TUDelft

Delft University of Technology

Unconventional Propeller–Airframe Integration for Transport Aircraft Configurations

van Arnhem, N.

Important note
To cite this publication, please use the final published version (if applicable).
Please check the document version above.

UNCONVENTIONAL PROPELLER–AIRFRAME INTEGRATION FOR TRANSPORT AIRCRAFT CONFIGURATIONS

UNCONVENTIONAL PROPELLER–AIRFRAME INTEGRATION FOR TRANSPORT AIRCRAFT CONFIGURATIONS

Dissertation

for the purpose of obtaining the degree of doctor
at Delft University of Technology,
by the authority of the Rector Magnificus prof.dr.ir. T.H.J.J. van der Hagen
Chair of the Board for Doctorates,
to be defended publicly on
Wednesday 16 March 2022 at 15:00 o'clock

by

Nando VAN ARNHEM

Master of Science in Aerospace Engineering,
Delft University of Technology, The Netherlands
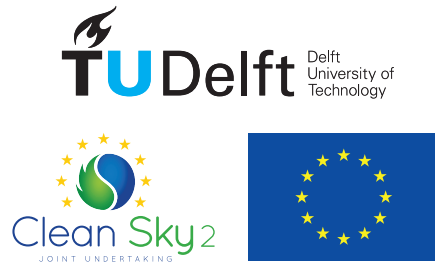
born in Amsterdam, The Netherlands

This dissertation has been approved by the promotor.

Composition of the doctoral committee:

Rector Magnificus	chairperson
Prof.dr.ir. L.L.M. Veldhuis	Delft University of Technology, *promotor*
Dr.ir. R. Vos	Delft University of Technology, *copromotor*

Independent members:

Prof.dr.ir. D. Casalino	Delft University of Technology
Prof.dr.ir. F.M. Catalano	University of São Paulo, Brazil
Dr.-ing. M. Hepperle	German Aerospace Center (DLR), Germany
Dipl.-ing D. Reckzeh	Airbus Operations GmbH, Germany
Prof.dr.-ing. E. Stumpf	RWTH Aachen University, Germany
Prof.dr.ir. F. Scarano	Delft University of Technology, *reserve member*

An electronic version of this dissertation is available at `http://repository.tudelft.nl/`.

SUMMARY

It is envisioned that the future generations of regional and short to medium-range aircraft employ a high level of propeller integration to achieve low-emission flight. The objectives of unconventional propeller installations include the enhancement of the airframe aerodynamic efficiency, increasing the propeller efficiency, improving cabin comfort, and improving the overall aircraft design by lower operating empty weight. Furthermore, by employing the aerodynamic interaction in specific phases of the flight, beneficial propulsion integration can also enable the use of alternative energy sources and increase the electrification level of the propulsion system.

The closer proximity of the propeller and airframe requires a more dedicated integral design (approach) of both the airframe and propulsion unit. The objective of this dissertation is *to characterize the role of the aerodynamic interaction between the propeller and the airframe on the performance and static stability characteristics for selected aircraft configurations which aim for a beneficial propeller–airframe interaction.* To this end, three different types of analyses are performed. First, fundamental phenomena are investigated which provide insight for related configurations and derivatives thereof. Second, a configuration study indicates the expected trends on various performance indicators. Finally, two detailed studies on aircraft level demonstrate the relative importance and the coupling between aerodynamic interactions.

The first configuration features propellers that are mounted to the horizontal tailplane. This is an example where there is a strong interaction between the propeller and airframe that affects performance, stability, and control, and contains various interaction mechanisms that are of interest for other configurations as well. A second specific case is the a distributed propulsion configuration with propellers mounted to the inboard part of the wing (in front of the high lift devices), together with a propeller mounted to the tip of the wing.

One of the focal points of the current study is extending the understanding of nonuniform inflow effects on propeller performance and its role in aircraft stability and trim. Compared to the conventional configuration, for various unconventional propeller installations, the nonuniform inflow to the propeller differs both in type and magnitude, and varies with flight condition. The slipstream shape and consequently its interaction with lifting surfaces are affected as well. These factors directly affect the gradients and offsets of the propeller force curves and therefore the aircraft stability and trim, respectively.

By employing CFD results, a study has been performed on the sensitivity of the radial load distribution to a change in inflow condition that is expressed as a change in local advance ratio. The constructed distributions provide insight into what region of the disk is responsible for the largest changes of the propeller forces. This has been demonstrated to be the region of highest loading. It is also shown that for a given propeller design, nonuniform inflow can be represented by an 'installation coefficient' κ such that the ef-

ficiency curve of this uninstalled propeller is scaled along the J and η_p directions by κ to obtain the installed propeller efficiency. Using the data of the isolated propeller for an arbitrary blade angle, the advance ratio at which the installed case has highest efficiency, as well as the value of the maximum efficiency, can be quantified immediately. The computational intensive analyses to find the optimum blade angle for the installed cases are therefore redundant and the formulation of the installation coefficient is therefore highly valuable to the aircraft designer. The installation coefficient also gives insight in what regime of the efficiency-advance-ratio curve the largest changes occur due to nonuniform inflow.

Since the impact of nonuniform inflow is a prominent factor on aircraft level and generally requires significant computational effort to characterize its impact on a single flight condition, an engineering method has been developed that predicts a time-resolved solution within several CPU seconds. The method relies on data either obtained from high-fidelity simulations, low-order models, or experiments. A validation of the method against full-blade CFD data and experimental data from four different cases demonstrates good agreement in both the prediction of the time-dependent solution and the time-averaged (integral) forces. Compared to relying on isolated performance data, this method allows for a better prediction of the performance of aircraft with tightly integrated propellers, as well as an estimation of the propeller contribution to the aircraft stability derivatives during the preliminary design phase.

The developed method allowed for the assessment of different propeller configurations, by varying the propeller location and diameter relative to an example full aircraft configuration. When the propeller is mounted ahead of the wing, the main installation effect is a change normal-force gradient compared to an isolated propeller and time-dependent loads. When the propeller is mounted behind the wing, the unsteady loads increase typically by a factor four compared to the tractor configuration. In line with other research, an over-the-wing installation especially leads to a reduction in effciency (highly dependent on chordwise location), significant unsteady loads, and a nonnegligible downforce. Analyses on propellers that are mounted in a side-by-side arrangement demonstrate a small reduction in efficiency, primarily caused by the presence of the nacelles. Unsteady loads are shown to be proportional to the thrust coefficient.

The impact of the propeller on lifting surfaces that are near or submerged in the slipstream has been investigated both on a fundamental level, as well as from an application level, by evaluating the impact on the two aircraft configurations. The fundamental study partially confirms the existing knowledge on the topic, while also new findings are presented for the time-averaged and time-dependent response of the lifting surface.

It is shown that the propeller installation especially leads to more suction on the leading edge, caused by the finite height of the slipstream relative to the chord length. When the propeller is operating and the angle of attack is increased, the experimental data shows that the normalized change in the pressure resembles the one of a propeller-off case. This result demonstrates that the propeller installation can be described by a change in lift curve slope. The propeller increases the effectiveness of the flap/elevator and is nearly inversely proportional with advance ratio. Also when a control surface/high-lift device is deflected, there is relatively more loading toward the leading edges of the main element and the control surface/high-lift device. The larger con-

tribution of the leading-edge is also observed by the kinetic energy deposition rate that is evaluated at a large number of stream-wise locations.

Three types of slipstream deformation have been identified that lead to vastly different unsteady loads on a lifting surface. The case where there is an alternating number of vortex pairs residing on the surface and in case there is a strong shear of the slipstream, the unsteady loads at a spanwise station are maximum. The local chord length relative to the pitch of the helical vortex is found to be the driving parameter to affect the unsteady loads. The largest unsteady loads can be expected on the inboard side of the lifting surface due to the higher lift-curve slope in this region compared to the tip region.

Several conclusions are presented on an aft-mounted propeller installation. Detailed analyses are presented on the installation effect on propeller efficiency, their contribution to trim and stability. It is shown that the rotation direction has a large impact on the propeller contribution to these aspects. Overall, mounting the propellers to the horizontal tailplane does not adversely affect the aircraft longitudinal static stability, which confirms the finding of previous studies. The neutral point shifts aft with increasing thrust coefficient, up to 5% of the mean aerodynamic chord for a thrust coefficient typical for climb/cruise with co-rotating propellers. At higher thrust settings, the neutral point shifts more aft. Exceptions to this are observed at high angles of attack.

At high angle-of-attack conditions, the flow separation from the wing–fuselage junction is shown to dominate the interaction for the aft-mounted propeller configuration. By evaluating the relative contributions of each force component, it was found that the propeller normal force is the dominant contribution to the pitching and yawing moment coefficient, next to the changes on the tailplane forces. Experimental data show that on aircraft level, the propeller installation leads to a nonlinear contribution to the pitching moment due to angle of attack (C_{m_α}) which depends rotation direction. The large variations of C_{m_α} start from the onset of the nonlinearity of the lift curve, because of the strong nonuniform inflow to the propeller. The slope of the pitching moment curve becomes up to 25% more negative for an outboard-up configuration, and up to 40% more negative for an inboard-up configuration. In addition, it is concluded that the propeller installation only has a minor impact on the offset and slope of the $C_n - \beta$ curve. The main installation effect is a higher/lower propeller side-force contribution, while the secondary effect is a lower effectiveness of the vertical tailplane. By means of microphones embedded in the fuselage outer surface, it is confirmed that nonuniform inflow also affects the unsteady pressures at the fuselage surface, that will directly translate to cabin noise. This is pronounced at high angle-of-attack conditions, but is even observable for the cruise condition. The current study displays that even for a suboptimal design, the beneficial propeller–airframe aerodynamic interaction could partially offset the drawbacks identified for the configuration. These benefits are present despite the fact that an aerodynamic performance benefit historically has not been the motivation for studying the configuration with propellers mounted to the horizontal tailplane.

For the study on the case with propellers mounted along the leading edge of a swept wing, the contributions of the propeller, wing, and the flowfield at the horizontal tailplane are quantified for longitudinal static stability and from a performance perspective. On average, the rotation direction "down between blades" has the smallest impact on the downwash angle at the horizontal tailplane relative to the propeller-off case.

Among other considerations such as unsteady loads, a slipstream impingement introduces rapid changes in the pitching moment curve with angle of attack. Therefore, it is recommended that the propellers and horizontal tailplane should be positioned such that the slipstream does not impinge on the horizontal tailplane. The main effect of the propeller installation is a more negative tail-off pitching moment and the slope of the tail-off moment curve becomes 5% more negative without significant difference between the rotation directions. It is demonstrated that the presence of the nacelle is the dominant factor of the installation when it comes to the slope of the pitching moment curve with angle of attack. Irrespective of the rotation direction of the inboard propellers, there is a net increase of the lift coefficient which is proportional to the thrust coefficient. The airframe lift-to-drag ratio increases between 5% to 8% depending on the reference drag and rotation direction. A design study on the tip propeller shows that the product $\eta_{\mathrm{p}} \frac{L}{D}$ remains approximately constant for a range of propeller radii. A smaller tip propeller may be advantageous in terms of weight since the torque of the motor is less (which in some cases is constraining the motor design).

The main two analyses methods that are employed are unsteady RANS simulations and a variety of experimental measurement techniques. Regarding the unsteady RANS simulations, the propeller performance for a cruise setting compares well with the experimental results, even when a relatively coarse mesh is used. Numerical diffusion is responsible for the large difference in vortex core radius and the associated velocity gradients, while the circulation of the tip vortex is nearly independent of the grid choice. However, for the computation of the integral forces of the lifting surface, the excessive numerical diffusion is not considered a major drawback of an unsteady RANS approach, as is demonstrated in several validation cases. Moreover, the results on a full aircraft configuration demonstrate that the CFD simulations are well suitable to predict the aircraft performance for the clean configuration. The estimated change in axial force component, i.e. the combined effect of propeller thrust variations and airframe drag, falls within 2% of the experimental result. The *change* in slope of the pitching moment curve is also predicted to differ up to 2% of the experimental result; nearly in the experimental uncertainty band. A comparison between two well-established models (the one-equation Spalart-Allmaras model and the two equation $\kappa - \omega$ shear stress transport model (SST) model) show significant difference in the flow structures. While the pressure distribution from the simulation using the Spalart-Allmaras model coincides with experiment, the $\kappa - \omega$ SST model greatly overpredicts the flow separation. The fact that two well-known models display such a significant difference highlights the importance of validation data.

Finally, recommendations for future work are presented. It is expected that future studies should especially focus on high lift conditions and design modifications that permits both high cruise and take-off/landing performance. For this, special attention needs to be paid to the nacelle installation, especially when a large number of nacelles are installed. Moreover, it is recommended that dedicated benchmark studies are published which accelerates further development of propeller-driven configurations.

SAMENVATTING

De verwachting is dat de toekomstige generaties van regionale vliegtuigen en vliegtuigen voor de korte tot middellange afstand gebruik zullen maken van een hoge mate van propeller-integratie om een vlucht met lage uitstoot te kunnen waarmaken. De intenties van onconventionele propellerinstallaties zijn onder meer de verbetering van de aerodynamische efficiëntie, de verhoging van de propeller efficiëntie, de verbetering van het cabinecomfort, en een verbetering van het algehele ontwerp van het vliegtuig door een lager leeggewicht. Verder, door gebruik te maken van de aerodynamische interactie in specifieke fasen van de vlucht, kan de installatie van propellers ook het gebruik van alternatieve energiebronnen mogelijk maken, net als een verdere verhoging van de mate van elektrificatie van het voortstuwingssysteem.

De nauwere nabijheid van de propeller en het vliegtuig vereist dat bij het ontwerpen van het vliegtuig en het voortstuwingssysteem meer kruisbestuiving is. Het doel van dit proefschrift is om de rol van de aerodynamische interactie tussen de propeller en het vliegtuig verder te karakteriseren met een focus op de prestatie en statische stabiliteits kenmerken voor een geselecteerd aantal vliegtuigconfiguraties. Deze specifieke configuraties hebben allen het oogmerk op een gunstige interactie tussen propeller en vliegtuig. Om dit doel te dienen, worden drie verschillende soorten analyses uitgevoerd. Ten eerste, fundamentele verschijnselen worden onderzocht die inzicht geven in de specifieke vliegtuigconfiguraties en afgeleiden daarvan. Ten tweede geeft een configuratieonderzoek de verwachte trends van verschillende prestatie-indicatoren aan. Tot slot tonen twee gedetailleerde studies op vliegtuigniveau het relatieve belang en de koppeling tussen aerodynamische interacties.

De eerste configuratie heeft propellers die aan het horizontale staartvlak zijn gemonteerd. Dit is een voorbeeld waarbij er een sterke interactie is tussen de propeller en het vliegtuig die de prestaties, stabiliteit en bestuurbaarheid beïnvloedt, en bevat verschillende interactie mechanismen die ook interessant zijn voor andere configuraties. Een tweede specifiek geval is een vliegtuig met verdeelde voortstuwing waarbij propellers gemonteerd zijn aan de voorrand van de vleugel, samen met een propeller gemonteerd op de vleugeltip.

Een van de aandachtspunten van de huidige studie is het uitbreiden van het begrip van niet-uniforme aanstroomeffecten op de prestaties van de propeller en de rol hiervan op de stabiliteit en trim van vliegtuigen. In vergelijking met de conventionele configuratie, hebben verschillende onconventionele propellerinstallaties een niet-uniforme aanstroming naar de propeller die verschilt in zowel het type als in de mate waarin deze niet uniform is. Deze aanstroming is tevens afhankelijk van de vliegconditie. De vorm van de slipstream en de interactie met de kleppen worden ook beïnvloed. Deze factoren hebben direct invloed op de hellingen en verschuiving van de momentcurves, en dus op de stabiliteit respectievelijk trim van het vliegtuig.

Door gebruik te maken van CFD-resultaten is er onderzoek gedaan naar de gevoeligheid van de radiale verdeling van de belasting op een propeller blad naar een verandering in aanstromingsconditie die wordt uitgedrukt als een verandering in lokale 'advance ratio'. De geconstrueerde distributies geven inzicht welk deel van de propeller schijf verantwoordelijk is voor de grootste veranderingen van de propellerkrachten. Dit bleek het gebied met de hoogste belasting te zijn. Verder wordt er aangetoond dat voor een bepaald propellerontwerp, een niet-uniforme aanstroming kan worden weergegeven door een zogenaamde 'installatiecoëfficiënt', zodanig dat de efficiëntiecurve van deze niet-geïnstalleerde propeller wordt geschaald langs de advance ratio en efficiëntie richtingen door deze installatiecoëfficiënt, om uiteindelijk de efficiëntiecurve van de geïnstalleerde propeller te verkrijgen. Op deze manier kunnen, gebruikmakende van de karakteristieken van de geïsoleerde propeller met een willekeurige bladhoek, de advance ratio waarbij de geïnstalleerde propeller de hoogste efficiëntie bereikt evenals de waarde van deze maximale efficiëntie, onmiddellijk gekwantificeerd worden. De rekenintensive analyses om de optimale bladhoek voor de geïnstalleerde propellers te vinden zijn daarom overbodig, en de formulering van de installatiecoëfficiënt is daarom zeer waardevol voor een vliegtuigontwerper. De installatiecoëfficiënt geeft ook inzicht in welk regime van de efficiency-advance-ratio curve de grootste veranderingen optreden als gevolg van een niet-uniforme aanstroming.

Aangezien het is aangetoond dat de impact van niet-uniforme aanstroming naar de propellers een prominente factor is op vliegtuig-niveau en het een aanzienlijke rekeninspanning vereist om de impact ervan te karakteriseren op zelfs een enkele vluchtconditie, is een versimpelde 'engineering method' ontwikkeld die een tijdsafhankelijk oplossing vindt binnen enkele CPU-seconden. De methode maakt gebruik van data die verkregen zijn van hoge-orde simulaties, van lage-orde modellen, of van experimenten. Een validatie van de methode waarbij een combinatie van CFD data van 'full-blade' simulaties en experimentele verkregen data van vier verschillende casussen, toont een goede overeenkomst in zowel de voorspelling van de tijdsafhankelijke oplossing en de tijdsgemiddelde (integrale) krachten. In vergelijk met het gebruik van karakteristieken van een geïsoleerde propeller levert deze methode een betere voorspelling van de prestaties van vliegtuigen, met name als de propellers dichtbij het vliegtuig zijn geinstalleerd. Eveneens kan een goede schatting worden gemaakt tijdens de voorontwerpfase van de propeller bijdrage aan de stabiliteitsafgeleiden.

De ontwikkelde methode is gebruikt om verschillende propellerconfiguraties te vergelijken door de propellerlocatie en diameter te variëren ten opzichte van een referentie vliegtuiggeometrie. Wanneer de propeller vóór de vleugel is gemonteerd, is het voornaamste installatie-effect een verandering normaalkrachtgradiënt in vergelijking met een geïsoleerde propeller, en tevens wordt de belasting op de propeller tijdsafhankelijk. Wanneer de propeller achter de vleugel is gemonteerd, nemen de tijdsafhankelijke belastingen typisch met een factor vier toe in vergelijking met de tractorconfiguratie. In lijn met ander onderzoek leidt vooral een installatie met propellers boven de vleugel tot een vermindering van de efficiëntie (alhoewel de afname sterk afhankelijk is van de locatie langs de koorde), aanzienlijke tijdsafhankelijke belastingen, en een niet te verwaarlozen neerwaartse kracht. Analyses op propellers die naast elkaar zijn gemonteerd tonen een kleine vermindering van de efficiëntie, voornamelijk veroorzaakt door de aanwezigheid

van de gondels. In deze gevallen blijkt de tijdsafhankelijke belastingen evenredig te zijn met de stuwkrachtcoëfficiënt.

Voor propellers die aan het horizontale staartvlak zijn gemonteerd, worden gedetailleerde analyses gepresenteerd over het installatie-effect op de propellerefficiëntie en de bijdrage van de propellers aan trim en stabiliteit. Het blijkt dat de draairichting een grote invloed heeft op de propeller bijdrage aan deze aspecten. Deze worden veroorzaakt door het complexe stromingsveld ter hoogte van de propeller, zelfs bij een lage aanvalshoek. Bij hoge aanvalshoeken blijkt de stroming die loskomt van de vleugel-romp overgang de interactie te domineren. Door middel van microfoons ingebouwd in de romp wordt er bevestigd dat niet-uniforme aanstroming ook invloed heeft op de tijdsafhankelijke druk op het oppervlak van de romp, die zich direct zal vertalen tot extra cabinegeluid. Dit wordt versterkt bij een hoge aanvalshoek, maar is ook waarneembaar voor de kruisconditie.

De impact van de propeller op draagvlakken die zich dichtbij of in een slipstroom bevinden is zowel op fundamenteel niveau als vanuit de toepassing onderzocht, door de twee vliegtuigconfiguraties te evalueren. De fundamentele studies bevestigen gedeeltelijk de bestaande kennis over het onderwerp, terwijl ook nieuwe bevindingen zijn gepresenteerd voor de tijdsgemiddelde en tijdsafhankelijke belasting op de draagvlakken.

Het blijkt dat de propellerinstallatie vooral leidt tot meer zuigkracht op de voorrand van een draagvlak, als gevolg van een eindige hoogte van de slipstroom ten opzichte van de lengte van de koorde. Wanneer de propeller draait en de invalshoek wordt vergroot, laten de experimentele gegevens zien dat de genormaliseerde verandering in de druk vrijwel hetzelfde is als het geval dat de propeller niet gemonteerd is. Dit resultaat toont aan dat de propellerinstallatie kan worden gevat in een verandering van de helling van de liftcurve. Verder verhoogt de propeller de effectiviteit van het draagvlak, die bijna omgekeerd evenredig is met de advance ratio. Ook wanneer een stuurvlak of een klep wordt uitgeslagen is er relatief meer belasting op de voorranden van het hoofdelement en het stuurvlak of de klep. De grotere bijdrage van de voorrand wordt ook waargenomen door de kinetische energie-depositie die wordt geëvalueerd op een aantal locaties in stromingsrichting.

Er worden verschillende conclusies gepresenteerd over een staart-gemonteerde propellerinstallatie. Voor de meerderheid van de vluchtomstandigheden heeft een dergelijke installatie geen nadelige invloed op de langsstabiliteit van het vliegtuig, wat de bevinding van eerdere studies bevestigt. Het neutrale punt verschuift naar achteren met toenemende stuwkrachtcoëfficiënt, tot 5% van de gemiddelde aerodynamische koorde voor een stuwkrachtcoëfficiënt die typisch is voor klim- of kruiscondities voor propellers die dezelfde draairichting hebben. Bij hogere stuwkrachtcoëfficiënten verschuift het neutrale punt meer naar achteren. Uitzonderingen hierop worden waargenomen bij hogere invalshoeken. De relatieve bijdragen van elke krachtcomponent laten zien dat de propellernormaalkracht de dominante factor is, naast de bijdragen van de krachten die werken op de staartvlak. Experimentele data laten zien dat op vliegtuigniveau de propellerinstallatie tot een niet-lineaire bijdrage aan de verandering van het duikmoment met de invalshoek, die afhangt van de rotatie richting. De grote variaties hierop beginnen vanaf het het begin van het niet-lineaire gedeelte van de liftcurve vanwege de sterke niet-uniforme aanstroming naar de propeller. De helling van de duikmoment-

curve wordt tot 25% negatiever voor een 'outboard-up' configuratie, en tot 40% negatiever voor een draairichting die 'inboard-up' is. Daarnaast wordt er geconcludeerd dat de propellerinstallatie slechts een kleine impact heeft op de helling en verschuiving van de giermomentcurve. Het belangrijkste installatie-effect is een hogere of lagere zijwaartse kracht op de propeller, terwijl een lagere effectiviteit van het verticale staartvlak een secundaire effect is. De huidige studie toont aan dat zelfs voor een suboptimaal ontwerp, de gunstige propeller–aerodynamische interactie met het vliegtuig gedeeltelijk de nadelen die zijn vastgesteld voor de configuratie compenseren. Deze voordelen zijn aanwezig ondanks het feit dat aerodynamische prestaties historisch niet de motivatie zijn geweest om de configuratie waarbij propellers gemonteerd op het horizontale staartvlak te bestuderen.

Voor de studie van het geval waarbij propellers gemonteerd zijn aan de voorrand van een gepijlde vleugel worden de bijdragen van de propeller, de vleugel, en het stromingsveld bij het horizontale staartvlak gekwantificeerd om de installatie-effecten op de langsstabiliteit en prestatie te bepalen. Op de tijdsgemiddelde belasting heeft de draairichting 'down-between-blades' de minste impact op het binnenste gedeelte van het horizontale staartvlak ten opzichte van situatie zonder propellers. Naast andere overwegingen, zoals de tijdsafhankelijke belastingen, introduceert een slipstream een snelle verandering in de duikmomentscurve met invalshoek. Daarom is het aan te raden om de propellers en het horizontale staartvlak zo te plaatsen dat de slipstream het horizontale staartvlak niet raakt. Het belangrijkste effect van de propeller installatie is een meer negatief duikmoment zonder het horizontale staartvlak, waarbij de helling van deze momentcurve 5% negatiever wordt zonder significant verschil tussen de rotatierichtingen. De aanwezigheid van de gondels is de dominante factor als het gaat om de helling van de duikmomentcurve. Ongeacht de draairichting van de binnenste propellers is er een toename van de liftcoëfficiënt die evenredig is met de stuwkrachtcoëfficiënt. De lift-over-weerstandsverhouding van het vliegtuig neemt tussen 5% en 8% toe, afhankelijk van de referentieweerstand en draairichting van de propellers. Een ontwerpstudie van de propeller die gemonteerd is op de tip van de vleugel toont aan dat het product van de propellerefficiëntie en de lift-over-weerstandsverhouding ongeveer constant blijft voor een redelijk groot bereik van propeller diameters. Een kleinere op de vleugeltip gemonteerde propeller kan voordelig zijn qua gewicht, aangezien het benodigde koppel van de motor lager is (wat in sommige gevallen de beperkende factor is het motorontwerp).

De twee belangrijkste analysemethoden die worden gebruikt, zijn tijdsafhankelijke RANS-simulaties en een verscheidenheid aan experimentele meettechnieken. Wat betreft de tijdsafhankelijke RANS simulaties blijkt dat al met een relatief grof grid de propellerprestaties voor een kruisconditie goed overeenkomen met de experimentele resultaten. Numerieke diffusie is verantwoordelijk voor het grote verschil in straal van de tipwervel en de bijbehorende snelheidsgradiënten, terwijl de circulatie van de tipwervel bijna onafhankelijk is van de keuze van het grid. Echter, voor de berekening van de integrale krachten van een dragend vlak is deze numerieke diffusie niet een dusdanig nadeel van de tijdsafhankelijke RANS-benadering, zoals is aangetoond in verschillende validatiecasussen. Bovendien tonen de resultaten op een volledige vliegtuigconfiguratie aan dat de CFD-simulaties goed geschikt zijn om de vliegtuigprestaties te voorspellen voor de kruiscondities. De geschatte verandering in axiale krachtcomponent, d.w.z. het

gecombineerde effect van propeller stuwkracht variaties en de weerstand van het vliegtuig, valt binnen 2% van de experimentele resultaat. De verandering in helling van de duikmomentcurve wordt ook goed voorspeld met verschillen oplopende tot 2% van het experimentele resultaat, en valt bijna binnen de experimentele onzekerheid. Een vergelijking tussen twee gevestigde turbulentie-modellen (het Spalart-Allmaras model en het κ-ω shear stress transport model (SST)) tonen een significant verschil in de voorspelling van loslating. Terwijl de drukverdeling van de simulatie met het Spalart-Allmaras model vrijwel op de experimentele drukverdeling valt, overschat κ-ω SST-model de loslating aanzienlijk. Het feit dat twee bekende modellen zo'n significant verschil laten zien benadrukt het belang van beschikbare validatiedata.

Tot slot worden aanbevelingen gepresenteerd voor toekomstig onderzoek. Naar verwachting zullen toekomstige studies zich vooral richten op vliegcondities waarbij kleppen worden uitgeslagen om een hoge lift te genereren, en zullen zich ook richten op ontwerpaanpassingen die tot goede prestaties leiden voor zowel de kruisconditie als in de start- en landingsfases. Hiervoor zal met name goed gekeken moeten worden naar de bevestiging van de gondels, vooral wanneer er een groot aantal gondels worden gemonteerd aan de vleugel. Bovendien moeten specifieke referentiedata worden gepubliceerd die de verdere ontwikkeling van propeller-aangedreven configuraties zullen ondersteunen.

CONTENTS

NOMENCLATURE

VARIABLES

a	=	speed of sound [m/s], induction factor [-]
$\mathcal{R}$	=	aspect ratio, b^2/S[-]
b	=	span [m]
B	=	number of blades [-]
BPF	=	blade-passing frequency, nB [Hz]
$c, \bar{c}$	=	chord, mean aerodynamic chord [m]
c_d	=	section drag coefficient, $\frac{d}{q_\infty c}$ [-]
c_l	=	section lift coefficient, $\frac{l}{q_\infty c}$ [-]
c_n	=	section normal-force coefficient, $\frac{n}{q_\infty c}$ [-]
C	=	Theodorsen's function
C_D	=	drag coefficient, $\frac{D}{q_\infty S_{\mathrm{w}}}$ [-]
C_L	=	lift coefficient, $\frac{L}{q_\infty S_{\mathrm{w}}}$ [-]
C_m	=	pitching-moment coefficient, $\frac{m}{q_\infty S_{\mathrm{w}} \bar{c}}$ [-]
C_{m_α}	=	gradient of pitching-moment coefficient with angle of attack [deg^{-1}]
$C_{m_{\delta_{\mathrm{e}}}}$	=	gradient of pitching-moment coefficient with elevator deflection [deg^{-1}]
C_n	=	yawing-moment coefficient, $\frac{n}{q_\infty S_{\mathrm{w}} \bar{c}}$ [-]
C_{n_β}	=	gradient of yawing-moment coefficient with angle of side slip [deg^{-1}]
C_N	=	normal-force coefficient, $\frac{F_N}{q_\infty S_{\mathrm{w}}}$ [-]
$C_{N_{\mathrm{p}}}$	=	propeller normal-force coefficient, $\frac{F_{N_{\mathrm{p}}}}{\rho_\infty n^2 D_{\mathrm{p}}^4}$ [-]
C_p	=	specific heat [J/(kg K)]
$C_{p_{\mathrm{s}}}$	=	static-pressure coefficient, $\frac{p-p_\infty}{q_\infty}$ [-]
$C_{p_{\mathrm{t}}}$	=	total-pressure coefficient, $\frac{p_{\mathrm{t}}-\bar{p}_{\mathrm{t\infty}}}{q_\infty}+1$ [-]
$C_{p,1}$	=	pressure coefficient in condition 1 [-]
$\Delta C_{p,12}$	=	difference in pressure coefficient beween condition 2 and 1 [-]
C_P	=	power coefficient $\frac{P_{\mathrm{s}}}{\rho_\infty n^3 D_{\mathrm{p}}^5}$ [-]
C_Q	=	torque coefficient $\frac{Q}{\rho_\infty n^2 D_{\mathrm{p}}^5}$ [-]
C_T	=	thrust coefficient, $\frac{T}{\rho_\infty n^2 D_{\mathrm{p}}^4}$ [-]
C_{T_β}	=	gradient of thrust coefficient with angle of side slip [deg^{-1}]
C_X	=	axial-force coefficient, $\frac{F_x}{q_\infty S_{\mathrm{w}}}$ [-]
C_Y	=	side-force coefficient, $\frac{F_Y}{q_\infty S_{\mathrm{w}}}$ [-]
$C_{Y_{\mathrm{p}}}$	=	propeller side-force coefficient, $\frac{F_{Y_{\mathrm{p}}}}{\rho_\infty n^2 D_{\mathrm{p}}^4}$ [-]

d	=	section drag [Nm^{-1}]
dT	=	local thrust [Nm^{-1}]
D	=	diameter [m] drag [N]
E_v	=	cross-flow kinetic energy [Pa]
$\dot{E}_v$	=	cross-flow kinetic energy deposition rate [Watt]
F	=	force [N]
F_N	=	normal force [N]
h_i	=	average cell size of grid i, [m]
J	=	advance ratio, $\frac{V_\infty}{nD_p}$ [-]
J_0, J_1	=	zeroth- and first-order Bessel functions of the first kind
k	=	wave number [m^{-1}]
k_T	=	thermal conductivity [W/(m K)]
K_0, K_1	=	modified zeroth- and first-order Bessel functions of the second kind
l	=	sectional lift force [N/m], length of a moment arm [m]
L	=	lift force [N], length [m]
m	=	pitching moment [Nm], molecular weight [kg/kmol]
M	=	Mach number [-]
n	=	rotational speed [s^{-1}], yawing moment [Nm]
N_{C_p}	=	propeller normal-force coefficient, $\frac{F_{N_p}}{q_\infty S_p}$ [-]
p	=	pressure [Pa], observed order of accuracy [-]
P_s	=	shaft power [W]
q	=	dynamic pressure [Pa]
Q	=	torque [Nm]
Q_C	=	torque coefficient, $\frac{Q}{q_\infty S_p D_p}$ [-]
r	=	radial coordinate [m]
R	=	radius [m]
Re_c	=	Reynolds number based on chord [-]
S	=	area [m^2], effective temperature [K], Sears function [-]
t	=	thickness [m]
T	=	thrust(along propeller rotation axis) [N], temperature [K]
T_C	=	thrust coefficient, $\frac{T}{q_\infty S_p}$ [-]
$T_{C,x}$	=	thrust coefficient along x-axis, $\frac{F_{x_p}}{q_\infty S_p}$ [-]
T_0	=	reference temperature [K]
u, v, w	=	velocity in Cartesian system [ms^{-1}]
U_s	=	standard deviation based on observed order
U_ϕ	=	estimated discretization uncertainty
V	=	velocity [ms^{-1}]
W	=	weighting function [-]
x, y, z	=	aircraft coordinate system [m]
X, Y, Z	=	propeller coordinate system [m]
y^+	=	dimensionless wall distance [-]
Y_{C_p}	=	propeller side-force coefficient, $\frac{F_{Y_p}}{q_\infty S_p}$ [-]

α	=	angle of attack [deg]
β	=	angle of sideslip [deg], blade pitch [deg]
γ	=	reference specific heat ratio [-]
Γ	=	circulation [m^{2}s^{-1}]
δ	=	deflection angle [deg]
ε	=	downwash angle [deg]
ϵ	=	tip clearance [-]
ζ	=	compressibility factor, $\sqrt{1-M^2}$
η_p	=	propeller efficiency, $\frac{TV_\infty}{P_\mathrm{s}}$ [-]
η_x	=	propeller efficiency in x-direction, $\frac{F_{xp}V_\infty}{P_\mathrm{s}}$ [-]
θ	=	phase angle [deg]
κ	=	installation coefficient [-]
μ_0	=	reference viscosity [kg/(m s)]
ξ	=	local coordinate, $\frac{x'}{c}$ [-]
ρ	=	density [kgm^{-3}]
σ	=	shear stress [N/m^2], sidewash angle [deg], solidity [-], reduced frequency, $\frac{knc}{4\pi V}$ [-]
ϕ	=	swirl angle [deg]
ω	=	vorticity [s^{-1}]
$\widetilde{\omega}$	=	normalized vorticity, $\frac{\omega \bar{c}}{V_\infty}$ [-]
ω^*	=	normalized vorticity, $\frac{\omega D_\mathrm{p}}{V_\mathrm{eff}}$ [-]
Ω	=	rotational speed [rad/s]

SUB- AND SUPERSCRIPTS

a	=	axial
ac	=	aircraft
af	=	airframe
b	=	bound, body
B	=	value related to blade
cfd	=	value from CFD
d	=	deflection
e	=	elevator
eff	=	effective
est	=	estimated
exp	=	value from experiment
f	=	flap
fus	=	fuselage
ht	=	horizontal tailplane
hel	=	helical
i	=	induced
ins	=	installed
iso	=	isolated
nac	=	nacelle

np	=	neutral point
off	=	propeller off
on	=	propeller on
opt	=	optimal
pp	=	propulsive
qs	=	quasi-steady
r	=	radial
ref	=	reference
s	=	static
ss	=	slipstream
t	=	tangential, total
tip	=	value related to tip
us	=	unsteady
v	=	vertical tailplane
wa	=	wake
wt	=	wind tunnel
x, y, z	=	Cartesian components
∞	=	freestream value
1,2,i	=	station 1, station 2, station i
I,II,...	=	indicators of trailing vortices along the span
$0.7R_\mathrm{p}$	=	related to radial station at $r/R_\mathrm{p} = 0.7$
$'$	=	local value
*	=	based on theoretical order of convergence

ABBREVIATIONS

CFD	=	computational fluid dynamics
CO	=	co-rotating
IU	=	inboard-up rotating
OU	=	outboard-up rotating
RANS	=	Reynolds-averaged Navier-Stokes
SPL	=	sound-pressure level

1

INTRODUCTION

With a growing worldwide population and improving average living standards, the impact of human activity on global warming has been increasing since 1800, coinciding with the beginning of the Industrial Revolution. Nowadays, the public awareness is raising that both technological advancements and human behaviour need to be adapted in order to facilitate a sustainable growth. Limiting the rapidly depletion of natural resources and reducing the emission of greenhouse gasses to halt further global warming cannot be done without systematic changes.

Transportation of people and goods is estimated to contribute around 24% of the total worldwide emissions of carbon dioxide from human activity [1]. About 2% is emitted by the aviation sector [2]. Besides the emission of carbon dioxide, the impact of aviation on global warming is higher (approximately 3.5%), if the effects of contrail formation and emissions of NO_x are also accounted for. With the exception of the worldwide pandemic in the years 2020 and 2021 that disrupted the aviation industry [3], both passenger numbers and passenger-kilometers have been increasing nearly every year since the introduction of commercial aviation, and are expected to rise with 4 to 5% per year throughout the year 2050 [4, 5]. While road transport is the fastest growing transportation sector [1], the implementation of technologies for more sustainable land-based transportation is accelerating. Therefore, the relative share of aviation in terms of environmental impact compared to other means of transportation is likely to increase with current operations [6], and with that, also the societal pressure to lower the environmental impact will rise. To guarantee that air transport remains a viable means of transportation for the general public for the coming decades, major advancements to the aircraft system are necessary.

As aviation is highly integrated in the world economy and in society, it also means that developments should not merely aim at reducing environmental impact, but they also need to comply with sustainability in a broader perspective. Ideally, current standards in terms of safety, comfort, financial cost, and availability should be met to at least comparable extent. As some of these aspects may hamper progress to lower environmental impact by aviation, the importance of these factors relative to reducing the environmental impact is a trade-off that society has to make. Provided that the European

Commission has announced the European Green Deal [7] to move forward, the environmental impact has a heavy weighting factor in this trade-off.

There are different areas of the aviation sector that have potential to be improved to reduce environmental impact [8, 9]. These include policies (e.g. refinement of environmental standards), (flight) operations, infrastructure, the transition to alternative fuels, and aircraft technologies. Even though most of the improvements could be implemented independently, the implementation of one can also enable another. For example, if (future) airports would allocate more space at the gates, aircraft with a larger span and therefore higher aerodynamic efficiency could enter service. If the airlines and routes would allow for more flexibility in terms of cruise Mach number, aircraft could be designed to fly at a Mach number that is most efficient for the configuration and mission [10]. If flight at a lower Mach number is beneficial for the fuel burn for a certain mission, the positive side effect is this flight is conducted at lower altitude and therefore contrail formation is reduced [10].

The current share of fuel cost relative to cash operating cost ranges between 30% to 45% for short to medium-range missions [8]. A significant reduction of 15% of fuel burn would therefore lead to only 5% lower cost for the airline. This may not be sufficient for an airline to invest in fleet renewal and leaves little room for the aircraft manufacturer to make significant investments in radical designs. If fuel consumption would be a more prominent factor over cost and flexibility for airlines, aircraft would be selected that are better suitable for a particular mission. Stepping away from the current top level requirements and today's standards may be inevitable to open the door for aircraft designs and propulsion systems that are more tailored for a particular mission [8].

Although improvements in operations can be made, the transition to alternative fuels and energy sources onboard the aircraft is inevitable to reach major reductions in environmental impact. Research on synthetic kerosene, fuel-cells, liquid hydrogen, and batteries is ongoing and will accelerate in the coming decades [11]. The implementation of these energy sources will depend on how successful the mitigation of certain drawbacks on aircraft and infrastructure level will be.

The first step within reach that could enable the implementation of radical new energy sources, is therefore to implement a highly efficient propulsion system and improve airframe designs. By integration of a propulsion system, that in itself is highly efficient, with the airframe, synergistic advantages can be employed [12]. The challenges that arise in the integration of such efficient propulsion systems with the airframe need to be tackled to enable further development of energy-efficient transport aircraft configurations for the future. This dissertation aims to address aspects of several of these challenges.

1.1. Efficient Aeropropulsion Systems

The main purpose of an *aeropropulsion system* for an aircraft, i.e. a *propulsor* coupled to a *motor*, is to provide thrust. This force is used to overcome aerodynamic drag, to accelerate the aircraft, and to gain altitude. Historically, the energy source has been a hydrocarbon-based fuel and the motor a reciprocating piston engine until the introduction of the gasturbine. Since the first powered flight conducted in 1903 by the Wright brothers, the propulsor in most cases has been a rotor. A ducted rotor is often referred to as a 'fan', while modern versions of an unducted propulsor are sometimes called 'open

1

rotor' or 'propfan' [13], and are typically driven by gasturbines. Because of the lack of fundamental differences for the propulsor, hereinafter the unducted propulsor is simply referred to as a 'propeller'.

The useful work that is performed on the flow that passes through the propulsor, i.e. the thrust multiplied by the flight speed ('thrust power'), requires power that has to be provided by the motor. The ratio of this useful thrust power to the power that is provided to the slipstream, is called the *propulsive efficiency* [14], and is a measure in how efficient a propulsor is in producing thrust. This efficiency depends on the relative increase in axial velocity through the propulsor, or alternatively, the pressure rise over the propulsor. A high propulsive efficiency can be obtained if the velocity rise is small. Therefore, to produce a certain thrust, a large disk area of the propulsor is beneficial from a propulsive efficiency point of view.

In order to achieve large disk areas, the bypass ratio of turbofan engines has been increasing over the past decades [15], leading to large nacelles. The nacelle has a profound effect on the performance of the propulsion system. For example, at low speed, the suction on the nacelle lip can lead to a thrust force that is over 50% of the thrust produced by the fan [16]. For a given fan diameter, the reduced tip-losses allow for a higher maximum thrust compared to propellers. Cruise at higher Mach numbers can be achieved because of lower compressibility losses from a carefully designed distribution of the duct area. The duct also shields noise, can house thrust reversers, and provides shielding in case of an in-flight blade failure.

Being the engine of choice in the last decades, research and development on turbofans has led to significant progress in terms of the gas turbine, the introduction of gearboxes, and lightweight composite fan blades. Today's state-of-the-art turbofans have bypass ratios between 10 to 12, a fan pressure ratio between 1.5 and 1.7, and propulsive efficiencies around 0.7 at Mach 0.8 [15]. Despite various developments on ultra-high bypass ratio turbofans with contra-rotating fans, the drag of large nacelles adversely affects the performance of the propulsion system and is a clear drawback of turbofans. The gain in net propulsive efficiency of turbofans with bypass ratios over 15 to 20 would be offset by the added nacelle drag and weight, and can therefore not be increased substantially from today's values [15, 17]. Instead, large propellers can be chosen, such that low pressure ratios around 1.1 can be achieved by the propulsor to realize propulsive efficiency gains of 10 to 15% compared to state-of-the art turbofans [18].

Research has not been limited to turbofans, as in particularly the increase of fuel prices around 1973 was a motivation to direct research programs to increase the fuel efficiency of transport aircraft. The high performance of unducted propellers compared to the ducted counterpart led to the development of an advanced turboprop concept known as the 'propfan', and was a focus point of research for about 15 years. Through a number of research programs initiated by NASA and conducted by both industry partners and research institutes, several areas of improvement were investigated to arrive at a complete propulsion system that could be installed on a passenger transport aircraft flying at high-subsonic Mach numbers. At these high Mach numbers, the propeller tip is supersonic, with typical values of the helical tip Mach number range from 1.1 during take-off up to 1.4 during cruise at Mach 0.8. These conditions were found to be detrimental to the propeller efficiency caused by compressibility losses. Both cabin noise

and community noise levels would be unacceptable if no adjustments were made to the propeller design. These included new airfoil designs, high solidity, modifications to spinner and nacelle, and blade sweep. These finding can be found in today's state-of-the-art turboprop, of which an example is shown in Fig. 1.1a. Thanks to a variable pitch, the propellers can achieve high efficiency for a large range of operating conditions, as the propeller can operate at its most efficient advance ratio*. This is reflected as improved climb performance for the turboprop aircraft [19], which is advantageous for airports in rural areas as community noise can be reduced. The use of variable blade pitch is also used as thrust reverser without the additional complexity that is otherwise required for turbofan engines.

(a) Variable pitch propellers of the Airbus A400M. Copyright: Airbus. (b) SAFRAN counter-rotating open-rotor test setup. Copyright: Safran No. SSAF04568.

Figure 1.1: State-of-the-art propeller propulsion systems.

During the investigations into the single-rotating propeller, the contra-rotating open-rotor became of interest because for its performance at high Mach numbers. In Ref. [20] it is predicted that at $M = 0.8$ a 7.5% higher propulsive efficiency can be obtained compared to the single-rotating propeller, in particular due to lower swirl losses. For a given fan diameter, this concept also achieves higher thrust than a single-rotating propeller, which can be beneficial if the disk diameter is constrained by the minimal ground clearance. Recently, the counter-rotating propeller propulsion concept was revisited in a CleanSky project and successful ground tests were performed (see Fig. 1.1b). Although such design is technically feasible, it was found that the disadvantages in terms of complexity and reliability are clear drawbacks compared to a single-rotating propeller [18].

The operational limitations for the single-rotating propeller are primarily related to the maximum flight Mach number. For the short to medium-range mission, a reduction of flight Mach number from the typical Mach 0.8 up to 0.6 to 0.7 would have a marginal effect on block time as the cruise phase is relatively short. Additionally, the consequence is that cruise should take place at lower altitude to fly at the optimal lift-to-drag ratio, which is therefore achieved relatively quickly. On average, a high propulsive efficiency is

---

*The advance ratio is the ratio of the flight speed relative to the tip speed

obtained over the whole mission as the propellers also have high efficiency during take-off and climb phases. For a typical 500 nautical mile mission, nearly half of the fuel is used in the take-off and climb phase [15], and a higher efficiency in this phase would reduce the block fuel significantly. For example, several studies in the 1980s estimated block fuel savings up to 20 percent can be realized compared to technology-equivalent turbofans for missions that are climb and approach dominated [13, 21–23]. Flights of medium-range (1,000-2,000 nautical miles) with design cruise Mach numbers between 0.7 to 0.8 are predicted to achieve fuel savings of 10 to 20 percent [13, 23, 24]. Therefore, the most suitable missions for propeller propulsion is short to medium range [15, 18, 21, 25–32].

Various roadmaps, for example Refs. [9, 11], have been constructed and supported by industry, universities, and research institutes which outline potential pathways to more sustainable aviation. Although each roadmap project had different time-lines and views on the role of certain energy sources, there is common ground that propeller propulsion is one of the fundamental building blocks for the energy-efficient aircraft of the future for short to medium range missions.

1.2. Opportunities and Challenges of Propeller Integration

As the propulsion system is mounted to the airframe, the flowfield of the propulsor locally influences the aerodynamic forces on the airframe. In its turn, the airframe changes the flowfield that is experienced by the propulsor. This *aerodynamic interaction* between the propulsor and airframe exists for any aircraft to a certain extent. Already the early days of aviation, for example in 1920 in Ref. [33], it was identified that by careful placement of the propulsion system relative to the airframe, in particularly close to the lifting surfaces and drag producing bodies, that the efficiency of the propulsor and airframe theoretically could be increased relative to their performance in isolated conditions. Around that time, it was realized that the propulsor and airframe should not be treated as individual components but instead their interaction should be taken into account to determine their combined performance. The careful installation of the propeller in such way that it leads to a performance benefit, is referred to as *beneficial propeller integration.*

1.2.1. Improved Airframe Performance

Today's state-of-the-art passenger and military transport aircraft have tractor propellers mounted to the wing, e.g. the ATR-72, Bombardier Q400 and Airbus A400M. Throughout history various other propeller configurations were selected. The choice for a particular propeller location relative to the airframe was be motivated by several design criteria [25], for example structural rigidity of the engine mounting, aircraft weight and balance, ground clearance constraints, and considerations for operation such as accessibility for maintenance. The choice for the type and number of engines was also constrained by the availability of power plants [34]. With a few exceptions, propellers that were mounted to the wing leading edge became mainstream since the introduction of the Douglas DC-1 in 1933.

The awareness of potential benefits of propeller installation on component level has recently led to the appearance of a wide range of alternative aircraft configurations with the objective of higher propeller efficiency or higher airframe efficiency. The performance benefit could be a direct result from propeller integration, e.g. a lower induced drag in cruise could lead to lower block fuel for a mission. Another form of beneficial propeller integration are indirect benefits that come from *design modifications* relative to the uninstalled configuration. These could be from e.g. improved stability characteristics from propeller installation that lead to smaller and lighter stabilizing surfaces.

It has been recognized by various studies that for a tube-and-wing aircraft that the wing lift-to-drag and high-lift characteristics to a large extent determine the overall aircraft performance. An enhancement of these performance indicators have therefore a large impact on the fuel consumption and need to be quantified already in the early stages of the design [35]. For propellers mounted to the leading edge, the swirl and increase in dynamic pressure changes the load distribution along the wing span. The wing removes some of the swirl in the propeller slipstream, and thereby reducing the wing induced drag [36, 37]. By careful installation, high-lift capabilities in take-off condition or approach condition can significantly be enhanced [38–41]. For example, the Antonov-70 STOL (short take-off and landing) aircraft with four engines has proven lift coefficients up to $C_L = 7$, allowing for take-off over a runway length that is only half of the one required for conventional aircraft of similar class with turbofan engines [42]. For twin-engine aircraft similar reductions in field length have been found [43, 44].

Alternative to reducing the wing's induced drag by mounting propeller on the inboard part, tip-mounted propellers have shown clear potential to reduce the induced drag even further. Already in 1969, Snyder [45] showed that by mounting the propeller to the wingtip can increase both lift and reduce induced drag of the wing where the effect of the wingtip vortex is partially cancelled by the propeller induced swirl [46]. In several fundamental studies, [36, 47–49], this benefit is confirmed and drag reductions between 10% to 15% are achievable for the wing, while on aircraft level this would translate to approximately 5% to 10% in cruise conditions.

The outlook that suitable electric motors could become available in the foreseeable future has led to a wide range of studies on distributed propulsion. The aerodynamic performance benefits that can be gained by the distributed propellers also makes the utilization of hybrid-electric propulsion more feasible [50]. By installing an array of propellers to the leading edge of the wing, a large portion of the slipstreams interacts with the wing. In such case, the propeller–wing interaction can therefore be better tailored for specific conditions, contrary to a conventional twin-engine configuration. Tailoring of the integration entails for example local enhancement of lift in select flight conditions by using only the propellers that are upstream of high lift devices [38]. The consequence of improved performance in low speed conditions, is that the wing area can be designed for cruise conditions, which is an important design consideration for the NASA X-57, see Fig. 1.2a. Distribution of thrust can also partially relieve the ground clearance constraint on the propeller diameter, such that a larger total disk area could be installed relatively easily, noticeable for the Airbus ZEROe concept with six electric motors, shown in Fig. 1.2b. In several studies [51–54] it was found that if propellers are mounted above the wing (i.e. over-the-wing propellers), higher maximum lift can also be achieved by delay-

ing separation on the high-lift systems. In cruise condition, such installation can also enhance the wing lift-to-drag ratio by increasing both the effective angle of attack and dynamic pressure to the wing.

(a) All electric NASA X-57.
Credits: NASA/Advanced Concepts Lab, AMA, Inc.

(b) Artist impression of the Airbus ZEROe 'pod' configuration (2020), with fuel-cell powered electric motors. Copyright: Airbus.

Figure 1.2: Envisioned aircraft configurations with a wing-mounted distributed propulsion system.

1.2.2. IMPROVED PROPELLER PERFORMANCE
Besides the potential of enhancing airframe performance, also the propeller performance can be significantly improved by careful installation. If the propeller is positioned in a flowfield with low axial momentum or high momentum in transverse direction, it exchanges the kinetic energy that is otherwise dissipated in the trailing vortex system [55, 56]. The most notable examples are the swirling flowfield induced by the wingtip vortex and the lower axial velocity as a result of friction on the fuselage. A pusher propeller that rotates opposite to the wingtip vortex can lead to propeller efficiency gains in the order of 10% [36, 57]. If the propeller operates in the wake or boundary layer of the fuselage efficiency gains between 5% and 10% are possible [58, 59]. While this integration technique is widely utilized to enhance the performance of marine propulsors, only a handful of manned aircraft have propellers mounted to the aft fuselage, e.g. the Dornier DO 334, Douglas XB-42, Saab 21, LearFan 2100, and more recently the Celera 500L.

1.2.3. AIRCRAFT STABILITY AND TRIM
The influence of the propellers is not limited to altering the aircraft's lift and drag: they directly and indirectly alter the aircraft's static stability, trim, and control characteristics as well, through several mechanisms. First, the propeller in-plane forces [60] alter the aircraft moment curves, depending on the propeller location relative to the center of gravity [61, 62]. These in-plane force gradients are affected by the airframe induced flowfield when the propeller is in proximity of the airframe. Although the classical linear models for the prediction of propeller in-plane forces may suffice for wing-mounted propellers [61, 63], but for configurations where propeller inflow highly depends on the

flight condition, these would be inaccurate. Secondly, the propeller induces aerodynamic forces on the airframe and therefore alters its moment coefficients, for example a wing that experiences the propeller slipstream. Finally, in its turn, the wing's downwash and therefore flowfield at the stabilizing surfaces is affected by the propeller as well. While this is an indirect effect of the propeller, it could be the primary installation effect on aircraft level [39, 62–66].

The most critical condition determines the size of the stabilizing surfaces, which is either driven by a trim, control, or stability constraint. This condition therefore directly influences the aircraft performance through the structural weight of the tail, the drag of the tail, and the trim drag resulting from deflecting the control surfaces to nullify the pitching moment about the center of gravity [67]. The consequences of the propellers on the aircraft's static stability and control characteristics therefore also indirectly play a role on the aircraft performance as found in several publications [39, 61, 63, 65, 66].

1.2.4. Noise and Unsteady Aerodynamic Loads

In conclusion, the goal of propulsion integration optimization should not be limited to achieving higher aerodynamic efficiency. Integration techniques to achieve high energy-efficiency is often accompanied with additional noise, as some form of nonuniform inflow to the rotor exists which can contain a high turbulence level [23, 68–70]. Mitigation of this interaction noise has been a focus point of propeller integration since the research on high speed and advanced turboprops. A drawback of unducted propellers is increased cabin noise [71, 72], in particular for flight Mach numbers above 0.6. This noise is caused by an airborne contribution due to the unsteady pressure field induced by the rotating blades, and a structureborne contribution due to vibrations from the engines, propellers, and propeller-airframe interaction [69, 73–75]. Despite successful reductions of cabin noise by employing various techniques [69, 71, 72, 76–83], the cabin noise levels of current turboprops are still several decibels higher compared to turbofan-driven aircraft [72, 74, 79]. This noise penalty is aggravated due to the tonal components of the noise spectrum, which are perceived by passengers as more annoying than broadband noise [72].

The turboprop is inherently noisier than a state-of-the-art turbofan engines for the same thrust level, due to the absence of a nacelle that acts as a noise shield [18]. Because from a certification point of view, only community noise is assessed, the superior climb performance is a clear advantage of the turboprop. Moreover, several studies have shown that community noise for typical regional turboprop aircraft is well below the certification standards [13, 23].

Wing-mounted tractor propellers of today's aircraft produce the highest sound pressure levels on the fuselage outer surface within ±30 deg from the propeller rotation plane [72, 84, 85]. A large reduction in perceived airborne and structureborne noise can potentially be achieved by mounting the propeller propulsion system to the tailplane or a pylon, as already proposed in the 1980s [21, 25, 29, 75, 86, 87], and this configuration is also proposed in more recent studies [18, 88]. Two examples are shown in Fig. 1.3. The General Electric GE36 counter-rotating propulsion system has made testflights fitted to a Boeing 727 in 1986. In 1990, Embraer made several test flights with prototypes of the CBA-123 aircraft, but production was never started. The NAL Saras, an aircraft designed

by the National Aerospace Lab of India, is the only production aircraft with aft-fuselage mounted propellers to date, and will be in service by 2025. Recently, Embraer announced the Energia Family with either propellers mounted to the vertical tailplane, or to pylons that are mounted to the rear part of the fuselage, shown in Fig. 1.3a. Embraer noted the significant (cabin) noise reductions of this particular layout as a key driver. Moreover, the aft-mounted layout also enables a relatively compact integration of alternative fuels (such as hydrogen) compared to a wing-mounted installation. A similar layout has been proposed by the company Eviation for the Alice aircraft (Fig. 1.3b).

(a) Embraer Energia Family. Copyright: Embraer.   (b) Eviation Alice. Copyright: Eviation Aircraft Ltd., with permission.

Figure 1.3: Examples of rear-mounted propeller configurations that are currently in development.

Integration techniques where the propeller operates in a highly nonuniform flow-field, also leads to cyclic loads on the motor, gearbox, and airframe, and therefore also impacts passenger comfort. Passenger comfort is also influenced by the unsteady loads on the airframe that are induced by the propeller slipstream and are experienced as vibrations. The aft-mounted propeller is therefore an excellent example where on the one hand, cabin noise is aimed to be reduced, while on the other hand, interaction noise and potential more pronounced vibrations arise from such installation [69, 74, 89]. Therefore, the understanding of the interaction phenomena is necessary to mitigate such adverse side effects.

1.3. OBJECTIVE OF DISSERTATION

The motivation of this dissertation is driven by the untouched potential of known propeller integration techniques that could lead to more efficient aircraft that are flying today. Existing studies on novel propulsion integration often focus on the aerodynamic benefits on component level. The assessment of the aerodynamic performance on aircraft level is often out of the scope of the study, which also means that the studied phenomena are confined to the ones that are relevant on component level. A translation of such results to aircraft level would require broader aerodynamic analyses that address the relevant flow quantities and force coefficients. On the other hand, conceptual and preliminary design studies aim at identifying the potential of a propeller configuration

on aircraft level, but often do not include sufficient detail to properly assess a performance gain. Also in these studies, the installation effects that go beyond the interaction of the propeller and a single component of the airframe are often neglected. The potential benefits of propeller integration can therefore be overestimated or underestimated.

Given the emerging interest in configurations with unconventional propeller installations, it follows that the dominant interaction effects which directly or indirectly contribute to performance, stability, and control need to be identified in order to establish fair comparisons. The notional sketch in Fig. 1.4 provides an overview of various propeller locations and the typical goal of such installation. Although various propeller configurations have shown either promising efficiency benefits or reductions in noise, these margins can quickly diminish if the complete aerodynamic interaction on aircraft level is quantified.
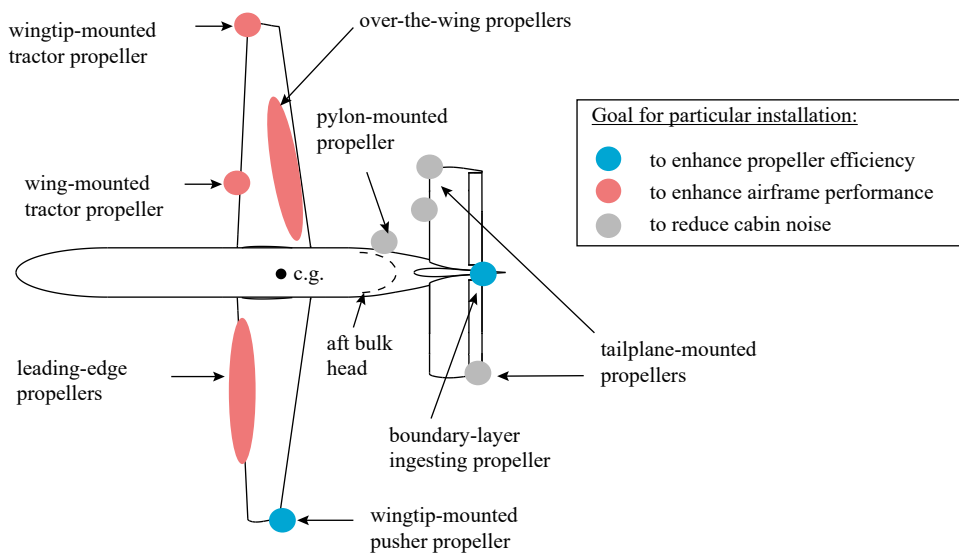
Figure 1.4: Examples of propeller integration at configuration level with main goals annotated.

From Fig. 1.4, several key differences in the type and magnitude of interaction can be recognized for the integrated configurations compared to the conventional, wing-mounted configuration:

- The aerodynamic forces on the propeller are a more prominent factor that influences aircraft stability.

- The effect of the propeller on the airframe aerodynamic forces could play a larger role on aircraft performance, stability, and control, as the aerodynamic interaction typically occurs far from the center of gravity. Moreover, undesired side effects from the propeller installation could be therefore be amplified.

- The interaction can be more complex, in particular when the propeller loading

and its slipstream are more affected by the airframe induced flowfield. In those cases, the aerodynamic interaction is more dependent on flight condition.

The understanding of the driving interaction phenomena that play a role on aircraft level is therefore crucial for comprehensive configuration studies, and ultimately, can lead to improved design choices. This has led to the following objective of this dissertation is:

> *.... to characterize the role of the aerodynamic interaction between the propeller and the airframe on the performance and static stability characteristics for selected aircraft configurations which aim for a beneficial propeller–airframe interaction.*

The main research question is:

> *What are the fundamental mechanisms that determine the airframe performance, static stability, and control characteristics when propellers are in close proximity to the airframe and how can these be predicted?*

The following sub questions will be addressed:

1. What are the physical mechanisms that determine the propeller performance in installed conditions?

2. What aspects need to be captured for a lower order method in order to accurately estimate the propeller loading caused by nonuniform inflow?

3. How do different propeller configurations compare in terms of cruise performance and what design guidelines can be formulated?

4. What are the physical mechanisms that determine aerodynamic forces on the airframe as the result of propeller installation?

5. What approaches should be followed to reduce or avoid unsteady loads on the airframe and propeller when they are in proximity to each other?

6. What are the key parameters that determine the airframe performance, static stability, and control characteristics when propellers are in close proximity to the airframe and what is their relation to aircraft design?

1.4. SCOPE AND RESEARCH APPROACH

The aerodynamic interactions are studied on a select number of configurations and conditions that would be representative for regional transport aircraft. For these type of aircraft, it is the airframe that typically produces the dominant flowfields and aerodynamic forces, while the propeller typically introduces a change to these, with magnitudes up to the ones introduced by the airframe. The scope is limited to fixed-wing aircraft. Therefore, cases where the propellers or rotors produce the dominant flowfields (such as vertical take-off and landing (VTOL) vehicles) or cases where there is significant flow separation from the propulsor and airframe (such as rotorcraft and other VTOL vehicles), are out of the scope.

The conventional, wing-mounted propeller configuration has been addressed in a large number of studies. This configuration therefore is not treated specifically in this thesis, although some of the fundamental interactions discussed herein apply to the wing-mounted configuration as well. For the selection of the configurations and cases, several aspects are taken into account: The propellers are located far from the center of gravity, typically experience a significant nonuniform flow induced by the airframe, the propeller inflow is a function of flight condition, and the airframe experiences a nonaxisymmetric slipstream. The following 'top level' configurations are studied on component and for some on aircraft level:

1. Propellers that are mounted *behind* the center of gravity and have *limited* effect on the wing:

    - Propellers behind a wing
    - Propellers in close proximity to the fuselage

2. Propellers that are mounted *far from* the center of gravity *in lateral direction* and have a *moderate* effect on the wing:

    - Wing-tip mounted pusher propellers
    - Over-the-wing propellers

3. Propellers that are mounted *ahead* the center of gravity and have a *large* effect on the wing:

    - Distributed propellers along the leading edge of the wing
    - Wing-tip mounted tractor propellers

A particular case that is treated in detail herein is a configuration where propellers are mounted to the horizontal tailplane. This case is motivated by the European Union CleanSky2 project IRON shown in Fig. 1.5 and serves as the starting point for this dissertation. The tail-mounted propeller configuration is an example where there is a strong interaction between the propeller and airframe that affects performance, stability, and control, and contains various interaction mechanisms that are of interest for other configurations as well. A second specific case is the a distributed propulsion configuration with propellers mounted to the inboard part of the wing (in front of the high lift devices) and a propeller mounted to the tip of the wing. In such configuration, the propellers are in front of the center of gravity, and the dominant aerodynamic interaction is the effect of the propeller on the wing, and which in its turn influences the flowfield at the horizontal tailplane. This particular configuration is part of the European Union CleanSky2 project NOVAIR.

The analyses that have been performed are a combination of studies on component level (in absence of the rest of the aircraft), as well as studies on full aircraft level which entails the full aerodynamic interaction. On a component level, a specific effect can be addressed as the aerodynamic phenomena are isolated or simplified. Figure 1.6 shows

Figure 1.5: The CleanSky IRON configuration with propellers mounted to the horizontal tail.
Credits: CleanSky.

the examples of the configurations on component level and aircraft level that are discussed throughout the thesis, with the aspects that are in particular of interest. The studies on component level can be considered simplifications of the integrated propeller. Besides the distributed leading-edge configuration and the horizontal tailplane configuration, the exploratory study to determine overall aircraft cruise performance considers a wider range of configurations. This is a study that focuses in particular on the propeller performance by comparing its performance that is influenced by the airframe induced flowfield, maintaining an equilibrium state, while the aircraft performance is affected by trim drag and changes in lift-to-drag ratio.

As highlighted in Section 1.2, aircraft design alternations as the result of propeller–airframe aerodynamic interaction may be the primary reason for the particular propeller position. However, aircraft (aerodynamic) design is not specifically discussed in this dissertation. Where applicable, it is noted that an effect is classified as 'small' or 'significant', based on the nondimensional force coefficients. It is attempted to put these values in perspective, but in end it is the aircraft designer that judges if the effect is indeed 'small' or 'significant'. The following practical constraints are set to further limit the scope of the research discussed herein:

- Despite the fact that modern propellers have swept propeller blades, the cases treated in this dissertation have unswept blades.

- As discussed in Section 1.2, airborne noise, structureborne noise, and airframe vibrations are crucial aspects for propeller-driven aircraft, in particular when the propellers are highly integrated. These aspects are briefly addressed in some of the analyses, but are by far not explored to the full extent. The discussions are therefore meant to identify possible future research areas.

1

- Although for the various engine configurations there is an exhaust jet that partially contributes to the thrust and also modifies the flowfield in the vicinity of the airframe [37]. These effects are not considered in this dissertation; the shaft power production is decoupled from the aerodynamic interaction study.

- The fundamental interactions are studied at low flight Mach numbers and the effect of compressibility is not treated specifically (although briefly discussed in Chapter 2). However, operating conditions and the nondimensional force coefficients are selected with care to represent a range of full-scale conditions.

A combined experimental and numerical approach is selected for several reasons. The experimental analyses are more suitable for various configurations and conditions where large gradients in the flowfield and flow separation dominate the forces on the airframe and propeller. The experimental work also provides validation data that is not only used to strengthen the presented numerical results in this dissertation, it also serves as validation material for studies by others. Numerical simulations are used to trace the cause of a certain aerodynamic phenomena, as the complete description of the flowfield can be analyzed, and some of the uncertainties that are present in experimental work are absent. Furthermore, distributions of loads are readily available in a numerical solution, even on components on which force distributions are difficult to measure (for example on the propeller blades). The choice for high fidelity CFD is motivated by the necessity of capturing both the primary interaction phenomenon as well as secondary interaction phenomena. Lower order models often lack the capability to estimate for example the development of the slipstream in the proximity of the airframe, in particular if the slipstream is deformed due to its encounter with the airframe. The exception of using high fidelity tools is the propeller analysis method which is developed as part of the dissertation (Chapter 5). Such lower order method also allows to understand the impact of the installation as it is sensitive to design changes and is therefore not a means to an end, but is an integral part of the analyses.

1

Fundamental interactions on component level

(distributed) angle of attack

wing-mounted
tractor propeller

vortex-impingement

Γ

Γ

V

propeller-propeller
interaction

wingtip-mounted
pusher propeller

wake encounter

fuselage

V

propeller in distributed
non uniform flowfield

tailplane-mounted
tractor propeller

Aspects of interest:

• propagation of nonuniform flow

• performance on component level

• time-averaged and time dependent
loads

Exploratory study on aircraft level

distributed along chord
on pressure/suction side

in fuselage wake

in wing downwash
and tailplane upwash

in wing upwash   distributed along span   tip-mounted pusher

Aspect of interest:

sensitivity of propeller
performance to propeller location

Configuration-specific interactions on aircraft level

Aspects of interest:

• aircraft performance

• static stability characteristics

• propagation of nonuniform flow

• performance on component level

• time-averaged and time dependent

Figure 1.6: Various levels of aerodynamic studies with each having a different focus and goal.

15

1.5. OUTLINE OF DISSERTATION

This dissertation contains ten chapters, each being linked as schematically shown in Fig. 1.7. In Chapter 2, the background information is provided and concepts are explained that will be used throughout the remainder of the dissertation and builds on existing knowledge of literature. This entails the characterization of the propeller slipstream that will interact with the airframe, propeller performance and load distributions in absence of the airframe.

In Chapters 3 and 4, the analysis methods and their validity are presented. In Chapter 3 the numerical and experimental methods are discussed and it provides an overview of the geometries that are used throughout, as well as the wind-tunnel setups, and measurement techniques. The validation of the numerical simulations is subsequently presented in Chapter 4.
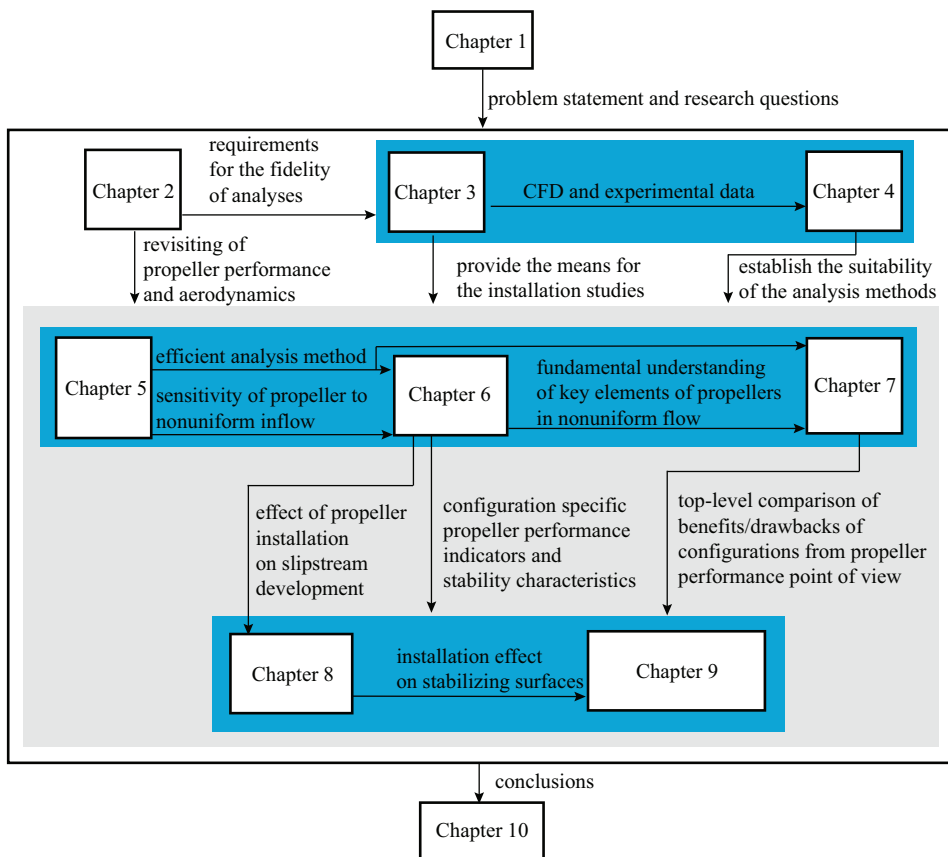
Figure 1.7: Flowchart indicating the connection between the chapters of this dissertation.

In Chapters 5 through 7, the detailed analyses on component and aircraft level are presented. First, in Chapter 5 a novel engineering method is developed that is useful to predict the propeller forces as the consequence of a nonuniform inflow. Airframe-induced inflow effects on installed propellers are further discussed in Chapter 6, as these findings are crucial for subsequent chapters. This chapter is followed by a configuration study of various propeller configurations, of which the findings are presented in Chapter 7. Readers who are interested in the comparison between different configurations to make design choices based on aerodynamic performance, will find useful trends and considerations in particular that chapter.

In Chapter 8, the effect of propeller installation on the flowfields and propeller-induced forces on downstream elements are discussed, which in particular contribute to aircraft stability and control. Aircraft performance aspects are presented in Chapter 9, by evaluating the two configurations of interest in more detail. Conclusions of the dissertation are presented in Chapter 10.

2

AERODYNAMIC CHARACTERIZATION OF THE UNINSTALLED PROPELLER

The understanding of the propeller-induced flowfield and the propeller forces in various conditions is crucial to characterize the aerodynamic interaction between propeller and airframe. This chapter forms the basis for that by evaluating the propeller in absence of the airframe. Already the analyses of the uninstalled propeller will provide directions of the impact of propeller installation on aircraft level. Later, when the airframe is included in the analyses, it becomes clear which phenomena are due to interaction and which are solely introduced by the propeller itself.

In various published works the performance, flowfields, and loading distributions have been described and quantified, for example in Refs. [14, 37, 91–93]. This chapter aims to introduce and revisit the propeller in uninstalled conditions, and specifically address the trends of flow quantities and forces that are of interest for performance and stability aspects, including:

- The extent in spatial directions to which the propeller influences the pressure and velocity field. This will illustrate what parts of the airframe directly experience the presence of the propeller.

- The variation of the loading distribution and flowfield as function of operating condition.

- Time-averaged slipstream characteristics. As shown in Chapter 8, the time-averaged flowfield is the dominant factor that determines the propeller–airframe interaction.

Parts of this chapter have been published in Ref. [90].

- The time-dependency of the flowfield quantities inside and outside the slipstream. A time-accurate flowfield reveals the regions of largest gradients in flow quantities and it is indicative for the unsteady forces on the airframe that are induced by the propeller [74, 94].

- The gradients of the propeller forces. The rates at which the propeller forces change with an angle of attack directly influences aircraft stability [61].

To address these, two cases are investigated: a propeller with axial inflow and a propeller experiencing an angle of attack, as sketched in Fig. 2.1. For the case with axial inflow, also a brief discussion is presented on scaling effects, as the analyses in subsequent chapters are conducted at low Reynolds number and low Mach number conditions, contrary to the conditions of typical transport aircraft. The relevance is discussed on the choice for a certain operating condition of the analysis when the propeller and airframe are in close proximity, as this choice has a profound effect on the quantification and assessment of the installation on aircraft level. It is therefore necessary to also introduce the key considerations of propeller selection. The insights on this aspect also form the basis for the propeller–airframe studies in the subsequent chapters. Detailed flowfield analysis of the case of a propeller experiencing an angle of attack is further discussed in Section 8.2.1.

(a) Symmetric inflow   (b) Asymmetric inflow
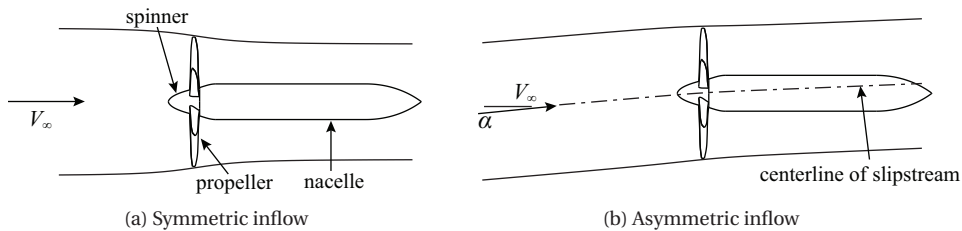
Figure 2.1: Schematic of an uninstalled propeller, spinner and minimum body nacelle.

In the following sections, both experimental and CFD data are used to show typical distributions, illustrate flowfield characteristics, and discuss scaling effects. The geometry of the particular propeller and analysis methods that are used to obtain these data are described in Chapter 3; such background information is superfluous at this stage.

2.1. GENERAL CHARACTERISTICS OF PROPELLER LOADS AND INDUCED FLOWFIELD

The two concepts that are often used to describe the working principle of a propeller are either based on the *forces* that act on the propeller, or on the *effect* that these forces have on the flowfield. First, the aerodynamic forces are discussed, followed by a simplification of the propeller to approximate the induced flowfield.

2.1.1. PROPELLER VORTEX SYSTEM

Propeller blades can be considered to be rotating wings. As a consequence of the local oncoming flow, aerodynamic forces act on the blade sections. The force distribution along the blade depends on the local flow angle, the local dynamic pressure, and the aerodynamic properties of each section. Figure 2.2a depicts relevant velocity vectors and flow angles. In most conditions where the propeller thrust is low, the local blade angle, and the ratio of V_∞ and Ωr determine the local angle of attack. Typically, a blade is twisted to account for the varying Ωr from hub to tip. The lift and drag forces can be decomposed in a component in the flight direction, i.e. the thrust force T, and a force opposite to the rotation direction, i.e. the tangential force F_t. The tangential force multiplied by its radial location is equal to the local torque, and the integral torque of all blades needs to be counteracted by the supplied torque on the propeller shaft.

(a) A blade section with aerodynamic forces

(b) Simplified propeller vortex system
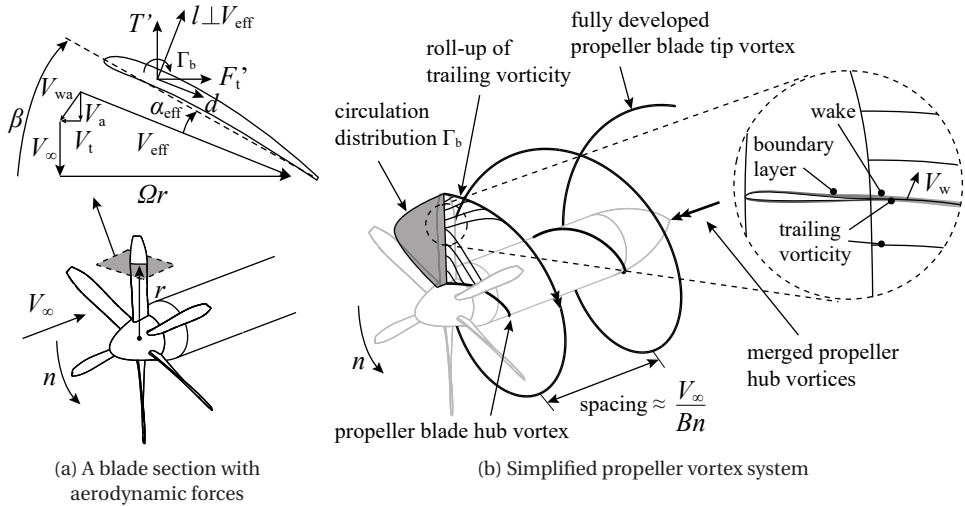
Figure 2.2: Schematic of a propeller, its bound circulation, and its vortex system that forms the slipstream. The relevant flow quantities and angles are annotated.

As each section experiences a different inflow condition and at the tip the pressure forces go to zero, the circulation varies along the propeller. This varying circulation distribution sheds vorticity, schematically shown in Fig. 2.2b. The vorticity in the tip region rolls up into a tip vortex, while the inboard vorticity rolls up into a hub vortex, opposite in sign to the tip vortex. While in the blade frame of reference the propeller induces a steady flowfield, in the aircraft frame of reference the rotating motion of the propeller blades results in a helical vortex system. The pressure, velocity, and vorticity vary for each location in the slipstream, especially close to the propeller disk. In conditions where the is no flow separation, the helical vortex system is periodic and the distance between the tipvortices (Fig. 2.2b) depends on the number of blades and the ratio of freestream velocity to rotational speed. The bound vortex Γ_b and this helical vortex system induce a certain flowfield, and the streamtube that passes through the propeller disk is referred to

as the 'slipstream', extending in downstream direction. At the propeller plane, the self-induced velocity field (V_a and V_t) partially determines the effective inflow at the propeller disk, as indicated by Fig. 2.2a. The figure also indicates the net induced velocity vector, V_w, which is the direction in which the trailing vortex sheet and blade wake are moving.

While the propeller-induced flowfield is periodic and well defined, the interpretation of the effect of a helical vortex sheet on the velocity at a location in space is still quite cumbersome. Instead, the helical vortex can be decomposed into vortex elements that have a clear orientation [95]. Such decomposition is sketched in Fig. 2.3. The slipstream can be considered, on average, on its edge to constitute of vortex rings containing the tangential component of vorticity, which are oriented perpendicular to the freestream direction. The helix also has a vorticity component in streamwise direction, ω_x, that is also situated at the slipstream edge, as well as on the center line. The consecutive vortex rings only induce an axial flow inside the tube. Outside of the tube, the apparent reduced velocity from each vortex element is cancelled due to the curvature of the vortex rings. Far downstream of the propeller disk, the axial velocity remains constant as the tube extends (nearly) symmetrically with respect to a location $x \gg 0$. At the propeller disk, the tube only extends in $x > 0$ direction, and therefore the axial velocity is only half of the value that exists far downstream. It may be observed that this is analogous with the flowfield induced by a semi-infinite vortex filament, which is half of the velocity induced by an infinite vortex filament.
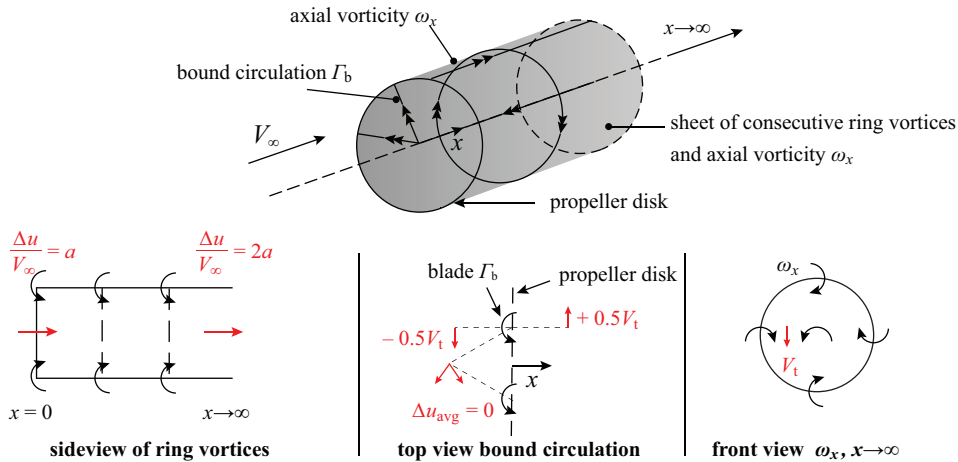
Figure 2.3: Representation of propeller slipstream as consecutive vortex rings, bound circulation, and axial vorticity. The lower subfigures indicate the effect of each component on the velocity field (in red).

The bound circulation does, on average, not induce an axial velocity component as the contribution of each blade is cancelled by the adjacent blades (assumed to have equal circulation and azimuthal spacing), shown in Fig. 2.3. However, it does induce a tangential component just upstream of the disk, and an equal but opposite tangential velocity just downstream the disk. At $x = 0$, it cannot induce a tangential velocity, i.e. $V_t = 0$. Yet, the flow that is approaching the propeller disk is irrotational, while just

behind the disk, the flow has a rotational motion that remains constant in downstream direction. Therefore, the tangential induced flow from Γ_B is exactly cancelled by the ω_x component of the tip and hub vortices. Again, the semi-infinite vortex filaments ω_x induce V_t far downstream, and half of that at the propeller disk. The net effect is $V_t = 0$ for $x = -\infty \rightarrow 0^-$ and V_t =constant from $x = 0^+ \rightarrow \infty$, if the slipstream tube diameter is assumed constant.

By distributing the vorticity in an axisymmetric tube instead of considering that the vorticity is concentrated in distinct regions for a real propeller, one only describes the average effect. In an instantaneous flowfield where there are individual vortex filaments, locally there is a tangential component upstream of the disk. Alternatively, this could be interpreted as the consequence of the pressure field around the blades that is not constant along the azimuth. On average, this component is cancelled due to the rotational motion of the blades. Effectively, such average distribution can only be achieved by having an infinite number of blades. In practice, there are distinct vortex sheets at a certain spacing. In that case, there is a local radial flow around the edge of the slipstream between the consecutive vortex sheets. Again, on average this component is cancelled out. The average radial velocity component that exists can only be the result from the varying strength of the tangential vorticity component along the x-direction. In case the vortex rings are not deformed and their strength is constant, this change only exists at the propeller disk itself. Hence, the radial velocity is only introduced at this location and is therefore symmetric around $x = 0$.

In this discussion so far, the role of viscosity on the development of the vortex system after its formation has been ignored. However, it does affect the development of the vortex system through the processes of diffusion and dissipation. From the moment that vorticity is shed, the vortex decays, such that its strength is reducing when it is moving in downstream direction, and at the same time, the high velocity gradients associated with the tip vortices are smeared through diffusion. Further downstream, it can be deduced that a reducing vortex strength leads to a (small) net radial component because subsequent tip vortices no longer cancel each other and therefore the slipstream is diverging. Furthermore, several vortex instabilities have been identified in literature [96] that that cause the destruction of the helical vortex system far downstream of the propeller. The instabilities are known to occur closer to the propeller if the axial spacing of the helical vortices is relatively small [96], e.g. if the number of blades is large or when the ratio V_∞/n is low [97].

2.1.2. SIMPLIFIED DESCRIPTION OF FLOWFIELD

Before the development of an actual slipstream is discussed in detail, the main characteristics of the slipstream can already be obtained by considering forces that are acting on the air, are the same and opposite to the forces introduced by the propeller. By realizing that the main purpose is to provide a thrust force T, one can simplify the propeller as a disk that produces a pressure jump. This disk represents the average effect of the propeller blades, which indeed also generates a low and high pressure field upstream and downstream of the disk, respectively. Such a disk is schematically shown in Fig. 2.4, with station 1 and 2 indicating each side of the disk.

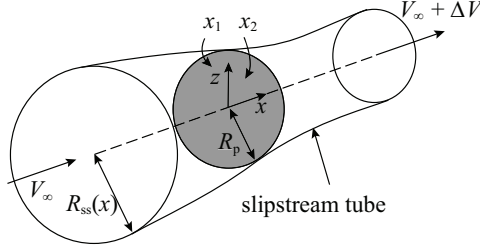The flowfield that is introduced by such an 'actuator disk' can be derived by the mo-

Figure 2.4: Representation of propeller as a thin disk.

mentum equations. In its simplest form it prescribes no tangential flow component and the pressure jump is constant over the disk, i.e. $(p_2 - p_1) = \frac{T}{\pi R^2}$, where p_2 is downstream of the disk, p_1 is directly upstream of the disk. Next to the disk loading, a relevant coefficient can be defined which expresses the (average) rise in pressure relative to the freestream dynamic pressure. The disk loading is often expressed relative to freestream dynamic pressure in the form of a coefficient T_C:

$$T_C = \frac{T}{q_\infty \pi R_p^2} \tag{2.1}$$

By neglecting viscosity and compressibility, the pressure and velocity field can be described by a set of closed form equations (e.g. in Ref. [14]), that provide insight in the slipstream development and spatial extent where the propeller is influencing the flowfield.

At the location of the disk, the pressure is discontinuous, while upstream and downstream of the disk the pressure is continuous. In those regions, the velocity can be described by a velocity potential. As shown in Ref. [14], the development of pressure can be obtained by covering the disk with doublets of strength $\Delta p = p_2 - p_1$. Along $r/R_p = 0$, the static pressure is:

$$\begin{aligned}
p_s &= \frac{p_2 - p_1}{2}\left(-1 - \frac{x}{\sqrt{R^2 + x^2}}\right), & x < 0 \\
p_s &= \frac{p_2 - p_1}{2}\left(1 - \frac{x}{\sqrt{R^2 + x^2}}\right), & x > 0
\end{aligned} \tag{2.2}$$

and is symmetric about $x = 0$, graphically shown in Fig. 2.5a.

Upstream of the disk, no momentum has been added yet, and total pressure is therefore constant until the disk. At the disk, the total pressure is increased by $(p_2 - p_1)$, and remains constant in downstream direction. The consequence is that upstream of the disk the axial velocity is increasing with the highest axial velocity gradient occurring at the disk. Although the pressure is discontinuous, the velocity has to be continuous if density is assumed to be constant and continuity is maintained. It is noted that for a propeller operating in high subsonic conditions, there is a change in density across the disk. In downstream direction, the flow continues to accelerate until the axial pressure gradient vanishes at $x \to \infty$. At $r/R_p = 0$, this development is given by:

$$v_x = \frac{p_2 - p_1}{2\rho V_\infty}\left(1 + \frac{x}{\sqrt{R^2 + x^2}}\right) \tag{2.3}$$

Instead of working with a dimensional velocity, it is more convenient to use the induction factor $a = \frac{v_{x,x=0}}{V_\infty}$, as discussed before. It can been shown that it depends on the thrust coefficient when it is constant over the disk:

$$a = \frac{1}{2}\left(\sqrt{1 + \frac{8}{\pi}T_C} - 1\right) \tag{2.4}$$

The profile of Eq. 2.3 is plotted in Fig. 2.5b, showing that the slipstream develops approximately between $\pm 4R_p$. Instead of the development of the velocity, the dynamic pressure is more relevant in case an aerodynamic surface would be located inside the slipstream. Figure 2.5c depicts both velocity and dynamic pressure increase as a function of thrust coefficient. For a typical range of T_C that occurs in flight (see Table 2.2), the dynamic pressure is significantly raised.

(a) Static pressure along $z/R_p = 0$

(b) Axial induction factor along $z/R_p = 0$

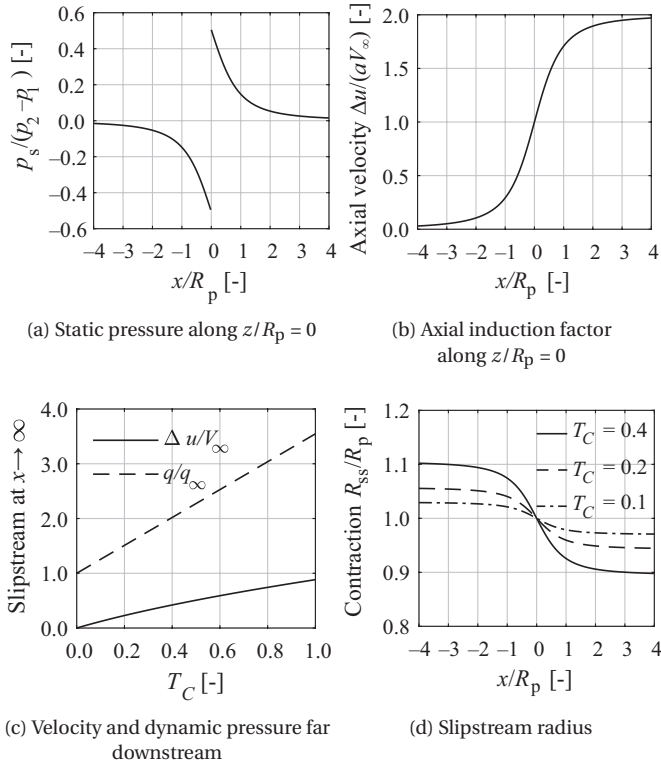(c) Velocity and dynamic pressure far downstream

(d) Slipstream radius

Figure 2.5: Pressure and velocity distributions for an actuator disk, based on derivations in Ref. [14]. In subfigures (a), (b), and (d) it is shown that at $x/R_p \pm 4$ the gradients of the flowfield are close to zero.

Next to the axial velocity, the radial velocity component has several consequences that can be important on aircraft level, as it influences the local flow angle and therefore the local angle of attack to a lifting surface. This radial component is the result of the boundary of the slipstream that can be considered a surface of revolution with no flow across this surface. As the continuity is maintained, the radius of this surface must vary along the axis of the propeller, with no radial flow at $x \to \pm\infty$, and a maximum value at the propeller disk, coinciding with the location of the highest velocity gradient in axial direction. The radius of the slipstream is given by:

$$\frac{R_{ss}}{R_p} = \sqrt{\frac{1+a}{1 + a\left(1 + x/\sqrt{R^2 + x^2}\right)}} \tag{2.5}$$

The fact that the slipstream tube is not parallel to the freestream, and outside the slipstream the total pressure remains constant, there is a non-zero pressure and velocity gradient in axial and radial direction. Although the propeller primarily influences the flow inside the slipstream tube, its presence therefore also influences the region outside this tube. The radial velocity component is maximum at the propeller tip, and zero on the symmetry axis of the disk, shown in Fig. 2.6a. The associate axial velocity field outside of the slipstream is depicted in Fig. 2.6b, indicating that upstream the flow is also accelerated, while downstream of the disk the velocity is lower than freestream conditions.

(a) Radial induction factor $\frac{V_r}{aV_\infty}$

(b) Approximate axial induction factor a
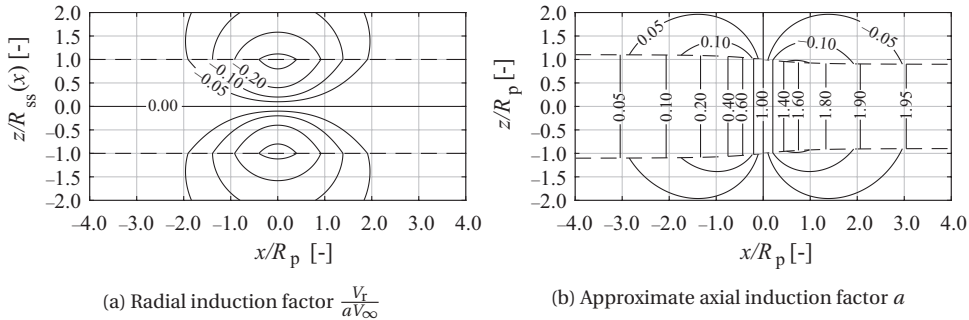
Figure 2.6: Approximated development of slipstream to show the spatial extent of the propeller influence on the flowfield. Based on derivations in Ref. [14].

In summary, the following is observed from these simplified flowfields:

- The extent at which the propeller influences the pressure and velocity field is limited to $x < \pm 4R_p$. Outside this domain the pressure perturbation is less than 1% of the pressure jump, independent of thrust coefficient. This implies that for interaction phenomena where the pressure gradient is important, the impact will be confined over a distance that scales with propeller radius and T_C. This is also confirmed in Ref. [98].

- The contraction is a function of thrust coefficient and is symmetric over $x = 0$. The largest gradient is found at the propeller tip.

- The shape of the flowfield outside the slipstream depends on T_C as the slipstream boundary depends on T_C. However, if the flowfield is expressed in terms of the induction factor, it is independent of the propeller thrust.

- Outside of the slipstream, the pressure and velocity gradients vanish quickly.

2.1.3. Ideal Propeller Efficiency

In an ideal situation, the propeller operates at its maximum efficiency. The shape of the slipstream that is introduced by the propeller in that case is most representative for the design condition. Off-design conditions are then a derivative of this ideal slipstream shape. To define an ideal propeller, first its efficiency needs to be defined. The consequence of the added momentum by the propeller is that the slipstream contains kinetic energy that is higher than the freestream value, and this kinetic energy deposition of requires power. The useful thrust power, TV_∞, relative to the power that is required to accelerate the slipstream is called the 'propulsive efficiency'. It is therefore a measure of how effective a propulsor is in producing thrust. If the axial induction a is constant over the disk, it can be shown that the propulsive efficiency is given by:

$$\eta_{\mathrm{pp}} = \frac{1}{1+a} \tag{2.6}$$

Note that when a approaches 0, there is maximum efficiency. To approach this, the diameter should be large and disk loading low. If a varies along the radius, the propulsive efficiency can be generalized by taking the area weighted average:

$$\eta_{\mathrm{pp}} = \frac{1}{1 + \frac{2}{R_{\mathrm{p}}^2} \int_0^{R_{\mathrm{p}}} r a(r) dr} \tag{2.7}$$

An actual propeller generates thrust by the rotating the propeller blades which requires a certain shaft power P_{s} to maintain rotational speed. It is this shaft power that is the actual input to the system. The *propeller efficiency* is therefore written as:

$$\eta_{\mathrm{p}} = \frac{TV_\infty}{P_{\mathrm{s}}} \tag{2.8}$$

The propulsive efficiency is therefore a measure of how efficient the axial component of a slipstream is in producing thrust. The propeller efficiency on the other hand describes how efficient the propeller is to convert mechanical power into thrust. This latter therefore includes the swirl and profile losses.

A relevant question is, what is the best distribution of the induction factor over the disk such that the kinetic energy loss is minimum for a given thrust? Effectively, the propeller can be divided into a set of concentric rings, such that the slipstream consist of annular tubes, each having an axial induced velocity. Then, a becomes a function of radius. As the kinetic energy deposition is proportional to a^3, while the change in momentum is proportional to a^2, a low value of a is desired. Therefore, any region where a is larger than necessary to meet the integral thrust requirement is an excessive loss. In this region a should be reduced, while in another region of low a its value should be increased. The optimal efficiency distribution over the disk is therefore constant.

Since the induction factor is a function of thrust coefficient (Eq. 2.4), the maximum propulsive efficiency can be determined and is plotted in Fig. 2.7a. Note that this is just a combination of Eq. 2.6 and Eq. 2.4 under the assumption that we have a uniform axial induction factor over the propeller radius. As the added momentum (or thrust) is proportional to a^2 and the disk area, a low 'disk loading' or thrust per unit area is desired. Therefore, a large disk is beneficial from a propulsive efficiency point of view to meet a required thrust. From an overall aircraft performance perspective, several studies [29, 86, 99] indicate that large propeller diameters do not necessarily lead to high fuel efficiency. This is primarily due to the weight increase of the gearbox, propeller, and the support structure with larger diameters. Secondly, the helical tip Mach number tends to go beyond the speed of sound resulting in a loss in efficiency and an increase in noise [80]. For high speed flight, even at Mach numbers around 0.7, high disk loading on the propeller disk have shown total efficiency benefits over larger, lightly loaded, propellers [13]. From an aircraft performance perspective, the optimal diameter needs to be selected carefully considering the aircraft system and its mission.

If for a given airspeed, the diameter should be maximal, a relevant question is whether the airspeed itself is also a dependent variable. This can be determined by minimizing the amount of energy in Watt·s per meter travelled, or power P absorbed by the propeller relative to flight speed V. If thrust equals drag, and the lift-to-drag ratio is assumed constant, then it can be shown that W·s/m is constant and independent on flight speed, if only the propeller is considered. Therefore, an aircraft with thrust equal to drag should fly at the conditions such that the product of propulsive efficiency with lift-to-drag ratio is maximal. From a *propulsor* point of view, a large disk area is most favourable in terms of energy consumption, while for the *aircraft*, it should fly at a flight speed that corresponds to the highest lift-to-drag ratio.

(a) Propulsive efficiency of an actuator disk

(b) Effect of swirl on optimal induction at propeller disk, $\eta_{pp} = 0.8$

(c) Effect of number of blades on optimal circulation distribution
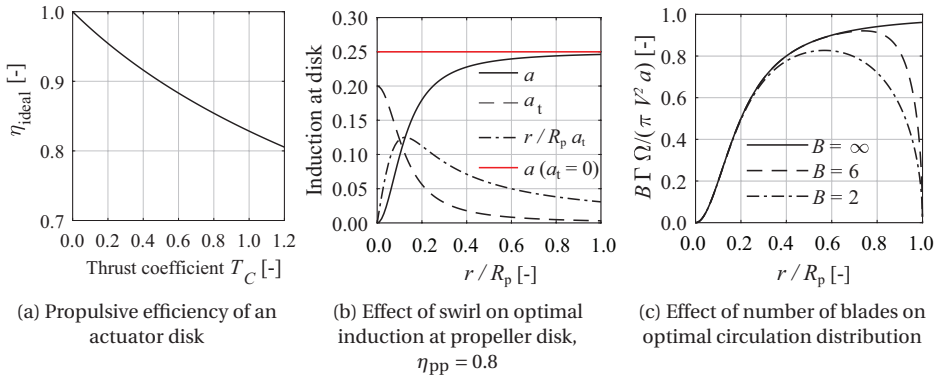
Figure 2.7: Efficiency and slipstream induction factors for an ideal propeller showing the effect of thrust coefficient, the role of swirl, and the effect of the number of blades.

The flowfield described by Fig. 2.5 is a simplification of an actual flowfield. In particular, there is no swirl velocity. Following the same line of thought as for the disk without swirl, if swirl is added, the optimal solution is still the one where the efficiency along the radius is constant. However, it is achieved with a drastically different induction factor

[14]. The two distributions are depicted in Fig. 2.7b. Since a is proportional to the local thrust, the shape of the induction factor resembles the ideal thrust distribution as well. The figure also shows that the highest axial induction occurs in the tip region. The low induction at the hub can be interpreted as follows: To add momentum in axial direction in a region where Ωr is low, a relatively large swirl is required. This swirl adds to the shaft power. A low a—in itself highly efficient—is required in that region to offset this relatively high loss to obtain a constant efficiency along the blade. The result is that the vortex sheet moves backwards with velocity V_{w} (Fig. 2.3a) and the angle $\arctan \frac{V_{\mathrm{t}}}{V_{\mathrm{a}}}$ is constant along the radius. This condition is the *minimum induced loss condition* [100]. It may be observed that this condition is similar to the constant downwash distribution of a wing that leads to lowest induced drag for a given wing span and wing lift [101].

As discussed in the previous section, a finite number of blades results in a flow around the edges of the vortex sheets that are shed by each blade. This has two consequences. First, the local induced angle of attack is highly influenced and there is a relatively higher loss towards the tip of the propeller blade. A large number of blades is therefore favourable in terms of induced losses. Second, the ideal solution of the induction factor (and therefore approximately circulation) is no longer the one plotted in Fig. 2.7b. The relatively larger loss at the blade tip requires the magnitude of a to reduce accordingly in order to maintain the optimal constant efficiency along the blade. To obtain this, the induction factor is also reduced in the tip region, such that the highest induction occurs at $r/R_{\mathrm{p}} < 1$, and typically between $r/R_{\mathrm{p}} = 0.5$ and 0.8. An approximate solution of such optimal distribution can be obtained by applying the Prandtl tip loss function [102] to the optimal solution for an infinite number of blades. Figure 2.7c depicts the impact of a finite number of blades on the induced flowfield.

It is noted that the situation for the ideal distribution of a and the value of maximum propeller efficiency is significantly different if the propeller operates in a flowfield that is not equal to V_∞, while the aircraft is flying at V_∞ or if the inflow is not uniform [14, 56, 103]. This is further discussed in Chapter 5. Moreover, for practical applications where the structure of the blade [104], noise considerations [81], or high thrust conditions are taken into account in the design of the blade, the efficiency distribution is not constant but still approximately resembles the optimal distribution.

2.2. CHARACTERISTIC PERFORMANCE CURVES

2.2.1. INTEGRAL FORCES

Propeller performance is expressed by a number of dimensionless coefficients. By these coefficients, similarity of loading distributions and slipstream can be maintained. A key parameter that describes the operating condition is the advance ratio:

$$J = \frac{V_\infty}{nD_{\mathrm{p}}} \tag{2.9}$$

which expresses the forward velocity relative to the rotational motion. For a propeller with a given blade pitch, by keeping the advance ratio the same while the propeller is scaled or freestream velocity is varied, the angle of attack remains the same along the blade, and with that, the shape of the load distribution. Furthermore, provided that the

tip vortices move backwards with approximately V_∞, the distance between tip vortices and therefore the helical vortex system is only a function of J.

In the discussion so far, the thrust has been related to the dynamic pressure of the freestream and the disk area as the thrust coefficient T_C (Eq. 2.1). Such definition is closely related to the aircraft aerodynamic coefficients C_L and C_D, and is therefore useful when the propeller thrust force is put into perspective on aircraft level. Figure 2.8a shows a typical $T_C - J$ curve. The slope is steep at low J, because only small reduction in J not only changes the angle of attack along the blade, it also leads to a high dynamic pressure on the blade sections relative to the freestream dynamic pressure. The figure also shows that a change in blade pitch primarily leads to a shift of the complete $J - T_C$ curve in horizontal direction, explained by the offset in section angle of attack along the blade which translates to an offset ΔJ. Again, the slope is slightly higher at low J and therefore it is not only a shift.
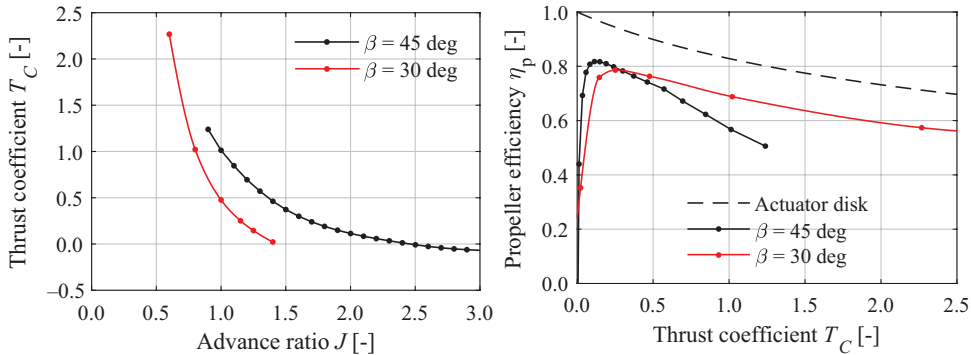
(a) Thrust coefficient. Note the difference in range of advance ratio for high to zero thrust.

(b) Propeller efficiency. Note the lower maximum efficiency for $\beta_{0.7R_p} = 30$ deg, while the efficiency is not compromised at high thrust coefficients.

Figure 2.8: Typical performance curves for two blade angles $\beta_{0.7R}$ for the XPROP propeller (Section 3.2), obtained from full-blade CFD simulations. The curves shows that the different ranges of operating condition for a low and high blade pitch angle.

When the efficiency of an actual propeller is compared to the ideal efficiency, shown in Fig. 2.8b, a number of observations can be made. First, the complete offset $\Delta\eta$ for a real propeller is caused by the higher induced losses and blade profile losses. Second, while maximum efficiency is also achieved at low T_C, it is not at $T_C = 0$. In this condition there are still profile losses and the shaft power is finite. Furthermore, while on average the thrust is zero, often part of the blade typically still experiences positive thrust, and a part negative, and also induced losses are still finite. The propeller therefore gradually transits from propulsive mode ($C_T, C_P > 0$), to braking mode ($C_T < 0$, $C_P > 0$), to windmill mode resulting in a net power absorption by the propeller and motor ($C_T, C_P < 0$). Third, at higher thrust coefficients ($T_C > 0.6$ for a blade pitch angle at 70% radius of $\beta_{0.7R_p} = 45$ deg) the efficiency drops more rapidly. This is caused by flow separation and the fact that blade sections do not operate at their highest lift-to-drag ratio. It is noted that at for a low blade pitch angle, the flow separation occurs at much higher T_C (not

shown in the graph), due to the relatively high dynamic pressure experienced by the blade section when the onset of separation is reached.

The definition of T_C does not express *how* the thrust is being generated. By observing that the $T_C - J$ curve depends approximately on J^{-2}, instead the thrust can be also normalized by the rotational speed, density, and propeller diameter:

$$C_T = \frac{T}{\rho_\infty n^2 D_p^4} \tag{2.10}$$

It may be observed that $C_T = \frac{\pi}{8} J^2 T_C$. Similarly, the torque, Q, is normalized as:

$$C_Q = \frac{Q}{\rho_\infty n^2 D_p^5} \tag{2.11}$$

while the power coefficient is $C_P = \frac{P_s}{\rho_\infty n^3 D_p^5}$, or equivalently $C_P = 2\pi C_Q$. By such normalization, better insight is gained in the state at which the propeller operates, for example whether it operates in the expected linear part of $C_T - J$ or in the nonlinear part, which would indicate that part of the blade experiences stall. Examples of typical performance curves are plotted in Fig. 2.9a. These curves show that indeed there is a (nearly) linear region from low to medium thrust, and a clear nonlinear region in case the advance ratio is reduced further. The fact that the curves are not exactly linear is a consequence of the data that was obtained at low Reynolds number (further discussed in Section 2.5), which influences influences zero-lift angle of attack and lift curve slope of the sections. Due to the cambered airfoils (see Section 3.2) also separation on the pressure side occurs at low J, leading to nonlinear behavior of the airfoil sections. As expected, and similar to the $T_C - J$ curve, a reduction in blade pitch shifts the curves in horizontal direction.

(a) Thrust and power coefficients

(b) Propeller efficiency. Indicated ideal efficiency at constant C_P and constant n
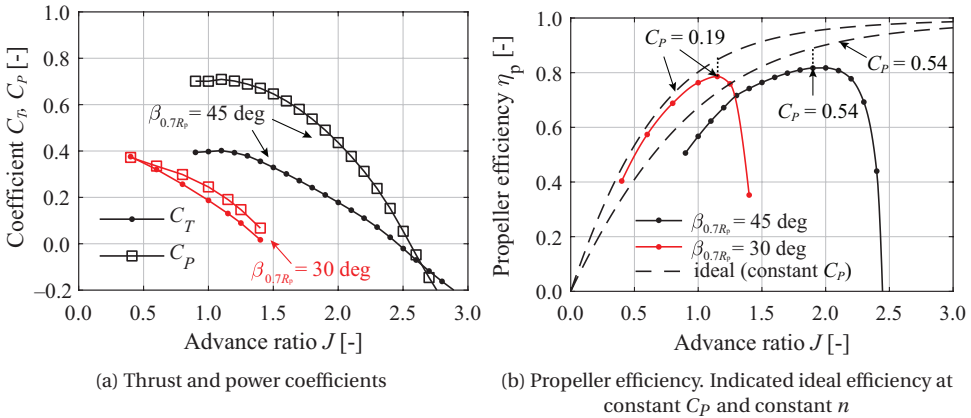
Figure 2.9: Typical performance curves for two blade angles $\beta_{0.7R_p}$ for the XPROP propeller (Section 3.2), obtained from full-blade CFD simulations

While it has become clear that a high efficiency can be achieved at low disk loadings, reaching a low T_C is not the only objective: it should be done such that the swirl losses

at this condition are also minimal. It is now of interest to determine how the operating condition and blade pitch play a role in achieving that objective. The dependency of efficiency on these two parameter is depicted in Fig. 2.9b. The advance ratio at which the highest efficiency occurs is highly dependent on blade pitch. At $J = 0$, the efficiency has to go to zero by definition. This means that the theoretical efficiency of unity can only be approached at high advance ratio, leading to the conclusion that high blade pitch could allow for high efficiency, also displayed by Fig. 2.8b. The figure shows that an imaginary curve can be constructed such that the blade pitch can be chosen to achieve the maximum efficiency for each J. In fact, such a curve can be constructed by the observation that the C_P curve shifts along the J axis if β is varied. For each J and an assumed C_P, there is a maximum theoretical efficiency. The blade pitch should be adapted such that the propeller operates near this maximum envelope. These ideal curves are plotted in Fig. 2.9b as dashed lines. The efficiency curves also demonstrate that a low pitch leads to a quite 'narrow' range of operating conditions where the propeller has high efficiency. Any change in inflow velocity, or ΔJ, that occurs rapidly reduces the efficiency, while for a large blade pitch this sensitivity is much lower.

From this discussion, it can be concluded that on an aircraft level, a low pitch is favourable in take-off and climb conditions as high thrust can be achieved. In cruise condition a high blade pitch is beneficial to achieve the highest propeller efficiency. Therefore, large turboprop driven aircraft feature a governor to automatically adjust the blade pitch over the flight for a given rotational speed and throttle setting of the engine. Although these observations are not new and in fact these are applied to today's aircraft, it is important to realize that the selection of the correct operating condition in any performance estimation is profoundly important, as various conclusions will strongly depend on this choice.

2.2.2. Force Distributions
In Section 2.1.3 has been shown that the ideal induction factors vary significantly along the radius. This also means that the load distribution varies in a similar way. By understanding how the thrust and torque are distributed along the radius and how this varies with operating condition, it also becomes clear how the associated slipstream depends on operating condition.

In the previous section it has been concluded that for a propeller with a finite number of blades, the load is zero at both $r/R_p = 0$ and at the tip, with a maximum ranging between $r/R_p = 0.5$ and 0.8 depending on the number of blades. In order to mount the propeller and allocate a possible variable blade pitch mechanism, there is a hub to which individual blades are mounted and spans typically 20% to 30% of the propeller radius. By the presence of this hub, the loading does not have to go to zero. In fact, this would also not be beneficial from an efficiency point of view. The circulation distribution is rarely exactly optimal in terms of induced and profile losses for various reasons, including:

- structural constraints: for root-bending moment constraints the airfoil at the hub need minimum thickness and thereby adding to viscous losses [87]

- noise considerations: by shifting the location of maximum loading more toward the hub the noise for a given thrust reduces [81]

- design for certain slipstream shape: either high swirl or high dynamic pressure can be directed to a certain portion of the disk with the objective of a more favourable forces of airframe components downstream of the propeller [38]

- operating conditions: a constant efficiency generally cannot be maintained if the propeller operates at off-design conditions

The results presented herein are typical as they were computed using a representative six-bladed propeller that is close to minimum induced loss. For example, structural considerations are included in the particular design. These radial distributions are depicted in Fig. 2.10. The maximum can be found around $r/R_p = 0.85$ and the value at the tip is not zero, as there the tip vortex introduces a shear force at the tip. Figure 2.10a shows that there is approximate similitude between the distributions if the C_T is matched with two different blade angles. For the same blade angle, the normalized thrust distribution has a relatively low dependency on advance ratio, shown in Fig. 2.10b. Only in the nonlinear part ($J < 1.5$) or in the condition with nearly zero thrust ($J \approx 2.3$) the distributions do deviate from the characteristic distribution. The finite dependency is attributed to two phenomena. First, the orientation location of the tip vortex is more in streamwise direction at high advance ratios. At low advance ratios, the tip vortex is in closer vicinity to the adjacent blade. The higher axial velocity introduced by the tip vortex leads to a lower loading at the tip of the neighbouring blade. Therefore, in a *relative* sense, the tip is higher loaded at high advance ratio, hence a gradual dependency of $C_T'/C_T(r)$ on J. Second, a lower Reynolds number at high J leads to lower lift coefficients towards the hub, given the relatively thick airfoil profiles in that region. Along those lines, compared to the $\beta_{0.7R_p} = 45$ deg case, the tip is less loaded for the $\beta_{0.7R_p} = 30$ deg case as on average the blade sections operate at higher Reynolds number. Figure 2.10a also shows that for the same T_C at two blade angles, the distribution is quite different, with a shift of the highest loaded region. Consequently, the slipstream induction factor will have comparable deviations.

The fact that the thrust distributions are rather consistent and predictable distributions has a distinct advantage: the thrust distributions in the linear part of the $C_T - J$ curve can be constructed once the gradient $\frac{dC_T}{dJ}$ is known. While the distributions in the linear part of the $C_T - J$ curve can be predicted with reasonable accuracy using blade-element models, the distributions in the nonlinear regions are more difficult, as part of the blade is stalled, which leads to complex three-dimensional flow near the surface of the blade that affects the local (maximum) lift coefficients [105].

It is now of interest to determine to what extent the efficiency along the radius depends on operating condition. In Fig. 2.11a it is observed that the efficiency is indeed nearly constant along the blade when the propeller operates at design conditions. Assuming that the sections operate at approximately their optimal $\frac{c_l}{c_d}$, the angle of attack is approximately constant along the blade. Reducing the advance ratio and thereby increasing the blade section angle of attack, shows a consistent reduction in blade section efficiency from hub to tip for $T_C = 1.01$. The fact that the efficiency is no longer constant but reduces towards the tip is a consequence of two factors. First, the relatively thin blade sections that are typically chosen for the tip region have a lower maximum lift coefficient and therefore c_d rises rapidly with α and therefore propeller torque. Second,

2
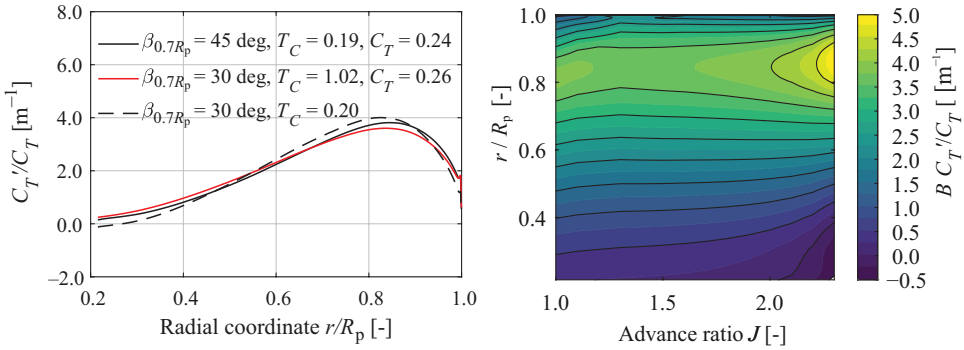
(a) Effect of blade pitch. A lower blade pitch leads to higher loading on the inboard part of the disk.

(b) Dependency on advance ratio, $\beta_{0.7R_p} = 45$ deg. For the nominal range ($J = 1.4$ to $J = 2$), the *shape* of the thrust distribution remains approximately constant.

Figure 2.10: Example of normalized thrust distributions to identify the differences in *shape* of the thrust distribution, based on full-blade CFD data from the XPROP propeller (Section 3.4).

when there is a strong radial flow component of the boundary layer when it is close to separation [106]. This radial component starts from the hub and results in a significant growth in boundary layer in the tip region, affecting the effective camber of the airfoil. The radial flow component and the associated decambering of the airfoils results not only in higher profile (pressure) losses, but the circulation distribution is not optimal any more causing the induced losses to increase as well. Hence, the efficiency along the span reduces when the advance ratio reduces significantly.
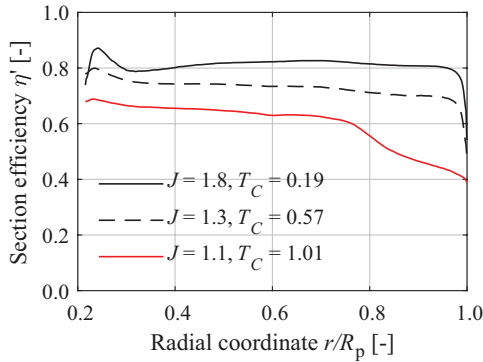

Figure 2.11: The effect of off-design condition on the efficiency distribution, $\beta_{0.7R_p} = 45$ deg. Note that at high thrust settings, the outboard part of the disk experiences flow separation due to the relatively thin blade sections. Full-blade CFD data for the XPROP propeller (Section 3.4).

2.3. CHARACTERISTIC FLOWFIELDS

Although the effect of the propeller on the airframe is inherently unsteady, the time-averaged flowfield leads to insight in the interaction that on average takes place. On the other hand, an instantaneous, time-dependent, flowfield reveals the regions of the largest gradients in the flowfield. These could lead to, among other phenomena, flow separation and unsteady loads on the airframe [54, 94].

The purpose of this section is to demonstrate how typical slipstreams develop without considering the simplifications that have been introduced in the previous sections. The selected geometry is the XPROP-S propeller, introduced in Section 3.2. While the slipstream shape depends on propeller geometry, similar geometries will have comparable trends and numerical values.

The results presented in this section illustrate the extent and the variation of the propeller-induced flowfield for the case of a propeller with finite number of blades, contrary to the simplified flowfields discussed so far. The difference in the slipstream distributions for various operating conditions, i.e. take-off, cruise, and approach conditions, will be discussed. These observations are relevant for subsequent analyses where aerodynamic surfaces are submerged in the slipstream at distinct locations relative to the slipstream.

2.3.1. TIME-AVERAGED FLOWFIELDS

The propeller increases the total pressure of the flow that passes through the disk. Its distribution in radial direction resembles the combination of thrust and tangential force components, as shown in the contour plot in Fig. 2.12a. At the propeller the total pressure is increased remains constant in downstream direction. The region of $C_{p_t} < 1$ indicates the boundary layer and wake from the nacelle. As the total pressure entails the pressure and velocity components of the slipstream, the development of these different contributions can be compared to the simplified model of the propeller, as presented in the previous sections. A decomposition is shown in Fig. 2.12b at a constant radial coordinate ($r/R_{\mathrm{p}} = 0.8$). As the contraction is relatively small at this thrust coefficient ($T_C = 0.18$), the streamlines are oriented approximately in parallel to the x-axis, and therefore the distributions are approximately along a streamline. The figure shows that only a minor part of the rise of C_{p_t} is the consequence of swirl, less than 2%, while the largest portion is caused by the added momentum in axial direction, displayed as a rise of axial velocity. Although the axial velocity profile seems to reach half of its final velocity at the propeller disk, the non-symmetric pressure profile indicates that there is more acceleration upstream than downstream. This non-symmetry partially is due to the increase in q that therefore also impacts the nacelle's contribution of the pressure and velocity field. However, the majority can be explained by the vorticity distribution along the surface of the airfoil surface, which is not equally divided on the suction and pressure side. Therefore, the propeller vortex field as depicted in Fig. 2.4 is indeed a simplification, in particular by describing the vortex field near the propeller.

Figure 2.12a also clearly shows an effect of the propeller on the nacelle's induced pressure field on the aft part of the nacelle. The consequence is that even though the nacelle geometry is aimed to have minimal influence on the propeller inflow, its presence does influence the pressure and velocity gradients in the slipstream.
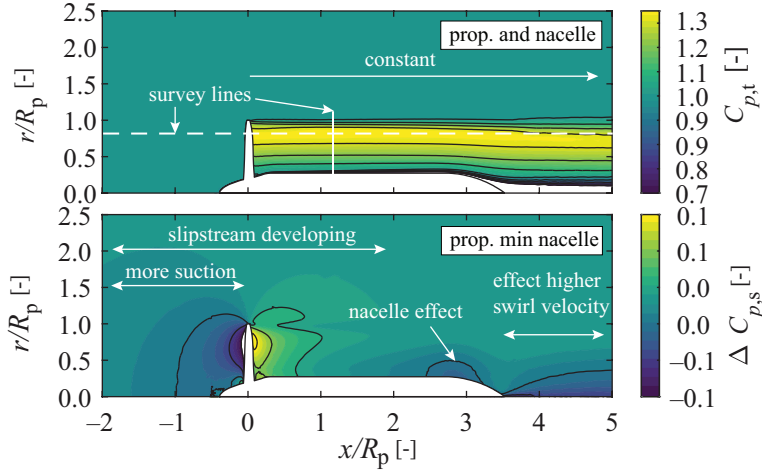
(a) Total-pressure distribution showing a nearly constant jump. The contour of static pressure indicates the extent of the propeller pressure field and the indirect effect of the nacelle shape. Conditions: $J = 1.8$, $C_T = 0.24$.
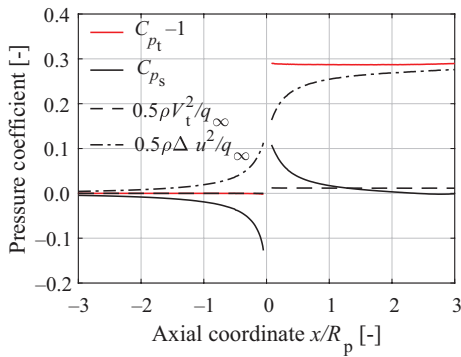
(b) Decomposition slipstream components at $r/R_p = 0.8$, nacelle effect subtracted. Conditions: $J = 1.8$, $C_T = 0.24$.
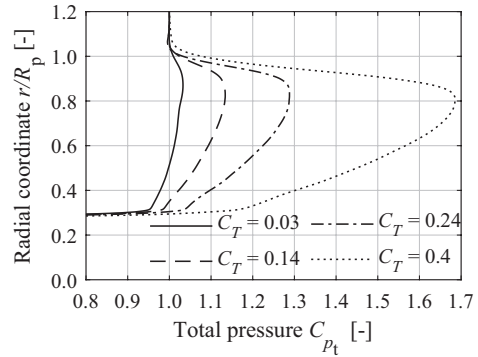
(c) Total pressure at $x/R_p = 1.1$

Figure 2.12: Effect of propeller installation on the local total and static pressure to show the spatial extent of the propeller influence on the flow field. Full-blade CFD data for the XPROP propeller with $\beta_{0.7R_p} = 45$ deg (Section 3.4).

When the thrust coefficient is increased, the magnitude of C_{p_t} increases accordingly. Figure 2.12c shows the radial distributions for several values of C_T. Although the profile appears to become sharper, it scales approximately linearly with T_C for the linear range of the $C_T - J$ curve, similarly to the thrust distributions that remain the same over a large part of the linear thrust curve. However, close to $C_T = 0$, the profile shows clearly a different behaviour due to an adapted load distribution, as explained in the previous section. Even though for a small positive net thrust ($C_T = 0.03$ for this case), the inboard part of the blade could lead to a deficit in total pressure, meaning it extracts momentum from the freestream flow. As the radial load distribution is not constant for all operating

conditions, the integral thrust coefficient does not directly indicate the state of the local slipstream; it only represents the average increase.

As was concluded in Section 2.1.2, the axial velocity reaches its maximum already at $x/R_p \approx 4$. However, in Fig. 2.12b it is shown that the largest change is already reached around $x/R_p = 3$ for this radial station. This is a consequence of several effects. First, the contraction of the nacelle for $x/R_p > 3$ limits u/V_∞ to increase further. Second, due to the larger suction upstream of the disk, the slipstream development is also slightly more upstream than for an actuator disk. Finally, it is also the result of dissipation in the shear layer of the slipstream that gradually decelerates the slipstream to V_∞ again. Figure 2.13 also shows that downstream of the nacelle, there is a clear redistribution of the dynamic pressure, leading to a lower velocity gradient at the edge of the slipstream. An aerodynamic surface (far) downstream of the propeller therefore also experiences a lower dynamic pressure than would be predicted with the idealized actuator disk model.
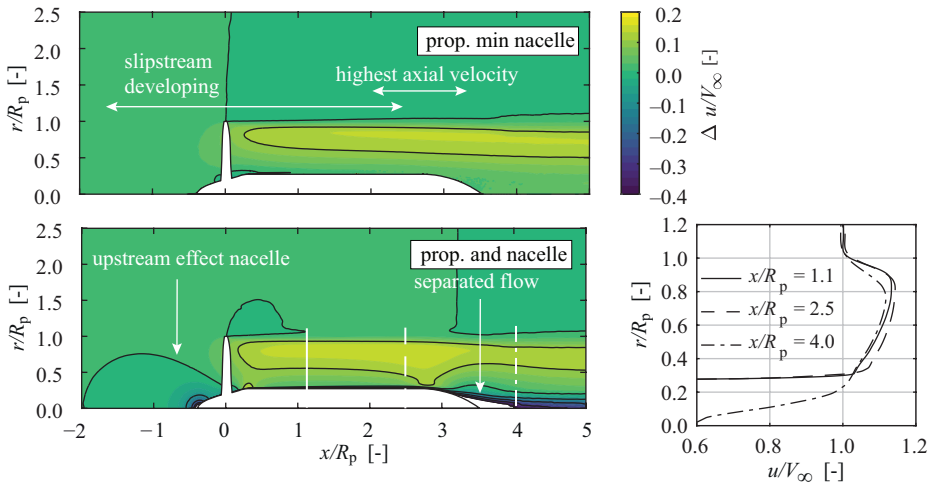
Figure 2.13: Time-averaged axial velocity flowfield to show the radial extent of the propeller influence and the relevance of the nacelle. Conditions: $J = 1.8$, $\beta_{0.7R_p} = 45$ deg, $C_T = 0.24$.

The development of the swirl angle is an important factor for propeller–airframe interaction. Although the swirl velocity may be constant, the swirl angle also depends on the axial velocity. The associated swirl for the particular example case is plotted in Fig. 2.14a. As expected, the swirl is confined to the slipstream only. Contrary to the axial velocity, the largest swirl occurs at around $r/R_p = 0.6$. From Fig. 2.14b it can be seen that the swirl angle reduces only slightly compared to the distribution just downstream the disk. Also its shape remains approximately constant. The largest deviation occurs when the nacelle is contracting. Since angular momentum needs to be conserved, the swirl velocity increases due to the tapered nacelle. This not only results in a significant swirl and high swirl angle on the centerline (in particular as the separated flow from the nacelle has a low axial component), it also causes the static pressure to reduce, shown in Fig. 2.12a.

In Fig. 2.14c it is shown that the (normalized) shape of the swirl distribution changes
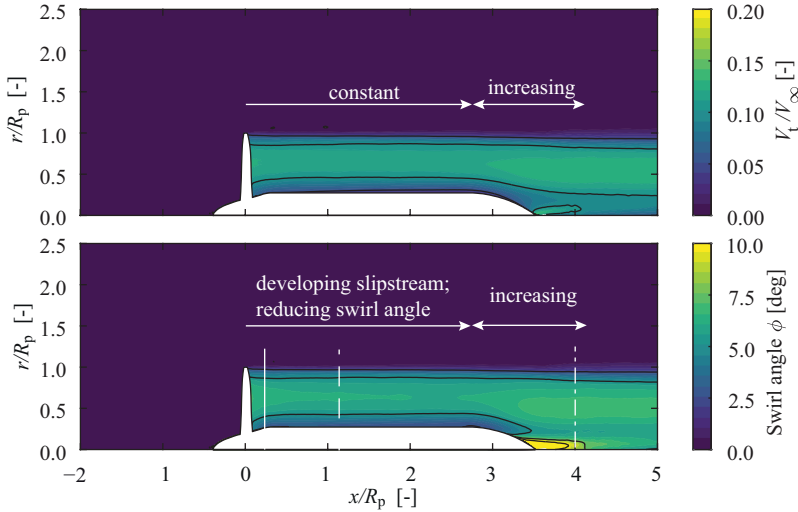
(a) Development of swirl and swirl angle. Note the effect of a finite nacelle length. Conditions: $J = 1.8$, $\beta_{0.7R_\mathrm{p}} = 45$ deg, $C_T = 0.24$.
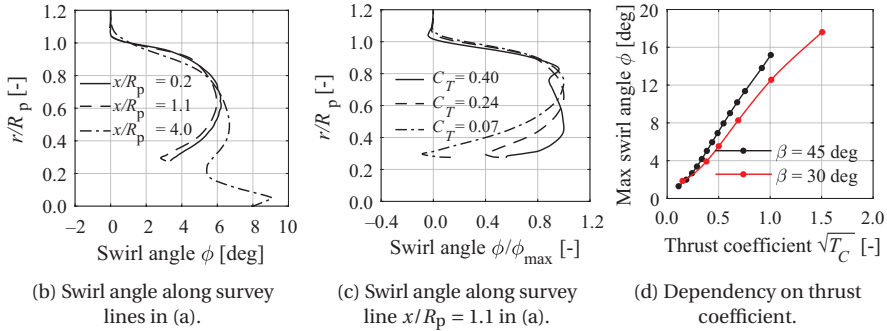
(b) Swirl angle along survey lines in (a).

(c) Swirl angle along survey line $x/R_\mathrm{p} = 1.1$ in (a).

(d) Dependency on thrust coefficient.

Figure 2.14: Time-averaged tangential velocity flowfield. Full-blade CFD data for the XPROP propeller (Section 3.4).

significantly if the thrust is low or high. In the former case, as was observed from the loading distributions in the previous sections, the swirl near the hub becomes negative, and the swirl is shifted towards the tip. For high thrust conditions ($C_T = 0.4$), the figure shows the opposite; the swirl is more concentrated towards the hub as the load is shifted towards the root.

The maximum value of the swirl angle in the slipstream, Fig. 2.14d, is proportional to $\sqrt{T_C}$. Its slope is only marginally different for two blade angles, each with a quite different $\eta - T_C$ curve (Fig. 2.8b). The reason for this is to be sought in the distribution of swirl. The drop in efficiency for $\beta_{0.7R_\mathrm{p}} = 45$ deg is primarily due to stall on the outboard part of the blade. This reduces the T_C, but at the same time the induced swirl around $r/R_\mathrm{p} = 0.5$ is maintained. In other words, if the efficiency curve would be the same, the

two curves in Fig. 2.14d would collapse to a single curve. In take-off and climb conditions with T_C ranging between 1 and 2 typically (Table 2.2), swirl angles well over 10 deg are to be expected. The property of the predictable maximum swirl for a given propeller is very useful in case the (maximum) swirl angle is relevant for propeller–airframe interaction. An example of such case is when the propeller causes local flow separation as the maximum angle of attack to the wing sections is surpassed, e.g. observed in [107, 108]

As already shown in Section 2.1.2, the radial component is limited to the region near the propeller tip. For the case shown in Fig. 2.15, with a thrust coefficient representative for cruise conditions, it becomes clear that the nacelle induces a radial component of nearly an order of magnitude larger than the propeller. Within $\pm R_p$ this propeller induced component leads to a negative flow angle arctan V_r/V_a of maximum -3 deg. Outside this tip region, the influence vanishes quickly. For cruise conditions, the radial velocity component is only of interest in the case where other propellers or airframe components are in close proximity to the propeller tip, for example for an array of distributed propellers or over-the-wing propellers.
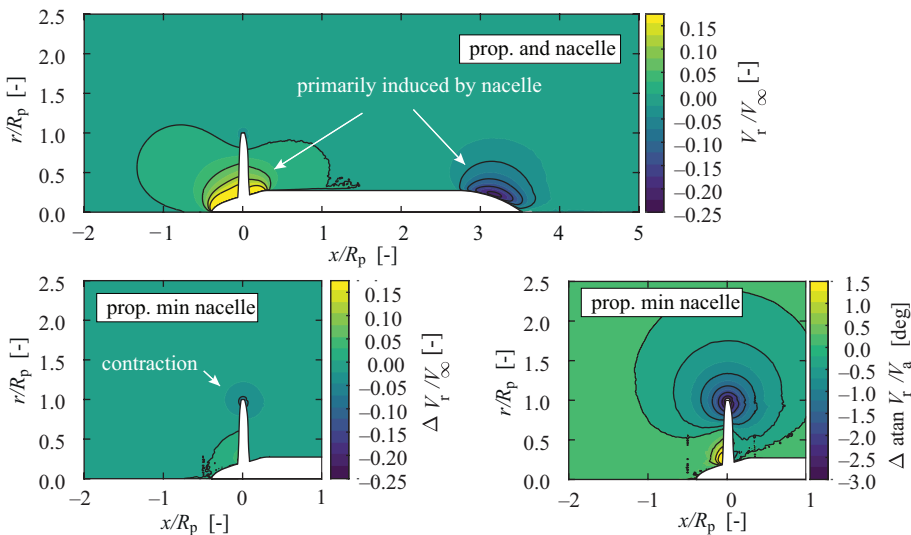
Figure 2.15: Time-averaged radial velocity flowfield to show the radial component of the velocity field in a typical cruise setting is primarily induced by the minimum-body nacelle. Full-blade CFD data for the XPROP propeller (Section 3.4). Conditions: $J = 1.8$, $\beta_{0.7R_p} = 45$ deg, $C_T = 0.24$.

2.3.2. SPINNER AND NACELLE FORCES

The flowfield induced by the rotating propeller blades also changes the forces on the spinner and nacelle, as schematically shown in Fig. 2.16a. The low pressure field that acts on the spinner geometry results in a net thrust force. Although it is a relatively small component compared to the propeller thrust (Fig. 2.16b), it should not be neglected. Since it depends directly on the pressure jump, it is nearly a constant fraction of the propeller thrust coefficient, in this case 1%. At low thrust coefficients ($T_C < 0.2$), the fraction

is higher, since at $T_C = 0$, the rotating motion of the spinner in combination with the no-slip boundary condition induces a swirl, and therefore a lower static pressure. Contrary to the added thrust on the spinner, the nacelle drag increases. In case the nacelle radius is still increasing behind the propeller disk, the higher static pressure behind the propeller acts as a bouyancy force on that part, as schematically shown in Fig. 2.16a. Subsequently, the higher dynamic pressure in the slipstream increases the wall shear on the straight part of the nacelle, while the higher swirl (Fig. 2.14) leads to primary a suction force on the aft cone, which is found to be the dominant part. However, it is noted that the shape of the cone highly affects the magnitude of the added drag [109]. Overall, the spinner and nacelle combination increase the drag, equivalent to approximately 3% of the propeller thrust.
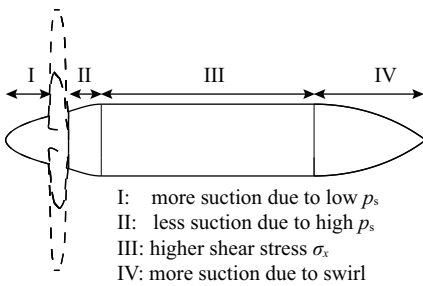
(a) Schematic of the dominating change in forces.
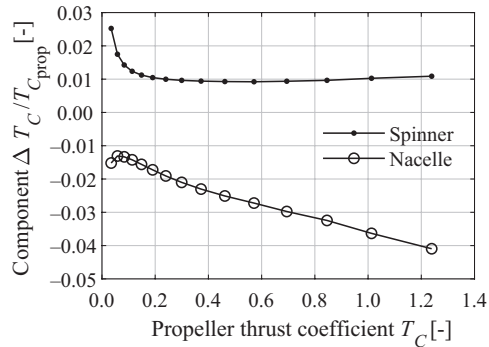
(b) Computed forces change in spinner and nacelle forces. Reference case has a non-rotating spinner. Conditions: $\beta_{0.7R_p} = 45$ deg, $V_\infty = 40$ m/s.

Figure 2.16: Change in the forces on the spinner and nacelle induced by the propeller.

2.3.3. TIME-DEPENDENT FLOWFIELDS

In the previous section, the time-averaged flowfield has been discussed. A finite number of blades introduces a flowfield that is periodic but not axisymmetric. The fluctuations around the time-averaged value of velocities, the pressure, and the flow angle are the source of vibrations on airframe components that are in close proximity to the slipstream. However, the magnitude is not the only indicator for the unsteady aerodynamic interaction. As the flowfield is highly three-dimensional, some regions may exhibit large fluctuations of a certain flow quantity, while the direction of these have no or limited impact on the airframe.

The dependency on various flow quantities is schematically shown in Fig. 2.17 for a number of typical locations and orientations of an aerodynamic surface relative to the slipstream. For example, variations in the swirl angle component are only relevant if an aerodynamic surface is in the slipstream and reasonably close to the propeller rotation axis. On the other hand, the radial component is only important for surfaces that are close to the propeller tip. The extent to which dynamic pressure fluctuations could be

experienced by the airframe, depends on the axial and radial distance to the disk.

Fluctuations in flow flowfield experienced by airframe	Typical locations of airframe components relative to the propeller				
Flow angle atan $\frac{V_r}{V_a}$	+ +	— —	— —	+ +	— —
Swirl angle	— —	+ +	— —	— —	— —
Dynamic pressure	+ +	+ +	+	+ +	+
Static pressure	+ +	+ +	+	+ +	+
Part of slipstream of interest	downstream	downstream	upstream	outside	outside

Figure 2.17: Expected dependency of unsteady airframe loads on the fluctuations of flow quantities.

Besides the orientation and magnitude, also a distinction can be made in terms of time and length scales. Flow structures that are time dependent and have a time-scale equal to the blade-passing frequency $BPF = nB$ include:

- Propeller tip and hub vortices

- Blade wakes

- Induced velocity field outside the cores of the tip and hub vortices

Within the viscous region of the blade wakes, increased levels of turbulence have been measured by e.g. Ref. [110]. These have significantly smaller time and length scales compared to the propeller induced unsteady flowfield. It is known from unsteady airfoil theory [111] that the smaller the length scale relative to the airfoil chord, the lower the unsteady loads on solid boundaries that are subject to this time-dependent inflow. For example, an angle of attack in the form of a pulse function with a short duration will lead to a negligible change in lift coefficient, while if the length scale is much larger than the chord length, the lift will approach the steady-state solution. Hence, the regions where turbulence is concentrated primarily affect the state of the boundary layer that forms on a surface in the slipstream and not significantly affect lift. Therefore, of interest here are the unsteady flowfield quantities at the blade-passing frequency.

In Ref. [94] it is shown that the tip vortex region introduces the largest pressure fluctuations on an aerodynamic surface that is submerged in the slipstream. Although it cannot be concluded that also the largest unsteady loads are to be found in the vortex impingement region, it is interesting to determine its development in downstream direction. The development of this vortex is depicted in Fig. 2.18, shown by an isosurface of vorticity from CFD simulations (Section 3.4) in Fig. 2.18a, and numerical values from experimental data (Section 3.3) in Fig. 2.18b. The orientation of the helical vortex remains approximately constant as the induced velocities on the mean remain approximately zero at the slipstream edge. The strength of the tip vortex is maximal just downstream

2

(a) Isosurface of vorticity magnitude, full-blade CFD results of the XPROP.

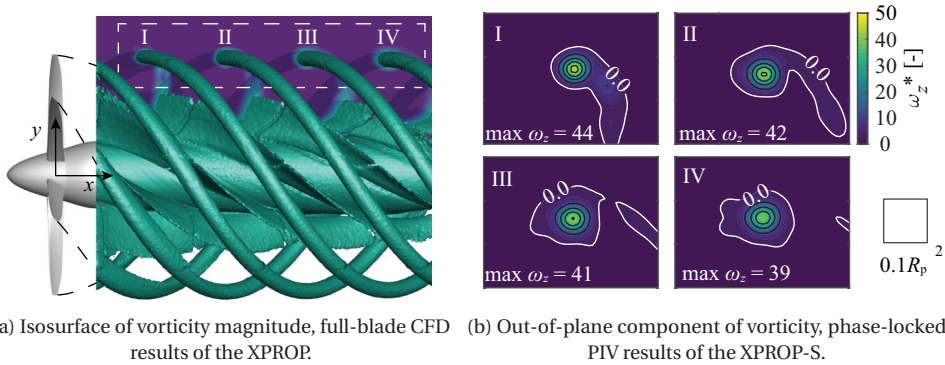(b) Out-of-plane component of vorticity, phase-locked PIV results of the XPROP-S.

Figure 2.18: Development of the propeller tip vortex in downstream direction. Phenomena that can be observed: reduction of the peak vorticity, diffusion of the vortex, roll-up process into a single vortex.

of the propeller. Further downstream, the vortex diffuses and dissipates due to viscosity. The tangential component of vorticity in the tip region, shown in Fig. 2.18b, indeed shows that around half a radius downstream the propeller the vortex still rolls up (vortex I), while three times the radius downstream a single vortex can be distinguished (vortex IV). Even further downstream, it is clear that its magnitude is reduced and it has spread in spatial direction due to diffusion. The measured flowfield indicates that the peak value of vortex IV is reduced by approximately 15%. The vortex core radius is approximately 10% of the propeller radius, while its effect on the velocity field reaches well beyond the vortex core.

Figure 2.19 shows the associated instantaneous flowfield measured using particle image velocimetry (PIV). The blade wakes are clearly visible as sharp reduction in axial velocity. In the hub region, these are the major unsteady contribution, while in the region of highest loading, the wake is thin, and the propeller induced flowfield can be described by potential flow is dominating. The figure also shows that just outside the slipstream, the axial velocity varies significantly, again as a consequence of the tip vortices. Clearly, the largest gradients in the flowfield are introduced by the tip vortices, with fluctuations of over 50% of the freestream velocity. The reduced frequency, i.e. the degree of unsteadiness in the flow, at which these flow quantities vary over a revolution also impacts the response of a submerged body [112]. The regions in which the fluctuation is concentrated in spatial direction, lead to sudden changes inflowfield. These are found in the regions with high gradients, i.e. in the vicinity of the tip-vortex region and the blade-wakes.

It is clear that the fluctuations in flowfield quantities vary significantly in radial direction, while the dependency on the axial location is limited. Figure 2.20 depicts the fluctuations around the mean of several relevant flow quantities at a distance of $x/R_p = 1.1$ downstream the rotation plane, for a cruise condition. The total pressure varies approximately ±10% around its mean value from the hub up to the highest loaded region at $r/R_p = 0.85$. This is not only due to the added momentum; it also entails the deficit in total pressure due to the blade wakes. Outside the slipstream, the flow locally experi-
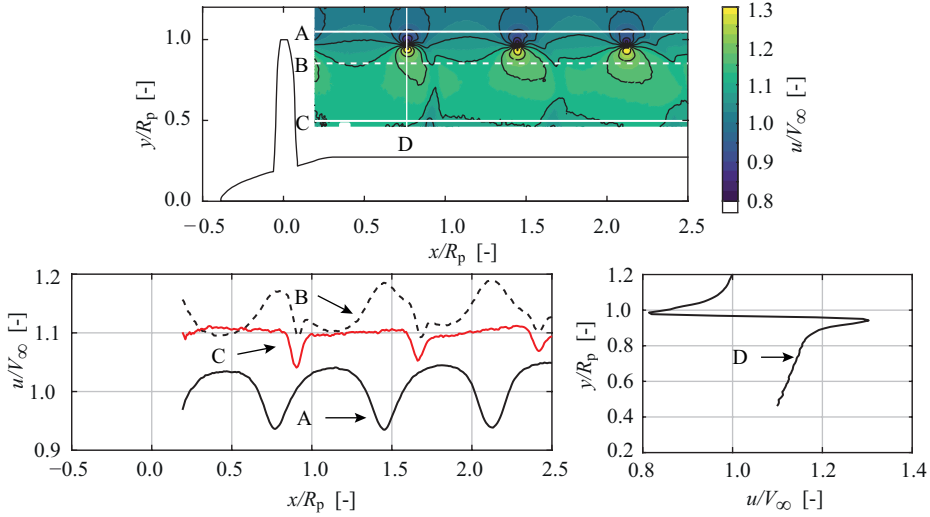
Figure 2.19: Experimental results of an instantaneous flowfield to show the strong variation of the velocity gradients in the slipstream. Survey lines A, B, and D indicate the effect of the tip vortex, while C shows the wake profiles. XPROP propeller with $J = 1.8$, $\beta_{0.7R_p} = 45$ deg, $C_T = 0.24$.

ences a strong gradient introduced by the tip vortices, leading to strong fluctuations of C_{p_t}. The largest peak-to-peak fluctuations span around 10% of the radius, coinciding with the radius of the vortex core. It is noted that the strength of the tip vortices reduces with increasing number of blades if the disk loading is maintained, and with that, the magnitude of unsteady flow.

(a) Total pressure

(b) Swirl angle

(c) Angle of attack
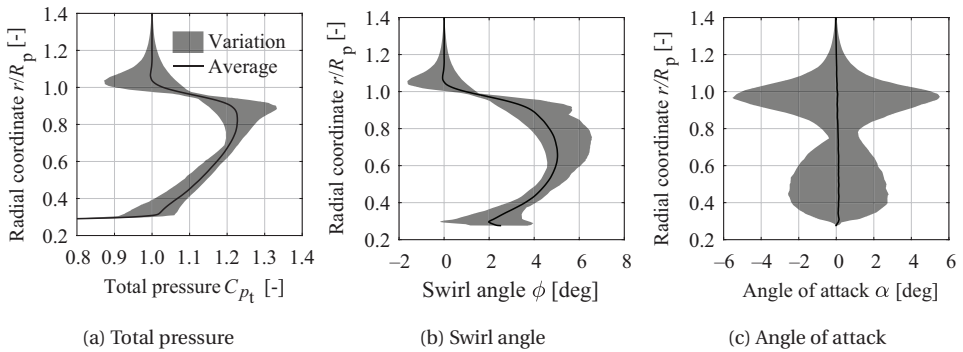
Figure 2.20: Mean and variation of slipstream quantities at $1.1R_p$ downstream the propeller. Full-blade CFD data for the XPROP propeller (Section 3.4). Conditions: $J = 1.8$, $\beta_{0.7R_p} = 45$ deg, $C_T = 0.24$.

The fluctuations around the mean swirl angle (Fig. 2.20b) are of the order of 0.5 to 1.0 deg for a cruise condition. The fact that the fluctuations are not symmetric around the mean is the consequence of the blade wakes, that consistently increase the swirl an-

gle when they move past the survey location. This is also visible by the nonsymmetric variations around C_{p_t}, indicating larger reductions than increments. It is noted that the swirl angle is influenced up to $r/R_p = 1.3$, similarly to the total pressure perturbations. At exactly the slipstream edge, i.e. the path of the tip vortices cores, the swirl induced by the tip vortex remains zero. Only for r not equal to slipstream radius there is a tangential velocity induced. To the contrary, the radial velocity is alternating from positive to negative along the slipstream edge. Therefore, the local angle of attack (defined as $\arctan V_r/V_a$) is fluctuating symmetrically around the mean (that is approximately zero). In this case fluctuations of up to ± 6 deg can be observed. This flow angle is not confined to the tip only, also for $r/R_p < 0.8$ this angle varies significantly. This is due to the radial velocity component on each side of the vortex sheets that move in downstream direction.

Finally, the root-mean-square values of the most important flow quantities are depicted in Fig. 2.21 to illustrate the magnitude of the fluctuations. Again, turbulence levels are not included herein. The purpose of the figure is to show that the extent to which the propeller has an effect upstream of the disk is very limited; the unsteady flowfield upstream is limited to approximately half a radius. The swirl angle, axial velocity, and static pressure resemble the load distribution along the blades. In line with the observations in Fig. 2.20, outside the slipstream the flow quickly approaches a steady condition, and its pressure and velocity field is dictated by the time-average effect of the slipstream. It is also noted that the static pressure inside the slipstream rapidly decreases and is only present in the path of the tip vortices.
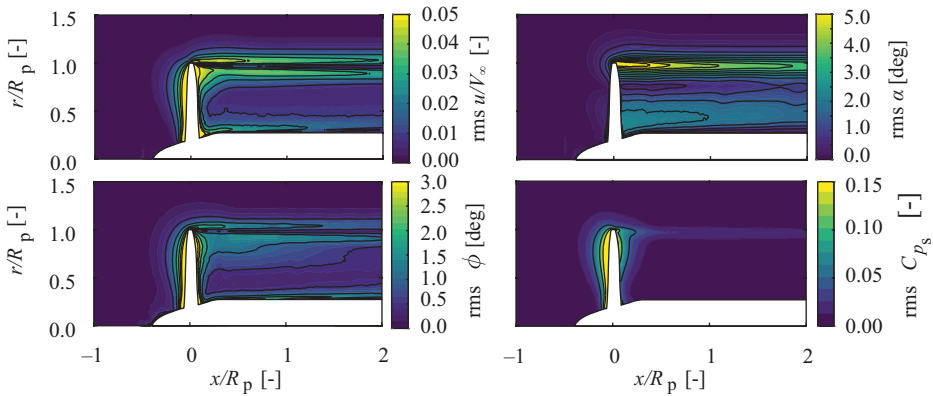
Figure 2.21: Root-mean-square values of the most important flow quantities that introduce unsteady loads and pressure fluctuations on the airframe and cause strong gradients in the flowfield. Full-blade CFD data for the XPROP propeller (Section 3.4). Conditions: $J = 1.8$, $\beta_{0.7R_p} = 45$ deg, $C_T = 0.24$.

2.4. EFFECTS DUE TO NONZERO ANGLE OF ATTACK

When the propeller inflow is no longer aligned with the propeller rotation axis, the effective angle of attack and velocity (indicated in Fig. 2.2) experienced by the blade sections become a function of azimuthal position. It is well known that in such case, the propeller generates in-plane forces and generally its thrust and efficiency increase slightly

[60, 92, 113]. Furthermore, both the slipstream dynamic pressure and local swirl angle depend on angle of attack as well [93]. In this section, the propeller loading and integral forces are discussed. The investigation of the slipstream is investigated in Section 8.2.1.

2.4.1. Propeller Forces

Figure 2.22a depicts the local change in advance ratio over the disk. The upgoing (retreating) blade experiences a higher advance ratio, leading to lower thrust, while for the downgoing blade the opposite is the case. Near the hub, the changes are largest primarily due to the relatively low Ωr. Secondly, the potential flow effect that the nacelle/spinner introduces is maximum near the hub. However, as the loading is low in this region, the absolute change of the blade forces is small as well. The same figure indicates that the largest change in thrust occurs around the same radial station at which the load is highest in case of uniform inflow. In the regions of high and low thrust, the torque is affected the same way. The consequence of the difference in torque on each side of the disk is a normal force, schematically shown in Fig. 2.22b, and has been quantified as a function of advance ratio, solidity, and thrust coefficient by e.g. Ref. [60]. The normal force coefficient C_{N_p} defined as:

$$C_{N_\mathrm{p}} = \frac{F_N}{\rho_\infty n^2 D_\mathrm{p}^4} \qquad (2.12)$$

and is positive, independent of rotation direction.

(a) Change in the inflow and thrust for $\alpha = 5$ deg, full-blade CFD data for the XPROP propeller (Section 3.4). Conditions: $J = 1.8$, $\beta_{0.7R_\mathrm{p}} = 45$ deg.

(b) Integral forces due to an angle of attack
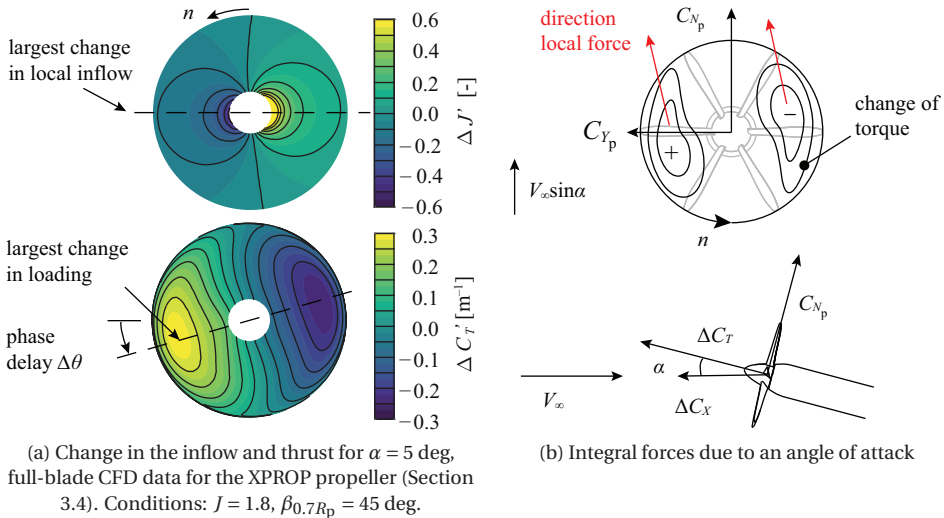
Figure 2.22: Effect of an angle of attack on the propeller load distribution that results in in-plane forces.

It can be observed that there is a distinct delay $\Delta\phi$ of the load increment and decrement relative to the location where the largest change in inflow occurs. This delay is equivalent to the delay of the forces on an airfoil that experiences an unsteady inflow

[111] and depends on the reduced frequency ($k = \frac{\omega c}{2V}$) of the inflow to the blade section with a chord length c. Since the inflow to the blade is sinusoidal, it is the blade chord length that determines the unsteady response. Therefore, the phase delay depends on the slenderness of the blades, with high slenderness resulting in a smaller phase delay. Since the slenderness ratio does not vary significantly between modern propellers, a typical phase delay of 15 deg can be expected for cruise conditions. The phase delay causes a sideforce, C_Y, defined as:

$$C_Y = \frac{F_Y}{\rho_\infty n^2 D_{\mathrm{p}}^4} \tag{2.13}$$

which can be approximated by $C_Y \approx C_N \sin \Delta\phi \approx 0.25 C_N$. The side force coefficient *is* dependent on rotation direction. Fig. 2.23 depicts a typical evolution of the blade forces over a full revolution, highlighting the phase shift and the change of the mean value.
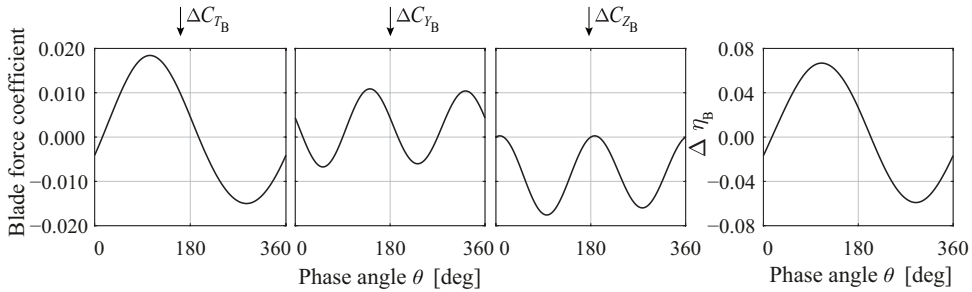
Figure 2.23: Unsteady blade forces over a full revolution, $J = 1.8$, $\alpha = 5$ deg. Full-blade CFD results.

Typical numerical values of the integral forces are plotted in Fig. 2.24. The figure indicates that for a cruise setting, a significant normal force is created relative to the thrust force. The in-plane forces are linear with angle of attack, as they are only a function of the difference in loading between the two halves of the disk, which is proportional to the angle of attack. In fact, the gradient C_{N_α} is positive such that the propeller has a destabilizing contribution on aircraft level, if it is located ahead of the center of gravity. The angle of attack also increases the thrust slightly, primarily due to a reduced axial inflow, approximately $\frac{\Delta u}{V_\infty} = 1 - \cos \alpha$, that translates to a lower advance ratio. Besides that, the axial inflow is nonlinear, the $T_C - J$ and $Q_C - J$ curves are proportional to J^{-2}, therefore the $C_T - \alpha$ and $C_Q - \alpha$ curves are nonlinear as well.

Besides a higher thrust, also the torque is affected, but to a lesser extent. This is because the effective inflow velocity is reduced, leading to a higher propeller efficiency for a given V_∞. This is indeed observable in Fig. 2.24b. While the efficiency increases, the efficiency defined along the direction of flight, $\eta_x = \frac{T_x V_\infty}{P_s}$, is reducing with angle of attack. This is caused by the normal force that has a $C_N \sin \alpha$ component in opposite direction to flight. However, the net effect is quite moderate and efficiency in the direction of flight is nearly independent of angle of attack. This is a striking result, as the propeller does generate a larger resultant force compared to $\alpha = 0$, while the power remains nearly the same. A small positive inclination angle may therefore be beneficial on aircraft level.

(a) Integral forces for cruise conditions ($J = 1.8$). For readability, C_N is scaled.

(b) Change in propeller efficiency, same conditions as in (a).

(c) Out-of-plane force gradients.
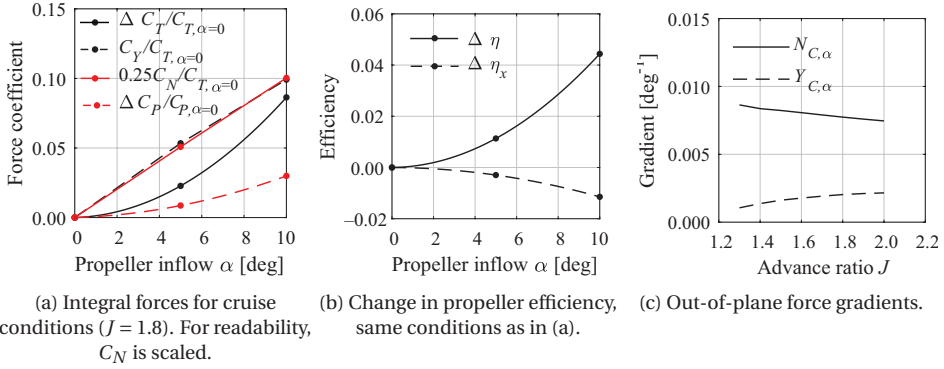
Figure 2.24: Effect of an angle of attack on the integral propeller forces, $\beta_{0.7R_\mathrm{p}} = 45$ deg. Full-blade CFD data for the XPROP propeller (Section 3.4).

The dependency of the propeller forces at a single advance ratio gives insight in the contribution of the propeller to aircraft stability in one condition. If the advance ratio is lowered, the relative impact of an angle of attack is lowered as well. The relative change in the force coefficients C_T, C_Y, and C_N therefore reduces with lower J. From an aircraft perspective, it is therefore more convenient to define in-plane force coefficients nondimensionalized with $q_\infty S_\mathrm{p}$, such that N_C and Y_C are similar to T_C:

$$N_C = \frac{F_N}{q_\infty S_\mathrm{p}}$$
$$Y_C = \frac{F_Y}{q_\infty S_\mathrm{p}} \tag{2.14}$$

With such definition, the absolute change in propeller forces become apparent. The gradient of the in-plane forces for a range of advance ratios is plotted in Fig. 2.24c. The normal force gradient slightly increases with lower J, because the $\Delta\alpha$ at by the blade sections is encountered with a higher effective velocity compared to the condition of a low J; the normal force increases and so is $N_{C,\alpha}$. It can therefore be concluded that the (de)stabilizing contribution of the propeller on aircraft level is slightly increasing with thrust, but at zero thrust, there is still a finite contribution. The opposite occurs for the side-force. This is due to the dependency of the phase delay $\Delta\phi$, which is reducing with lower J and tends to 0 at $J = 0$.

2.5. Scaling Effects

If one is interested in the propeller installation effect on large transport aircraft, the effect of *scale* on the results needs to be understood. It is common that propeller–airframe aerodynamic interaction studies rely on experimentally obtained data of subscale aircraft and propeller models. Also numerical studies frequently perform analyses at the same scale at which validation data is available, i.e. subscale as well. Only a handful of datasets of propeller performance are available that were obtained at high subsonic Mach numbers, e.g. Ref. [24]. A relevant question is, to what extent can propellers be modelled or experimentally tested at small scale, such that conclusions (on trends) at full scale still hold? If the effect of scaling is known, it may not be required to match full-scale conditions in all aspects in order to still produce relevant results.

To address the topic of scaling, first the flowfield quantities and forces that are relevant for the aerodynamic interaction should be identified. These include (from e.g. Refs. [14, 37]):

- Relative increase in dynamic pressure inside the slipstream

- Mach number in the slipstream

- Slipstream contraction, in particular to match the flowfield outside of the slipstream

- Characteristics of the unsteady flowfield, i.e. the reduced frequency, Strouhal number ($St = \frac{fL}{V}$), and relative magnitude of the time-dependent flowfield quantities

- The flow angles inside the slipstream, i.e. the shape of the slipstream in radial direction

- Forces on the propeller relative to the airframe forces

The relevant parameters are given in Table 2.1, indicating what coefficient need to be met to obtain similitude between different scales. The blade geometry in this case refers in particular to the planform, which influences the in-plane force gradients. In addition to the values of the performance related coefficients, Mach number plays a role in the response of the airframe to an unsteady inflow [112]. Reynolds number directly influences the momentum loss in the boundary layer and blade wakes, and therefore affects the swirl velocity and the dynamic pressure.

Table 2.1: Requirement of propeller operating condition and geometry to meet various parameters that are necessary to obtain same level of similitude. A ($\checkmark$) indicates the dependency is weak, a $\times$ indicates a negligible dependency. Marks are based on the theory presented in this chapter.

	J	T_C	Q_C	B	Blade planform	M	Re
Dynamic pressure, $\frac{q_{ss}(r)}{q_\infty}$	$\checkmark$	$\checkmark$	($\checkmark$)	($\checkmark$)	($\checkmark$)	($\checkmark$)	($\checkmark$)
Swirl angle, $\phi(r)$	$\checkmark$	$\checkmark$	$\checkmark$	($\checkmark$)	($\checkmark$)	($\checkmark$)	($\checkmark$)
Flow angle, $\arctan \frac{V_t}{V_a}$	$\times$	$\checkmark$	$\times$	$\times$	$\times$	($\checkmark$)	$\times$
Unsteady forces of lifting surface	$\checkmark$	$\checkmark$	$\checkmark$	$\checkmark$	$\checkmark$	$\checkmark$	$\checkmark$
Propeller in-plane force gradients	$\checkmark$	($\checkmark$)	$\times$	$\checkmark$	$\checkmark$	$\times$	$\times$
Propeller forces relative to airframe	$\checkmark$	$\checkmark$	$\checkmark$	$\times$	$\times$	$\times$	$\checkmark$

From Table 2.1 is becomes clear that the advance ratio is a parameter that should be properly scaled if unsteady forces and force gradients are to be predicted with sub-scale models. This is generally not an issue for a subscale (experimental) setup. If the aerodynamic analyses of a subscale propeller are performed at ambient conditions, the freestream Mach number is often lower, and with that the tip Mach number if advance ratio is maintained. The smaller blade chord also leads to lower Reynolds number. Besides, experimental simulation often comes with practical limitations, such as a limited number of blades and the absence of a variable pitch propeller due to manufacturing constraints. The question arises whether certain conditions can be matched such that either the time-averaged, time-dependent flowfield, and/or the propeller forces are similar to full scale.

An overview of typical conditions of a full-scale propeller for transport aircraft is summarized in Table 2.2, based on various sources. The indicated ranges depend on cruise Mach number, number of propellers, and mission requirements. For example, design studies (e.g. Refs. [29, 86, 99]) discuss that for high cruise Mach numbers of $M = 0.7$, the propeller diameter is restricted, which in its turn leads to higher thrust coefficients, larger swirl angles, lower efficiency, and higher advance ratio. The aircraft design, such as the choice of a high or low wing, also impacts the maximum propeller diameter. These values therefore should only be used as indicative.

Table 2.2: Typical propeller operating conditions and planform for regional turbo-prop aircraft with variable pitch propellers. Based on Refs. [19, 22, 29, 31, 82, 86, 99, 114].

	Geometry	Take-off	Climb	Cruise	Approach
Number of blades B	6-10	$--$	$--$	$--$	$--$
Blade pitch [deg]	$--$	20-30	30-45	45-60	<45
Thrust coefficient T_C	$--$	≥ 0.8	0.2-0.6	0.1-0.4	≈ 0
Propeller efficiency η_p	$--$	≥ 0.8	≥ 0.8	≥ 0.8	≤ 0.6
Advance ratio J	$--$	<1.0	1.5-2.0	2.0-3.0	>3.0
Maximum swirl ϕ [deg]	$--$	10-20	10-12	4-6	≈ 0

The effect of a lower Reynolds number on the propeller performance has been identified by e.g. Refs. [115, 116]. The maximum efficiency is dramatically lowered in case of low Reynolds number conditions, a consequence of the large swirl at a given thrust setting. A lower Reynolds number on the blade section leads to a relatively thick boundary layer, earlier separation, and a nonlinear lift curve slope due to the formation of laminar separation bubbles. This has several implications: a lower two-dimensional lift curve slope, a lower zero-lift angle of attack for cambered airfoils, a more pronounced radial flow due to the centrifugal acceleration, and lower maximum two-dimensional lift coefficient. The affected section properties are also displayed in the flowfield, as the momentum thickness of the boundary layer is not matching the one of the full-scale propeller.

The effect of freestream velocity and therefore section Reynolds number on the propeller thrust curve is shown in Fig. 2.25a. The experimental $C_T - J$ curves are constructed from external balance measurements. Several observations can be made. First, the offset of the thrust curve is a direct consequence of the decambering effect from the blade sections. Secondly, the thrust curves at low V_∞ show a more erratic behaviour, expected to come from shifting transition location and laminar separation bubbles (confirmed by two-dimensional analysis of the airfoil sections in Section 4.2.1). By reducing J, two phenomena occur simultaneously. First, the angle of attack increases, and second, the Reynolds number increases. Provided that the lift curve slope and α_0 increase with Re, an *effective lift curve* of each airfoil section can be constructed as illustrated in Fig. 2.25b. This apparent curve has a relatively high slope.
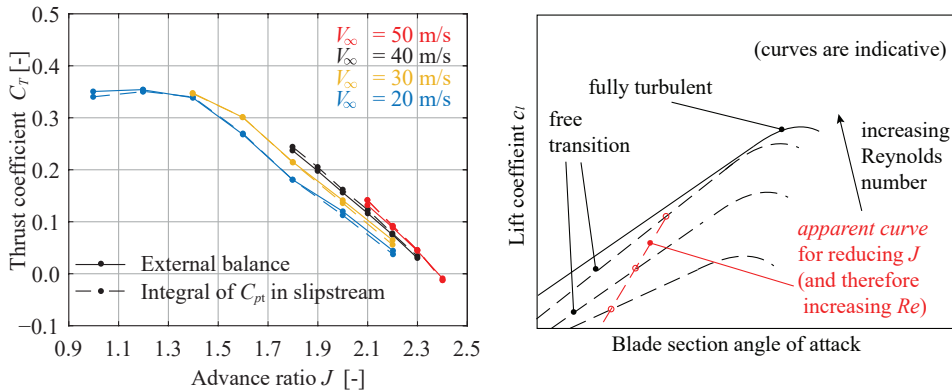
(a) Propeller thrust coefficient, experimental data of the XPROP propeller (Section 3.2).

(b) Illustration of apparent lift curve for a cambered blade section by varying J.

Figure 2.25: to Illustration of the effect of Reynolds number on propeller performance.

Besides the fact that the integral forces are dependent on the Reynolds number, so is the shape of the slipstream. This is in particularly observable in Fig. 2.26, which depicts an experimentally obtained slipstream profile for various advance ratios. As the advance ratio was varied by varying the rotational speed, the Reynolds number based on chord was significantly higher at low J. The total pressure in the slipstream shows an erratic distribution at high J, while the profile becomes more defined and consistent only at low

J conditions. In other words, the scaling of the load distribution with thrust coefficient, as was observed in Section 2.2.2, does not apply if the Reynolds number is significantly affecting the state of the boundary layer.
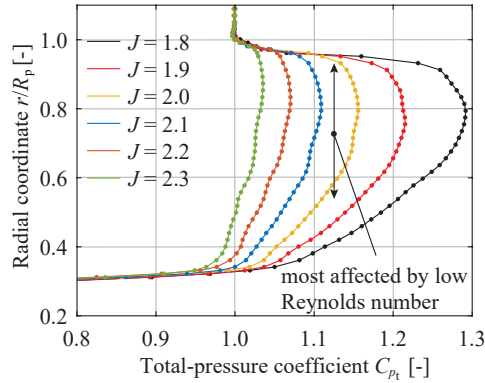
Figure 2.26: Slipstream of the XPROP propeller (Section 3.2) for various advance ratios by varying rotational speed, $V_\infty = 40$ m/s to illustrate of the effect of Reynolds number on propeller performance.

Although the $C_T - J$ is a nondimensional performance curve, it is shifted and the slope is increased when the helical tip Mach number becomes larger. This is primarily due to the effect of compressibility on the aerodynamic properties of the two-dimensional blade sections. At a given advance ratio, the thrust and torque coefficients are therefore increasing with M_{hel}. The consequence is that the total pressure and swirl angle in the slipstream are increasing accordingly, shown in Fig. 2.27a and Fig. 2.27b, respectively. Along the blade, in particular the outboard sections experience the effect of compressibility.

However, compared to the thrust distribution in Fig. 2.27c, the normalized thrust distribution in Fig. 2.27d indicates that there is only a minor effect on the shape of the radial distribution. It is mentioned that this would only apply if there is no significant shock-induced separation on the outboard part of the blade. In this case, even though the blades are unswept, the effect of a supersonic tip does not significantly affect the thrust distribution. This leads to the conclusion that the same slipstream shape can be obtained if J and C_T are matched. This would be possible by slightly increasing the blade pitch for low Mach number conditions. For the XPROP propeller at the operating condition close to maximum efficiency, a linear dependency of T_C on Mach number was found: $T_C(M_{\mathrm{hel}}) = T_{C,M_{\mathrm{hel}}=0} + 0.037 M_{\mathrm{hel}}$ for $M_{\mathrm{hel}} < 0.8$.

2

(a) Total-pressure distribution

(b) Swirl angle distribution

(c) Sectional thrust

(d) Sectional thrust normalized with integral value
to demonstrate that the *shape* of the distribution
is not affected by Mach number
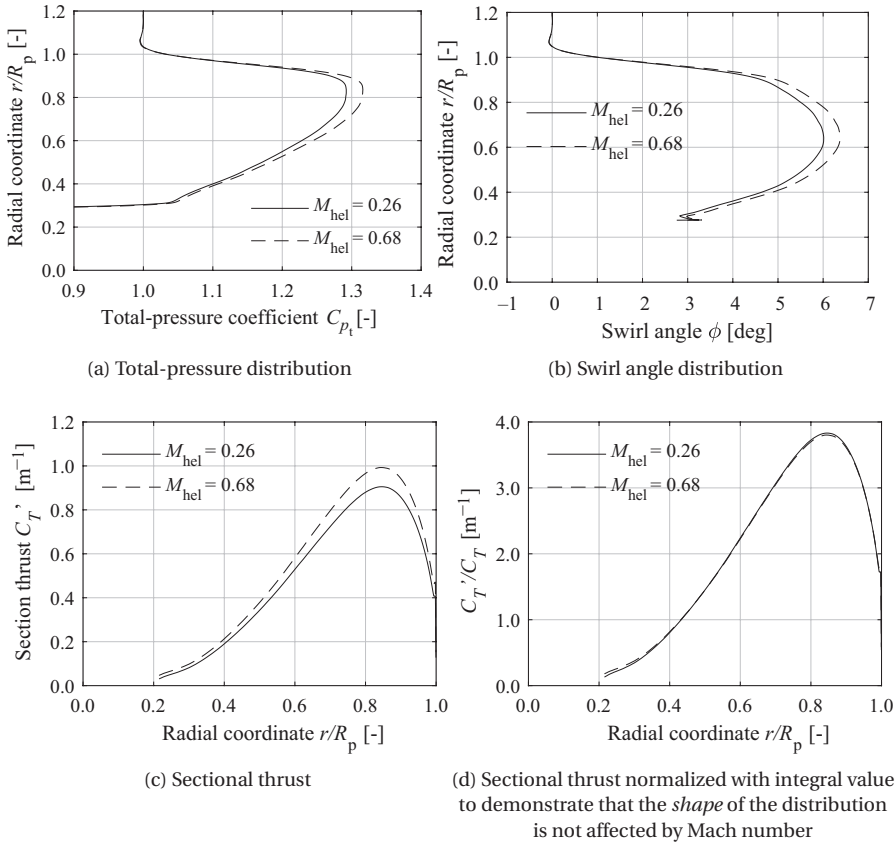
Figure 2.27: Illustration of the effect of Mach number on the propeller forces and slipstream shape. Propeller coefficients and advance ratio representative for cruise phase. Full-blade CFD results of the XPROP propeller.

The net effect of Mach number on efficiency is depicted in Fig. 2.28. Up to $M_{hel} = 0.6$, the profile losses reduce with higher tip Mach number (linked to the higher Reynolds number), while at high subsonic Mach numbers, the efficiency starts to reduce due to compressibility losses in the tip region. However, the drop is quite moderate, in line with observations in Refs. [82, 117]. At higher thrust coefficients, these losses would occur at lower M_{hel}.
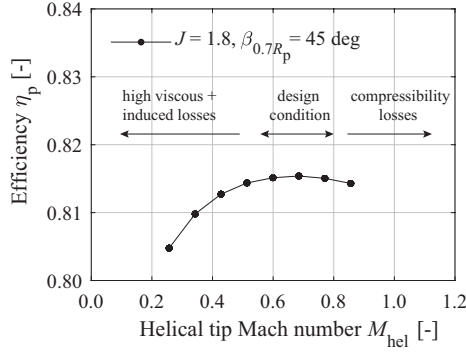
Figure 2.28: Illustration of effect of Mach number on the propeller efficiency for a constant blade pitch and advance ratio. The expected factors that affect the efficiency are annotated. Full-blade CFD results of the XPROP propeller.

Finally, it is common that full-scale propellers have variable pitch [72], such that the maximum in efficiency can be obtained in each flight condition (see Section 2.2). As analyses on subscale propellers require the Reynolds number and Mach number to be relatively low, which in their turn is shifting the performance curves, the blade pitch angle can be tuned to compensate for this. This is schematically shown in Fig. 2.29. A shift of the $C_T - J$ curve could be achieved by selecting a larger blade pitch angle. However, this has a consequence for the advance ratio of maximum efficiency. In Ref. [116] it is shown that the maximum efficiency is achieved at lower J for low Reynolds number conditions. This implies that, with a higher blade pitch, only the $C_T - J$ curve is shifted and the maximum efficiency is not achieved at the same J that belongs to the full-scale design. The maximal thrust coefficients of the scaled-down experimental setup are inherently lower because of the lower tip Mach number and lower Reynolds numbers of the blade sections. High thrust conditions are less suitable to predict with subscale models. Typical take-off conditions (see Table 2.2) are therefore impracticable to achieve when scaled models are used. On the other hand, climb, cruise, and approach conditions are less problematic, if the conditions and blade angle are selected accordingly.
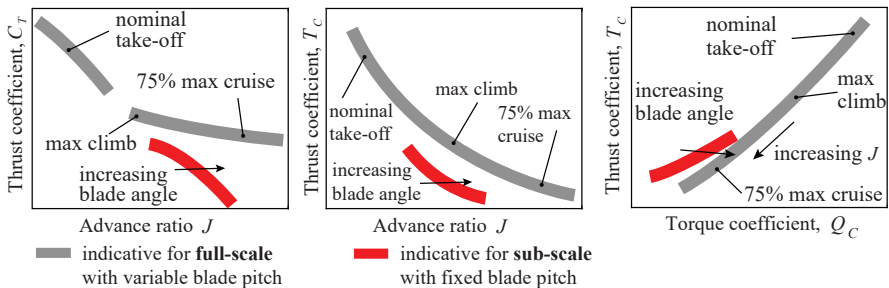

Figure 2.29: Illustration of typical performance curves of full-scale versus the wind-tunnel scale propellers. The typical phases of flight are annotated.

3

MODELS AND CFD METHODS

3.1. INTRODUCTION

The research questions in this dissertation are addressed by employing a variety of models and analyses methods. The selected cases represent aspects of the two configurations of interest: the leading-edge distributed propeller configuration and the configuration with propellers mounted to the horizontal tailplane. These are divided into subproblems with the goal to remove the influence of other airframe components. The advantage of the investigations on subsystems is that the findings are not configuration specific but instead can be used for a broader range of applications. The models range from relatively straightforward setups, to more complex setups where multiple interaction phenomena are present simultaneously. The goal of this chapter is to provide an overview of each setup. These are summarized in Table 3.1, where the increasing level of propulsion-integration effects is indicated with an arrow.
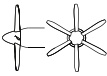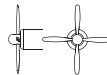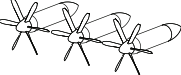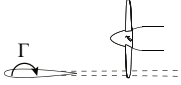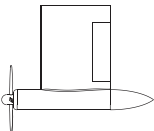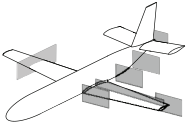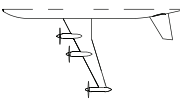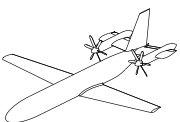
For all cases, propeller setups with an undisturbed inflow serve as the reference. For the propeller–airframe interaction studies, a distinction is made between the cases where primarily the propeller is affected, and the cases where in particular the airframe component is affected by the propeller slipstream. Finally, the analyses of a complete aircraft not only reveal the more complex aerodynamic interactions, but also put the findings into perspective. To this end, two reference aircraft have been used for the analyses of propeller installation effects on aircraft performance, stability, and control.

Both experimental and numerical analyses have been performed on nearly all cases, with only a few exceptions, as listed in Table 3.1. The following benefits of experimental methods have been employed herein:

- Flexibility to assess the complete flight envelope and to identify the regions of the envelope where the aerodynamic interaction is most profound at a relatively low cost.

Parts of this chapter have been published in Refs. [90, 118–120].

Table 3.1: Overview of setups, their objectives, and analysis methods.

3

Increasing level of propulsion integration effects

Setup	Objectives/aspects of interest	Geometry	Analysis method	Chapter(s)
Isolated propellers	• validation data • reference condition • gradients of flowfields for $\alpha > 0$ conditions		experimental, CFD-full blade	Ch. 2-9
			experimental, CFD-full blade	Ch. 2, 4, 6
Distributed propellers	• unsteady interaction • propagation of interaction in downstream direction		CFD-full blade	Ch. 6
Wing–propeller model	• unsteady propeller loads • induced effect of wing on propeller	Γ	CFD-full blade experimental	Ch. 6
Propeller–tailplane model	• upstream effect on propeller • propeller–tip-vortex interaction • propagation of interaction downstream		experimental, CFD-full blade, CFD-actuator disk	Ch. 6,8
Configuration study	• airframe-induced effect on propeller loads		CFD, engineering method	Ch. 7
Leading-edge distributed propellers	• propagation of interaction in downstream direction • stability and control characteristics • performance of leading-edge distributed propellers		CFD-actuator disk	Ch. 9
Tail-mounted propellers	• propagation of nonuniform flowfield in downstream direction • time-averaged and unsteady aircraft loads • stability&control characteristics		experimental, CFD-full blade	Ch. 8, 9

- The analyses of high-lift conditions and interaction phenomena that are driven by flow separation do not suffer from limitations of the turbulence models in predicting flow separation.

- Analyses of the interaction where large gradients of the flowfield are relevant, do not suffer from artificially introduced diffusion and dissipation.

On the other hand, numerical analyses compensate for some of the distinct disadvantages of experimental analyses, including:

- The complexity to determine forces on a component level.

- The difficulty to simulate isolated conditions due to the presence of support structures and wind-tunnel walls.

- The limited accessibility to the model for flowfield measurements due to obstruction by the model itself and by the wind-tunnel walls.

- The difficulty to characterize the full interaction with sufficient resolution.

- The limited flexibility to modify the geometry.

- Limitations of the wind-tunnel setups in terms of Mach number and Reynolds number.

- The limited ability to determine the state of all relevant flow quantities simultaneously.

- The introduction of measurement errors and uncertainties.

3.2. PROPELLER MODELS

Since the propeller plays a key role in the propeller–airframe interaction, the choices for the propeller geometries are based on several considerations. In particular, the performance characteristics are attempted to match the ones listed in Table 2.2. Although a large range of thrust coefficients is required to simulate cruise and climb conditions, the maximum thrust coefficient T_C is limited by the low Reynolds number. To still achieve moderately high T_C, the blade sections should have a relatively high maximum lift coefficient. This leads to lower limits on blade thickness, in particular for low Reynolds number conditions. Furthermore, the blade design should be such that it is close to minimum induced loss; this ensures a slipstream shape that is comparable to full-scale designs. Finally, availability of the geometry, the existence of previous studies using the same geometry, and manufacturability also have played a role in the selection.

The majority of the work presented in this dissertation relies on the use of the XPROP propeller; a six-bladed propeller with a suitable range of thrust coefficients, a high maximum efficiency, and a representative solidity of $\sigma = 0.29$. It is a propeller that is also extensively used in other studies, for example in Refs. [109, 116, 121, 122]. Its geometry is depicted in Figs. 3.1a and 3.1b. The ARA-D airfoil profiles are designed to operate at high lift coefficients [123] and the stall is gradual. This is an advantage as it leads to a consistent shape of the slipstream for a large range of advance ratios. The airfoils are stacked on the blade pitch axis, and because the chord is not constant, this leads to a slight forward-backward sweep when going from hub to tip. Two blade pitch settings at 70% of the radius are analyzed: $\beta_{0.7R_p} = 30$ deg and $\beta_{0.7R_p} = 45$ deg. The CAD geometry of the model is attached as Supplemental Data in Ref. [90].

Two variants of the XPROP are utilized. For the CFD simulations, a 50% scaled version of the original XPROP ($D_p = 0.4064$ m) is used, denoted as 'XPROP'. The only modification is the removal of the gap that exists near the hub, as shown in Fig. 3.1d. For the experimental model, the trailing edge region was slightly modified to maintain a minimum

(a) XPROP-S blade with airfoil sections.

(b) Pitch and chord distribution

(c) Difference in rear part of airfoils between XPROP and XPROP-S.

(d) Main dimensions of propeller and nacelle, XPROP. Dimensions in mm.
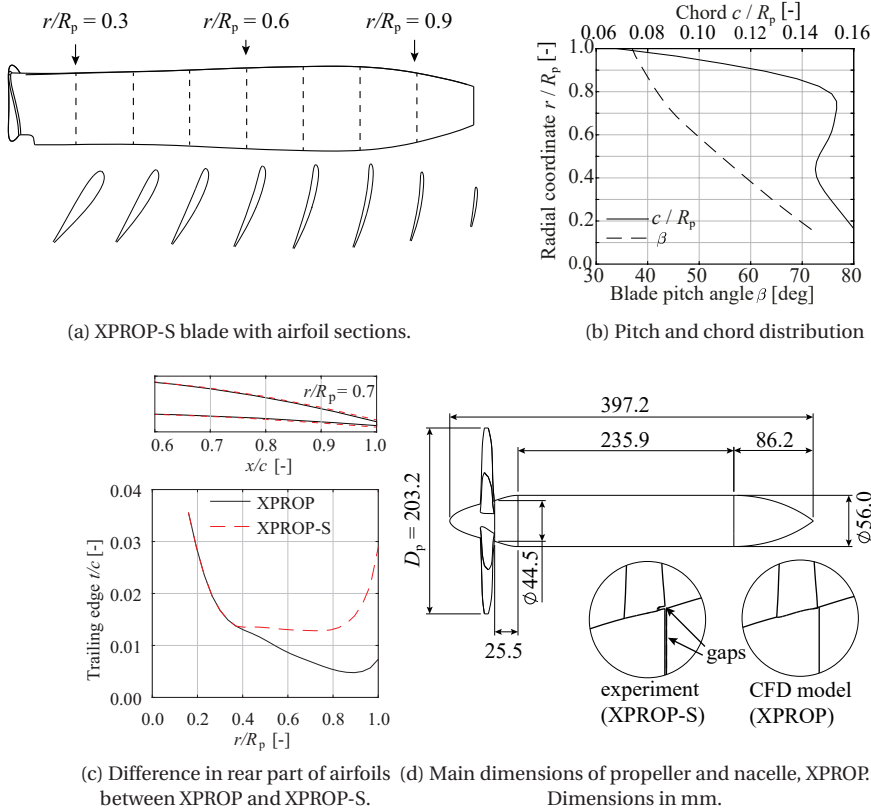
Figure 3.1: XPROP(-S) propeller geometries.

trailing edge thickness of 0.2 millimeter to comply with manufacturing constraints. The thickness of the last 30% of the blade chord was adapted for $r/R_\mathrm{p} > 0.4$, while the camber line was maintained, as shown in Fig. 3.1c. This is referred to as the 'XPROP-S'. The reason for the inconsistency was a matter of timing: most simulations were performed prior to the manufacturing of the experimental model. Yet, a two-dimensional analysis of the two airfoil profiles at $r/R_\mathrm{p} = 0.7$ indicates that the lift curve slope of the modified version reduced by less than 1% and zero-lift angle of attack increased by 0.05 deg. Although the value of c_{d_0} was increased with 40 %, since profile drag typically accounts only a few percent to the torque and even less to the thrust [91], this modification has no significant impact on the results. For clarity, Table 3.2 lists the different variants of the propeller.

Table 3.2: Different propellers and their notation used in this dissertation.

Notation	Method	Diameter	Hub	Trailing edge
XPROP	CFD	0.2032 m	without gap	original
XPROP-S	Experimental	0.2032 m	modified gap	modified
Beaver	Experimental & CFD	0.2370 m	original	original

For the propeller–tailplane study, a scale model of a rather dated propeller design that was mounted on the de Havilland DHC2 Beaver was used. This propeller is denoted as the 'Beaver propeller', of which an overview is provided in Fig. 3.2. The choice for this propeller was mainly based on the availability of the setup at the time when the experiment and the first numerical analyses were conducted. Also this propeller has been employed by various authors [37, 109, 116, 124, 125]. The four bladed propeller has a solidity of $\sigma = 0.20$ and features Clark-Y profiles and nearly circular root sections. The blades are set to a blade angle of 23.9 deg at 75% of the radius. Compared to the XPROP propeller, the lower solidity results in a lower normal force gradient and lower maximum thrust coefficients. Since structural rigidity constraints the section thickness-to-chord ratio, and the geometry in the hub region, its efficiency distribution is not ideal (contrary to the nearly optimal distribution for the XPROP). This also leads to a relatively low maximum efficiency for the Beaver propeller.

(a) Blade planform and airfoil sections.

(b) Pitch and chord distribution and main dimensions of propeller and nacelle.

Figure 3.2: Beaver propeller geometry, dimensions in mm.

A quantitative comparison between the more modern XPROP geometry and the Beaver propeller is depicted in Fig. 3.3, which shows the load distributions and time-averaged slipstreams. Contrary to the XPROP, the loading (Fig. 3.3a) is time-dependent up to $r/R_p = 0.4$, and its mean value is even negative for $r/R_p < 0.3$. Part of this differ-
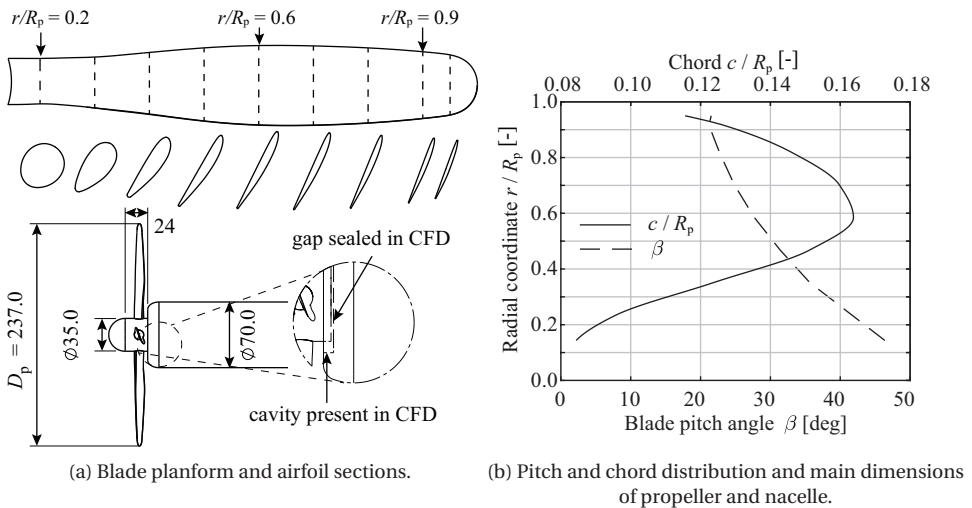
ence in loading can be attributed to the nearly circular root sections on which the flow separates. Furthermore, there is clear difference in nacelle geometry, shown in Figs. 3.1d and 3.2a. While the relative maximum nacelle diameters are comparable (27.5% for the XPROP, 29.5% for the Beaver propeller), the contour of the XPROP spinner is smooth and is tangent to the nacelle, whereas the connection of the cylindrical Beaver spinner is normal to the nacelle, which also causes a time-dependent flowfield near the root sections of the Beaver propeller.

The ineffective root sections of the Beaver propeller lead to a relatively high loading on the outboard part. This has clear implications on the blade loading and flow field in that region. For the same thrust coefficient T_C, a much higher axial induced velocity for $r/R_p > 0.5$ (Fig. 3.3b), while the XPROP slipstream is more gradual in radial direction. This is a clear sign of lower propeller efficiency. As a consequence of the outboard load, the average swirl angle is also relatively low for the Beaver propeller. These different flowfields are indicative that the interaction with an aerodynamic surface will be quite different, as the location of the higher induction and swirl angle are driving factors for the loads that are generated on the surface. For example, if mounted to a tip of a wing, the swirl of the XPROP is more concentrated in the hub region, and therefore will lead to a different interaction with the wing-tip vortex for the same thrust coefficient.

(a) Normalized propeller thrust along blade.

(b) Time-averaged axial velocity at $x/R_p = 1.1$.

(c) Time-averaged swirl angle at $x/R_p = 1.1$.
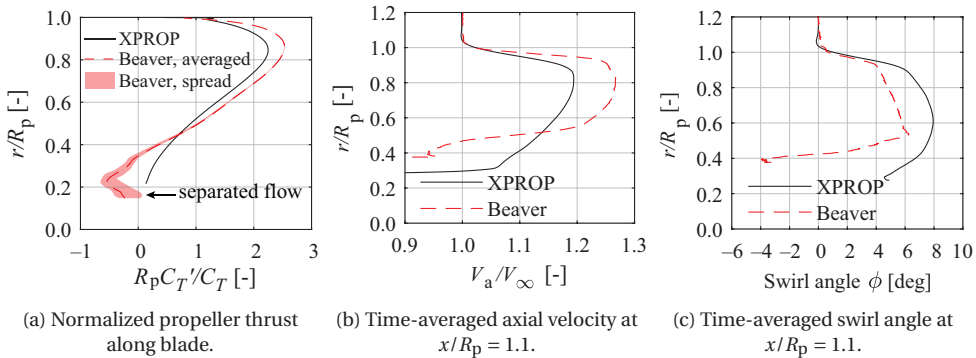
Figure 3.3: Comparison between Beaver and XPROP propeller characteristics, full-blade CFD results (Section 3.4). XPROP: $T_C = 0.37$, $\eta_p = 0.76$. Beaver: $T_C = 0.36$, $\eta_p = 0.71$.

3.3. EXPERIMENTAL SETUPS

3.3.1. WIND-TUNNEL FACILITY AND OPERATING CONDITIONS

The majority of the experimental work was performed in the Low-Turbulence Tunnel (LTT) at the Delft University of Technology. This is a low-speed, closed-return tunnel, with a maximum velocity of 120 m/s. A schematic of the tunnel is depicted in Fig. 3.4. The removable test sections have an octagonal cross sections with a dimension of 1.80×1.25m. These are slightly diverging to compensate for the streamwise pressure gradient that is introduced by the boundary layer on the wind-tunnel wall. This zero pressure gradient condition only exists for an empty tunnel. The freestream dynamic

pressure is determined by a combination of the measured pressure increase in the set-
tling chamber, a calibration of the test section, and the measured total pressure in the
test section.

The measurements were performed at a freestream velocity of 40.00 ± 0.02 m/s, un-
less specified otherwise. The turbulence level at these conditions is below 0.03% [126].
The freestream velocity was limited by the maximum available power and torque of the
electric motors that drive the propellers. A trade-off was made between the achievable
thrust coefficients and still an acceptable Reynolds number (see Section 2.5). Thanks to
the very small fluctuations of the freestream velocity, results can be compared at con-
stant advance ratio. Since the $T_C - J$ curve is not linear, the average measured thrust
would be higher in case of large velocity fluctuations, and therefore a measurement er-
ror would be introduced.
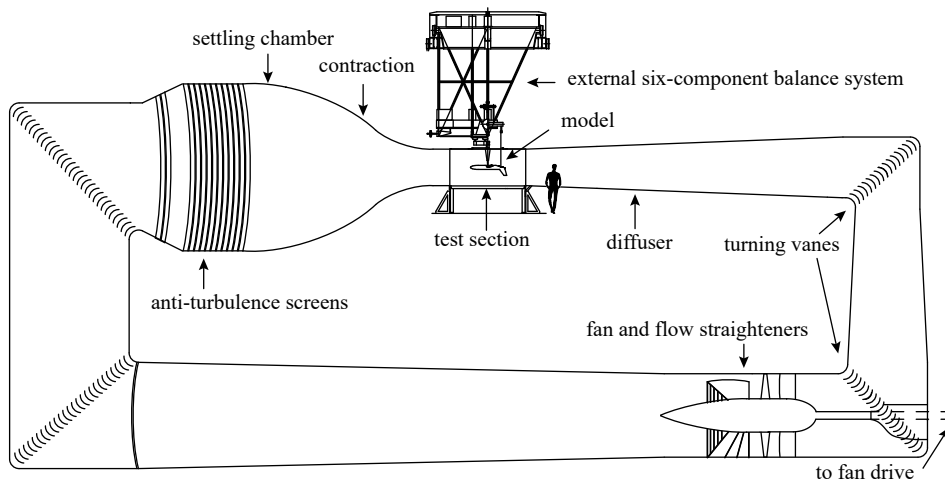
Figure 3.4: Simplified side view of the low turbulence tunnel (LTT) at Delft University of Technology.

3.3.2. EXTERNAL BALANCE

The models installed in the LTT were connected to a six-component external balance
which allows for variation of both angle-of-attack and side-slip, as depicted in Fig. 3.4.
The advantage of such large external balance compared to internal load cells or force
measurements based on strain-gauges, is that the measurements are nearly indepen-
dent of temperature variations and creep. Additionally, high accuracy can be achieved
for a large range of applied forces. For the considered range in aerodynamic forces, the
balance readings have an uncertainty up to 0.02 N [127, 128]. Two times these values are
included in the error-bars of the respective force measurements. These error-bars also
include the spread in data of repeat measurements due to hysteresis, small variations in
operating conditions, and remaining random errors. Tare measurements were taken to
account for the aerodynamic forces of the support struts. Typical acquisition times of
20 seconds were selected to average the measured force data, based on a convergence
study with the model installed at a high angle of attack, which is the critical condition.

The acquisition frequency was 10 Hz.

3.3.3. PRESSURE MEASUREMENTS

Various pressure measurements were conducted for the purpose of quantifying the load distribution on lifting surfaces, for the quantification of the propeller slipstream for validation purposes, and for qualitative assessment of the slipstream deformation due to interaction. These measurements were conducted using surface-pressure tabs, a Pitot probe, and a wake-rake. Measurements taken in the test section were acquired using a DTC Initium pressure scanner system. A calibration of this system indicated an average bias of -0.3 Pa over the all channels. In addition, maximum random errors of ± 4Pa were registered, which in line with the value noted by the manufacturer. These random errors are included in the errorbars of the presented data. The pressures are averaged over the acquisition time of 5 seconds, and were acquired at a sampling rate of 5 Hz. After a change of angle of side slip or angle of attack, or when the probe has traversed to a new location, a waiting time of three seconds was applied to avoid the transient to be part of the measurement.

The probes and wake-rake have an internally conical shaped tip. Although the local flow is not aligned with the pressure probes, in Ref. [129] it was found that angles up to 20 deg yield a total pressure with a maximum error of 1% for such tips. The flow angle in the majority of the slipstream is well below this value, except in the tip-vortex region, where the measured total pressure is inaccurate. For the balance measurements, the Pitot-tube and its support were removed to eliminate their upstream effect on the model.

3.3.4. MOTOR CONTROL SYSTEM

A motor control system was specifically designed to drive the Lehner 2260/40 electric motors to which the propellers are mounted. This EPTR (Electric Propeller Test Rig) system is shown in Fig. 3.5. The system consists of TDK GEN-60-85-3P400 DC power supplies, an inhouse developed power dissipator, MGM HBC25062-3E electronic speed controllers, and several data acquisition units from National Instruments. The rotational speed was measured by means of an optical rotary encoder mounted to the motor shaft.

An inhouse developed LabView program sets a setpoint for the speed controller, and through a PID-controller controls the rotational speed of the motor, by adjusting the voltage of the DC power supplies through the DAQ system. The setpoint could be set with a precision of 0.01 Hz. Maximum fluctuations of 0.1 Hz were registered around the setpoint (typical operating range is 82 to 126 Hz).

To allow for control of the rotational speed in windmilling and close to windmilling conditions, the power generated by the motor is dissipated by the power dissipators as heat. This system also allows for rapid control of the rotational speed in case the torque on the propeller shaft is fluctuating (for example in case of flow separation on the propeller blades or in nonuniform inflow conditions).

(a) EPTR system

(b) Schematic of the EPTR motor control system
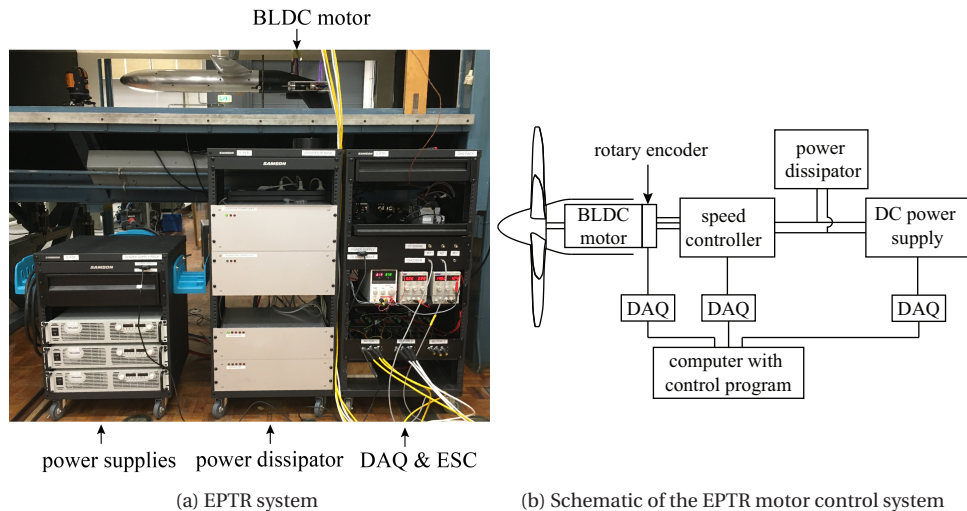
Figure 3.5: Schematic of electric motor control setup 'EPTR' in the LTT wind tunnel.

3.3.5. MODELS AND MODEL-SPECIFIC MEASUREMENT TECHNIQUES

ISOLATED PROPELLERS

The XPROP-S propeller was milled out of stainless steel (material code: 1.4104), shown in Fig. 3.6a. The nacelle was airtight, while a gap exists between the spinner and nacelle. The nacelle was connected to a support strut, which was in turn connected to the external balance of the LTT, schematically shown in Fig. 3.6b, such that the propeller was in the center of the test section. The distance between the leading edge of the support and the propeller plane measured approximately $2.67R_p$, and the support featured a NACA0030 profile of 100 millimeter ($\approx 1.0R_p$). The out-of-plane velocity at the propeller plane that is induced by the support is estimated to be in the order of 0.1% of the freestream velocity at $\alpha = 0$ deg. A 2.5mm wide transition strip with carborundum particles with an average size of 150 μm was applied to the nacelle, while zig-zag tape was applied to the support strut. Transition was verified by means of an electronic stethoscope. No transition was enforced on the propeller blades. The blades are individually set to the desired blade pitch angle at 70% of the radius using a special bench, shown in Fig. 3.6c. It was found by a large number of trials that the blade could be set with an accuracy of ± 0.05 deg. The associated forces of this uncertainty are determined by means of CFD simulations, and are included in the error-bars indicating the uncertainty of the force measurements.

Tare measurements were taken with the same setup but the rotating part replaced by a non-rotating dummy-spinner. It is noted that the propeller thrust measured with this approach also includes the change in nacelle drag due to its interaction with the propeller slipstream, for which no correction is applied. An estimate of the added nacelle drag is discussed in Section 2.3.2. Only a thrust-dependent correction in line with Ref. [130] for slipstream blockage was applied to the experimental data to obtain the equivalent advance ratio to compare with the numerical results that do not include the effect

of wind-tunnel walls.

(a) Propeller model

(b) Schematic of the wind-tunnel cross section

(c) Bench to set blade angle
to ±0.05 deg

(d) Pitot probe

(e) Stereoscopic PIV
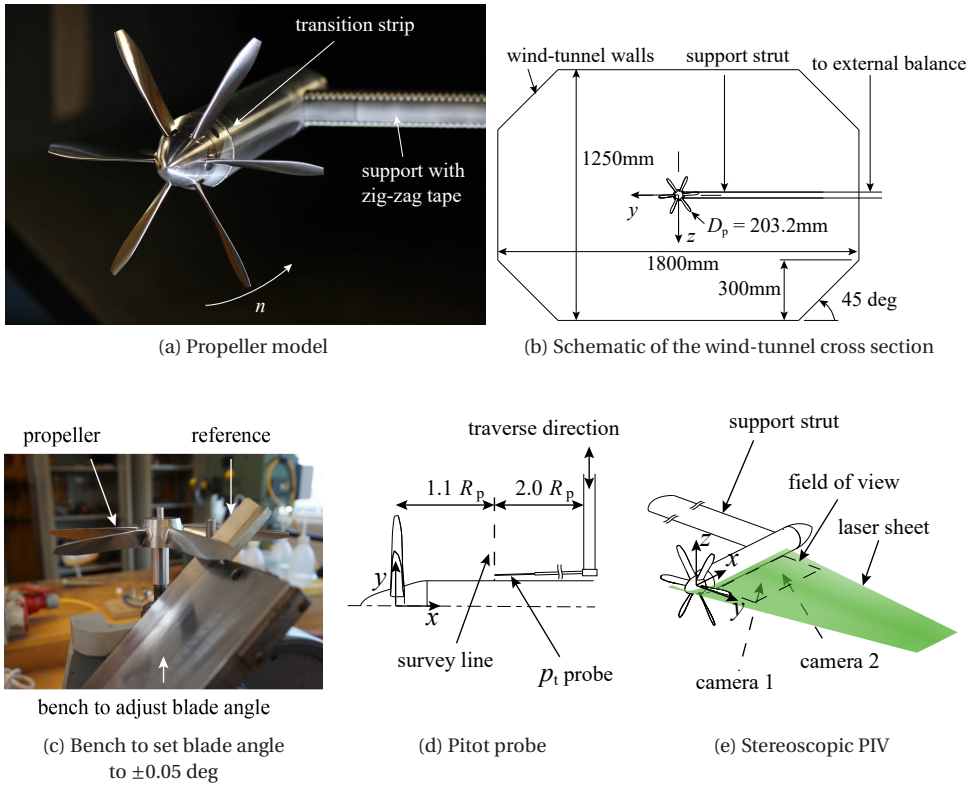
Figure 3.6: Isolated XPROP-S propeller installed on a support in Low Turbulence Tunnel at Delft University of Technology.

For validation purposes, total-pressure measurements were taken using a Pitot probe at a survey line $1.1R_p$ downstream of the plane of rotation, with a minimum clearance to the nacelle of 0.2mm, as sketched in Fig. 3.6d. These were taken on the opposite side to the support strut, such that the measured upstream effect by the support on the propeller disk loading is minimized.

In addition to the total-pressure distribution, the velocity field in the slipstream was measured by means of stereoscopic particle image velocimetry (PIV). Both axial and swirl velocity were measured in a plane aligned with the propeller rotation axis, schematically shown in Fig. 3.6e. Phase-averaged measurements were performed by acquiring 500 image pairs at arbitrary phase angles. Also phase-locked measurements were performed using a one-per-revolution trigger signal from the rotary encoder, and are used to compare the velocity field of individual tip vortex and wake structures, which was constructed by averaging 300 image pairs. Table 3.3 lists further details of the PIV setup.

Table 3.3: Measurement and processing characteristics of the PIV setup for the XPROP-S.

Parameter	Value
PIV setup	Stereoscopic
Cameras	$2\times$ 6 Mpixel sCMOS
Focal length	105 mm
Laser	200 mJ Nd:YAG
Field of view	260×100 mm
Pulse separation	$14\mu s$
Image resolution	19 [pixel/mm]
Interrogation window size	24 [pixel^2]
Window overlap	50 %
Image pairs	300^a, 500^b
Uncertainty mean velocity magnitude	$0.025 V_\infty$

[a] phase-locked measurements, [b] phase-uncorrelated measurements

HORIZONTAL TAILPLANE MOUNTED PROPELLER

For the characterization of the aerodynamic interaction between a propeller and a horizontal tailplane, the Beaver propeller was mounted to the tip of a tailplane featuring a 25%-chord elevator, referred in this dissertation as the *PROWIM-HTP*. The ratios of propeller diameter-to-chord and diameter-to-span are comparable to the ones used in several conceptual design studies, for example Refs. [25, 86, 131, 132]. A technical drawing of the setup is depicted in Fig. 3.7a. One could recognize this model as a low-aspect-ratio wing with a plain flap. The CAD geometries of the model and wind-tunnel section are attached to the Supplemental Data in Ref. [133].

A cylindrical nacelle was connected to a straight, symmetric tailplane model with a chord length of 0.240 m, a span of 0.292 m, and a NACA 64$_2$A015 profile. The nacelle is parallel to the chord of the tailplane. The streamwise propeller–tailplane spacing was fixed to 43% of the propeller diameter. The tailplane model was connected to a rotating disk integrated into the ground plane, allowing for measurements at nonzero angle of incidence. Photographs of the propeller–tailplane model installed in the LTT are depicted in Fig. 3.7b. Transition was forced using a 2.5 millimeter wide trip wire made out of carborundum particles, applied at 12% of the chord from the leading edge of the tailplane model.

The tailplane model contained 408 pressure taps in chordwise direction, providing local measurements of the pressure distribution at eight spanwise locations:
$2y/b_\mathrm{h} = [0.19, 0.34, 0.49, 0.55, 0.61, 0.68, 0.74, 0.80]$. Since at each chordwise position the pressure ports were cross-connected in spanwise direction, the measurements were taken per pressure row, with all other rows closed by tape. The pressures from each spanwise row were simultaneously recorded at a sampling rate of 5 Hz using an electronic pressure scanner and averaged over a measurement time of 3 seconds to obtain the final results per data point.

Flowfield measurements were taken in the wake of the model using stereoscopic particle-image velocimetry (PIV). Three measurements planes were used, oriented per-

(a) Technical drawings

(b) *PROWIM-HTP* setup installed in the Low-Turbulence Tunnel at Delft University of Technology.
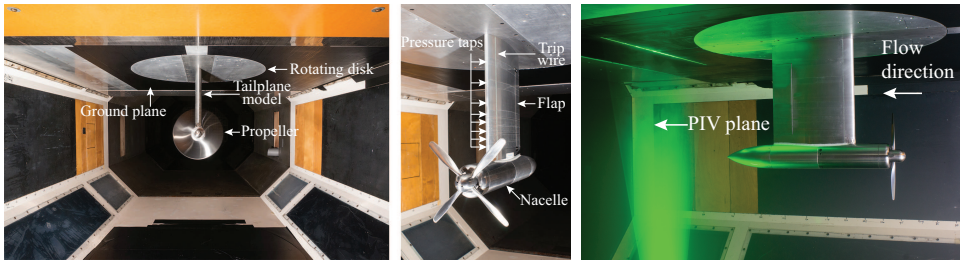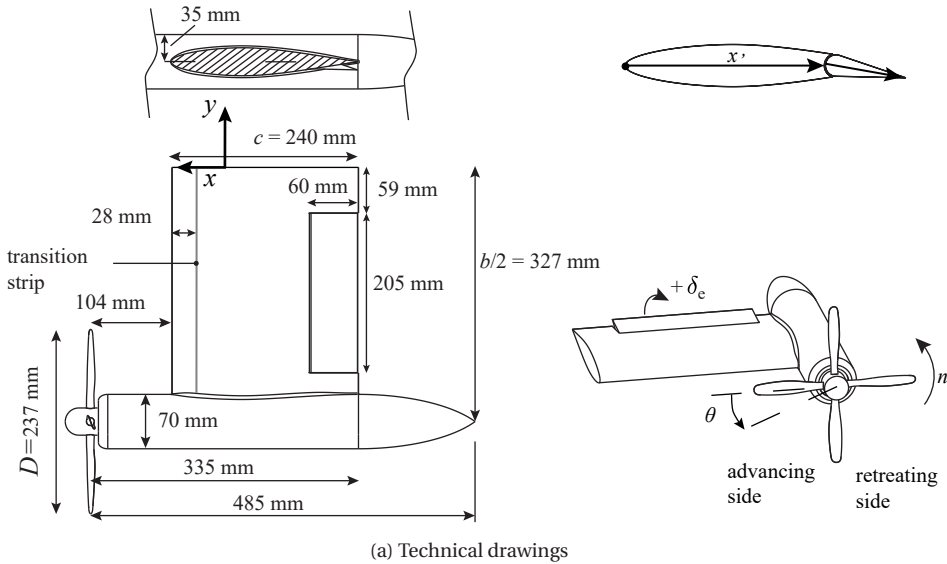
Figure 3.7: Tip-mounted propeller model *PROWIM-HTP*.

pendicularly to the flow at $1.5c_{ht}$ from the trailing edge of the tailplane model, see Fig. 3.7b. Table 3.4 provides an overview of the data-acquisition and postprocessing characteristics of the PIV setup. The cameras were traversed simultaneously in the vertical direction to allow for measurements in three different planes, together covering the entire wake of the propeller–tailplane model. The results from the three measurement planes were combined in postprocessing to obtain a final field of view with dimensions of 360×485 mm. Both phase-uncorrelated and phase-locked measurements were taken, with phase-locking achieved using a one-per-revolution-trigger signal integrated into the motor driving the propeller.

Table 3.4: Measurement and processing characteristics of the PIV setup for the Beaver propeller.

Parameter	Value
PIV setup	Stereoscopic
Cameras	2× 16 Mpixel CCD
Focal length	200 mm $f/4$
Laser	200 mJ Nd:YAG
Field of view	360×485 mm
Pulse separation	$40\ \mu$s
Max. particle displacement	25 pixel
Image resolution	19 [pixel/mm]
Interrogation window size	24 [pixel^2]
Window overlap	50 %
Vector spacing	0.9 mm
Image pairs	300^a, 1000^b

^{a} phase-locked measurements, ^{b} phase-uncorrelated measurements

AIRCRAFT WITH PROPELLERS MOUNTED TO HORIZONTAL TAILPLANE

For the characterization of a series of propulsion integration effects on aircraft level, a conceptual aircraft model was designed that features propellers mounted to the horizontal tailplane of a low-wing aircraft. This model is called the *VGM-HTP* (*V*ariable *G*eometry *M*odel with *H*orizontal *T*ailmounted *P*ropellers). The geometry of the conceptual aircraft model was based on Refs. [25, 86, 131, 132]. The main dimensions were selected to be representative for such layout, of which an overview is provided in Fig. 3.8 and Table 3.5.

The wing has no sweep, a linear washout of 2 deg, an aspect ratio of 8.46 and a taper ratio of 0.40. The selected cambered airfoil has a 15% thickness-to-chord ratio and is described in Appendix A. High-lift configurations were simulated by removable Junkers flaps. The nacelles are aligned with the fuselage centerline and are mounted at 69% of the horizontal tail semi-span, comparable to Ref. [25]. Both inboard and outboard parts of the horizontal tail are equipped with elevators with a chord ratio of 25%. The rounded tip of the symmetric horizontal tail extends up to $0.85R_p$ from the propeller rotation axis such that propeller tip-vortex cores do not impinge on the tailplane in clean configuration with no side slip angle. The distance between the propeller rotation plane and the leading edge of the tailplane is selected as $1.2R_p$, based on suggestions in Ref. [94]. The CAD geometries of the model and wind-tunnel section are attached to the Supplemental Data in Ref. [120].

The model was supported to the external balance of the LTT wind tunnel, by three support struts. The struts connected to the wing were shielded by a fairing that was not connected to the balance system (see Fig. 3.9a). Separate measurements were taken with the model removed to subtract the forces generated on the isolated support struts (and thereby neglecting the interference drag between the model an struts (see Ref. [134]). No wind-tunnel-wall corrections were applied, as the numerical simulations also include wind-tunnel walls and the objective is to focus on the aerodynamic phenomena trends,
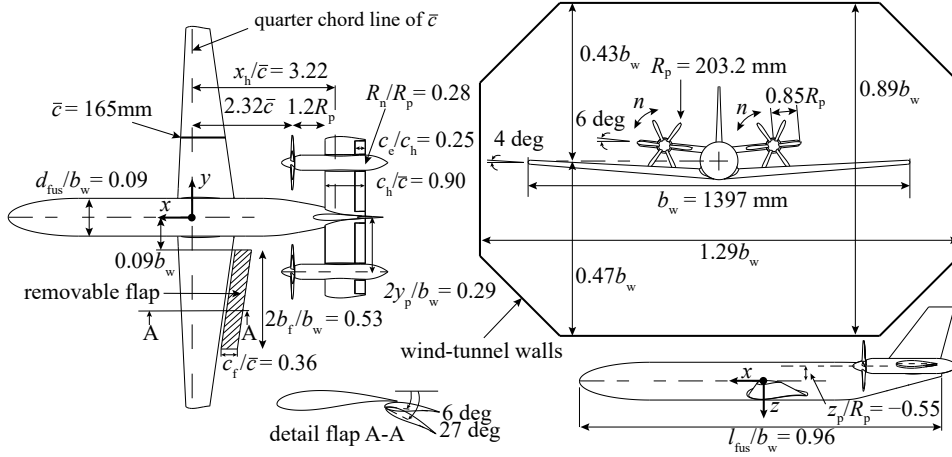
Figure 3.8: Technical drawing of the *VGM-HTP* aircraft model and wind-tunnel test section.

Table 3.5: Main dimensions of the aerodynamic surfaces. The vertical tail is defined up to the curved fuselage centerline.

	Wing w/o flap	Flap	Horizontal tail	Vertical tail
Area	0.2163 m^2	$\frac{2S_f}{S_w} = 0.19$	$\frac{S_h}{S_w} = 0.37$	$\frac{S_v}{S_w} = 0.18$
Airfoil	DU 96-150	DU 96-150	NACA 64$_2$A015	NACA 0015
Root incidence	0 deg	–	0 deg	0 deg
Washout angle	2 deg	0 deg	0 deg	0 deg
Aspect ratio	8.46	6.10	2.85	1.50
Taper ratio	0.40	1.00	1.00	0.41
Volume coefficient	–	–	1.14	0.54
Control surface area	–	–	0.17S_h	0.28S_v

rather than the performance curves of the model in absence of wind-tunnel walls. An acquisition time of 20 seconds was selected to average the measured forces. This resulted in converged mean force estimates at all operating conditions considered.

The boundary layers were tripped with 2.5mm wide transition strips with carborundum particles with an average size of 150 μm on the fuselage, wing, nacelle, and tail surfaces. On the tail surfaces and wing pressure side, the strips were applied at 10% of the chord, while on the wing suction side a strip was applied at 5% chord. Transition was verified by means of an electronic stethoscope for the considered range of operating conditions. The model was manufactured with a surface roughness of less than 0.4 μm and surface irregularities (e.g. countersunk holes) were filled with plasticine.

The blade pitch of the XPROP-S propellers (see Fig. 3.9c) were set to of 45±0.05 deg at 70% radius and the advance ratios were selected such that the range of nondimensional force coefficients (C_T, C_P, T_C, Q_C, C_{N_α}) and the pitch of the tip vortex obtained in the experiment are comparable to those of full-scale propellers operating at cruise to climb

(a) Horizontal tail-mounted propeller configuration

(b) Horizontal tail with split elevators

(c) Detail of XPROP-S propeller and tailplane

(d) Installation of the wake rake and Junkers flap
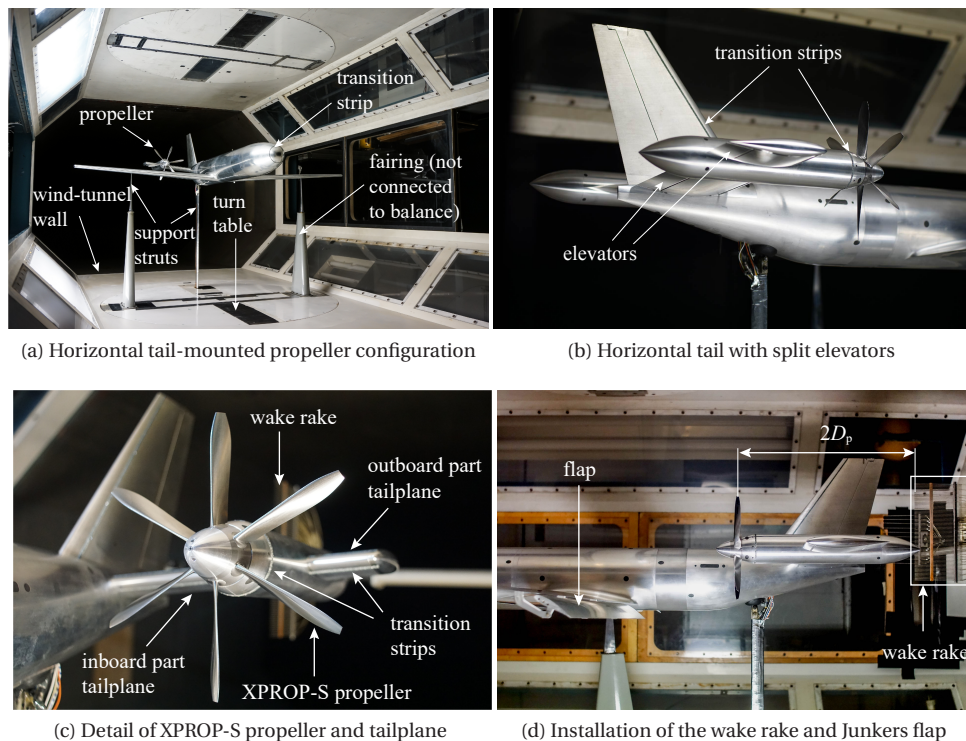
Figure 3.9: Experimental setup of the *VGM-HTP* configuration installed in the Low Turbulence Tunnel at Delft University of Technology.

conditions (see Table 2.2). The advance ratio was varied between $J = 2.3$ and $J = 1.6$ by changing the rotational speed to achieve thrust coefficients from $T_C = 0.01$, representing approach conditions, up to $T_C = 0.28$, typical for cruise and climb conditions. Both inboard-up (IU), outboard-up (OU) and co-rotating (CO) propeller configurations were tested to quantify the effect of rotation direction, which will be shown to play a key role on the effect of propeller installation on stability. For the propeller-off conditions, that serve as the reference, the propellers were replaced by non-rotating dummy spinners.

To illustrate the propeller-airframe interaction for a range of conditions as well as for validation purposes, the total pressure was measured by traversing a rake with 74 probes in a plane perpendicular to the freestream at two propeller diameters behind the propeller rotation plane, see Fig. 3.9d. The measurements were taken in a rectangular grid with resolution of 3 mm in vertical and lateral directions.

The propeller forces were measured by attaching the electric motors to ATI-SI-40 load cells, connected to National Instruments NI-9239 modules. The six forces and moments were measured simultaneously. The uncertainty of presented propeller force coefficients are equal to the spread of the data of the repeat measurements. This installation is depicted in Fig. 3.10a. Despite the thermal isolation layer between the electric

motor and load cell, the temperature of the load cell rises during operation, which affects the load cell readings [135, 136]. A calibration campaign of the installed setup was performed to determine linear temperature compensation coefficients for each force component, of which an example is shown in Fig. 3.10b. The average readings of two thermocouples mounted close to the load cell registered the temperature during operation. Because the load cell temperature response is only linear after a transient response, the load cell bias of each measurement was determined at elevated temperature, such that it fell in the linear part of the temperature-force curve. It was found that the calibration curves were nearly independent on the applied load, hence the same calibration constants were applied on all measurements. Separate calibration curves are used for each of the load cells.

(a) Load cell assembly to measure propeller forces

(b) Example of calibration curves of one of the two load cells
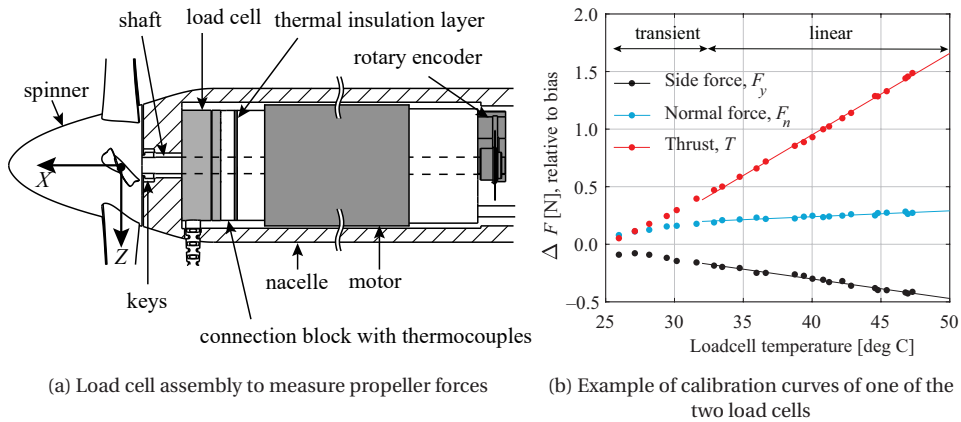
Figure 3.10: Load cell assembly to measure propeller forces.

At a certain angle of attack, the wing wake is encountered by the propeller. This encounter not only affects the propeller loading, but the interaction between the (vorticity of the) wing wake and the propeller tip vortices also affect the flowfield downstream the disk. To further study the spatial extent of this interaction, a stereoscopic PIV setup is employed with a field of view that contains a portion of the flowfield upstream and downstream the propeller disk and is aligned with the freestream flow direction, as highlighted in Fig. 3.11. The lasersheet and two cameras traversed in the spanwise direction to evaluate the locations where the wake is encountered by the propeller, as well as locations where the blades remain above the wake. Table 3.6 lists the measurement and processing details of the PIV fields. An experimental approach is selected over a numerical approach, as it is known that the velocity gradient at the propeller slipstream edge is not well captured in the CFD simulations, which would complicate the quantification of the associated deformation of the wing wake.
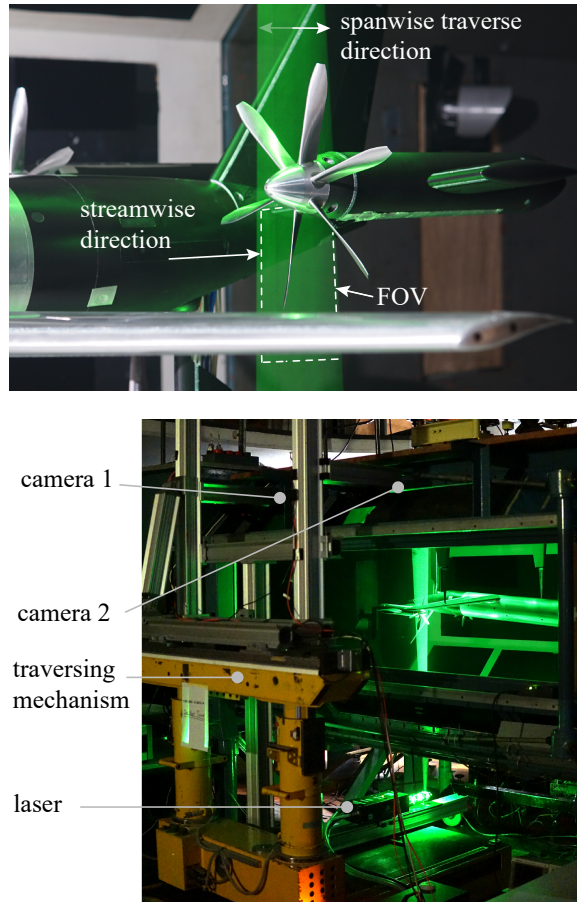
Figure 3.11: Definition of the field of views for stereoscopic PIV of the *VGM-HTP* model.

Table 3.6: Measurement and processing characteristics of the PIV setup for the *VGM-HTP* model.

Parameter	Value
PIV setup	Stereoscopic
Cameras	2× 6 Mpixel sCMOS
Focal length	105 mm
Laser	200 mJ Nd:YAG
Field of view	85 × 150 mm
Pulse separation	$14\mu s$
Interrogation window size	24 [pixel^2]
Window overlap	50 %
Image pairs	300[a], 500[b]

[a] phase-locked measurements, [b] phase-uncorrelated measurements

71

In addition to the quantitative visualizations of the flowfield constructed from the PIV and wake rake measurements, qualitative flow visualization was done by applying a mixture of Shell Ondina 32/15 and A-680 fluorescent particles on the surface of the model. This was in particularly done to visualize the flow separation that originates from the wing–fuselage junction. To avoid that the photographs were taken of a still developing flow, the conditions were maintained for about one minute until no transient state was observed.

The effect of the propeller installation on the unsteady pressure fluctuations on the fuselage can be indicative for a part of the interior noise. In a similar fashion to Ref. [137], five Sonion 8044 microphones are embedded in the aft-fuselage outer surface on the fuselage centerline, as shown in Fig. 3.12. The figure also depicts the cavity and distance from the microphones up to the fuselage surface. The microphones measured a frequency range of 20 Hz–15 kHz, with a maximum input level of 123.5 dB (re $20 \cdot 10^{-6}$ Pa) at 1 kHz and an equivalent noise level of 35 dBA. A calibration using a white-noise sound source was performed by placing a LinearX M53 microphone next to each microphone, which was calibrated using a GRAS 42AA piston phone. The microphone data was acquired with a sampling frequency of 51.2 kHz, synchronously with the once-per-revolution trigger signal from the optical encoder. The measurement time of 30 seconds corresponded to approximately 15,000 to 23,000 blade-passages for each measurement point.
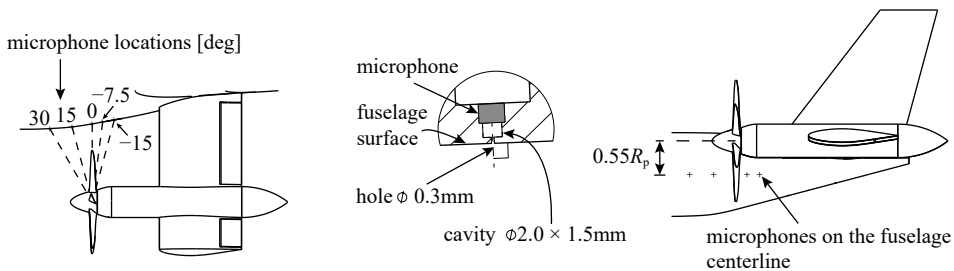
Figure 3.12: Locations of microphones embedded in the aft-fuselage of the *VGM-HTP* model.

3.3.6. Effect of Low Reynolds Number on Interaction

Compared to the undisturbed flowfield that a lifting surface experiences without the propeller, a propeller slipstream introduces a periodic flowfield that on the one hand changes the local lift coefficient, and on the other hand introduces regions that contain elevated levels of turbulence. These regions are the tip vortices and the blade wakes. From Refs. [110, 138] it is shown that the boundary layer transition does move towards the leading edge of the lifting surface due to these disturbances. However, at certain locations on the wing the boundary layer becomes laminar between blade passages. The time-averaged effect of the slipstream is leading to earlier transition [37]. This topic does not specifically get attention in this dissertation, as the aim is to investigate installation effects for transport aircraft that typically fly at relatively high speed, hence transition occurs already close to the leading edge. For this reason, the experimental setups include

forced transition (see Section 3.3.5) and the simulations make use of turbulence models.

The necessity of such approach in the quantification of installation effects becomes clear by the photos taken of fluorescent oil that was applied on the *VGM-HTP* model, shown in Fig. 3.13. The figure depicts three cases; a propeller-off case with a transition strip, a propeller-off case without strip, and a case with propeller and without strip.

a. laminar boundary layer
b. laminar separation
c. turbulent boundary layer

d. path core of tip vortex
e. vortex deformation
f. turbulent fuselage boundary layer
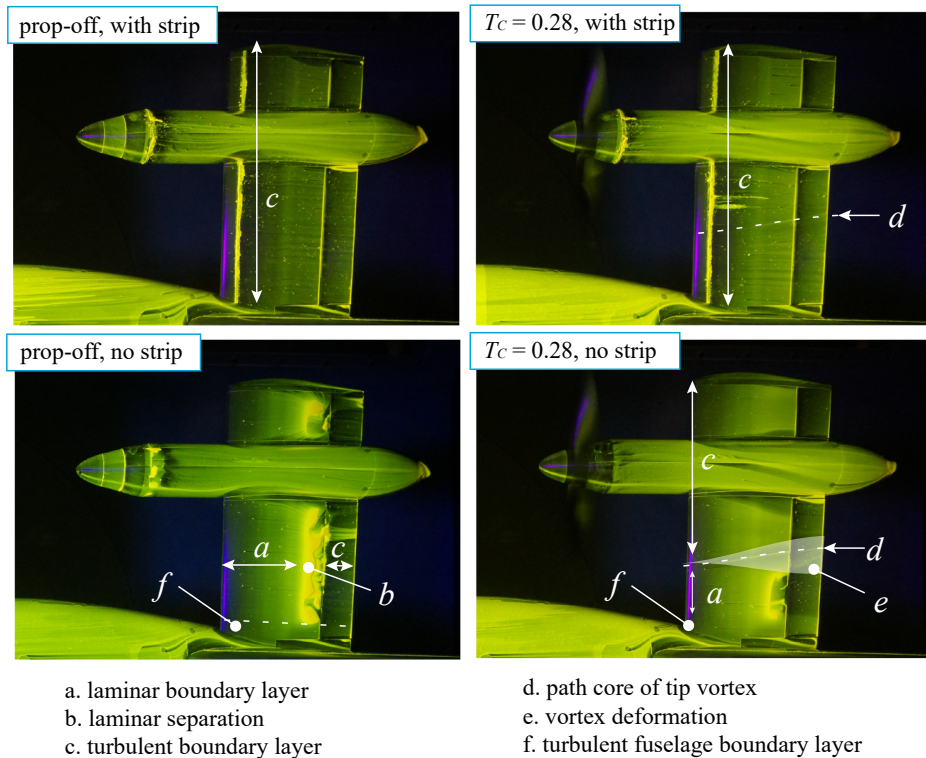
Figure 3.13: Effect of propeller installation on the transition and laminar separation on the tailplane at $\alpha = 0$ deg. Reynolds number based on tailplane chord is 400,000.

The fluorescent oil is too viscous to adapt to the local flow direction in a time-accurate manner. However, after a short period (typically less than 30 seconds), the regions of transition, separation, and reattachment can be distinguished.

For the case with strip, a turbulent boundary layer is formed over the majority of the chord. At this low Reynolds number based on chord (400,000), approximately 50% of the chord is laminar, after which laminar separation and reattachment is achieved. From this location onwards, the flow is turbulent. With the propeller installed, the slipstream region as well as a wedge from the impingement of the helical vortex on the leading edge becomes turbulent nearly immediately. The consequence is that if no transition is enforced, one would quantify also the effect of transition on the drag, lift, maximum lift coefficient, and effectiveness of trailing edge devices. Especially if the model scale of the model relative to the envisioned scale is not matching, this is an unwanted artefact of

testing at smaller scales.

3.4. RANS CFD SETUPS

Numerical models are employed to support and complement the experimental analyses. The majority of the aerodynamic simulations of the various interaction phenomena are performed by solving the Reynolds-averaged Navier-Stokes (RANS) equations. This approach is chosen over lower-order methods, for example panel methods or other vortex-based methods, based on the several considerations. A RANS approach is considered most suitable to maintain consistency with the experimental setup. The geometry can be maintained to a large extent and it is possible to predict flow separation with reasonable accuracy. Lower order models often require the flowfield close to the model to be defined/enforced a-priori, for example by defining collocation points of vortex panels. Such a choice influences the solution. Since the studied flowfields are highly three-dimensional and the model consists of a combination of lifting surfaces, nacelles, fuselage, and junctions between these, it is an advantage to use RANS instead.

3.4.1. RANS CFD SOLVER AND SETUP

ANSYS® Fluent Release 18.1 [139], a commercial, unstructured, finite volume, and cell-centered solver was used for all simulations. The meshing was performed with ANSYS Meshing Release 18.1. The details regarding grids per case are discussed in Section 3.4.4.

Since the aerodynamic interaction is driven by the relatively large length and time scales, i.e. multiples of the blade-passing frequency, the smaller scales of turbulence are not of interest. The flow is therefore prescribed to be fully turbulent. This is in line with the experimental setups, which employ transition strips near the stagnation points/lines on the models, except for the propeller blades. As discussed in Section 4.2.1, this discrepancy between experiment and simulation of the flowfield around the propeller blades leads to quite significant deviations at high advance ratios.

The choice for the turbulence model to close the system of equations has a profound effect on the prediction of flow separation [140]. The one-equation Spalart-Allmaras model and the two-equation $\kappa - \omega$ shear stress transport model (SST) model are widely used models for simulations of external flows for a large range of Reynolds numbers, Mach numbers, and pressure gradients. The $\kappa - \omega$ SST model was designed to accurately predict the onset and the severity of flow separation under adverse pressure gradients [141]. The performance of this model has been demonstrated by several validation studies, for example Refs. [141, 142], and in various propeller related studies [92, 113, 143–146]. The Spalart-Allmaras model was developed in particular for typical aerospace applications [147]. Also this model was successfully applied in simulations of propellers in various studies, e.g. Refs. [148–151]. Provided that all simulations approximately have the same range of Reynolds number based on the chord of the lifting surface of interest, a brief validation study is performed in this section to determine the most suitable turbulence model for the cases presented herein. A modification as proposed by Ref. [152] to the Spalart–Allmaras model with a strain/vorticity-based production equation is used which improves the development of tip-vortices by suppressing the artificial build-up of turbulent viscosity in these regions.

Figure 3.14 depicts a comparison between these two turbulence models on the test case of a horizontal tailplane with a deflected elevator ($\delta_e = -10$ deg). It was found in the experimental campaign that at a mid-span location, the flow separated from approximately 75% of the flap chord up to the trailing edge. The path lines depicted in Fig. 3.14a, clearly indicate that the point of the trailing edge separation strongly differs between the two turbulence models, with the SST model predicting separation nearly immediately downstream of the flap gap. The pressure distributions in Fig. 3.14b show that the SST model indeed predicts the separation prematurely compared to the experimental data, and consequently leads to less suction on the elevator and main element. The associated decambering of the streamlines, well observable in Fig. 3.14a, leads to a lower section lift coefficient for the SST model. On the other hand, the Spalart–Allmaras model clearly shows better agreement with the experimental data, with a nearly identical suction peak on the elevator.

(a) Detail of flow separation

(b) Pressure distributions
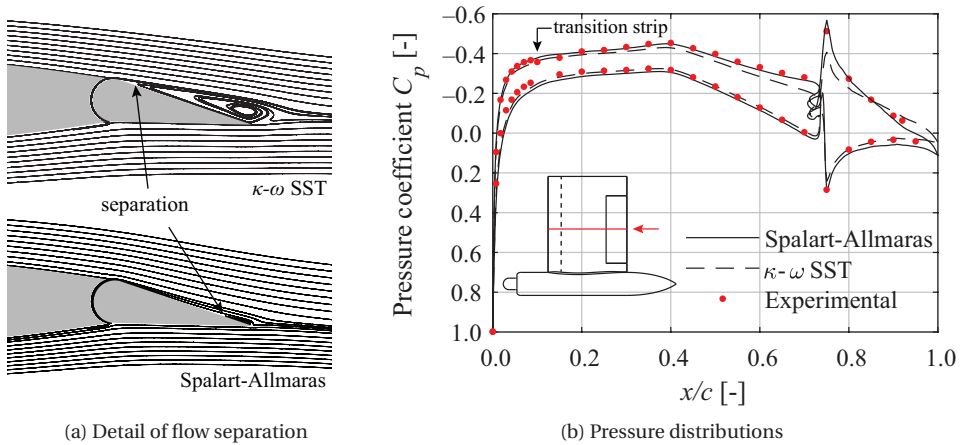
Figure 3.14: Comparison between two turbulence models and experimental data for the horizontal tailplane model (prop-off) at $2y/b = -0.5$. Conditions: $Re_c = 660,000$; $\delta_e = -10$ deg; $\alpha = 0$ deg.

The experimental data suggests that the trailing edge separation occurs slightly ahead of the separation line predicted by the Spalart-Allmaras model. However, the Spalart–Allmaras turbulence model shows a satisfactory prediction and was therefore selected for all cases considered herein. The fact that two well established models display such a significant difference also highlights the importance of validation data.

For the spatial discretization of the RANS equations, a second-order upwind scheme is selected. The momentum and pressure-based continuity equations are solved simultaneously by a coupled algorithm. Such an implicit approach is selected as it is advantageous in terms of computational resources over segregated algorithms, in particular for the time-dependent simulations. A Courant number of 1.0 is used, which is a compromise between numerical stability and the required number of iterations to reach a converged solution. Convergence is determined by a maximum normalized residual of 10^{-5} and by evaluating the convergence history of the forces on the component of inter-

est. For the steady simulations this typically required around 5,000 iterations.

Since the maximum helical Mach number of the propeller tip cannot be considered low subsonic, the simulations are of a compressible fluid. For the equation of state, an ideal gas is assumed, and Sutherland's law is applied to predict the dynamic viscosity. In line with the experiments, ambient conditions are set to sea level conditions. Although temperature and pressure varied during the experimental campaigns, these did not substantially differ from sea level conditions and therefore no adjustments to the flow properties were made in the CFD simulations. For completeness, the associated flow properties are listed in Table 3.7.

Table 3.7: Fluid properties for the CFD simulations.

Quantity	Expression	Value
Molecular weight, m [kg/kmol]	–	28.9644
Specific heat, C_p [J/(kg K)]	$C_p = \frac{\gamma R}{m(\gamma-1)}$	1004.69
Thermal conductivity, k_T [W/(m K)]	$k_{\mathrm{t}} = \frac{2.64638 \cdot 10^{-3} T^{1.5}}{T + 245.4 \cdot 10^{\frac{-12}{T}}}$	0.025326
Reference viscosity, μ_0 [kg/(m s)]	–	$1.7894 \cdot 10^{-5}$
Reference temperature, T_0 [K]	–	288.15
Effective temperature, S [K]	–	110.40
Reference specific heat ratio, γ [-]	–	1.4
Reference pressure, p_0 [Pa]	–	101325

3.4.2. TYPES OF BOUNDARY CONDITIONS AND INTERFACES

In most of the evaluated cases, the same boundary conditions were set. An overview is provided here:

- *No-slip wall.* This boundary condition is used on all surfaces of each model. Since the first layer height of the cells, determined by the desired y^+ value, is an order of magnitude larger than the sand grain roughness of the experimental models (typically $Ra = 0.4\mu m$), all no-slip walls are simulated as hydro-dynamically smooth boundaries.

- *Slip wall.* All wind-tunnel walls are simulated as a slip wall boundary condition by setting the shear stresses on these walls to zero. This condition allows for non-zero gradients normal to the boundary.

- *Symmetry.* For the cases where there is symmetry, this condition is applied on the symmetry plane. There is no flux through this plane; the normal velocity is set to zero, and there is no shear stress. This condition therefore does not allow for non-zero gradients normal to the boundary.

- *Pressure inlet.* This condition is placed far upstream of the model. The turbulent viscosity ratio, gauge total pressure, and total temperature are required, as well as the direction of the freestream flow.

- *Pressure outlet.* This condition is placed far downstream of the model. It is assumed that, on average, over the outlet the static pressure has developed to ambient conditions. On average, the propeller-induced pressure field has reached that value already within two diameters (see Section 2.1.2). Furthermore, in-plane velocities, such as the downwash induced by the model or the propeller induced swirl are not influenced by this boundary condition.

- *Pressure far-field.* This characteristic condition is specified on the remaining boundary that is not an inlet or outlet. The freestream Mach number, turbulent viscosity ratio, static pressure, temperature, and freestream flow direction comply with the inlet conditions.

- *Cyclic periodic conditions.* This condition is set on the two sides of a wedge-shaped domain that contains one propeller blade. In these isolated propeller simulations, the flow is rotationally periodic. In this way, the solver treats the two planes as direct neighbours. To avoid unnecessary interpolation, the mesh on these boundaries are conformal.

3

To avoid that the proximity of the boundary condition has an effect on the flow direction, pressure and velocity experienced by the model, the boundary conditions are placed far from the model. The distances to the model that can be freely chosen (that excludes the wind-tunnel walls) are determined by first simulating the model in a large domain. The final (smaller) domain is selected based on a certain chosen threshold of the gradient of static pressure and flow angle that exist in the large domain; these conditions are therefore freestream conditions.

Although needless to say, it is important that the specified flow quantities at the boundary conditions should be consistent. This entails that total pressure, total temperature, Mach number, temperature, and the ratio of turbulent viscosity should match the desired flow condition in the far field. Inconsistent boundary conditions not only lead to poor convergence, it can introduce e.g. an erroneous flow angle in the domain. For completeness, the equations used to determine the flow quantities are repeated here. Based on the freestream velocity V_∞ and assumed sea level conditions, the Mach number follows as

$$M_\infty \equiv \frac{V_\infty}{a} \tag{3.1}$$

The total pressure and total temperature then follow from the isentropic relations:

$$p_t = \frac{p_\infty}{\left(1 + \frac{\gamma-1}{2}M^2\right)^{\frac{-\gamma}{\gamma-1}}} \tag{3.2}$$

$$T_t = \frac{T_\infty}{\left(1 + \frac{\gamma-1}{2}M^2\right)^{-1}} \tag{3.3}$$

The inlet eddy-viscosity ratio of 0.21044 was based on recommendations by Spalart and Rumsey [153].

3.4.3. PROPELLER MODELLING

The propeller is modelled with two levels of fidelity: a full-blade approach and an actuator disk approach. The former is particularly used when the loads on the propeller are to be determined and when the unsteady interaction with the airframe is to be characterized. This is the case when the airframe or flow condition introduces a strong nonuniform inflow to the propeller. The actuator disk approach is used when the time-averaged effect of the slipstream on the airframe is of interest. The two methods are schematically shown in Fig. 3.15.

In a full-blade approach, the propeller geometry is treated as a no-slip boundary condition. The propeller blade is placed in an axisymmetric domain, containing the spinner and the front part of the nacelle. For the isolated propeller, this domain is a wedge that contains one blade, with periodic boundary conditions on the sides. For the installed propeller cases, or when the inflow is not uniform, a full annulus is constructed by copying the domain of a single blade. This ensures an axisymmetric mesh. The domain containing the propeller is coupled to the stationary domain through interfaces. The interpolation of the flow quantities on this interface introduces artificial diffusion and dissipation. Therefore, the grid is further refined on these interfaces.

(a) Representation with a full-blade approach

(b) Representation with an advanced actuator disk model
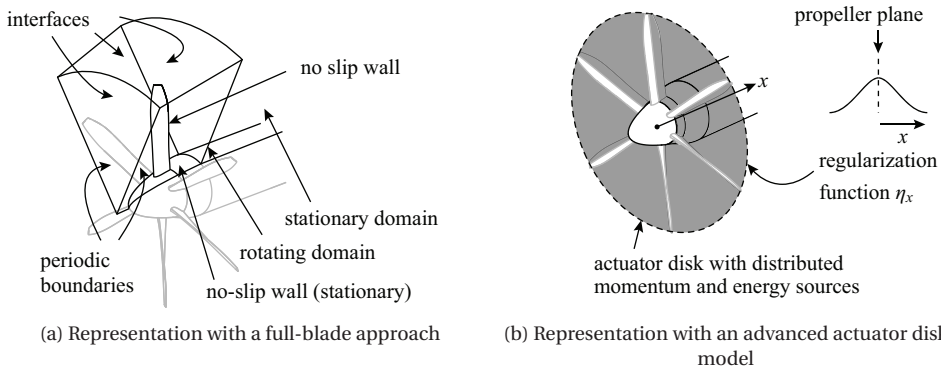
Figure 3.15: Schematic of the full-blade approach and the actuator disk approach.

The rotational motion of the propeller is simulated by a multiple reference frame approach for the steady simulations, for example used in Ref. [154]. In order to maintain a helical vortex system, also the stationary domain is simulated with the same rotational speed as the propeller, while the nacelle remains stationary. If this frame transformation is not also prescribed in the stationary domain, the helical vortex system would not be present, and instead the tip vortices would follow a straight path. The consequence would be that the induced velocity field at the propeller disk is not representative. For consistency, the steady isolated propeller simulations also include the interfaces, such that the flowfields and loading distributions can directly be compared to the installed cases. It is noted that this approach is only valid if there is no significant flow separation from the propeller blades.

For the time-dependent these cases, the mesh containing the propeller rotates at

the propeller rational speed relative to the stationary domain, and is coupled through the sliding mesh approach [139], by using interfaces from the stationary to the rotating domain. This is the most used CFD method for propeller–airframe interaction studies in case the blade is modelled as a full blade, for example in Refs. [72, 109, 155–159]. A time step equivalent to 2 deg propeller rotation with 35 inner iterations per time step, using a second-order implicit temporal discretization.

An advanced actuator disk approach is used, developed in Ref. [133], to simulate the propeller slipstream that interacts with the airframe for the *A320-DP* model and a specific case of the *PROWIM-HTP* model, see Section 3.4.4. Instead of a discontinuity of pressure in the domain, the thrust and tangential forces acting on the propeller blades are represented by axial momentum sources, tangential momentum sources, and energy source terms. Since the region that is swept by the propeller has a finite thickness, these source terms are distributed along the x-direction through a regularization function, as described in Ref. [133] and sketched in Fig. 3.15b. The method allows for a nonuniform load distribution in radial and azimuthal directions, and therefore the effect on nonuniform inflow on the propeller slipstream development is captured. A similar approach is followed in Ref. [125]. The distributions are determined a-priori by the method described in Chapter 5 or by full-blade simulations of the installed configuration. In Ref. [133] it is shown that even though a relatively accurate representation of the flowfield can be obtained by using an actuator disk model, stability analysis of turboprop, e.g. in Ref. [160], therefore require the propeller load distribution should be known in advance. Moreover, for an aerodynamic surface like the tailplane that is submerged in a highly distorted and time-dependent flowfield, a time-accurate representation is most suitable to accurately determine the time-averaged normal force on this aerodynamic surface, as demonstrated in Ref. [133].

3.4.4. MESH DETAILS PER CASE

XPROP AND BEAVER ISOLATED PROPELLER

The isolated propellers are solved in the wedge-shaped domains consisting of subdomains with refined grids, as depicted in Fig. 3.16. The propeller blades, spinner and nacelle are no slip walls, while the nacelle is a moving wall. Periodic conditions are used on the sides of the wedge. The inlet is a pressure inlet, while the outlet is a pressure outlet boundary condition. A pressure far-field condition is specified on the remaining boundary. The size of the domain of the Beaver propeller is smaller than the domain of the XPROP, since lower thrust coefficients were simulated with this propeller.

Table 3.8 summarizes details about the selected meshes. The choice for the propeller grids is based on a grid refinement study presented in Section 4.1. The nacelle, rotating, and outer domains have tetrahedral shaped elements, while the domains upstream and far downstream the propeller are hex dominated. The inflation layers on the nacelle, spinner, and blade have a different first layer thickness, to comply with the maximum y^+ of 1. The number of elements is chosen to capture the boundary layer profile in the prism shaped elements. The surface mesh on the blade is a mapped, rectilinear grid, with refinements towards the leading/trailing edges and the hub/tip regions.

(a) XPROP propeller

(b) Beaver propeller
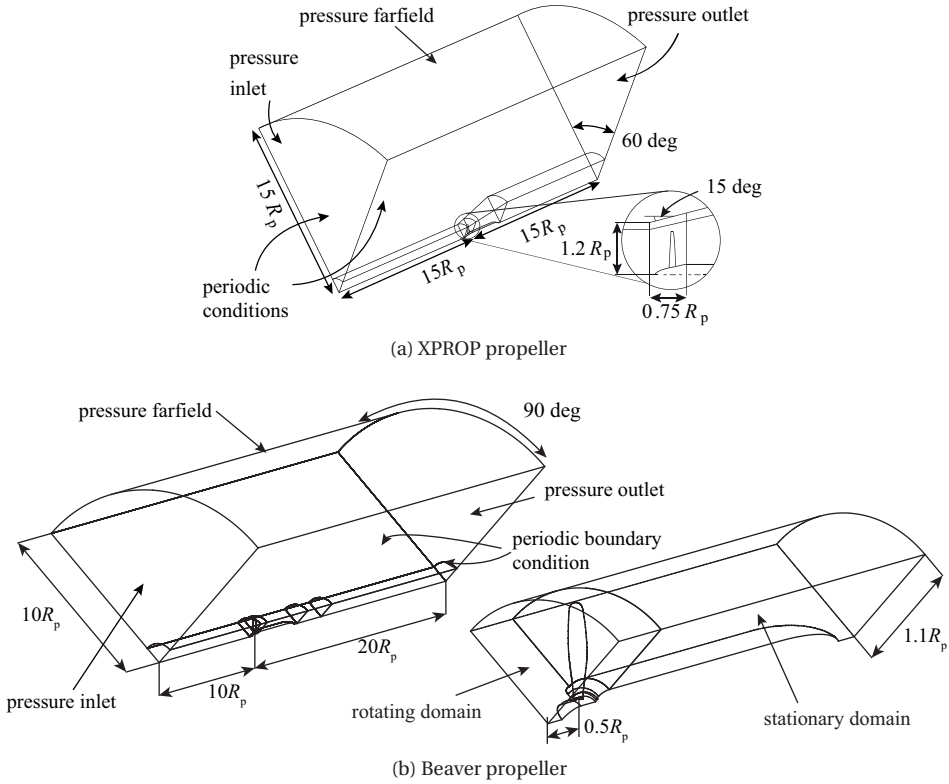
Figure 3.16: Computational domain and boundary conditions for the simulations of the propellers in isolated conditions.

Table 3.8: Mesh details of the CFD simulations for two different propellers in isolated conditions (see Fig. 3.16).

Parameter	XPROP ($\beta_{0.7R_p} = 45$ deg)	Beaver
Prism layers		
• Spinner	28	28
• Blade	28	26
• Nacelle	28	32
• Growth rate	1.2	1.2
Number of divisions surface mesh		
• Chordwise	141	82
• Spanwise	154	128
Max. element size rotating & nacelle domains	$(0.032R_p)^3$	$(0.025R_p)^3$
Number of elements		
• Rotating domain	1,912,719	2,658,134
• Nacelle domain	1,852,244	2,387,459
• Total	4,841,676	7,373,636

ARRAY OF DISTRIBUTED PROPELLERS

The effect of the installation of a propeller as part of an array of distributed propellers is simulated by placing a full XPROP propeller and nacelle in a domain with symmetry boundary conditions on each side, shown in Fig. 3.17. By placing these boundary conditions, the situation is simulated where the 'middle' propeller is part of an infinite array, with the adjacent propeller rotating in opposite direction. Furthermore, the imaginary adjacent propellers have the same rotational speed and are in phase with the middle propeller. The blade angle is set to $\beta_{0.7R_p} = 30$ deg, which is in line with the available experimental data, presented in Ref. [161].
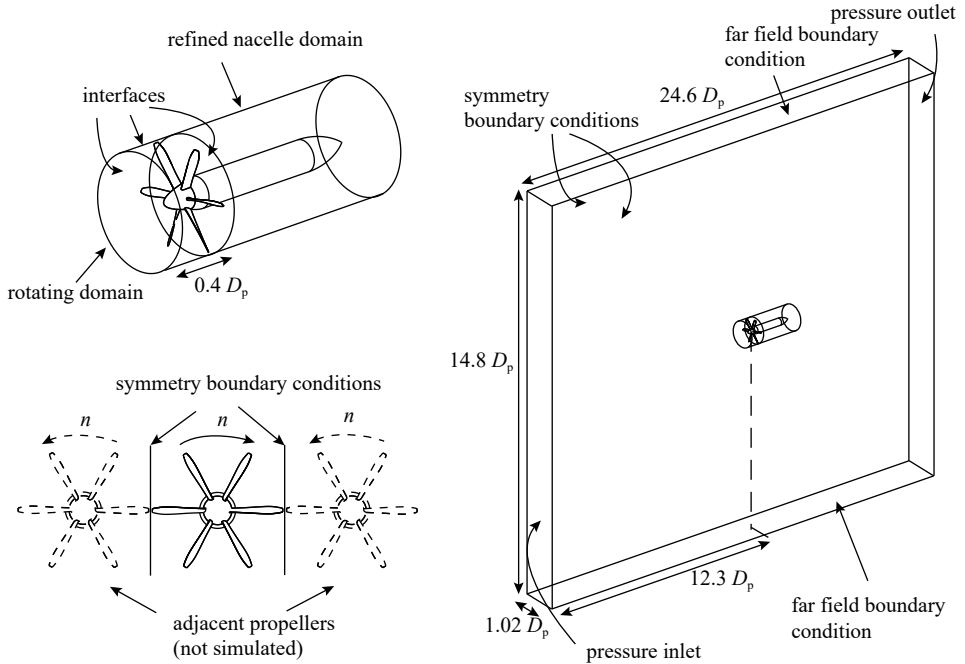
Figure 3.17: XPROP propeller simulated as part of an array of distributed propellers.

As noted in Refs. [96, 97], vortex pairs that have equal strength and are counter rotating, will lead to an instability when the critical distance is met, such that the helical vortex systems start to break down. It is noted that this instability introduced by the tip vortices near the symmetry planes is being obstructed by the symmetry boundary condition. However, from experimental data obtained prior to these simulations (see Ref. [161]), the merging process was not observed relatively close to the propeller disk. Therefore, it is concluded that the boundary condition does influence the development of the flowfield (far) downstream, but is not expected to influence the solution close to the disk. Since it is this latter region that is of interest in this study, a symmetry boundary condition is deemed adequate herein.

The propeller domain has the same characteristics as presented in Table 3.8, with only a slightly different total number of elements. The outer domain contains 6.7 million

elements, while the full setup contains 64.3 million elements.

WING UPSTREAM OF PROPELLER

A wake-encounter by a propeller is simulated by placing a straight wing with no twist upstream of the XPROP propeller ($\beta_{0.7R_\mathrm{p}}$ = 45 deg). A symmetric, NACA0015, airfoil is selected to decouple the viscous and the potential flow contributions of the nonuniform inflow to the propeller. The setup is a conceptual representation of the horizontal tail-mounted propeller configuration shown in Fig. 3.8 and typical values of wing–propeller spacing and the relative size of the wing for an aft-mounted configuration are used [25]. This leads to the selection of a wing chord-to-diameter ratio of 0.8 and a spacing between the wing trailing edge and propeller of $3.2R_\mathrm{p}$. Three wing locations are evaluated to vary the location of the wake-encounter: $z_\mathrm{w}/R_\mathrm{p}$ = [0.50, 0.75, 1.00]. The setup is depicted in Fig. 3.18.

A symmetry boundary condition is set on the symmetry plane. The other boundary conditions are a pressure inlet, pressure outlet, and pressure farfield. The domain containing the wing is coupled to the rotating domain by means of interfaces. The domain that captures the wing wake is refined to avoid excessive diffusion of the wing wake. The full wing–propeller mesh contains 49.1 million elements for the case $z_\mathrm{w}/R_\mathrm{p}$ = 0.75, of which 36% is located the domain containing the wing.
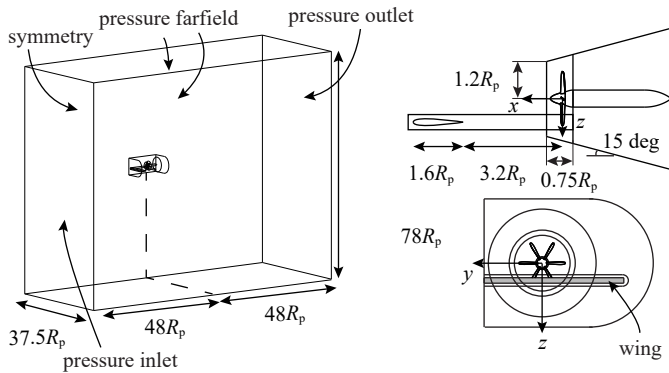
Figure 3.18: Schematic of the CFD domain of the wake-encounter case.

PROPELLER MOUNTED TO TIP OF HORIZONTAL TAILPLANE

The geometry of the case with a propeller mounted to the tip of a horizontal tailplane is the same as discussed in Section 3.3.5. The propeller-tailplane model is simulated in a domain representing the wind-tunnel test section, as shown in Fig. 3.19. The results can therfore be compared to the experimental results. The propeller blades, spinner, nacelle, tailplane, and elevator were modelled as no slip walls, while the front part of the nacelle in the rotating domain was modelled by a moving wall. All wind-tunnel walls were modelled as slip walls, except the top wall on which a no-slip condition was enforced to capture the development of the boundary layer on the tunnel ceiling and its interaction with the tailplane. An angle of attack to the model is simulated by rotating

the model with respect to the wind-tunnel inlet plane. The gaps between the elevator and main element are maintained.

The mesh of the rotating domain containing the propeller is the same as the mesh of the Beaver propeller in isolated conditions. As indicated in Fig. 3.19, the mesh contains several domains, each with a different volume sizing. The inflation layer on the wing consists of 30 layers. The domain downstream of the model that contains the propeller slipstream and wake is refined. This is done to compare the simulation results with the experimentally obtained flowfield data in the PIV plane (as indicated in Fig. 3.19). For each elevator and angle of attack adjustment, a new mesh is constructed. The total number of elements for the case of $\alpha = 0$ deg and $\delta_e = -10$ deg is 49.4 million. An extensive validation study of the mesh that is constructed for the wing is presented in Ref. [133].
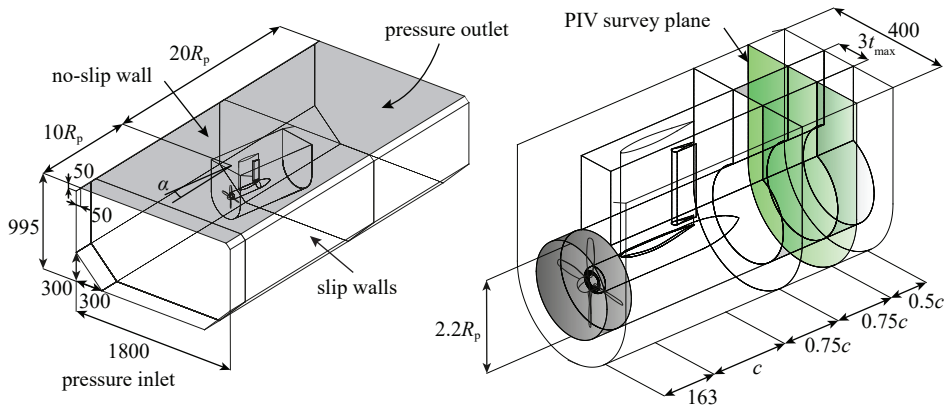
Figure 3.19: Computational domain and boundary conditions used for the simulations.

AIRCRAFT WITH HORIZONTAL-TAIL-MOUNTED PROPELLERS

For the simulation of the full aircraft configuration that features propellers mounted to the horizontal tailplane, the experimental setup of the *VGM-HTP*, discussed in Section 3.3.5, is replicated. A half-model of the clean configuration is placed in a domain resembling the walls of the LTT wind tunnel, shown in Fig. 3.20. The simulations excluded the support struts. The geometry contains the gaps around the elevators, while the gap between the spinner and nacelle, and the gaps associated with the rudder, were sealed for simplicity. The model was placed in a domain with parallel outer boundaries on which a free-slip boundary condition was specified (as sketched in Fig. 3.8), to resemble the wind-tunnel walls that are diverging by approximately 0.5 deg to compensate for buoyancy effects.

A pressure inlet boundary condition was placed far upstream of the model at $x/b_w = 2.7$. The flow direction is enforced to be normal to this boundary, and the magnitude matches the conditions of the experiment. The domain size is chosen based on the gradients $d\alpha/dx$ and dC_{p_s}/dx. Already at $x/b_w = 2.0$ these gradients have reached negligible values (see Fig. 3.21a), while the boundary is placed further upstream. One indication of a small but appreciable effect of the presence of the wind-tunnel walls on

(a) Computational domain with boundary conditions. (b) Detailed view of the rotating domain containing the propeller.
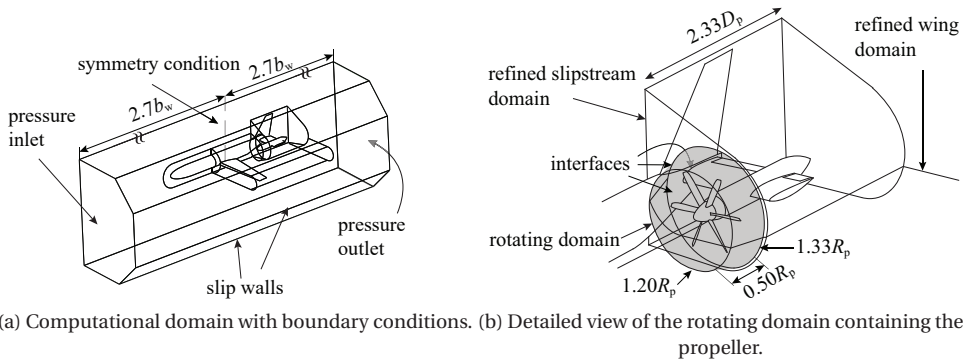
Figure 3.20: Overview of computational domain and boundary conditions for the simulations of the *VGM-HTP* model.

the forces acting on the airframe when the propellers are operating, is obtained by comparing the static pressure along the centreline of the test section. The non-zero gauge-pressure is indicative of a wall effect. The figure shows that the wall effect due to the propellers is a combination of a scaling of C_{p_s} from a ΔC_L, and a distribution of C_{p_s} along x. Relatively simple wind-tunnel corrections do not suffice since the source of momentum is introduced close to the model at a distinct location. A wall correction that is determined with a numerical model would be the most suitable solution, which requires significant resources, while it is not expected to influence the conclusions on the interaction. Therefore, no wall correction is computed.

The unstructured volume grid contained tetrahedral elements with refined grids in the proximity of the model, indicated in Fig. 3.20a. The propeller was placed in a rotating domain, indicated in Fig. 3.20b, using the sliding mesh approach [139] by defining interfaces on each side. The cell size of the domain adjacent to the rotating domain containing the horizontal tail, is the same as the size of the volume elements of the isolated propeller setup (see Table 3.8). Wall-refinements are applied and an inflation layer of 25 layers with a growth rate of 1.20 is constructed on all no-slip walls (except for the propeller). On the wing a mapped, rectilinear surface mesh is constructed. The selected grid including propeller contained 60.5 million cells, while the grid of the propeller-off condition contained 51.8 million cells.

(a) Wall pressure along the centerline of the tunnel, $\alpha = 0$ deg.

(b) Flowfield along centerline, $y/b_w = 0$.
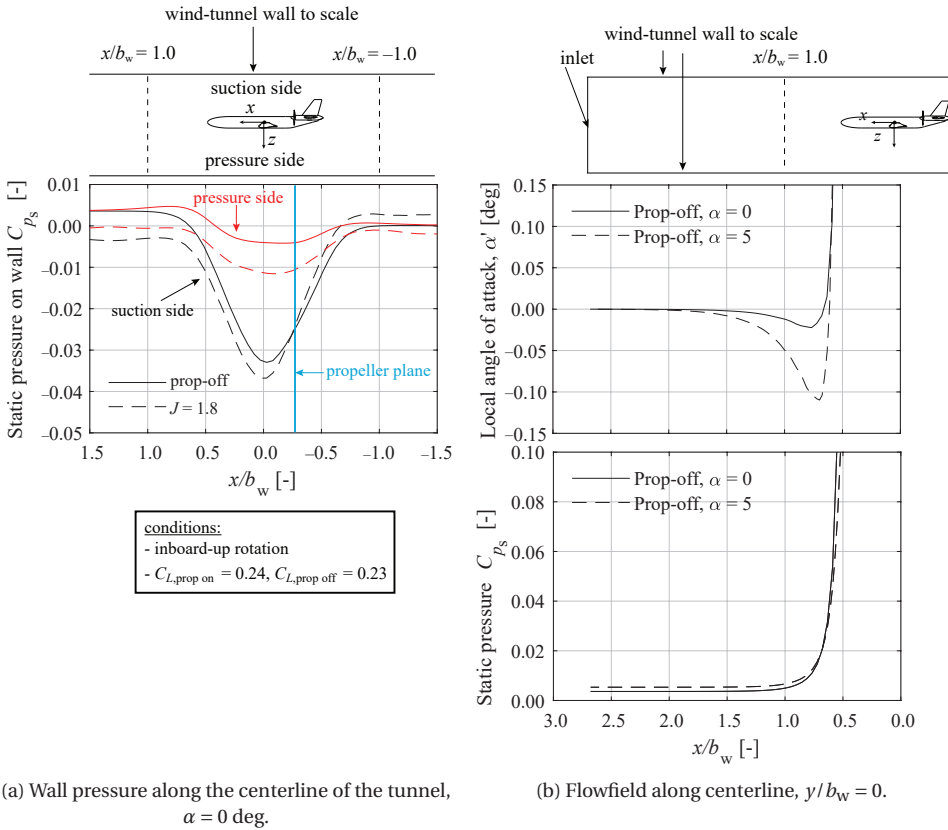
Figure 3.21: Indication of the effect of finite domain with boundary conditions on the flowfield upstream and downstream of the model at $y/b_w = 0$.

AIRCRAFT WITH LEADING EDGE DISTRIBUTED PROPELLERS

The last configuration that is studied is a full aircraft configuration with propellers mounted to the leading edge of the wing, referred to as *A320-DP*. Contrary to the other cases, for this configuration in particular the propulsion installation effects on the wing performance and aircraft longitudinal stability are of interest. The geometry resembles an Airbus A320, a geometry that was defined in the European Clean-Sky project NOVAIR. Because of the confidential geometry, only a schematic is provided in Fig. 3.22 that outlines the general characteristics. Several considerations and constraints are taken into account for the propeller location, operating condition, and diameter. This is a trade-off between cruise, climb, and ground-roll performance, the landing gear position, cruise angle of attack, and unsteady loads that can be expected to act on the wing.

Since the nonuniformity of the inflow to the propellers is relatively small, and only the mean performance of the wing is of interest, the propeller installation is modelled by the actuator disk approach, as discussed in Section 3.4.3. The upstream effect of the
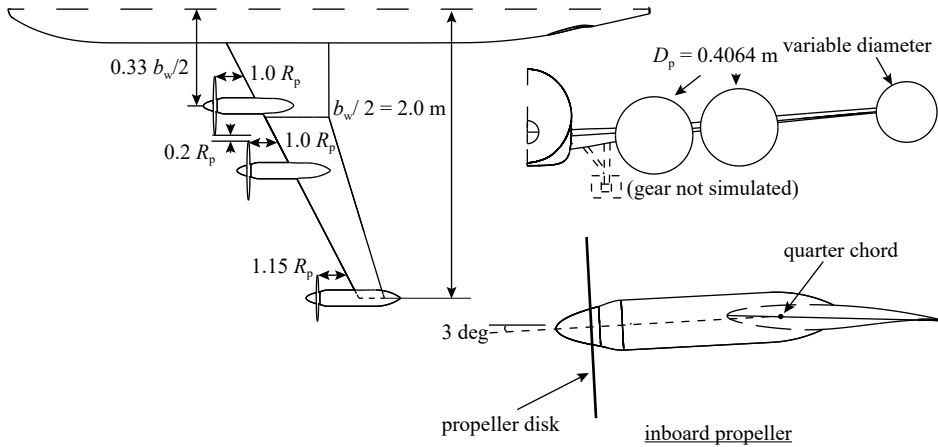
Figure 3.22: Technical drawings of the leading edge distributed propeller configuration, as studied in the CleanSky project NOVAIR.

wing on the propeller loading is included in the simulations. The characteristics for the actuator disk is determined based on the method described in Chapter 5. As indicated in Fig. 3.22, the disks are tilted downwards with 3 deg, to compensate for the positive angle of attack during cruise condition, as well as the upwash of the wing, which both would induce an angle of attack to the propeller. It is noted that there is no fillet to make the junction between the nacelle and wing leading edge less pronounced (see e.g. Ref [162]) with the goal of preventing flow separation. It will be shown that the separated flow in this region due to the sweep angle is influenced by the installation of the propeller. The model dimensions and flight conditions are that of a scaled version of the full aircraft. The flight speed is set to 46 m/s, and ambient conditions are specified as 600m above mean sea level.

The inboard propeller locations are chosen on sufficient clearance to the fuselage and main landing gear and a small clearance between the propeller tips to avoid propeller–propeller interaction. A propeller is mounted to the wing tip to increase the lift-to-drag ratio, in particular in cruise condition (see e.g. Ref. [49]).

The half model is placed in the middle of a rectangular domain with a symmetry boundary condition on the symmetry plane. A pressure inlet, pressure outlet, and pressure far field boundary conditions are specified on the remaining boundaries. The domain measures $7.5b_w$ in spanwise direction, $15b_w$ in z-direction, $15b_w$ upstream, and $25b_w$ in downstream direction. An inflation layer is constructed from the no-slip walls with 26 layers and a growth rate of 1.25. The domain containing the model is refined, with a maximum element size of $(0.03R_p)^3$, which is in line with the selected sizing in the other cases. The domain containing the model has 31.2 million elements, while the total mesh consists of 36.9 million elements.

4

ASSESSMENT AND VALIDATION OF CFD METHODS

The numerical simulations that are used in subsequent chapters are compared with experimental data to demonstrate to what extent the goal of the particular simulation can be met, either qualitatively or quantitatively. The following simulated cases are validated, with increasing level of integration:

- Case I: **Isolated propellers** in Section 4.2.1. These serve not only as reference condition, but the propeller disk and slipstream also act as a boundary condition to the airframe components that are submerged in the slipstream. Therefore, besides the comparison of the forces acting on the propeller, also agreement of the slipstream shape is of importance for the subsequent analyses of the installed configurations.

- Case II: A **propeller–tailplane combination** in Section 4.2.2. This validation study demonstrates the capability of simulating the interaction of the slipstream with a lifting surface by comparing load distributions and the associated flowfields.

- Case III: An **aircraft with horizontal-tailplane-mounted propellers** in Section 4.2.3. In this study, the validity of the simulations of a full aircraft configuration is quantified, since they entail interactions that are dominated by both airframe-to-propeller and propeller-to-airframe interactions.

Even though the geometry of cases II and III are different, the computational strategy, operating conditions, and choices for mesh sizing are similar. Therefore, although indirectly, general conclusions can be formulated on the validity of the numerical approach. First, an estimation of the discretization error for the isolated propeller simulation is given in Section 4.1, followed by the validation studies in the subsequent sections.

Parts of this chapter have been published in Refs. [90, 118, 120, 133].

4.1. ESTIMATION OF DISCRETIZATION ERROR FOR ISOLATED PROPELLER SIMULATIONS

The mesh of the XPROP propeller is selected based on a trade-off between on the one hand achieving sufficient accuracy of the quantities of interest, and computational cost on the other hand. First, the discretization errors of the integral forces are estimated prior to a comparison of the propeller slipstream. An estimation of the discretization error for the Beaver propeller is presented in Ref. [133] and not repeated herein.

Since the temporal and spatial discretization of the RANS equations are close to second-order (see Section 3.4), a minimum of three meshes is required to determine the discretization error if the quantity of interest indeed follows a second-order convergence. Since not all quantities of interest necessarily behave in such way, four meshes of different refinements are used. In line with the suggestions presented in Ref. [163], the refinements are systematically varied with a refinement factor of 1.3, applied to volume and surface refinements, while the inflation layer is kept approximately constant. If also the inflation layer is varied, modelling error will play a role of the estimated discretization error. The mean refinement factors for the complete wedge-shaped domain are listed in Table 4.1, where h_i is the average cell size of grid i. More specific details of the mesh can be found in Table 3.8 in Chapter 3.

Table 4.1: Different grids for the simulation of a single XPROP propeller blade in uninstalled conditions.

Grid	h_i/h_1	Number of elements
Grid 1	1.00	17,986,198
Grid 2	1.25	9,163,007
Grid 3	1.55	4,841,676
Grid 4	1.87	2,744,493

A least-squares version of the grid convergence index (GCI) as proposed by Ref. [164] is applied to estimate the discretization error, in a similar manner as the study performed by Ref. [133]. Figure 4.1 shows two force coefficients for the different meshes for the design condition of $J = 1.8$. The thrust, respectively, power coefficients in Figs. 4.1a and 4.1b decrease with a finer mesh due to a better description of the suction peak on the blade sections with more elements along the chord.

In Table 4.2 the observed order p is listed, which is lower than the order of the discretization, indicating that these coefficients have a relatively low dependency on the choice of mesh. The fact that the order of convergence is not equal to the theoretical order of the schemes is explained by the coupling between the load distribution and the formation of the helical vortex system. Furthermore, the airfoil geometry varies along the blade and each section may have a different resulting lift coefficient due to grid refinement. Although the orders are quite different than second-order, the fitting error for a second-order fit (U_s^*) is still small. For grid 3, the estimated discretization error U_ϕ falls within 2% for both C_P and C_T, depending on the selected order of convergence. If a second-order convergence is assumed, the error reduces to less than 0.5%. Since the

thrust is dominated by pressure forces, while the power coefficient also has a relatively large contribution from the shear stress, the thrust and power coefficients have different discretization errors since the inflation layer is not altered between the different grids. Therefore, also the propeller efficiency is slightly dependent on the choice of the mesh.

(a) Thrust coefficient   (b) Power coefficient
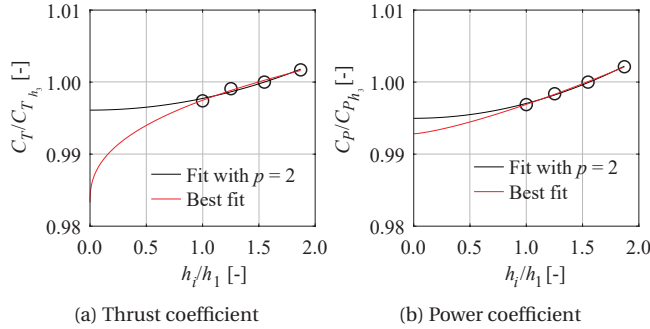
Figure 4.1: Mesh refinement study for the XPROP propeller blade in uninstalled conditions.

Table 4.2: Results of the for the XPROP propeller blade in uninstalled conditions.

	C_T	C_P
Observed order p	0.40	1.31
Standard deviation w.r.t observed order, U_s [%]	0.04	0.01
Standard deviation w.r.t second-order fit, U_s^* [%]	0.06	0.03
Extrapolated value relative to grid 3, U_ϕ [%]	−1.7	−0.7

Since the sizing used for the slipstream domain is a key parameter to capture the propagation of the slipstream to airframe components, also the shape of the slipstream is compared between the different grids. Instead of assessing a flow quantity at a single point, the relevant distributions are compared. Figure 4.2a depicts the phase-averaged total-pressure distribution downstream the propeller, which is a good indication of the blade loading as the integral value approximately represents the thrust (see Fig. 4.3b). The low dependency of the distribution on the different grids over the majority of the radius is as expected: the thrust and power coefficients vary less than 1% between the grids, and therefore the integral value of C_{p_t} should not vary significantly. The largest deviations are present near the edge of the slipstream, where large velocity gradients are present as it is the shear layer of the slipstream. The figure shows a lower gradient for the grids with less refinement. The edge of the slipstream is slightly wider for the coarser meshes, indicating the effect of numerical diffusion on the solution.

A comparison of the instantaneous flowfield shows where these differences originate. Figure 4.2b depicts the total pressure along a radial line passing through the propeller tip-vortex. The figure shows a consistent increase in the gradient of the tip vortex when the grid become more refined, but also indicates that the radius of the vortex core

reduces. This is especially observable in Fig. 4.2c, which depicts the out-of-plane component of vorticity in the tip-vortex region between the least and most refined grids. The larger discrepancy in the tip region is caused by dissipation and in particularly diffusion of the tip vortices, in line with the results of e.g. Ref. [133, 152]. Besides the radius that is larger for grid 4, also the shape of the vortex is clearly different than the one in grid 1. The vortex in grid 1 has not yet fully rolled up into a single vortex, which is another indication that numerical diffusion impacts the vortex development in grid 4. Interestingly, there is a minimal difference in the circulation of the tip vortices, of which the out-of-plane component is plotted in Fig. 4.2d. Only the spread is shown, as it was found that due to inaccuracies in interpolation and integration of ω_z^* no clear trends are observable. Besides, since only a component of the vorticity is integrated here and not the vorticity magnitude, slight changes in helicity also impacts the value of Γ_z^*. Nevertheless, the figure indicates that indeed the dissipation is minor as the circulation does not vary significantly between the grids. This is the reason why outside the vortex, there is nearly no difference between the grids.

(a) Phase-averaged total-pressure distribution at $x/R_p = 1.1$

(b) Instantaneous total-pressure distribution along a survey line at $x/R_p = 1.1$

(c) Comparison shape and concentration of tip vortex between two meshes. Normalized out-of-plane component.

(d) Variation of tip-vortex circulation between meshes, only out-of-plane component.
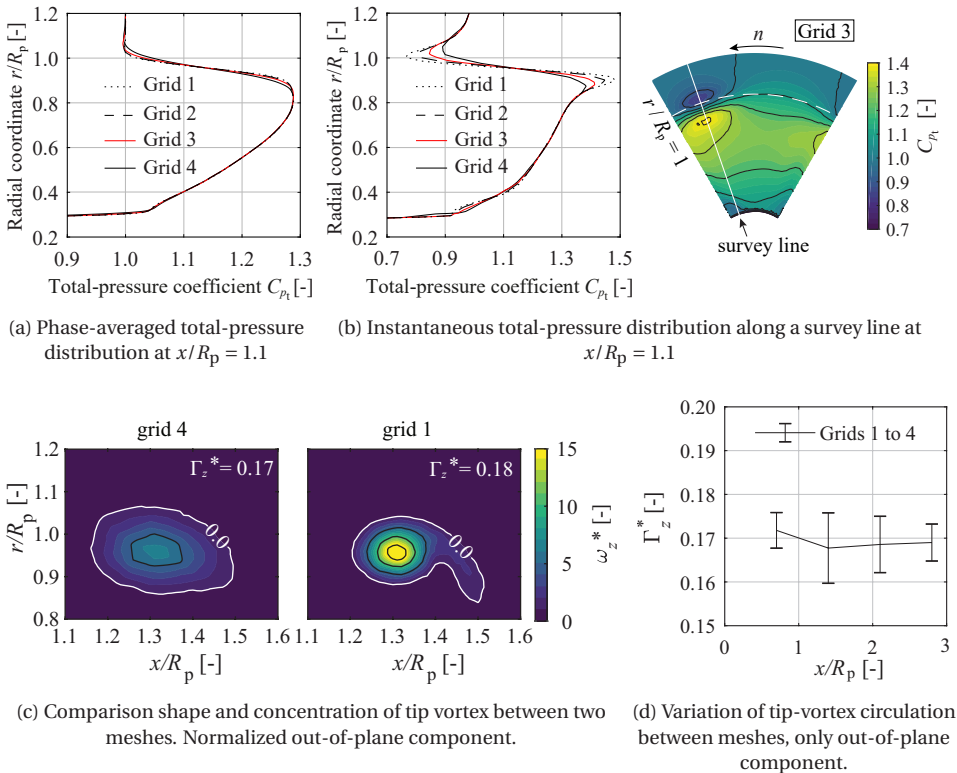
Figure 4.2: Comparison of the flowfield for different grids of the XPROP propeller blade in uninstalled conditions.

The fact that the instantaneous velocity and pressure field is vastly better described by a fine mesh, which means that such a grid will therefore be more suitable if e.g. the unsteady pressure fluctuations on an airframe component submerged in the slipstream are required to be captured. If the description of the average slipstream is desired, a coarse mesh will still be suitable. However, it is noted that the interaction between vortices, for example the propeller helical vortex system with the vortex system of a lifting surface, is influenced by the radius of the vortex core [165], which does depend on the choice of the mesh size. Therefore, for such interaction studies, the flowfield and the gradients should still be sufficiently captured. To demonstrate that for the selected mesh this is the case, in the following section the installed configuration is assessed.

Provided that the majority of the time-averaged slipstream profile does largely not depend on the mesh choice, the largest mesh that can still be computed within the available computational resources is therefore desired. Grid 3 is selected as a compromise between computational efficiency and accuracy, as the finer grids only lead to marginal improvement of the propeller slipstream quantities and integral forces. The corresponding discretization error listed in Table 4.2 is included in the error bars of the isolated propeller simulation.

Unfortunately, second-order schemes require extremely dense grids to avoid excessive numerical diffusion. This would result in an excessively high computational cost [166], and was not within the reach of this research. Provided that the path of the vortical structures can be estimated relatively easily, local grid adaptation could be a more efficient way if the numerical diffusion is to be avoided. Alternatively, as suggested by Ref. [166], a higher-order scheme is a computationally more efficient way than further refinement of the grid. However, this is not further explored in this research.

4.2. Validation of CFD Methods

4.2.1. Isolated Propeller Simulations

For the XPROP propeller, the nominal condition of $J = 1.8$ at $V_\infty = 40$ m/s is the most important condition to quantify the difference with experimental data, since the majority of the simulations of the installed configuration are performed at this condition. Because in the installed cases the inflow varies from this freestream condition, and therefore different advance ratios are experienced by the blade sections locally, also off-design conditions are assessed in this section. In contrast, the flowfield and thrust generated by the Beaver propeller is compared in only one condition ($J = 0.8$ at $V_\infty = 40$ m/s), since the airframe induced inflow for that propeller in installed conditions is relatively uniform, no other operating conditions are compared with the experimental data.

Thrust Curve of XPROP Propeller

Figure 4.3a shows the computed $C_T - J$ curve compared to the experimental data. In the experiment no direct thrust was measured (for example by an internal load cell). Instead, the experimental $C_T - J$ curves are constructed from by integrating the total-pressure coefficient in the slipstream, and by estimating the propeller thrust by means of the external balance. Since the C_{p_t} profile of the propeller-on condition also contains the boundary layer formed on the nacelle and spinner, the difference in propeller-on and

propeller-off, ΔC_{p_t}, is integrated from the nacelle surface up and to a radial coordinate corresponding again to freestream condition:

$$T \approx \int_r 2\pi r q_\infty \left(C_{p_{t\mathrm{on}}}(r) - C_{p_{t\mathrm{off}}}(r) \right) dr \qquad (4.1)$$

Since the total-pressure profile is slightly contracted, an integration along the radial direction inherently does not exactly represent the loading on the disk; the streamlines with a constant total pressure are displaced. Furthermore, the total pressure also contains the contribution of swirl [167]. In Fig. 4.3b it is shown that for the CFD results the integration of the total pressure is for this case an excellent method to determine the thrust, compared to integrating the pressure and viscous forces on the blades. In this case, the deviation over the majority of advance ratios is only $\Delta C_T \approx 0.0005$—equivalent to 0.3% of the thrust at design condition of $J = 1.8$. It is noted that for a different nacelle geometry such integration may lead to much larger errors. Only at high thrust condition, the loss in total pressure due to flow separation from the blades leads to an underprediction of thrust.

The curves in Fig. 4.3a show that the balance data and the integration of total pressure yield comparable results. The slope of the $C_T - J$ curve obtained from the external balance data deviates from the pressure integration results depending on the free stream velocity, indicating that the Reynolds number has quite a distinct effect on the drag of the support strut, on which also the changes in forces are included (see Section 3.3.5).

Compared to the experimental data at $V_\infty = 40$ m/s, Fig. 4.3a indicates that CFD overpredicts the thrust, while the slope of the linear part of the $C_T - J$ curve is approximately 20% lower. The onset of the nonlinear part of the thrust curve is observed around $J = 1.4$ in the experiment, while the CFD simulations predict it to initiate at $J = 1.3$. The computed curve also is more gradual around this onset, indicating that the predicted stall on the blades is more gradual. It becomes clear that only near the advance ratio for cruise conditions ($J = 1.8 - 1.9$) the experimental data shows good agreement with the measured data, deviating around 2%, which falls within the discretization error of the CFD simulation (Table 4.2).
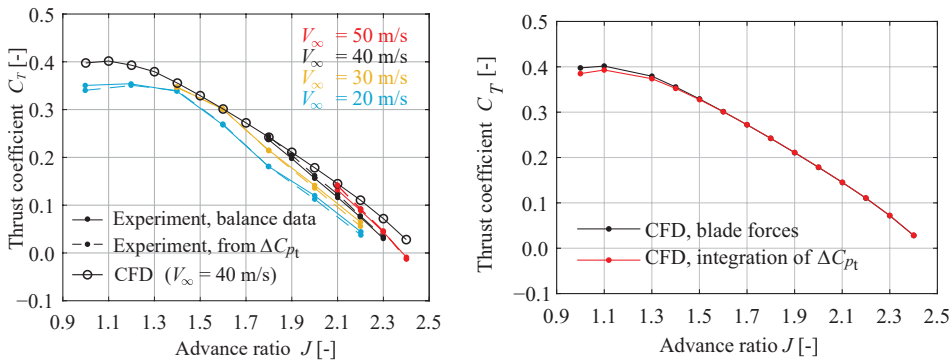
(a) Thrust coefficient at different freestream velocities   (b) Comparison of blade forces vs. integration C_{p_t}

Figure 4.3: Comparison of the thrust curve for the XPROP propeller with experimental data.

Figure 4.3a also shows a significant offset of the measured C_T curve between $V_\infty = 20$ m/s and 50 m/s. As already discussed in Section 2.5, there is a clear influence of the freestream velocity on C_T since the Reynolds number along the blade depends on V_∞. The boundary layer formed on the blade is expected to be predominately laminar in the experiment, while it is enforced to be turbulent in the CFD simulations. Part of these deviations can therefore be attributed to the different aerodynamic properties of the blade sections.

To identify whether the trend in the C_T curve can be traced to the different state of the boundary layer, the slope of the two-dimensional lift curve, the zero-lift angle of attack, and the local flow angle are the key parameters that should be compared. Analyses using a two-dimensional viscous-inviscid coupled panel code at low Reynolds number can therefore provide insight into the airfoil characteristics. Since no measurements were performed on the propeller blades, the findings will only be used qualitatively. To this end, a representative airfoil at the radial location of $r/R_\mathrm{p} = 0.7$ (close to the highest loaded location on the blade) is selected for further investigation using XFOIL [168]. At the selected radial location, the Reynolds number varies over a wide range, shown in Fig. 4.4a for a range of freestream velocities. At the advance ratio of interest ($J = 1.8$), the value is approximately $Re_{c,0.7R} = 40,000$ for the freestream condition of interest ($V_\infty = 40$ m/s).

At a given angle of attack, equivalent to a constant advance ratio, this airfoil lift coefficient is strongly dependent on Reynolds number if transition is not enforced, as shown in Fig. 4.4b, in particular for Reynolds numbers below $80,000$. This is a combination of $c_{l\alpha}$ and α_0 being both dependent on Re, which is especially the case for cambered airfoils [169]. It is noted that the nonlinear range is exactly the range of Reynolds number that is of interest for the experimental campaigns. Even at the highest freestream velocity considered, over the full range of advance ratios, the Reynolds number on this section remains below this critical value. This behaviour is caused by the formation of a laminar separation bubble on both the suction and pressure side at $\alpha = 0$. For $\alpha > 2$ deg, these disappear, and laminar separation on the suction side occurs that does not reattach and initiates around $x/c = 0.5$. The pressure side remains laminar, while transition on the suction side occurs close to the trailing edge and downstream of the separation point. At higher angle of attack ($\alpha > 4$ deg), the separated flow on the suction side reattaches, and the transition point moves towards the leading edge. This leads to a nonlinearity of the lift curve at low Reynolds number, of which a few examples are depicted in Fig. 4.4c. To the contrary, the airfoil with a fully turbulent boundary layer shows a gradual behaviour as expected, since the state of the boundary layer is constant and only the boundary layer displacement thickness is a function of Reynolds number.
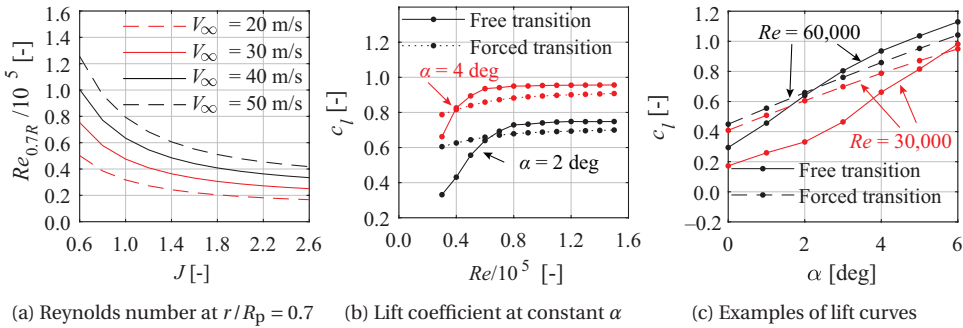
(a) Reynolds number at $r/R_p = 0.7$ (b) Lift coefficient at constant α (c) Examples of lift curves

Figure 4.4: Effect of Reynolds number on the two-dimensional lift coefficient of the airfoil at $r/R_p = 0.7$ of the XPROP propeller.

Since a reducing J, does not only lead to a higher angle of attack but also a higher Reynolds number, the *apparent lift curve* of each airfoil section is a combination of $c_{l\alpha}(Re)$ and $\alpha_0(Re)$. The net effect is that this apparent curve has a relatively high slope (Fig. 2.25b) and directly translates to a higher slope of the $C_T - J$ curve, shown in Fig. 4.5a which is an enlarged version of Fig. 4.3b. To the contrary, the thrust curves from CFD simulations have a significantly lower dependency on freestream velocity, in line with the analyses of the two-dimensional airfoil section. The observed shift of the CFD curve is a consequence of the effective camber of the profiles that is smaller at low Reynolds number, hence a horizontal and vertical shift of the $C_T - J$ curve. The reduced effective camber is visible in the pressure distribution along the full chord of the airfoil, shown in Fig. 4.5b, extracted from the propeller CFD simulation. It may be noted in Fig. 4.4a that the increase in Reynolds number going from $J = 2.4$ to 1.7 is nearly the same for $V_\infty = 30$ m/s and 40 m/s. The fact that the boundary layer thickness of a turbulent boundary is nearly inversely proportional to the Reynolds number [170], the *slope* of $C_T - J$ curve remains nearly the same since ΔRe is nearly the same. It is noted that the situation is drastically different in case the airfoils would be symmetric: the shift in the experimental $C_T - J$ curve would be smaller since α_0 remains zero.

Next to the two-dimensional situation, where transition is caused by Tollmien-Schlichting waves, a more pronounced cross-flow exists at high advance ratios, as shown in Ref. [171], which could lead to a cross-flow induced transition on the blade in the experiment, prior to the transition induced by Tollmien-Schlichting waves. This is for example demonstrated in Ref. [172], and would increase the similarity between experiment and CFD. The radial acceleration on the boundary layer on the rotating blades is largest at low advance ratio. However, at high advance ratios, the *relative* contribution of viscous forces is large compared to the pressure forces. Therefore, the relative error between CFD and experiment in Fig. 4.3 is more pronounced as well.

It is stressed that since the slope of the thrust curve is underestimated by approximately 20%, a change in advance ratio that is caused by the propeller installation, would therefore also lead to a smaller change in propeller forces compared to the experimental setup. Nevertheless, provided that in a full-scale situation, the state of the actual bound-

(a) Performance curves, detail

(b) Pressure distribution from CFD normalized with $q_{helical}$ at $r/R_p = 0.70$, $J = 1.8$.
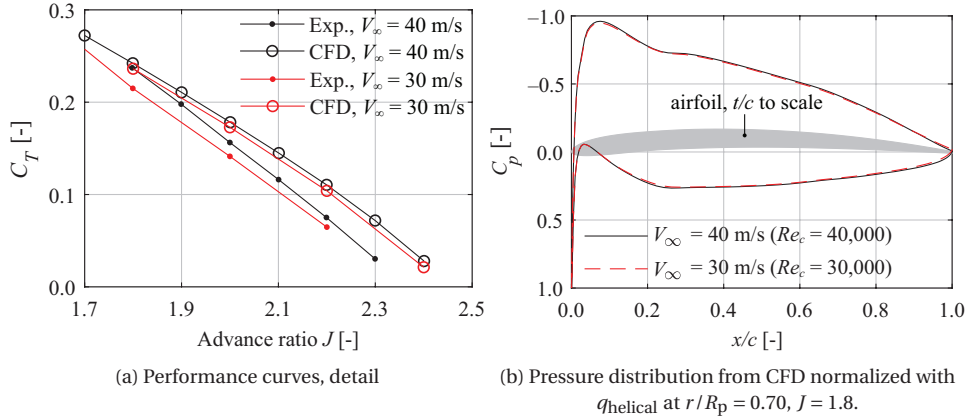
Figure 4.5: Comparison of thrust and pressure distributions for the XPROP propeller at different freestream velocities.

ary layer on the blades is closer to CFD simulations than in an experiment, the CFD results and observed trends of the propeller forces are therefore particularly relevant. It is also observed that, while the predicted integral thrust nearly coincides with the experimental value in the design condition, it is no guarantee that the computed slipstream also matches the experiment. In fact, due to the known difference in boundary layer state along the blade, the slipstream will by definition not match. This is further investigated in the following subsection.

To conclude, the deviation of the integral thrust at the cruise condition (around $J = 1.8$) with experiment is 2% and is considered an acceptable overprediction to perform further analyses of the installed condition. Since it is this condition that is most of interest for the subsequent CFD simulations, no reduction of the blade angle in the computational model is implemented to obtain a better match with the experimental data. A lower blade angle would also reduce the gradient of the propeller normal force, which is not desired.

SLIPSTREAM OF XPROP AND BEAVER PROPELLERS

Next to the forces that act on the isolated propeller, for the propeller–airframe interaction studies in particular both time-dependent and the time-averaged flow quantities in the slipstream are relevant. These are compared with experimental data for both the XPROP and Beaver propeller. These flowfields will also provide further insight into the deviations observed in the offset of the $C_T - J$ curve of the XPROP propeller in the previous subsection.

The total-pressure profile in the slipstream entails the load distribution on the blade. Figure 4.6 shows the distribution at $1.1R_p$ behind the XPROP propeller for various advance ratios. The profiles show a slightly irregular loading distribution at high advance ratios at a radial location with highest loading ($r/R_p = 0.6 - 0.9$), which is expected to be the result of local laminar separation, as observed in the analyses of the two-dimensional airfoil sections. At lower advance ratios the waviness in the loading distributions disap-

pears and the numerically computed total-pressure distribution approaches the measured distribution. The higher pressure losses near the nacelle in the experiment are attributed to the transition strip on the nacelle. From the figure it becomes clear that the contraction of the slipstream is slightly underestimated by the numerical simulations, similarly to the results in e.g. Ref. [133], which is shifting the momentum rise towards the hub. As discussed in Section 2.1.2, a smaller contraction could be caused by diffusion of the tip vortex. Note that the shaded region around the computed C_{p_t} at $J = 1.8$ indicates the uncertainty in the slipstream distribution due to uncertainty in the blade pitch angle and fluctuations in rotational speed in the experiment. These uncertainties are much smaller than the deviation from the experiment and are not a significant factor. Although the maximum rise in total pressure is well predicted at $J = 1.8$, the lower values up to $r/R_p = 0.8$ in the simulations is due to a combination of a lower contraction ratio, higher viscous losses, and lower axial induced velocity.

4
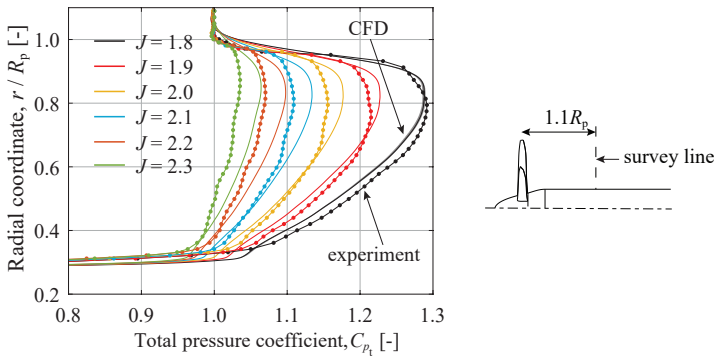
Figure 4.6: Time averaged C_{p_t} for the XPROP propeller at $x/R_p = 1.1$, $V_\infty = 40$ m/s. Uncertainty of $\beta_{0.7R_p}$ and n indicated by the shaded area for $J = 1.8$ (nearly indistinguishable).

A better insight in the relative contributions to the total-pressure rise, the time-averaged velocity fields between CFD and experiment are compared. Figure 4.7 depicts axial and tangential velocity field in a plane parallel to the freestream. At half a radius downstream the propeller, the surveylines indicate good agreement between CFD and experiment, both the distribution and magnitude of the averaged induced velocities are well predicted. Although the PIV results are not available up to $r/R_p = 0.5$, the trend is indicating that there is larger swirl in that region and a lower axial induced velocity in the CFD results, explaining the lower C_{p_t}. Figure 4.7 also shows that the development of the slipstream in axial direction is very well captured at $r/R_p = 0.8$. Towards the hub ($r/R_p = 0.6$) the simulation result shows a lower axial induction, in line with the higher momentum loss in the turbulent boundary layer.

Figure 4.7: Comparison of the computed and measured phase-averaged slipstream by means of stereoscopic PIV for the XPROP propeller. The shaded are indicates the uncertainty band of the measured PIV result, which is omitted for survey line A for the sake of readability. Conditions: $V_\infty = 40$ m/s, $J = 1.8$.

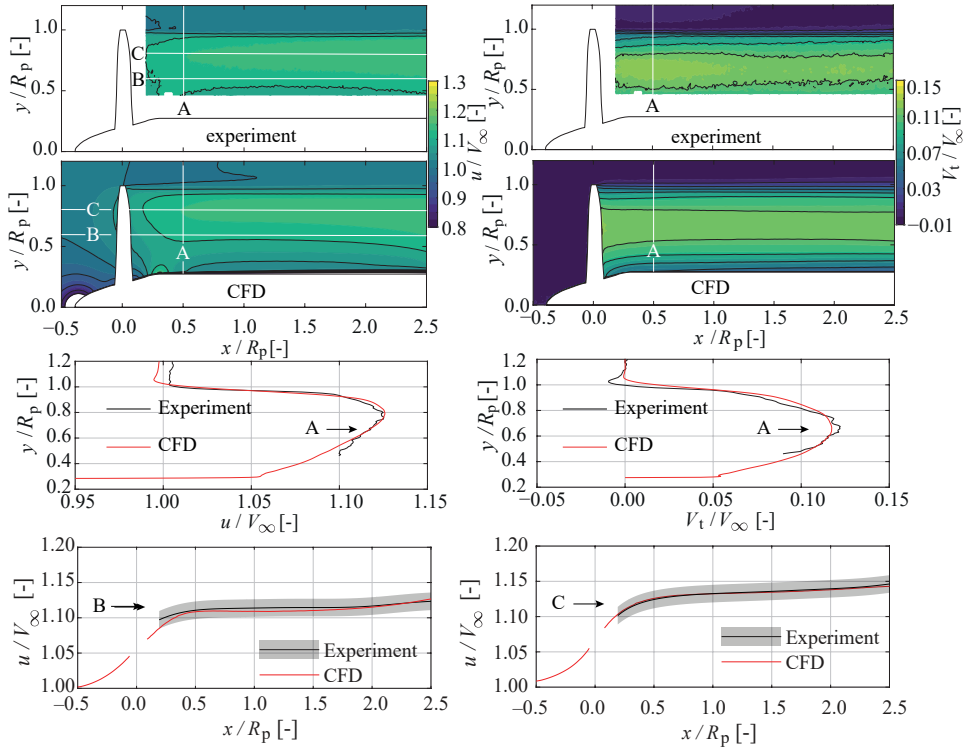A comparison of the phase-locked velocity fields obtained from the CFD simulations and PIV measurements is shown in Figs. 4.8a and 4.8b. The velocity distribution along a vertical survey line (D) through the first tip vortex reveals a lower velocity gradient through the vortex in the computed velocity field, comparable to the findings in Ref. [133]. While the velocity distribution along the survey line suggests the vortex is significantly weaker in the CFD simulation, instead, the vortex is more diffused in the CFD computation than in the experiment. Outside the tip vortex region, the computed velocity distribution matches well with the measured distribution, although the deviation grows downstream of the propeller plane. It is expected that the growing difference between measured and computed phase-locked axial velocity for the three radial stations, is primarily caused by diffusion of the vortex structures in the CFD simulation that occurs downstream of the propeller. Comparisons of the wake profiles in the CFD along the horizontal survey lines also reveal more diffusion of the blade wakes.

Figure 4.8c clearly shows the profound effect of diffusion on the transport of the vorticity in the tip vortices in downstream direction. While the experiment shows a small region of concentrated vorticity which requires several radii downstream of the propeller to form a axisymmetric vortex, the CFD simulations show the vorticity to be distributed

97

over a much larger area. Again, the observation can be made that the circulation in the vortex is comparable to the experimental value, depicted in Fig. 4.8d. The lower circulation for $x/R_p > 1$ is expected to be a combination of dissipation and a slightly different helicity.

From the phase-locked results, it can be concluded that the magnitude of the unsteady forces resulting from vortex impingement on a lifting surface should therefore be interpreted with care. As the loading distribution is the primary focus of the studies with the XPROP propeller, the slipstream development far downstream and the local gradients in velocity are of secondary importance. It is therefore concluded that the validity of the CFD model of the isolated propeller is sufficient to be used in subsequent analyses.

(a) Comparison of phase locked velocity field

(b) Velocity along survey lines defined in (a)

(c) Vorticity distribution, out-of-plane component

(d) Vortex strength
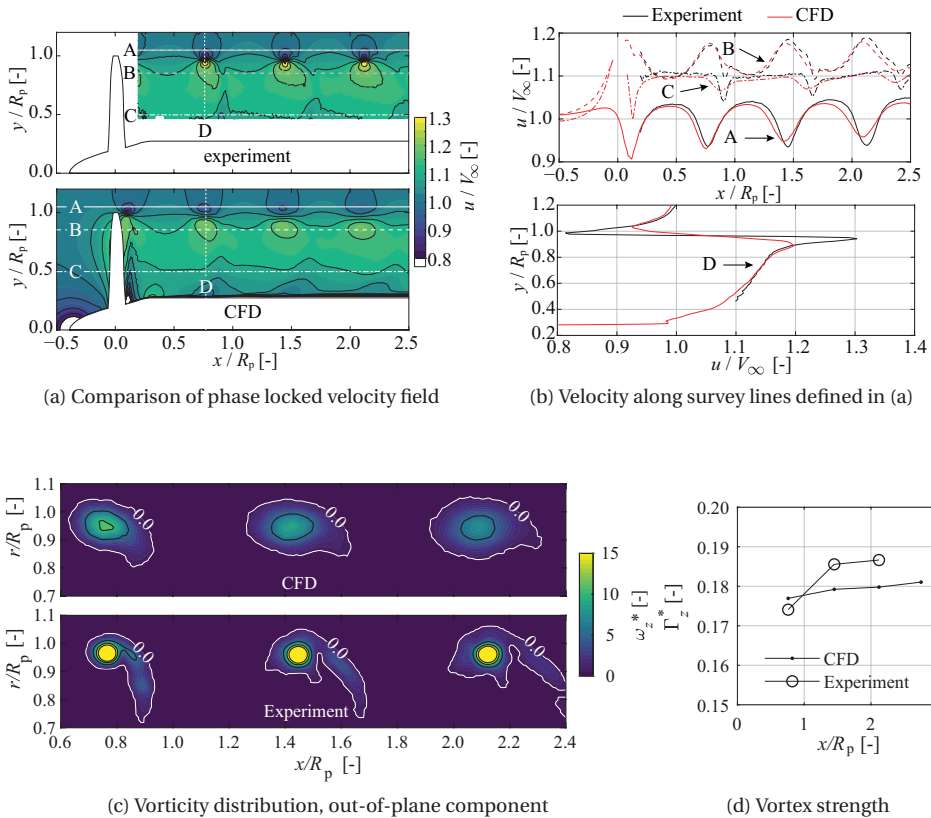
Figure 4.8: Comparison of the computed and measured instantaneous slipstream by means of stereoscopic PIV for the XPROP propeller. Propeller blade at same phase angle. Conditions: $V_\infty = 40$ m/s, $J = 1.8$.

As discussed, the slope of the propeller thrust curve computed using CFD and the curve from the experiment differ significantly and have a relatively large offset. Besides the design condition that matches well in terms of forces and flowfield, the flowfield belonging to a condition of a different J will therefore, by definition, also vary significantly. However, if variable pitch would be available, this difference in C_T could be compen-

sated in CFD and be matched with the experiment, or vice-versa. To demonstrate that this is indeed possible, one can compare flowfield quantities as function of disk loading, or T_C. Figure 4.9 depicts the axial velocity and swirl angle at radial stations that correspond to approximately the maximum values of these quantities. The figures show that the experimental values collapse on the CFD curve, although these values are obtained at different advance ratios. This means that one can indeed select a blade pitch to match the T_C and match the flowfield to a large extent. If one would maintain the blade pitch and vary J to obtain $T_{C,\mathrm{CFD}} = T_{C,\mathrm{exp}}$, the shape of the helical vortex will not match (see Section 2.5). It is therefore preferred to adjust the blade pitch instead.

(a) Axial velocity at $r/R_\mathrm{p} = 0.8$ 　　　　　　 (b) Swirl angle at $r/R_\mathrm{p} = 0.5$

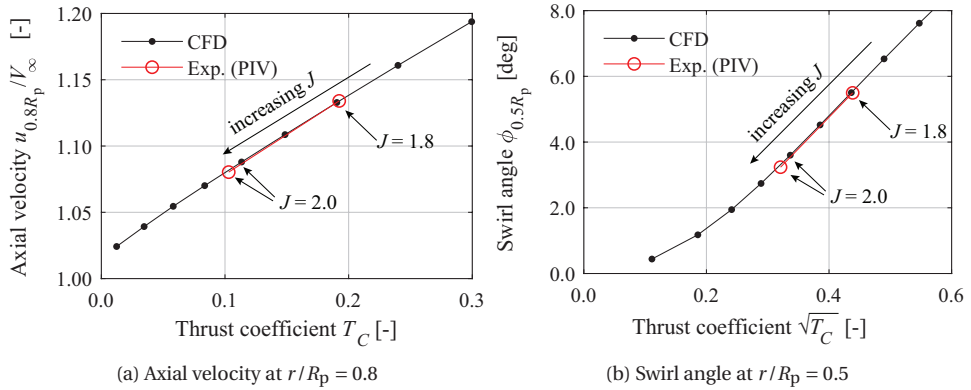Figure 4.9: Phase-averaged axial velocity and swirl angle at $x/R_\mathrm{p} = 1.1$ as function of thrust coefficient. Radial locations correspond to approximately the maximum values of each quantity. The figure shows that the a comparison at the same thrust coefficient leads to better agreement between CFD and experiment than comparison at same advance ratio. Conditions: $V_\infty = 40$ m/s, $\beta_{0.7R_\mathrm{p}} = 45$ deg.

The differences observed so far for the XPROP propeller are generally also observable for the Beaver propeller. In the condition of interest ($J = 0.8$ at $V_\infty = 40$ m/s), the computed thrust coefficient is $C_T = 0.0911$, taken as average over a full rotation. The experimental value is $C_T = 0.0936$ [49]. The Reynolds number along the blade is approximately a factor two higher than for the XPROP case. Nevertheless, extent of the separated flow in the hub region ($r/R_\mathrm{p} = 0.2 - 0.4$) is influencing the result considerably, resulting in a 2.7% lower thrust in CFD. The computed time-averaged slipstream is compared to PIV results in Fig. 4.10. Figure 4.10a shows that the swirl velocity is excellently predicted by CFD for $r/R_\mathrm{p} > 0.6$. Due to the underpredicted axial velocity, the swirl angle is only slightly larger than the measured profile in this region. In the hub region ($r/R_\mathrm{p} < 0.6$), the swirl is overpredicted, indicative that in the experiment there is a lower loading due to more severe flow separation. Additionally, the boundary layer on the nacelle is not properly captured: the experimental data indicates a significantly larger boundary layer, that merges with the root-separation from the blades. Despite the deviations within this region, that in particular will influence the propeller–nacelle interaction and the flow at the nacelle–tail junction, the majority of the slipstream in terms of slipstream area is properly captured in the simulation.
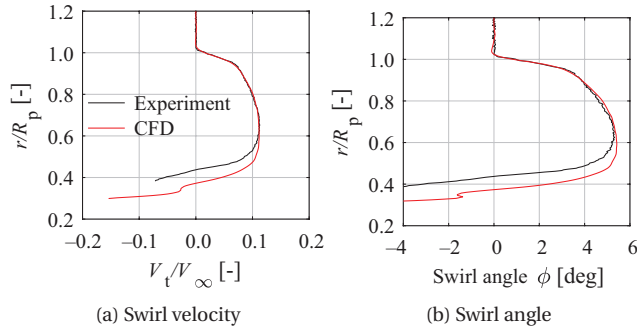
(a) Swirl velocity   (b) Swirl angle

Figure 4.10: Time-averaged slipstream of the Beaver propeller at $x/R_p = 0.19$ from CFD compared to the experimental values. Conditions: $V_\infty = 40$ m/s, $J = 0.8$.

4.2.2. PROPELLER–TAILPLANE INTERACTION (*PROWIM-HTP* MODEL)

The validation of the simulations of the *PROWIM-HTP* model focusses on the forces acting on the tailplane, provided that the slipstream generated by the Beaver propeller corresponds well with experiment for the majority of the propeller disk, as discussed in the previous section. As shown in Chapter 5, the installation of a propeller to the tip of a tailplane results in a relatively small upstream effect, and is therefore not further investigated in this validation study.

    The computed pressure distributions for a range of cases are compared to the measured values in Fig. 4.11. The selected spanwise locations correspond to the location where the tip vortex impinges, the swirl angle of the slipstream is maximum, and a location far from the slipstream impingement. Figure 4.11a shows that for the propeller-off condition, excellent agreement is obtained between CFD and experiment, where the largest deviation from the experiment occurs around $x/c = 0.12$, which corresponds to the location of the transition strip. While the stagnation point on the elevator and the suction peak on the elevator are exactly captured, on the suction side the experiment shows a smaller pressure recovery, indicating that the trailing edge separation is slightly overpredicted. The same is observed towards the trailing edge of the main element around $x/c = 0.7$. The same minor differences can be observed at a more inboard location, Fig. 4.11b. The consequence is that the simulations predict a slightly higher normal-force coefficient along the span, depicted in Fig. 4.12.

    With the propeller installed, rotating inboard-up, the lift on the tailplane is increased, as the pressure distribution in Fig. 4.11a indicates. In Figure 4.10 it is shown that the swirl of the slipstream nearly coincides with the experimental value. Comparable agreement as the propeller-off condition is reached; there is only a slight underprediction of separation at the trailing edge of the elevator. At the leading edge, the suction peak is slightly larger in the experiment. This is likely due to the lower dynamic pressure in the slipstream of the propeller. The Δc_n due to the propeller is therefore also slightly larger at this location in the experiment, shown in Fig. 4.12.
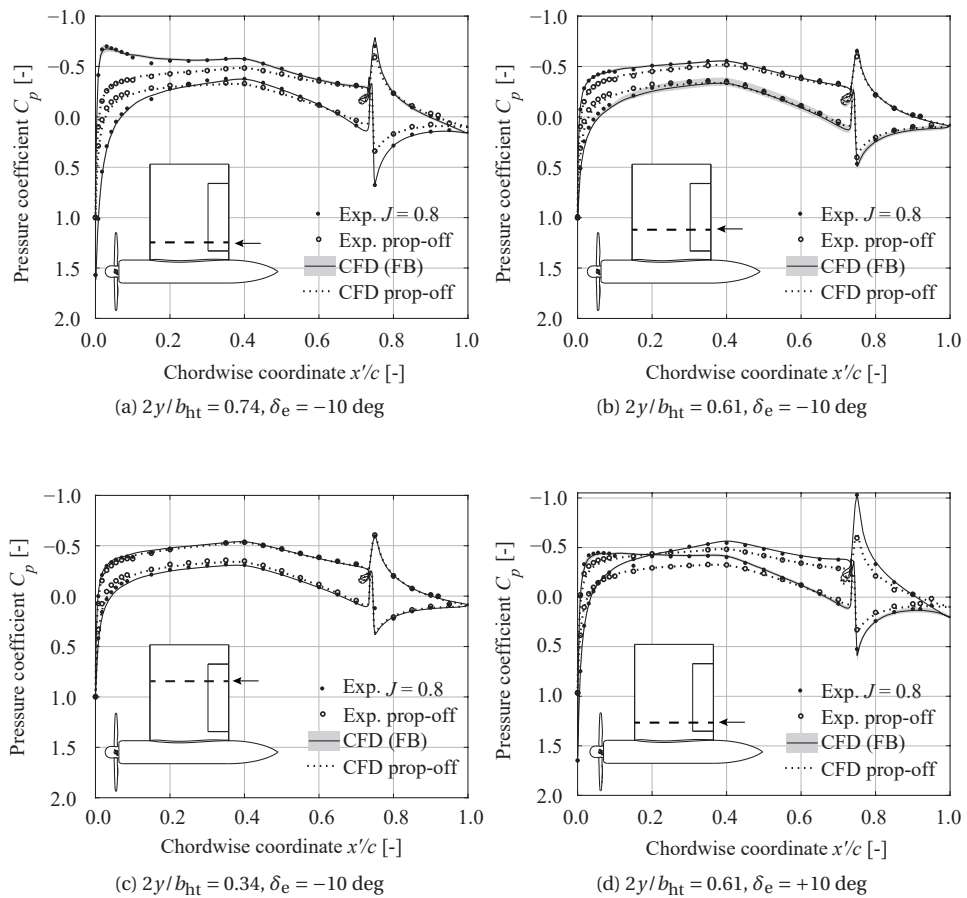
Figure 4.11: Comparison of pressure distributions on the tailplane at $\alpha = 0$ deg with an elevator deflection. Propeller rotating inboard-up. The shaded area indicates the spread computed over a full revolution.

Figure 4.11b depicts the C_p distribution at a spanwise location that approximately corresponds to the location where the tip vortex impinges the leading edge. On the suction side, the helical vortex system moves towards the tip, while on the pressure side it is skewed towards the symmetry plane. Since in this region the gradient of the tailplane's circulation is largest, the comparison of C_p at this location is indicative of the propeller–tailplane interaction. Since it is a time-dependent loading, the C_p distribution in the simulation shows a small range within the C_p fluctuates over a full revolution. The computed pressure distribution is again close to the experiment, although the figure indicates a slightly smaller shear of the slipstream in the simulation. However, as depicted in the normal-force distribution along the span, the change in c_n is more abrupt in the experiment, since the shear layer at the slipstream edge is more confined. In Appendix B it is shown that if a concentrated disturbance in spanwise direction is distributed over a larger portion of the span, the integral value between these two cases is comparable. Along this line, even in the region of high velocity gradients, the CFD model shows acceptable agreement. At a spanwise location far from the slipstream impingement (Fig. 4.11c), the computed pressure distributions nearly coincide with the measured pressures. This is indicative that the change in spanwise loading is also well captured, which further strengthens the confidence in the CFD simulations. For the case where the elevator is deflected to $\delta_e = +10$ deg, i.e. the tip vortex of the tailplane is in the same direction as the propeller-induced swirl, the same agreement is found, as shown in Fig. 4.11d. Quantitative conclusions on the interaction between the helical vortex system and the propeller-vortex system based on the CFD model are therefore valid.
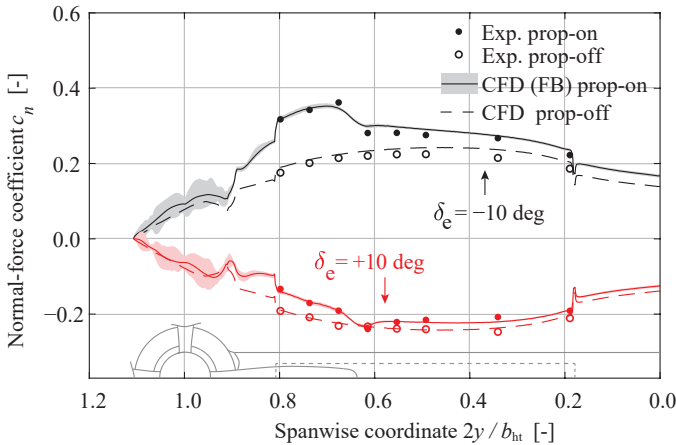

Figure 4.12: Comparison of the normal-force distribution at $\alpha = 0$ deg, $J = 0.8$. To quantify the relative contribution of the nacelle, the normal force acting on the nacelle is normalized with the tailplane chord length.

    The slightly lower influence of the propeller on the tailplane load distribution can also be understood by assessing the total-pressure distribution in a plane downstream of the model, as depicted in Fig. 4.13. The contour in Fig. 4.13a shows that the rise in C_{p_t} in highest loaded region on the blades is slightly larger in the experiment, also evident in the survey lines in Figs. 4.13b and 4.13c. The wake originating from the blade hub region is larger in the CFD case, leading to, on average, a lower dynamic pressure in the slipstream. It is noted that the contour is constructed from one propeller rotation. Provided the severe separation, a fully converged average of the flowfield in that region would require a (much) larger number of rotations. This is the main reason of the discrepancy in the shape of the flowfield in the contour plots, where the CFD result is more erratic. The regions where the flow is periodic, shows good resemblance with the experiment, where the deformation of the slipstream (indicative of the interaction between propeller and tailplane) is adequately captured, also the magnitude and shape of the slipstream show good agreement. A surveyline through the elevator-edge vortex (Fig. 4.13c) indicates that the deficit in C_{p_t} is well predicted, but the wakes from the boundary layer on the suction and pressure side are quickly diffused at the distance of the survey plane. It is also noted that the overprediction of the normal force (Fig. 4.12) leads to a slighly larger displacement of this vortex due to the larger downwash angle ϵ.

(a) Total-pressure coefficient downstream the model

(b) $C_{p,t}$ at $2y/b_{ht} = 1.20$ (c) $C_{p,t}$ at $2y/b_{ht} = 0.80$ (d) $C_{p,t}$ at $2y/b_{ht} = 0.19$
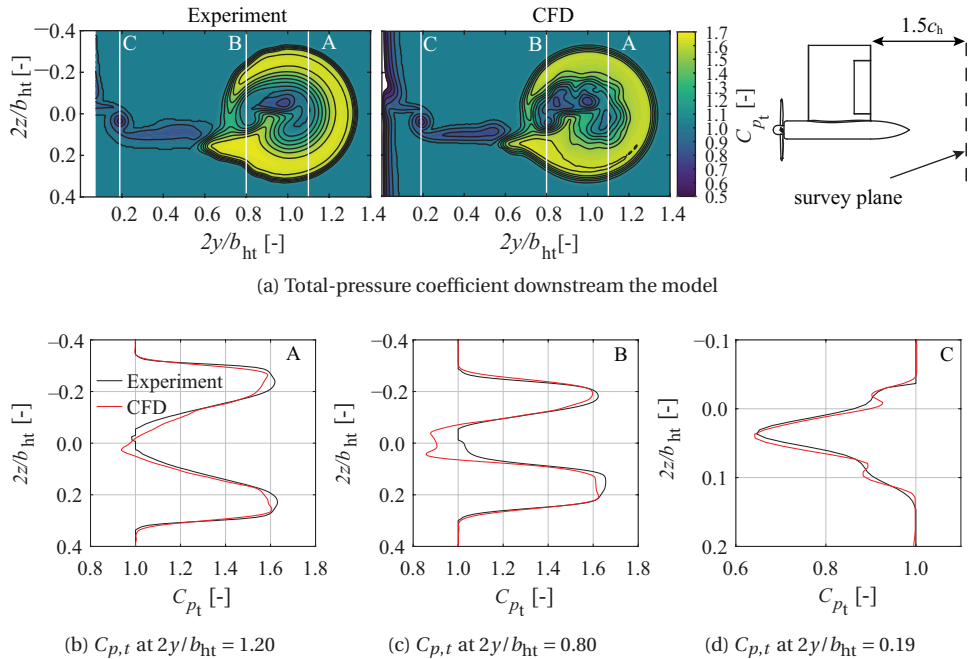
Figure 4.13: Total-pressure coefficient at $1.5c$ behind the trailing edge of the propeller–horizontal tailplane model. The flowfield of the full-blade simulations are the average over one rotation, while the experimental results are a phase-average.
Conditions: $J = 0.8$, $\alpha = 0$ deg, $\delta_e = -10$ deg.

A representation of the downwash field behind the tailplane, which entails the load distribution as well as the swirl recovery by the tailplane, is presented in Fig. 4.14. The slightly larger downwash due to the larger lift force in the CFD is clearly visible along the tailplane. The downwash near the propeller disk (Fig. 4.14c) shows that the swirl recovery is indeed captured properly by the CFD simulations. Worth noting is the stronger upwash and downwash that is concentrated near $2y/b_{ht} = 1.0$. The CFD simulations suggest a stronger vortex that originates from the propeller hub. In fact, the load distribution along the blade indeed shows a more rapid reduction in thrust here, hence a stronger hub vortex is shed. The sign of this vortex is opposite to the tip vortex of the tailplane. This leads to a local overprediction of the down and upwash in this region. Also these figures indicate that in particular the gradients in the flowfield are diffused by in the CFD simulation, in particularly visible in Fig. 4.14b. However, the fact that the resulting flowfield does resemble most of the details *on average*, and the deformation of the slipstream is adequately captured, indicates that the diffusion of the vorticity does not impact the flowfield significantly.

(a) Flowfield in PIV plane

(b) C_{p_t} at $2y/b_{ht} = 0.19$ (c) C_{p_t} at $2y/b_{ht} = 0.80$
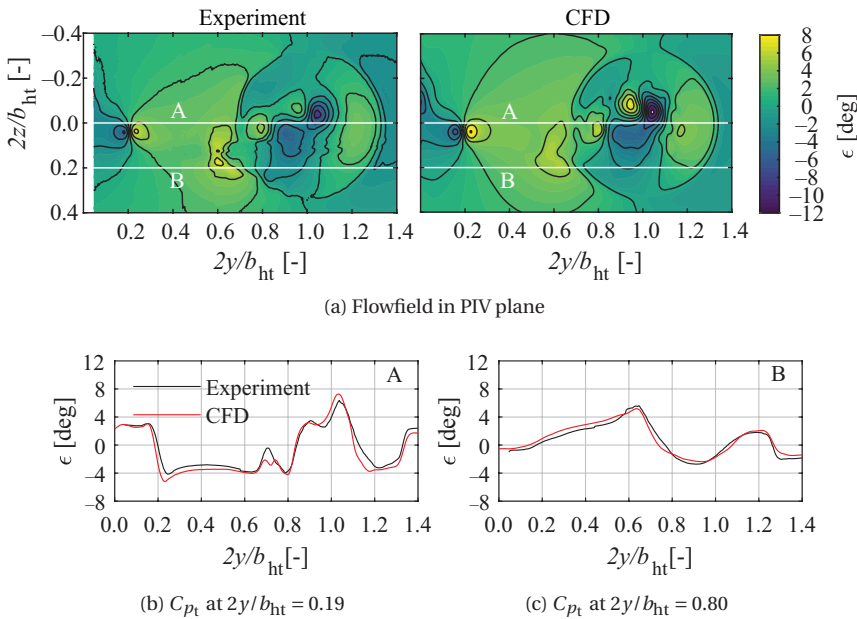
Figure 4.14: Downwash behind at $1.5c$ behind the trailing edge of the propeller–horizontal tailplane model. The flowfield of the full-blade simulations are the average over one rotation. Conditions: $J = 0.8$, $\alpha = 0$ deg, $\delta_e = -10$ deg.

Finally, also cases were simulated with an angle of attack. In these cases, the loading on the propeller disk, and the relative strength of the vortices that trail from the elevator and tailplane tip compared to the propeller swirl differ from the ones at $\alpha = 0$. Figure 4.15 depicts the tailplane pressure distributions at two spanwise locations. The agreement that was observed at $\alpha = 0$ deg is also achieved at $\alpha = 10$ deg, in this case with an elevator deflection ($\delta_e = -10$ deg), which reduces the lift on the tailplane. This is a situation that
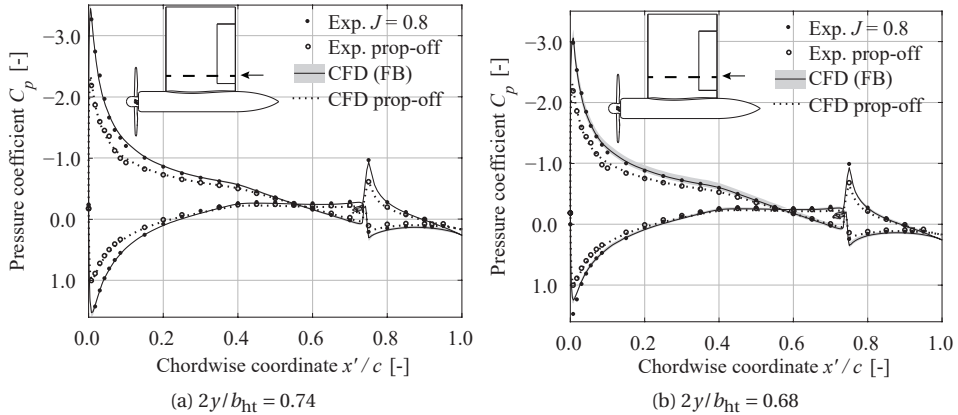
Figure 4.15: Comparison of pressure distributions on the tailplane at $\alpha = 10$ deg with an elevator deflection of $\delta_e = +10$. Propeller rotating inboard-up. The shaded area indicates the spread computed over a full revolution.

could represent a trim condition at high angle of attack. The quite significant added lift by the propeller on the main element is excellently captured in the CFD simulation. The stagnation point, suction peak, and the pressure distribution on the elevator are nearly coinciding with the experimental result. Again, the largest deviations occur near the transition strip and the last few percent of the chord. This result provides sufficient confidence that at these more extreme conditions, the loading on the propeller as well as the propeller–tailplane interaction is also captured by the CFD model.

In conclusion, the propeller installation is well predicted by the CFD model, in terms of force distributions on the tailplane, the deformation of the slipstream, and the flow-field far downstream of the model. The conclusions that can be drawn from the results are not limited to identify in terms of trends, but instead, the quantitative values that characterize the propeller–tailplane interaction can be used as well.

4.2.3. FULL AIRCRAFT SIMULATIONS (*VGM-HTP* MODEL)

The previous sections have established the validity of the CFD simulations to solve the flowfield around the propeller blades and to capture the aerodynamic interaction between the propeller and a tailplane. In this section, the simulations of a full aircraft configuration with horizontal tail-mounted propellers is assessed, where in particular the inflow field to the propeller and the propeller-airframe interaction are important flow phenomena that are required to be captured.

First, the total-pressure field downstream of the model is compared with the experimental result. This flowfield encompasses the added momentum by the propeller, the momentum loss by the airframe, and the propeller–airframe interaction. Figure 4.16 compares measured and computed the C_{p_t} fields at a plane two diameters downstream of the propeller plane with the model installed at an angle of attack of $\alpha = 5$ deg. Qualitatively, all flow features observable in the experimental data are also present in the CFD results. To compare quantitatively, the C_{p_t} is plotted along four survey lines, depicted

105

in the same figure. Survey lines *a* through *c* show that the location of the wing wake is excellently predicted by the CFD on the inboard side, with only a slight underprediction of the downwash on the outboard sections. While the minimum C_{p_t} almost coincides with the experimental result, the wake thickness in the CFD is slightly underpredicted. It is expected that this is associated with the applied transition strips on the model, which are relatively thick and therefore lead to a more rapid growth of the boundary layer. The deviation of the C_{p_t} of the tailplane wake (survey line *a*) is a combination of the underprediction of viscous drag and diffusion of the wake. However, the corresponding *z*-location is predicted well, which indicates that the combination of local downwash produced by the wing and tailplane is captured. Also the prediction of the nacelle wake (survey line *b*) shows excellent agreement with experimental results, including the two minima originating from the merging of upper and lower boundary layer formed on the nacelle. The deviation of the reduced C_{p_t} in the vortex core (survey line *c*) is found to be due to a slightly more inboard location of the tip-vortex in the experiment. The largest deviation in the wake plane can be observed in the vicinity of the fuselage (survey line *d*), where the experiment clearly shows a larger momentum defect, although the particular shape from the merging of the boundary layer on each side is clearly present in the CFD result.
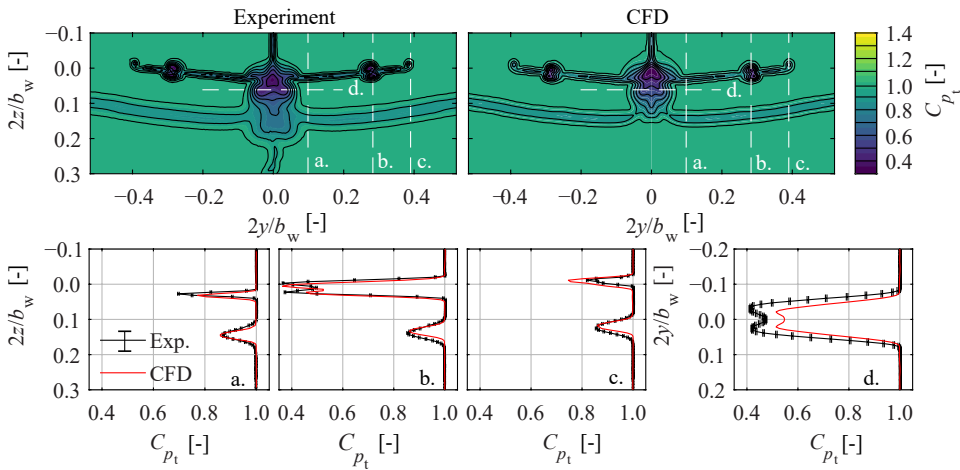
Figure 4.16: Comparison of the CFD result to the measured total-pressure coefficient in a wake survey plane downstream the model. Several survey lines are indicated by letters a through d. Clean configuration of the *VGM-HTP* model with CFD, propeller off, $\alpha = 5$ deg.

The underprediction of fuselage drag will primarily lead to an underprediction of C_{D_0}, but is not considered to be detrimental to the propeller–airframe interaction study. This is also observable in Fig. 4.17a which depicts the integral force coefficients. The drag-curve from the simulations has clear offset with the experimental data, attributed to an underprediction of drag, particularly for the fuselage. The lift-curve shows that there is good agreement with the experimental data, although there is a slightly lower lift curve slope in the experiment, possibly due to the decambering-effect of the boundary layer at higher lift coefficients. It is noted that a typical cruise lift coefficient of 0.5 to

0.6 [132] is only attained at a relatively high angle of attack of $\alpha = 4$ deg. The figure in particularly indicates the regions of interest for the subsequent chapters. At high angle of attack, the flow separation from the wing will influence the flowfield near the propeller and tailplane. Aspect of performance in cruise conditions are especially at low angle of attack. The quantitative agreement with experiment is especially good for these low angles of attack.
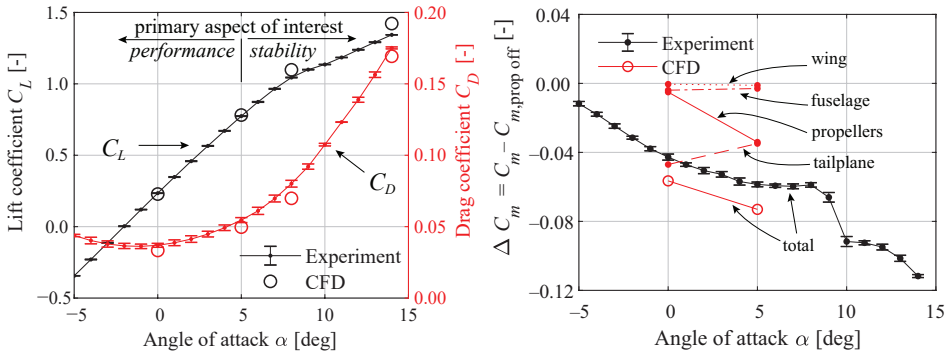
(a) Lift and drag coefficients, propeller off. Indicated regions represent aspect of interest for analyses in subsequent chapters.

(b) Comparison of the *change* in pitching moment for the inboard-up rotation direction ($J = 1.8$).

Figure 4.17: Comparison of the measured integral force coefficients of the clean configuration of the *VGM-HTP* model with CFD.

The change in axial force relative to the drag of the isolated airframe, $\Delta C_X = C_{X,\text{prop-on}} - C_{X,\text{prop-off}}$, is a quantitative measure of the propeller-airframe aerodynamic interaction and it is not dependent on the underprediction of C_{D_0}. Table 4.3 shows that the predicted *change* of C_X nearly falls within the experimental uncertainty, especially at $\alpha = 0$ deg. The difference between inboard-up and outboard-up is primarily a difference in tailplane drag. At $\alpha = 5$ deg, the net axial force is reduced in the CFD simulation, while in the experiment it remains nearly constant. It is expected that this is in particular due to the lower slope of the $C_T - J$ curve in CFD (see Section 4.2.1), since the higher angle of attack slightly reduces the inflow to the propeller, that is equivalent to a change in advance ratio.

Table 4.3: Change in axial force on the airframe and propeller from the CFD simulations relative to the experimental results. Indicated uncertainty corresponds to the experimental values.

Angle of attack [deg]	0	0	5	5
Rotation direction	inboard-up	outboard-up	inboard-up	outboard-up
$\frac{\Delta C_{X,\text{CFD}}}{\Delta C_{X,\text{exp}}} - 1$	$+0.6\% \pm 0.5\%$	$+1.1\% \pm 0.6\%$	$-2.5\% \pm 0.7\%$	$-1.8\% \pm 0.7\%$

Since the quantification of the stability derivatives and the conclusions that are drawn from the particular configuration are an important aspect in this dissertation, the computed change in the pitching moment coefficient due to the propeller installation is compared to the experimental data in Fig. 4.17b. The breakdown of the CFD

results reveals that the propeller installation has negligible effect on the fuselage and wing forces. The propellers are a stabilizing contribution, while the tailplane contribution to stability reduces due to propeller installation. Since the magnitude of the change in pitching moment is significant, the comparison with experimental data is therefore important. The figure shows that the gradient over the interval $\alpha = [0, 5]$ deg from the CFD is $\Delta C_{m_\alpha} = -3.24 \cdot 10^{-3} \, \mathrm{deg}^{-1}$, while in the experiment the gradient is $\Delta C_{m_\alpha} = -3.17 \pm 0.03 \cdot 10^{-3} \, \mathrm{deg}^{-1}$. These values indicate that the change in stability is captured with sufficient agreement to formulate qualitative and quantitative conclusions based on these simulations. The slightly larger nose-down pitching moment is attributed to the slightly higher thrust of the propellers, which are situated above the moment reference point.

To compare the propeller-airframe aerodynamic interaction, the slipstream deformation and the magnitude of the C_{p_t} of the propeller-on configuration are shown in Fig. 4.18. The time-accurate CFD results are time averaged to compare with the measured C_{p_t}. Only for the co-rotating case experimental data is available, while only the inboard-up and outboard-up cases are simulated. It is noted that for the co-rotating case there is a sidewash as a result of the slipstream–tailplane interaction (see Refs. [62, 173, 174]) which is absent in the CFD simulations due to the symmetry condition. The slipstream location is slightly different and hence pressure data along the survey lines should be compared with care. The cropped contours on the upper side of the slipstream are an artefact of lower resolution of the wake rake data in the upper region of the plane.
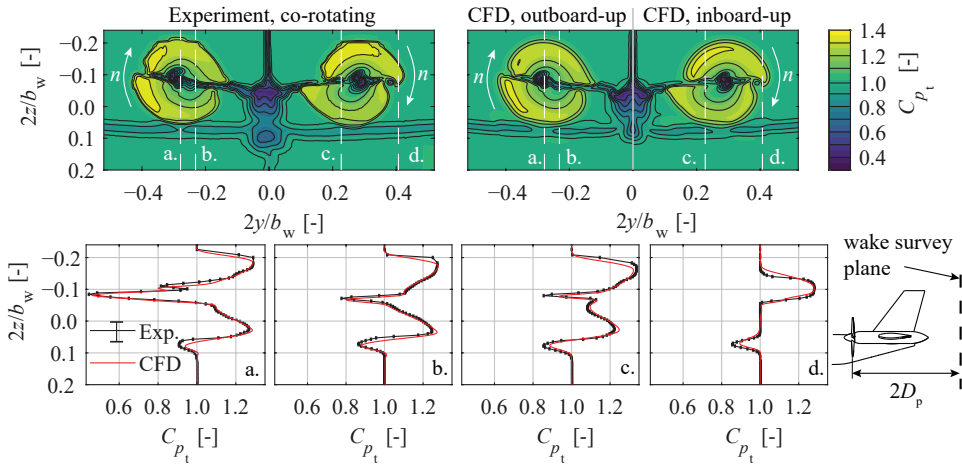
Figure 4.18: Measured total-pressure coefficient in a wake survey plane behind the *VGM-HTP* model compared with CFD. Time-accurate CFD results are time averaged over 60 deg of rotation (30 time steps). Clean configuration, J=1.8, $\alpha = 0$ deg.

Qualitatively, all details of the measured flow field are also present in the CFD results, i.e. the shear of the slipstream, the non-axisymmetric loading of the propeller and the interaction of the propeller tip-vortex with tailplane tip-vortex. Quantitatively, the survey lines show excellent agreement as well, except for the regions near the edges of the propeller slipstream. As previously discussed, the large gradients in the shear layer of

the wing wake quickly diffuse downstream of the propeller in the numerical simulation, despite the fine grid in the slipstream domain. Therefore, also the interaction of the wing wake with the propeller tip is less pronounced.

It is concluded that the agreement of the CFD model with experiment for both the integral forces and flowfields for this scale is sufficiently accurate to predict the aerodynamic interactions and the associated trends.

4.3. CONCLUSIONS

RANS SIMULATIONS OF ISOLATED PROPELLERS

For the two propellers analyzed, good agreement was found between the RANS CFD simulations and experimental data for the design condition of the propeller in terms of force coefficients and the slipstream. The following conclusions are made:

- In line with other publications, the dependency of several force coefficients and the slipstream shape on the mesh size is low. Already with a relatively coarse mesh, the propeller performance is well captured, and the time-averaged slipstream is well defined. A grid refinement study indicated a discretization error less than 1% for the selected grid on the propeller thrust and power coefficients. No major differences were found in the flowfield, except in the shear layer of the slipstream, for both an instantaneous flowfield, as well as for the time-averaged flowfield.

- Numerical diffusion is responsible for the large difference in vortex core radius and the associated velocity gradients, while the circulation of the tip vortex is nearly independent of the grid choice. The fact that numerical diffusion plays such an important role in the vorticity transport is also observed in the roll-up process. In the experiment, the complete roll-up takes place significantly further away from the propeller disk, while the velocity gradients are still large, even close to the disk. For installation studies where the unsteady component of lift is important, a combination of a higher-order model and a fine grid is required.

- Since the experiment was conducted on a small scale model operating at relatively low freestream velocity, the low Reynolds number on the blade section significantly influenced the thrust curve, which is in line with the observations by other researchers. Because of this dependency, CFD primarily overpredicts the thrust, while the slope of the linear part of the $C_T - J$ curve is approximately 20% lower. Through two-dimensional airfoil analyses of a representative blade section, it was found that the airfoil operates in a highly nonlinear region, where both the lift curve slope and zero-lift angle of attack change with Reynolds number. This combination leads to a higher slope of the $C_T - J$ curve.

- When the flowfields were compared at the same T_C instead of the same advance ratio, the phase-averaged slipstreams between CFD and experiment nearly collapse. Therefore, the blade-pitch should be adjusted to match T_C at the same J to obtain an equivalent slipstream, although the swirl is still slightly higher in the experiment due to larger viscous losses.

The CFD simulations are considered well suitable for the analyses of the installed conditions because both instantaneous (phase-locked) flowfields, as well as the time-averaged

flowfield match to a large extent with the experiment.

RANS Simulations of Installed Propellers

For the two validation cases of installed propellers, again excellent agreement was found in terms of flowfields and force coefficients between the RANS CFD simulations and experimental data. The following conclusions are made:

- The response of a tailplane to the propeller installation is well captured, both at the spanwise location of the slipstream impingement, the location where the tip vortices impinge, as well at a location outside the region where the slipstream impinges. This indicates that the aerodynamic interaction between the helical vortex system and the vortex system of the lifting surface is captured well.

- The main deviation of CFD relative to experiment is found at the slipstream edges, in line with the observations of the isolated propeller. The consequence is a more confined region along the span of the lifting surface where the bound circulation varies. However, the results also show that excessive diffusion of the (propeller) tip vortices does not impact the integral forces on the lifting surfaces.

- The minor differences in the magnitude of the induced velocity in the installed case are traced back to the slipstream of the isolated propeller. This also holds for the negligible differences of the loading of the tailplane. This demonstrates that, if the slipstream is well defined, excellent agreement of the time-averaged loading on lifting surfaces can be expected, even at large angles of attack.

- The results on a full aircraft configuration demonstrate that the CFD simulations are well suitable to predict the aircraft performance. The estimated change in axial force component, i.e. the combined effect of propeller thrust variations and airframe drag, is within 2% of the experimental result. The *change* in slope of the pitching moment curve is also predicted to differ up to 2% of the experimental result, which therefore falls nearly in the experimental uncertainty band.

Concluding Remarks

As a general conclusion, this chapter demonstrates that both the flowfields and the forces generated on the propeller and airframe can be well predicted with unsteady RANS simulations with a second-order scheme. Despite the relatively large amount of computational resources required to obtain a single solution, the excellent agreement indicates that the main flow phenomena on each component can be studied in further detail. The power of CFD, in case of a small amount of operating conditions, is therefore clearly displayed herein. Flow phenomena observed in the experiment can therefore even be explained by subsequent CFD simulations. Nevertheless, this chapter also shows the value of validation data, and especially the different types of validation data. Differences observed in time-averaged data cannot be explained by itself without consulting time-accurate flowfield data. Since the vast majority of propeller-integration studies performed today rely on time-averaged results, CFD can be considered a very viable analysis method. If one is interested in trends (i.e. in case of a large number of operating conditions) and in the time-accurate response of a lifting surface in an unsteady flowfield, experimental campaigns are in particular useful.

5

ENGINEERING METHOD TO ESTIMATE THE BLADE LOADING OF PROPELLERS IN NONUNIFORM FLOW

5.1. INTRODUCTION

The simulation of a propeller and airframe using a full-blade CFD approach is time-consuming. If one is in particularly interested in the forces on the propeller that are caused by the airframe-induced flowfield, for example the normal-force gradient, or the change in propeller efficiency, performing a series of full-blade simulations may not be within reach, in particular in (the preliminary) design stages. Furthermore, a single full-blade simulation will not provide direction to the designer to make improvements or draw conclusions on part of the propeller installation effects. While experimental approaches are generally suitable to identify trends for a given geometry, changing the geometry in an experimental setup is often laborious, and therefore these methods are often not suitable for design studies. Furthermore, deducing the propeller blade loading from a flowfield measured at some distance downstream of the installed propeller is not straightforward, in particular when the slipstream is distorted due to interactions with the airframe [27, 37, 175–177]. Despite the introduced modelling errors, an analytical or numerical prediction of the installed propeller performance may be preferred instead, in particular if relatively small performance changes are expected.

Next to a range of prediction methods for axisymmetric inflow [178–180], several authors have published work on load prediction and analyses of propellers in nonuniform inflow, ranging from experimental, numerical and analytical methods. A number of analytical expressions for the in-plane forces for an isolated propeller at angle of attack have

---

Parts of this chapter have been published in Ref. [90].

been formulated, of which the formulae by de Young [60, 181] are widely used. These formulae were adapted in Refs. [62, 182] to account for the induced inflow by the fuselage and wing for wing-mounted tractor propellers. However, a generic nonuniform inflow can rarely be reduced to an equivalent angle of attack, which makes such analytical expressions less suitable for nonuniform inflows that only influence part of the propeller disk.

Numerical methods are therefore often preferred, as the actual constitution of nonuniform inflow can be taken into account. In coupled approaches, the flow solution of the combined airframe and propeller is solved directly. These include unsteady RANS CFD methods [133] and panel methods [183] with a full representation of the propeller blade. Such approaches are particularly useful if the propeller has a strong effect on the airframe. If one is primarily interested in the propeller performance, the additional accuracy may not outweigh the additional computational cost and effort to analyze a full configuration, compared to a superposition of the individual contributions of the propeller–airframe interaction. If the nonuniformity of the inflow is dominated by the isolated airframe, one can argue that the dominant changes in propeller loading due to the interaction are already captured if the inflow is treated as being decoupled. However, even with this simplification, the cost can still be significant if the full propeller is modelled. On the other hand, lower-order models are generally not able to account for nonaxisymmetric flows and may lack the fidelity to capture the relevant flow phenomena.

In this chapter, a computationally efficient *engineering method* is presented to determine the response of propeller forces and moments due to an arbitrary nonuniform flow, based on blade-loading distributions in uninstalled conditions and an inflow field. A prediction of these loads is useful in both the preliminary and the detailed design phase, as it can assist aircraft designers to select appropriate locations of the propeller along the airframe in a multidisciplinary design synthesis, for example to improve the time-averaged performance of the propeller, or to reduce unsteady loads. An efficient prediction method of the load distribution can also be used to provide inputs in noise studies [81, 181, 184], or provide inputs for actuator disk and actuator line models to assess propeller–airframe aerodynamic interaction [133].

The engineering method initially assumes that the propeller response to a nonuniform inflow is a quasi-steady problem. The solution is later improved by applying a correction to account for unsteady effects. The validation of the method is presented in Section 5.4.

5.2. Quasi-Steady Solution Method

The developed method to estimate propeller blade loading, treats the nonuniformity of the inflow field induced by the airframe and flight condition, i.e. the inflow at the propeller plane that exists in absence of the propeller, as a local disturbance to the nominal operating condition. The main principle of the method is that it is assumed that a change in local advance ratio $\Delta J'$ at r/R_p results in a local change in load, C_T' and C_Q', and therefore induced velocity field, with a magnitude equal to the one that would be obtained if $\Delta J'$ is applied to the full propeller disk as $\Delta J = \Delta J'$. The prime indicates a local quantity at a determined location on the propeller disk, given by its azimuthal and radial posi-

tion. This principle is schematically shown in Fig. 5.1. The underlying assumption of the method is based on three principles:

1. It is assumed implicitly that the local sensitivity of a section at r/R_{p} to a disturbance is determined by the nominal load distribution that exists in uniform inflow conditions. The analogy can be made to a three-dimensional wing, for which the local slope of the lift-curve along the span is proportional to its nominal lift distribution. It is shown in Section 2.2.2 that for a propeller blade the normalized thrust distribution is nearly independent of advance ratio, hence the sensitivity to a change in advance ratio is also proportional to the nominal load distribution.

2. Since a perturbation of the inflow leads to a variation of the bound circulation relative to the one obtained in uniform inflow, the associated shed vorticity induces an upwash/downwash to adjacent sections. It is assumed that the redistribution of loading along the radius is a second-order effect. Since thrust and torque are dominated by the lift force and induced drag on a blade section, the response to a nonuniform inflow for a propeller is analogous to the resulting changes in lift and drag due to a perturbation distributed along the span of a wing. It is shown in Appendix B that the error of the estimation of the integral forces by neglecting this redistribution becomes indeed a second-order effect if the spanwise gradient of the perturbation is small. A similar approach is utilized in blade-element momentum models, where the direct influence of adjacent blade sections is also neglected in the computation of local blade forces, and only a tip-loss factor is applied along the blade.

3. The blade–blade mutual interference as a consequence of the perturbation in loading is proven in Ref. [185] to be an effect of several orders of magnitude smaller than the primary change in load due to the perturbation, if the average spacing between blades is several chord lengths. Therefore, it is assumed for the quasi-steady solution that a blade response to a disturbance is confined to the same azimuthal angle at which the disturbance is encountered by a blade. The propeller–airframe interaction is therefore linearized, i.e. the perturbations $\Delta u, \Delta v, \Delta w$ at the location of the propeller disk, are the ones that exist in absence of the propeller. In this way, a computationally intensive analysis of the full annulus is avoided.

For the computation of the quasi-steady load distribution, both the propeller performance—that is, the radial load distribution for a range of advance ratios—of the isolated propeller in uniform flow and the propeller inflow field V and ρ are assumed to be known in advance. These quantities can be obtained by various analysis methods.

The propeller blade is described as a line, spanning from hub to tip, sweeping through an arbitrary flow field, as depicted in Fig. 5.2. Along this line, the local inflow at location (r, θ) is used to compute the local forces and moments. The temporal resolution of the estimated solution depends on the spatial resolution of this flowfield.

In the presented approach, the propeller load distribution is treated as a linear superposition of the response to in-plane disturbances $\Delta v, \Delta w$ and out-of-plane disturbance Δu, permissible when the perturbations are small. This separation gives insight in their relative contribution to the change in propeller forces. Additionally, the response of the
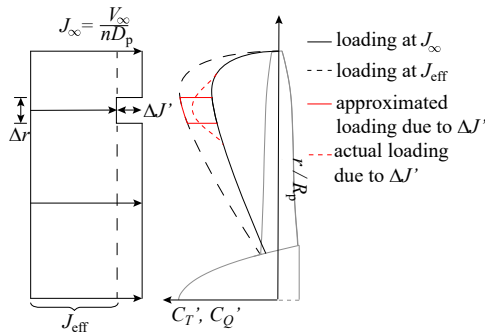
Figure 5.1: Illustration of relation between local effective advance ratio and change in blade-loading.
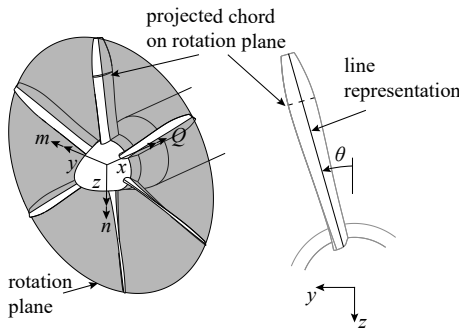
Figure 5.2: Definition of the propeller rotation plane on which the inflow is determined.

propeller to a change in tangential or axial inflow is different. At a given rotational speed n, the disk loading varies approximately *linearly* with a change in *axial* velocity, as $C_T - J$ is approximately linear and J is linear with V:

$$\frac{T}{S_\mathrm{p}} = \frac{4}{\pi} \rho D_\mathrm{p}^2 n^2 C_T, \text{ where } C_T \propto J \tag{5.1}$$

Similarly, at no change in axial velocity but an inflow constituted of tangential velocity components, the disk loading varies *quadratically* with a *tangential* inflow velocity V_t, as the $T_c - J$ curve is hyperbolic:

$$\frac{T}{S_\mathrm{p}} = \frac{1}{2} \rho V^2 T_C, \text{ where } T_C \propto \frac{1}{J} \tag{5.2}$$

Therefore, for a propeller operating at a given condition, i.e. V_∞ and n, the thrust and torque are more sensitive to a change in advance ratio caused by V_t than V_a at moderate to high thrust conditions. This is illustrated in Fig. 5.3. At high advance ratios, i.e.
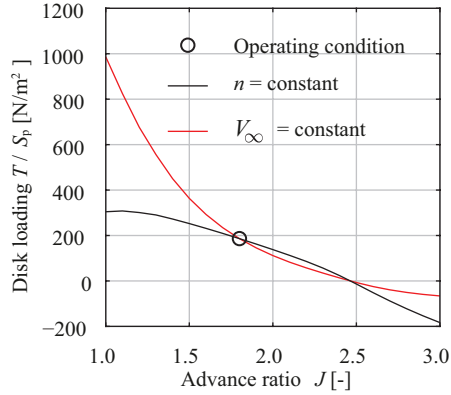
Figure 5.3: Effect of varying either rotational speed or axial velocity on the disk loading around a certain operating condition.

near windmilling conditions, the trend is reversed, and instead, the blade sections are more sensitive to a change in V_a than V_t. Therefore, the inflow disturbance needs to be associated with the corresponding sensitivity around the operating condition. This observation is in particularly apparent when the thrust distributions are compared at various advance ratios, shown in Fig. 5.4a and 5.4b. The two figures show that there is a significant difference in disk loading if either V_∞ or n is varied. The *gradient* of these maps, depicted in Fig. 5.4c and 5.4d, also display that the sensitivity to a ΔJ depends on radial location. The following important observation can be made that is useful for the interpretation of nonuniform inflow effects on propellers:

A nonuniform inflow expressed as $\Delta J(r)$ results in a change in propeller load that is proportional to the propeller load distribution that exists in uniform inflow. If this disturbance $\Delta J(r)$ is in the propeller rotation plane, it has a significantly larger impact than an out-of-plane disturbance of the same magnitude.

Since the radial distribution of thrust and torque, $C_T'(r, J_\infty)$ respectively $C_Q'(r, J_\infty)$, are known for the isolated propeller (for example the maps shown in Fig. 5.4a and 5.4b), these need to be evaluated at the local, effective advance ratio, determined by the nonuniform inflow. This distinction is made such that J_{eff_a} is the effective advance ratio due to *axial inflow*, while J_{eff_t} is the effective advance ratio only due to *tangential inflow*. At constant rotational speed, the effective advance ratio due to axial inflow is:

$$J_{\text{eff}_a}(r, \theta) = \frac{\Delta u(r, \theta)}{n D_p} + \frac{V_\infty}{n D_p} \tag{5.3}$$

Only the tangential components of the in-plane velocities Δv and Δw are of interest, and are decomposed into a tangential velocity using the local phase angle θ:

$$\Delta V_t = -\Delta v \cos\theta - \Delta w \sin\theta \tag{5.4}$$

115

(a) Distribution of sectional disk loading with
$V = 40$ m/s (constant)

(b) Distribution of sectional disk loading with
$n = 109.4$ Hz (constant)

(c) Derivative of sectional disk loading
with respect to J. Constructed from (a).

(d) Derivative of sectional disk loading with
respect to J. Constructed from (b).
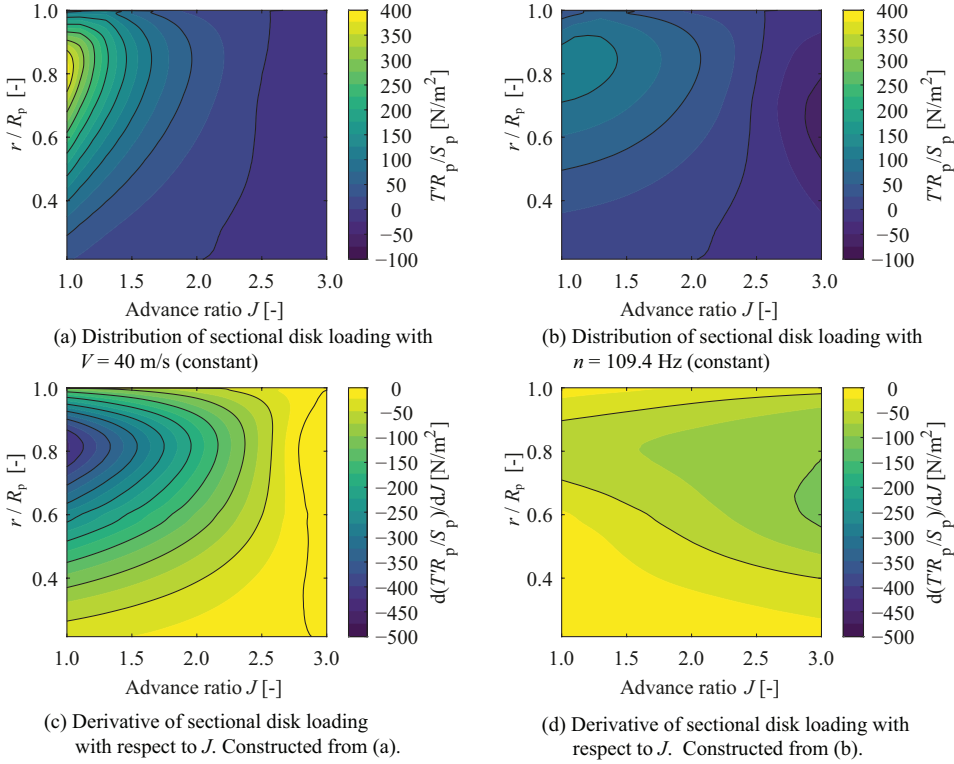
Figure 5.4: Effect of varying either rotational speed or axial velocity on the disk loading around a certain
operating condition.

which yields an effective advance ratio of:

$$J_{\text{eff}_t}(r,\theta) = \frac{V_\infty}{\left(n + \frac{\Delta V_t}{2\pi r}\right) D_p} - \frac{V_\infty}{n D_p} \tag{5.5}$$

For the uniform inflow case, it follows that $J_{\text{eff}_t} = 0$ and $J_{\text{eff}_a} = J_\infty$. If $C'_T(J_{\text{eff}})$ is the local
section thrust coefficient on a blade operating in *uniform inflow* at the corresponding
effective advance ratio J_{eff}, the corresponding changes in local thrust and torque due to
ΔJ_{eff_a} are:

$$T'_a(r,\theta) = \left[C'_T(J_{\text{eff}_a}) \frac{\rho}{\rho_\infty} - C'_T(J_\infty) \right] \rho_\infty n^2 D_p^4 \tag{5.6}$$

$$Q'_a(r,\theta) = \left[C'_Q(J_{\text{eff}_a}) \frac{\rho}{\rho_\infty} - C'_Q(J_\infty) \right] \rho_\infty n^2 D_p^5 \tag{5.7}$$

Equivalently, the change in thrust due to an in-plane disturbance J_{eff_t} is:

$$\Delta T'_t(r,\theta) = \left[C'_T(J_{\text{eff}_t}) \cdot \left(n + \frac{\Delta V_t}{2\pi r} \right)^2 \frac{\rho}{\rho_\infty} - C'_T(J_\infty) n^2 \right] \rho_\infty D_p^4 \tag{5.8}$$

116

$$\Delta Q'_{\text{t}}(r,\theta) = \left[C'_Q(J_{\text{eff}_{\text{t}}}) \cdot \left(n + \frac{\Delta V_{\text{t}}}{2\pi r} \right)^2 \frac{\rho}{\rho_\infty} - C'_Q(J_\infty)n^2 \right] \rho_\infty D_{\text{p}}^5 \tag{5.9}$$

To determine the thrust and torque expressed by Eqs. 5.6 through 5.9, one needs to compute or measure $C'_T(r,J)$, $C'_Q(r,J)$ for a range of advance ratios of the propeller in isolated condition. Furthermore, one needs to determine the flow field in which the propeller is operating. The summation of the in-plane and out-of-plane contributions yields the total change in normalized propeller loading at a particular blade section position (r,θ):

$$\Delta C'_T(r,\theta) = \frac{\Delta T'_{\text{a}} + \Delta T'_{\text{t}}}{\rho_\infty n^2 D_{\text{p}}^4} \tag{5.10}$$

$$\Delta C'_Q(r,\theta) = \frac{\Delta Q'_{\text{a}} + \Delta Q'_{\text{t}}}{\rho_\infty n^2 D_{\text{p}}^5} \tag{5.11}$$

Once the load distribution is found by evaluating Eqs. (5.3) through (5.11) at each phase angle, the integral propeller forces are computed by integration:

$$\Delta C_T = \frac{1}{2\pi} \int_0^{2\pi} \int_{R_{\text{h}}}^{R_{\text{p}}} \Delta C'_T(r,\theta)\,\mathrm{d}r\,\mathrm{d}\theta \tag{5.12}$$

$$\Delta C_Y = -\frac{1}{2\pi} \int_0^{2\pi} \int_{R_{\text{h}}}^{R_{\text{p}}} \frac{\Delta C'_Q(r,\theta)}{r} \cos\theta\,\mathrm{d}r\,\mathrm{d}\theta \tag{5.13}$$

$$\Delta C_Z = -\frac{1}{2\pi} \int_0^{2\pi} \int_{R_{\text{h}}}^{R_{\text{p}}} \frac{\Delta C'_Q(r,\theta)}{r} \sin\theta\,\mathrm{d}r\,\mathrm{d}\theta \tag{5.14}$$

and the integral propeller moments become:

$$\Delta C_Q = \frac{1}{2\pi} \int_0^{2\pi} \int_{R_{\text{h}}}^{R_{\text{p}}} \Delta C'_Q(r,\theta)\,\mathrm{d}r\,\mathrm{d}\theta \tag{5.15}$$

$$\Delta C_n = -\frac{1}{2\pi D_{\text{p}}} \int_0^{2\pi} \int_{R_{\text{h}}}^{R_{\text{p}}} \Delta C'_T(r,\theta)r\sin\theta\,\mathrm{d}r\,\mathrm{d}\theta \tag{5.16}$$

$$\Delta C_m = -\frac{1}{2\pi D_{\text{p}}} \int_0^{2\pi} \int_{R_{\text{h}}}^{R_{\text{p}}} \Delta C'_T(r,\theta)r\cos\theta\,\mathrm{d}r\,\mathrm{d}\theta \tag{5.17}$$

The change in power coefficient follows from Eq. 5.15 as $\Delta C_P = 2\pi\Delta C_Q$. Conventionally, the efficiency is defined as the ratio of useful work done on the fluid per unit time to the power that is put into the system to perform the useful work. Although the propeller is doing work on a fluid having a velocity $V = (u,v,w)$, generally not equal to V_∞, one is only interested in the change of the thrust-to-power ratio of the propeller, at the flight speed of the vehicle. Therefore, the efficiency of a propeller in close proximity of the airframe with a nonuniform inflow, is determined in a straightforward way, by using the computed thrust and torque:

$$\Delta \eta_{\text{p}} = \frac{(\Delta T + T_\infty)}{(\Delta P_{\text{s}} + P_{\text{s}_\infty})} V_\infty - \frac{T_\infty}{P_{\text{s}_\infty}} V_\infty \tag{5.18}$$

117

The treatment of the local response to a nonuniformity of the inflow is in particular suitable for unswept propeller blades, as a high sweep angle leads to a more pronounced coupling between adjacent sections along the radius. Furthermore, the evaluation of inflow along the line assumes the chord length is effectively zero. However, as observed in Ref. [89], the forces on the blade sections are particularly influenced by the flow conditions around the propeller leading edge, analogous to the sensitivity to a change in angle of attack of the load distribution along the chord for typical two-dimensional airfoils [111]. Hence, an improved representation of the inflow can be obtained when the inflow at location (r, θ) is determined by a weighted velocity along the projected chord in the plane of rotation:

$$\Delta V_{\text{weighted}}(r, \theta) = \overline{\Delta V W} \tag{5.19}$$

with $\Delta V = (\Delta u, \Delta v, \Delta w)$.
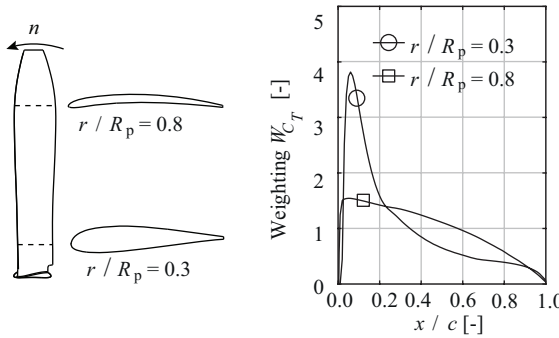
Figure 5.5: Example of distribution of thrust in chordwise direction.

Herein, a weighting function W is used for illustration purposes, which is based on the thrust distribution along the blade chord, projected in the plane of rotation, as illustrated in Fig. 5.5. The weighting depends on the airfoil shape and operating condition. If c_T is the local thrust coefficient per unit area at a determined projected chordwise location, such that the thrust coefficient at a radial location is $C_T'(r, J) = c(r) \int_0^1 c_T(r, \xi, J) d\xi$, then the weighting function is:

$$W(r, J, \xi) = \frac{c_T(r, \xi, J) c(r)}{C_T'(r, J)} \tag{5.20}$$

and equivalently for torque:

$$W(r, J, \xi) = \frac{c_Q(r, \xi, J) c(r)}{C_Q'(r, J)} \tag{5.21}$$

Such weighting function has not been employed in the presented analyses and validation cases, as it was found that it led to only a small phase difference between the load and the disturbance in the flowfield. Furthermore, the assumption representing the propeller as a line did not have significant impact on the magnitude of the predicted forces.

5.3. ACCOUNTING FOR UNSTEADY EFFECTS

The response of a two-dimensional airfoil to a change in inflow is not instantaneous. As explained by Sears [112], a downwash is induced at the leading edge by the bound vorticity and wake vorticity. This not only reduces the section lift coefficient, but also introduces a difference in phase between unsteady motion of the inflow and the response to the disturbance. By accounting for these unsteady effects, the temporal response of the blade forces, and therefore also the relative importance of the resulting in-plane loads, are predicted more accurately compared to the quasi-steady solution. The utilization of the Sears function is a well accepted approach to determine the transient lift response of a two-dimensional airfoil to a gust [186–188]. The response of the introduced induced drag and the change in profile drag of the two-dimensional airfoil can be determined using the approach of Ref. [189], and is comparable to the lift response. However, the application of a separate correction on lift and drag would require an estimation of the local induced velocity to obtain the local velocity vector to decompose lift and drag. As the thrust and torque forces on a section are typically dominated by the lift force, instead, a straightforward approach is used here. The radial load distributions of thrust and torque are corrected by directly applying Sears' function. The quasi-steady forces of Eqs. 5.6 through 5.9 are transformed to the frequency domain and are multiplied with Sears' function:

$$T'_{\text{us}}(r,\sigma) = T'_{\text{qs}}(r,\sigma)S(r,\sigma) \tag{5.22}$$

and

$$\frac{Q'_{\text{us}}(r,\sigma)}{r} = \frac{Q'_{\text{qs}}(r,\sigma)}{r}S(r,\sigma) \tag{5.23}$$

with σ being the reduced frequency $\sigma = \frac{k\Omega c}{2V}$, and S the Sears function. V is the magnitude of the local helicoidal inflow velocity to a section in the nominal, isolated conditions, and therefore includes the induced velocity. In case the induced velocities are unknown, actuator disk theory could be used as a first-order estimate. The Sears function for incompressible flow, $S_{M=0}$, is defined by Ref. [112] as:

$$S_{M=0}(\sigma) = [J_0(\sigma) - \mathrm{i}J_1(\sigma)]\,C(\sigma) + \mathrm{i}J_1(\sigma) = \frac{J_0(\sigma)\,K_1(\mathrm{i}\sigma) + \mathrm{i}J_1(\sigma)\,K_0(\mathrm{i}\sigma)}{K_1(\mathrm{i}\sigma) + K_0(\mathrm{i}\sigma)} \tag{5.24}$$

with C Theodorsen's function, J_0 and J_1 the zeroth- and first-order Bessel functions of the first kind, K_0 and K_1 the modified zeroth- and first-order Bessel functions of the second kind. A compressibility correction in line with Ref. [186] is applied to account for compressibility effects, which are typically not negligible on outboard sections. Ref. [186] applies a compressibility correction on both the lift curve slope and the reduced frequency. As the predicted quasi-steady loads already include the effect of compressibility on the section forces through the analysis of the isolated propeller, only the reduced frequency is corrected:

$$S(\sigma, M) = S_{M=0}(\sigma/\zeta^2)\left\{J_0\left(\frac{M^2\sigma}{\zeta^2}\right) + \mathrm{i}J_1\left(\frac{M^2\sigma}{\zeta^2}\right)\right\}\mathrm{e}^{\frac{-\mathrm{i}\sigma f(M)}{\zeta^2}} \tag{5.25}$$

119

with M the effective Mach number, ζ the Prandtl-Glauert compressibility factor based on the effective Mach number, and f a correction factor defined by:

$$f(M) = (1 - \zeta)\ln(M) + \zeta\ln(1 + \zeta) - \ln(2) \tag{5.26}$$

Equation (5.25) is valid for $\sigma M/\zeta^2 < 1$ [186]. The unsteady response over a full revolution in the time-domain is computed by taking the inverse Fourier transform of the product of the quasi-steady loading and the Sears function, Eqs. 5.22 and 5.23.

5.4. Validation

The predicted propeller forces by the engineering method are compared to full-blade CFD simulations and experimental data. The comparisons are presented for various cases that each have their own specifics in terms of the magnitude of the inflow relative to the size of the propeller disk, and the relative magnitude of the in-plane and out-of-plane velocity contributions. The various cases are selected to demonstrate the applicability of the method for a range of aircraft configurations.

5.4.1. Definition of Validation Cases

The engineering method is validated by comparing the predicted load distributions, integral blade loads, and integral propeller forces with unsteady RANS simulations (explained in Chapter 3) and experimental data of four representative validation cases. These cases are selected to feature a range of different types of inflow, summarized in Table 5.1. For each of the four validation cases, the inflow fields are evaluated at the plane of the propeller and are summarized in Fig. 5.6.

Table 5.1: Characteristics of the validation cases.

	Validation case #			
	1	2	3	4
In-of-plane disturbance ΔJ_t	✓		✓	✓
Out-of-plane disturbance ΔJ_a	✓	✓	✓	✓
Vortical inflow				✓
Defect in total pressure		✓		✓
Local disturbance		✓		✓
Disturbance over full disk	✓		✓	✓
Small propeller–airframe separation			✓	✓
Large propeller–airframe separation		✓		

An in-plane nonuniformity that is distributed over the propeller disk is simulated by providing an angle of attack (case 1) to the XPROP propeller. Figure 5.6a depicts the change in effective advance ratio and shows that the dominating component is the result of the in-plane velocity field, leading to changes in effective advance ratio of up to 35% of the freestream value, with a minimum at $\theta = 90\,\text{deg}$ and a maximum at $\theta = 270\,\text{deg}$. The axial induced velocity by the nacelle introduces only a slight asymmetry in the inflow.

A concentrated disturbance is simulated by generating a wake at different vertical locations which is encountered by the propeller (case 2), Fig. 5.6b. The viscous wake trails from a straight, untapered, and untwisted wing that is situated upstream the XPROP propeller with a separation of $3.2R_p$. The corresponding dimensions, computational domain and boundary conditions are presented in Section 3.4.4. For a wing that is situated at $z/R_p = 0.5$, the change in advance ratios is depicted in Fig. 5.6b, showing a maximum reduction of $\Delta J_a = 0.27$, caused by a maximum velocity defect of $0.15V_\infty$. As the in-plane induced flowfield downstream of the wing is negligible, the tangential velocity is nearly zero, and therefore $\Delta J_t \approx 0$.

(a) Case 1: Angle of attack, $\alpha = 5$ deg

(b) Case 2: Propeller encountering a wake. Wing at $z/R_p = 0.5$

(c) Case 3: Conceptual representation of an over-the-wing propeller. Flowfield with tip clearance $\varepsilon/R_p = 0.07$.

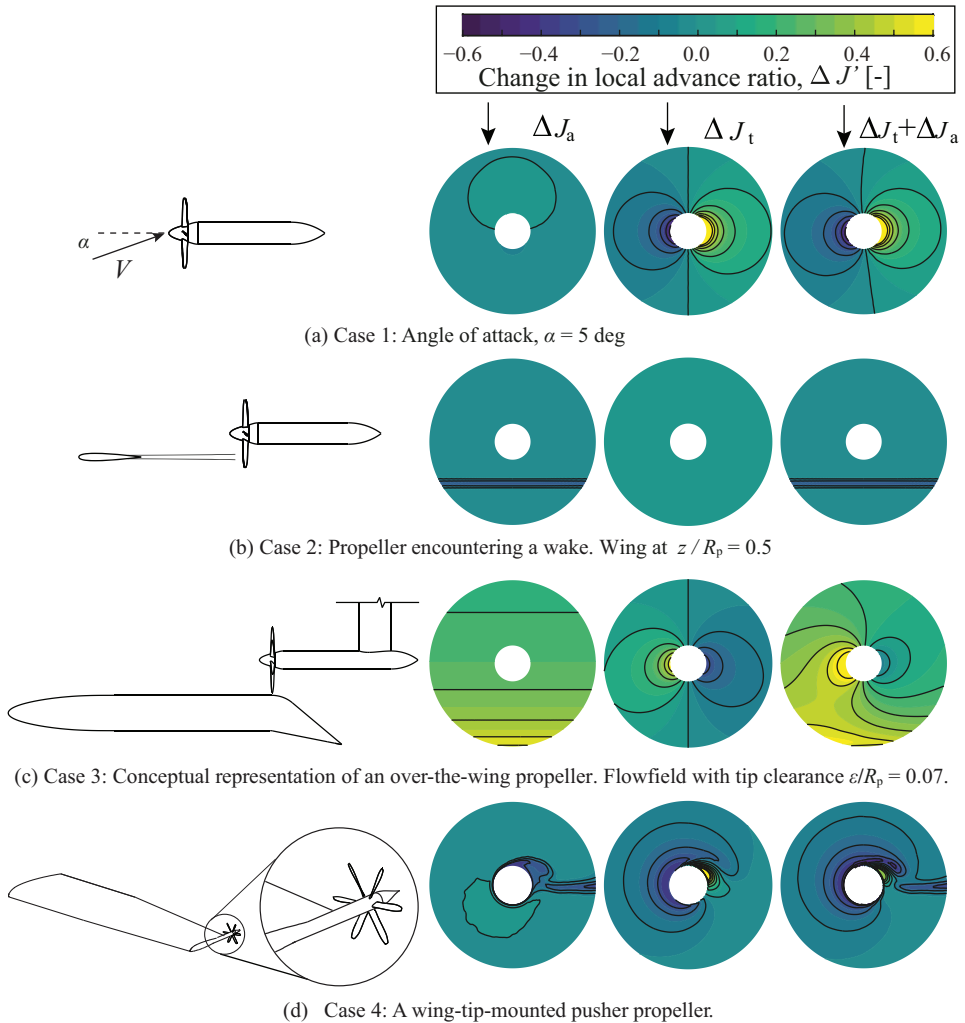(d) Case 4: A wing-tip-mounted pusher propeller.

Figure 5.6: Schematic of the four configurations used to validate the method. On the right, computed inflow profiles of the four validation cases that are used as input to the method.

A flow field consisting of both in-plane and out-of-plane flow was generated by mounting the XPROP-S propeller above a wing with a plain flap (case 3), Fig. 5.6c. The predicted integral thrust as function of tip-clearance is compared to experimental data from de Vries et al. [54]. The inflow to the propeller was obtained by simulating the wing section in a domain including wind-tunnel walls, but excluding the support strut. To gain confidence that simulated inflow field is close to the one in the experiment, the measured and computed pressure distribution are compared in Fig. 5.7a, which shows three is good agreement of the pressure distribution around the chordwise location where the propeller is installed. The extracted velocity profiles at this location are shown in Fig. 5.7b. The propeller experiences a strong variation of ΔJ_a over the disk, depicted in Fig. 5.6c, caused by the variation of axial velocity at the propeller location from $0.1V_\infty$ to $0.3V_\infty$. The in-plane velocity due to the wing circulation and curvature also varies over the propeller disk and is observed by the propeller as a negative angle of attack.

5

(a) Comparison of the measured and computed wing pressure distribution.

(b) Velocity profiles at the propeller location for different tip-clearances.
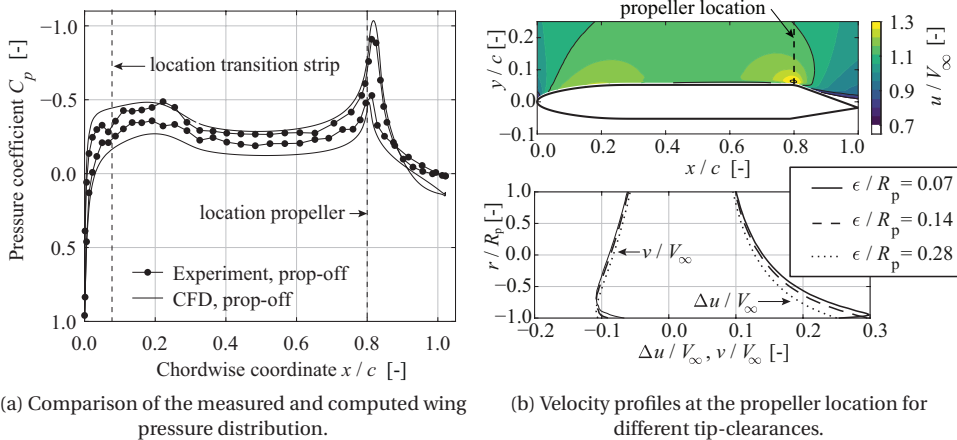
Figure 5.7: Validation and inflow profiles for the over-the-wing propeller configuration, propeller-off condition. Experimental data from Ref. [54].

Finally, a combination of a distributed and concentrated nonuniform inflow is generated by mounting a pusher propeller to the tip of a wing (case 4), Fig. 5.6d, such that the propeller encounters both a swirling inflow (due to the wingtip vortex), as well as a wing wake. This is a typical example where as a concept, often a relatively simple inflow is envisioned consisting of only a swirling inflow, while in practice the inflow is highly distorted and nonuniform. The mesh and inflow distribution from Ref. [190] were used to obtain the required validation data. The propeller is again the XPROP, but with a blade pitch of $\beta_{0.7R_p} = 30$ deg and a diameter of $D_p = 0.4046$ m. The performance maps in Fig. 5.4 were separately quantified for this propeller (not shown in this dissertation). Figure 5.6d shows a highly nonaxisymmetric inflow, caused by the swirling flow induced by the wing-tip, the wing downwash, and the viscous wing wake. The axial induced flow is driven by the viscous wake and the junction flow between the nacelle and wing surface.

122

Although the wing-tip and propeller axis are aligned, the wing-tip vortex rolls over the nacelle causing a large variation of J_t.

5.4.2. VALIDATION OF THE PROPELLER BLADE LOADS

Figure 5.8 depicts the predicted change of integral blade thrust, torque, side force and normal force coefficients over a full revolution, for the propeller at angle of attack (case 1). The blade loads are nearly sinusoidal, with a period of one-per-revolution for the thrust and torque, and a period of two-per-revolution for the in-plane forces. The quasi-steady method underpredicts the peak-to-peak load and introduces a phase advance with respect to the full-blade simulations. The maximum change in advance ratio occurs at $\theta = 90\,\text{deg}$ and $\theta = 270\,\text{deg}$ (Fig. 5.6a), while the maximum change in load occurs with approximately a 15 deg lag in the full-blade CFD results, in line with findings by Refs. [92, 113] and the discussion in Section 2.4. This delay is accurately captured by applying the unsteady correction to the quasi-steady result, and indicates that it can be predominantly attributed to the response of the two-dimensional blade sections that experience an unsteady inflow, and not due to blade-to-blade interaction. This behaviour is also clearly visible by comparing the C'_T distribution over the disk in Fig. 5.8b and is approximately constant along the blade. As the predicted load distribution has a phase advance, the relative values of the integral in-plane forces (depicted in Fig. 5.8c) are inaccurate, in particular the predicted C_Y shows a relatively large deviation. The non-zero C_Y from the quasi-steady solution is attributed to the difference in thrust at $\theta = 0$ deg and $\theta = 180$ deg due to the nacelle induced axial velocity field. By using the unsteady correction, the $C_Y - \alpha$ curve is closer to the full-blade CFD result. The strong variation of loading over the disk for this case results in a significantly nonuniform propeller slipstream and leads to an increase of the force magnitude in the full-blade simulation. As the actual slipstream is not computed, the predicted quasi-steady loads are too low, and these are further reduced by the application of the unsteady correction model. This is for discussed in Section 6.2. Despite that the root-mean-square of the blade thrust is underpredicted by 12% and 24% by the quasi-steady and unsteady methods, the integral thrust and torque nearly coincide with the full-blade simulation. It is noted that the integral thrust and torque are not affected by the application of Sears' function over a full revolution and the quasi-steady and unsteady result are identical, as can be deduced from Eq. 5.24.

5

(a) Blade forces, $\alpha = 5$ deg, $J = 1.8$

(b) Load distributions, $\alpha = 5$ deg, $J = 1.8$

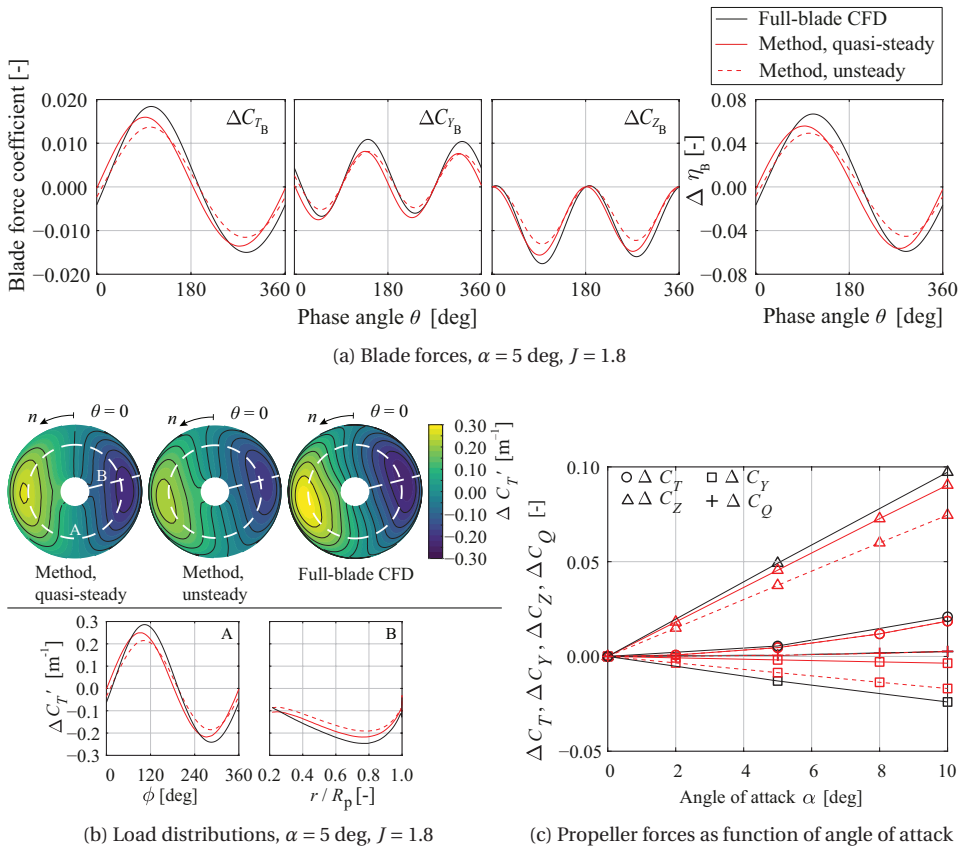(c) Propeller forces as function of angle of attack

Figure 5.8: Comparison of the forces predicted by the engineering method and computed by means of full-blade CFD simulations. Case 1: angle of attack.

For validation case 2, where the propeller encounters a wake, the predicted evolutions of integral blade forces compare well with the full-blade CFD simulation in terms of magnitude and phase, shown in Fig. 5.9a. The transient after the steep rise and fall of load is inherently not captured by the quasi-steady approach, but is shown to be quite well predicted when the Sears function is applied. It is worth noting that the character of the blade force over a revolution is highly dependent on the location at which the wake is encountered. The fact that two distinct peaks are present when the wing is at $z/R_{\mathrm{p}} = 0.5$, is attributed to the more sensitive response to a change in advance ratio in the highest loaded region of the blade, as shown in Fig. 2.10. If the wake is encountered towards the tip, the two peaks in Fig.5.9b merge into a single peak. From Fig. 5.9b, it also follows that even though in the full-blade simulation the load is slightly more smeared in radial direction, the unsteady method already shows excellent agreement of the radial load distribution for a range of phase angles. The relative change of the thrust and torque is also in line with the full-blade CFD simulations, reflected in the change in blade efficiency,

Fig. 5.9a. The integral forces depicted in Fig. 5.9c are close to the ones computed in the full-blade simulation. The trends of the forces as function of the location of the wing wake relative to the propeller are in line with the full blade simulations. It is noted that even though the axial separation between the wing and propeller is $3.2R_p$, the propeller still has an upstream effect on the wing. For a wing location of $z/R_p > 0$, the propeller induces an angle of attack to the wing, and leads to a small lift coefficient.

(a) Blade forces, wing at $z/R_p = 0.5$

(b) Load distributions, wing at $z/R_p = 0.5$
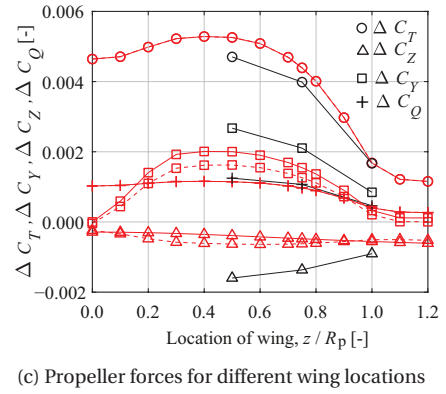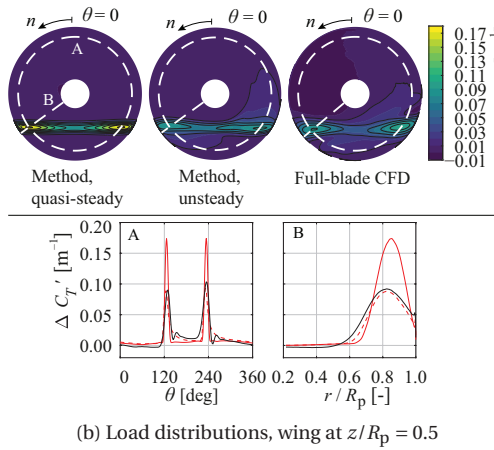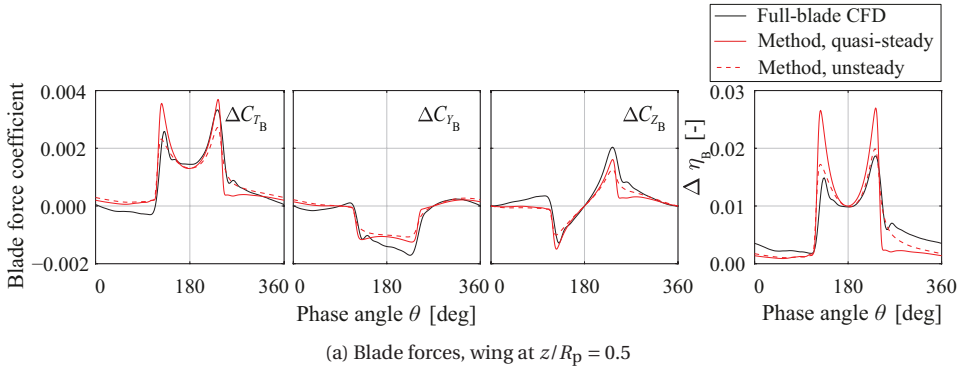
(c) Propeller forces for different wing locations

Figure 5.9: Comparison of the forces predicted by the engineering method and computed by means of full-blade CFD simulations. Case 2: wake encounter, $J = 1.8$.

This leads to a nonzero wing downwash, reflected as the sinusoidal blade force over a revolution, Fig. 5.9a. Consequently, the propeller normal force in the full blade simulations is higher than estimated using the engineering method (Fig. 5.9c). This interaction becomes stronger with higher thrust coefficients and smaller wing–propeller spacing.

For case 3, where the propeller is placed above a wing, the large reduction in thrust observable in Fig. 5.10a is caused by the higher axial inflow velocity induced by the wing's circulation. When the tip-clearance is increased, the reduction in thrust becomes smaller due to the reduced axial inflow. This trend is very well predicted by the method,

despite the complex flowfield, the proximity of the propeller to wing which will cause the wing lift to change, and with that the propeller inflow. The predicted magnitude of the ΔC_T almost coincides with the measured values, and shows the ability of the method to predict the propeller performance for such configuration. The model is also able to capture the different response of the propeller thrust coefficient to the nonuniform inflow for each advance ratio, as the sensitivity to a change in advance ratio depends on the nominal operating condition. Since at higher thrust coefficient, the effect of the propeller on the wing increases, the reducing offset towards lower J is the consequence of higher wing lift in the experiment. Since the inflow profile used for the method does only entail the airframe induced inflow without the propeller present, this interaction is not captured. The dominant inflow to the propeller is therefore the airframe in absence of the propeller and the propeller has a secondary effect on the inflow. Therefore, as a first prediction of the propeller performance loss in such configuration, the method will provide an excellent first estimate.
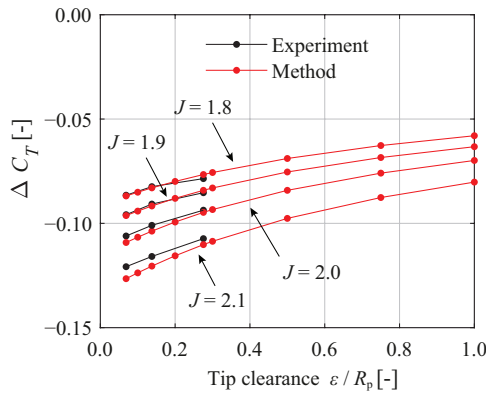

Figure 5.10: Comparison of the change of the integral propeller thrust predicted by the method and experimental data of the over-the-wing propeller configuration from Ref. [54].

Finally, case 4, where a pusher propeller is mounted to the tip of a wing, exhibits comparable trends as validation cases 1 and 2 in terms of integral blade forces if the quasi-steady method is used, as depicted in Fig. 5.11a. First, there is a local overprediction in the regions of a local disturbance induced by the wing wake, secondly there is an underprediction of the effect introduced by a distributed nonuniformity over the disk, i.e. the swirling inflow, and finally there is a phase advance with respect to the full-blade simulation. Similarly to the previously discussed cases, the contour plot in Fig. 5.11b reveals that the shape of the thrust distribution is very well captured by the method, despite the overpredictions in the regions where there is a strong gradient of the inflow: the encounter of the wing-wake and the impingement of the wing-tip vortex. In a qualitative manner, one can directly relate the relative importance of the different flow phenomena on the propeller loads, by relating the thrust distribution to the inflow field of Fig. 5.6d. Figure 5.11c shows that the integral thrust is close to the computed value of the full-blade CFD simulation, and the order of magnitude and direction of the in-plane forces is correctly captured. Quantitatively, the in-plane forces of this case are relatively small, and a

difference in phase quickly causes a relatively large offset.

(a) Blade forces, $J = 1.17$

(b) Load distributions, $J = 1.17$

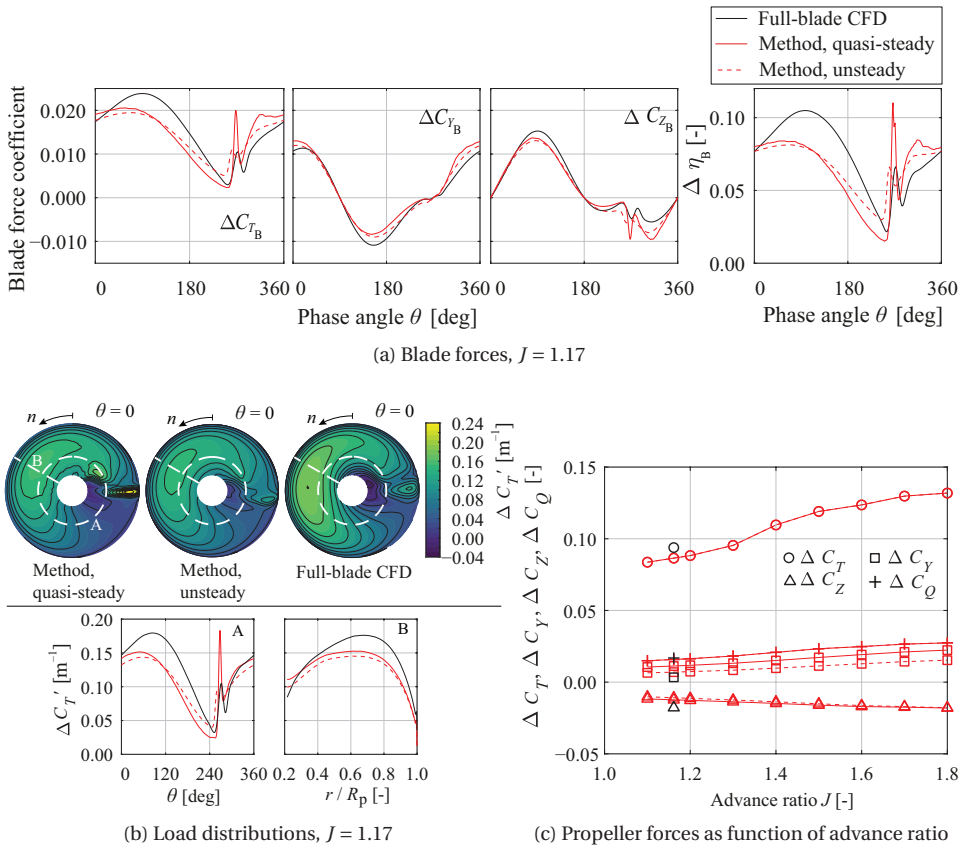(c) Propeller forces as function of advance ratio

Figure 5.11: Comparison of the forces predicted by the engineering method and computed by means of full-blade CFD simulations. Case 4: wing-tip mounted pusher propeller.

For the cases evaluated, it was found that the change of the integral thrust and torque compared to uniform inflow condition were within a range of 0.5% to 12% compared to the validation data. It is concluded that the method is able to capture the relevant changes in propeller loading, and can predict both the magnitude and trends well for a wide range of operating conditions and nonuniform inflows. Provided that this method provides a solution with seven orders of magnitude lower computational resources than a full blade simulation (Table 5.2 in Section 5.5), it is a powerful tool for relatively accurate propeller performance prediction in several stages of the design of unconventional propeller installations.

5.5. COMPUTATIONAL EFFICIENCY BENEFITS

The computational cost of a single condition using the engineering method was found to be in the order of several seconds, while a significant amount of computational efforts

were spent on the unsteady full-blade CFD simulations to evaluate a single operating
condition, as listed in Table 5.2. The table lists results of typical propeller–airframe inter-
action studies, presented in Section 5.4. The additional time to correct the quasi-steady
results for unsteady effects is negligible. If one is only interested in the change in inte-
gral thrust or torque, the unsteady correction is even redundant. The construction of the
performance maps in Fig. 5.4 required approximately 2000 CPU hours, while it is noted
that the large number of conditions (20 advance ratios) could be reduced to a minimum
of two conditions in case the nonlinear regime is not of interest. The values in Table
5.2 clearly demonstrate the advantage of using the engineering method for an initial es-
timate of the propeller performance as well as the phase-accurate blade responses, in
particular if a large number of conditions are to be evaluated. This makes the proposed
method highly valuable for the design of vehicles with tightly integrated propellers.

Table 5.2: Comparison computational effort of engineering method to full-blade CFD. The cases are
described in Section 5.4.

Propeller test case	Characterization $C_T - J$ [CPU hr.]	Simulate inflow [CPU hr.]	Method [CPU sec.]	Full-blade CFD [CPU hr.]
Angle of attack	~2000	160	~3	7000
Wake encounter	~2000	180	~3	7500
Tip-mounted pusher	~1900	210	~4	8500

5.6. CONCLUSIONS

This chapter has presented an engineering method to estimate the propeller load dis-
tribution for propellers operating in arbitrary nonuniform flow. The method is com-
putationally extremely efficient, as the input is based on the distribution of the thrust
and torque along the propeller radius to a change in advance ratio for the uninstalled
propeller in uniform inflow. It is shown that the shape of the sensitivity distributions is
nearly independent of propeller advance ratio, and can therefore be approximated by
simulating only two operating conditions. The construction of these sensitivity distribu-
tions also provides insight into what region of the disk leads to the largest response in
propeller forces, this was demonstrated to be the region of highest loading.

The method was applied to four representative validation cases: a propeller at an an-
gle of attack, a propeller encountering a wake, an over-the-wing propeller, and a wing-
tip mounted pusher propeller. The method has been applied for slender blades, repre-
sented as a line through the mid chord. A phase difference with respect to full-blade CFD
simulations is present in case of a distributed disturbance, leading to slight inaccuracy of
the prediction of the in-plane forces. The application of a correction on the quasi-steady
results nearly removes the difference in phase between the responses of the validation
data and the method, and also improves the difference in magnitude of the blade re-
sponse as the result of local disturbances in inflow. The integral forces on the individual
blades over a full revolution as well as the integral propeller forces compare well with
the validation data, both in terms of predicted trends and magnitude. For the evaluated

cases, it is shown that the change in the load due to the nonuniform inflow is predicted with errors ranging from 0.5% up to 12% compared to the validation data. The acceptable agreement with full-blade simulations and experimental results also demonstrates that, for most configurations, the dominating factor to alter the propeller performance is the flowfield induced by the airframe in absence of the propeller.

The proposed method offers significant efficiency benefits over conventional unsteady CFD analyses of installed propeller. The unsteady analyses of the full annulus of the installed propeller are avoided, while still a time-resolved solution is obtained, with a temporal resolution depending on the spatial resolution of the inputs. The proposed method provided a time-resolved solution within several CPU seconds, which was seven orders of magnitude faster than with the full-blade RANS CFD computations. The low computational cost makes the proposed method suitable for both design and analyses of propellers in arbitrary nonuniform flows. Compared to relying on isolated performance data, this method will allow for a better prediction of the performance of aircraft with tightly integrated propellers, as well as an estimation of the propeller contribution to the aircraft stability derivatives during the preliminary design phase. Such a comparison between propeller configurations by the application of this method is presented in Chapter 7.

5

6

AIRFRAME INDUCED INFLOW EFFECTS ON INSTALLED PROPELLERS

6.1. INTRODUCTION

As discussed in Chapter 1, for numerous existing and proposed configurations, the propeller installation is carefully chosen with the objective to gain an overall aircraft performance benefit by increasing the propeller efficiency, improving the airframe performance, and/or by reducing the noise footprint [12, 25]. Since the early days of propeller-driven aircraft [14] it is known that the installation of propellers in the vicinity of the airframe leads to an aerodynamic interaction: the propellers alter the airframe forces by inducing a pressure and velocity field, while the airframe induces a flowfield that affects the propeller forces. The airframe-induced inflow effects for both conventional and unconventional configurations are the subject of this chapter.

Since the airframe rarely induces a uniform flowfield relative to the freestream condition, a propeller operating near the airframe experiences a nonuniform inflow. As introduced in Chapter 5, in a general sense, an arbitrary, time-averaged inflow to the propeller disk can be characterized as a combination of out-of-plane and in-plane momentum transport. A reduction in local effective advance ratio locally results in a higher thrust, higher torque, and a higher thrust-to-power ratio [14]. An azimuthal variation in advance ratio has a number of consequences. First, the propeller rotation makes the loads on the blade periodic, typically leading to additional noise [26, 191, 192], fatigue loads on the blades [193], and vibrations to the airframe [156]. Second, in-plane forces and moments are generated [60], which alter the trim condition and stability characteristics, as observed in Refs. [25, 62, 194]. These propeller out-of-plane moments that originate from the nonzero in-plane forces are small compared to the moment coefficients

---

Parts of this chapter have been published in Refs. [90, 118–120].

on aircraft level [195, 196], and will therefore not be discussed. Finally, the slipstream development as a consequence of the redistribution of the blade loading, as is demonstrated for a propeller at angle of attack in Chapter 2, can play an important role in the aerodynamic interaction [197].

Various studies have been conducted on the effect of a fuselage, swept and unswept wing, and the nacelle on the propeller inflow [198–200]. Several authors have discussed the effect of a nonuniform inflow on various propeller performance indicators. References [48, 63, 184, 201, 202] demonstrate that by careful installation, significant propeller efficiency gains can be achieved relative to a propeller that operates in freestream conditions. For example, axisymmetric inflow that covers a large part of the propeller disk, such as a swirling inflow to a wing-tip mounted pusher-propeller or a boundary layer inflow, have shown to enhance the propeller efficiency typically by 5% to 10% [56, 57, 190, 203]. Local disturbances, such as the propeller encountering a wake or vortex, have a small effect on the mean propeller forces, while they do cause significant unsteady loads and noise [89, 187, 204–208]. Asymmetric inflow, such as a propeller at an angle of attack or a propeller operating in the upwash or downwash of a wing, only changes the propeller efficiency slightly, but still leads to significant unsteady loads and in-plane forces [49, 92, 93, 113, 144, 156, 202]. Structural and aerodynamic design considerations for rotors in highly distorted flowfields (e.g. boundary layer ingestion configurations or in case of a wake encounter) have been addressed in e.g. Refs. [193, 209]. These studies concluded that the blade design (procedure) is to be adapted to account for the additional loads and it can be expected that for other unconventional installations similar design adaptations are required to meet operational standards. Other adverse consequences of nonuniform inflow include an increase in airborne noise and higher levels of structureborne noise [68, 70, 181, 206, 208, 210]. Special mitigation strategies could be applied to reduce this noise penalty, for example demonstrated in Ref. [205] by applying a blowing system to reduce the nonuniformity of the inflow. However, such system would add more complexity to the installation and it can be expected to lead to lower payload-range energy efficiency due to increased mass and required power for the blowing system.

The relative impact of nonuniform inflow on propeller forces compared to the installation effect on the airframe forces depends on several factors, including the location, the flight condition, and the relative size and aerodynamic characteristics of the airframe and propeller. While for the conventional configuration the propeller operates in a relatively undisturbed flowfield which therefore has a small effect on efficiency, normal-force coefficient, and periodic loading (see Ref. [49]), the recent rise of interest in unconventional propeller-driven aircraft configurations demands design guidelines and the need of understanding the nonuniform inflow effects of inflows that deviate from the conventional configuration. For example, the altered stability characteristics could require design modifications to the airframe, and the change in propeller efficiency could lead to performance predictions that are far from a prediction based on the consideration of uniform inflow. An estimation of aircraft performance based on propeller data for isolated conditions is therefore insufficient, especially if the propellers are more distributed along and in close proximity with the airframe.

Even for configurations where the objective is not a higher propeller efficiency,
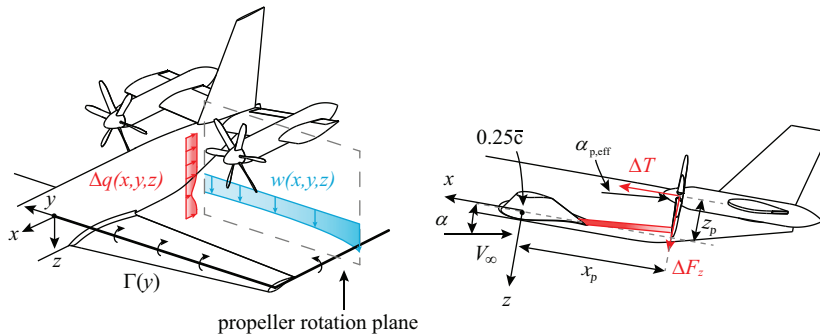
6

Figure 6.1: Illustration of an unconventional propeller installation where the propeller experiences various types of nonuniform inflow (simplified representation).

the propeller will experience nonuniform inflow. An example of such case is the tail-mounted propeller configuration. Figure 6.1 illustrates various sources of inflow for this configuration: a wake that trails from the wing is encountered at higher angles of attack, the wing-induced downwash field is distributed over the propeller disk and varies with angle of attack, the fuselage induces an upwash to the disk due to the upsweep angle and introduces a distorted flowfield in the case of a side-slip angle. Finally, the tailplane introduces an upstream effect to the disk. It may be observed that for unconventional configurations, the *inflow varies with flight conditions*. Such a highly three-dimensional flowfield therefore impacts the propeller's contribution to the moment coefficients, the unsteady loads, and propeller efficiency. Moreover, the stabilizing surfaces are submerged in the slipstream and any changes in propeller slipstream directly affect the forces acting on these surfaces.

Not only the inflow varies with the flight condition (i.e. angle of attack, angle of side slip, deflection of control surfaces, and deployment of high-lift devices), also the effect of the inflow on the propeller is dependent on the flight condition. One of the key elements needed to understand the trends of force coefficients and slipstream development of installed propellers, is how different regions on the disk respond to a disturbance. In Section 2.2.2 it is shown that not only the load distribution varies along the radius, but the *change* of the loading to a ΔJ depends on the radial station as well. Figure 5.4 in Chapter 5 therefore depicts a key property of propeller blades that encounter a nonuniform flowfield. From this characteristic, one can directly deduce that the response of the propeller is highly dependent on the location on the disk where the nonuniformity is encountered, as illustrated in Fig. 6.2. This figure shows that a disturbance that is off-center relative to the propeller can still have a larger impact than a centered disturbance, since the product of this sensitivity with swept area is still larger. Herein, this is referred as the 'donut effect', similar to Ref. [37]. The nonlinear sensitivity of the disk already indicates that the size of the propeller relative to the disturbance, their relative locations, and the gradient of the inflow will largely determine how the propeller performance is affected. Furthermore, due to the transient response (Section 5.3), the response of the blade loading does not directly correspond to the inflow profile, and therefore the direction and magnitude

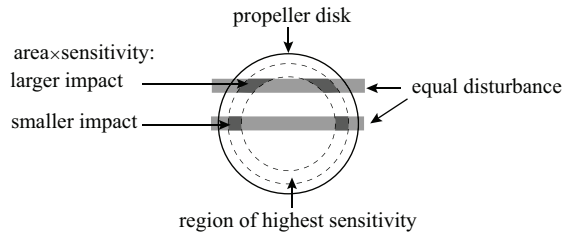of the resulting force vector is not apparent.

Figure 6.2: Illustration of a disturbance that is encountered at a different location on the propeller disk.

This chapter will demonstrate that the airframe-induced inflow directly influences the propeller efficiency and forces and in the estimation of the *overall aircraft performance*, the *propeller performance* should therefore be determined based on the airframe-induced inflow conditions. Various authors have analyzed aspects of nonuniform inflow effects. In this chapter, more specific research questions are posed that extend the current knowledge on this topic:

- *RQ 6.1:* What is the relation between the changes in load distribution to the propeller sensitivity distribution?

- *RQ 6.2:* What are the key drivers that determine the response of a propeller in installed conditions?

- *RQ 6.3:* To what extent can a nonuniform inflow be averaged to estimate the propeller forces?

- *RQ 6.4:* How are the gradients of propeller forces related to the gradient of the inflow?

These questions are addressed first by assessing the different sources that cause nonuniform inflow in Section 6.2. Subsequently, various cases are discussed, each having a specific focus. These cases are subproblems of full-aircraft configurations, and therefore serve as more fundamental problems. Finally, a practical example of propeller installation is discussed to identify the key phenomena that play a role on aircraft level. The findings in this chapter are relevant to understand the trends presented in Chapter 7, which presents a comparison of different propeller configurations.

6.2. Various Sources of Nonuniform Inflow

The flowfield at the propeller disk is a combination of the *airframe-induced flowfield* and the *propeller-induced flowfield*. The relevance and scope of these contributions are discussed in the following.

Airframe-Induced Flowfields

The flowfield at the propeller plane is described by the velocity perturbations, density variations, turbulence level, and pressure gradient. The velocity variations directly determine the local inflow vector to the blade sections. The relevance of density variations

becomes more apparent for high subsonic flight, and are not further discussed in this dissertation. Turbulence levels of the inflow alter the transition location and therefore the sectional lift and drag coefficients. This is especially relevant for small propellers that have extended laminar flow due to the low Reynolds number on the blade sections (see Section 2.5). The blade loading caused by this type of inflow is also out of the scope of this dissertation and the interested reader is referred to Ref. [171].

Figure 6.3 depicts a number of typical cases of nonuniform inflow caused by the presence of the airframe, which can be divided into three categories with each having their specific characteristics. These specifics are summarized in Table 6.1.

First, the most common type of flowfield is the one that can be described by a velocity potential. The vorticity distribution along the boundary of a solid surface, or in a more simplified representation, by a bound vortex for lifting surfaces, induces a nonuniform flowfield around the airframe. For these inflows, the in-plane and out-of-plane velocity gradients vanish at a large distance from the airframe, the velocity profile generally is smooth, and the velocity distribution strongly depends on the flight condition. Contrary to the flowfields in the other two categories, there is a strong spatial dependency, and therefore the effect of the inflow can be manipulated by the careful selection of propeller diameter and location. Additionally, pressure forces act on the propeller blades due to the static pressure gradients in streamwise and in-plane directions. Since the blades have finite chord and thickness, this gradient alters the forces on the blades as well. However, it is demonstrated in Ref. [211] that, compared to the thrust coefficient, this is a negligible effect for typical applications and is therefore not discussed further.

6
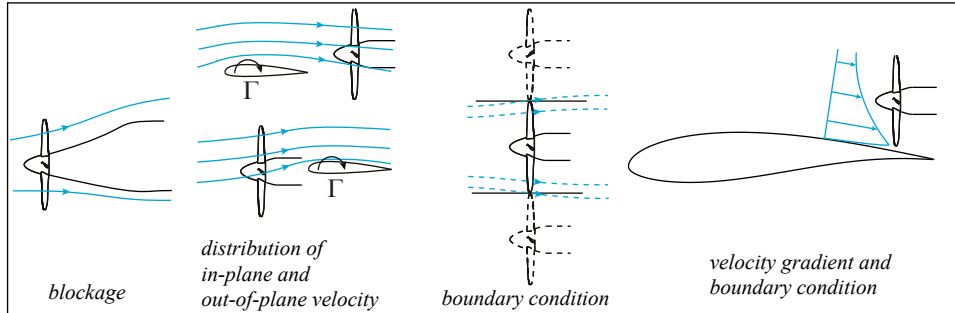
(a) Examples of flowfields that can be described as velocity potential that is externally induced
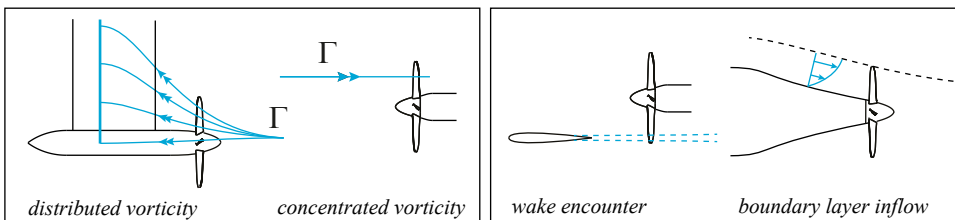
(b) Examples of flowfields vortical inflow

(c) Examples of flowfields with a deficit in total pressure

Figure 6.3: Various types of nonuniform inflow for conventional and unconventional configurations.

Table 6.1: Different types of nonuniform inflows and their typical characteristics. Practical examples are depicted in Fig. 6.3, indicated by letter between brackets.

Type	Velocity gradient	Dominant component perturbation	Contains turbulence	Variation with flight condition	Dependency on proximity to airframe
Potential flow (a)	smooth	axial and tangential	no	strong	moderate
Vortical inflow (b)	strong	depends on orientation	yes	strong	weak
Deficit of p_t (c)	strong	axial	yes	moderate	strong

Second, in case of vortical inflow, the distributed or concentrated vorticity introduces a sharp gradient of the velocity with the largest gradient at the core of the vortex. The dominant velocity component depends on the orientation: a vortex aligned with the propeller rotation axis induces primarily an in-plane velocity component, while a transverse vortex induces primarily an out-of-plane component. For this type of inflow, the vorticity that is encountered by the propeller blades interacts with the propeller-induced vortex system and therefore the slipstream deforms. Since the strength and path of the vortex depends on the flight condition, these flowfields also strongly vary with flight condition. Outside the core of the vortex, the velocity can be described by a velocity potential, while inside the vortex core there are elevated levels of turbulence due to the presence of viscosity [152].

Finally, due to the no-slip condition at the solid walls, the airframe introduces a deficit of total pressure, e.g. a wake trailing from the wing or fuselage, which is primarily a velocity perturbation in axial direction. In nominal conditions, its shape does not vary significantly with flight condition. An exception to this are the situations of flow separation. The location of the wake relative to the propeller is dependent on flight condition in case of a wake encounter and the axial distance between trailing edge and propeller is large. The profile is typically the shape of a free-wake or boundary layer and the velocity gradient reduces rapidly after the boundary layer is shed from the airframe [170]. The disturbance is limited in spatial direction and therefore affects only part of the propeller disk. These flowfields also contain elevated levels of turbulence.

The following distinction can be made in the *source* of the nonuniform inflow, as schematically shown in Fig. 6.4:

1. The flowfield induced by the airframe *without propellers*

2. The flowfield induced by the changes in airframe forces *caused by propeller installation*

The airframe-induced flowfield in absence of the propellers is referred to as the 'direct contribution'. In addition, the *change* in airframe forces caused by *propeller installation*, also influence the inflow to the propeller. For example, it alters the lift of a lifting surface upstream or downstream of the disk. Figure 2.5 in Section 2.1.2 shows that the influence of the propeller vanishes within two propeller diameters upstream of the disk. The impact of the propeller-induced airframe forces on the propeller inflow therefore depends on the relative size of the propeller to the airframe, their proximity, the thrust coefficient,

and the aerodynamic characteristics of the airframe. In most cases, this installation effect is secondary compared to the direct effect, shown in e.g. Refs. [37, 54] and Chapter 5. Examples where the installation effect becomes more important include over-the-wing propellers for lift enhancement and delay of flow separation [52, 54] and leading-edge mounted tractor propellers in high thrust conditions [12]. In other cases, it can be reasoned that the change in airframe lift is significantly smaller than lift present without the propellers, for example for wing-mounted tractor or pusher propellers at moderate thrust coefficients.
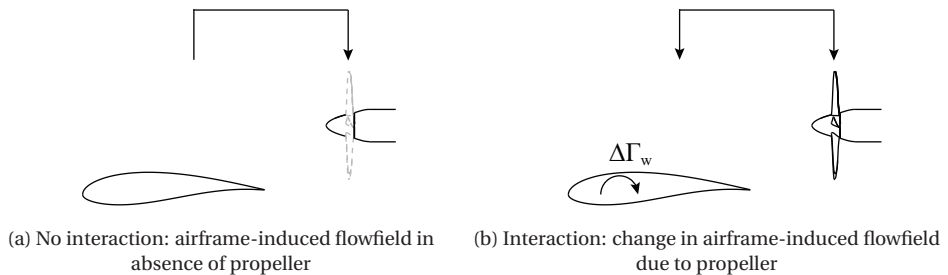

(a) No interaction: airframe-induced flowfield in absence of propeller

(b) Interaction: change in airframe-induced flowfield due to propeller

Figure 6.4: Schematic of the direct (in a) and indirect (in b) causes of the airframe-induced flowfield at the propeller disk.

6

PROPELLER-INDUCED FLOWFIELDS

For the installed propeller, the nonuniform inflow at the propeller plane is partially modified by the propeller vortex system in three ways: an upstream effect, a near-field effect, and a downstream effect. These three phenomena are schematically shown in Fig. 6.5.

Firstly, since the slipstream tube extending upstream of the disk has a larger diameter than the propeller, it is this momentum that will enter the propeller plane. The higher the thrust coefficient, the larger the radius of this upstream part of the slipstream (see Chapter 2). This upstream effect will redistribute the airframe-induced inflow to different radial locations, also observed in Ref. [212]. This is illustrated for a propeller operating in the boundary layer of a fuselage in Fig. 6.5a. This effect is especially present if there is a strong gradient of the flowfield around edge of the slipstream tube, for example if a wake is encountered at the edge of the propeller disk. However, in Ref. [211] it is shown that this upstream effect is generally small for thrust coefficients corresponding to cruise condition.

Secondly, there is a near-field effect, schematically shown in Fig. 6.5b. Since the induced velocity field depends on the circulation distribution, a varying bound circulation and varying vortex strength of the helical vortex caused by nonuniform inflow affects the inflow to the adjacent blades. The effect of nonuniform inflow is therefore not confined to its azimuthal location. In Ref. [185] it is proven that the influence of a change in load distribution on a propeller blade on adjacent blades is at least two orders of magnitude smaller than the change in load itself. This is particularly the case for a low number of blades and in case the disturbance is encountered towards the blade tip because the distance to adjacent blade sections is large.

(a) Upstream effect: slipstream contraction modifies inflow

(b) Nearfield effect: blade loading affects inflow to adjacent blades

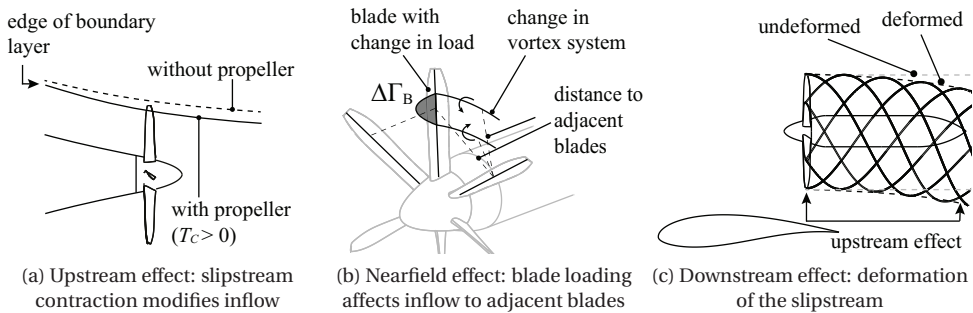(c) Downstream effect: deformation of the slipstream

Figure 6.5: Nonuniform inflow to the propeller disk that is caused by the propeller vortex system for the installed condition in three ways.

Finally, the airframe-induced flowfield translates and deforms the propeller slipstream. This can be the consequence of e.g. a vortex that is encountered by the propeller and interacts with the helical vortex system [204], the slipstream that is curved due to the airframe-induced in-plane velocity, or the interaction of the slipstream with the airframe will deform the slipstream [37]. An example of such deformation is depicted in Fig. 6.5c. Since the helical vortex system determines the induced velocities at the disk, a displacement and deformation of this vortex system relative to the disk leads to a different inflow than the case of an undisturbed vortex system.

To the knowledge of this author, the downstream effect of slipstream deformation on the propeller inflow is not clearly demonstrated in open literature. To indicate the relevance for this type, the slipstream is modelled as a series of ring vortices which are displaced with respect to the propeller disk. For this exercise, the analytical expressions from Ref. [213] are used. Two cases of interest can be deduced from Fig. 6.6a. In the first case, the slipstream is deflected by an angle δ at a certain distance x_d from the propeller disk (this represents a slipstream deformation after it impinges a wing leading edge, see Chapter 8). The second case with $x_d = 0$ represents a propeller at an angle of attack or the slipstream is deformed by the airframe. The flowfield depicted in Fig. 6.6b is the flowfield in uniform flow conditions. In Fig. 6.6c the deviation from the axisymmetric case is shown along the propeller disk for different distances x_d. The figure shows that for $x_d = 0$ the inflow deviates less than 1% per degree from the induced velocity of the isolated condition. As expected, this deviation quickly reduces when the distance is enlarged. Therefore, the first few tip vortices near the disk are the dominant source of the induced velocity field at the disk, and further downstream the helical vortex system has limited impact on the propeller inflow and is not a key driver that determines the response of a propeller in the installed condition.

(b) Axial velocity induced by ring vortices extending to $x \to \infty$. u_1 is half the velocity at $x = \infty$.

(a) Illustration of ring vortices. At $x = x_d$ these have a constant deflection angle δ.

(c) Effect of a deflection ($\delta = 1$ deg) on axial velocity at the propeller disk
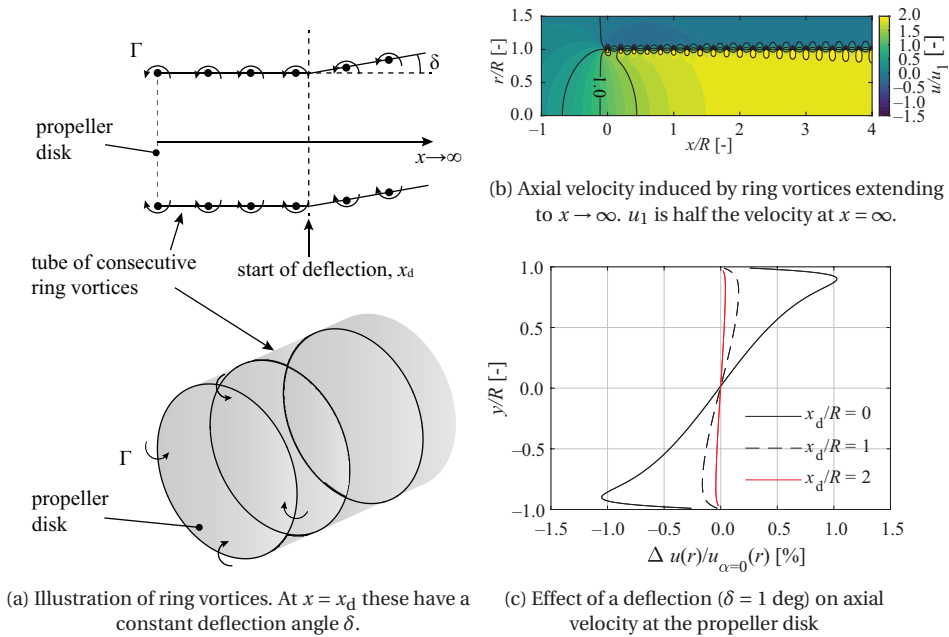
Figure 6.6: Illustration of modifying the propeller slipstream at a downstream location on the velocity at the propeller disk, modelled by consecutive ring vortices, based on Ref. [213].

6.3. PROPELLER IN PROXIMITY OF A LIFTING SURFACE

For various configurations, the propeller operates in a flowfield induced by a lifting surface, i.e. in an upwash or downwash, for example discussed in Refs. [199, 200, 214, 215]. Near the lifting surface, the pressure distribution of the airfoil dominates the flowfield and is therefore geometry specific, particularly if the propeller is positioned above or below the wing. In addition to the lift-dependent flowfield, a surface of finite thickness also induces a displacement effect, that can vary in spanwise direction. Further away, the problem becomes more generic and the propeller experiences only an upwash and downwash. A schematic of this problem is depicted in Fig. 6.7.
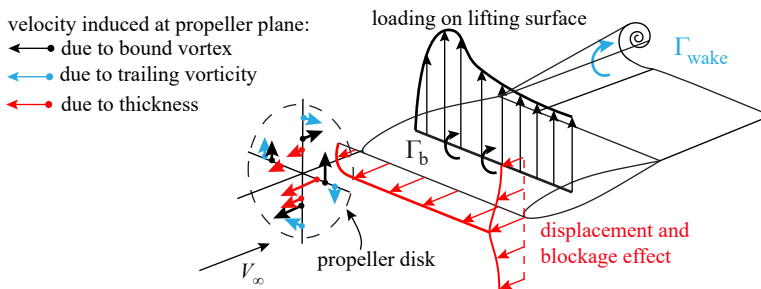

Figure 6.7: Schematic of a propeller that is influenced by the presence of a lifting surface with finite thickness.

139

An example of the nonuniform loading on the propeller that is introduced by the lifting surface is illustrated in Fig. 6.8 for a propeller that is mounted to a low aspect ratio tailplane where the loading is influence by the deflection of an elevator. The thrust is increased on the side where the blade sweeps past the leading edge of the tailplane, slightly increasing the average loading on the blades. When the lift on the lifting surface is altered, it is directly observable in the propeller loading as well, and the change is not limited to the leading-edge region.

(a) Radial thrust distribution of one propeller blade, installed versus isolated

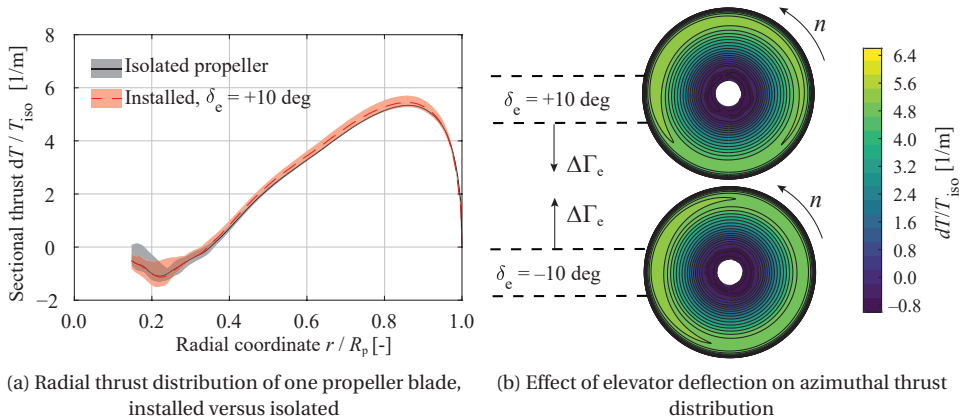(b) Effect of elevator deflection on azimuthal thrust distribution

Figure 6.8: Effect of tailplane installation on the propeller loading at $\alpha = 0$ deg. Beaver propeller mounted to the *PROWIM-HTP* model. Full-blade CFD simulations, $J = 0.8$.

In this section, the nearfield and farfield effects are treated separately by computing the propeller forces and load distributions by the method described in Chapter 5. In this section not only part of the research questions *RQ 6.2*, *RQ 6.3*, and *RQ 6.4* are discussed, also practical examples of the effect of lifting surfaces on propeller forces are given.

6.3.1. PROPELLER IN FLOWFIELD INDUCED BY HORSESHOE VORTEX

For relatively large propellers at a large distance to the leading edge, the blockage upstream of a wing due to thickness is small, and the circulation generated by the wing's surface can be modelled by a lifting line with trailing vorticity. In this section, the effect of the nonuniformity of the flowfield induced by the horseshoe vortex is investigated. This investigation highlights the importance of including nonuniformity of the inflow in analyses and shows an example of how the gradient of the inflow relates to the gradients of the propeller forces. The effect of chordwise varying vorticity is presented in Section 7.4.

Figure 6.9 shows two cases where the bound vortex induces an in-plane and out-of-plane velocity field at the propeller disk. For a wing of finite span, the upwash field is primarily induced by the bound vortex, while a pusher propeller experiences a flowfield constituting of a contribution from the bound vortex and trailing vorticity. The relative importance of the bound and trailing vorticity depends on the wing's aspect ratio. In Fig. 6.10a it is shown that the downwash upstream of the wing is not negligible rela-
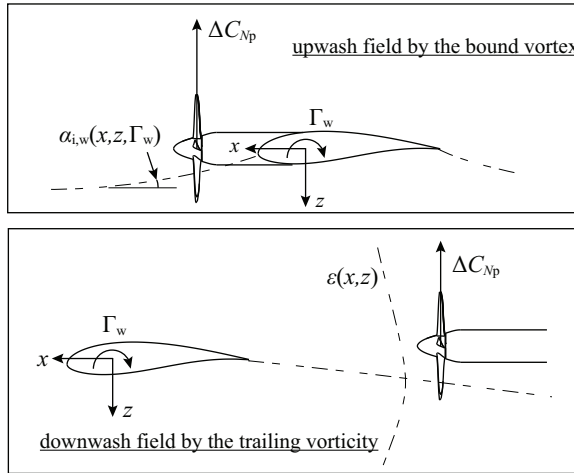
Figure 6.9: Schematic of a propeller that is influenced by the upwash and downwash of a lifting surface.

tive to the bound vortex for typical wing aspect ratios. As expected, the contribution of the bound vortex vanishes if the distance to the bound vortex is increased. Because the bound vortex Γ_B produces an upwash in the propeller plane, the problem resembles to a propeller at angle of attack. However, this upwash is not perceived by the propeller as a uniform angle of attack over the full disk, but as a distribution [37] such that the local angle is $\alpha'_p = \alpha_\infty \left(1 + \frac{d\alpha_{i,w}}{d\alpha_\infty}(x,y,z)\right)$ with $\frac{d\alpha_{i,w}}{d\alpha_\infty}(x,y,z)$ being the gradient of the local angle of attack caused by the wing.

Since the flowfield induced by a lifting line is primarily in the plane of the propeller, the propeller normal-force coefficient is the most important propeller force that is influenced by it. To obtain a general understanding of how this coefficient is influenced by the wind-induced flowfield, the propeller forces are computed with the method presented in Chapter 5. To illustrate this effect, the induced flowfield of a lifting line with an elliptical lift distribution is used to determine the propeller normal-force coefficient (see Fig. 6.10b). For $\mathcal{R} \to \infty$, the problem reduces to a propeller that experiences the induced velocity by the bound vortex. For this case, the ratio $C_{Np,\text{ins}}/C_{Np,\text{iso}}$ is above unity for the upstream propeller, and below unity in case for a propeller downstream of the bound vortex. For lower aspect ratios, the downwash reduces the ratio $C_{Np,\text{ins}}/C_{Np,\text{iso}}$, similar to a stabilizing surface downstream of a wing for which the effectiveness reduces. At $\mathcal{R} \approx 10$, the propeller normal-force gradient remains at a constant value downstream of the wing, and remains the value of the isolated propeller upstream of the wing. For typical aspect ratios of $\mathcal{R} = 8-20$ [25, 31, 216–220] and an assumed location of center of gravity close to the wing's quarter chord, the wing causes a neutral to destabilizing contribution for a propeller mounted ahead of the wing, and a $10-20\%$ reduction in the stabilizing contribution were the propeller mounted behind the wing, in line with the findings of Ref. [200].

Downstream of the bound vortex, the axial-dependency is low due to the compensating in-plane velocity induced by the bound vortex and trailing vorticity. It is noted

(a) Induced angle of attack along the centerline ($z = 0$) by bound and trailing vorticity of a lifting line with an elliptical lift distribution

(b) Installation effect on the gradient of the propeller normal-force coefficient for three different aspect ratios
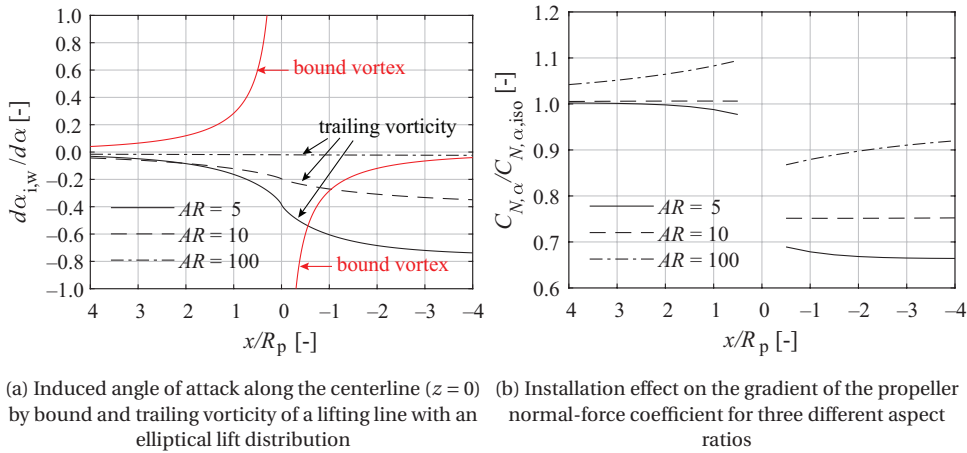
Figure 6.10: Effect of a flowfield induced by a lifting line of finite span with an elliptical lift distribution on the propeller normal-force coefficient.

that the assumption of the trailing vorticity remaining in the xy-plane has a large impact on the inflow to the propeller and therefore the normal-force gradient, especially if it is mounted downstream of the wing.

From an aircraft design perspective, it is important to establish an understanding of the relevance of this nonuniformity; if the problem can be reduced to a simple angle-of-attack problem, analytical equations [60] or available data for the propeller at angle of attack can be used to determine the normal-force coefficient for such installation. Such an approach would be computationally efficient and the accuracy may be sufficient for conceptual and preliminary design studies. The role of this distribution is therefore an aspect that requires further investigation. To this end, the flowfield induced by an infinite bound vortex is used as the propeller inflow, depicted in Fig. 6.11. The largest in-plane velocity is induced at $z = 0$ and the largest angle of attack is found close to this location. Especially for a small spacing between propeller and bound vortex (or alternatively, a large propeller diameter), the profile varies significantly.

Two cases are compared that are simplified relative to the actual inflow, i.e. a uniform angle of attack is used as inflow. For the first case, this angle is equal to the value that exists at the z-location at which the blade is horizontal, schematically shown in Fig. 6.12a. This seems a representative value as in Section 2.4 it is shown that the horizontally orientated blades are the dominant factor to determine the in-plane forces [215]. For the second test case the angle of attack is the area-averaged value over the disk and is denoted as $\bar{\alpha}$. The perturbation of u is set to zero for all considered cases.

Figure 6.12b shows the error introduced by simplifying the inflow. As expected, this error highly depends on the location of the propeller disk, since in the far field the velocity gradients over the disk approach zero and indeed can be represented by a constant value. The right contour depicts the result for $\alpha = \bar{\alpha}$ and clearly demonstrates that the sensitivity of the propeller to an inflow depends on the radial station. If this would have

(a) Schematic of the inflow that is distributed over the disk
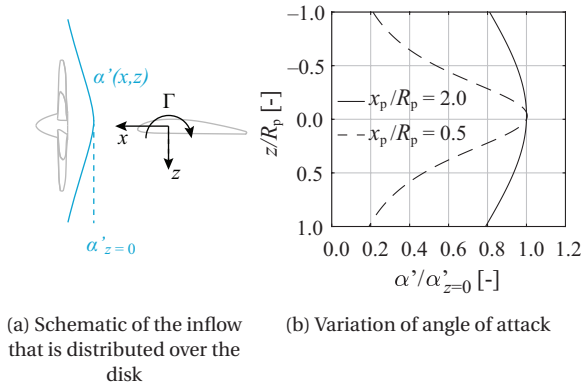
(b) Variation of angle of attack

Figure 6.11: Schematic of a propeller upstream of an infinite bound vortex, of which the inflowfield is computed by the Biot-Savart law for a propeller at $x = 0, z = 0$. Thickness effect of the airfoil not included.

been constant along the blade, the area-averaged inflow would coincide with the solution computed using the nonuniform inflow. The contour on the left side ($\alpha = \alpha^*$) shows that the normal force would be slightly overestimated. However, for a first estimation of the propeller normal-force coefficient, one could assume a constant (average) angle of attack and consult the C_{N_α} curve of the isolated propeller, since the error for a typical spacing to the bound vortex leads to an error less than 5%.

(a) Definition of α^*
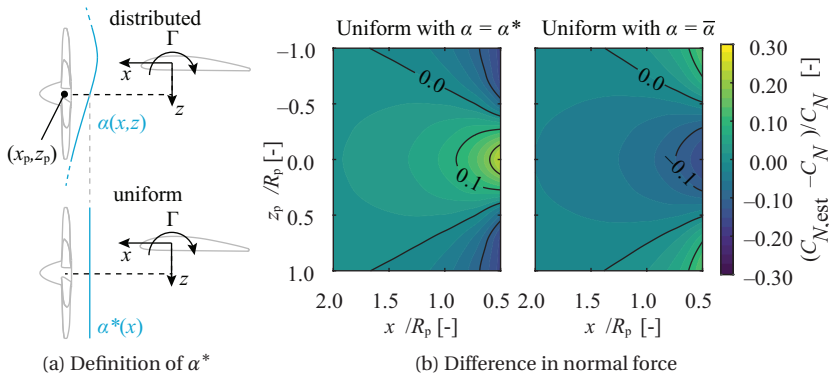
(b) Difference in normal force

Figure 6.12: Difference in normal force by assuming a uniform angle of attack over the disk instead of a distribution.

Next to the integral forces, the wave form of the blade forces is also of interest from a structural and noise point of view. For the propeller at an angle of attack, it is known that the blade forces are nearly sinusoidal and the amplitude of the unsteady forces on the propeller shaft is negligible since the blade forces cancel each other over a full revolution (see Section 2.4). In the case of the flowfield induced by a bound vortex, a complete can-

cellation does not occur, and larger unsteady forces on the shaft may arise [221]. In Fig. 6.13a the difference in blade loading is evident. While the angle-of-attack cases display a nearly symmetric change in thrust distribution, the case of a distributed inflow leads to distinct peaks, especially for the horizontally oriented blades. This loading pattern clearly leads to a blade force that is not sinusoidal, as shown in Fig. 6.13b. Consequently, the summation for the blade forces makes the propeller normal force phase-dependent, unlike the propeller at constant angle of attack, as shown in Fig. 6.13c. A similar result is found for the thrust coefficient. Although the unsteady component is fairly small, on the order of 0.5% of the thrust in this example, the shape of the inflow distribution is therefore key for the magnitude of the unsteady loads.

(a) Disk loading over a full revolution

(b) Blade loading over a full revolution

(c) Propeller shaft forces. The curves C_T and C_Z for the uniform cases are on top of each other.
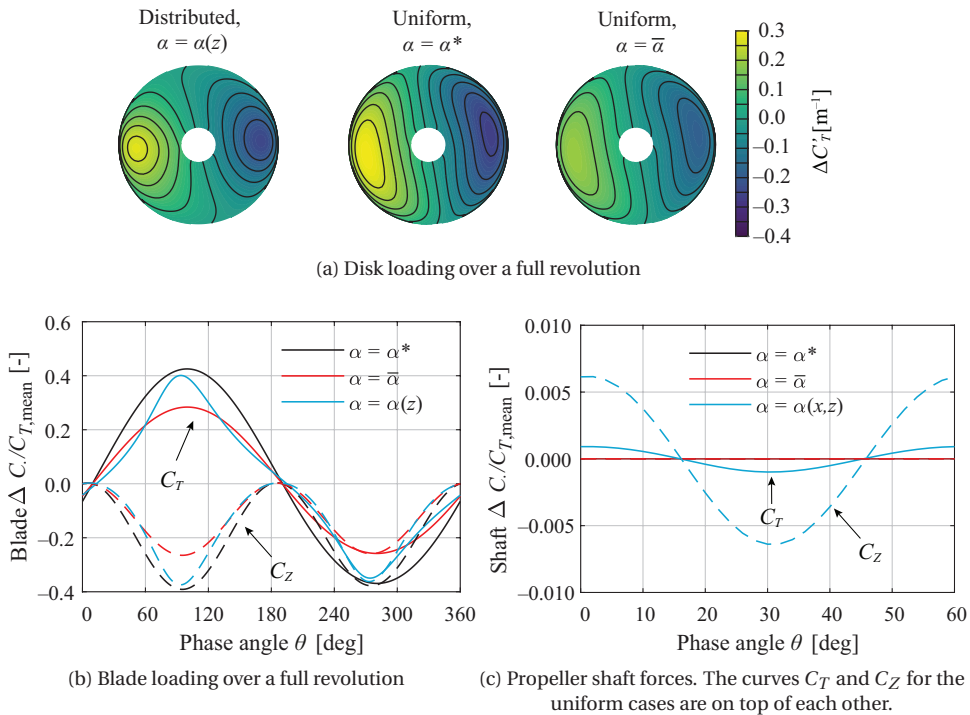
Figure 6.13: Comparison of the propeller blade forces for the uniform angle of attack case versus the distributed inflow case. Loading at $x/R_p = 1$ and $z/R_p = 0$, with $\alpha^* = 7.3$ deg and $\tilde{\alpha} = 4.9$ deg.

6.3.2. DISPLACEMENT EFFECT OF LIFTING SURFACE

In addition to the lift-induced flowfield discussed in the previous section, a propeller near a lifting surface also experiences the displacement effect because of the finite thickness of the surface. Fundamentally, there is no difference compared to the in-plane and out-of-plane induced velocity by a horseshoe vortex, but the velocity distributions are different, since now there is a nonzero axial perturbation in the xy-plane. Especially for low diameter-to-chord ratios (e.g. for distributed propellers along the leading edge), the

upstream effect of a wing with high t/c ratio becomes more pronounced. For example, regional aircraft with short take-off and landing capabilities have a wing with a high t/c ratio. This section therefore puts the relative contributions of the bound and trailing vorticity relative to the displacement of the streamlines into perspective, and thereby addressing research question *RQ 6.2*.

Although the velocity distribution depends on the thickness distribution along the chord, typical profiles obtained by XFOIL [168] are depicted in Fig. 6.14 for symmetric NACA 4-series airfoils with no lift. The profiles are extracted in a survey plane at half a chord upstream of the leading edge for $D_p/c = 1.0$. Since the magnitude of the axial and in-plane velocity perturbations are proportional to the airfoil t/c, the different curves are plotted for illustrative purposes.

Figure 6.15a shows that in the azimuthal direction the inflow, expressed as a change in local advance ratio ΔJ, varies quite significantly up to $\Delta J = -0.12$. The combination of in-plane and out-of-plane perturbations leads to shift in the minimum advance ratio relative to the airfoil chord. The load distribution in Fig. 6.15b shows a resemblance of this inflow profile. Provided that the most sensitive region on the disk is close to $r/R_p = 0.8$, it is this region that experiences the largest increase in load. The phase delay observed for propellers at an angle of attack is much smaller, due to the rather confined region in spatial direction where there is a disturbance. The inflow in this case leads to unsteady loads of $\pm 0.05 C_T$ in the thrust and z-direction, where the thrust is periodic with a two-per-revolution excitation, while the in y- and z-directions the excitation of the blade forces is not sinusoidal due to the decomposition of the force vectors. The magnitude of these loads scale linearly with the displacement effect of the airfoil, i.e. with the t/c ratio. The particular inflow profile leads to unsteady blade loads along the three principle axes, but the in-plane components cancel over a full revolution because of the even number of blades. For the current case, the unsteady shaft loads are therefore only relevant in the thrust direction. In case of an uneven number of blades or when $z_p \neq 0$, also in-plane shaft loads would be introduced.

(a) Schematic of the propeller upstream a symmetric airfoil

(b) In-plane velocity at $x/D_p = 0.5$
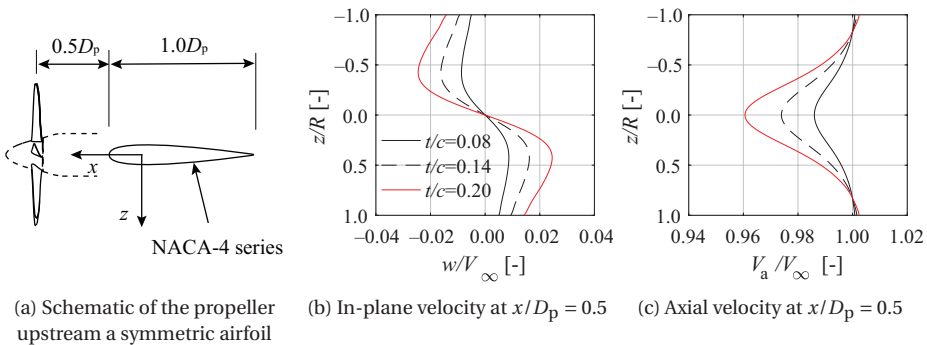
(c) Axial velocity at $x/D_p = 0.5$

Figure 6.14: Effect of a finite thickness airfoil on the flowfield at the propeller plane ($c_l = 0$).

In case the displacement varies along the span, unsteady shaft loads are introduced in the y and z-direction. This is clearly depicted in Fig. 6.15c for the symmetric case

to a tip-mounted case, where the latter is the most extreme case of a varying thickness in the y-direction. The sum of the root-mean-square contributions for the tip-mounted case is even slightly higher than the root-mean-square of the three components in the symmetric case. This displays that while the average perturbation is smaller, the inflow could lead to more unsteady shaft loads. The asymmetry of the inflow clearly plays a key role in the shaft loads.
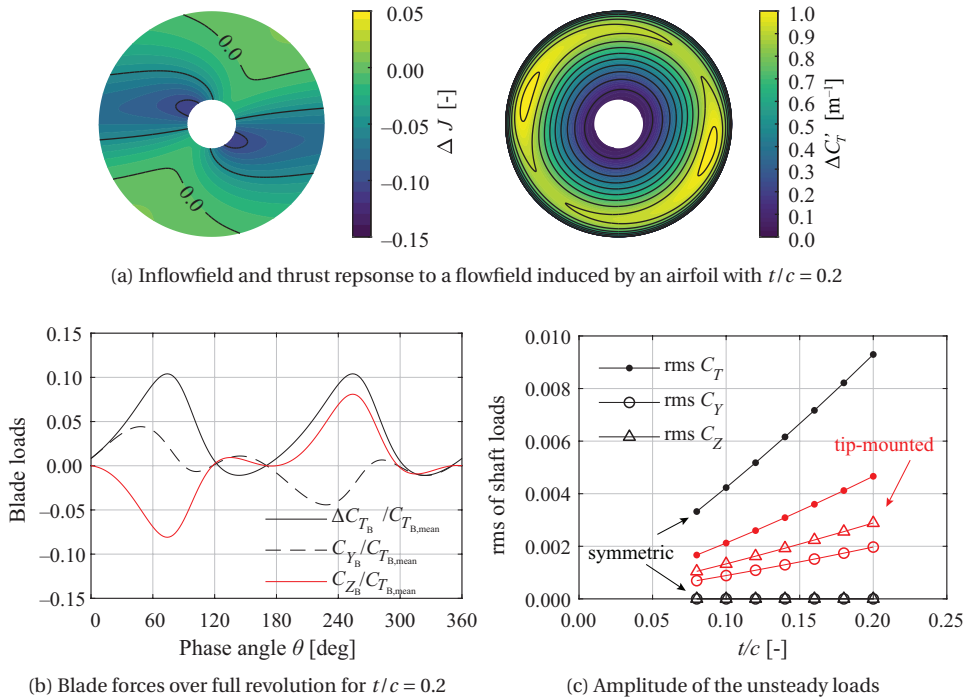

(a) Inflowfield and thrust repsonse to a flowfield induced by an airfoil with $t/c = 0.2$

(b) Blade forces over full revolution for $t/c = 0.2$

(c) Amplitude of the unsteady loads

Figure 6.15: Displacement effect on the propeller blade forces for XPROP at $J = 1.8$, $C_{T,\mathrm{iso}} = 0.24$. Nacelle effect and interaction are excluded in analysis ($c_l = 0$).

The relative increase in relevant integral forces, i.e. the thrust coefficient, normal-force coefficient, and efficiency, are shown in Fig. 6.16. For typical wing thickness-to-chord ratios (between 0.15 and 0.20), the displacement effect leads to a higher thrust (up to 4%) in case of a wing that extends in both positive and negative y-direction. Half of this would be obtained for a tip-mounted application. The lower inflow velocity directly increases the propeller efficiency, for the typical thickness ratios with approximately $\Delta\eta = +0.01$. Since the blade forces in the propeller plane cancel over a full revolution for the symmetric case $\Delta C_Z = 0$, while for the tip-mounted application there is a lift reduction for an inboard-up rotation. Depending on rotation direction and in what direction the displacement effect reduces, this can lead to a higher or lower normal-force coefficient. For a wing-mounted configuration with a displacement effect that reduces towards the wing tip, an inboard-up rotating propeller will create a (small) negative contribution to aircraft lift.
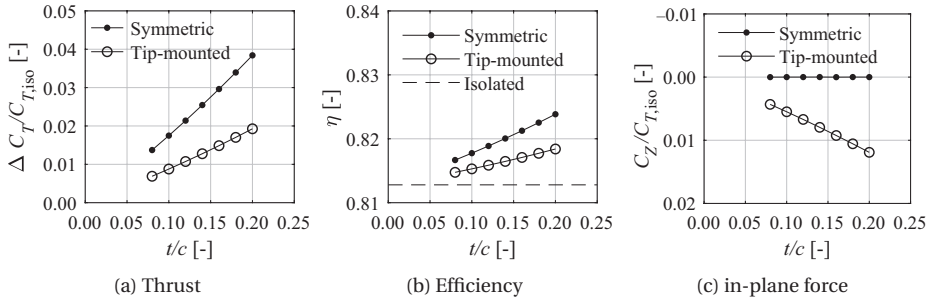
146

(a) Thrust (b) Efficiency (c) in-plane force

Figure 6.16: Displacement effect of a finite thickness airfoil on the integral propeller forces for XPROP at $J = 1.8$, $C_{T,\text{iso}} = 0.24$

Compared to a lifting surface that induces an average upwash at the propeller plane of approximately 5 deg (Fig. 6.13) and lead to unsteady loads of 40% of the thrust, the displacement effect leads to unsteady loads of approximately 10% of the thrust. These values indicate that the displacement effect is a relevant factor for the unsteady loads which may influence the design choice for the spacing between propeller disk and leading edge of the wing.

6.4. WAKE ENCOUNTER

The flowfields that can be described by potential flow generally are distributed over the disk with relatively small gradients in spatial direction. In contrast, a viscous wake that trails from a wing or pylon has a high velocity gradient and when it is encountered by a propeller, this gradient is confined to a distinct region on the disk. Research on propellers that encounter a wake has demonstrated significant increases in noise levels caused by the pressure fluctuations on the blade sections that sweep through the wake [89, 187, 204–208]. Additional noise is generated by the higher turbulence levels in this region [222]. Although it is well known that such an encounter changes the blade forces, for the installation of a propeller that in various flight conditions may encounter a wake, it is of interest how the blade loading is affected. The effect of the location of the wing relative to the disk is therefore a key parameter of interest herein. For example, if the propeller is mounted to the horizontal tailplane and the angle of attack is increased, the wing wake will be encountered on the lower part of the disk. Ultimately, in the installed configuration, the trends identified in this section will support the understanding of the magnitude and direction of the propeller force gradients. This section therefore specifically addresses research question *RQ 6.1*.

To this end, a conceptual wing model is used with a symmetric airfoil that is placed upstream of the propeller at various z-locations. For a description of the setup, see Section 3.4.4. Figure 6.17 shows the wing wake at the propeller plane for a trailing edge–propeller spacings of $\Delta x = 3.2 R_\text{p}$. At this location, the maximum velocity defect is 10% of the freestream flow, equivalent to a maximum $\Delta J = 0.18$ for the reference propeller operating condition of $J = 1.8$. Based on the total-pressure profile, the boundary-layer

thickness of the reference case is $0.20R_p$ with the edge defined as $C_{p_t} = 0.99^2$.
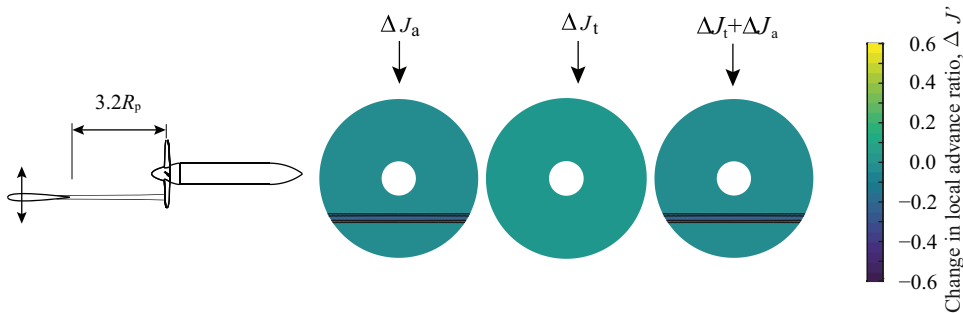

Figure 6.17: Change in advance ratio caused by the wake encounter at $z/R_p = 0.50$, with $J_\infty = 1.80$. Wake thickness is $0.2R_p$, with the edges defined as $C_{p_t} = 0.99^2$

The three considered wing locations at $J = 1.8$ are $z_w/R_p = 0.50, 0.75, 1.00$ are sim-ulated using a full-blade unsteady RANS approach. The propeller thrust distributions for these wake encounters are shown in Fig. 6.18a. For the $z_w/R_p = 0.50$ case there are two distinct regions with increased thrust, while for $z_w/R_p = 0.75$ there is a quite grad-ual increase of thrust at the location of wake encounter. The case where the wake is encountered at the propeller tip shows a minor variation in thrust. A better insight is gained by plotting the difference with the isolated propeller thrust distribution, shown in Fig. 6.18b, with the dashed line indicating the blade section with highest sensitivity to a change in advance ratio. The increase in thrust for both $z_w/R_p = 0.50$ and $z_w/R_p = 0.75$ occurs at a phase angle at which the blade sections with the highest sensitivity encounter the wing wake. For the wake encounter at the propeller tip, there is only a small region with higher loading.

This strong dependency of the vertical position of the wake relative to the disk is also observable for the integral blade load for each phase angle, depicted in Fig. 6.19b. For the considered cases, the maximum deviations to isolated conditions are 3 to 8%. For the wake encountered near the blade tip, there is a one-per-revolution thrust increment. At $z_w/R_p = 0.50$, there is first a peak in blade thrust at $\phi = 130$ deg, then a reduction followed by a higher second peak. The second peak is higher due to the thrust enhancement around $\phi = 180$ deg at which the circulation has already developed. The strongly varying blade responses are a direct result of the nonlinear sensitivity distribution over the disk. From a noise and vibration perspective, the dominant frequencies therefore depend on the location at which the wake is encountered. The frequency of the blade forcing is therefore either n if $z_w > 0.8$ or $2n$ if $z_w < 0.8$.

The apparent sinusoidal thrust with a period equal to one revolution is expected to be a combination of two effects. First, there is the near-field effect due to blade-to-blade interaction (Fig. 6.5b), such that the blades advancing towards the wake experience a lower angle of attack. In addition, the propeller is found to have a small upstream effect to the wing by introducing a positive angle of attack, which leads to a non-zero wing lift and therefore a downwash to the propeller. This downwash leads to the typical sinu-soidal blade forcing.
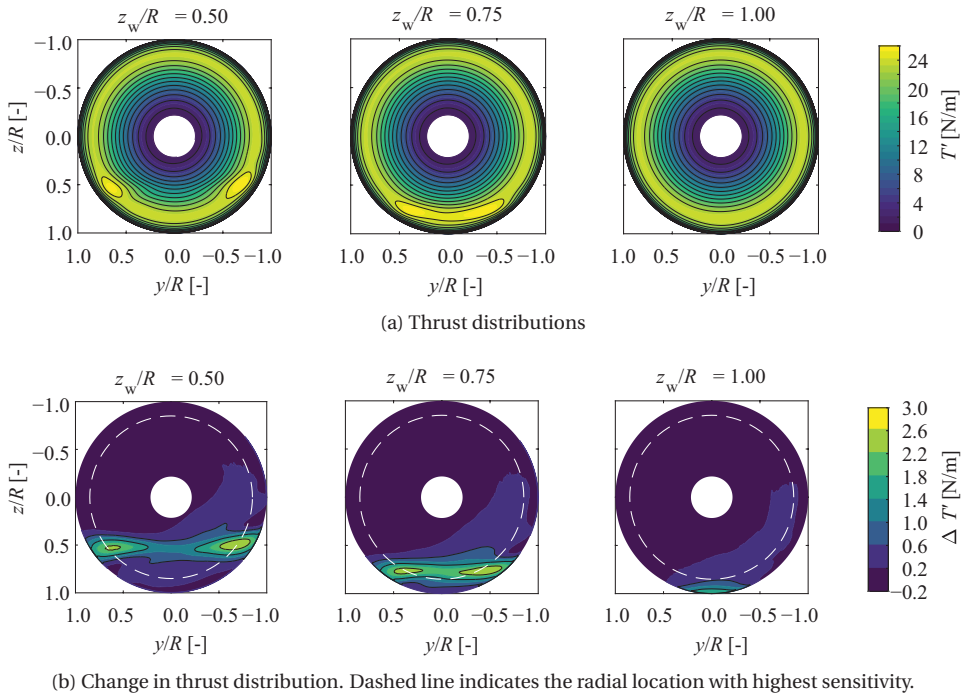
(a) Thrust distributions

(b) Change in thrust distribution. Dashed line indicates the radial location with highest sensitivity.

Figure 6.18: Blade thrust distribution over the azimuth as the result of a wake encounter. Three different z-locations of the wake are evaluated using full-blade CFD of the XPROP propeller with $\beta_{0.7R_p} = 45$ deg at $J = 1.8$.

The integral thrust of the propeller is depicted in Fig. 6.19c, showing fluctuations around 1%-2% of the propeller thrust at the blade passing frequency. At a blade phase angle of $\phi = 0$ deg, both the $z_w/R_p = 0.50$ and $z_w/R_p = 1.00$ show the maximum propeller thrust, coinciding with the phase angle at which the blades encountering the wake. At $z_w/R_p = 0.75$, this is the case for $\phi = \pm 30$ deg, explaining the phase shift of the integral propeller thrust. Again, if the number of blades would be uneven, the forces on the propeller shaft do not fluctuate at the blade-passing frequency. The figure also shows that the torque follows the same trend as the thrust. Since this rise in torque is smaller than the rise in thrust, the propeller efficiency slightly increases.

Finally, the effect of a wake encounter on the time-averaged forces is shown in Fig. 6.20. The rise in thrust is, as already apparent from the blade forces, maximal if the wake is encountered at $z_w/R_p = 0.5$. In addition to changes in propeller thrust, the change of the in-plane forces are an important aspect, especially for the force-gradients as a function of angle of attack. In increment of thrust, and therefore torque, which arise from an asymmetric wake encounter, lead to a net side force. A torque distribution that is not symmetric with the xz-plane results in a net normal force.

For all wing positions, the side force is positive and does not exceed 2% of the propeller thrust. The higher second peak of thrust and torque when the blade tip is encountering the wake for the second time in a revolution results in a net force on the propeller
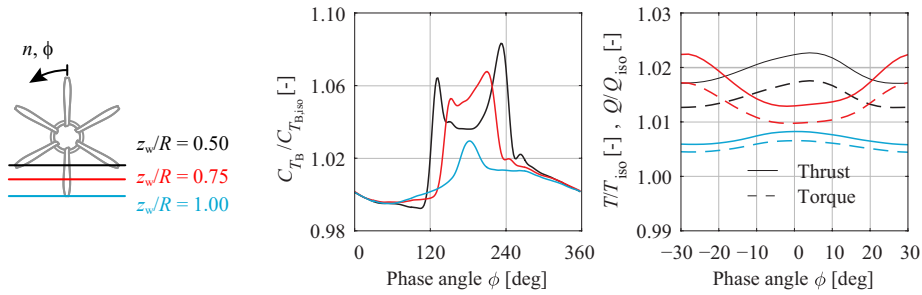
(a) Illustration of the wing locations for (b) and (c)

(b) Blade force over a full rotation

(c) Periodic propeller shaft forces

Figure 6.19: Installation effect on the unsteady forces on the blade and propeller shaft as the result of a wake encounter at different z-locations. The figure shows the difference in amplitude and frequency of the unsteady response. Computed using full-blade CFD simulations of the XPROP propeller with $\beta_{0.7R_p} = 45$ deg at $J = 1.8$.

(a) Out-of-plane components
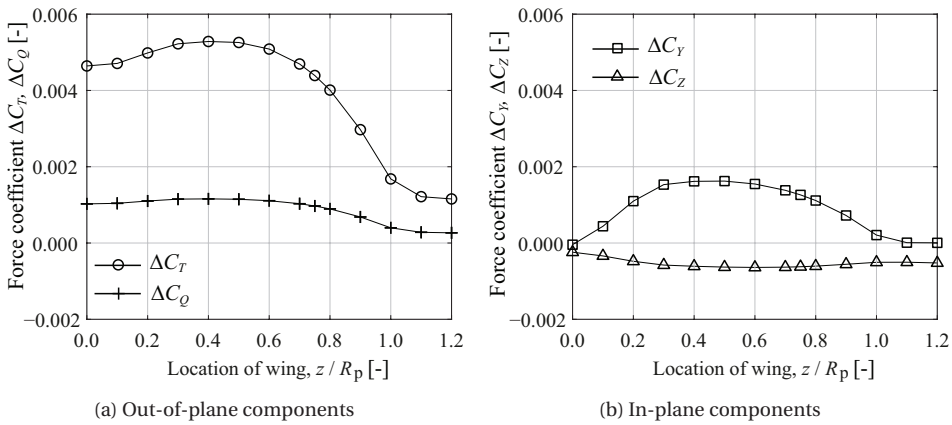
(b) In-plane components

Figure 6.20: Installation effect of a wake encounter on the integral propeller forces to show that the maximum response (around $z/R_p = 0.5$) does not coincide with the situation where the maximum area of the disk is affected (at $z/R_p = 0.0$). Results computed with the analysis method described in Chapter 5, using the XPROP propeller with $\beta_{0.7R_p} = 45$ deg, $J = 1.8$ ($C_{Tiso} = 0.24$).

in negative z-direction. To put the magnitude of these in-plane forces in perspective, one can compare them to the normal force arising from an angle of attack. A force of 1% of the isolated thrust is equivalent to a propeller with an inflow at 0.25 deg. This indicates that these in-plane forces are small if installed on an aircraft, since a force equilibrium is found at a different yaw and pitch angle than the equilibrium condition without wake encounter. These forces therefore contribute to a different trim condition, rather than altering the longitudinal and lateral stability significantly. The unsteady loads and the consequences in terms of noise and vibrations that originate from such installation are therefore more relevant than the small changes of the integral forces.

150

6.5. PROPELLER–PROPELLER INTERACTION: AN ARRAY OF DISTRIBUTED PROPELLERS

Propellers that are mounted side-by-side in leading-edge-mounted or over-the-wing configurations experience not only a distorted inflow from the airframe, but also experience the flowfield induced by adjacent propellers. Existing research on rotor-rotor interaction primarily focuses on specific configurations that experience a large inflow angle and, in some cases, a large spacing between the rotors, such as unmanned aerial vehicles, tilt rotors, and vehicles for urban air mobility [223, 224]. The relevant flight conditions for these configurations are high-thrust conditions (such as hover) and phases of transitional flight. Also significant reductions in propeller efficiency are reported in cases the propellers have a small spacing with high thrust coefficients [225–227]. For cases with a small spacing, those flight phases largely determine the design of the propulsion system and overall layout, and the cruise condition is of secondary importance. Therefore, significantly less research has been conducted on propeller–propeller interaction where the propeller rotation axes are (nearly) aligned with the direction of flight and the propellers have relatively low thrust coefficient, which are of interest for transport aircraft configurations.

A recent publication [161] presents an extensive study on the propeller performance of an array of distributed propellers, where several design variables are varied. This reference identifies that the propeller–propeller interaction is relevant in three ways. Firstly, there is a reduction in the performance of the propellers through a reduction in thrust and efficiency. Secondly, the slipstream is affected through the boundary condition that is imposed at the midplane between the rotors that constrains the slipstream contraction. Thirdly, the noise production of the system is affected by cancellation and superposition of noise sources, and by the introduction of additional noise sources caused by the interaction between passing propeller blades. This study concluded that a major part of the thrust reduction is introduced by the presence of the nacelles. On the other hand, the nonuniform loading is primarily affected by the in-plane velocity, introduced by a local reduction of slipstream contraction.

This section complements the results discussed in Ref. [161] by an assessment of the unsteady propeller loads for a small tip-clearance, as well as the slipstream development downstream of the array of propellers. The same geometry and operating conditions are used herein, and the focus is mainly on the propeller blade loading and the slipstream development. More specifically, this section has the following objectives:

1. Determine the dominant factors that affect the blade section loads, blade loads, and shaft loads

2. Quantify the relation between installed thrust and unsteady thrust component

3. Confirm the conclusions in terms of overall performance loss in Ref. [161]

For the study presented in this section, an infinite array of counter-rotating propellers is selected, with all propellers at the same axial location, i.e. in one plane. Furthermore, to demonstrate the blade-to-blade interaction, the blades of the propellers are

in-phase, such that for the horizontally oriented blades the distance between the tips is equal to the tip-clearance.

Prior to an assessment of the performance reductions that can be expected through the installation of adjacent propellers, first the propeller inflowfield is investigated on a conceptual level by using the principle of superposition and thereby ignoring any changes in blade loading for the moment. In Section 2.1.2 it is shown that a propeller induces a radial flow component that is proportional to the axial induction factor and is maximal at the edge of the disk (Fig. 2.6a). In case this propeller is part of an array, locally, this radial component reduces since a symmetry condition is imposed. In fact, the normal velocity at the plane of symmetry is zero on average. This is schematically shown in Fig. 6.21a. Since the cases are simulated by means of a symmetry condition (Section 3.4.4), at each timestep the normal velocity is zero. It is shown in Ref. [161] that the slipstream is not deforming significantly when going in downstream direction and the slipstreams are not merging. This representation is therefore valid, at least in the nearfield of the propeller. Far downstream, the tip vortices are expected to interact and merge when the tip clearance is small [165], but based on the discussion in Section 6.2 the effect on propeller loading can be ignored.
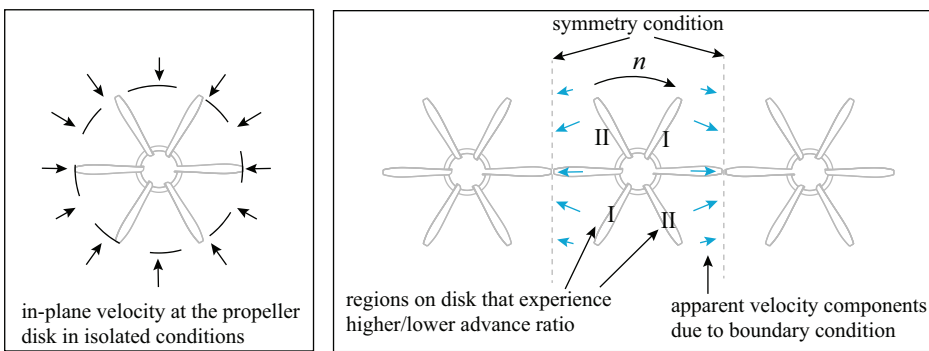
(a) Schematic of the *slipstream effect* that introduces an in-plane velocity for distributed propellers
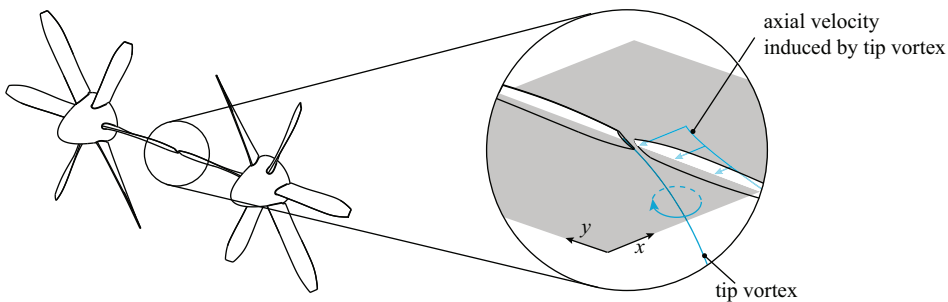
(b) Schematic of the *local inflow effect* at the blade tip due to an adjacent tip vortex

Figure 6.21: Schematic of a local and a slipstream effect that both introduce a nonuniform flow to the propeller.

The mirrored propeller at the symmetry plane leads on average to an in-plane velocity field that affects the blade loading. From Fig. 6.21a is can be observed that the blade approaching the symmetry plane (regions I) experiences a higher advance ratio and therefore a reduced loading, while the blade moving away (regions II) experiences a lower advance ratio and therefore higher loading. It is noted that this is independent of the rotation direction and the magnitude only depends on the thrust coefficient. This is therefore referred to as the 'slipstream effect'. For a windmilling propeller ($T_C < 0$), this effect is inverted.

In addition to the slipstream effect, the displacement effect of the nacelle leads to a locally disturbed axial inflow velocity in the plane of the propeller. The magnitude and sign of this $\Delta u / V_\infty$ depends on the spinner and nacelle geometry. For the case considered herein, there is a slight increase in axial velocity, up to 1% of the freestream value.

Next to the boundary condition that constrains the slipstream contraction, there is also a local effect caused by the blade tip vortices that affect the propeller inflow, as schematically shown in Fig. 6.21b. For a positive thrust condition, this leads to a local reduction in advance ratio. In Ref. [161] is was found that the difference in phase angle between the blades is small, although small variations can be distinguished. A small phase difference between the passing blades seems to have the largest impact, since the propeller tip vortex strength is maximal at a finite azimuthal distance from the trailing edge of the tip.

Figure 6.22 depicts the changes of the integral forces due to the installation. As confirmed in literature [161, 227], the installation leads to a lowering of the $C_T − J$ curve. The nearly constant offset with respect to the curve of the isolated propeller is indicative that this is the result of the axial inflow perturbation. The reduction in thrust at the condition $T_{C,\text{iso}} = 0$ is a direct result of the nacelle, indicated in Fig. 6.22b. At this condition, the installed propeller (on average) is wind milling, and the slipstream effect is approximately zero. The further reduction of T_C at higher thrust settings is still partially caused by the nacelle: the higher dynamic pressure induced by the propeller also raises the absolute induced velocity by the nacelles of the adjacent propellers. This component is approximated in Fig. 6.22b as a component proportional to T_C by taking the average induction factor of the disk and by using the ΔT_C at the windmilling condition. This figure confirms the conclusion in Ref. [161] that the nacelle is the primary factor to change propeller thrust. The remainder of the thrust reduction is caused by the higher axial inflow due to the larger contraction on the top and bottom part of the slipstream. In line with these observations, the efficiency curve is also lower than the one for the isolated propeller, leading to changes of approximately 0.5% for typical cruise thrust settings, as depicted in Figs. 6.22c and 6.22d. Although these reductions are small, these are present in all flight conditions and therefore still relevant for the total energy consumption for a mission.

6

(a) Thrust coefficient

(b) Change in thrust coefficient

(c) Propeller efficiency
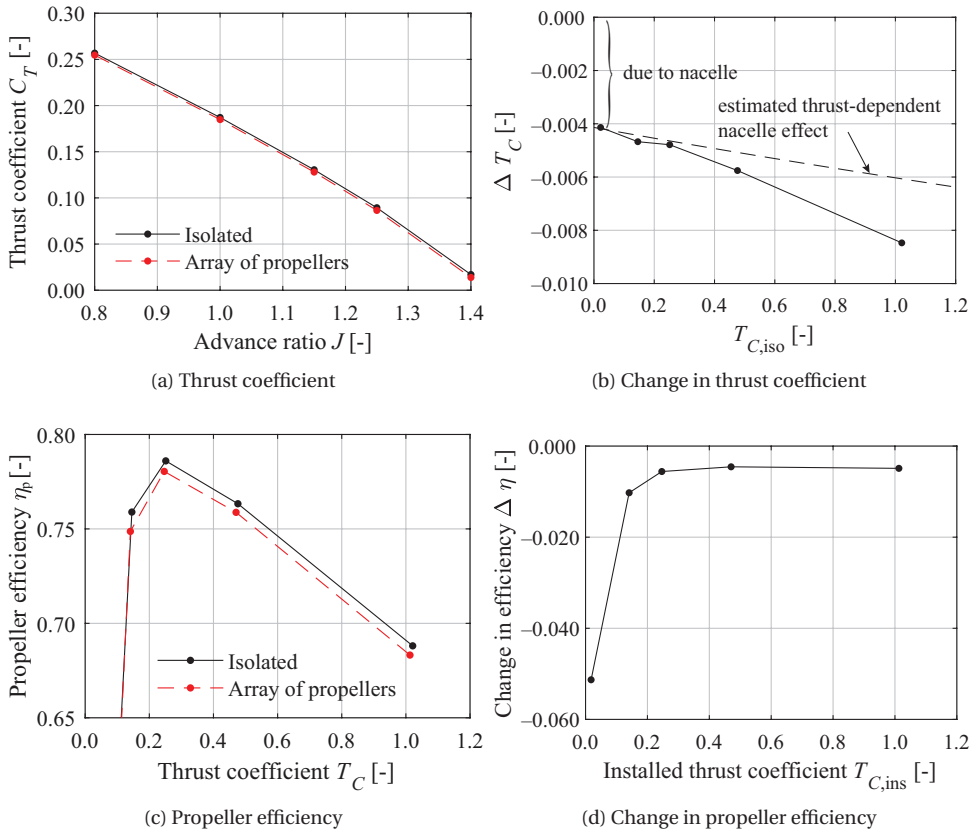
(d) Change in propeller efficiency

Figure 6.22: Installation effect of adjacent propellers on the propeller forces and efficiency. CFD results.

The understanding how the local effect and slipstream effect relate to the blade loading, the propeller thrust is compared to the isolated loading in Fig. 6.23a. Compared to the nominal load distribution, the propeller thrust varies relatively smoothly over the azimuth, with two regions of enhanced loading, and two regions of lower loading. These correspond to the regions I respectively II in Fig. 6.21a. The figure clearly shows that the majority of the variations in blade thrust are caused by the slipstream effect. This can be deduced from Fig. 6.23b, in which the change in thrust along the radial direction is plotted for regions I and II, and for the horizontal orientation of the blade. For the advancing and retreating blades, the respective increase/reduction in thrust resembles the sensitivity distribution along the radius (Section 5.2), and the inflow can therefore be interpreted as a disturbance that is distributed over the disk. The exception to this is when the blade tips are close to each other, i.e. for the horizontally oriented blades. In this case, there is a rapid rise in thrust from $r/R_\mathrm{p} = 0.8$ to $r/R_\mathrm{p} = 1.0$, caused by the local axial flow induction of the tip vortex of the blades from the neighbouring propeller. Although this unsteady component does not significantly change the integral trust, the fact that

these pressure fluctuations occur at the tip, the high Mach number at this station leads to a relatively large impact on the noise production, as can be deduced from analytical expressions (e.g. Ref. [228]). The rather local character becomes visible for a survey line along the azimuth for $r/R_p = 0.98$ in Fig. 6.23c. Near $\phi = 90$ deg and $\phi = 270$ deg, there is a peak in the local thrust component, attributed to the local effect of the tip vortex. There is a slight phase shift of this peak, since the reduced frequency becomes higher at lower advance ratio (see Section 5.3). The remainder of the unsteady loads is introduced by the slipstream effect, that is present over the other phase angles, with the exception of $\phi = 0$ and $\phi = 180$ deg, where the effect of the boundary condition is negligible.

(a) Thrust distribution $T_{C,\text{ins}} = 1.01$

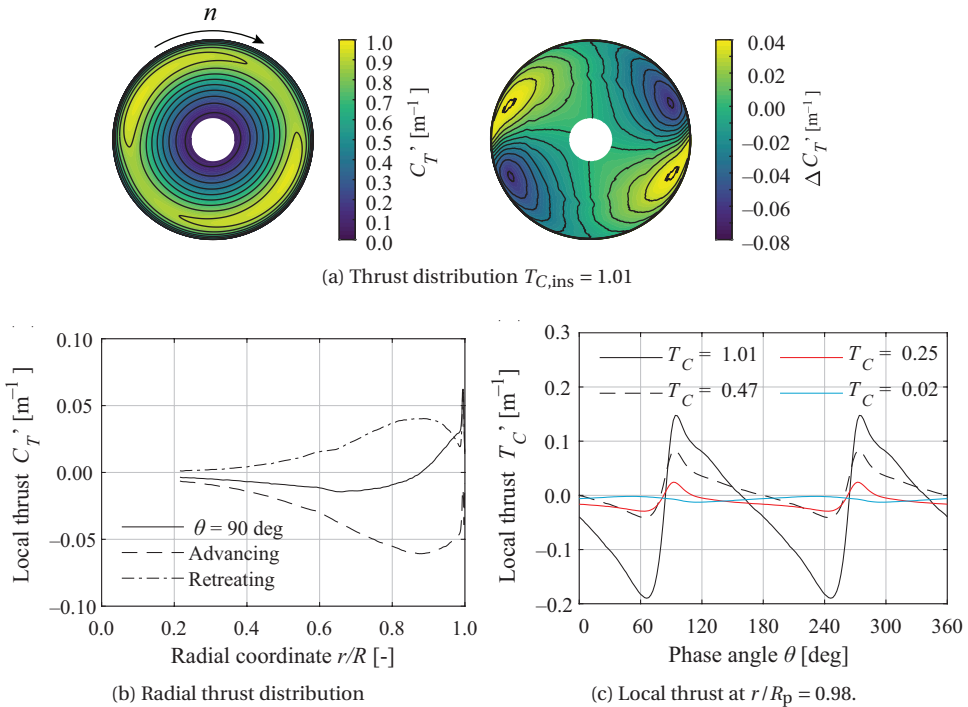(b) Radial thrust distribution

(c) Local thrust at $r/R_p = 0.98$.

Figure 6.23: Variation of blade loading in azimuthal direction for a propeller as part of an array of counter-rotating propellers. CFD results.

From Fig. 6.23 it can be deduced that the blade thrust over a revolution is not sinusoidal. This is confirmed in Fig. 6.24a. Due to the unsteady aerodynamics, the fall of the blade thrust is less steep compared to the rise in loading. This leads to an unsteady shaft load at the blade passing frequency. It is noted that the local effect is not observable in the blade load, which supports the conclusion that the slipstream effect is the primary contributor to affect unsteady loads. In Fig. 6.24b it is shown that the unsteady loads are thrust dependent. The nacelle-induced flowfield, which is largely independent of thrust, is not as pronounced, since at $T_C \approx 0$ the thrust fluctuations are negligible. The reason for this is that the number of blades is even and the nacelle induced inflow influences the two sides of the disk evenly. The figure therefore indicates that the largest vibrations

transferred to the airframe occur in high thrust conditions.

(a) Unsteady blade and shaft thrust over full revolution, $T_{C,\text{ins}} = 1.01$, $J = 0.8$ (b) Amplitude of the unsteady thrust on the propeller shaft
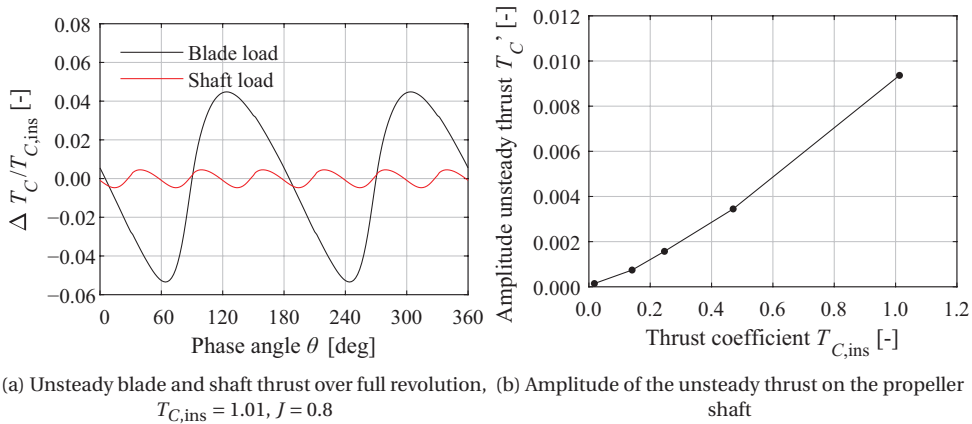
Figure 6.24: Unsteady loads for a propeller as part of an array of counter-rotating propellers. Full-blade CFD results.

To conclude, the performance reduction in terms of propeller efficiency that has been observed in other literature, in particular Ref. [161], is confirmed in the analyses presented in this section. Furthermore, the following conclusions are formulated:

- The presence of the nacelle leads to an increase in axial inflow and is responsible for the majority of the reduced propeller efficiency. Its presence does not lead to unsteady loads; at $T_C = 0$, the amplitude of the unsteady loads reduces to zero.

- The blade–blade interaction is confined to the tip-region only and does not lead to significant blade loads, but instead to sharp rises in local loading, potentially important for noise radiation [161].

- The primary installation effect is the local modification of the slipstream and inflow to the propeller that leads to a nearly sinusoidal loading. The loading on the blade advancing the symmetry condition reduces, while the retreating blade increase its loading.

6.6. PROPELLERS MOUNTED TO THE HORIZONTAL TAILPLANE

The previous sections have investigated the various interaction effects that impact the propeller performance. In this section, the focus is on an example case where there is a combination of various airframe-propeller interactions: propellers mounted to the horizontal tailplane, of which an example is given in Fig. 6.25. For such configuration, the propeller inflow is influenced by the wing's circulation and wake, the upstream effect of the tailplane, and the flowfield induced by the fuselage, and therefore entails all three types of inflow presented in Fig. 6.3. While the previous sections address several sub-problems of a full aircraft configuration, a dedicated study considering a full aircraft allows for the remaining inflows that cannot be simulated on a component level. A specific

example are the high lift conditions, achieved by a high angle of attack or a flap deflection. Moreover, the gradient of the inflow with flight condition is more representative as well. An advantage of using a full aircraft geometry is that the corresponding findings can directly be put into perspective. The findings on propeller level are directly useful for the assessment of propeller integration on aircraft level, presented in Section 9.2. These results are a major extension of the initial work performed on aft-mounted propeller configurations presented in Refs. [25, 194, 229], which do not present investigations on component level.
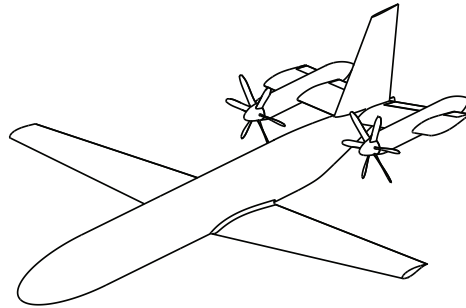

Figure 6.25: Schematic of an aircraft with propellers mounted to the horizontal tailplane. Details of this *VGM-HTP* model are listed in Section 3.3.5.

6

The full aircraft configuration is an extension of the analyses presented in Sections 6.3 and 6.4 in several ways. First, there is the introduction of the fuselage, which leads to a more distorted flowfield near the wing–fuselage junction, it introduces a sidewash and upwash component to the propeller. Second, (local) flow separation not only introduces a more distorted inflow at a given angle of attack, the gradient of the flowfield is highly affected as well. Finally, high-lift conditions obtained by the deflection of flaps illustrate the effect of a flap-edge vortex in the vicinity of the propeller.

For these analyses, the *VGM-HTP* model (Section 3.3.5) is used. In case of large changes in inflow, the principle of superposition no longer holds, such that the method presented in Chapter 5 cannot be applied, and instead an experimental or full-blade CFD analysis is required. The results are a combination of the flowfields that are introduced by the airframe, the propeller loading distributions and integral forces, and flowfield measurements taken downstream of the model, which encompasses the full interaction.

For the assessment of the airframe-induced propeller forces, a distinction is made between the types of flowfield at the propeller plane. Both stability and performance aspects are relevant for cruise conditions, i.e. the linear region of the lift curve, for which the flowfield can primarily be described as potential flow. For the nonlinear region, where the characteristic flowfield at the propeller is also determined by flow separation, especially aspects that influence the longitudinal and directional static stability are of interest. These relevant interaction phenomena and their effect on aerodynamic performance and static stability are described in the following subsections.

6.6.1. Interaction in Cruise Conditions

In cruise conditions, the aircraft angle of attack typically ranges between zero and three degrees. The propeller operates close to the maximum efficiency, at a high advance ratio, and at a medium thrust condition (see Table 2.2). In addition to the geometric angle of attack, the propellers operate in the wing-induced downwash field and a fuselage-induced sidewash, schematically shown Fig. 6.26a. The downwash affects the region on the disk with the up- and down-going blades, which reduces the contribution to longitudinal stability, introduces a normal force in downward direction, and leads to unsteady loads, as discussed in Section 6.3. The sidewash affects the region where the blades have a vertical orientation, as indicated by the quadrants I and III in Fig. 6.26a. The difference in loading between each quadrant pair (I&III and II&IV) leads to a side force and a normal force, with the direction determined by the propeller rotation direction, as sketched in Fig. 6.26b. Due to the effect of unsteady aerodynamics, which introduces a difference between the phase angle of the inflow disturbance and blade response, velocity component w results in an additional side force, while v introduces an additional normal force, as depicted in Fig. 6.26b. The direction of these secondary in-plane forces depends on the propeller rotation direction. From this figure, it becomes clear that depending on how the downwash and sidewash vary with angle of attack and side slip, the gradients of the propeller force curve are influenced.

(a) Downwash and sidewash distribution.

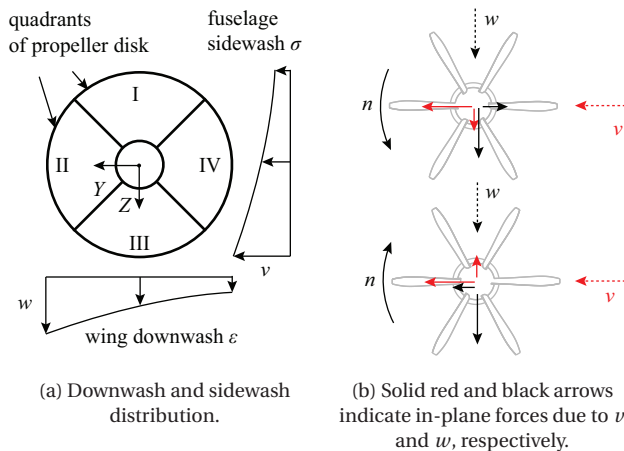(b) Solid red and black arrows indicate in-plane forces due to v and w, respectively.

Figure 6.26: Schematic in-plane velocity distributions at $\alpha = 0$ deg that affect the load distribution in the quadrants, leading to a net in-plane force on the port propeller.

From the flowfields obtained of the *VGM-HTP* testcase at $\alpha = 0$ deg, the wing downwash angle varies from $\varepsilon = 1$ deg to $\varepsilon = 4$ deg over the propeller disk, with the maxima around $z_p/R_p = 0.5$. The conically-shaped aft fuselage induces a sidewash at the propellers, which varies from $|\sigma| = 1$ deg at $z_p/R_p = -1$, to $|\sigma| = 3$ deg at $z_p/R_p = 1$. To relate the propeller load distribution to this nonuniform inflow, the time-averaged velocity field is expressed as a change in local advance ratio J' consisting of an axial component and tangential component: $J' = J'_a + J'_t$. Figure 6.27a depicts the change in local advance

(a) Change in advance ratio

(b) Change in thrust

(c) Change in torque. Arrows indicate the
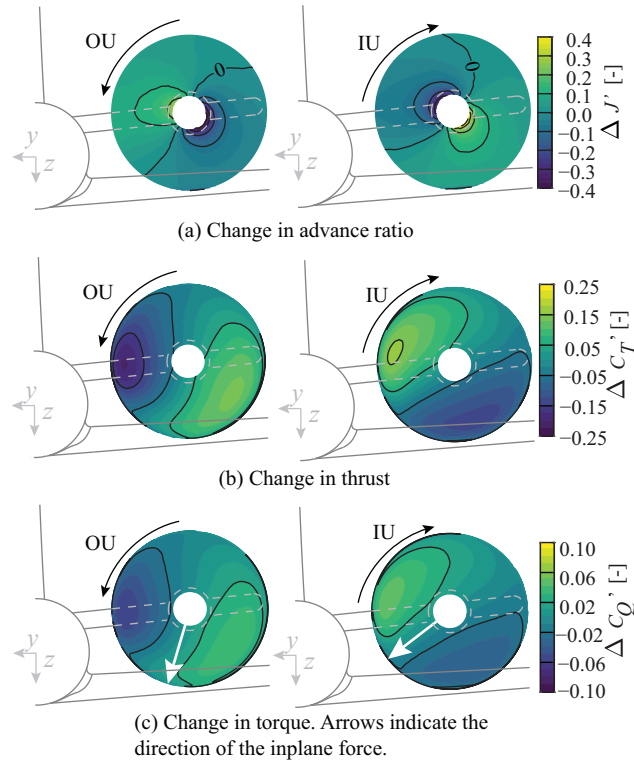direction of the inplane force.

Figure 6.27: Effect of airframe installation on the propeller loading at $J_\infty = 1.8$ and $\alpha = 0$ deg, relative to an isolated propeller. CFD results of the clean configuration, $\beta = 0$ deg.

ratio extracted from the CFD simulations of the propeller-off condition at $\alpha = 0$ deg. The up-going blades and the blades that move away from the fuselage experience a reduction of the local advance ratio, and therefore higher thrust and torque, as shown in Figs. 6.27b and 6.27c, respectively. Such a loading distribution is comparable to the one of a propeller at an angle of attack [90, 113], but the distribution is less symmetric for the installed case.

For the installed propeller, the change in out-of-plane velocity is small compared to the total change in advance ratio (Fig. 6.27a): on average $\Delta J'_a = +0.02$ at $\alpha = 0$ deg. Approximately half of this value is estimated to be from the presence of the wind-tunnel walls (for which the data is not corrected), and the remainder is attributed to the presence of the curved aft-fuselage with the associated pressure field. The dominant inflow perturbation is in the in-plane direction. At a nonzero angle of attack, the inflow to the propeller is a superposition of the geometric inflow and an airframe-induced inflow. The result is that at $\alpha = 5$ deg (Fig. 6.28a), the magnitude of $\Delta J'$ is significantly reduced compared to the propeller in isolated conditions (Fig. 6.28b). The regions of higher and lower advance ratios shift approximately 90 deg clockwise for the propeller on the port side. This shift leads to a change in thrust distribution. Relative to $\alpha = 0$ deg, the av-
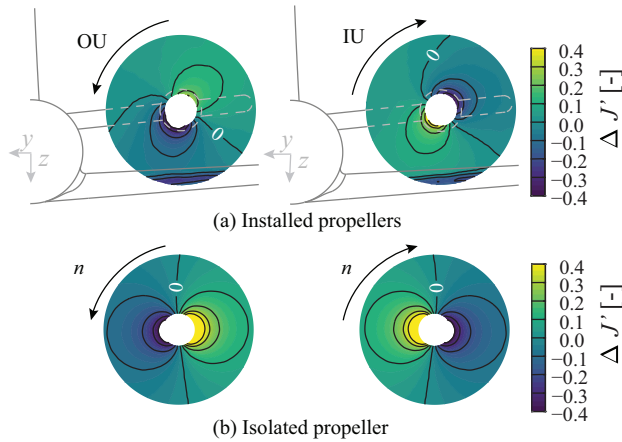
(a) Installed propellers

(b) Isolated propeller

Figure 6.28: Comparison of inflow expressed in local J value at $J_\infty = 1.8$ and $\alpha = 5$ deg for the installed and isolated propeller, relative to $\alpha = 0$ deg. CFD results of the clean configuration, $\beta = 0$ deg.

erage change in J_a is negligible, except for the lower side of the disk where the wake is encountered. The change in axial inflow is negligible because $\Delta J_a = (\cos\alpha - 1)J_\infty$ is offset by the downwash component $\Delta J_a = J_\infty \sin\alpha \sin\varepsilon$. Furthermore, downstream of the wing at the propeller plane (outside the viscous region), the axial velocity induced by the wing is negligible. Because the perturbations of the in-plane and out-of-plane velocity fields are reduced in magnitude and distributed over the disk for the installed propeller, it follows that the downwash cannot be considered as a pure angle-of-attack effect, i.e. $\alpha_{\text{eff,prop}} \neq \alpha - \varepsilon$, in line with the observations made in Section 6.3.

For the isolated propeller, the thrust increases with angle of attack, as shown in Fig. 6.29a. Approximately half of this increase is caused by the reduced axial inflow, determined by evaluating the propeller at $J = J_\infty \cos\alpha$. The other half comes from the in-plane velocity component because T_C varies quadratically with J and the thrust rise on the advancing blade is larger than the reduction in thrust on the retreating blade [90].

From Fig. 6.29a it follows that for the installed propellers, the combined in-plane and out-of-plane flowfields cause only a slight reduction in C_T at $\alpha = 0$ deg compared to the same propeller in isolated conditions. As the axial inflow remains nearly constant and the in-plane velocity component that appears at increasing angle of attack is compensated by the downwash, in the installed configuration, C_T is less dependent on α than in the isolated configuration. This directly leads to a lower contribution of the thrust to longitudinal stability for propellers that are positioned above the aircraft center of gravity, which is the case for this example.

The installation also changes the in-plane forces, as shown in Fig. 6.29b. The $C_{Y_p} - \alpha$ curve is shifted, primarily as a result of the sidewash that leads to a sideforce towards the fuselage symmetry plane. The shift is larger for the inboard-up rotating propeller because for that case the downwash causes an additional sideforce in the same direction as the one induced by the fuselage. The gradient C_{Y_α} for the outboard-up propeller is higher than the one for the isolated propeller for two reasons. First, the average wing-

(a) Propeller thrust (b) In-plane forces C_{Y_p} and C_{Z_p} (c) Propeller efficiency
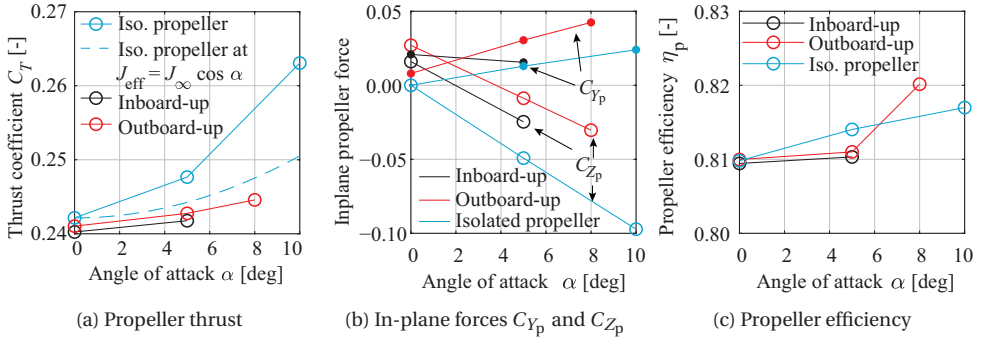
Figure 6.29: Computed changes in forces due to installation on the port propeller, $J = 1.8$. CFD results of the clean configuration, $\beta = 0$ deg.

induced downwash at the propeller disk increases with angle of attack because the maximum downwash angle shifts in z-direction in the propeller plane. The side force associated with the wing downwash therefore increases with angle of attack. Second, with increasing angle of attack, the wing-wake encountered around $\frac{z_p}{R_p} = 1$ also leads to a side force which acts in the same direction as the one that is induced by the fuselage sidewash. The opposite is the case for the inboard-up rotating propeller, hence its lower slope compared to the isolated propeller.

The propeller normal-force curves for both rotation directions are shifted up and their slope is reduced compared to the isolated propeller. The gradients of the normal force curve, $C_{N_{p,\alpha}}$, are lowered by -27% and -17% compared to the isolated propeller for the outboard-up and inboard-up propeller, respectively. This reduction is a consequence of the propeller experiencing a downwash gradient $\frac{d\varepsilon}{d\alpha}$ from the wing and fuselage that increases with angle of attack from on average $\frac{d\varepsilon}{d\alpha} = 0.15$ at $\alpha = 0$ deg to $\frac{d\varepsilon}{d\alpha} = 0.25$ at $\alpha = 5$ deg. These values indicate that by taking the average downwash gradient, the propeller normal force can be predicted with reasonable accuracy, even though the maximum value of this gradient shifts upwards (in negative Z-direction) with angle of attack. The difference between the two rotation directions is primarily caused by the increasing sidewash with angle of attack, which makes C_{Z_p} more positive for the outboard-up rotating propeller, hence reducing $C_{Z_{p,\alpha}}$ for this rotation direction. The offset at $\alpha = 0$ deg is larger for the outboard-up rotating propeller as the airframe induced sidewash positively contributes to C_{Z_p} for this rotation direction.

The axial velocity field is responsible for a negligible difference in propeller efficiency at $\alpha = 0$ deg, as shown in Fig. 6.29c. For the isolated propeller, the propeller efficiency slightly increases with increasing the angle of attack due to the lower axial inflow and the in-plane velocity component. In line with the moderate increase in thrust due to the lower effective advance ratio when installed, the efficiency is nearly independent of angle of attack for the cruise condition. For $\alpha > 5$ deg, the efficiency increases due to the installation as the result of the wake encounter.

The highly nonuniform flowfield that is introduced at high angles of attack, as well

as the distorted axial and in-plane flowfields at low angles of attack change the propeller efficiency map. Figure 6.30 demonstrates for the two rotation directions the importance of including the installation effects in the quantification of the efficiency. As expected, the efficiency along the propeller rotation axis slightly increases with angle of attack, with a maximum for the inboard-up rotating case around $J = 1.9$, close to the advance ratio at which the isolated propeller has its maximal efficiency. Approximately the same trend is followed by the outboard-up rotating propeller. However, the reduction of η_p at $\alpha = 8$ deg, corresponding to the condition with swirling inflow, is only present for the inboard-up rotating propeller, since it operates locally at a higher effective advance ratio. The efficiency of the outboard-up rotating propeller continues to increase up to values close to unity. These high efficiencies are possible because η_p is defined with V_∞, while there is kinetic energy deposition induced by the airframe at the propeller plane.
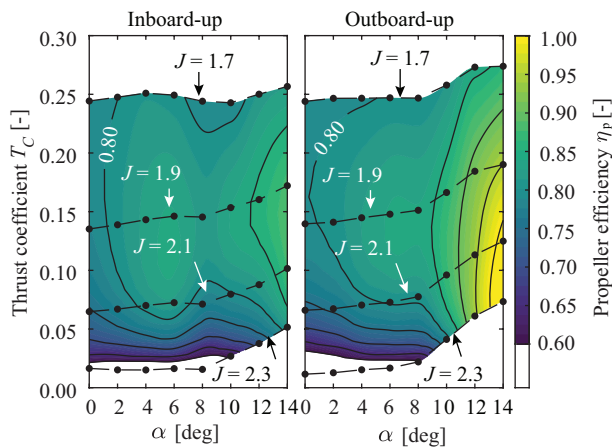

Figure 6.30: Installation effect on propeller efficiency. Experimental results (clean configuration, $\beta = 0$ deg).

In summary, the installation effects of the propeller forces in cruise condition are not negligible. The largest difference with the uninstalled propeller is a reduced gradient of the propeller normal force with angle of attack. The observed differences between the two rotation directions are caused by the translation of the maximum downwash gradient with angle of attack and by the different response to the fuselage-induced sidewash. The installation also leads to a modification of the propeller efficiency curves, such that the maximum efficiency is achieved at a nonzero angle of attack. The magnitude of the interaction effects on aircraft level are put in perspective to the aircraft forces and moments in Section 9.2.

6.6.2. EFFECT OF A FLAP DEFLECTION
In high-lift conditions, achieved by deflecting high-lift devices, the aircraft angle of attack typically ranges between zero and five degrees. In addition to the fuselage and main-wing-induced flowfield, a flap deflection leads to an additional nonuniform inflow to the propellers. Figure 6.31a depicts the measured total-pressure field behind the aircraft at $\alpha = 0$ deg with a 27-degree flap deflection, and illustrates a highly distorted

flowfield. The strong flap-edge vortex induces a swirling inflow on the inboard and lower part of the propeller disk, in addition to a strong downwash of approximately 16 deg. It is apparent from the region's increased total pressure that the thrust distribution is highly affected in this condition in comparison to the case without a flap deflection, as shown in Fig. 4.18.

(a) Measured total pressure downstream at $\alpha = 0$ deg.

(b) side force coefficient, port side, outboard-up.

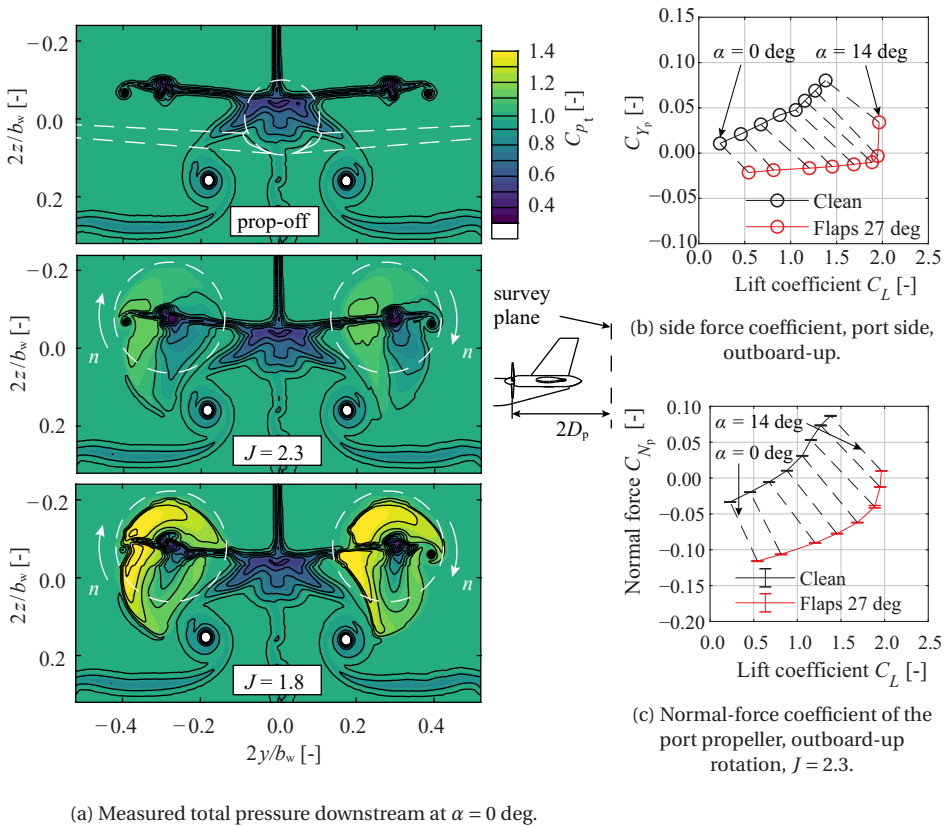(c) Normal-force coefficient of the port propeller, outboard-up rotation, $J = 2.3$.

Figure 6.31: Effect of a flap deflection of $\delta_f = 27$ deg on the propeller slipstream development and propeller normal force. Experimental results, $\beta = 0$ deg.

The resulting effect on the integral propeller forces is depicted in Fig. 6.31b. The in-plane velocity induced by the flap-edge vortex introduces a compensating effect on the propeller sideforce, such that $C_{Y_p,\alpha} \approx 0$ for the outboard-up rotating propeller. In that case, the propeller and flap-edge vortex are counter-rotating. With the flap installed, also $\frac{d\varepsilon}{d\alpha}$ increases due to higher induced losses and a higher lift curve slope (Fig. 9.17). Consequently, the slope of the propeller normal-force curve with angle of attack reduces by approximately 50% compared to the clean condition. Moreover, the larger downwash angle at $\alpha = 0$ deg leads to a significant force on the propellers in negative z-direction, which affects the trim condition. The thrust is found to remain nearly independent of

flap deflection. Figure 6.31a shows that there is a significant lateral translation of the thrust vector, which in case of a co-rotating configuration leads to a yawing moment around the aircraft center of gravity, further discussed in Section 9.2.3.

6.6.3. Effect of High Angle-of-Attack

The effect of a high-lift condition by employing a flap on the propeller forces were quantified in the previous section. In that case, the wing wake and flap edge vortex are significantly displaced with respect to the propeller plane, while there is a strong downwash. High-lift conditions that are achieved by a high angle of attack differ in several ways from a flap deflection. Firstly, for the same wing circulation, the downwash and wake are closer to the propeller disk, due to the z-location of the wing trailing edge. Secondly, the angle of attack leads to a fuselage-induced upwash instead of a downwash in the case of a flap deflection (at $\alpha = 0$ deg). Thirdly, the flap-edge vortex is not present in this case. Finally, the flowfield near the propeller at high angle of attack is strongly influenced by the flow structures that originate from the wing–fuselage junction. The objective of this section is therefore to characterize the impact of the inflow that is achieved at a high angle of attack on the propeller forces. As will be shown in the following, the characteristic flowfield in this condition differs significantly from the types of inflow that have been discussed so far. Although it is a flight condition that is rarely achieved, from a phenomenological point of view, it is illustrative as an extreme case.

In Fig. 6.32 it is shown that there is a strong three-dimensional separation at $\alpha = 14$ deg, in combination with a trailing edge separation. Already at $\alpha = 5$ deg, the wing–fuselage junction causes a vortex that trails from the junction in downstream direction. An improved fairing design compared to the one of the model analyzed herein would reduce the flow separation at the wing–fuselage junction and therefore the relative strengths of the separation-induced vortices. However, the qualitative development of the flow reversal is still representative, since it also has been identified in previous studies [230, 231], and such a flowfield is present to some extent near any wing-fuselage junction.

The installation effect on the propeller forces up to $\alpha = 8$ deg in the clean configuration is moderate and is nearly linear with angle of attack, as shown in Fig. 6.29. By increasing the angle of attack further into the nonlinear region of the aircraft lift-curve, the propeller thrust rises rapidly over the complete range of advance ratios, in particular for the outboard-up rotating propeller, as shown in Fig. 6.33. This trend can be understood by assessing the flowfield at an angle of attack of $\alpha = 14$ deg, as shown in Fig. 6.34a. In this condition, the maximum changes in local advance ratio at the propeller disk are $\Delta J' = -1.8$ and $\Delta J' = +0.6$ for the outboard-up and inboard-up configurations, respectively. Based on the performance curves of the isolated propeller in Fig. 4.3, these values indicate that the blades experience either windmilling conditions or a large angle of attack that leads to flow separation, and the blades for both rotation directions therefore experience significant time-dependent inflow. An appreciable part of the reduction in advance ratio, up to $\Delta J'_a = -0.6$ (Fig. 6.34b), comes from the deficit in total pressure by the separated flow from the wing root that is encountered by part of the propeller disk. This velocity component leads to the same change in thrust for either rotation direction.

The significant difference in thrust between the rotation directions is caused by the

(a) $\alpha = 0$ deg
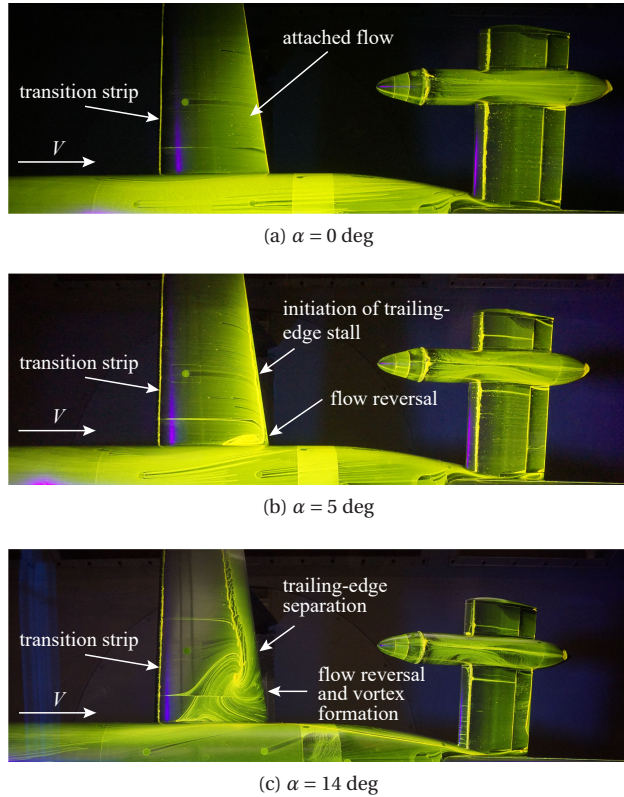

(b) $\alpha = 5$ deg

(c) $\alpha = 14$ deg

Figure 6.32: Flow visualization by means of fluorescent oil on the surface of the *VGM-HTP* model to illustrate the initiation of flow separation at the wing–fuselage junction for $\beta = 0$ deg, propeller-off. Top view.

in-plane velocity components. The regions of positive and negative axial vorticity in and adjacent to the propeller plane, shown in Fig. 6.35a, are indicative of circulation that changes the inflow encountered by the blades. The cause of the negative component of the axial vorticity, $\widetilde{\omega}_x$, is the significant drop in wing lift from the wing–fuselage junction up to 40% span (Fig. 6.35b), which sheds a sheet of trailing vorticity that rolls up into a strong vortex opposite in sign to the wing-tip vortex, indicated by Γ_I in Fig. 6.35c. From the isosurfaces of vorticity depicted in the same figure, two more vortices can be distinguished that are opposite in sign to Γ_I. First, a vortex is formed on each side of the fuselage [230], originating close to the fuselage nose, denoted by Γ_{II}. Secondly, the root separation leads to a pressure gradient along the fuselage [232], that results in a vortex denoted by Γ_{III}. This pair of co-rotating vortices rapidly merge into a single vortex ($\Gamma_{II} + \Gamma_{III}$) that is counter-rotating to Γ_I and contains approximately three times the circulation of Γ_I. The relative distance and strength is such that vortex Γ_I displaces in vertical direction and towards the symmetry plane of the aircraft, over a relatively short distance [165]. The net effect of the vortex pair is a significant in-plane velocity component, equivalent to the large change in J', depending on rotation direction. In particular
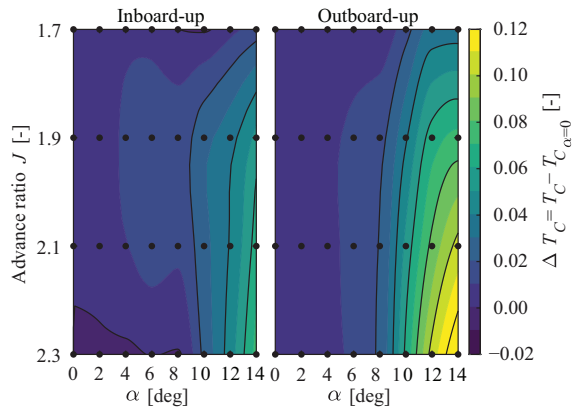
Figure 6.33: Installation effect on propeller thrust at increasing angle of attack. The black dots indicate the measurement points. Experimental results of the clean configuration, $\beta = 0$ deg.

(a) Change in local advance ratio relative to isolated conditions at $\alpha = 0$ deg, $J_\infty = 1.8$.

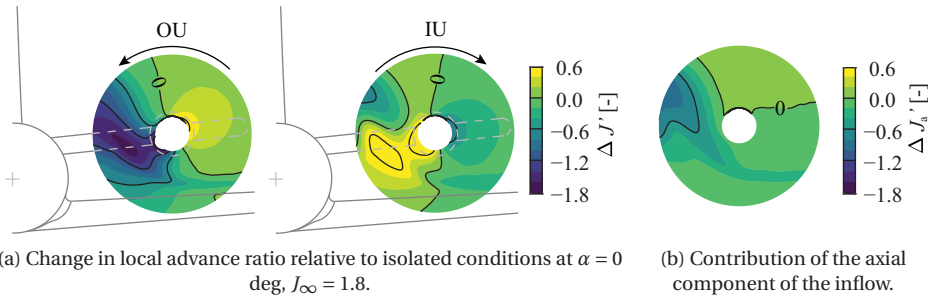(b) Contribution of the axial component of the inflow.

Figure 6.34: Nonuniform inflow to the propeller at $\alpha = 14$ deg, propellers-off. CFD results of the clean configuration, $\beta = 0$ deg.

the outboard-up rotating propeller experiences a large reduction in advance ratio, as the propeller rotation is opposite to the resulting swirling inflow, and is further reduced by the deficit in total pressure. These phenomena are also reflected in the efficiency maps for the two rotation directions, shown in Fig. 6.30. At high angle of attack, the outboard-up rotating propeller has a significantly higher efficiency than the inboard-up rotating propeller.

(a) Axial component of normalized vorticity.

(b) Wing lift distributions

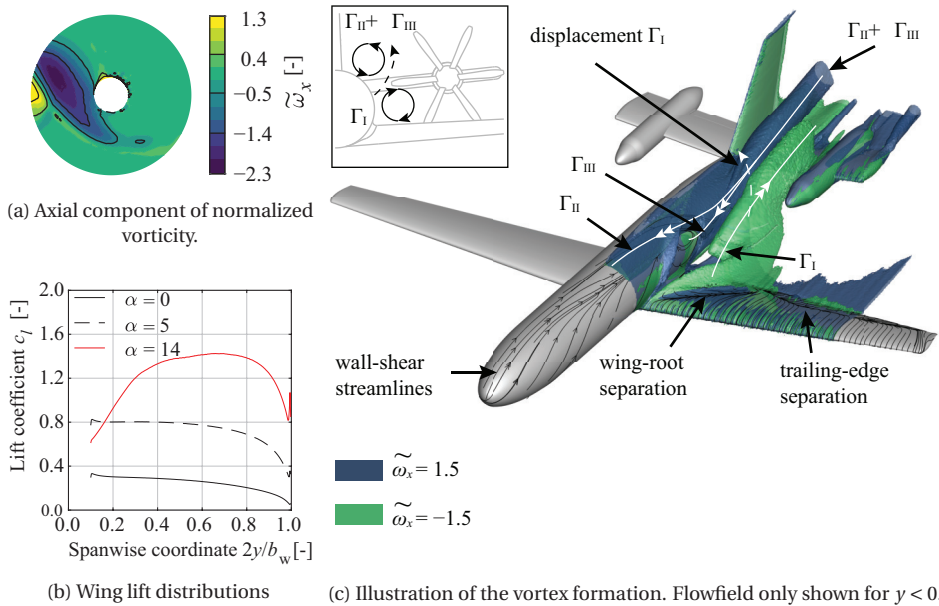(c) Illustration of the vortex formation. Flowfield only shown for $y < 0$.

Figure 6.35: Vortex formation and nonuniform inflow to the propeller at $\alpha = 14$ deg. CFD results of the clean configuration, $\beta = 0$ deg, propellers-off.

6

Next to the rise in thrust, the vortex-induced inflow also leads to a large normal force that is in negative z_p-direction for the outboard-up rotating propeller, while it is in opposite direction for the inboard-up rotation direction. The propeller contribution to overall aircraft stability and trim therefore varies with angle of attack if such a swirling inflow impinges on the propeller or is in the vicinity of the propeller disk. Figure 6.36a shows that $C_{N_{p,\alpha}}$ continuously increases for the outboard-up rotating propeller, and reduces up to $C_{N_{p,\alpha}} = 0$ for the inboard-up rotating propeller at high angle of attack. Such an irregular normal-force curve clearly adversely affects the flight dynamic characteristics of the aircraft. These forces are put into perspective on aircraft level in Section 9.2.1. As can be deduced from the velocity triangle on each blade section, any nonuniformity in the form of a velocity disturbance has the largest effect at high advance ratios. This is clearly visible in Fig. 6.36b for the inboard-up rotating propeller, where the highest advance ratio leads to the largest absolute changes in the normal-force coefficient N_C, and N_{C_α} is even negative; the rear-mounted propeller can have a destabilizing contribution to the aircraft.

In summary, the separated flow from the wing–fuselage junction, present at high angle of attack for the configuration considered herein, significantly influences the propeller forces. The swirling character of this flowfield in particular leads to an increase in thrust and propeller normal force for the outboard-up rotating propeller and thus a stabilizing contribution at aircraft level, while the inboard-up rotating propeller has approximately no stabilizing contribution at aircraft level in these conditions.
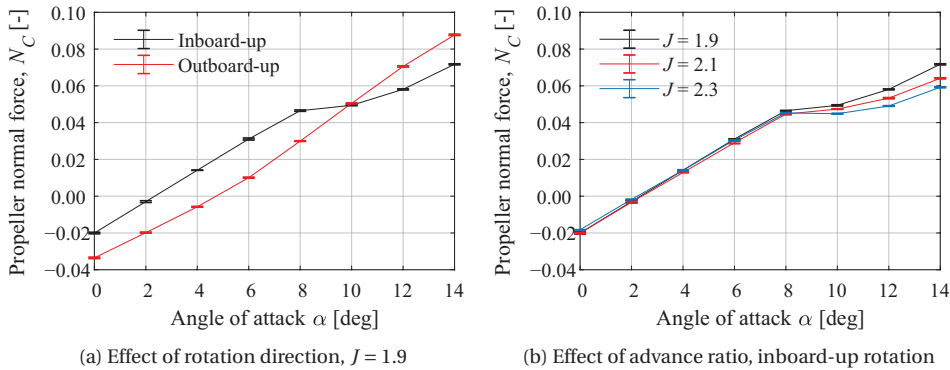
(a) Effect of rotation direction, $J = 1.9$

(b) Effect of advance ratio, inboard-up rotation

Figure 6.36: Installation effect on the propeller normal force, experimental results at $\beta = 0$ deg.

6.6.4. INSTALLED PROPELLERS AT AN ANGLE OF SIDE SLIP

Propellers that experience an angle of side slip generate a side force in the same direction of the transverse velocity component and a normal force of which the direction depends on the rotation direction. For propellers that are mounted behind the aircraft center of gravity, the sideforce acts as a stabilizing contribution, and the normal force affects the trim condition. In the installed configuration, the airframe induces additional velocity components to the propeller, which also vary with angle of attack, and thereby affecting the stability characteristics. For the case considered herein, the propellers are close to the fuselage, in the vicinity of the vertical tail, in a wing-induced downwash field, and near the curvature of the aft fuselage. These factors complicate the interpretation of the resulting propeller forces, which have not been discussed in open literature for this configuration specifically. Despite only experimental results are available for this condition and no distinction is made between each of these contributions, the assessment in this section further helps to understand the relevant interaction phenomena for this configuration.

Part of the nonuniform loading can be attributed to the fuselage-induced flowfield. In case the propellers are mounted above the fuselage centerline, the propeller load distribution is not symmetric. Figure 6.37a shows the in-plane velocity field of an infinite cylinder in a crossflow, using potential flow equations. The figure shows that the fuselage induces an in-plane flowfield such that:

- Quadrant I is more affected by β than quadrant III. The largest changes in loading will be observed in quadrant I.

- Quadrant II is more affected by the in-plane component w than quadrant IV.

This flowfield leads to a thrust distribution that is illustrated in Fig. 6.37b. The particular load distribution leads to a shift of the resultant force vector in z and y-directions. However, this is a simplification of the situation, since also the wing introduces a non-symmetric flowfield with respect to the symmetry plane. A first indication of the effect of a side slip angle can be obtained from the flowfield downstream of the model. Figure
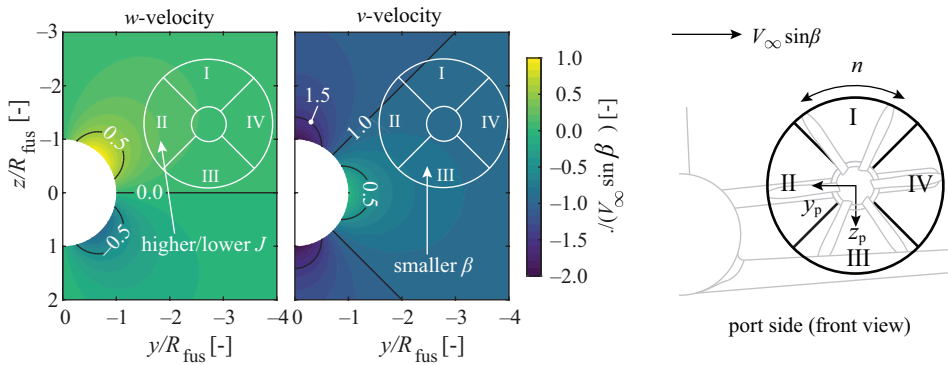
(a) Fuselage induced flowfield affecting different quadrants of the disk (not to scale). Potential flow solution of an infinite cylinder in a crossflow.

higher T, Q

lower T, Q
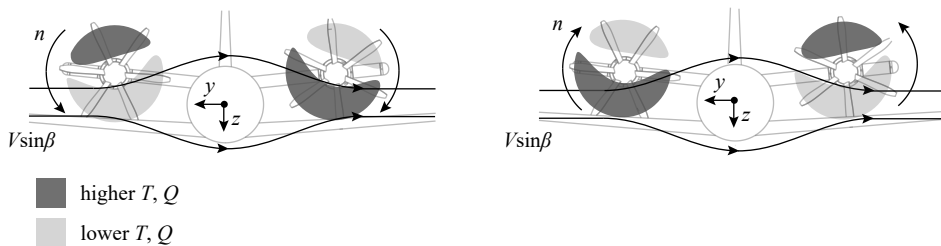
(b) Differences in loading due to the fuselage-induced flowfield

Figure 6.37: Qualitative effect of fuselage-induced flowfield on the propeller loading.

6.38 depicts the total-pressure distribution in a wake-survey plane for the case of $\alpha = 0$ deg and a side slip of $\beta = -5$ deg. In line with the case of a propeller at angle of attack, the thrust is higher on the advancing side of the disk, while a reduction in thrust is observed on the retreating side. However, it is clear that the thrust distributions are not (anti) symmetric; the airframe-induced flowfield is not small relative to the sidewash component $v/V_\infty = \sin\beta$.

As discussed before, if a ΔJ is encountered, the increase in loading is larger than the reduction in loading. Based on these observations, one can already conclude for the port propeller that an inboard-up rotating propeller will produce a larger side force than an inboard-up rotating propeller, due to the flowfield in the dominant quadrant I. This is confirmed in Fig. 6.39a, which shows that the outboard-up rotating propeller has a substantial 10% more negative C_{Y_β}. Furthermore, it can also be concluded that an inboard-up rotating propeller will produce a larger downforce, due to the w-component that affects quadrant II. This is confirmed in Fig. 6.39b. This downforce is further increased by the larger wing circulation on this side of the aircraft because of the low-wing configuration: the fuselage induces an additional angle of attack in the root region, leading to a net downwash behind the wing. In case a full aircraft has two inboard-up rotating propellers and experiences a side slip, this normal force is equal on each side of the air-
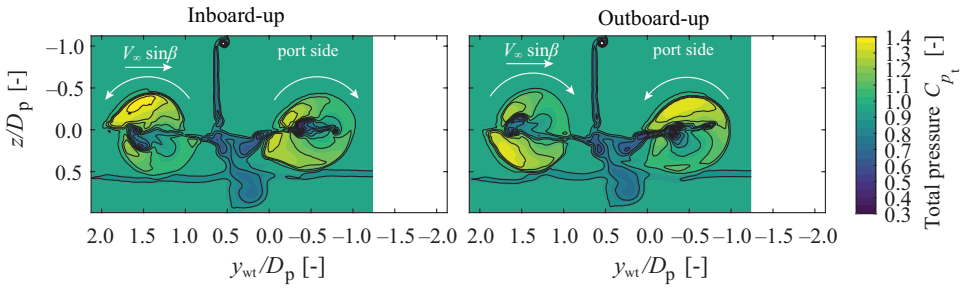
Figure 6.38: Effect of sideslip on propeller loading and slipstream deformation. Experimental results. Conditions: $J = 1.9$, $\alpha = 0$ deg, $\beta = -5$ deg.

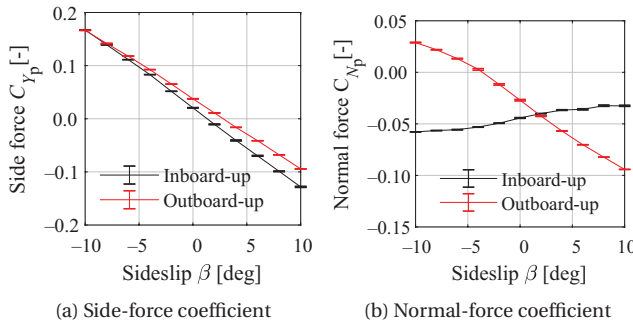(a) Side-force coefficient

(b) Normal-force coefficient

Figure 6.39: Effect of side-slip angle on the integral in-plane forces on the port propeller of the clean configuration, $J = 1.9$, $\alpha = 0$ deg. Experimental results.

craft but opposite in sign. However, for a co-rotating configuration, there is a pitch-up or pitch-down moment depending on the angle of side slip.

At high angle of attack, the shape and magnitude of the flow separation originating from the wing–fuselage junction (discussed in Section 6.6.3) also depend on β. The significant installation effect that was observed in Section 6.6.3 on $C_{N_{\alpha,p}}$ therefore occurs at a lower angle of attack: an angle of sideslip lowers the critical angle of attack at which this flow separation initiates. Furthermore, the location of the vortex relative to the propeller disk also depends on side slip as well. This is clearly observable in Fig. 6.40a, showing that for a $\beta = 5$ deg angle of sideslip, the port propeller does not experience this highly nonuniform flow, while the starboard propeller does. This asymmetric flow separation has a distinct effect on the normal-force gradient as function of sideslip. Figure 6.40b shows that $C_{N_{p,\alpha}}$ increases up to three times the value that corresponds to the one at $\alpha = 0$ deg for the outboard-up rotating propeller, and reduces up to $C_{N_{p,\alpha}} = 0$ for the inboard-up rotating propeller at high angle of attack. Such an irregular normal-force curve clearly adversely affects the flight dynamic characteristics of the aircraft.
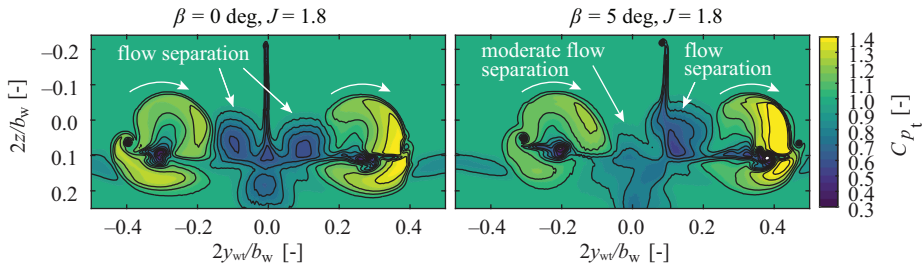
(a) Asymmetric flow separation from wing–fuselage junction at an angle of sideslip for co-rotating propellers, $\alpha = 10$ deg. Viewed from behind.
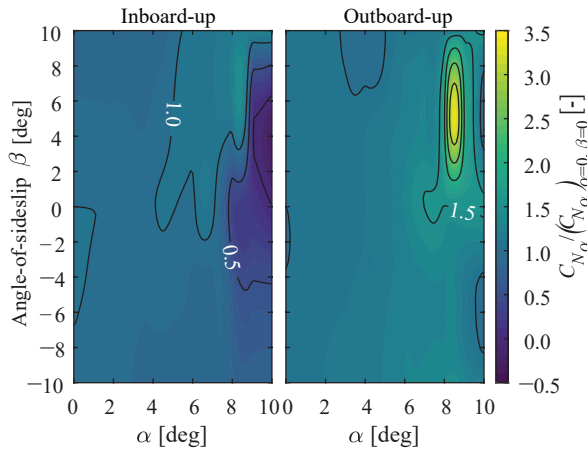
(b) Installation effect on the propeller normal-force gradient, $J = 1.9$

Figure 6.40: Effect of sideslip angle on the propeller normal-force gradient and inflow. Experimental results.

Next to the variations in in-plane forces, also the thrust depends on angle of sideslip. This is relevant for directional stability, since the propellers have an offset from the aircraft symmetry plane. The fuselage produces a circulation such that for a positive side slip, the port propeller experiences a higher axial inflow, schematically shown in Fig. 6.41a. This is especially the case as the propellers are mounted close to the curved part of the fuselage. This leads to a $C_{T_\beta} < 0$, independent of rotation direction. On the other hand, the axial flow component is reduced by a factor $\Delta u / V_\infty = 1 - \cos \beta$. This factor is dominant, as depicted in Fig. 6.41b, provided that the thrust increases independently of the direction of side slip. Finally, the gradient C_{T_β} varies significantly: each rotation direction has a higher gradient depending on $\beta > 0$ or $\beta < 0$. This is again attributed to the magnitude of the rise in thrust in quadrant II.
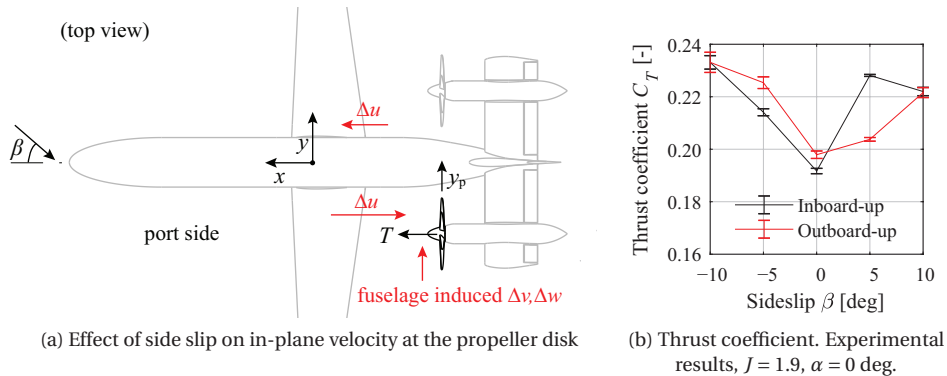
(a) Effect of side slip on in-plane velocity at the propeller disk

(b) Thrust coefficient. Experimental results, $J = 1.9$, $\alpha = 0$ deg.

Figure 6.41: Effect of side-slip angle on the thrust on the port propeller of the clean configuration.

6.6.5. Effect of Nonuniform Inflow on a Structureborne Noise Indicator

The previous sections show that the installation of propellers in a nonuniform flowfield leads to time-dependent shaft loads, which are transferred to the airframe. If no appropriate damping system is applied to damp this transfer at the relevant frequencies [78], it leads to periodic forcing of the structure that comprises passenger comfort through vibrations and additional cabin noise [77, 233]. Another part of the noise perceived by passengers is can be sought in the airborne noise that is radiated from the propellers, as well as the hydrodynamic pressure fluctuations on the fuselage surface, which also leads to structureborne noise.

It is known (e.g. shown in Refs. [72, 84, 181, 234]) that turboprop aircraft that fly at an angle of attack produce asymmetric cabin noise if the propellers are corotating. For a propeller that is mounted above the cabin centerline, the downgoing blades closes to the cabin are known to produce higher noise levels due to the higher loading on these advancing blades. For the horizontal-tail-mounted propellers, the loading distribution is significantly different between the two rotation directions, especially at a high angle of attack. This clearly has an influence on the nearfield noise. Since the propellers are relatively close to the fuselage surface, the hydrodynamic pressure fluctuations (i.e. the rotating pressure field outside of the slipstream) leads to periodic pressure fluctuations on the fuselage outer surface. This is a part of the structureborne noise [74] experienced by passengers. On top of that, the acoustic waves from the rotating propeller blades also lead to airborne noise.

In this section, it is shown that the nonuniform inflow does indeed affect the sound-pressure levels on the outer surface of the aft-fuselage, which is shown in more extensive studies by other authors [68, 70, 222]. Besides the findings on the effect of nonuniform inflow to the contribution to aircraft stability and unsteady loads, findings in terms of cabin noise could contribute to design choices, for example rotation direction. Since these experimental analyses are performed on a small model at low flight Mach number, the results are meant to provide a qualitative indication. Since no measurements are performed of the propeller in isolation, the observed trends should be illustrative.

Additionally, as only a single z-location is assessed (which is known to be an important parameter [234]), no quantitative conclusion can be drawn on the interior noise.

The results consist of microphone measurements of which the setup is described in Section 3.3.5. To illustrate the significance of the propeller-induced pressure fluctuations on the fuselage surface relative to the boundary-layer noise and background noise, the spectra obtained at two angles of attack are shown in Fig. 6.42. The tonal components at the blade-passing frequency (BPF) are clearly identifiable, with the fundamental frequency being 15 dB above the propeller-off baseline noise, and the second and third harmonic still identifiable. Also at high angle of attack (Fig. 6.42b), the propeller-induced pressure fluctuations are still dominant and allows further investigation of the installation effect on the noise level at the dominant, fundamental frequency.
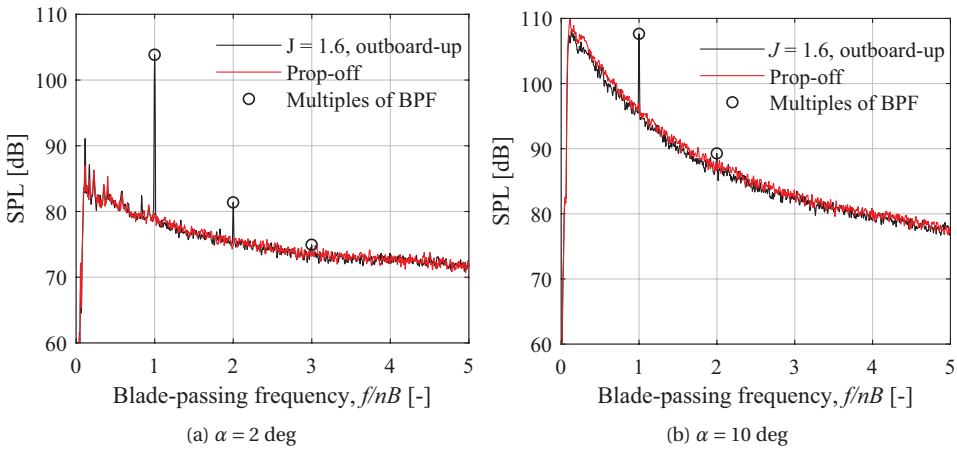

(a) $\alpha = 2$ deg

(b) $\alpha = 10$ deg

Figure 6.42: Spectra at two angles of attack of the microphone at the propeller plane ($x_\mathrm{p} = 0$).

To show how the rotation direction and therefore the load distribution near the fuselage outer surface affects the unsteady pressures, Fig. 6.43 depicts the sound-pressure level at the blade-passing frequency along a portion of the aft fuselage. The propeller-off noise levels vary slightly in x-direction due to the on the one hand growth of the boundary layer and on the other hand the thickness variation due to the curvature of the aft fuselage. At $\alpha = 14$ deg, the relative location of the separated flow from the wing–fuselage junction to the microphones plays an important role. For the propeller-on measurements, the highest propeller-induced noise levels are found slightly aft of the propeller plane, similar to the findings in Ref. [85]. From the Figs. 6.43b through 6.43e it is clear that at high angle of attack, for the outboard-up rotating propeller, the downgoing blades experience a net reduction in advance ratio and generate a higher loading. The inverse is the case for the inboard-up rotating propeller. If the propellers–fuselage spacing would be reduced, these levels would increase even further [234]. Around the cruise condition ($\alpha = 4$ deg), both rotation directions lead to the same noise levels. This coincidence is a combination of several factors. Although the loading on the inboard side of the disk is slightly higher if the propeller rotates outboard-up (Fig. 8.13), it is the Mach number

173

at which the loading is approaching and retreating to the microphone. A different z-location of the microphones would therefore lead to a slightly different result [234] and it can be expected that the overall sound-pressure level inside the cabin is still higher for an outboard-up rotation. The effect of a lower loading due to installation is particularly demonstrated in Fig. 6.43e. At this angle of attack, the loading on the inboard side of the inboard-up rotating propeller reduces to zero (see Fig. 6.40a). Although not shown herein, a similar but less pronounced effect would be the case if the installation effect is not present and the propeller would operate at an angle of attack.

6

(a) Microphone locations and legend

(b) $\alpha = -2$ deg

(c) $\alpha = +4$ deg

(d) $\alpha = +8$ deg
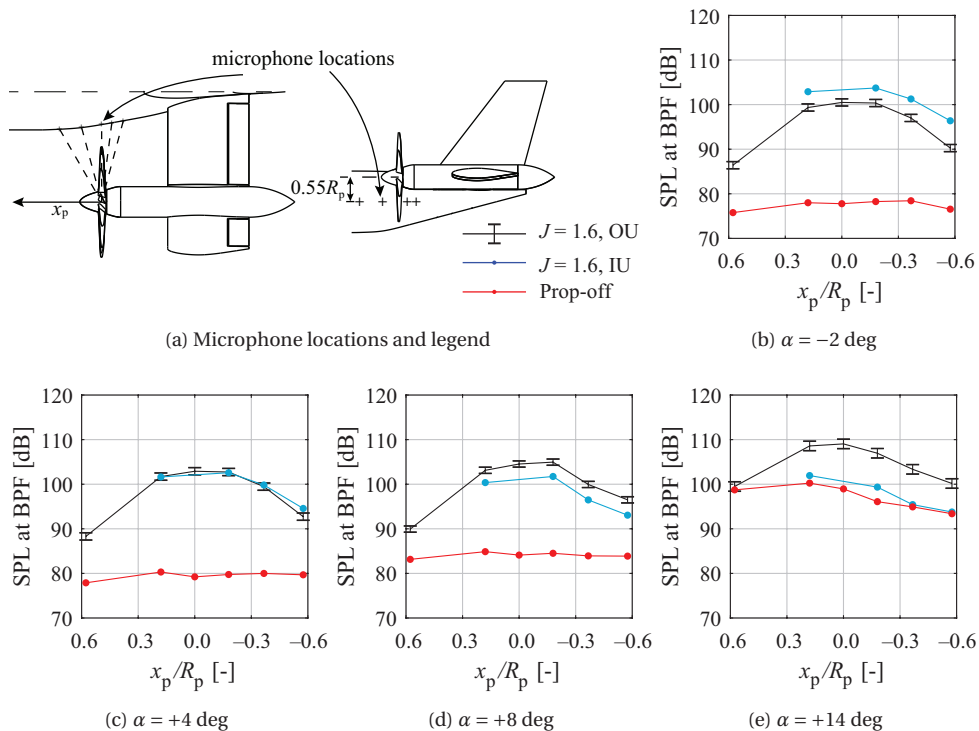
(e) $\alpha = +14$ deg

Figure 6.43: Effect of rotation direction on the sound-pressure level on the fuselage surface at various angles of attack. The errorbars are only plotted for one curve to improve readability.

As the trend of the sound-pressure level as function of angle of attack is irrespective of the axial location, a single x-location can be further investigated. The dependency of angle of attack is more clearly demonstrated in Fig. 6.44, showing the results for an upstream location $x_p/R_p = 0.18$. As at high advance ratio the effect of nonuniform inflow is more pronounced, the trends of the sound-pressure level are steeper for $J = 2.3$ relative to $J = 1.6$, shown in Figs. 6.44a and 6.44b, respectively. The subfigures also indicate that for $\alpha > 5$ deg, the noise levels increase for the propeller-off condition, the result of on the one hand trailing-edge separation and the more severe flow separation from the wing–fuselage junction. In line with the results in Fig. 6.43, the inboard-up rotating propeller
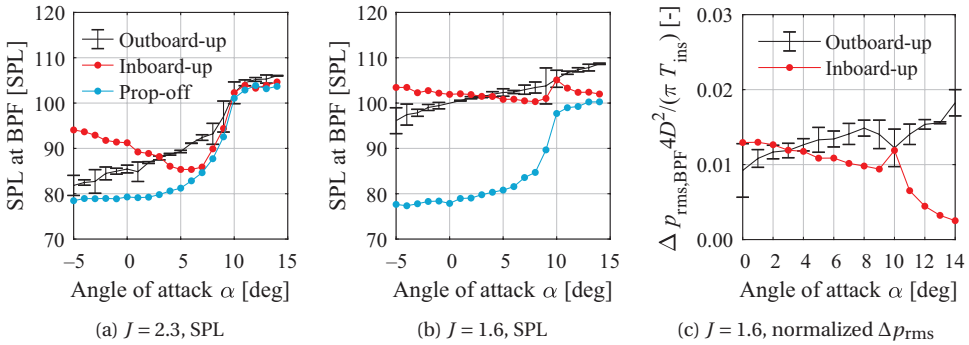
Figure 6.44: Effect of rotation direction on the sound-pressure levels at $x_p/R_p = 0.18$ for a range of angles of attack. Indicated errorbars are representative for other cases as well.

approaches the propeller-off sound-pressure levels for $\alpha > 10$ deg. However, in Fig. 6.33 it is shown that the installed thrust is vastly different between the two rotation directions at these high angles of attack. Therefore, a more fair comparison is to compensate the rise in thrust and therefore compare the noise relative to the disk loading. To this end, the pressure fluctuations relative to the propeller-off condition (Δp_{rms}) are normalized with the disk loading. Figure 6.44c shows that the *relative* noise levels indeed increase with angle of attack for the outboard-up rotating propeller, and reduce for the inboard-up rotating propeller.

It can therefore be concluded that the installation indeed leads to a significantly higher noise level for the same thrust coefficient. This suggests that the installation effect on interior noise can be reduced by either selecting an inboard-up rotating propeller, or by mounting the propeller such that the nonuniform inflow is reduced.

6.7. CONCLUSIONS

In this chapter the effect of nonuniform inflow on the propeller loading, propeller efficiency, and gradients of propeller forces are identified for a range of typical types of inflows that are induced by the airframe. The following conclusions are formulated that are independent on the particular propeller configuration:

- The flowfield that is induced by the airframe at the propeller disk is the dominant flowfield that determines the propeller forces. Velocity perturbations at the disk caused by slipstream deformation downstream of the disk and blade-to-blade interaction as a consequence of nonuniform loading are of secondary importance.

- The regions on the disk that produce the largest change in load correspond to the radial locations with the highest sensitivity.

- If the actual shape of the nonuniform inflow is not taken into account, but instead is averaged over the disk, the installation effect is underestimated. For a propeller operating in the upwash field of a wing, this error amounts up to 10% for the normal-force coefficient.

- Due to the nonlinear sensitivity distribution over the disk, the gradient of the propeller integral forces can be higher or lower than the gradient of the inflow.

- Compared to a lifting surface that induces an average upwash at the propeller plane of approximately 5 deg (Fig. 6.13) and lead to unsteady loads of 40% of the thrust, the displacement effect leads to unsteady loads of approximately 10% of the thrust. These values indicate that the displacement effect is a relevant factor for the unsteady loads which may influence the design choice for the spacing between propeller disk and leading edge of the wing.

The following main conclusions are configuration specific:

- **Propeller near a lifting surface**

  – A propeller in the proximity of a horseshoe vortex generates larger unsteady loads than a propeller at angle of attack with a magnitude equal to the average of the vortex-induced flowfield. The magnitude of the normal-force gradient depends on the relative position of the maximum downwash gradient and propeller disk.

  – The upstream effect due to displacement of the streamlines is proportional to the airfoil thickness-to-chord ratio

- **Propeller encountering a wake**

  – The encounter of a wake especially leads to unsteady loads and the changes in integral forces are small. For a typical propeller diameter-to-wing chord ratio, the integral forces amount up to 2% of the installed thrust in cruise condition. The largest installation effects occur if the wake is encountered at $z/R_\mathrm{p} = 0.5$.

- **Array of distributed propellers**

  – The largest unsteady loads occur due to the boundary condition that limits the slipstream to contract. The corresponding in-plane velocities lead to periodic loading and these linearly increase with the thrust coefficient. The unsteady loads from the interaction between tip vortices only leads to very local changes in load. Furthermore, the unsteady shaft loads are nearly proportional to the installed thrust coefficient.

- **The tail-mounted propeller configuration**

  – The separated flow from the wing–fuselage junction significantly influences the propeller forces. The swirling character of this flowfield in particular leads to an increase in thrust and propeller normal force for the outboard-up rotating propeller and thus a stabilizing contribution at aircraft level, while the inboard-up rotating propeller has approximately no stabilizing contribution at aircraft level in these conditions.

- The installation effect at lower angles of attack is also not negligible, because the stability characteristics are adversely affected as the normal-force coefficient is lowered by up to 30% for the outboard-up rotating propeller for the cruise condition. At high angle of attack, the normal-force gradient becomes even slightly negative for an inboard-up rotating propeller, while the magnitude increases by a factor of three times the value existing at $\alpha = 0$ deg for the outboard-up rotating propeller.

- Due to the nonuniform inflow, the maximum propeller efficiency is achieved at a small positive angle of attack if the propellers are aligned with the fuselage centerline.

- A propeller installation above the fuselage centerline leads to a rotation-dependent effect of a side slip. The changes in propeller loading are primarily caused by the fuselage-induced flowfield in case of a sideslip.

- Although limited in scope, microphone measurements suggest that the adverse installation effect on interior noise can be reduced by either selecting an inboard-up rotating propeller, or by mounting the propeller such that the nonuniform inflow is reduced.

In the next chapter an exploratory study is presented where for a specific aircraft geometry a number of propeller performance indicators are compared. Findings in the current chapter in terms of propeller disk loading are further employed in Chapter 8, where the effect of the propeller installation on lifting surfaces is discussed, for which the change in slipstream due to nonuniform inflow is an essential aspect. Findings in the current chapter regarding the horizontal-tail mounted propeller configuration are put into perspective by comparing their contribution to the airframe contribution in terms of forces and moments.

6

7

EXPLORATORY CONFIGURATION STUDY ON PROPELLER-PERFORMANCE INDICATORS

The performance of unconventional propeller-driven aircraft configurations is a combination of both propeller and airframe performance in the installed condition. In this context, 'performance' is referred to as the product of propeller efficiency and lift-to-drag ratio. Once the propeller performance is known, minimum the change of the airframe L/D due to the aero-propulsive airframe interaction can be determined to arrive at a net benefit on aicraft level. A direct comparison of different propeller configurations on aircraft level is challenging, since the outcome will depend on various factors, for example:

- top-level requirements
- aircraft configuration
- location of the center of gravity
- propeller blade design
- nacelle integration
- flight condition

A study that shows how sensitive the propeller performance is to the choice of propeller location relative to the airframe would provide insight in the design freedom of an aircraft designer. Even though the design process is iterative, such comparison based on a given representative reference geometry is still relevant since different propeller installations can be put in perspective and the most important contributions of the flowfield

to the propeller forces can be identified. The associated trends cannot only be used in aircraft design, but can also support further developments of mitigation strategies on the adverse performance effects.

Despite numerous publications exist on the fundamentals of the impact of the airframe on the propeller, for those studies, different geometries, conditions, or performance indicators are used which complicates a comparison. Before particular propeller–airframe interactions are investigated in detail in subsequent chapters, in this chapter first a more high-level comparison is made on the effect of the airframe on the propeller for various configurations. These outcomes also form a starting point and a motivation for the detailed analyses of particular aerodynamic phenomena in subsequent chapters. The approach at this stage therefore is to not go into the details regarding the particular installation, but instead, highlight the important outcomes in the form of an exploratory study. It is noted that no conclusions are drawn on the 'optimal' configuration from a propeller performance point of view, for reasons discussed earlier, but to provide handles for the reader to conduct aircraft design studies. The outcome of this chapter is an overview in the form of a bar chart for various configurations for which three performance indicators are computed.

The approach of the evaluation of the different propeller configurations is described in Section 7.1. Section 7.2 introduces a novel and particularly useful *installation coefficient* that can be used for comparisons of the configurations. This is followed by configuration assessments, discussed in Sections 7.3 through 7.6. Finally, a summary and the main findings are presented in Section 7.7.

7.1. APPROACH AND DEFINITION OF TEST CASE

The performance indicators of interest in this chapter are schematically shown in Fig. 7.1 and include:

- **Maximal efficiency**; since the airframe induced inflow will typically affect the optimal advance ratio, the assessment of the propeller at a constant advance ratio, could give a biased view, depending on the advance ratio of the analysis. A more relevant approach is to compare the change of the *maximal* efficiency.

- **Optimal thrust coefficient**; the thrust coefficient T_C that corresponds to the maximal efficiency indicates the need to adjust blade pitch or disk area to achieve a certain installed thrust.

- **Normal-force coefficient**; this force component adds to or reduces the system lift, and therefore lift-to-drag ratio

- **Unsteady blade loading**; a low value is preferred for various reasons, including structural design, passenger comfort, and noise, as is discussed in Section 1.2.4

The comparative study is performed using a reference transport aircraft, operating at a cruise condition. To quantify the installation effects for each propeller configuration, the propeller diameter and proximity to the airframe are altered, such that both the magnitude and the distribution of nonuniform inflow is varied throughout. A straightforward approach is used, where both the propeller design and aircraft design are not
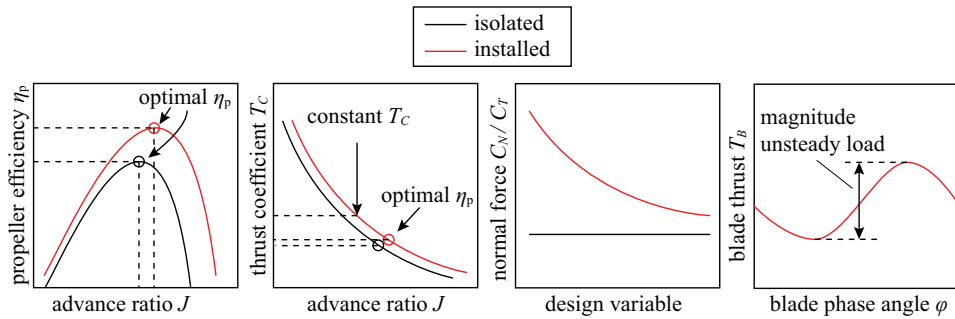
Figure 7.1: Propeller performance characteristics of interest for the comparative study.

altered throughout the analyses. The different configurations are schematically shown in Fig. 7.2, each introducing a specific *type* of inflow:

1. A flowfield induced by the *bound vortex*; upstream and downstream of the wing

2. A flowfield induced by the *chordwise circulation distribution*; above and below the wing

3. A flowfield induced by the *wing-tip vortex*; downstream of the wing-tip

4. A flowfield induced by a *no-slip condition*; in the wake of the fuselage and in the wake of the wing
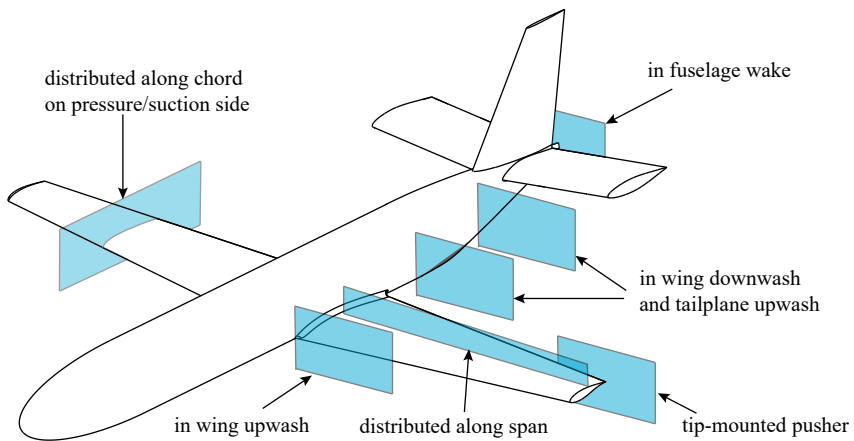

Figure 7.2: Conceptual representation of different propeller-configurations.

The aircraft geometry is the clean configuration of the *VGM-HTP* model (see Section 3.3.5). Provided that the geometry itself is not optimized to account for possible propeller efficiency benefits, without doubt, design changes to the model can be made

such that a configuration could achieve a higher gain (or smaller loss) of propeller efficiency. However, since the wing geometry in terms of thickness, spanwise loading distribution, and fuselage geometry are comparable to transport aircraft, the *relative* differences between propeller configuration are still representative. For the comparison, the clean configuration at $\alpha = 0$ deg is taken as reference condition, with the propeller disk perpendicular to the freestream. This leads to a propeller-off aircraft lift coefficient of $C_L = 0.23$. For lift coefficients that are more representative for transport aircraft ($C_{L,\text{cruise}} = 0.5$ to 0.7 [132]), the installation effects observed in this chapter will be more pronounced for installation effects that depend on lift. The cruise condition is an attractive choice since it directly highlights the performance change for an important portion of a mission. However, it should be kept in mind that other phases of the flight may be constraining the propeller design, e.g. diameter to achieve a certain thrust in take-off and climb, as discussed in e.g. Refs. [29, 86, 99]. The presented results for a range of diameter can therefore be interpreted in a design loop.

The predictions of the propeller performance are made using the engineering method introduced in Chapter 5. This analysis method is proven to be adequate for all of the types of nonuniform inflow in Fig. 7.2. The airframe-induced flowfield—the input to the engineering method—is obtained from the CFD simulations described in Chapter 3. In these simulations, the effect of the nacelle on the airframe-induced flowfield is not included. This is an important simplification that particularly will influence the propeller inflow in case there is a large angle of attack to the nacelle, or in case the nacelle is relatively close to the airframe. For the cases with a large inflow angle, for example in the proximity of the wing leading edge, the presence of the nacelle would increase installation effect.

7.2. Definition of Installation Coefficient κ

The maximum efficiency of a propeller that operates in freestream conditions is achieved at a certain advance ratio depending on the blade pitch angle (see. e.g. Fig. 2.8). Provided that a certain thrust coefficient T_C is desired to at least balance the airframe drag, the diameter, advance ratio, and blade pitch are to be selected in order to achieve maximum efficiency at this desired thrust setting. For an installed propeller, the optimal condition is not necessarily at the same advance ratio, hence, the blade pitch and diameter should be adjusted accordingly. To find this optimal point, often aimed for during cruise, but also the off-design points, the installation effect on the full $\eta_p - J$ curve is required.

It is hypothesized that a factor can be formulated that describes the *installation effect as a change in advance ratio*, such that it can be applied to the performance curves of the isolated propeller to arrive at the performance curves of the installed propeller configuration. The underlying motivation for this hypothesis is that it is shown in Chapter 5 that a nonuniform inflow on a blade section can be described as a change in the local advance ratio. If that correction factor is identified for one blade pitch angle, it can subsequently be used to scale the data for different blade pitches. The benefit of such scaling is significant reduced computational effort; it is not required to assess the installed configuration for a large number of operating points.

The existence of such factor can be reasoned by making the analogy to a wing that

operates in a disturbed flowfield. As example, one can define two wing geometries 'A' and 'B' of different aspect ratio that both are to be analyzed in the installed condition, e.g. a reduced dynamic pressure relative to freestream condition. If for wing geometry 'A' the slope of the lift curve is determined in both installed condition (= $C_{L_\alpha,\text{ins}}$) and isolated conditions (= $C_{L_\alpha,\text{iso}}$), then the lift curve slope of wing 'B' in isolated conditions can directly be scaled by $\frac{C_{L_\alpha,\text{ins}}}{C_{L_\alpha,\text{iso}}}$, without a specific analysis of wing 'B' in the installed condition. In other words, the aerodynamic coefficients of a surface that operates in other conditions than freestream, can be normalized to freestream conditions using a factor that describes this installation effect. This statement holds in case there is no coupling between wing and inflow field and in case the perturbations are small (i.e. the effects of a change in Reynolds number and Mach number are negligible). These are also assumptions made for the engineering method for the propeller analysis.

This concept is illustrated for a propeller by considering two simplified disturbances to the freestream: an axial and a tangential disturbance, as illustrated in Fig. 7.3. The goal is to find the optimal advance ratio for the two 'installed' cases. For the case of an axial disturbance (Fig. 7.3b), the propeller should operate at the same advance ratio as the propeller in uniform flow but with a different (local) inflow velocity V_{ins}. The rotational speed of that propeller is therefore to be adjusted by a factor $\frac{V_{\text{ins}}}{V_\infty}$. The (optimal) advance ratio based on the freestream velocity ($J_{\text{opt},\infty}$) therefore changes by a factor $\frac{V_\infty}{V_{\text{ins}}}$. Equivalently, if the inflow contains a swirl such that the local advance ratio is altered (Fig. 7.3c), the optimal advance ratio J_{opt} can directly be determined by introducing a change in rotational speed, Δn. Similarly, the efficiency of the propeller can be adjusted accordingly, which alters with the same factor as the advance ratio.

$$J_\infty = J_{\text{opt}}$$
$$n_{\infty,\text{opt}} = \frac{V_\infty}{J_{\text{opt}}D_p}$$

(a) Freestream inflow

$$J_{\text{ins}} = J_{\text{opt}}$$
$$n_{\text{ins,opt}} = \frac{V_{\text{ins}}}{J_{\text{opt}}D_p}$$
$$n_{\text{ins,opt}} = n_{\infty,\text{opt}}\frac{V_{\text{ins}}}{V_\infty}$$
$$J_{\text{opt},\infty} = J_{\text{opt}}\frac{V_{\text{ins}}}{V_\infty}$$

(b) Axial disturbance

$$V_t(r) = \frac{\Delta n}{2\pi}r$$
$$J_{\text{ins}} = J_{\text{opt}}$$
$$n_{\text{ins,opt}} = n_{\infty,\text{opt}} - \Delta n$$
$$J_{\text{opt},\infty} = \frac{V_\infty}{(n_{\infty,\text{opt}} - \Delta n)D_p}$$
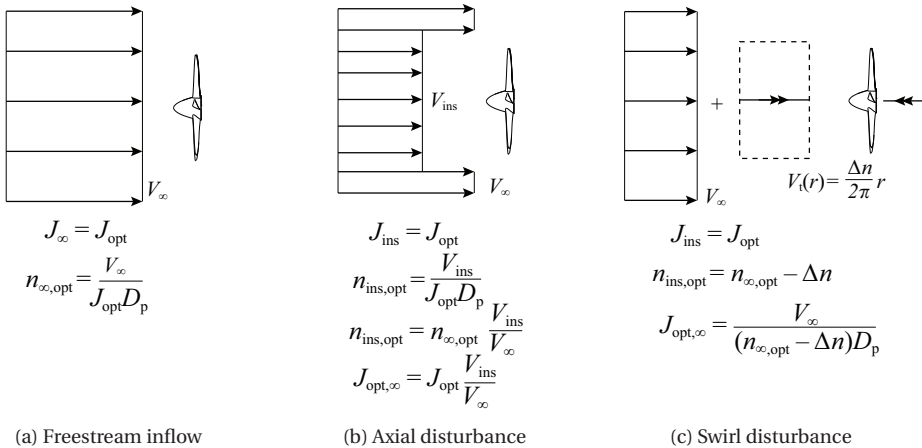
(c) Swirl disturbance

Figure 7.3: Schematic of relation of optimal advance ratio expressed in the freestream conditions using two theoretical inflows.

The relation between the installed and isolated propeller efficiency is herein denoted as κ and is referred to as the *installation coefficient*. The aforementioned rather straight-

forward observations suggest that for more complex inflows, an installation coefficient can be determined as well. In Chapter 3 it is shown that treating the disk as discrete areas on which the change in loading is computed leads to satisfactory prediction for the blade forces. Therefore, this coefficient can be determined for each element on the disk, and it follows directly that an equivalent value can be computed for the entire disk as well.

Figure 7.3 already indicates that a disturbance on the axial velocity is a factor independent of advance ratio, while for a swirling inflow it depends on the rotational speed and therefore on advance ratio. The correction to the efficiency curves therefore contains an axial and tangential contribution. In line with the approach of Chapter 3 these components are superimposed:

$$\kappa = \kappa_a + \kappa_t(J) \tag{7.1}$$

where κ_a is the contribution due to a disturbance in axial direction, while κ_t is the contribution due to a disturbance in tangential direction. This factor is used to correct the propeller efficiency curve by changing both η_p and J:

$$\eta_{ins}(J_{ins}) = \kappa\eta_{iso}(J_{iso}) \tag{7.2}$$

with

$$J_{ins} = \kappa J_{iso} \tag{7.3}$$

The axial component of the installation coefficient is independent of the advance ratio:

$$\kappa_a = \frac{\eta_{a,ins,max}}{\eta_{iso,max}} \tag{7.4}$$

with $\eta_{a,ins,max}$ the maximal efficiency achieved with only a disturbance of the flowfield in *axial* direction. The tangential component of the installation coefficient *is* dependent on the advance ratio:

$$\kappa_t(J_{iso}) = \left(\frac{\eta_{t,ins,max}}{\eta_{iso,max}} - 1\right)\frac{J_{iso}}{J_{iso,\eta_{max}}} \tag{7.5}$$

with $\eta_{t,ins,max}$ the maximal efficiency achieved with only a disturbance of the flowfield in *tangential* direction. The following regimes can be identified:

$$\kappa > 1 \qquad \text{higher propeller efficiency}$$
$$\kappa = 1 \quad \text{no change in propeller efficiency}$$
$$\kappa < 1 \qquad \text{lower propeller efficiency}$$

with the efficiency based on the freestream velocity, V_∞. To illustrate the applicability of the installation coefficient, the propeller performance is computed for two theoretical inflows, shown in Fig. 7.4. Two curves are presented, corresponding to two blade pitch angles: $\beta_{0.7R_p} = 30$ deg and $\beta_{0.7R_p} = 45$ deg. The installation coefficient is determined from equations Eqs. 7.4 and 7.5 of one of the two blade angles, and subsequently applied to the isolated propeller curves at both blade pitches. The figures confirm that the corrected curves collapse to the curve of the installed propeller performance.

(a) Uniform axial disturbance, $\frac{u}{V_\infty} = 0.9$, $\frac{V_t}{V_\infty} = 0.0$ (b) Uniform tangential disturbance, $\frac{u}{V_\infty} = 1.0$, $\frac{V_t}{V_\infty} = 0.1$
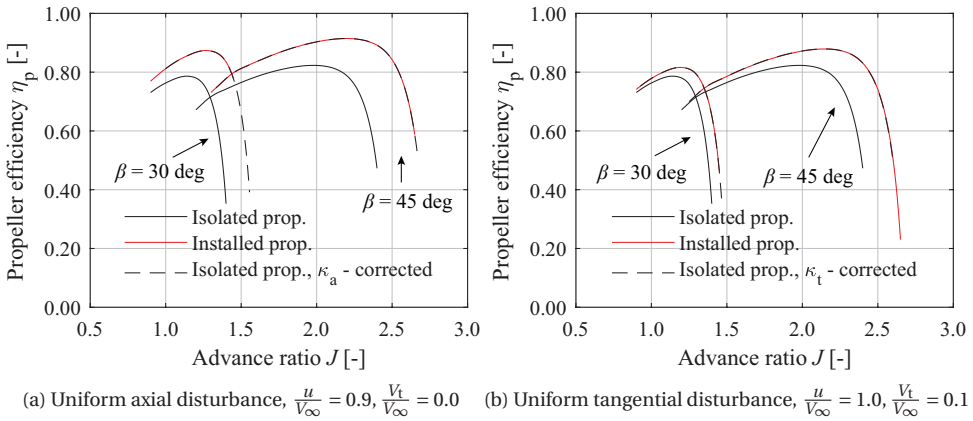
Figure 7.4: Illustration of the installation coefficient applied on efficiency curves using two theoretical inflows. Installed propeller data from the engineering method (Chapter 5).

For a more complicated inflow, the example of a tip-mounted propeller is taken (Section 7.5), where the inflow contains both axial and tangential disturbances. In line with the flowchart in Fig. 7.5, κ_a and κ_t are computed separately. In case the axial and tangential contributions cannot be separately determined, for example when the $\Delta\eta$ is determined in a complex experimental setup, the most important component can be identified to arrive at a reasonable prediction for the other advance ratios as well. As will be shown in subsequent examples, the κ_a is dominant for most cases, unless the in-plane velocity gradients $\frac{dw}{dy}$ and/or $\frac{dv}{dz}$ vary over the disk, for example for a flow that contains a swirl component. The application of κ_a and κ_t is shown in Fig. 7.6a and 7.6b. Since the axial and tangential contributions are superimposed, also the combined curve in Fig. 7.6c coincides with the computed curve.
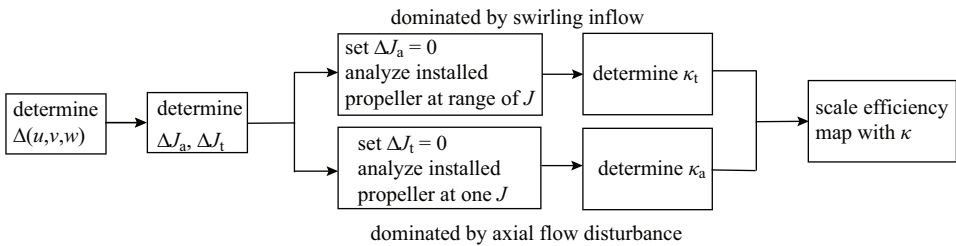

Figure 7.5: Flow diagram to determine installation coefficient for an arbitrary inflow.

(a) Only swirl contribution, $\frac{u}{V_\infty} = 1$ (b) Only axial contribution, $\frac{V_t}{V_\infty} = 1$ (c) Both swirl and axial contribution
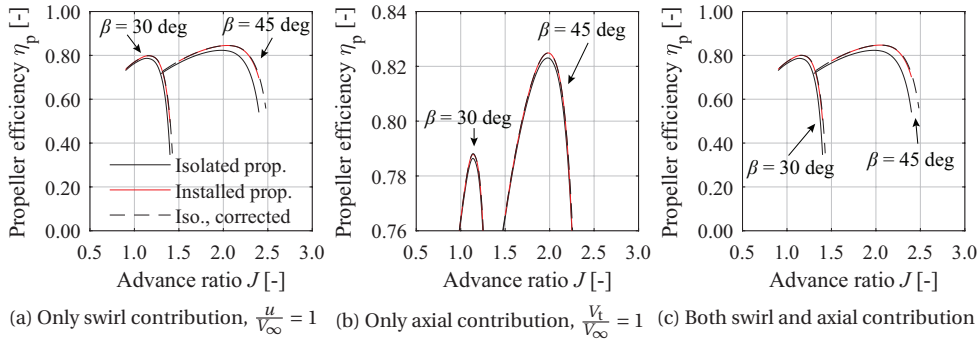
Figure 7.6: Illustration of the installation coefficient applied a practical example of a tip-mounted pusher propeller (Section 7.5). Installation coefficient determined for $\beta_{0.7R_p} = 45$ deg, and applied to propeller data for both blade angles.

These examples demonstrate that indeed an installation coefficient can be used to scale the propeller curves. Therefore the following can be formulated:

For a given propeller design, nonuniform inflow can be represented by a factor κ such that the efficiency curve of this uninstalled propeller is scaled along the J and η_p directions by κ to obtain the installed propeller efficiency.

If the maximum efficiency is to be achieved for a certain thrust coefficient by adapting the blade pitch, no further analyses are required to obtain that efficiency curve. The computational intensive analyses to find the optimum blade angle for the installed cases is therefore redundant. The formulation of this coefficient is therefore highly valuable to the aircraft designer. Using the data of the isolated propeller for an arbitrary blade angle, the following can immediately be identified:

- The advance ratio at which the installed case has highest efficiency

- The maximum efficiency of the installed case

Furthermore, by observing that the installed configuration is a variation of the uninstalled condition, the following can be observed from the definition of κ:

- For a given inflow disturbance, the largest effect is achieved at high advance ratio, i.e. cruise conditions

- An axial disturbance results in a benefit/loss in efficiency as a fraction of η_{iso}

- A tangential disturbance results in a benefit/loss in efficiency that is linearly increasing with J

- Any benefits/losses on the maximum efficiency will be more pronounced for large blade pitches

However, since the coefficient essentially describes the difference in momentum in the flowfield relative to the isolated condition, it does not reveal how the propeller loading is altered due to the installation. The unsteady loads and in-plane forces are therefore not reflected by this coefficient.

7.3. CASE 1: PROPELLER INSTALLATION UPSTREAM AND DOWNSTREAM WING

Figure 7.7a depicts a conventional tractor-propeller and pusher-propeller in the proximity of a wing. For positive lift coefficients, the wing's bound circulation induces an upwash and downwash upstream and downstream of the wing, respectively. Additionally, there is a reduced axial velocity at these locations, while downstream there is also a velocity deficit in the wake. Figures 7.7b and 7.7c depict these characteristic flowfields for a spanwise location of 40% of the semi-span, and at half a chord from the leading and trailing edges. From these flowfields it becomes clear that the vertical separation between propeller and wing chord line, as well as the diameter, are key parameters that determine the inflow and consequently the propeller forces.

(a) Schematic (to scale) of z-variation.

(b) Velocity distribution, $\Delta u / V_\infty$.
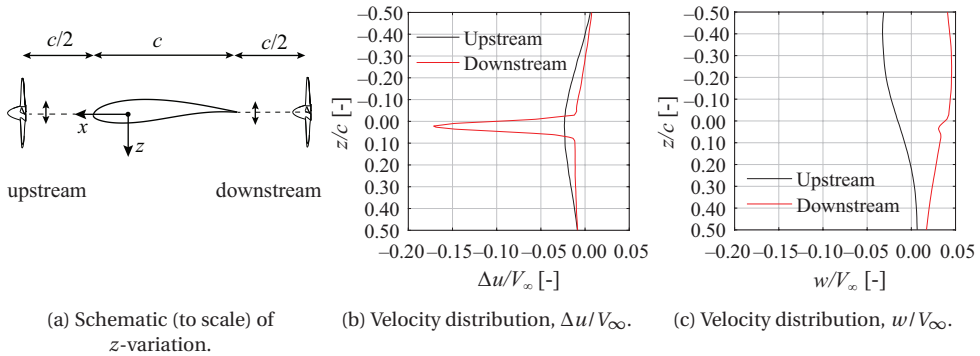
(c) Velocity distribution, w / V_∞.

Figure 7.7: Definition of the propeller upstream/downstream of a wing. The flowfields in (b) and (c) are along a surveyline at $c/2$ upstream of leading edge and at $c/2$ downstream the wing trailing edge, $2y/b = 0.4$.

For these upstream and downstream locations, the lower axial inflow relative to freestream velocity directly leads to an increase of the maximum efficiency that can be achieved for a given blade angle, as shown in Fig. 7.8a. The figure shows a moderate dependency of the efficiency on the z-location. Since the velocity profiles upstream of the wing are smooth in z-direction, so are the changes in the propeller efficiency. Downstream of the wing, the velocity deficit is confined to a small region, and consequently the effect of the vertical location of the propeller relative to the wing is more pronounced. The maximum $\Delta \eta_p$ does not correspond to the location where the axial velocity is lowest. This small offset is directly caused by the 'donut effect', as discussed in Section 6.1. Since the efficiency benefit is a fraction of the efficiency in isolated conditions, the efficiency

gains are smaller for $\beta_{0.7R_p} = 30$ deg, as indicated in Fig. 7.8a.

By definition, the installation coefficient follows the same trend as η_p, shown in Fig. 7.8b. By the separately determining κ_a, Fig. 7.8b reveals that $\kappa \approx \kappa_a$. The in-plane velocity components have a negligible effect on the efficiency. This figure directly indicates that the optimal efficiency increases by a factor 0.0 to 0.03, depending on z_p, and the optimal advance ratio increases by the same factor. Since the installation coefficient is larger than unity, for the full range of T_C, there is a net efficiency benefit. This is shown in Fig. 7.8c for the upstream propeller at $z/R_p = 0$. Therefore, there is a net benefit independent of the flight condition. Figure 7.8d also shows that the optimal thrust coefficient reduces relative to the optimal T_C in isolated conditions. Depending on z-location, these optimal values reduce with up to 5%, indicating that either a larger disk area to fulfil a thrust requirement at maximum efficiency, or a lower blade pitch angle is required if the thrust coefficient is to be maintained.
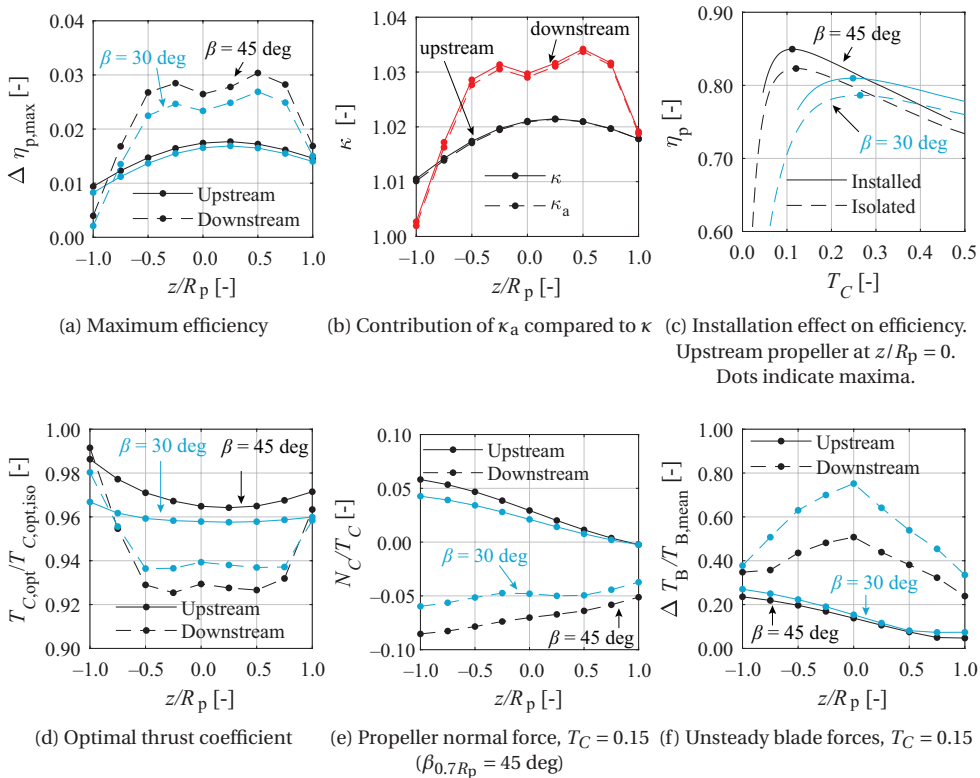

(a) Maximum efficiency

(b) Contribution of κ_a compared to κ

(c) Installation effect on efficiency. Upstream propeller at $z/R_p = 0$. Dots indicate maxima.

(d) Optimal thrust coefficient

(e) Propeller normal force, $T_C = 0.15$ ($\beta_{0.7R_p} = 45$ deg)

(f) Unsteady blade forces, $T_C = 0.15$

Figure 7.8: Installation effect of a propeller at $0.5c$ upstream or downstream of a wing. Propeller diameter is $D_p/c = 0.5$, and $\beta_{0.7R_p} = 45$ deg.

The efficiency gain of nearly 2% for the upstream propeller also comes with a net lift benefit caused by the upwash: the normal force is approximately 5% of the thrust force (Fig. 7.8e), and will increase with higher lift coefficients. For a given lift-to-drag ratio

of the airframe at the current lift coefficient, it would increase by $\Delta \frac{C_L}{C_D} = 0.05$, in case thrust equals drag. On the other hand, a downstream propeller generates a downforce of 10% of the thrust (larger than the lift-force of the upstream propeller because of the larger downwash than upwash). Consequently, the lift-to-drag ratio would decrease due to this downforce by 0.1. Comparing the increase in η_p by 4% to this change in L/D, the net benefit disappears when $L/D \leq 2.5$. The gain in efficiency will therefore compensate the reduced L/D for the pusher configuration. The normal force for $\beta_{0.7R_p} = 30$ deg is smaller than $\beta_{0.7R_p} = 45$ deg, since the normal force gradient is smaller [60].

Besides the installation effect on efficiency, also significant unsteady loads are introduced since the inflow is nonuniform. Figure 7.8f shows that in particularly the wake that is encountered by the propeller introduces unsteady loads that are a factor two to four larger than the ones for the upstream propeller. The figure also confirms that for the upstream propeller, a lower mounting reduces the unsteady loads quite considerably as the result of a more uniform inflow, particularly due to a lower w/V_∞ (Fig. 7.7c).

In Fig. 7.9a the portion of the nonuniform inflow that is encountered by the disk is altered by varying the propeller diameter. Since the upstream location is $0.75c$ to the bound vortex at the quarter chord, the variation of the upwash and axial velocity in z-direction is relatively small. The dependency of efficiency on diameter are therefore small as well, with the deviations to undisturbed condition approaching zero for $D_p/c \gg 1$. However, since the efficiency of the downstream propeller is particularly altered due to the wing wake, the smaller the disk, the larger the gain in efficiency (Fig. 7.9a).

(a) $0.5c$ upstream/downstream   (b) Installation coefficient   (c) Normal force, $T_C = 0.15$
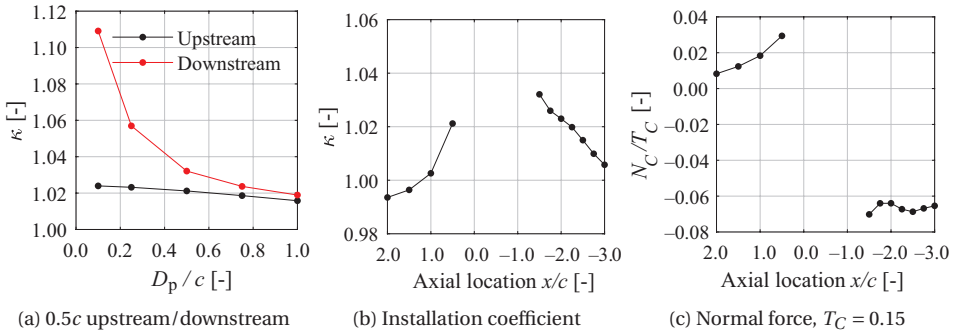
Figure 7.9: Effect of diameter and axial position of an upstream/downstream propeller at $z_p = 0$.

The effect of axial spacing to the wing is clearly depicted in Fig. 7.9b, showing a profound dependency of the installation coefficient with axial location. For the propeller mounted upstream of the wing, κ has a nonlinear character, due to the upstream blockage effect. To the contrary, downstream of the wing, the gain in efficiency is linearly decreasing. This is a consequence of first an acceleration of the potential-flow component of $\Delta u/V_\infty$ back to zero, and secondly the wake is being filled and its momentum deficit is diffused. Downstream of the wing, the normal force is partially introduced by the wake encounter, but primarily due to the downwash which does not vary significantly with x. The irregular normal force for the downstream propeller in Fig. 7.9c is

the result of the wake that is translating in z-direction, the upsweep of the aft-fuselage, and the downwash that is developing. Upstream of the wing, the normal force is more predictable, due to the bound vortex that causes the normal force to rise proportional to approximately $1/x$ for $x > 0$.

7.4. CASE 2: PROPELLER INSTALLATION OVER/UNDER-THE-WING

A propeller that is placed above a wing operates in the induced flowfield of the wing. Compared to the upstream or downstream installation where the induced flowfield can be represented by the bound vortex, for these propellers the circulation distribution that *varies along the chord* determines the propeller inflow. Although most novel configurations are mounted over-the-wing (OTW), the under-the-wing (UTW) configuration is of interest for the comparison as well.

The evaluated cases are schematically shown in Fig. 7.10a, also indicating a selected tip clearance. At a spanwise location of $2y/b = 0.4$ ($c_l = 0.29$), the axial and in-plane velocity profile at three chordwise locations are depicted in Figs. 7.10b and 7.10c. Except towards the trailing edge, the velocity profiles show a strong negative gradient in y' direction. This already indicates that besides the chordwise location, the diameter is a key parameter that determines the changes in propeller performance.

(a) Schematic of x-variation. To scale for $R_p/c = 0.2$.
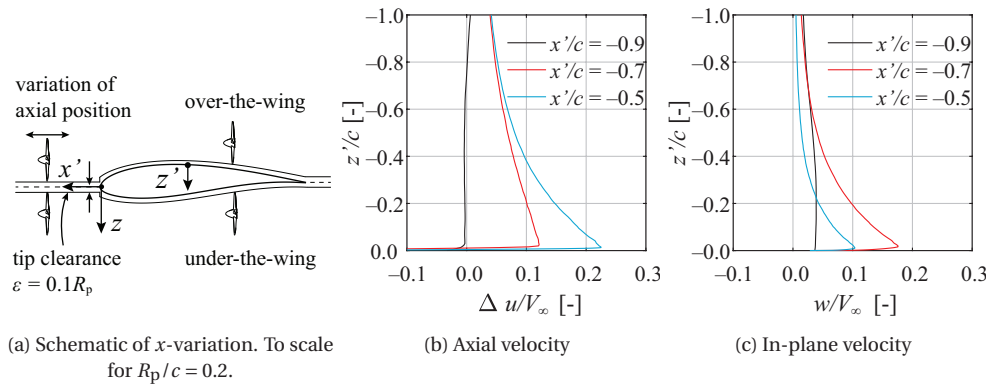
(b) Axial velocity

(c) In-plane velocity

Figure 7.10: Definition of propellers located above/below the wing with a tip-clearance of $0.1R_p$ in (a). Examples of the flowfield above the chord at $2y/b_w = 0.4$ are provided in (b) and (c).

Upstream of the leading-edge, for both above and below the wing installations, the installation coefficient is larger than unity, caused by the blockage induced by the wing, as shown in Fig. 7.11a. Further downstream, the wing causes the majority of x_p/c to lead to $\kappa < 0$ (and therefore lower efficiency), and is not constant since the inflow varies along the chord. The largest reduction of efficiency is achieved close to the quarter-chord location. As shown in Fig. 7.11b, this can almost completely be attributed to the axial flow perturbation, since $\kappa \approx \kappa_a$. The over-the-wing installation only causes an efficiency benefit for $x/c < 0.9$. This is caused by the pressure recovery and slightly lower axial velocity

than freestream condition.

(a) Installation coefficient

(b) Installation coefficient, κ_a contribution

(c) Effect for over-the-wing installation on efficiency. Dots indicate maxima.

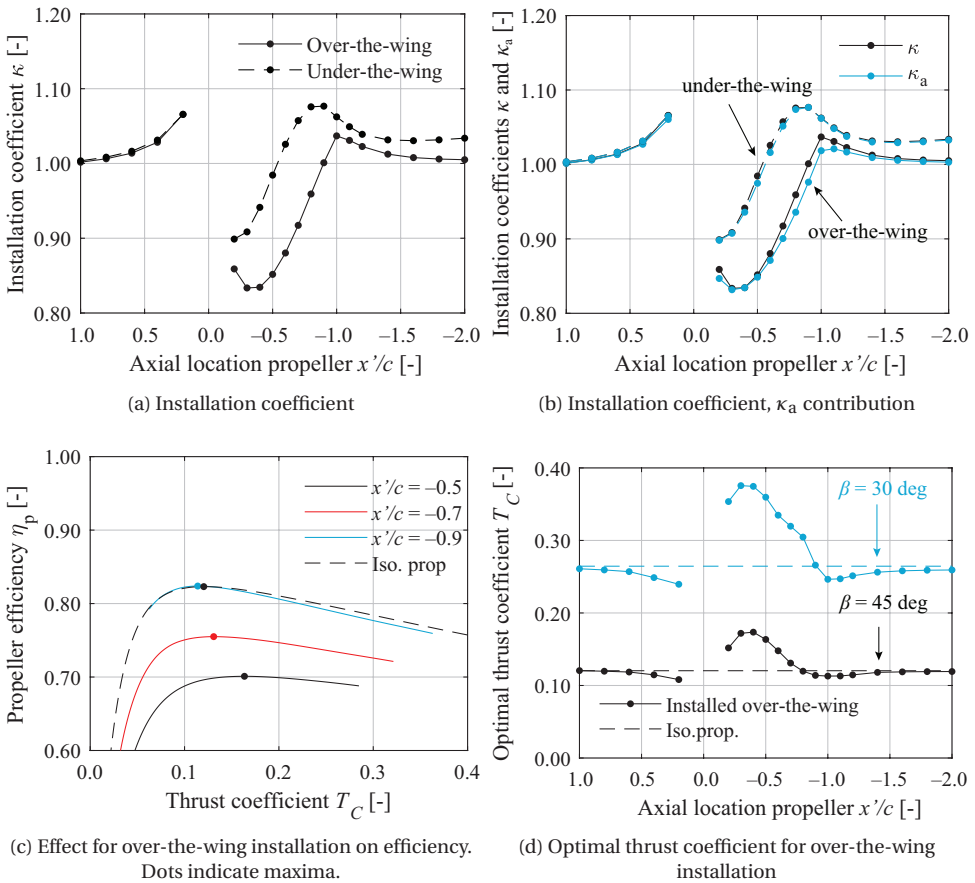(d) Optimal thrust coefficient for over-the-wing installation

Figure 7.11: Installation effect on a propeller above or below the chord line. Tip-clearance is $0.1R_p$, $D_p/c = 0.2$.

As the installation coefficient is significantly influenced, so is the efficiency curve as a function of thrust coefficient, as shown in Fig. 7.11c. Again, because $\kappa < 1$, the effective advance ratio experienced by the propeller is higher, and therefore the disk loading is to be increased to achieve the highest efficiency for a given blade pitch. For a constant T_C the blade angle is to be reduced, or alternatively, the thrust coefficient to be increased according to Fig. 7.11d while maintaining the blade pitch.

Although the in-plane velocity has nearly no effect on the installation coefficient, it does introduce a significant in-plane force, as depicted in Fig. 7.12a. A propeller below the wing experiences, on average, a positive angle-of-attack, causing a positive contribution to the aircraft lift. On the contrary, the over-the-wing propeller displays a negative lift force of $0.3T$ if it is located around 70% of the chord. This negatively affects the system L/D ratio. Since the in-plane flow is most disturbed for the over-the-wing installation,

the unsteady loads are also largest for this installation case, shown in Fig. 7.12b. The observed fluctuations are maximal around $x'/c = -0.7$ and are an order of magnitude larger than for the under-the-wing installation.

(a) Normal force, $T_C = 0.15$ (b) Unsteady blade thrust, $T_C = 0.15$, $\beta_{0.7R_p} = 45$ deg
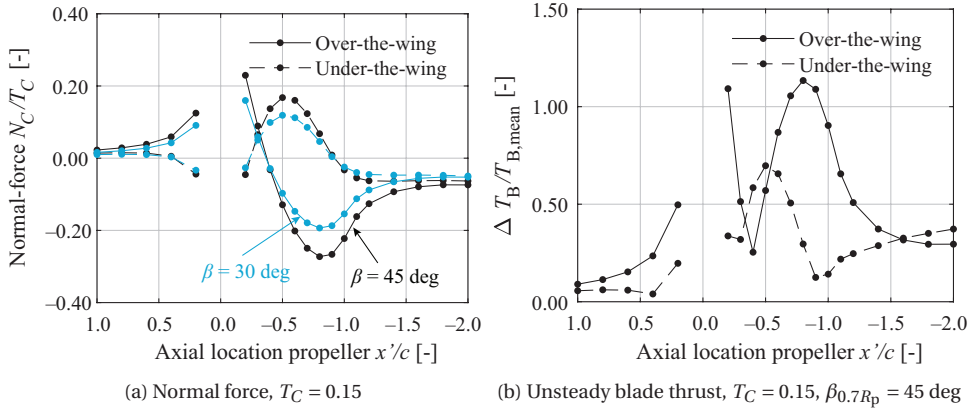
Figure 7.12: Effect of axial position of a propeller above or below the chord line. Tip-clearance is $0.1R_p$, $D_p/c = 0.2$.

Since the velocity varies significantly in the vertical direction, the diameter is an important design variable. Figure 7.13a shows that κ approaches unity if the diameter becomes large compared to the chord, in line with the observed velocity profiles. The performance penalty is therefore relatively large for low diameter-to-chord ratios. The figure also indicates that the sensitivity to diameter varies along the chord; a direct result from the particular inflow profiles.

(a) Installation coefficient   (b) Normal force, $T_C = 0.15$ (c) Unsteady blade thrust, $T_C = 0.15$
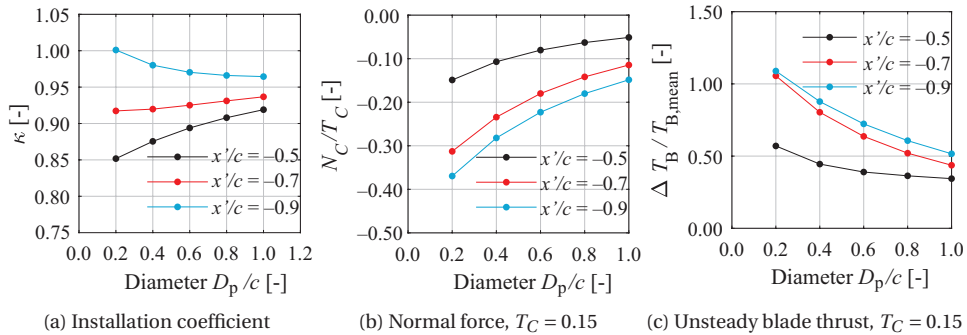
Figure 7.13: Effect of diameter position of a propeller ($\beta_{0.7R_p} = 45$ deg) above the wing at with a constant tip-clearance of $0.02c$.

The normal force (Fig. 7.13b) reduces with larger diameter-to-chord ratios, since the local flow angle approaches zero far from the wing's surface. For the same reason, the unsteady loads are also reducing with larger disk area, as shown in Fig. 7.13c. The

installation penalties are therefore maximal for an array of over-the-wing propellers with a small tip-clearance and a low diameter-to-chord ratio.

Because the lift coefficient varies along the span, it can be expected that the performance of an over-the-wing propeller depends on the spanwise location. For comparison, the (unswept) quarter chord location is selected as baseline and the spanwise location of the propeller is varied along this line, schematically shown in Fig. 7.14a. For the selected angle of attack of $\alpha = 0$ deg, the sectional lift coefficient has a maximum of approximately 0.3 at the wing-fuselage junction, and reduces towards the wing tip (Fig. 7.14b). Two types of diameter variations are chosen: a constant diameter based on the mean-aerodynamic chord ($D/\bar{c} = 0.2$), and a varying diameter with a constant ratio of $D/c(y) = 0.2$. For these two cases, the installation coefficient exhibits a comparable trend (Fig. 7.14c). The largest installation effect occurs towards the wing-fuselage junction and a reducing penalty in η_p towards the wing tip. The constant-diameter case, the efficiency penalty becomes smaller towards the tip, since in Fig. 7.13a it is shown that a larger diameter leads to a smaller installation effect, because in a relative sense, the propeller experiences less distorted inflow.
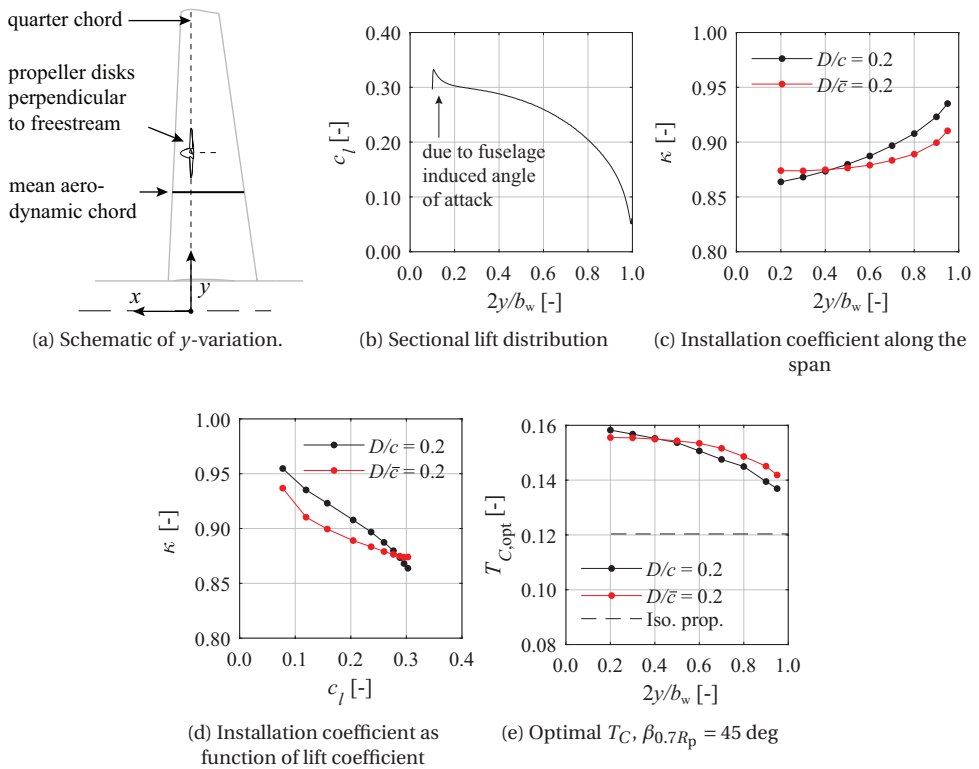

(a) Schematic of y-variation.

(b) Sectional lift distribution

(c) Installation coefficient along the span

(d) Installation coefficient as function of lift coefficient

(e) Optimal T_C, $\beta_{0.7R_p} = 45$ deg

Figure 7.14: Effect of spanwise position of an over-the-wing installation. Tip-clearance: $0.1R_p$, $D_p/c = 0.2$.

When κ is plotted against local lift coefficient (Fig. 7.14d), there is no clear trend for the $D/c(y) = 0.2$ case. Although not shown in the graph, at $c_l = 0$, there is still a $\kappa < 1$

as the airfoil has a finite thickness which leads to a higher axial velocity at the propeller plane due to the displacement of the streamlines. At nonzero lift coefficients, the effect of circulation starts to dominate, which makes the $c_l - \kappa$ curve nonlinear.

As expected, the optimal thrust coefficient also varies along the span, shown in Fig. 7.14e. The decreasing κ towards the root explains the trend for the optimal thrust coefficient, . If an array of propellers is to be installed along the span, ideally, these would either have a different blade pitch, or a different diameter, such that each could still operate at its maximum efficiency point in cruise in case the propellers are sized such that the operating point corresponds to a thrust equals drag balance.

7.5. Case 3: Pusher Propeller Mounted to the Wingtip

A pusher propeller that is mounted to the tip of a wing operates in the flowfield induced by the wing tip-vortex and the bound vortex, and in the wing wake, with the objective of high propeller efficiency caused by the swirling inflow [36]. Several authors have confirmed the propeller efficiency benefit [57, 190]. A comprehensive analysis of the unsteady blade loads, the shift in the propeller efficiency curve, and the dependency of diameter and vertical position on these performance indicators is not known from literature.

The configuration assessed herein is schematically shown in Fig. 7.15a. A spacing between the propeller plane and the wing trailing edge is selected as half the chord of the tip section. The propeller disk is at $\alpha = 0$ deg, and the baseline configuration has the rotation axis aligned with the trailing edge ($z_\mathrm{p}/z' = 0$). Figure 7.15b depicts the typical flowfield at the propeller plane, consisting of an axial disturbance primarily caused by the wing wake, and in-plane contributions that are induced by the wing-tip vortex and the bound vortex. It is noted that in case the nacelle installation is modelled, the flowfield would be redistributed due to the displacement effect of the nacelle such that at the propeller disk the tangential flow field is more outboard and the magnitude is reduced. It is shown in e.g. Ref. [109] that the change in axial force on the spinner is not negligible compared to the propeller thrust. This component is omitted in this analysis. The performance benefit in this case is therefore illustrative for such configuration. The asymmetry in the flow field leads to periodic blade loading and in-plane forces. From this flowfield, it is clear that the propeller diameter, its spanwise and vertical location affect the propeller performance.

The swirl in opposite direction to the propeller rotation increases the installation coefficient, shown in Fig. 7.16a. It is noted that since the lift coefficient is relatively low, the velocity deficit in the wing's wake therefore plays still a moderate contribution, as indicated by κ_a, especially for small propeller diameters. For higher lift coefficients, the in-plane velocity distribution will further dominate the performance benefit.

The trend of lower κ_a for larger diameter is a consequence of the reducing portion of the disk that encounters the wake. The trend of lower κ is the cause of two phenomena. First, the most sensitive blade sections ($r/R_\mathrm{p} = 0.85$, see Fig. 5.4) operate further from the region of highest swirl, which is close to the wing tip. Second, the overall swirl relative to the propeller slipstream becomes smaller with larger diameter, since the tip-
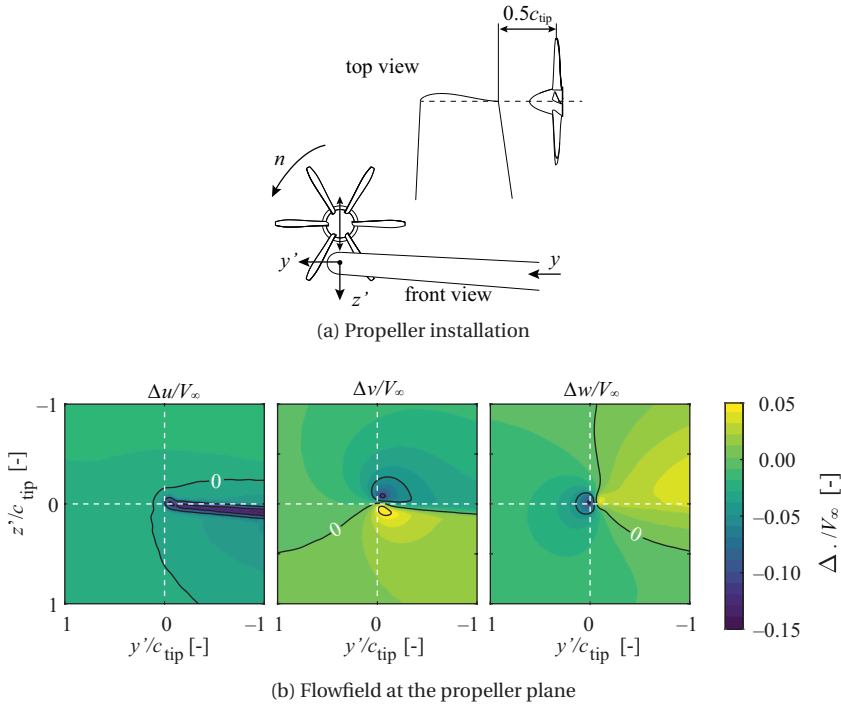
(a) Propeller installation

(b) Flowfield at the propeller plane

Figure 7.15: Schematic and inflow of the tip-mounted pusher-configuration.

7

vortex strength remains constant. For large diameters, part of the disk even experiences nearly undisturbed conditions, since the tangential velocity caused by the tip vortex has approximately a $1/r$ character. Therefore, not only $\kappa_a \to 0$ for $D_p \gg c_{tip}$, so is κ_t. However, these figures also show that even for a propeller that is not designed for the strong varying inflow along the radius, a moderate performance benefit can be achieved, even at an aircraft lift coefficient of $C_L = 0.23$.

Again, since the installation coefficient is above unity, the optimal thrust coefficient is slightly reduced compared to the isolated propeller. This effect is depicted in Fig. 7.16b for two blade angles. For large diameters, the installation effect reduces, and therefore the optimal disk loading approaches the one for the isolated propeller (Fig. 7.16c).

Contrary to the propeller efficiency, the normal force relative to the propeller thrust is only weakly dependent on diameter. The sign of this normal force is negative, as the upgoing blade side experiences a higher torque. This is in line with the finding in Ref. [57], where it was shown that at $\alpha = 0$, the propeller has a small negative contribution to lift. The primary causes of the normal force are first the presence of the wake on one side of the disk, and second, the larger downwash that spans between the fuselage and the wing tip. These two contributions lead to higher torque on the inboard side of the disk, hence a negative normal force is generated. In line with earlier discussions, the normal force for a low blade angle ($\beta_{0.7R_p} = 30$ deg) is low due to the lower projected disk area and the higher advance ratio for the same thrust coefficient. This normal force

negatively contributes to the system lift-to-drag ratio, and partially offsets the efficiency benefit for the propeller.

(a) Installation coefficients κ_a and κ

(b) Efficiency, $D_p/c_{tip} = 1.0$

(c) Optimal thrust coefficient

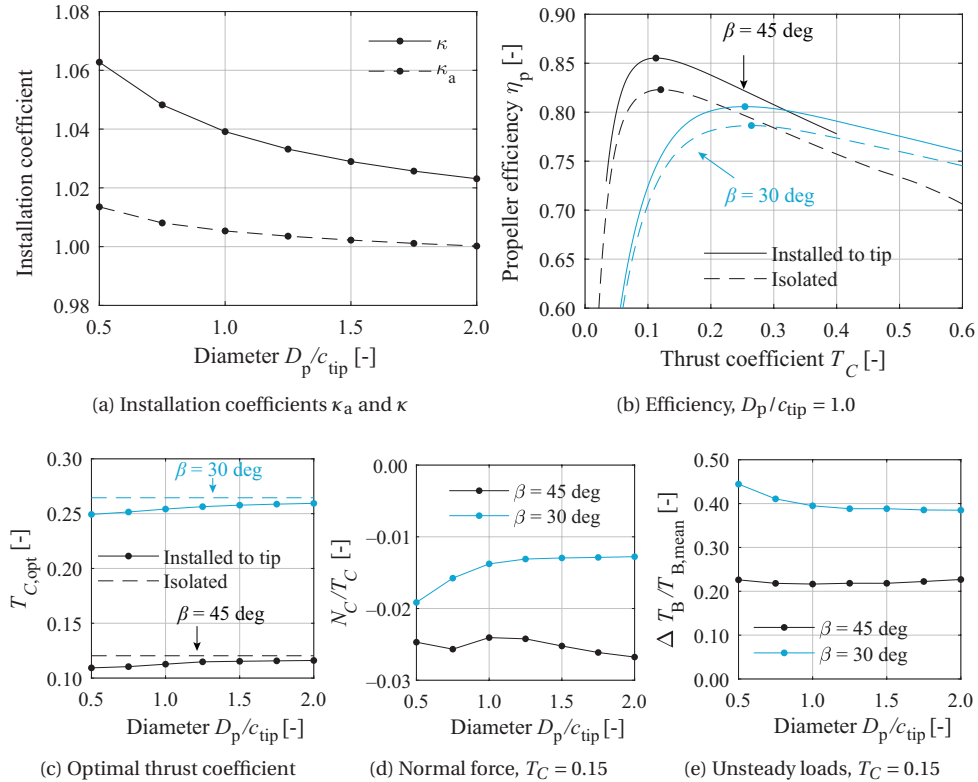(d) Normal force, $T_C = 0.15$

(e) Unsteady loads, $T_C = 0.15$

Figure 7.16: Effect of tip-mounted installation on the propeller performance, $z_p/z_{tip} = 0.0$.

Finally, to illustrate the sensitivity of the propeller location on its performance, the z-location is varied in Fig. 7.17 for $D_p/c_{tip} = 1.0$. Since the propeller is installed downstream of the tip, the wake and tip-vortex have been translated in z-direction as well, also observable in Fig. 7.15b. This causes the installation coefficient to be maximal for a propeller that is installed slightly below the wing plane, as depicted in Fig. 7.17a. For the normal force, this is also the case (Fig. 7.17b), but to a much lesser extent. This is explained by the v-component of the velocity that is also producing an in-plane force, but opposite to the one generated by the wing downwash and wake. Since it is a combination of these, it is also more sensitive to the vertical location. The same trend from switching sign of the normal force is observed in Ref. [109] for a propeller that operates behind another propeller where the two rotation axes are not aligned.
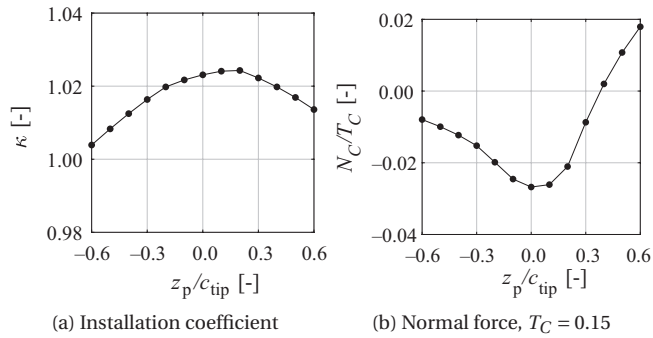
(a) Installation coefficient

(b) Normal force, $T_C = 0.15$

Figure 7.17: Effect of vertical location of the propeller relative to the wing tip, $D_p/c_{tip} = 2.0$.

7.6. Case 4: Propeller Mounted to the Rear Part of the Fuselage

A propeller that is positioned at the aft fuselage operates in the boundary layer of the fuselage, the wakes of the vertical and horizontal tailplane, the fuselage-induced upwash, and the wing-induced downwash. This complex flowfield is shown for the *VGM-HTP* model in Fig. 7.18. In this case, a small clearance is selected to the end of the fuselage, since the tail surfaces are no adapted to install the propeller closer to the fuselage. For a diameter equal to the fuselage diameter, a strongly varying flowfield is encountered by the propeller, with both in-plane and out-of-plane velocity components. This case represents a more realistic case than an axisymmetric inflow (e.g. [56, 59]).

The two design variables that are considered herein are the vertical location and the propeller diameter to demonstrate the variation of the nonuniformity of the inflow over the disk. Figure 7.19 depicts the dependency of the key propeller performance indicators on diameter, normalized with the fuselage diameter. It is clear from Fig. 7.18b that the fuselage wake is approximately contained within $0.5R_{fus}$, while outside this radius, the wakes of the tail are the dominant source of disturbance. The installation coefficient is significantly increased, particularly for small propellers, shown in 7.19a. Benefits of over 30% are registered if the propeller is of the size of the fuselage wake. This also leads to propeller efficiencies close to unity. It is noted that larger propeller efficiency benefits can be obtained if the blade pitch distribution is adjusted to account for the strong inflow variation along the radius, as demonstrated in Ref. [56]. The values presented in Fig. 7.19 are in line with the findings in e.g. Refs. [56, 58, 59, 201, 209, 235–237].

The upsweep angle of the fuselage introduces an upwash to the propeller. The associated normal force reduces with diameter, since the compensating wing-induced downwash becomes more prominent when the diameter increases. The unsteady loads are also maximal for small propeller diameters, since the main disturbances are introduced within the fuselage wake, as shown in Fig. 7.19c. Besides the beneficial contribution of the propeller to lift, the normal force also introduces a nose down pitching moment. This seemingly positive contribution to L/D is likely to cause additional trim drag instead, in case this force component is not accounted for in the aircraft design.
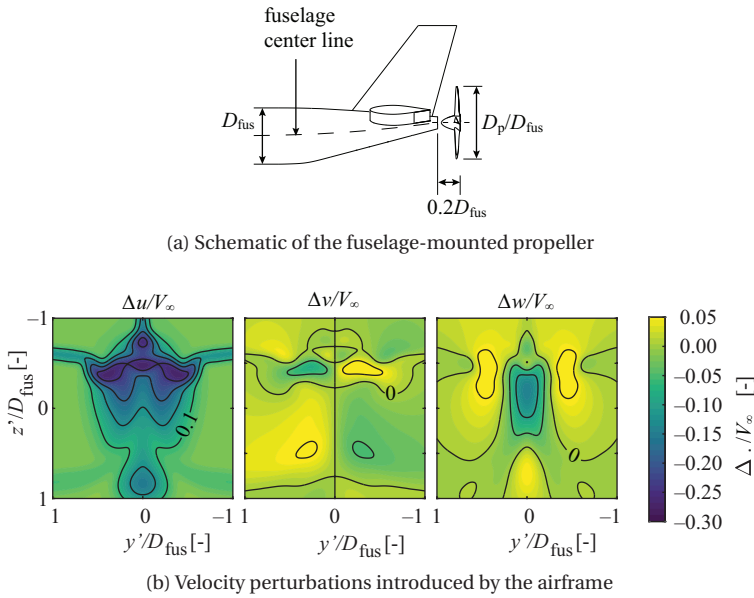
197

(a) Schematic of the fuselage-mounted propeller

(b) Velocity perturbations introduced by the airframe

Figure 7.18: Schematic and inflow of the fuselage-mounted propeller configuration.

(a) Installation coefficient

(b) Normal force, $T_C = 0.15$
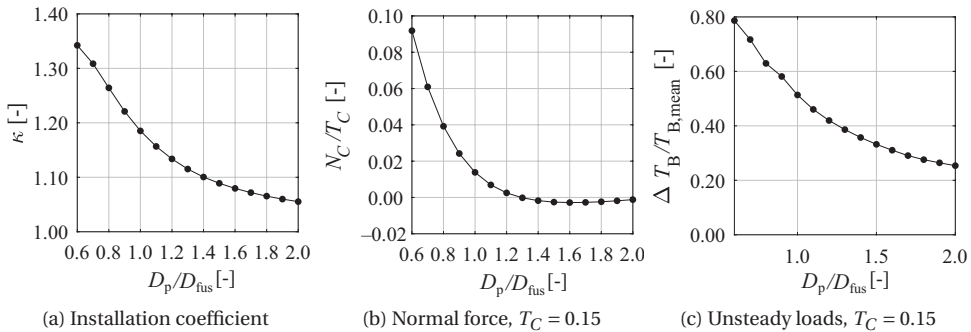
(c) Unsteady loads, $T_C = 0.15$

Figure 7.19: Change of the installation coefficient and propeller forces for the fuselage-mounted configuration.

7.7. CONCLUSIONS

In this chapter an approach has been presented where the installation effect of the airframe on the propeller is represented by a factor κ such that the efficiency curves of this propeller in uninstalled condition is scaled along the J and η_p directions by κ to obtain the propeller efficiency in the installed condition. This removes the need to asses a certain propeller design at different blade pitch settings and advance ratios. Only a limited number of analyses are required to determine this coefficient, which means a significant benefit in term of the number of computations to construct a propeller efficiency map.

Figure 7.20 provides an overview of the three performance indicators that have been computed for the various configurations. The range for each indicator depends on design choices, such as the propeller diameter, and location relative to the airframe. Since the numerical values are specific to the case assessed herein, the figure should be interpreted as a qualitative overview. An indicator with a narrow range implies that design choices have minimal impact on that propeller performance indicator. For those cases, the particular choice for propeller diameter or proximity to the airframe are motivated by other considerations, for example the performance of the airframe. It is noted that the performance benefit/loss for higher lift coefficients are likely larger than presented in Fig. 7.20, such that the spread of the performance benefit/loss becomes even larger. This also implies that off design conditions, e.g. high lift conditions, would lead to large performance changes compared to the isolated case. Furthermore, the propeller behind the fuselage encounters a quite significant wake from the fuselage. At Reynolds numbers that are more representative for cruise condition, this performance benefit would be reduced. On the other hand, a dedicated propeller design to operate in the distorted flowfield (in particular for the installations to the tip and behind the fuselage) would increase the installation coefficient [56].
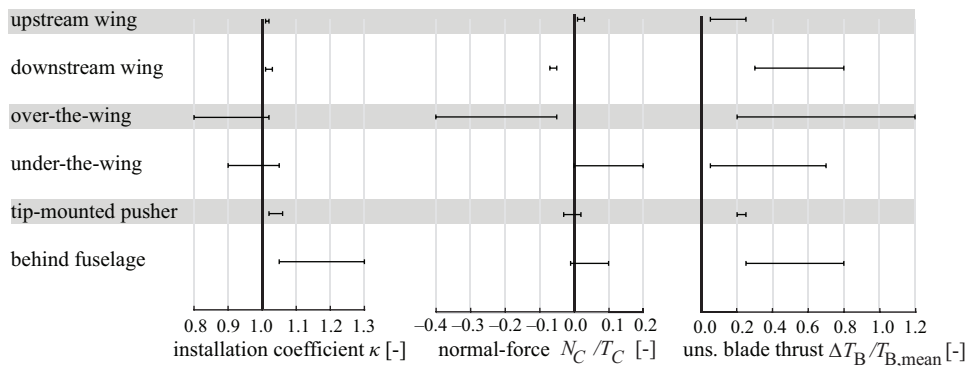

Figure 7.20: Comparison of propeller performance between the different configurations. Changes in airframe performance are not included in this comparison.

The findings of the previous sections are summarized as follows:

- **Upstream/downstream of wing:** The blockage effect of the wing slightly enhances the installation coefficient. The small values indicate that the benefit should not be the main objective for this installation. The upwash in front of the wing enhances the normal force, while the downwash leads to a down force on the propeller. Both upwash and downwash lead to unsteady blade loads. For the propeller behind the wing, the unsteady loads are more pronounced due to the wake that is encountered, in addition to a larger downwash.

- **Over-the-wing/under-the-wing:** The higher axial inflow leads to significant reduction in installation coefficient. This reduction strongly depends on chordwise location. The over-the-wing installation also leads to a significant downforce on

199

the propeller, contrary to the under-the-wing installation, which produces a lift force. Due to the strong varying velocity profile normal to the airfoil's surface, these installations lead to the largest unsteady loads of all configurations. The diameter is a key parameter that influences the propeller performance.

- **Tip-mounted pusher:** A moderate increase of the installation coefficient is caused by the tangential velocity of the wing-tip vortex. A small normal force is produced, depending on the vertical location of the propeller. The presence of the wake and downwash on the inboard side of the disk leads to moderate unsteady blade loads, which are nearly independent of diameter.

- **Behind fuselage:** The momentum deficit in the fuselage wake significantly increases the installation coefficient, particularly for small propellers. The fuselage-induced upwash dominates the in-plane velocity, leading to a net lift force on the propeller. This component vanishes if the diameter is increased, approaching a normal force close to zero. The highly distorted flowfield introduced by various airframe components leads to large unsteady loads. These decrease with increasing propeller diameter.

Again, the findings presented in this chapter are only related to the propeller performance, without taking the potentially (un)favourable effect of the installation on the airframe lift-to-drag ratio. The identified losses in propeller efficiency are therefore to be compensated by a favourable effect of the propeller on airframe components, for example for the over-the-wing installation.

7

8

AERODYNAMIC RESPONSE OF LIFTING SURFACES DUE TO A PROPELLER SLIPSTREAM

8.1. INTRODUCTION

In the previous chapters numerous effects are addressed that are relevant for the propeller when it is mounted in proximity to the airframe. This chapter discusses the effects of propellers on lifting surfaces that have particular relevance for unconventional propeller installations. This entails configurations where the propeller loading is nonuniform, are mounted near the stabilizing surfaces, or are mounted in such way that the slipstream affects the stabilizing surfaces, for example if the propellers are mounted to the inboard part of the wing. The scope of this chapter is limited to tractor propeller installations where part of the lifting surface encounters a propeller slipstream. It is shown in Ref. [98] that if the propeller is two diameter-to-chord ratios away from the trailing edge of a wing upstream of the propeller, the propeller-induced effect on the wing is negligible. For example, for a tail-mounted propeller configuration, this distance is large enough such that the upstream effect is limited to the propeller only. The presented findings will, in conjunction with the previous chapters, lead to the understanding of the installation effects on aircraft level, discussed in Chapter 9.

Contrary to a situation where a lifting surface is not near another aerodynamic surface, the flowfield induced by the propeller has a different magnitude and direction at every coordinate and is time-dependent. As will be shown in the following, the flowfield is strongly dependent on flight condition, i.e. angle of attack and propeller operating condition. The interaction between the propeller and lifting surface is relevant from aircraft performance, stability, control, and overall design perspectives in several ways, as can be deduced from typical effects that are extensively discussed in literature:

Parts of this chapter have been published in Refs. [119, 120, 133].

- *An offset and a higher slope of the $C_L - \alpha$ curve* [116, 238, 239]. Depending on the location of the lifting surface, this leads on aircraft level to a shift in the neutral point [64] and a change in pitching moment for a given angle of attack.

- A *modified downwash gradient* $\frac{d\epsilon}{d\alpha}$ depending on the interaction with the lifting surface (e.g. rotation direction) [14, 61, 62, 64, 160, 238]. Any lifting body downstream the propeller–wing combination experiences this altered flowfield. In some circumstances, the stabilizing contribution of the lifting surfaces is compromised.

- *More effective trailing edge devices*, i.e. a larger lift contribution due to a flap deflection, delayed flow separation, and more effective control surfaces [41, 64, 194].

- *Higher maximum lift coefficient* while approximately maintaining the angle of attack at which the maximum is achieved [38–41, 238].

- *Higher lift-to-drag ratio*, mainly caused by a reduction of induced drag depending on the flight condition, propeller location relative to the lifting surface, and rotation direction [36, 37, 45, 47, 48, 109, 116]. For a one-engine-inoperative condition or in case of a co-rotating installation, this also affects the yawing moment through a difference in drag on each side of the aircraft [173, 240].

Some of these known effects will be put into perspective on aircraft level in Chapter 9. Prior to the identification of the knowledge gap relevant for the propeller-installations considered in this dissertation, it is necessary to briefly revisit the typical interaction between a slipstream and lifting surface. Conceptually, as discussed in Chapter 2, a lifting surface submerged in a slipstream experiences a flowfield that entails:

- Regions of concentrated vorticity, i.e. the vortex cores

- Regions that can be modelled as potential flow, i.e. outside the vortex cores

- Regions where viscous forces dominate, i.e. the blade wakes

Although these characteristics cannot be fully separated since they are closely related, by separating them the interaction may be broken down into different mechanisms. A conceptual representation of the propeller flowfield relative to a lifting surface is shown in Fig. 8.1, indicating the four relevant regions that describe the interaction:

1. *Propeller loading and flowfield.* The flowfield can be described as a time-averaged distribution, with, on top of that, a time-dependent component, as discussed in Chapter 2. In Chapter 6 it is shown that the propeller loading generally is nonuniform as the result of installation. This leads to a nonaxisymmetric propeller vortex system and a nonuniform flowfield experienced by part of the lifting surface. A key observation that can be made is that the flowfield experienced by the lifting surface therefore also changes with flight condition, e.g. an angle of attack.

2. *Direct effect on lifting surface.* The local changes in dynamic pressure and angle of attack affect the lift coefficient and drag coefficient of the lifting surface. The loading is increased on the upgoing blade side, and reduced on the downgoing blade

side. In Chapter 2 it is shown that the relative location of the lifting surface to the slipstream is a key factor that determines the local flow quantities, together with the propeller incidence angle. Since the local flow angle is not aligned with the freestream, the direction of the resultant force vector changes, and therefore can change the section lift-to-drag ratios [37, 116]. Furthermore, since the slipstream turbulence level is on average higher than the freestream value (in particular in the tip-vortex region [241]), the skin friction is increased by influencing the transition location [110]. On top of that, the skin friction increases by the surface washed by the slipstream due to the higher dynamic pressure.

3. *Indirect effect on lifting surface.* Generally, only part of the lifting surface directly experiences the presence of the propeller and outside the slipstream it experiences the undisturbed flowfield. As is widely known, the surface of discontinuity does not split the wing into regions that are either 'disturbed' or 'undisturbed' [14], but instead the response is smeared in spanwise direction. The circulation along the full span is affected by the shed trailing vorticity that introduces an induced angle of attack to the lifting surface [37, 242]. A simplified representation of this is shown in Fig. 8.1. From the figure, it becomes apparent that the relative strength of the trailing vortices $\Gamma_{\text{root,p}}$, Γ_{I}, and Γ_{II} ultimately determine the induced angle of attack. The value of $\Gamma_{\text{root,p}}$ depends on the propeller operating condition J and T_C. On the other hand, Γ_{I} and Γ_{II} depend on the rise of Γ_{B}. Therefore, the ratios of $\frac{\Gamma_{\text{I}}}{\Gamma_{\text{root,p}}}$ and $\frac{\Gamma_{\text{I}}}{\Gamma_{\text{II}}}$ largely determine the net effect of the propeller on the downwash (gradient) and lift-curve slope of the lifting surface.

4. *Slipstream deformation.* The propeller vortex system deforms through two mechanisms. First, by encounter of the lifting surface, the vortex deforms through the no-slip boundary condition and the presence of the boundary layer [243]. Second, because the loading varies along the span, there is a spanwise flow component that shears the slipstream [37, 174]. This deformed slipstream not only has a different interaction with the lifting surface compared to an undeformed slipstream, it also affects the flowfield far downstream.
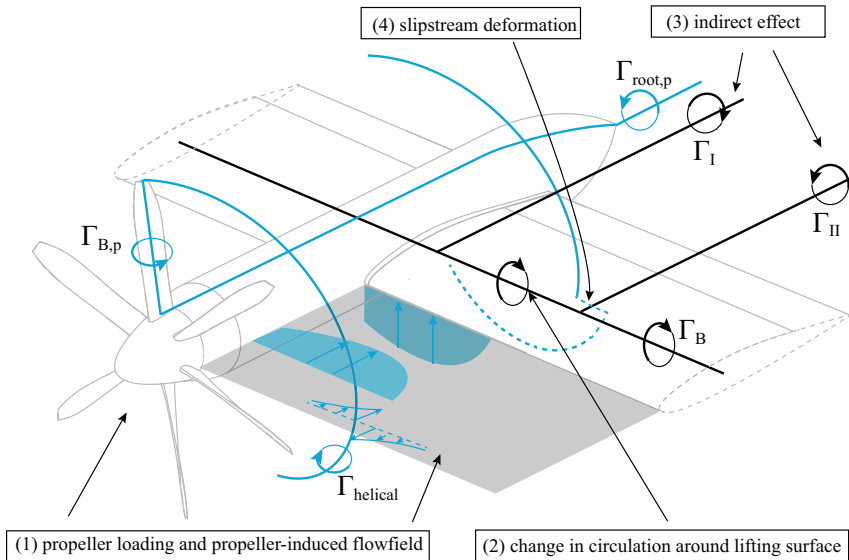
8

Figure 8.1: Simplified representation of a lifting surface submerged in a propeller slipstream with four major effects annotated.

Most of these fundamental interactions have been discussed in numerous publications. The analysis of a tractor propeller in close proximity with an aerodynamic surface has primarily been conducted for the wing-mounted propeller configuration, e.g. in Ref. [37]. The typical configuration that is studied is either a twin-propeller configuration, with propellers mounted on the inboard parts of the wing, or tip-mounted propellers. Existing studies on tip-mounted propellers (e.g Refs [36, 45, 47, 48]) have mainly focused on the efficiency benefits for wingtip-mounted propeller configurations. Limited work has been performed on pylon-mounted propellers, propellers mounted to the horizontal tailplane, or propellers mounted in a distributed propulsion layout.

Compared to wing-mounted propeller installation, there are a number of significant differences in the type and magnitude of aerodynamic interaction for these nontraditional propeller installations. Tailplane-mounted propellers interact with an aerodynamic surface which has a low aspect ratio and the propeller is relatively large compared to the tailplane span. The result is that the propeller affects a lift distribution which strongly varies in spanwise direction. As noted before, the relative strength of the vortex systems determines the trend of the integral forces. The magnitude of the propeller–tailplane interactions is therefore also influenced by an elevator deflection to change the tailplane loading.

For the tail-mounted configuration, especially the effect of propeller installation on the normal-force gradient of the tailplane is of interest. The mechanisms that cause the higher gradient are therefore required to be understood in order to interpret its contribution to aircraft stability. Since the gradient of the inflow directly affects the gradient of the force curve, the flowfield experienced by the aerodynamic surface should specifically

be analyzed. Subsequently, the further understanding of the flowfield will also be useful to understand the level of fidelity that is required in the analyses of propeller–wing systems. The key areas that currently are not sufficiently addressed in open literature are:

- The development of the flowfield experienced by the lifting surface inside and outside the slipstream

- The understanding what part of the airfoil with a trailing edge device is most affected by the slipstream

- The time-averaged and time-dependent interaction of a propeller that is relatively large compared to the chord of a low-aspect ratio lifting surface in its slipstream.

In this chapter, the following research questions are addressed:

- *RQ 8.1:* How does propeller installation affect the development of the flowfield that is experienced by the lifting surface?

- *RQ 8.2:* How do the presence of swirl, the rise of dynamic pressure, and the induced drag reduction affect the forces on a lifting surface that are relevant from a performance, stability & control perspective?

- *RQ 8.3:* What are the key aerodynamic phenomena that alter the normal-force curve of a nacelle–tailplane combination when (partially) submerged in a slipstream? How can this be explained by the vortex systems?

- *RQ 8.4:* What is the effect of the spanwise location of a propeller on the wing lift-to-drag ratio if the wing has a typical lift distribution?

Through a number of test cases, simulated using full-blade CFD setups as well as experimental setups, these areas are further explored with the objective of providing handles that are useful for 1) developing an understanding what level of modelling is required to capture the relevant effects, 2) support design choices, and 3) further development of knowledge on the interaction between the vortex systems of the propeller and lifting surface. Moreover, the test cases also provide insight in typical values and trends that can be expected, which may be useful for engineering problems. First, in Section 8.2 the flowfield that is experienced by the lifting surface is investigated in detail. Subsequently, Section 8.4 describes the time-averaged effect of the propeller installation by quantifying the fundamental mechanisms of induced drag reduction and swirl recovery. The same section also describes the flowfield downstream of a propeller–wing combination. Finally, the unsteady aerodynamic interaction is discussed in Section 8.5.

8.2. Installation Effect on Flowfields Experienced by Lifting Surfaces

The flowfield introduced by the propeller directly influences the forces on the lifting surface that is in its slipstream. When installed, this flowfield is no longer the flowfield that

exists when the propeller operates in isolation, and the interaction with a lifting surface is therefore affected by the installation. In this section, three cases are discussed of which an overview is given in Fig. 8.2.

The first case is a propeller at an angle of attack, which is a case that exists in a wide variety of installations. For example, for a wing-mounted case, the propeller loading is closely related to a propeller at angle of attack (see Section 7.3). The second case is a variation on the first, where the propellers are mounted to the horizontal tailplane. The change in the slipstream with angle of attack directly affects the loads on the tailplane, and therefore aircraft stability. The third case is an array of distributed propellers, where adjacent propellers influence the propeller loading and vortex field. This is in particular of interest for aircraft with leading-edge distributed propellers. Only flowfields downstream the propeller are investigated, in line with the remainder of the chapter where only tractor propellers are considered. The key question that will be addressed in this section is *RQ 8.1*, while the findings are also related to *RQ 8.3*.
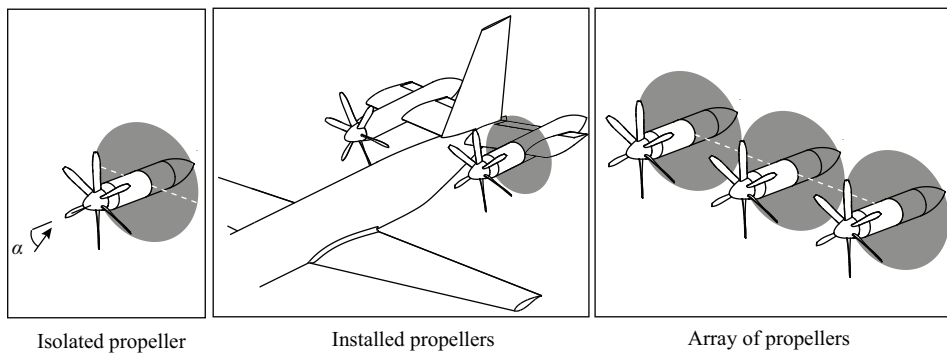

Isolated propeller   Installed propellers   Array of propellers

Figure 8.2: Examples of cases where the operating condition and interaction cause slipstream quantities to be a function of angle of attack.

8

8.2.1. EFFECT OF ANGLE OF ATTACK

The case of a propeller ahead of a lifting surface at angle of attack appears for a large range of aircraft configurations. In Chapter 6 it is shown that the load distribution is strongly varying in case of an angle of attack, which also indicates that the slipstream is affected. The effect of an angle of attack on the slipstream development is therefore especially relevant for the interaction with a lifting surface from both a modelling perspective and from a fundamental interaction perspective.

Historically, specific assessments of such a flowfield have often been performed in the light of vertical lift, including research on tilt rotors, helicopters, and other vertical take-off and landing (VTOL) vehicles [203]. In those cases, the slipstream location relative to the airframe varies significantly as a function of angle of attack. Recently, the ongoing developments of electrically driven VTOL aircraft (eVTOL) using unconventional propeller installations that undergo transition from hover to forward flight also require analyses of this flight condition.

For a propeller–lifting surface combination that operates at a lower angle of attack

($\alpha < 15$ deg), generally (part of) the lifting surface remains submerged in the slipstream, although the slipstream does not remain aligned with the rotation axis. In that case, both the slipstream location as well as the flow quantities within the slipstream that change with angle of attack are relevant. However, only few publications have reported on the development of the flowfield. An example of these works is Ref. [114], where the flowfield downstream of a turboprop are analyzed to provide guidelines on the most appropriate inlet location. The paper demonstrates that the effect of small angles of attack on a single-rotating and counter-rotating propeller are nonnegligible and indicate that it is a relevant case to be further understood. Even though only a limited number of locations within the slipstream were considered, the results show that the local flow angle is proportional to the geometric angle of attack. Up to $\alpha = 10$ deg, the gradient of the flowfield with respect to angle of attack at a given (x_p, y_p, z_p) location is approximately constant. This is a highly relevant observation, as it indicates that:

> *the lifting surface behind the propeller experiences a different angle-of-attack gradient than the freestream flow condition.*

Due to limited resolution and extent of the presented measurements, insight in the full flowfield is missing, as well as a quantification of the relative contributions of the nacelle and propeller. This knowledge gap is addressed in this section.

Before quantifying typical numerical values that can be expected for these gradients, a qualitative assessment of the slipstream deformation already provides an insight what trends can be expected. The difference in local angle of attack on each side of the propeller is the combination of various sources:

1. Slipstream deflection

2. Change of disk loading

3. Nacelle-induced flowfield

4. Slipstream deformation

Figure 8.3 schematically illustrates how the deflected slipstream affects the flowfield and the change of the flowfield at location (x_p, y_p, z_p). Even if the loading of the propeller is unaltered, the shift of the slipstream relative to a point in space leads to a gradient of the local flow angle and local dynamic pressure. This rate of change depends on the values of (x_p, y_p, z_p) and the propeller loading and can be positive or negative.

Figure 8.4a visualizes this deflection that at two planes at a distance from the nacelle ($|y| > R_{nacelle}$). Due to the swirl and increased axial velocity in the slipstream, the local angle of attack is unequal to α_∞. Outside the slipstream, there is still a limited influence of the propeller due to slipstream contraction and a contribution from the nacelle. At these locations, the slipstream edge follows approximately the freestream flow angle α_∞. The small reduction that can be observed is the result of the slightly higher axial velocity in this shear layer due to viscous forces, hence a lower local angle of attack. This reduction is therefore directly related to the thrust coefficient T_C, with a higher thrust coefficient leading to a smaller deflection angle [244].
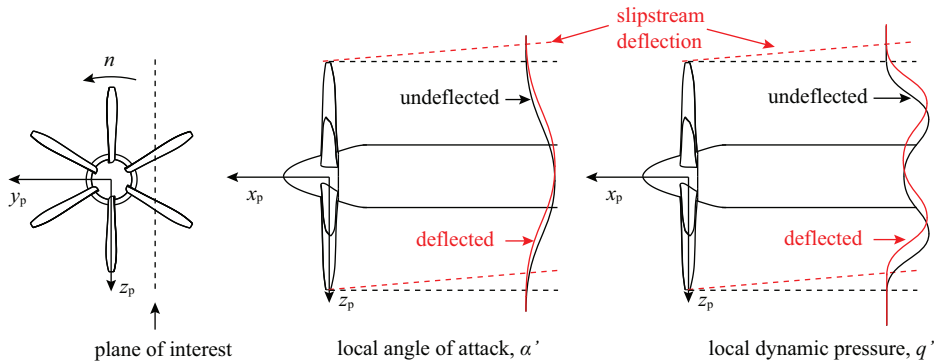
Figure 8.3: Illustration of the effect of a slipstream deflection angle on the local change in flow quantity.
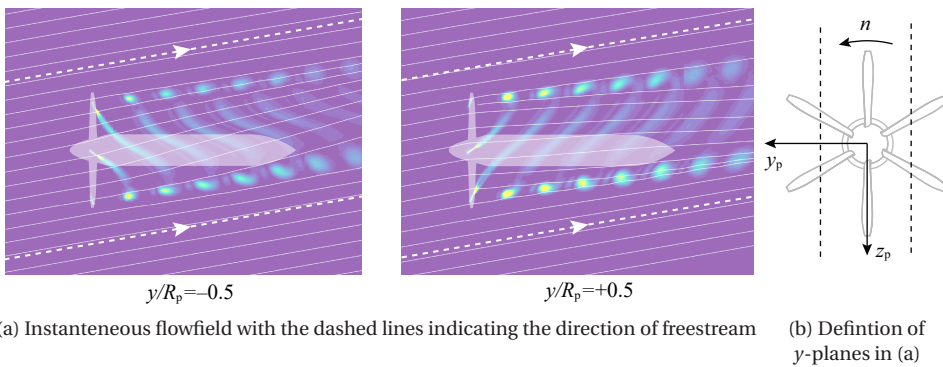

(a) Instanteneous flowfield with the dashed lines indicating the direction of freestream

(b) Defintion of y-planes in (a)

Figure 8.4: Deflection of the slipstream on the upgoing and downgoing side. The contours are of vorticity magnitude indicate the boundary of the slipstream. Pathlines in the y-plane are indicated in white. Instantaneous flowfield from full-blade CFD simulations of the XPROP propeller, $J = 1.8$, $\beta_{0.7R_p} = 45$ deg, $\alpha = 10$ deg.

One of the factors that plays an important role in the slipstream development is the nonaxisymmetric load distribution on the propeller disk (see Fig. 2.22a). The region of higher thrust and torque adds more momentum to the freestream, while on the retreating side the added momentum is lower compared to the case of a symmetric inflow condition. Furthermore, the normal force and the side force lead to a net deflection of the slipstream. Figure 8.5 illustrates this rather complex flowfield that is caused by an angle of attack. The isosurface of constant axial velocity is far from axisymmetric: on the downgoing blade there is significant rise in axial velocity, while on the upgoing blade the induced velocity is strongly reduced compared to a propeller in axial inflow.
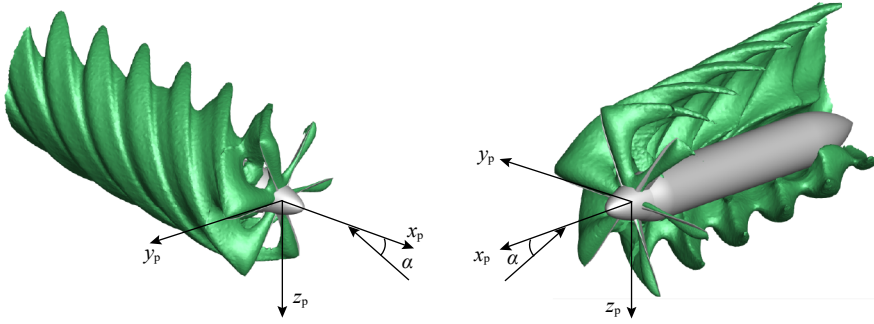
Figure 8.5: Isosurface of constant axial velocity $u/V_\infty = 1.13$ to illustrate of strongly nonuniform slipstream. Instantaneous flowfield from full-blade CFD simulations of the XPROP propeller, $J = 1.8$, $\beta_{0.7R_p} = 45$ deg, $\alpha = 10$ deg.

To analyze the dependency of the velocity magnitude and direction on α, the time-averaged local angle of attack and dynamic pressure can be defined as:

$$\alpha'(x, y, z) = \alpha_\infty + \Delta\alpha(x, y, z)$$
$$\frac{q'}{q_\infty}(x, y, z) = 1 + \frac{\Delta q}{q_\infty}(x, y, z)$$

(8.1)

with the prime indicating a local quantity and the Δ indicates the change due to the propeller relative to the freestream value. These latter terms can be further divided into:

$$\Delta\alpha(x, y, z) = \Delta\alpha_{\alpha=0}(x, y, z) + \Delta\alpha_{\alpha\neq0}(x, y, z)$$
$$\Delta q(x, y, z) = \Delta q_{\alpha=0}(x, y, z) + \Delta q_{\alpha\neq0}(x, y, z)$$

(8.2)

The values at $\alpha = 0$ represent the slipstream of the isolated propeller and are constant for a given J (i.e. the swirl angle and rise in dynamic pressure). The terms with $\alpha \neq 0$ entail the effect of an angle of attack. Because the aerodynamic forces of a lifting surface in a slipstream are proportional to αq, the magnitude and sign of the terms $\left(1 + \frac{d(q'/q_\infty)}{d\alpha_\infty}\right)$ and $\frac{d\alpha'}{d\alpha_\infty}$ give an indication whether the presence of the slipstream further increases the lift curve slope of an aerodynamic surface at that location. This contribution is therefore an additional effect that determines the change in c_{l_α}, in addition to the rise in dynamic pressure and the interaction of the slipstream with the lifting surface.

As will be shown later in this section in more detail, the nacelle has a profound effect on the flowfield in three ways. First, its cylindrical cross section experiences a crossflow, which introduces an in-plane velocity field. Secondly, it becomes a lifting body, generating an out-of-plane flowfield. Thirdly, its presence modifies the vortex field and the resulting induced velocities. The latter contribution is closely linked to the *deformation* of the slipstream, which is also caused by other phenomena. For example, the varying circulation along the helix induces a flowfield such that the tip vortices do not convect downstream in a straight path, but instead interact with each other [97, 165]. This asymmetry leads to deformation of the slipstream, which becomes more prominent in downstream direction. Not only the helical vortex itself leads to its self-induced deformation,

8

Fig. 8.6 also reveals that for certain angles of attack, the edge of the slipstream is close to the nacelle and propeller hub vortices. Hence, the shedding of the propeller hub vortices is off-center relative to the helical tip vortex. From the CFD results it was found that the strong hub vortex modifies the path of the tip vortices that are in their vicinity, although the impact on the overall flowfield is limited. This can be a relevant factor only if the angle of attack is large (i.e. the slipstream deflection is such that helical tip vortex is close to the nacelle) and when the lifting surface is far from the propeller disk. Even at three diameters downstream the disk, the slipstream remains approximately circular (see e.g. Fig. 8.10). For the typical configurations that are of interest in the following sections, the lifting surface is either sufficiently close to the propeller disk, or the slipstream is already distorted by the lifting surface, such that the interaction between hub vortices and tip vortices becomes less relevant. A case where the relative location of the slipstream to the nacelle is more pronounced, are VTOL vehicles, for example with a tip-mounted propeller, in transition from hover to forward flight, further discussed in Ref. [224].
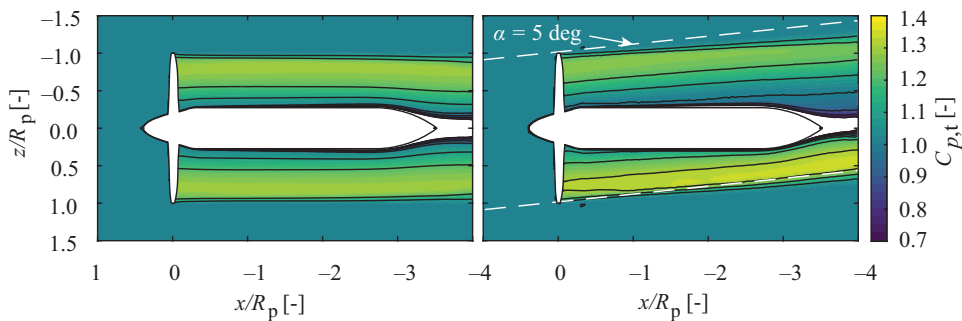

Figure 8.6: Illustration of the deflected nonuniform and displaced slipstream for the XPROP propeller. Time-averaged total-pressure field at a $z = 0$ plane for $\alpha_\mathrm{p} = 5$ deg, $J = 1.8$, $\beta_{0.7R_\mathrm{p}} = 45$ deg.

Figure 8.7 provides a more concrete view of the changing flowfield when going from $\alpha = 0$ deg to $\alpha = 5$ deg in a plane at $1.1R_\mathrm{p}$ downstream the propeller disk. This location typically corresponds to the leading edge of a wing, tailplane, or pylon for a tractor propeller configuration. It can be observed that the dynamic pressure is significantly affected along the complete survey line. The rise is larger than the reduction on the retreating side as the $T_C - J$ curve is nonlinear. This can also be shown through the velocity triangles in Fig. 2.2. This means that, on average, the dynamic pressure increases inside the slipstream when the propeller is under an angle of attack. On the other hand, on both upgoing and downgoing blades, the local angle of attack reduces between $r/R_\mathrm{p} = [0.5, 1.0]$ due to the change in tangential force on the blade sections.

To quantify the gradient of flowfield quantities with angle of attack, the change of the time-averaged flowfield when the angle of attack is increased from $\alpha = 0$ deg to $\alpha = 5$ deg is plotted in Figs. 8.7d and 8.7e. This gradient is linearized over the interval $\alpha = [0, 5]$. In Ref. [114] it is shown that for small angles of attack, the gradient is constant most of the locations within the slipstream, therefore the presented values are representative. On the advancing side, the gradient of the dynamic pressure is positive, indicating an increase of 1.5% per deg, while on the retreating side the loss in dynamic pressure is

approximately 1% per deg. On the other hand, the change of the angle of attack on *both sides* of the disk is smaller than the change of $\Delta\alpha$ since $\frac{d\alpha'}{d\alpha} < 1$.
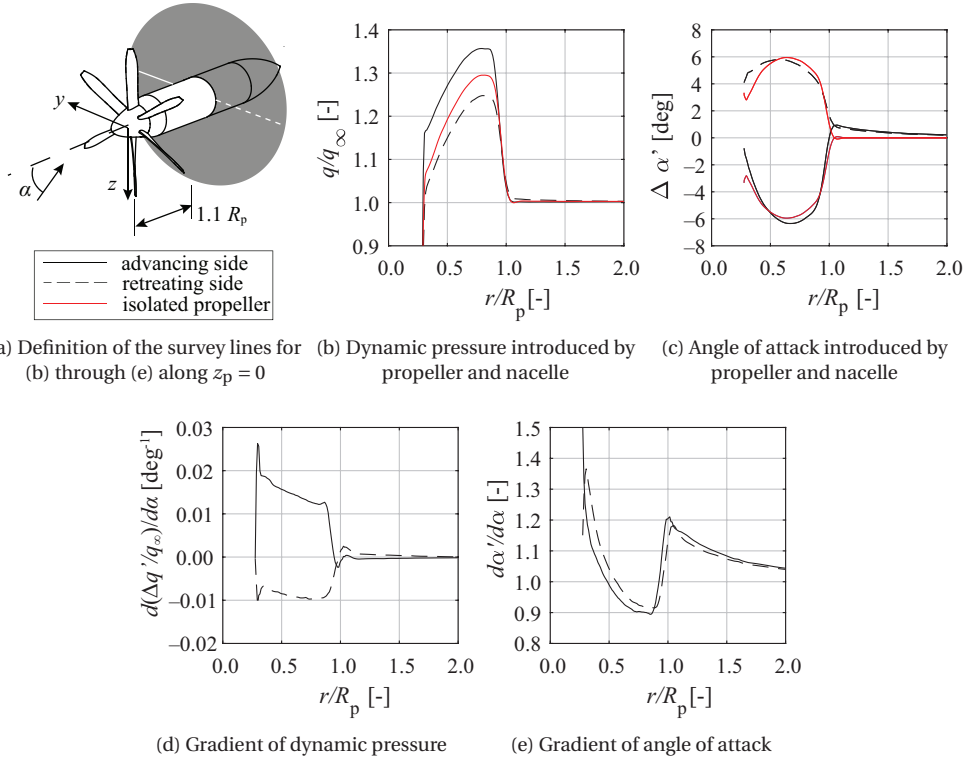

(a) Definition of the survey lines for (b) through (e) along $z_p = 0$

(b) Dynamic pressure introduced by propeller and nacelle

(c) Angle of attack introduced by propeller and nacelle

(d) Gradient of dynamic pressure

(e) Gradient of angle of attack

Figure 8.7: Time-averaged flowfield at a $x_p = 1.1 R_p$ plane along $z_p = 0$ to show the effect of a nonzero angle of attack ($\alpha = 5$ deg). Full-blade CFD data for the XPROP propeller, $J = 1.8$, $\beta_{0.7 R_p} = 45$ deg.

While the propeller primarily has a negative contribution to the local angle of attack, the nacelle is partially compensating this. In fact, the gradient is below unity between $r/R_p = [0.5, 1]$ and above unity outside the slipstream. Effectively, this means the lifting surface experiences a 10% reduction in angle of attack within the slipstream, while the dynamic pressure is only raised by 0.5% on average. This indicates that α' is the prominent value that changes with α_∞. To put this into perspective, the average raise in dynamic pressure in the slipstream far downstream is still $\Delta q \approx +0.2 q_\infty$ for these thrust coefficients (see Eqn. 2.4). A lifting surface therefore still has a higher lift curve slope than when operating in freestream condition (discussed in Section 8.4).

A remarkable observation is that the *change* in the flowfield is primarily happens *outside the slipstream*. This is especially visible in Fig. 8.8. Since this effect is so prominent, it requires further investigation. This is found to be the consequence of two phenomena:

- Deflection of the slipstream, i.e. the shear of the ring vortices relative to each other

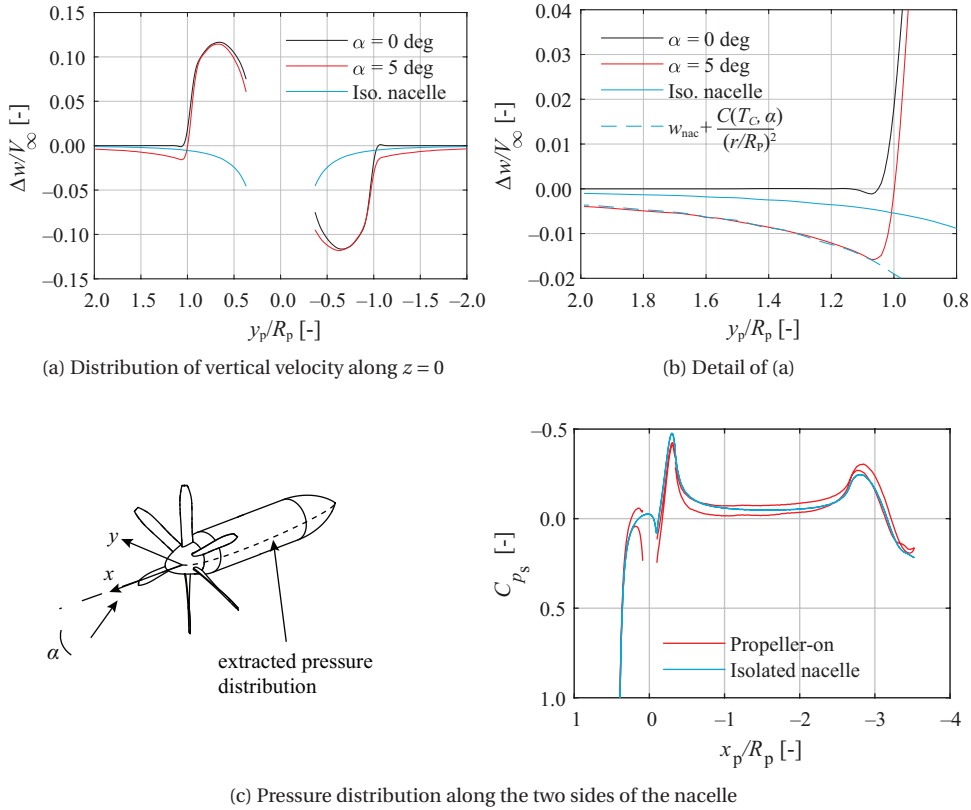- A higher dynamic pressure that is experienced by the nacelle

211

(a) Distribution of vertical velocity along $z = 0$

(b) Detail of (a)

extracted pressure distribution

(c) Pressure distribution along the two sides of the nacelle

Figure 8.8: Time-averaged normal velocity component inside and outside the slipstream at $x_p = 1.1 R_p$ and $z_p = 0$. Full-blade CFD data for the XPROP propeller, $J = 1.8$, $\beta_{0.7R_p} = 45$ deg.

The isolated nacelle introduces a cross flow velocity component, with a $1/r$ character (if the flowfield is approximated as a potential flow). Figure 8.8 shows that the effect of the propeller–nacelle combination on the in-plane velocity w can be approximated by a factor proportional to thrust coefficient in addition to the in-plane velocity of the nacelle: $w_{\text{prop+nac}} \approx w_{\text{nac}} + \frac{C(T_C, \alpha)}{(r/R_p).^2}$. The nacelle induced flowfield is only marginally affected by the propeller, as can be concluded from the differences in nacelle pressure distribution in Fig. 8.8c. The remainder of the in-plane velocity field outside the slipstream is therefore caused by the slipstream itself. It may be recalled from Section 2.1.1 that the radial velocity outside the slipstream is only nonzero near the propeller disk. Far away from the disk the consecutive ring vortices cancel each other contribution. However, if the ring vortices are displaced with respect to each other due to a slipstream deflection, the vortex-induced velocity fields do not cancel completely. This causes an in-plane velocity component in the same direction as the angle of attack. This is relevant in case the inflow condition to a propeller–wing combination is to be defined. Lower order models that do not consider this effect will therefore underestimate the effect of the propeller on

212

the lift distribution.

To obtain an understanding of the change in flowfield behind the propeller, the local angle of attack and axial velocity is depicted in the contours in Fig. 8.9. For the axial velocity, there is again a strong difference between upgoing and downgoing blades, but its maximum remains on the lower side of the disk for this particular condition. As expected, the effect of the nacelle on the local angle of attack is maximal along the $z_p = 0$ and $y_p = 0$ directions. In the same figure, it becomes clear that the largest change in local flow angle achieved within the slipstream is translated in negative z-direction. These results demonstrate that the gradient of the angle of attack and dynamic pressure have a different distribution over the disk.
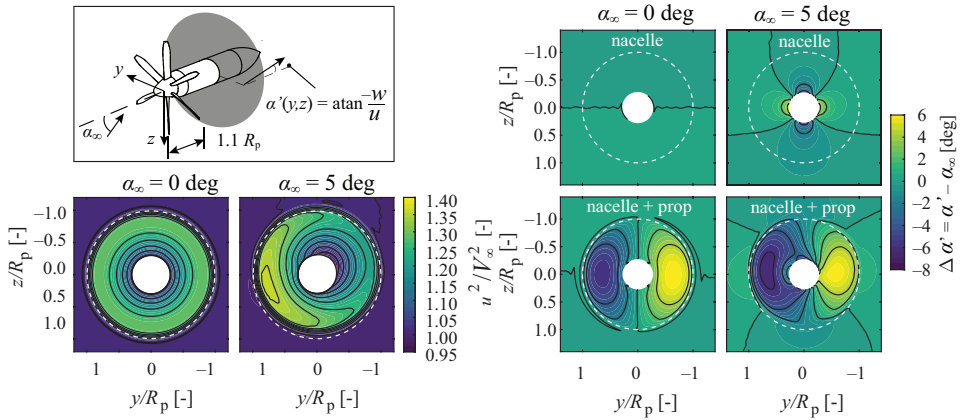
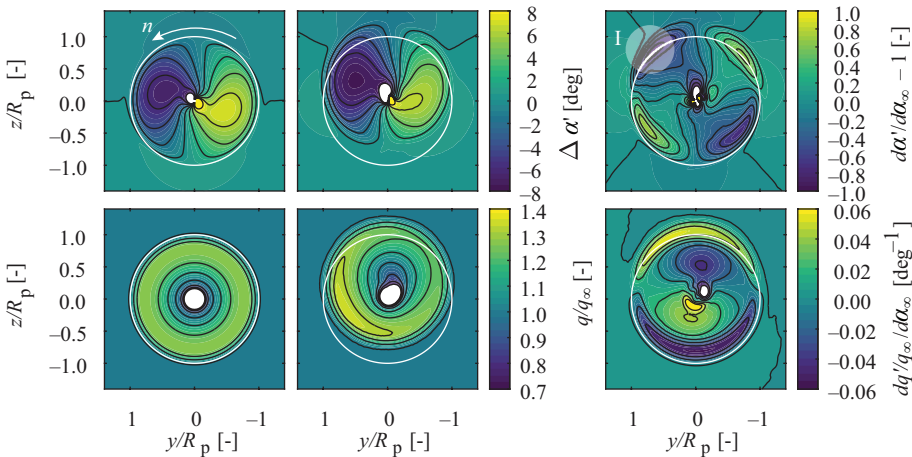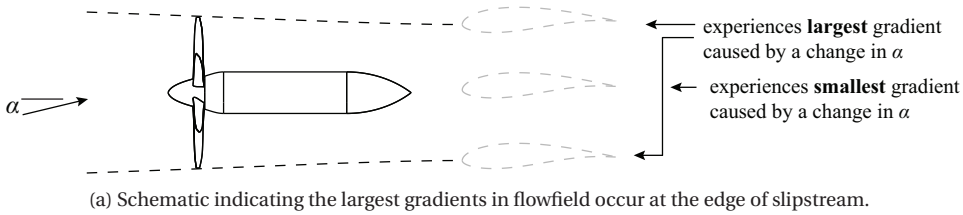(a) Effect of an angle-of-attack on the time-averaged flowfield
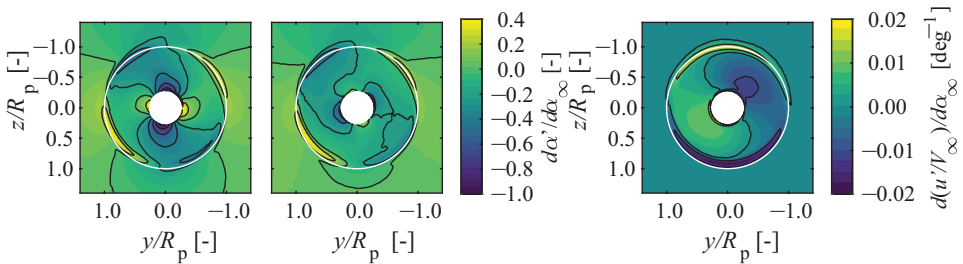
(b) Gradients of time-averaged flowfield. The figure shows that at the edges of the slipstream the magnitude of the gradient of the local flowfield with freestream angle-of-attack is largest.

Figure 8.9: Effect of an angle of attack on the axial velocity and local angle of attack. Full-blade CFD data for the XPROP propeller, $J = 1.8$, $\beta_{0.7R_p} = 45$ deg.

In Fig. 8.9b it is shown how the gradient of the angle of attack and axial velocity vary in y_p and z_p directions. This value is not constant but has a nonlinear character, especially near the edge of the slipstream. When the nacelle contribution is subtracted, it becomes clear that indeed over nearly the entire disk the propeller itself has a negative contribution to $\frac{d\alpha'}{d\alpha_\infty}$. Around the edge of the slipstream that is present at $\alpha = 0$ deg, the *change* is largest, because the slipstream is deflected. This corresponds with the swirl

distribution of Fig. 8.9. As expected, the largest *change* of the axial velocity occurs on the extremes of the upper and lower sides of the slipstream, although the magnitude is relatively small.

The flowfield is not only influenced in the nearfield, also the flow gradients (far) downstream of the propeller–nacelle combination are influenced by the presence of the propeller slipstream. In Fig. 8.10 the time-averaged angle of attack and dynamic pressure are plotted in a plane at $x/R_p = -3$, confirming the observation made earlier that the slipstream remains approximately circular. If an aerodynamic surface would be

(a) Schematic indicating the largest gradients in flowfield occur at the edge of slipstream.

(b) Flowfield at a $x/R_p = 3$ plane. White contour indicates propeller disk. Region I is indicated in the top-right figure as a white transparent disk.

Figure 8.10: Flowfield far downstream the propeller–nacelle combination, excluding the presence of a lifting surface. The figure shows that at the edges of the slipstream the magnitude of the gradient of the local flowfield with freestream angle-of-attack is largest. Full-blade CFD data for the XPROP propeller, $\alpha = 5$ deg, $J = 1.8$, $\beta_{0.7R_p} = 45$ deg.

installed at this distance, the largest gradients of angle of attack and dynamic pressure would again be encountered near the upper and lower part of the slipstream. If it is installed at the propeller rotation axis, neither angle of attack nor dynamic pressure are significantly affected by the slipstream. Region I as indicated in Fig. 8.10b, would lead to a *negative* $\frac{d\alpha'}{d\alpha_\infty}$; $\Delta\alpha_\infty > 0$ would be experienced as a $\Delta\alpha' < 0$. If there is a lifting surface placed in this region, the force gradient with angle of attack would therefore be negative.

The positive $\frac{dq'/q_\infty}{d\alpha_\infty}$ in that region would even aggravate this response, since the magnitude of the aerodynamic force would increase as a function of angle of attack. Although this is a quite unique characteristic, the spatial extent of this region is limited and therefore only relevant for a small range of angles of attack.

In Ref. [37] it is shown that a significant difference in lift and drag is achieved at a given angle of attack for a high or low wing location relative to the propeller axis. The effect of an angle of attack to the flowfield at a certain the vertical location of a lifting surface relative to the propeller is therefore relevant, since it is a major design variable. The flowfield experienced by the lifting surface as the result of installation (i.e. in this case an angle of attack) is shown in Fig. 8.11. A lifting surface experiences on average a smaller angle of attack than the freestream value, with the largest deviations observed if the surface is off-center with respect to the propeller rotation axis. The differences in dynamic pressure are varying between the different locations, as the distribution is not symmetric with respect to the xz-plane, while the local angle of attack is nearly antisymmetric (see Fig. 8.9). On the downgoing blade side, $q' > q_\infty$, and for the considered range of angle of attack, $\frac{d\Delta q'/q_\infty}{d\alpha_\infty} > 0$. The opposite is the case for the side where the blades are rotating up. For the considered case, representative for cruise condition, these flowfields reveal that when this actual flowfield is not taken into account, the estimated forces are likely to be overpredicted. It is therefore highly relevant to prescribe the loading distribution on an actuator disk that exists in case $\alpha \neq 0$, for example, by using the method presented in Chapter 5.

Not only variation of the propeller load distribution with angle of attack plays an important role in the response of the lifting surface, also the relative position of the helical vortex system to the lifting surface influences the response. For the axisymmetric condition, the tip vortices on $\pm y$ side are at the same axial location. This means that, if an unswept wing leading edge is situated at a location x, these vortices impinge at the same time instance. However, at an angle of attack, the tip vortices are no longer in phase, as depicted in Fig. 8.12a. Besides the tip vortices, also the flow structures inside the slipstream appear to have a phase shift, of which an example is depicted in Fig. 8.12b. Relative to the isolated propeller, the pitch of the flow structure on the advancing side is decreasing, while it is increasing on the retreating side. Recalling that the tip vortices move downstream with freestream velocity, the growing axial distance is not the result of the induced flowfield that is unequal on either side of the nacelle. Figure 8.12c shows that this is purely the consequence of the pitch of the tip vortices that are evaluated on an inclined plane (or alternatively, an inclined slipstream with respect to the propeller axis). This apparent phase difference grows in downstream direction, shown in Fig. 8.12d and has a cosine shape. Further downstream than is shown in the figure, the phase difference becomes zero again. This will have a profound effect on the unsteady loads an aerodynamic surface downstream, as in case the unsteady loads are in-phase at $\alpha = 0$ deg, they will be out-of-phase at a nonzero angle of attack. This dependency on angle of attack grows with increasing distance between to the propeller disk. A phase shift of the loading of subcomponents can lead to a reduction of this integral force through cancelling terms of out-of-phase periodic loads.

8

(a) Horizontal survey lines

(b) Survey along $z_p/R_p = 0.0$

(c) Survey along $z_p/R_p = -0.5$

(d) Survey along $z_p/R_p = +0.5$

(e) Survey along $z_p/R_p = 0.0$

(f) Survey along $z_p/R_p = -0.5$
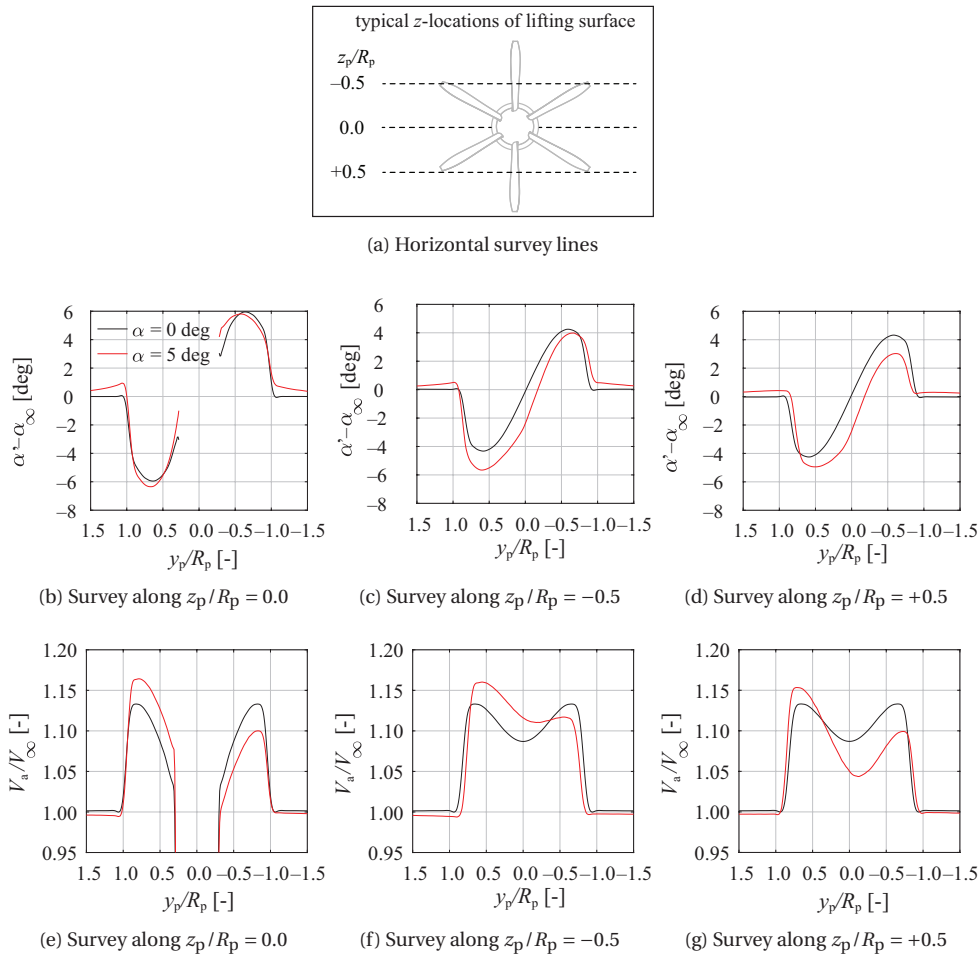
(g) Survey along $z_p/R_p = +0.5$

Figure 8.11: Effect of an angle of attack of $\alpha = 5$ deg on the development of the slipstream that would affect airframe components just downstream of the propeller. Time-averaged full-blade CFD results of XPROP, $J = 1.8$, $\beta_{0.7R_p} = 45$ deg.

8.2.2. PROPELLERS MOUNTED TO A TAILPLANE

A variation of the propeller at angle of attack is the case of a propeller operating in the downwash of a wing, where the distorted flowfield behind the propeller is experienced by a horizontal tail that is downstream of the propeller. In Chapter 6 it has been shown that the distribution of the downwash field has a somewhat different shape than a pure angle of attack: it varies in y and z directions. In the case of a propeller mounted to a horizontal tailplane, the gradient of the flowfield is especially relevant as the tailplane directly influences the aircraft stability. For this case, the flowfield between the propeller and tailplane for the *VGM-HTP* configuration (see Fig. 3.8) is analyzed.

Figure 8.13 depicts the time-averaged total-pressure coefficient and local angle of at-
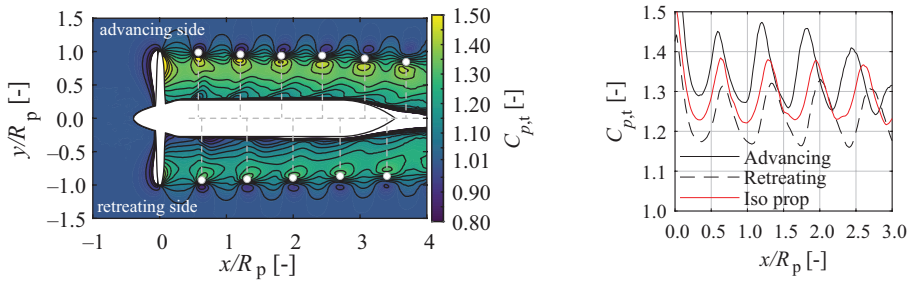
(a) Total pressure in survey plane of an instantaneous flowfield (top view). Dots indicate cores of tip vortices.

(b) Total pressure at $r/R_p = 0.85$.
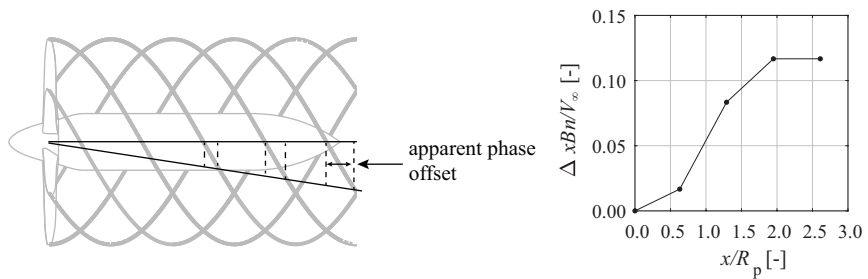
(c) Effect on the location of tip vortices by slicing a helix at an angle. Viewed from retreating side.

(d) Absolute phase offset between advancing and retreating side on flow structures (from (b)).

Figure 8.12: Effect of slipstream deflection on the instantaneous flowfield to show that a phase difference arises because of the deflected slipstream. Conditions: $\alpha = 5$ deg, $J = 1.8$, $\beta_{0.7R_p} = 45$ deg.

tack caused by the propeller for the two rotation directions. As will be shown in Section 8.3 the inboard part of the tailplane is responsible for the largest forces. Therefore, the distribution of total-pressure and local propeller-induced angle-of-attack along a survey line on the *inboard part* of the tailplane are indicative of the local change in forces on the *complete* tailplane. By increasing from $\alpha = 0$ deg to $\alpha = 5$ deg, ΔC_{p_t} changes with ± 0.1 and the swirl-angle changes by ± 1 deg due to the higher thrust and torque, respectively. Therefore, an outboard-up rotation indicates $\frac{dC_{p_t}}{d\alpha_\infty} > 0$, while for the inboard-up rotation it is the inverse, and for both rotation directions $\frac{d\alpha'}{d\alpha_\infty} < 0$. Compared to the change in dynamic pressure, the angle-of-attack is the primary factor to change the lift of a two-dimensional airfoil section. In line with the uninstalled propeller at $\alpha > 0$, the slipstream remains circular, even though the airframe-induced downwash field is not homogeneous. This indicates that the slipstream deformation ahead of the lifting surface does not play a significant role. The figure also demonstrates the effect of installation, the slipstream deflection is significantly smaller than for the propeller at $\alpha = 5$ deg. The variation of the slipstream with angle of attack is therefore also smaller than for a wing-mounted tractor propeller.

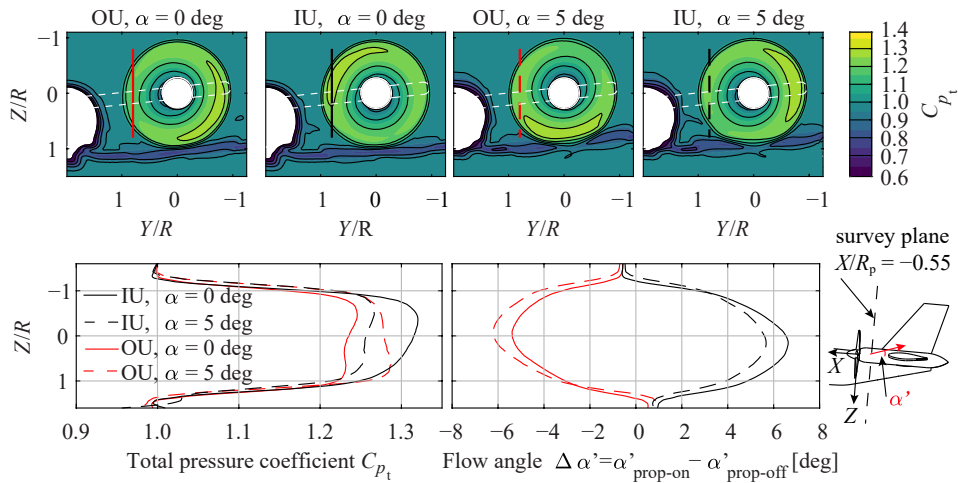In Fig. 8.13 it is shown that for this particular case, the lower part of the propeller disk

Figure 8.13: Computed time-averaged flowfield between the propeller and horizontal tail for two angles-of-attack at $J = 1.8$ and $\beta_{0.7R_p} = 45$ deg (cruise condition).

encounters the wake. Since the largest radial flow component is at the edge of the propeller disk, any nonuniformity of the flowfield outside the propeller disk is also modified by the propeller-induced velocity and pressure field. This deformation is for example shown in Ref. [98]. To visualize this, the wake-encounter at the edge of the propeller disk is further explored by means of PIV measurements (see details in Section 3.3.5). Figure 8.14a depicts three different PIV planes between the fuselage and propeller rotation axis. At the most inboard plane *b*, the wing wake is relatively far from the propeller disk, while the blade tips sweep through the wake at plane *d*. The survey lines (indicated by the dashed line in Fig. 8.14a) indicate that the wing wake is slightly displaced in vertical direction. At the most inboard plane (Fig. 8.14b), a slight increase in axial velocity can be observed. However, in Fig. 2.6 it is shown that outside the slipstream, the axial velocity is lower. This discrepancy indicates that the slightly different velocity profile in Fig. 8.14b compared to the propeller-off case is mainly caused by contraction and a redistribution of the airframe-induced flowfield. Overall, these results confirm that the location of the wing wake is not significantly altered by the propeller. Moreover, it can be observed in Fig. 8.14d that part of the wake is 'filled' by the propeller, which reduces the nonuniformity of the wake region and increases the mixing of the low momentum region with the slipstream; the propeller acts as a 'filter' to reduce the nonuniformity of the airframe-induced flowfield.
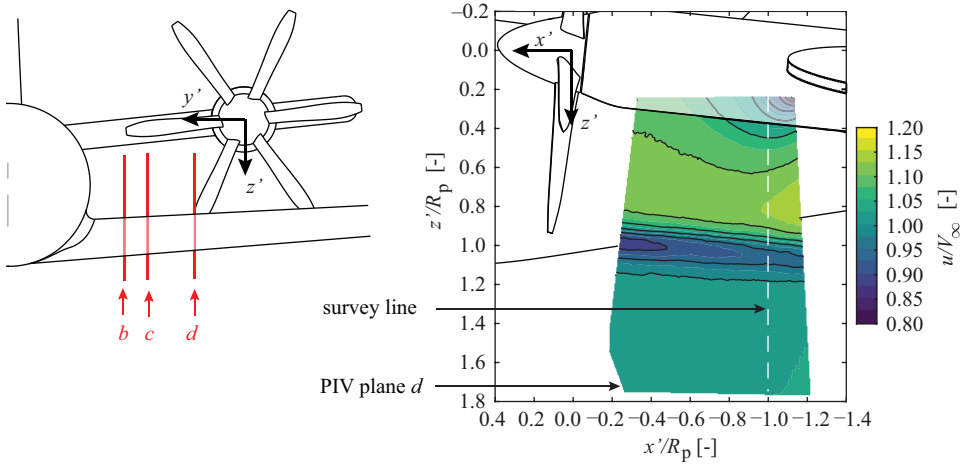
(a) Left: locations of the PIV planes at different spanwise locations. Right: a phase-averaged slipstream at plane d with a vertical survey line indicated for Figs. 8.14b through 8.14d.

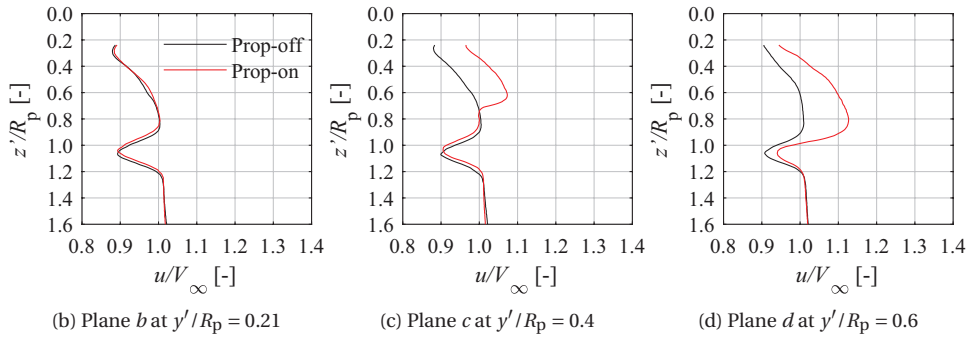(b) Plane b at $y'/R_p = 0.21$ (c) Plane c at $y'/R_p = 0.4$ (d) Plane d at $y'/R_p = 0.6$

Figure 8.14: Phase-averaged axial velocity profiles indicating the effect of the propeller installation on the location of the wing wake at $\alpha = 6$ deg. Propeller operates at $J = 1.9$ with $\beta_{0.7R_p} = 45$ deg. PIV results.

The interaction between the wing wake can be split into two phenomena. First, the tip-vortex does not remain helical, as the vorticity is convected in downstream direction with the local velocity, which is lower in the wake region than in the nonviscous region (also observable in Fig. 8.42). This could potentially lead to an instability of the helical vortex system [97] which would affect the flowfield at a lifting surface that is located downstream of the propeller. Second, the tip-vortex will entrain the wake. This causes the center of the wake to fluctuate in the vertical direction, as is indicated in Fig. 8.15b. The magnitude of the tangential vorticity of the propeller tip vortex is an order of magnitude higher than the out-of-plane vorticity of the wing wake, and will therefore convect in downstream direction in a relatively straight path. The dominant factor that determines the roll-up is therefore the propeller tip vortex. In this case, the break-down of the helical vortex system and the diffusion of the wing wake take place relatively far from the

219

propeller disk and the lifting surfaces. It can therefore be expected to play only a minor role in the actual inflow to the horizontal tailplane.
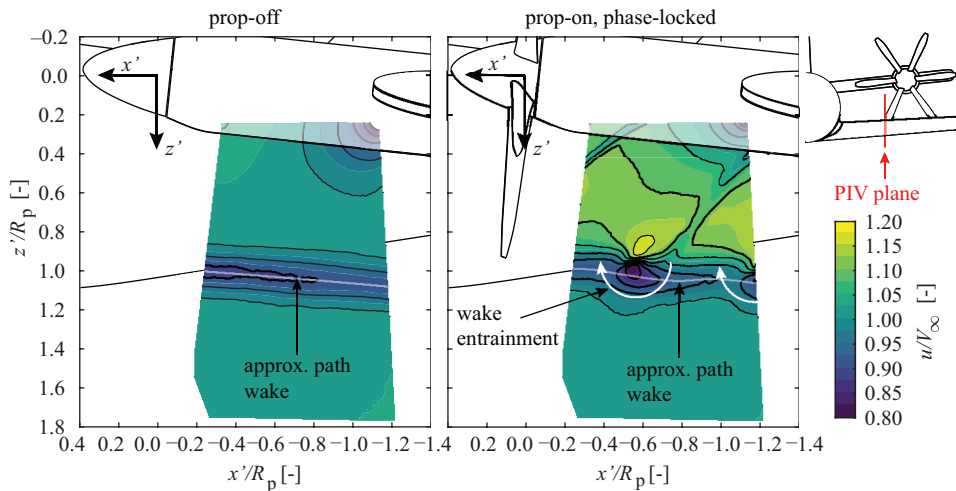

Figure 8.15: A phase-averaged flowfield for a fixed propeller phase angle to show the wake entrainment caused by the propeller tip-vortices, PIV results.

An example of an instantaneous flowfield between the propeller and horizontal tailplane for the *VGM-HTP* model is depicted in Fig. 8.16a and confirms the varying loading on the disk. For this particular example with a thrust setting and flight condition typical for cruise flight, the tailplane experiences significant variations in the local angle of attack, axial velocity, and static pressure, which further increase at higher thrust settings. Furthermore, in Fig. 8.16b it is shown that the pressure fluctuations that are in the vicinity of the tailplane greatly depend on the rotation direction and angle of attack: either the inboard part or outboard part of the tailplane experience the largest fluctuations.

8
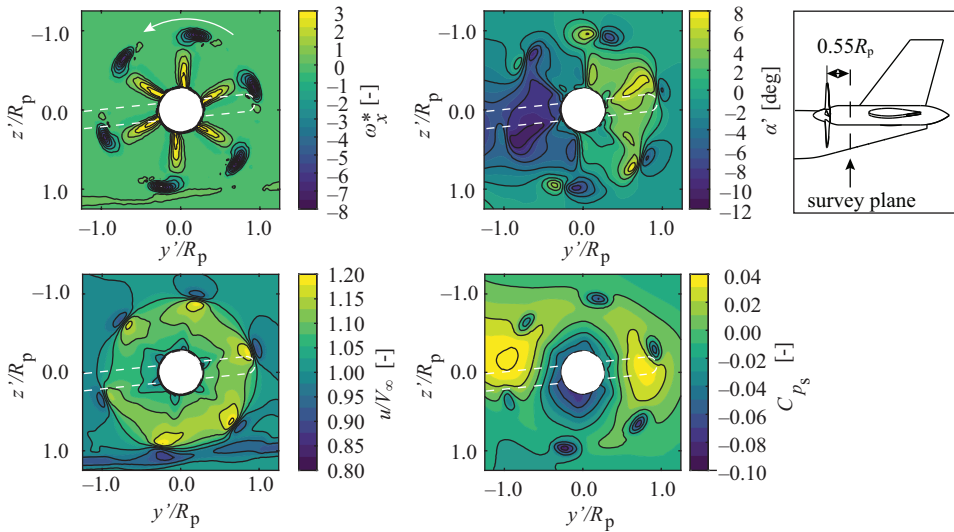
(a) Instanteneous flowfield at $\alpha = 0$ deg with an outboard-up rotation. The white dashed lines indicate the location of the horizontal tailplane.
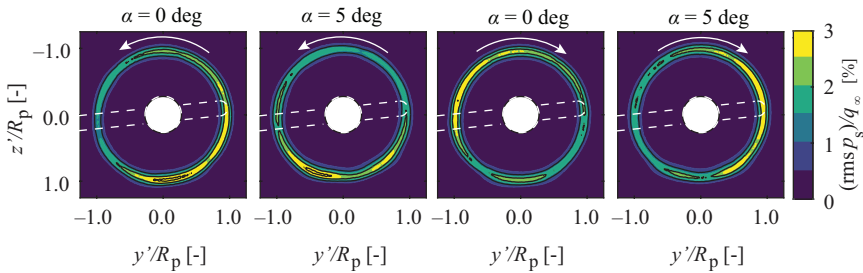
(b) Effect of rotation direction and angle of attack on the root-mean-square value of the static pressure

Figure 8.16: Nonaxisymmetric flowfield between the propeller and horizontal tailplane of the *VGM-HTP* model at $J = 1.8$ (cruise conditions). CFD results.

8.2.3. ARRAY OF PROPELLERS

In case of an array of distributed propellers, the propeller loading is not axisymmetric, as shown in Section 6.5. When the propellers are in close proximity to each other, the flow-field is no longer a superposition of the flowfields induced by the individual propellers, as identified by others (e.g. in Ref. [161]). An understanding of the installation effect on the slipstream can be used to analyze and design the propeller–wing combination.

Figure 8.17 depicts the time-dependent flowfield in a plane $0.2R_p$ downstream of the propellers. The effect of blade-blade interaction is apparent from the time-dependent flowfields at different propeller phase angles. The alternating reduction and increase of axial velocity when the blades are approximately in horizontal orientation lead to large gradients both in temporal and spatial domain. The combination of superposition and at the same time an increase in the tip-vortex strength (Section 6.5) aggravate these gra-
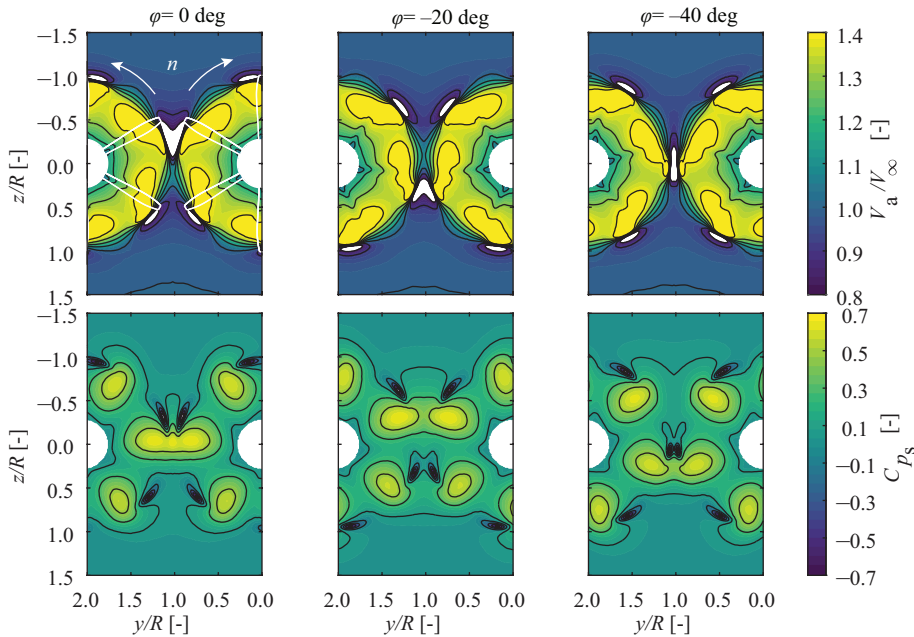
221

dients.

Figure 8.17: Installation effect on the time-accurate flowfield behind an array of propellers in a plane $0.2R_\mathrm{p}$ downstream the propeller disks, $J = 0.8$.

The load distribution in Fig. 6.23a is clearly observable in the total-pressure distribution in the first contour of Fig. 8.18a. The latter figure shows that, even though there is a restriction of the radial flow component at the symmetry planes, the slipstream remains approximately circular at this downstream location. The varying radial flow component is apparent in the second contour of Fig. 8.18a. However, a wing that is installed at $z = 0$ experiences strong gradients in the inflow field, especially near the edges of the slipstream. The reduction of the axial velocity for $r/R_\mathrm{p} > 1$ is now more concentrated in the region between the disks. This is also clearly observable in Figs. 8.18b and 8.18c, which show that the local angle of attack remains approximately the same when compared to the isolated propeller, with a strong negative angle of attack between the propeller blades. This local character is a direct result of the tip vortices that increase in strength over a finite azimuthal span $\Delta\theta$ and produce a net swirl outside the slipstream (unlike a propeller with an axisymmetric loading). The time-averaged slipstream is only locally slightly modified due to installation. The velocity gradient of the shear layer becomes larger at the symmetry plane, while the overall distribution is not significantly modified, as also observed in Ref. [161].

(a) Time-averaged flowfield, $J = 0.8$

(b) Axial velocity along a horizontal survey line, $z = 0$

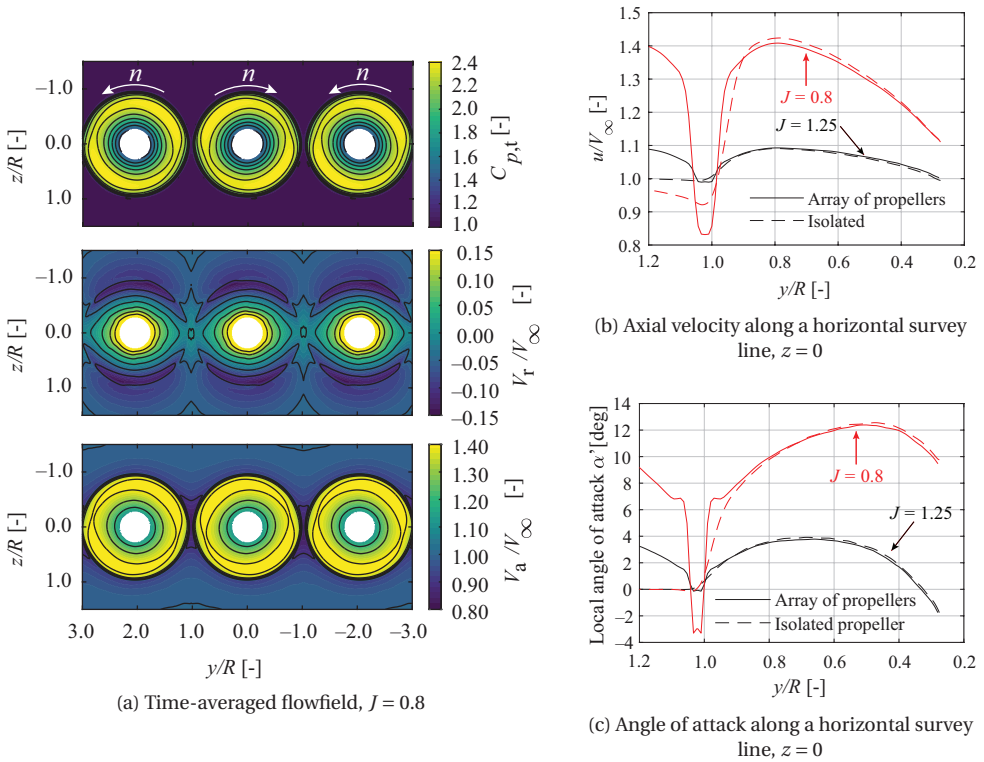(c) Angle of attack along a horizontal survey line, $z = 0$

Figure 8.18: Installation effect on the time-averaged flowfield behind an array of propellers in a plane $0.2R_p$ downstream the propeller disks.

A wing that is positioned above or below the propeller rotation axes will experience a more uniform angle of attack along the span compared to an array of propellers with larger spacing, as depicted in Fig. 8.19. Due to the larger contraction on the upper part of the slipstreams, a wing would, on average, experience a smaller angle of attack if it is positioned off-center relative to the propeller rotation axis. To counteract this, either the propellers are required to be tilted down, or the wing should have a higher incidence angle to obtain the same lift coefficient as the propeller-off condition for particular given angle of attack.

8

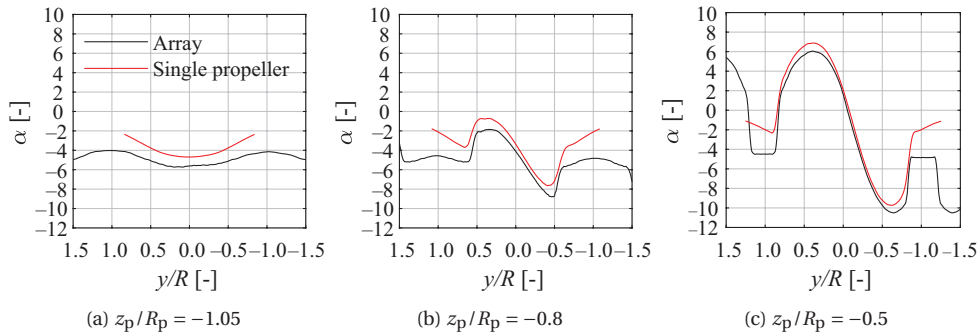(a) $z_p/R_p = -1.05$ (b) $z_p/R_p = -0.8$ (c) $z_p/R_p = -0.5$

Figure 8.19: Installation effect on the time-averaged, lateral angle of attack distribution in a plane $0.2R_p$ downstream the propeller disk, for $J = 1.8$, $\beta_{0.7R_p} = 45$ deg, $\alpha_\infty = 0$ deg.

8.3. AERODYNAMIC INTERACTION MECHANISMS

Prior to the quantification of the propeller installation on the aerodynamic forces on lifting surfaces, the aerodynamic interaction mechanisms need to be understood. This section revisits some of the findings from other authors and makes the link to the quantities of interest from a performance, stability, and control perspective. The results and observations also extend the knowledge on propeller-lifting surface interaction.

Other authors have identified that the propeller installation in front of a wing can lead to a beneficial effect on the induced drag of the wing [37, 45, 116]. From a performance perspective, this is advantageous, since the overall aircraft lift-to-drag ratio can be raised. However, not only L/D is modified, the flowfield downstream of the propeller–wing combination is influenced as well, in particular the dynamic pressure, downwash, and sidewash. These quantities contribute to the lift-curve slope of the lifting surface itself, but also to any aerodynamic surface (far) downstream, e.g. a tailplane that is located in the wing-induced flowfield. The propeller–lifting surface interaction is therefore also of profound importance to understand the installation effect on stability, for both wing-mounted propeller configurations, as well as horizontal-tailplane-mounted propeller configurations. Moreover, enhancements of the control effectiveness and offsets in the trim curve are relevant on aircraft level as well.

The interaction may be split up into a quasi two-dimensional problem, where an airfoil section experiences a different dynamic pressure and angle of attack. On top of that, there is a three-dimensional interaction, which in turn affects the local induced angle of attack. The initial impingement could be considered as a quasi two dimensional problem, where the slipstream locally adjusts the inflow vector to the airfoil. In Ref. [37] it is shown that if the lift coefficient is zero, a propeller swirl that leads to either $\alpha' > 0$ or $\alpha' < 0$ will tilt the resulting force vector into the direction of flight. If the local induced angle of attack from the trailing vorticity is reduced by the propeller installation, usually the term 'induced drag reduction' is used. This mechanism is therefore called herein as 'induced drag reduction'. Since this mechanism is a two-dimensional effect, *beneficial use of swirl* would be a more appropriate term. Alternative applications of this mecha-

nism are swirl-recovery vanes (SRV) [245, 246] which beneficially use this local flow angle to produce a force that has a component in the direction of flight. As discussed in Ref. [247], the finite slipstream height limits the ability to increase lift and potentially reduce drag. If the propeller diameter-to-chord ratio is infinite, a certain spanwise section will only experience the propeller-induced flow conditions, i.e. $\alpha = \alpha'$ and $q = q_s$. It can be hypothesized that for all other cases, especially the leading-edge region will experience the higher/lower angle of attack compared to the freestream value, while the remainder of the airfoil effectively experiences the freestream value.

In addition to the two-dimensional mechanism that depends on the slipstream shape, the axial components of vorticity from the two vortex systems of the propeller and lifting surface combined affect the local downwash angle at the lifting surface. If this local induced angle of attack is reduced by the propeller installation, usually the term 'swirl recovery' is used, which is inherently a three-dimensional effect. It is noted that this term in essence is not strictly correct. 'Recovery' suggests that the swirl is lost by the action of the propeller and is regained by the presence of the lifting surface. In essence, the propeller turns axial flow in a swirling motion, which is altered by the lifting surface. In that sense *axial flow recovery* would be a more suitable term, but is omitted due to the wide use of *swirl recovery* in other publications.

It is noted that both 'swirl recovery' and 'induced drag reduction' effectively lead to a forward tilt of the resultant force vector. Therefore they are closely related. For a wing, conventionally the terms 'lift-induced drag' and 'induced drag' are interchangeable. In the case of a propeller that is mounted to a wing, the term 'lift-induced drag' as the result of propeller installation has to be used with care. Induced drag reduction implies that the downwash gradient is lower than without propeller installed. However, if the propeller-induced flowfield would not change while the tip-vortex of the lifting surface increased, there would only be an offset of the downwash, not a change in the downwash gradient with angle of attack. On the other hand, an offset in downwash still leads to a ΔC_D. The situation is not straightforward, as the propeller loading changes with angle of attack and the relative location of the propeller hub vortices and tip-vortex of the lifting surface vary with angle of attack and lift coefficient as well. In other words, the principle of 'drag reducing mechanism that depends on lift' therefore applies to both 'swirl recovery' and 'induced drag reduction', and could be a better description of the two effects.

To better understand the mechanisms that contribute to the drag reduction mechanisms, the following quantities should be analyzed:

- Axial vorticity in-plane kinetic energy

- Load distribution along the chord of the lifting surface

- Slipstream deformation

The analyses of these quantities are done using two test cases. The first case is a tip-mounted propeller which directly influences the flowfield by the tip-vortex of the lifting surface. The second test case addresses the effects occuring for a more inboard mounted propeller, where the tip-vortex of the lifting surface resides between the propeller rotation axis and the edge of the propeller disk. As will be shown, different trends in terms of the flowfields are realized.

8.3.1. Interaction with Tip Vortex

The selected tip-mounted propeller model is the *PROWIM-HTP* model (see Fig. 3.7). The lift on the tailplane is altered by an elevator deflection, while the angle of attack remains zero. In this way, the propeller loading remains approximately constant, while the loading on the tailplane is altered, and therefore the strength and direction of the tip vortex also changes. The axial vorticity in a survey plane downstream the model is depicted in Fig. 8.20. In Fig. 8.20a the propeller-induced axial vorticity is clearly observable: $\omega_x^* > 0$ in the helical tip-vortex, while the inboard regions close to the tip of the tailplane the vorticity is opposite in sign.
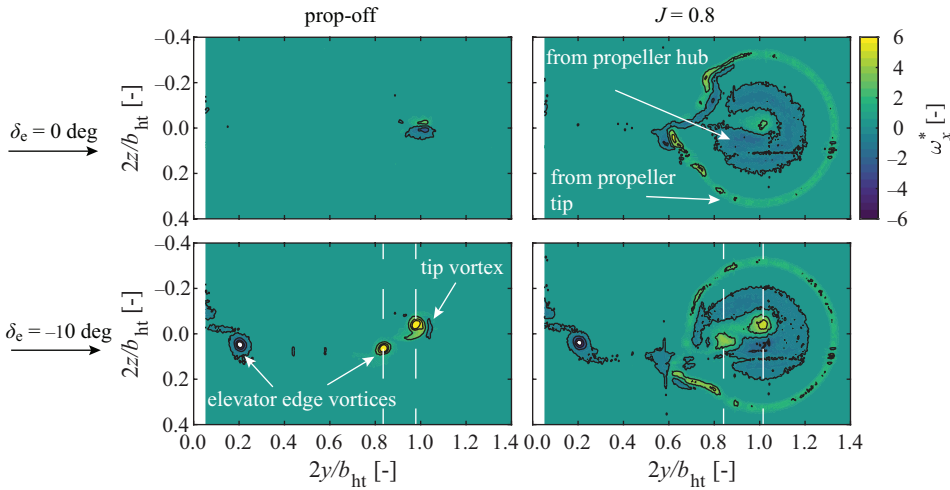
(a) Axial vorticity distribution. Dashed lines in dicate survey lines for (b) and (c)
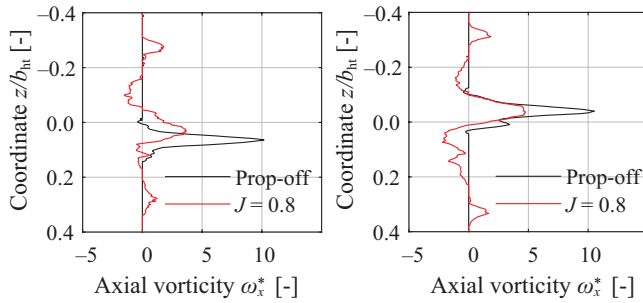
(b) Elevator-edge vortex, $\delta_e = -10$ deg   (c) Tailplane tip vortex, $\delta_e = -10$ deg

Figure 8.20: Phase-averaged axial vorticity xfrom a tip-mounted propeller (*PROWIM-HTP* model) in a plane $1.5c$ downstream the trailing edge, PIV results.

Due to the propeller installation, the part of the slipstream that impinges the tailplane has been strongly deformed (further discussed at the end of this section). The increased trailing edge vorticity from the tailplane is an indication of the higher loading.

It is also clear that a tailplane tip vortex is formed, which is opposite in sign compared to the vorticity shed from the blade roots. When the elevator is deflected, the propeller-off case has three strong vortices: two from the edges of the elevator and a tip vortex with approximately the same strength, see the surveylines in Figs. 8.20b and 8.20c. With the propeller on, the situation changes drastically. Even though the loading on the tailplane increases, the phase-averaged axial vorticity field is reduced: the propeller-induced vorticity from the hub appears to cancel the tip vortex. It is noted that the vorticity from the tailplane is not destroyed. According to Helmholtz's theorem, once vorticity is created, it can only be redistributed and converted into heat through viscosity. The effect is that the phase-average axial vorticity and therefore the circulation is lower.

The swirl angle, defined with respect to the propeller rotation axis, is depicted in Fig. 8.21. The swirl that is introduced by the propeller opposed to the tailplane induced flow-field leads to locally lower in-plane velocities, and therefore swirl angle. The same effect is observed as in the vorticity distribution: when the propeller is rotating in the opposite direction as the tailplane-induces swirl, the net effect is (on average) a lower swirl angle downstream of the model. The opposite is the case when the elevator is deflected such that the propeller and tip vortex are co-rotating. The same trend can be observed in the cross-flow kinetic energy $E_v = \frac{1}{2}\rho(v^2 + w^2)$, depicted in Fig. 8.22, where a co-rotating vortex pair leads to a significant higher cross-flow kinetic energy. Note that the lift force on the tailplane is even lower than for the case where the propeller and tailplane tip vortex are partially cancelling (see Fig. 8.31), which is in line with other research.
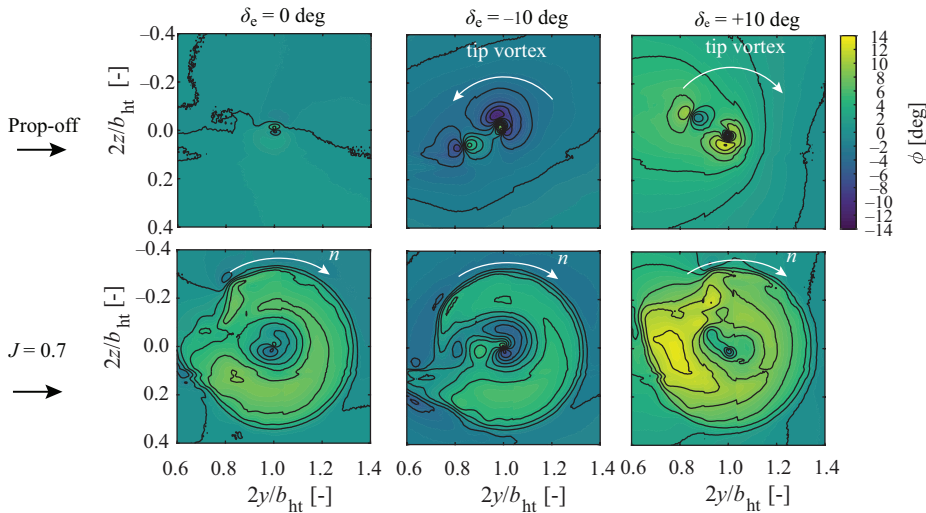

Figure 8.21: Effect of propeller installation on the swirl angle at $1.5c$ behind the trailing edge of the propeller–horizontal tailplane model. Propeller at constant advance ratio, $J = 0.7$, $\alpha = 0$ deg, PIV results.
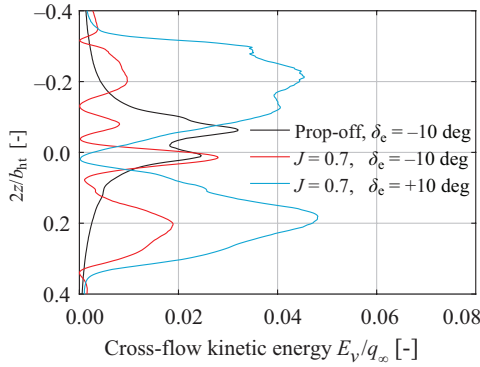
Figure 8.22: Cross-flow kinetic energy along a vertical survey line at $2y/b_{ht} = 1.0$ at $1.5c$ behind the trailing edge of the *PROWIM-HTP* model. Conditions: $J = 0.7$, $\alpha = 0$ deg. PIV results.

For the evaluation of the installation effect on the induced drag, the downwash distribution far enough from the lifting surface is required, such that the static pressure is equal to the ambient value. In Fig. 8.23a it is shown that for the case of $\delta_e = 0$, the downwash locally is negative and becomes more negative for larger thrust coefficients.
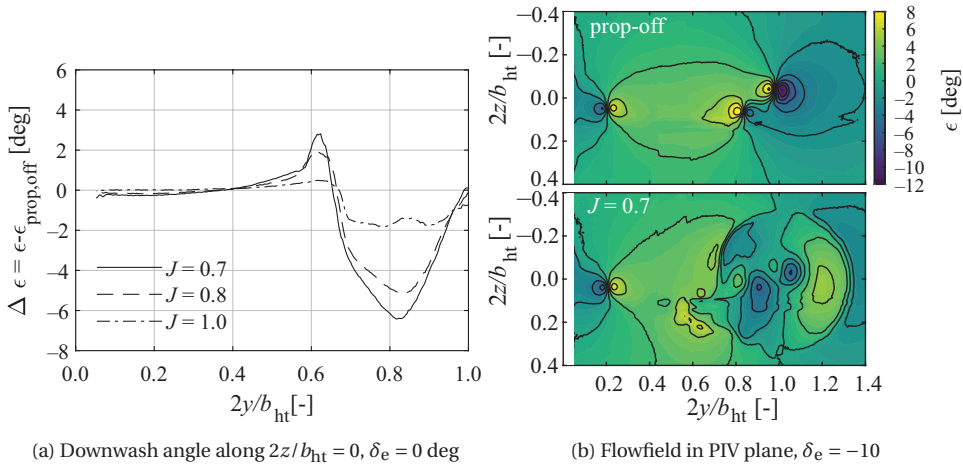
(a) Downwash angle along $2z/b_{ht} = 0$, $\delta_e = 0$ deg

(b) Flowfield in PIV plane, $\delta_e = -10$

Figure 8.23: Phase-averaged downwash distribution at $1.5c$ behind the trailing edge of the propeller–horizontal tailplane model. Conditions: $J = 0.7$, $\alpha = 0$ deg, $\delta_e = -10$ deg. Propeller swirl is opposite to the tailplane tip vortex.

At the edge of the slipstream, there is a sudden rise relative to propeller-off condition. This is caused by the strong gradient in loading at this location, that causes a vortex to trail from the tailplane, which induces a downwash. Towards the root there is nearly no effect on the downwash field; the propeller effect is relatively confined to the part that is washed by the tailplane. When the elevator is deflected, the same can be observed in

Fig. 8.23b: On the part washed by the tailplane there is a strong reduction in downwash.

The observations made so far are in line with research on tip-mounted propellers. From the survey plane downstream it is not clear *where* the reductions of the in-plane velocity components are achieved, which is also not clear from previous research. The relative importance of swirl recovery and induced drag reduction can be investigated by assessing the cross-flow kinetic energy at various survey planes that are normal to the freestream flow. In fact, a more suitable quantity is the kinetic energy deposition rate from Ref. [103]:

$$\dot{E}_{\mathrm{v}} = \iint \frac{1}{2}\rho(\Delta v^2 + \Delta w^2)u\mathrm{d}S \tag{8.3}$$

and describes the flux of the in-plane velocity component through a Trefftz plane with boundary S provides. A nonzero value behind the model indicates that there is a loss; transverse momentum in itself does not propel. A reduction of this transverse momentum caused by the lifting surface is indicative of improved performance of the lifting surface: the transverse momentum is employed and turned into a useful lift force and reduced drag. For this analysis, the Trefftz planes taken are enclosed by the wind-tunnel walls (see Fig. 8.24a). In Fig. 8.24b the integral values are plotted for the two different rotation directions. It is noted that these cases, in addition to the propeller-off case, have not the same lift value. However, the case of a counter-rotating tip vortex has a lower value of $\dot{E}_{\mathrm{v}}$, even though its lift force is higher. This is another confirmation that for the same propeller setting, the tailplane interaction can lead to higher/lower losses.

(a) Definition of integration planes used for (b)   (b) Change in $\dot{E}_{\mathrm{v}}$ with respect to the propeller-off case
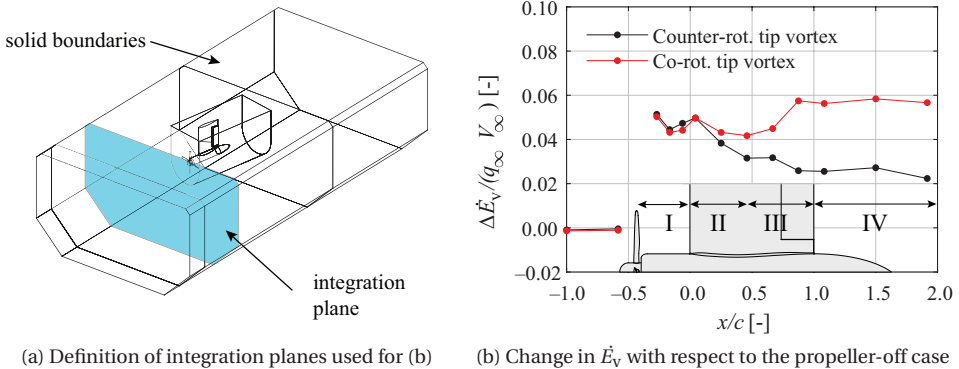
Figure 8.24: Crossflow kinetic energy deposition due to propeller installation. Full-blade CFD results of PROWIM-HTP, $J = 0.8$, $\alpha = 0$ deg, $\delta_{\mathrm{e}} = 10$ deg.

From Fig. 8.24b it can be deduced that the value of $\dot{E}_{\mathrm{v}}$ is not constant and four distinct regions can be identified aft of the propeller plane. In region I, $\dot{E}_{\mathrm{v}}$ is changing slightly due to the blockage and upwash from the tailplane, the accelerating slipstream, and more suction on the front part of the nacelle. From the leading edge, there is a reduction in $\dot{E}_{\mathrm{v}}$ for both cases up to the mid chord line. This part of the reduction is the 'induced drag reduction' through the solid boundary that limits the cross flow. From the mid chord to the

trailing edge, the $\dot{E}_v$ for the counter-rotating case continues to decrease up to approximately half the value that was caused by the propeller. To the contrary, the co-rotating tip vortex rises again to a value higher than introduced by the propeller alone. This is caused by the developing tip-vortex that becomes stronger towards the trailing edge and reaches its maximum value at a distance downstream the model. From the trailing edge onwards, $\dot{E}_v$ remains approximately constant for both cases.

8.3.2. Role of Finite Chord Length

From Fig. 8.24b it is clear that along the chord, reduction in cross flow is primarily achieved towards the leading edge. In other words, a portion of the $\dot{E}_v(x)$ curve seems to resemble the loading distribution on the tailplane in chordwise direction. If this is the case, the leading edge is the most suitable to be adapted to alter the aerodynamic characteristics. An investigation on the chordwise loading distribution can confirm this observation.

The pressure difference on each side of an airfoil section is a measure of the local vortex strength at the corresponding x/c. By comparing the ΔC_p along the chord between to conditions 1 and 2, one can identify what part of the airfoil is primarily responsible for this change. By normalizing this quantity by its integral value, the distribution along the chord then does not quantify the slope of a force coefficient, but it reveals what part of the airfoil is most productive to generate a normal force. Hence, two case can be compared that have a different lift-curve slope. The quantity of interest is defined by:

$$\Delta C_{p,12}(x) = \frac{\Delta C_{p,2}(x) - \Delta C_{p,1}(x)}{\int \left(\Delta C_{p,2}(x) - \Delta C_{p,1}(x)\right) d(\frac{x}{c})} \tag{8.4}$$

with ΔC_p the pressure difference between upper and lower side of the aifoil. The subscripts 1 and 2 refer to two conditions that lead to a change in pressure on the airfoil, e.g. propeller-on and propeller-off, or two different angles of attack.

Figure 8.25 depicts the distributions of $C_{p,12}$ for a number of cases at a spanwise location corresponding the highest loading on the propeller blade. In Fig. 8.25a it is shown that the *change* in loading due to an angle of attack is more concentrated towards the leading edge and:

> When the propeller is on and the angle of attack is raised from α_1 to α_2, the change in loading resembles the distribution of the propeller-off case

This is a highly relevant observation, as it indicates that even though the magnitude of the change in loading is not the same, the normalized change is. In other words, the propeller-tailplane combination behaves in the same way as the propeller-off case:

> The presence of the slipstream can be described as a change in local lift curve slope.

The same is observable for the case of an elevator deflection, Fig. 8.25b. On the other hand, if the change in loading is obtained through a change in advance ratio, i.e. going from $T_{C,1}$ to $T_{C,2}$, the distribution is not the same as a change in angle of attack. This is clearly visible in Fig. 8.25c:

The propeller installation leads to a more loaded leading edge. This may be interpreted as the consequence of a finite height of the slipstream.

(a) Angle-of-attack effect, $\delta_e = 0$ deg.

(b) Angle-of-attack effect, $\delta_e = -10$ deg.

(c) Propeller effect, $\delta_e = 0$ deg.
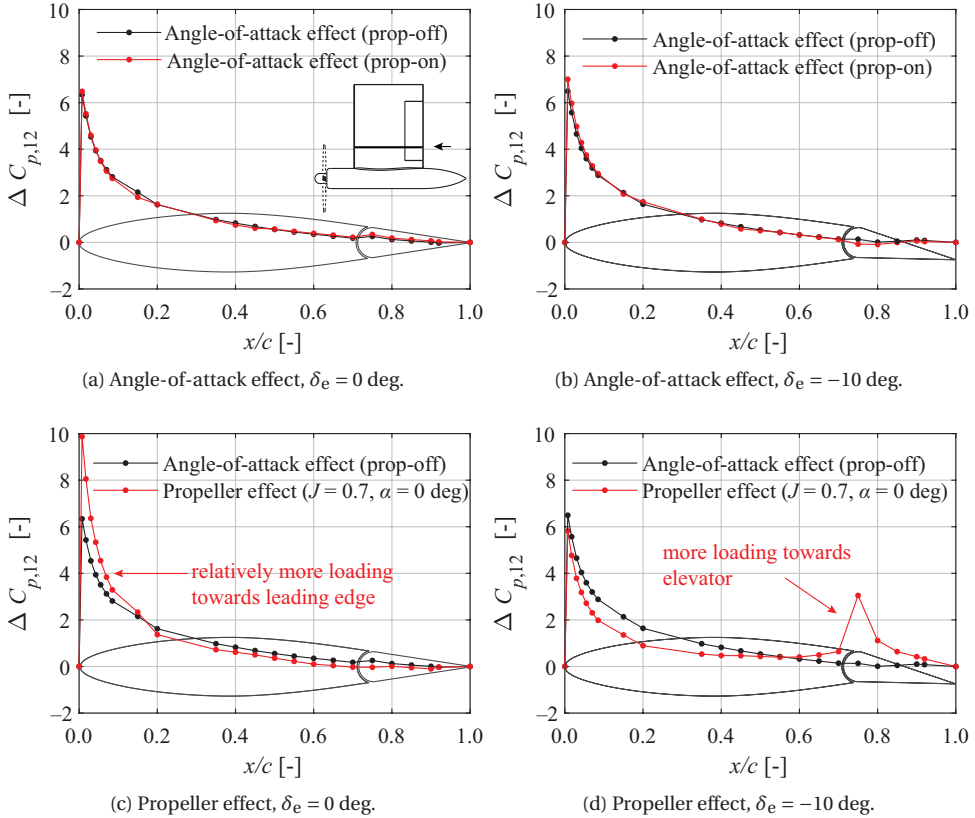
(d) Propeller effect, $\delta_e = -10$ deg.

Figure 8.25: Distribution of $\Delta C_{p,12}$ (Eqn. 8.4) for different loading conditions. Obtained from experimental data. Propeller on condition is $J = 0.7$ with a rotation direction opposite to the tailplane tip vortex.

If the ratio $D_p/c = \infty$, a two-dimensional airfoil would only experience a flow condition that is equal to an equivalent freestream condition. This also means that for low D_p/c ratios, which is the case for distributed propellers along the leading edge, the design of the leading edge of the wing becomes even more important. Again, if the T_C is maintained and the angle of attack is increased, one gets the distribution in Fig. 8.25a. In case the elevator is deflected, and the thrust is increased from $T_{C,1}$ to $T_{C,2}$, another distribution is obtained, shown in Fig. 8.25d. In that case, the change in loading is also strongly shifted to the leading edge of the elevator. This indicates the relevance of the elevator design, or in more general terms, trailing edge devices, if the objective is to gain a large lift change from the propeller in case such device is deflected. This also is an indication that the elevator effectiveness is to be enhanced by the propeller. This is further discussed in the next section.

8.3.3. Slipstream Deformation

When a slipstream washes over a lifting surface, the slipstream does not remain circular, which is also observed in numerous publications [37, 109, 116, 144, 185, 197, 248, 249]. The part of the slipstream that impinges on the lifting surface deforms, and with that, the whole slipstream deforms. The spanwise deformation is causing a larger part of the surface to be affected by the propeller, it leads to more unsteady loads (Section 8.5), and it leads to a crossflow component further downstream. For a wing-mounted propeller configuration, this leads to a crossflow to the vertical tailplane [173, 240]. Figure 8.26 shows such a deformation on each side of the lifting surface. Besides the shear, the iso-surface also indicates that near the surface there is a strong change in the direction of the vorticity; near the surface the vorticity vector is almost fully aligned with the local flow direction. The role of this change in helicity can be understood by considering the deformed flowfield for different tailplane loadings.

isosurface of vorticity magnitude at 800 s^{-1}

tip-vortex path

increased ω_x

decreased ω_x

−800 −400 0 400 800
axial vorticity ω_x[s^{-1}]

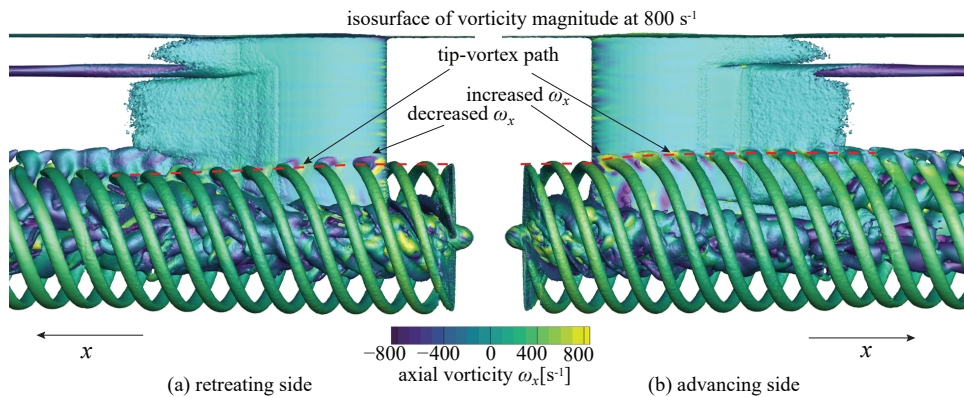(a) retreating side   (b) advancing side

Figure 8.26: Isosurface of vorticity illustrates a typical helical vortex field including slipstream deformation. Full-blade CFD results, $\alpha = 0$ deg, $\delta_e = +10$ deg.

From Fig. 8.27a it is evident that a higher propeller thrust leads to a larger deformation. In literature, this deformation is fully attributed to the spanwise gradient of loading. This gradient in circulation sheds trailing vorticity, which in its turn introduces a crossflow on the upper and lower surface, which is opposite in direction on each side. This cross flow then deforms the slipstream. However, as is evident in Fig. 8.27b, the spanwise gradient for $\delta_e = -10$ deg is significantly lower than for $\delta_e = +10$ deg, while for all cases the deformation is nearly the same (apart from the z-location of the deformation, which is determined by the trailing edge location of the tailplane). This already indicates that the spanwise gradient of circulation is certainly not the only factor that deforms the slipstream.
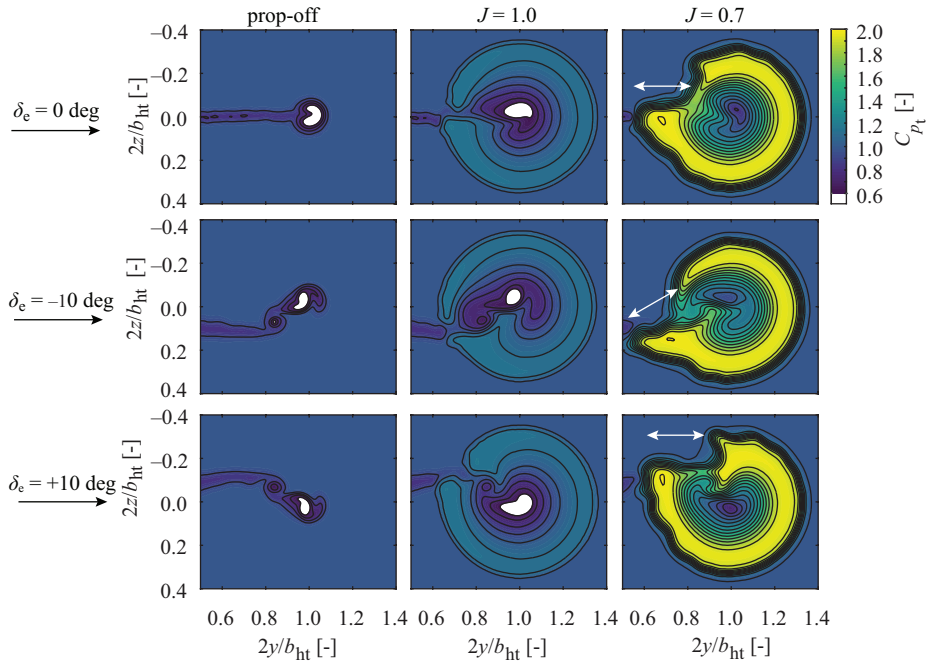
(a) Measured total-pressure coefficient at $1.5c$ behind the trailing edge of the propeller–horizontal tailplane model. White arrows indicate slipstream deformation due to interaction with the tailplane.
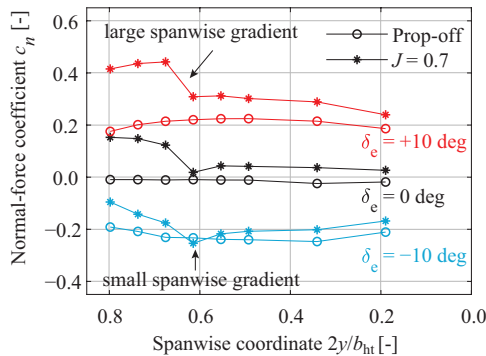
(b) Spanwise distribution of the loading

Figure 8.27: Slipstream deformation for the *PROWIM-HTP* case in (a). In (b) the spanwise normal-force distributions to demonstrate the weak link between spanwise gradient and slipstream deformation; for $\delta_e = -10$ deg and $\delta_e + 10$ deg the gradient is vastly different, while deformations are comparable.

Another factor that is likely to contribute is the deformation of the propeller helical tip vortex when it impinges on the leading edge. As shown in Refs. [94, 174], the vortex bends around the leading edge. Because of the no-slip boundary condition, it is also highly curved inside the boundary layer. The reorientation of the vorticity component in

axial direction therefore also leads to a spanwise translation. On each side of the lifting surface the axial component near the surface is opposite in direction, hence the spanwise translation is also in opposite direction.

8.3.4. EFFECT OF SPANWISE LOCATION

Until now, the focus has been on the tip region where the propeller and tip vortex of a tailplane interact. When the propeller is mounted more inboard, there is still a tip vortex from the lifting surface, while the propeller hub vortex is no longer shed at that location. Instead, the propeller tip vortices are then also in the vicinity of the tip of the lifting vortex, illustrated in Fig. 8.28. Furthermore, the edge of the slipstream on the inboard side is now impinging on the lifting surface closer to the root. Moreover, a more inboard positioned propeller also affects the lifting surface to a larger extent, since now both sides of the slipstream interact with the lifting surface. This not only leads to a larger jump in circulation at the propeller rotation axis, it also leads to a more complex vortex-vortex interaction. To understand the trends of the force coefficients for this case, i.e. the gradient of the normal-force coefficient and the (induced) drag coefficient, the flowfields behind the *VGM-HTP* model are assessed.
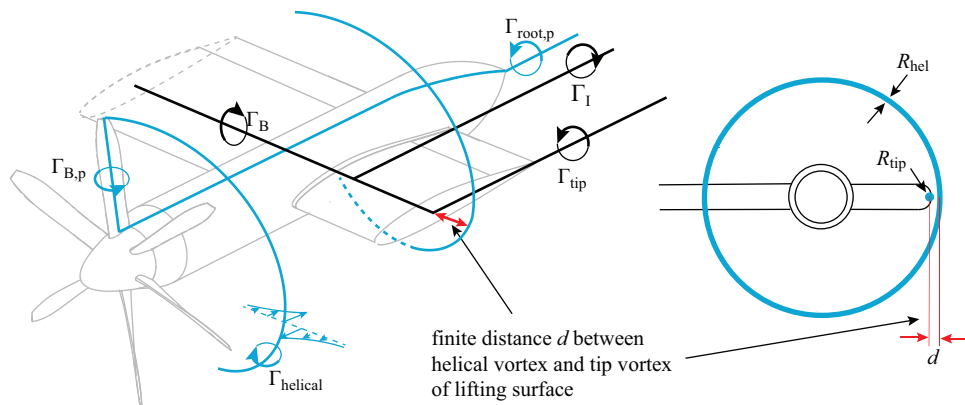

Figure 8.28: Simplified representation of a lifting surface submerged in a propeller slipstream where the tip vortex and helical tip vortex are in close proximity.

A schematic of the tailplane vortex system is shown in Fig. 8.29a. The vortex shed from the tailplane–fuselage junction is indicated as Γ_I and its direction is opposite to the tip vortex, denoted by Γ_{III}. The gradient of the circulation along the span also sheds a vortex Γ_{II} at the nacelle. These vortices can also be distinguished in the axial vorticity distribution downstream of the model, shown in Fig. 8.29b. With the installation of the propeller, two vortex systems can be identified: a helical vortex system from the propeller and the shed vorticity from the tailplane. Conceptually, the combined propeller–tailplane vortex system can be simplified as schematically shown in Fig. 8.29a: a tailplane root-vortex (Γ_A), a vortex around the tip vortex impingement (Γ_B), a vortex shed at the propeller rotation axis (Γ_C), the tailplane tip vortex (Γ_D), the propeller hub-vortex and the circular sheet containing the vorticity shed by the propeller tips. In ad-

dition to the local swirl induced by the propellers, the relative strength and direction of this vorticity dictate the local downwash distribution and the rate at which these change with angle of attack partially determines $c_{n_{\alpha,\text{ht}}}(y)$.

For the outboard-up rotation, $\frac{d\Gamma_A}{d\alpha}$ is opposite to $\frac{d\Gamma_I}{d\alpha}$ and $\frac{d\Gamma_C}{d\alpha}$ is opposite to $\frac{d\Gamma_{II}}{d\alpha}$. The net result is that on the inboard part of the tailplane, the outboard-up rotation leads to a smaller downwash. The opposite is the case for the inboard-up rotation direction. The consequence is that for the outboard-up case, the root vortex shed from the tail is nearly nonexistent if the angle of attack is increased from $\alpha = 0$ deg to $\alpha = 5$ deg. At the tip of the tailplane, the axial component of the propeller tip vortex is opposite in sign to the tip vortex of the tailplane for the inboard-up rotating propeller (contrary to a propeller that is mounted on the tip of the horizontal tailplane). The net effect is locally a higher induced loss, hence a lower $c_{n_{\alpha,\text{ht}}}$ in the tip region. This is an indication that the particular position of the propeller relative to the root and tip vortex of the tailplane is such that the typical trend of a higher C_{L_α} for an inboard-up rotating propeller (e.g. Ref. [116]) does not hold. This observation is confirmed in Section 8.4.2.

(a) Schematic of the propeller and tailplane vortices at $\alpha = 0$ deg

(b) Time-averaged normalized axial vorticity in a plane downstream of the model, $J = 1.8$. Full-blade CFD results.
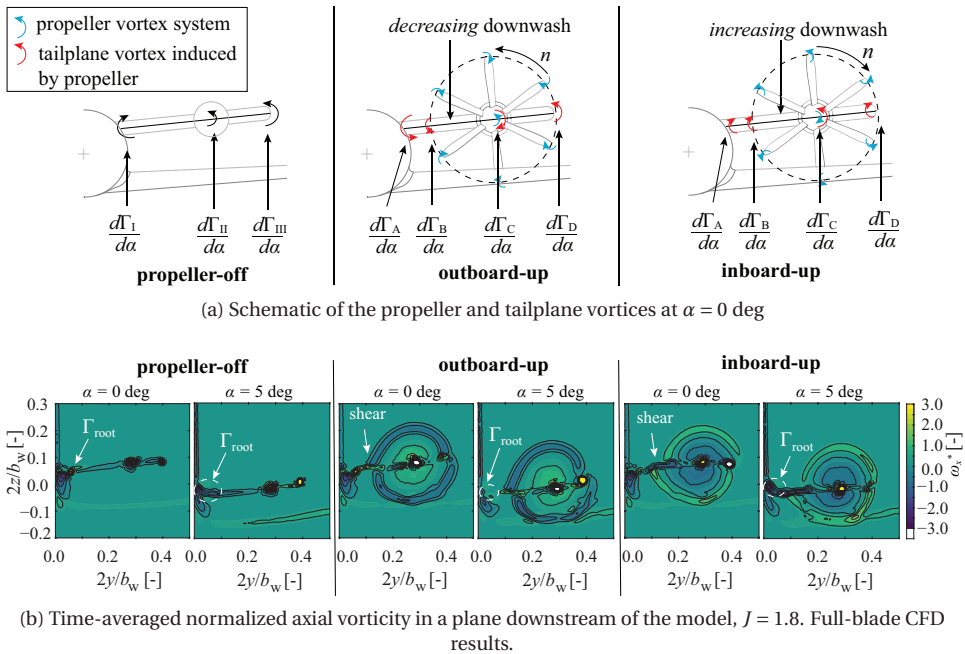
Figure 8.29: Vortex structures of the propeller–tailplane combination of the *VGM-HTP* model.

8.4. TIME-AVERAGED RESPONSE OF LIFTING SURFACES TO A SLIPSTREAM

In the previous section, it has been shown that the dominating fundamental mechanisms of the aerodynamic interaction strongly depend on the relative position of the
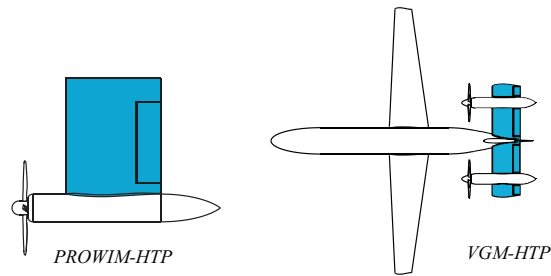
PROWIM-HTP

VGM-HTP

Figure 8.30: Two test cases to quantify the propeller installation on different types of surfaces (in blue).

propeller to a lifting surface. In this section, the time-averaged response of the lifting surface of two example cases are investigated. Again, a tip-mounted propeller is selected, and a case where the propeller is mounted more inboard, schematically shown in Fig. 8.30.

Key elements for these configurations are the offset of the $C_N - \alpha$ curve (which influences the trim on aircraft level), the slope of the $C_N - \alpha$ curve (that determines part of the changes in longitudinal static stability), the maximum lift coefficient, and the control surface effectiveness (which both determine the installation effect on control authority). Although the findings discussed in this section are in particular tailored to the application of a tailplane, the results also confirm the findings of other authors for a wing-tip mounted application.

8.4.1. *PROWIM-HTP*: Tip-Mounted Propeller

The impact of propeller thrust setting and elevator setting on the change in tailplane loading is analyzed using both experimental and numerical data. Figure 8.31 depicts the measured spanwise distributions of the normal-force coefficient for the three elevator deflections and a range of advance ratios. The normal force is computed by integrating the experimentally obtained pressure distributions. Two angles of attack are considered: $\alpha = 0$ deg and $\alpha = +10$ deg.

The propeller installation increases the normal force on the tailplane by locally inducing a larger angle of attack and a higher dynamic pressure, with the largest increase in c_n observed in the part of the tailplane immersed in the propeller slipstream. The loading distribution on the part of the tailplane outside of the slipstream is also altered due to the changed trailing vorticity compared to propeller-off conditions, as discussed in the previous section. The $\alpha = 0$ deg case (Fig. 8.31a) shows that a positive deflection of the elevator results in a significantly larger change of the normal force compared to a negative deflection. Increasing the angle of attack to 10 deg, the difference between prop-off and prop-on increases slightly. At this angle of attack, the net normal force on the tailplane is positive and the tailplane tip-vortex is contra-rotating to the propeller for $\delta_e \pm 10$ deg. Consequently, the change in aerodynamic interaction between the two elevator settings is now only related to a difference in tip-vortex strength. Two observations can be made. First, a propeller that is co-rotating with the tailplane tip vortex still increases the normal force due to the higher dynamic pressure in the slipstream. Second,

the ΔC_N of the counter-rotating case ($\delta_e = -10$ deg) appears slightly higher at $\alpha = 10$ deg, indicating a higher C_{N_α}. Figures 8.31c and 8.31d demonstrate the effect of the slipstream on the local lift coefficient and shows that:

- The maximum lift coefficient is enhanced by up to $\Delta C_L = 0.25$ for the measured range of advance ratios and is reached at approximately the same angle of attack, in line with Ref. [238].

- There is an offset of the lift curve which changes the equilibrium condition.

- The lift-curve slope increases which is a combination of the higher dynamic pressure, the fact that $\frac{d\alpha'}{d\alpha_\infty} < 1$ (see Section 8.2), and the reduced downwash gradient.

- The change in lift due to an elevator deflection at the same angle of attack is larger, because the elevator itself is also increasing its effectiveness in addition to the more effective main element.

- The stall behaviour is not significantly altered.

(a) $\alpha = 0$ deg

(b) $\alpha = +10$ deg

(c) Section lift coefficient, $\delta_e = 0$ deg. Only pressure forces.

(d) Section lift coefficient, $\delta_e = -10$ deg. Only pressure forces.
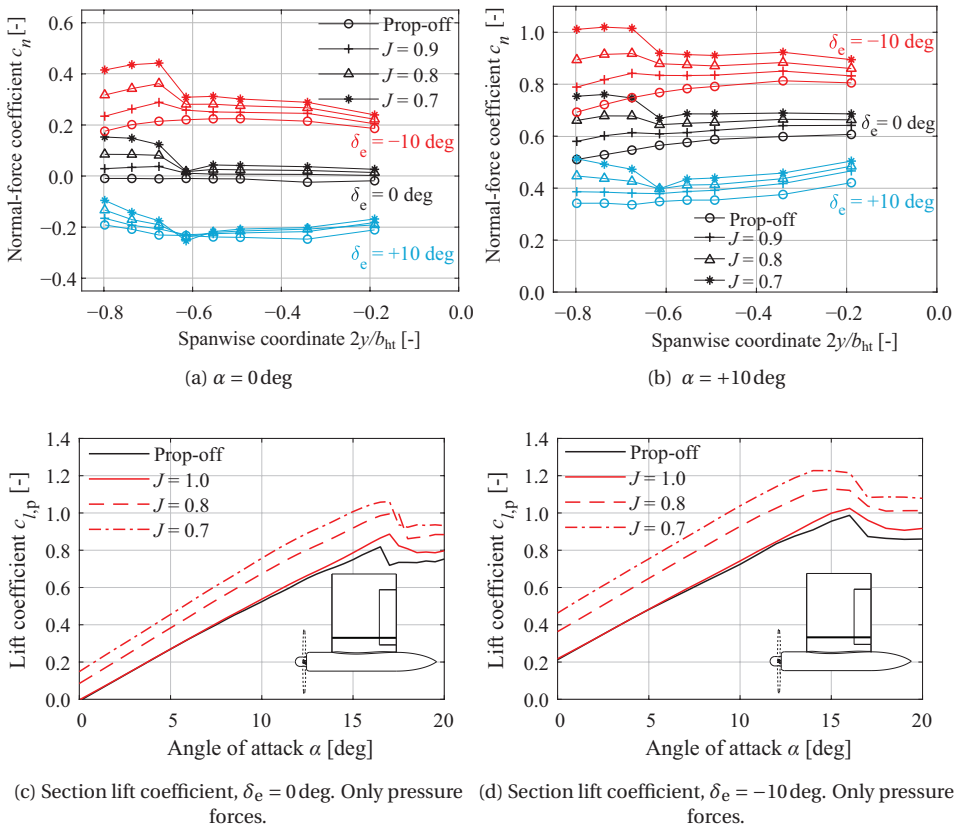
Figure 8.31: Normal-force and lift coefficients obtained by integration of the measured pressure distributions. Experimental data of the *PROWIM-HTP* model.

To assess the local changes to the tailplane loading caused by the interaction with the slipstream, the pressure distributions are analyzed. Figure 8.32 displays the measured and computed pressure distributions at a spanwise station located inside the propeller slipstream, for both the positive and negative elevator settings. The interaction with the propeller slipstream introduces a number of differences in the pressure distribution on the tailplane compared to the propeller-off case. First, for the case with the propeller present the pressure coefficient at the stagnation point is above unity due to the increased total pressure in the slipstream. This effect can also be observed on the pressure side of the elevator. Second, the increased suction occurs primarily in the leading-edge region, as is highlighted in the previous section. For the case with $\delta_e = +10$ deg (Fig. 8.32 (a)), this is reflected in a clear increase in the suction peak, while for the case with $\delta_e = -10$ deg the suction and pressure sides are interchanged compared to the propeller-off condition. For both cases, this is due to a local increase in the angle of attack experienced by the tailplane. The effect is especially pronounced in the leading-edge region of the tailplane due to the finite height of the slipstream, as discussed in the previous section. As already observed in Fig. 8.25, a change in angle of attack from α_1 to α_2 with the propeller present is not changing the shape of the pressure distribution. This means that also at a higher angle of attack, the largest effect on the pressure distribution remains in the leading-edge region. This is especially confirmed by the distributions in Figs. 8.32c and 8.32d. These results suggest that the lift vector is tilted into the freestream direction, and at the same time, the aerodynamic center of the airfoil is shifted towards the leading edge. This also means that the adverse pressure gradient becomes steeper with the propeller installed. From the perspective of control, the integral force on the propeller-tailplane model that are introduced by an elevator deflection is relevant. As already indicated in Fig. 8.25, the elevator effectiveness is significantly increased by the propeller installation, shown in Fig. 8.32e. The difference between the two elevator deflections can be explained by the downwash distribution along the tailplane. In Fig. 8.27a it is clear that the induced velocity field as a consequence of the slipstream deformation differs between $\pm \delta_e$. This is observable in Fig. 8.32f in the downwash distribution, where $\delta_e = -10$ displays a smaller reduction in downwash along the span. This means that there is a lower impact of propeller installation on the lift distribution, hence a slightly lower elevator effectiveness.

8

(a) $2y/b_{\mathrm{ht}} = 0.74$, $\delta_{\mathrm{e}} = +10\,\mathrm{deg}$

(b) $2y/b_{\mathrm{ht}} = 0.74$, $\delta_{\mathrm{e}} = -10\,\mathrm{deg}$

(c) $\delta_{\mathrm{e}} = 0\,\mathrm{deg}$

(d) $\delta_{\mathrm{e}} = -10\,\mathrm{deg}$

(e) Elevator effectiveness of full tailplane, including propeller forces. Evaluated at $\alpha = 0\,\mathrm{deg}$.

(f) Difference in phase-averaged downwash distribution along a horizontal surveyline at $2z/b_{\mathrm{ht}} = 0.1$, PIV results
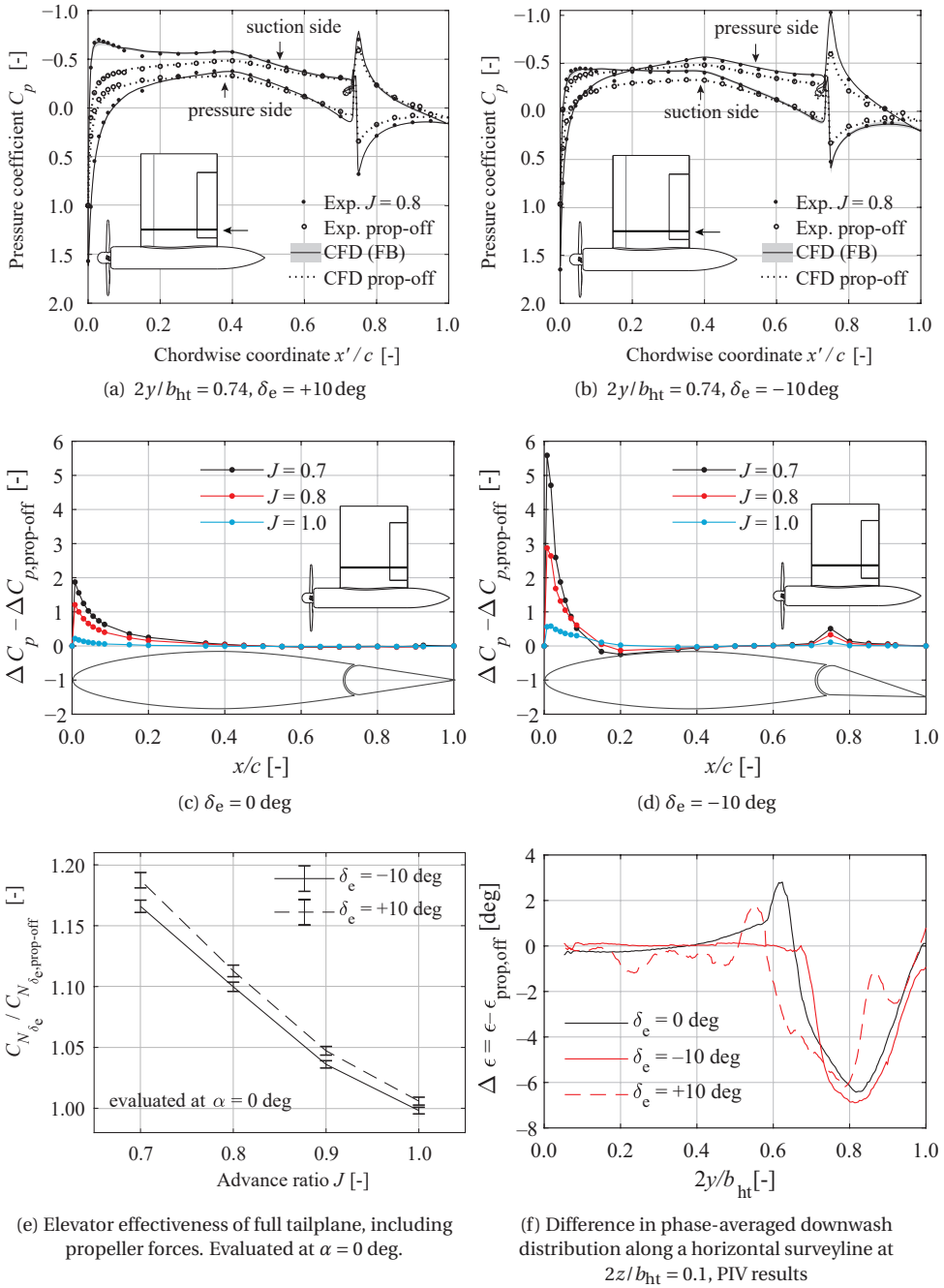
Figure 8.32: Effect of propeller installation on tailplane pressure distributions and integral loads, $\alpha = 0\,\mathrm{deg}$.

239

The tilting of the lift vector corresponds to the two drag-reducing mechanisms (see Section 8.3.1). The beneficial effect of propeller installation on the lift-to-drag ratio is demonstrated in Fig. 8.33, which depicts the lift-to-drag ratio by the integration of the experimentally obtained pressure distributions. The shear forces are therefore not included. Since these are values for a certain section washed by the slipstream, the benefit for the full lifting surface will obviously be lower, although the same trends will apply. The following can be observed in case the propeller is rotating against the tailplane tip vortex:

- The maximum two-dimensional c_l/c_d ratio increases with propeller thrust coefficient.

- The maximum c_l/c_d occurs at a higher lift coefficient but at the same angle of attack.

- The maximum lift coefficient increases significantly.

In case of a wing-mounted propeller configuration, these observations have a direct implication on the aircraft performance. To achieve optimal cruise performance, either the wing area is to be reduced if it were designed for propeller-off conditions, or the aircraft should fly at a higher altitude. This also means that at low lift coefficient, the propeller-off condition outperforms the propeller-on condition. This means that the propeller installation is not beneficial for all lift coefficients. In other words, from the perspective of the lifting surface, the installation benefit on lift-to-drag ratio is especially present for medium to high lift coefficients. If a low lift coefficient is to be maintained (e.g. for a tailplane mounted propeller), then additional drag is introduced if the propeller-induced lift is to be counteracted by a trim deflection (further discussed in Section 9.2.2).

(a) Section $\frac{c_{l,p}}{c_{d,p}}$ ratio vs. c_l (b) Section $\frac{c_{l,p}}{c_{d,p}}$ ratio vs. α

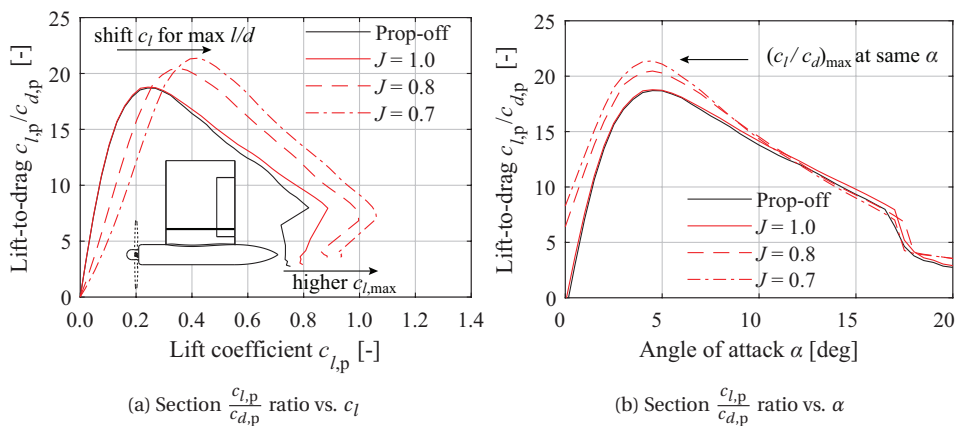Figure 8.33: Effect of propeller installation on lift-to-drag ratio of a section washed by the slipstream, $\delta_e = 0$ deg. Results obtained by pressure integration for the particular spanwise section (shear forces not included).

The limited spatial resolution of the experimental data in the spanwise direction masks the gradients in the loading distribution near the slipstream edge and the flap

edges. Therefore, the CFD data are assessed to obtain more detailed loading distributions for the case at $J = 0.8$. Figure 8.34 presents the resulting spanwise distributions of the time-averaged normal-force coefficient for the positive and negative flap settings. For comparison reasons, both the propeller-off and propeller-on configurations are considered, while the available experimental data are also included. The presence of the elevator is reflected in the loading distributions by the rapid changes in c_n along the span at $2y/b_{\mathrm{ht}} = 0.18$ and 0.81. The local decrease of c_n at the spanwise location where the propeller tip is located, is likely the result of the locally decreased static and total pressure at the edge of the propeller slipstream introduced by the propeller tip vortices, observed before in e.g. Ref. [250]. The fluctuations in normal force obtained from the CFD analysis highlight that variations in c_n occur primarily in the propeller slipstream region, with a magnitude of $c_n = \pm 0.01$. The magnitude of these fluctuations is comparable for the cases at $\delta_e = +10$ deg and $\delta_e = -10$ deg. Variations on the mean c_n outside the slipstream may be considered negligible. These changes are an effect of the time-dependent vortex field associated with the tailplane sections immersed in the propeller slipstream, further discussed in Section 8.5. The change in the time-average of the normal force on the nacelle with respect to the prop-off case is limited. The non-negligible c_n fluctuations on the nacelle should be considered as an artefact of the selected propeller geometry, and are not a general characteristic of the tailplane-mounted propeller configuration.
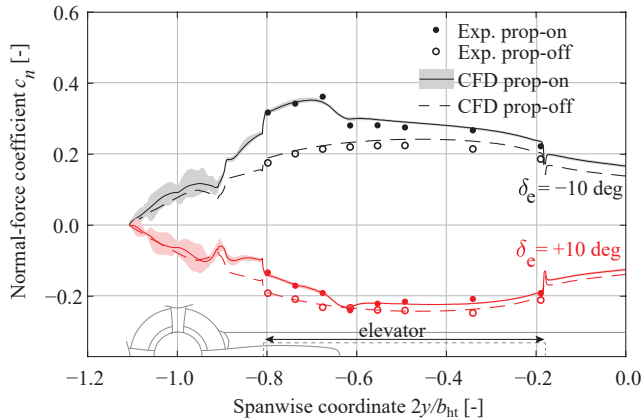

Figure 8.34: Spanwise distributions of normal-force coefficient for positive and negative elevator deflection.

The results in Figs. 8.31 and 8.34 resemble two counter-rotating propellers mounted on each tip of a horizontal tailplane. To quantify the differences between the co-rotating and counter-rotating cases for the current geometry, the full span of the tailplane is simulated with both elevators deflected by $+10$ deg for the co-rotating case, as depicted in Fig. 8.35a. This reveals to what extent a superposition can be applied for each side of the tailplane to arrive at a co-rotating propeller configuration. The input for the actuator-disk model (see Ref. [133]) is the extracted blade loading from both the $\delta_e = +10$ deg and $\delta_e = -10$ deg full-blade propeller simulations. This approach assumes that the nonuniform propeller loading for the co-rotating case is the same as for the counter-rotating

case.

In Fig. 8.35b is shown that a co-rotating propeller installation leads to a loading distribution that is different than a superposition of each side. The fact that the loading on the full tailplane is affected, including the circulation at the mid-plane, causes the change in loading to be smaller. Additionally, at the mid-plane there is a finite gradient in loading, which indicates that there is a cross-flow component. The appreciable effect of this component on the aircraft yawing moment is demonstrated in Section 9.2.3. In that case, there is also a fuselage that largely prevents the pressure communication, as it act as a boundary condition with a certain height in z-direction [251].

(a) Schematic of the analyzed co-rotating case by means of actuator-disks.
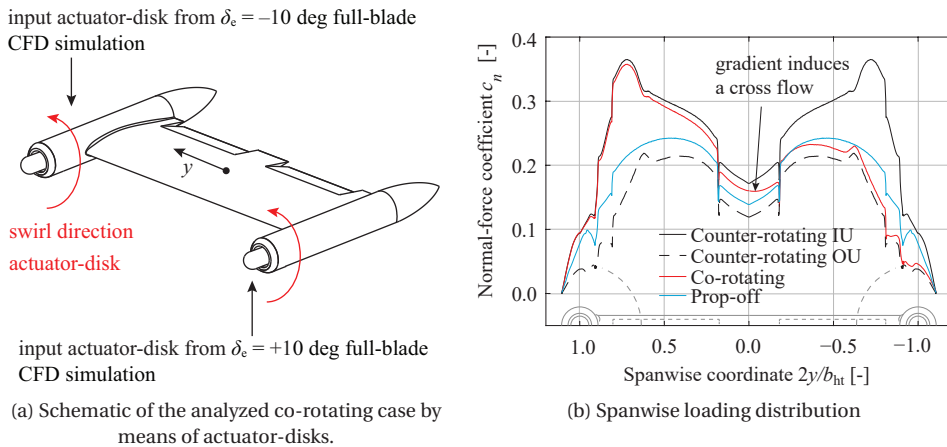
(b) Spanwise loading distribution

Figure 8.35: Computed spanwise load distribution on the *PROWIM-HTP* tailplane model for a co-rotating and two counter-rotating propeller installations at $J = 0.8$ and $\alpha = 0$ deg. The propellers are modelled by actuator disks.

8.4.2. *VGM-HTP*: Tail-Mounted Propeller

In Section 8.3 it is shown that compared to a tip-mounted propeller, a more inboard mounted propeller has quite a different interaction with the lifting surface as the vortex systems of the two elements are displaced with respect to each other. The strength of the trailing vortices shed from the lifting surface vary significantly between the two rotation directions, and it can therefore be expected that such installation also affects the aircraft trim and stability characteristics. In terms of performance, in particular the change in drag characteristics and the offset in the normal-force curve are of interest, as they influence the aircraft drag in trimmed conditions. From a stability perspective, primarily the gradient of the normal-force curve, herein referred to as the effectiveness of the tail, is a relevant quantity.

Since propeller installation is quantified relative to the propeller-off condition, it is necessary to first assess the propeller-off condition. The propeller-off normal-force coefficient is plotted in Fig. 8.36a. At $\alpha = 0$ deg, there is a downforce on the tailplane due to the wing-downwash. The presence of the fuselage leads to a drop in c_n near the tail–fuselage junction, such that a vortex is shed that is opposite in sign to the tip-vortex. This

is the case for both $\alpha = 0$ deg and $\alpha = 5$ deg. The added loading by the propellers, shown in Fig. 8.36b, are typical for an aerodynamic surface behind a propeller: the direction of the local swirl determines the direction of the change in lift-force, and the distribution of circulation redistributes the additional load in spanwise direction such that the changes are not contained in the region where the slipstream impinges on the tailplane [37]. It is noted that a normal force should not be mistaken with a lift-force: at a nonzero angle-of-attack, the tailplane-drag also enhances the force normal to the tailplane. For either rotation direction, the largest change in load occurs on the inboard part of the tailplane. This can directly be related to the distribution of $c_{n_\alpha}(y)$ of the propeller-off condition, which reduces towards the tip because of the tip-relief effect. This effect is depicted in Fig. 8.36c which is computed over the interval $\alpha = [0, 5]$. For the propeller-off case, the average c_{n_α} of the outboard part is 39% lower than the one of the inboard part and would be even lower if the tailplane had a lower aspect ratio.
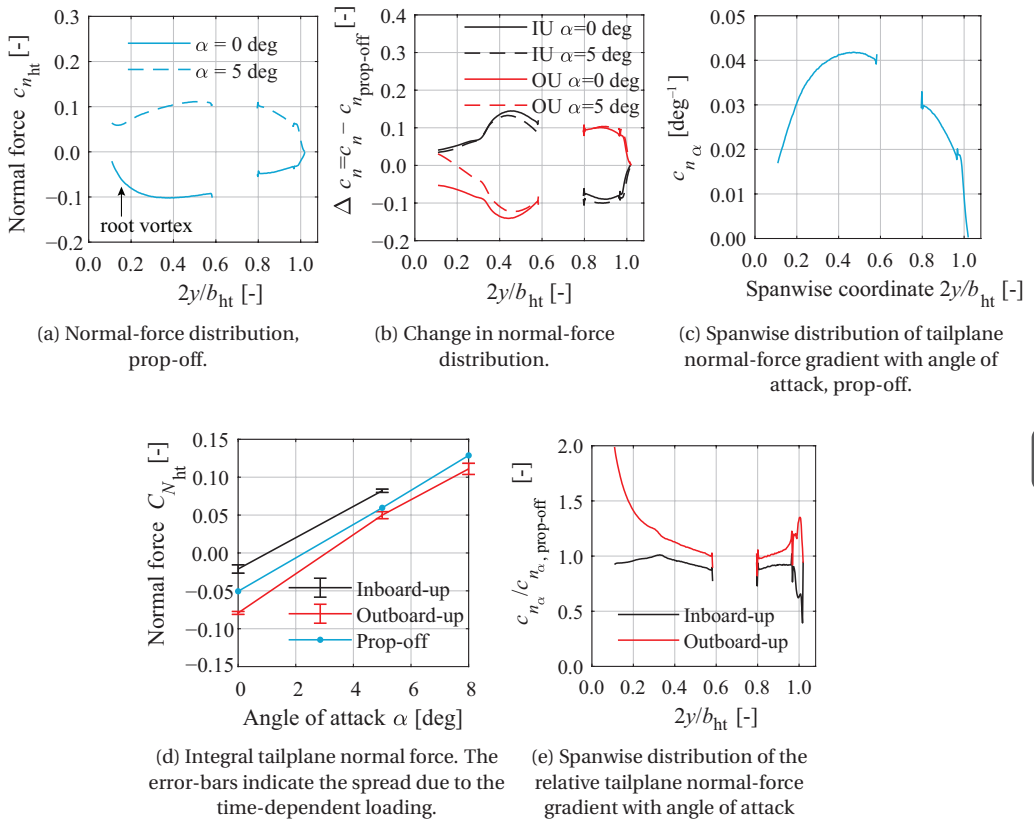

(a) Normal-force distribution, prop-off.

(b) Change in normal-force distribution.

(c) Spanwise distribution of tailplane normal-force gradient with angle of attack, prop-off.

(d) Integral tailplane normal force. The error-bars indicate the spread due to the time-dependent loading.

(e) Spanwise distribution of the relative tailplane normal-force gradient with angle of attack

Figure 8.36: Effect of propeller installation on the tailplane load distributions and integral forces on the *VGM-HTP* model, time-averaged results of full-blade CFD simulations, $J = 1.8$.

The combination of the varying c_{n_α} and the higher dynamic pressure in the slipstream leads to a net normal force on the tailplane with the direction depending on the

rotation direction of the propeller, shown in Fig. 8.36c. Besides the offset at $\alpha = 0$, the gradient $C_{N_{\alpha_{ht}}}$ relative to the propeller-off condition is 17% higher for the outboard-up configuration while the inboard-up rotation shows a 7% reduction for the cruise condition ($J = 1.8$). The difference between the two rotation directions is due to a combination of the downwash distribution that is a function of the vorticity shed by the tailplane and the varying inflow angle with angle-of-attack. Figure 8.36e reveals that the tailplane sections towards the root, are particularly affected by the propeller installation as locally c_{n_α} is twice the value of the propeller-off condition, despite the fact that these are outside of the region on which the propeller slipstream impinges. The $1/y$ character of c_{n_α} for the outboard-up rotation indicates that in particular the vortex stemming from the tailplane–fuselage junction is manipulated by the propeller. This is confirmed in Fig. 8.29. Therefore, the rate at which the slipstream is changing on the inboard part of the tailplane is yielding an *opposite* trend to what is observed in Fig. 8.36e: for the outboard-up rotating propeller the swirl and dynamic pressure increase which reduce C_{N_α}. Therefore, the observed trends of C_{N_α} are attributed to the interaction of the propeller vortex system with the tailplane and not to the changing slipstream characteristics with angle-of-attack.

The drag force on the tailplane is changed by a higher friction drag, a change of drag as the added lift ΔL is titled relative to the freestream because of the swirl in the slipstream, and by the induced drag as the tailplane vortex system is influenced by the propeller. A swirl which locally enhances the normal force in propeller-off condition, locally leads to a larger swirl-recovery by the tailplane [37]. Therefore at $\alpha = 0$ deg, there is a reduction of tailplane drag on the side of the downgoing blades as the tailplane in propeller-off condition produces a positive normal force in z-direction, as shown in Fig. 8.37a. The tailplane sections that exhibit a high lift-to-drag ratio in propeller-off condition, i.e. towards the root, also have a higher potential to reduce the drag locally for a given swirl angle. At $\alpha > 0$ deg, the drag reduction becomes less for the outboard-up rotating propeller. Not only the absolute drag is reduced at a constant angle-of-attack, also the integral tailplane drag at the same C_N depends on rotation direction, shown in Fig. 8.37b. For higher angles-of-attack, for which there is a positive $C_{N_{ht}}$, an inboard-up rotating propeller leads to a lower drag at the same normal force.
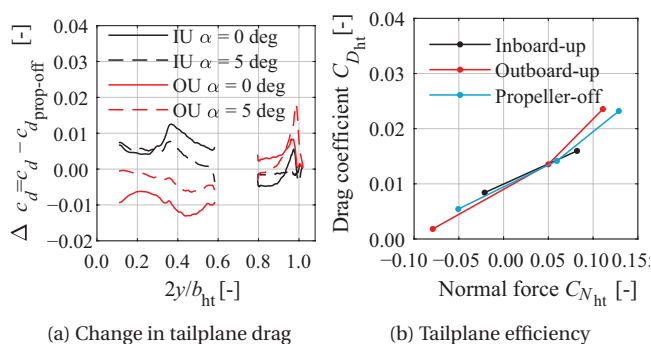

(a) Change in tailplane drag

(b) Tailplane efficiency

Figure 8.37: Effect of propeller installation on the tailplane load distributions and integral forces, $J = 1.8$.

8.5. UNSTEADY RESPONSE OF LIFTING SURFACES

The previous sections have established the understanding of the time-averaged effect of propeller installation on the forces acting on lifting surfaces that are relevant for the overall aircraft stability and control characteristics. By analyzing time-dependent load distributions on the lifting surface, not only insights are gained for structural design perspective, they also reveal opportunities to reduce the unsteady loads produced by the propeller–lifting surface combination. The observations made from those analyses may drive design choices such as rotation direction, propeller position relative to the airframe, and the tail size.

In Chapter 2 it is discussed that the local angle of attack, dynamic pressure, and static pressure vary at each location inside and outside the slipstream. It is widely known that this time-dependent slipstream induces unsteady pressures on a lifting surface [94, 249, 252, 253]. These fluctuations lead to a relevant increase in noise compared to the propeller loading noise [254, 255] and, in most circumstances, also cause the circulation around a section of the lifting surface to be time-dependent. For pylon-mounted propellers, several publications have shown significant reductions in unsteady pressures by applying porous material near the leading edge of lifting surfaces [256–258], which is the region where the largest pressure fluctuations occur [94, 112]. Even though these strategies exist, the application of such material adds significantly to the profile drag and reduces the lift performance [256]. Furthermore, while the reported reductions are significant, these fluctuations cannot be removed completely by the application of such material. The understanding which factors drive the unsteady response may therefore lead to less intrusive design modifications, such that the lifting capability is not compromised. For example, a slight adjustment of the propeller operating condition or local adaptations to the geometry such as the selection of the local chord length may already be effective.

Previous studies on unsteady response of a surface in the proximity of a lifting surface [94, 197, 245, 248, 253], have not discussed the role of nonuniform propeller loading on the unsteady loads on the lifting surface. Furthermore, the focus on the effect of an angle of attack, the rotation direction, and the spanwise location on the magnitude of these unsteady loads is limited. In this section, these factors are addressed by quantifying the unsteady component of the loading that manifest in structureborne noise and vibrations to the rest of the airframe. The approach is therefore to limit the analyses by only considering the aerodynamic phenomena that are dominant. The following questions are addressed herein:

- What is the effect of the spanwise location of a propeller on the unsteady loads on the lifting surface?

- How does the nonuniform disk loading affect the time-dependent loading on a lifting surface?

- What implication has a displaced slipstream due to an angle of attack on the loading on a lifting surface?

- What design choices can be made that would reduce the overall vibrations transmitted from the lifting surface to the fuselage?

These questions are evaluated for propeller–tailplane combinations, where the lift coefficient remains in the linear part of the lift curve, and the ratio of the diameter to chord is relatively high. Nevertheless, the trends and conclusions that are identified are also applicable for wing-mounted configurations where the lateral spacing of the propellers is such that there is no aerodynamic interaction between adjacent propellers. First, an overview of the mechanisms that lead to unsteady loads is provided, based on previous literature. This is required to explain the findings of this section, but also to prioritize the phenomena that are relevant for further investigation. Subsequently, Section 8.5.2 presents CFD results of the unsteady interaction by using a representative test case.

8.5.1. Mechanisms Leading to Unsteady Loads

The mechanisms that lead to unsteady loads on the lifting surface have been presented in several studies, of which a brief overview is given in this section. Prior to assessing the impact of the unsteady flowfield on the loading on the lifting surface, it is necessary to revisit the instantaneous flowfield introduced by the propeller. The flowfield will provide an indication what regions of the lifting surface will generate unsteady loads, of what trends can be expected, and will allow for hypotheses to be formed such that specific quantities are investigated in the following.

A typical instantaneous flowfield behind a propeller in isolated conditions is depicted in Fig. 8.38. The tip vortices are clearly visible, which introduce strong velocity and pressure gradients to a lifting surface. From the horizontal survey lines it is clear that even outside the slipstream, there is a time-dependent flowfield. Inside the slipstream, in addition to the velocities induced by the helical vortex system, the blade wakes also introduce local variations.
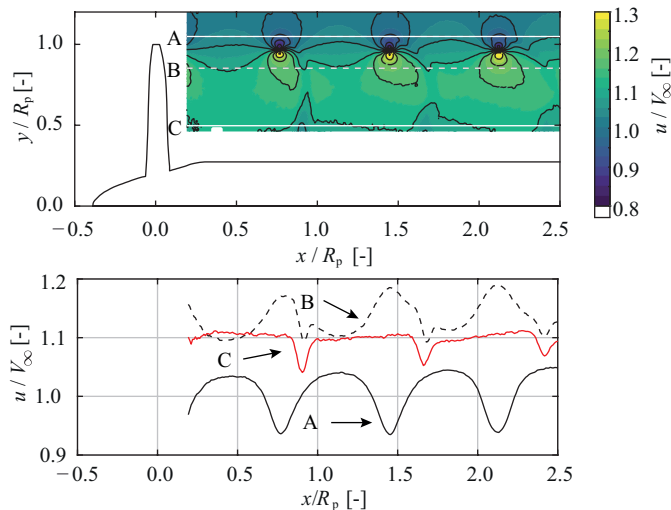

Figure 8.38: Experimental results of an instantaneous flowfield showing that the length scale of the perturbation strongly varies in the slipstream. PIV results of the XPROP propeller (Section 3.4). Conditions: $J = 1.8$, $\beta_{0.7R_p} = 45$ deg.

In Section 2.3.3, more specifically Fig. 2.20, it is shown for an isolated propeller that the time-dependent component of a typical slipstream is primarily confined to the shear layer of the slipstream, introduced by the tip vortices that convect downstream. This is a well-known characteristic, e.g. also shown in Refs. [109, 116, 259]. As it is the vortex system that is the main cause of the unsteady flowfield, the magnitudes of these fluctuations are directly related to the blade loading. This is visualized in Fig. 8.39, which depicts the spread of local swirl angle and axial velocity around their mean values as a function of T_C. It is clear that with higher T_C—therefore stronger tip vortices—the magnitude of the fluctuations in the flowfield increase. A relevant condition is therefore a case of high disk loading.

(a) Radial variation of the unsteady flowfield

(b) Illustration of the axial velocity variations in the slipstream
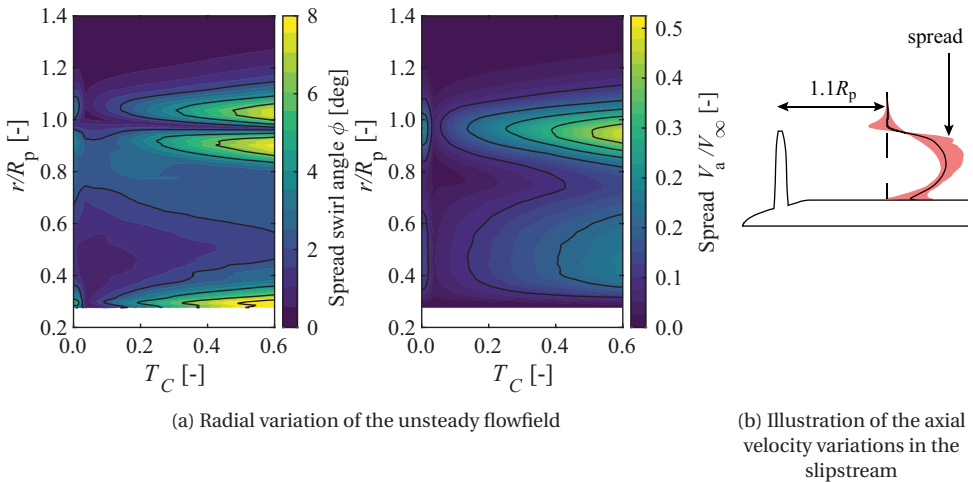
Figure 8.39: Unsteady flowfield in the slipstream of the XPROP propeller ($\beta_{0.7R_p} = 45$ deg) at $\alpha = 0$ deg as a function of thrust coefficient. Time-averaged full-blade CFD results.

Figure 2.21 in Section 2.3.3 shows that the extent of the fluctuations in the flowfield depends on the considered flow quantity. The static pressure perturbations are primarily confined in the core of the tip vortices, while the velocity perturbations are distributed over a larger region. It is noted that since this flowfield is obtained from CFD simulations, the spatial extent is larger than would occur in an experimental setup due to numerical diffusion. The time-dependent flowfield along the remainder of the propeller radius is partially introduced by the blade wakes and partially by the induced velocities (see Section 2.1.1). This will lead to fluctuations in the force coefficient along a large part of the span.

Figure 8.40 provides a few examples of the mechanisms. A distinction can be made in the effect of the periodic inflow on the response of the lifting surface: 'Direct lifting-effects' and 'Lifting-effects due to interaction'.
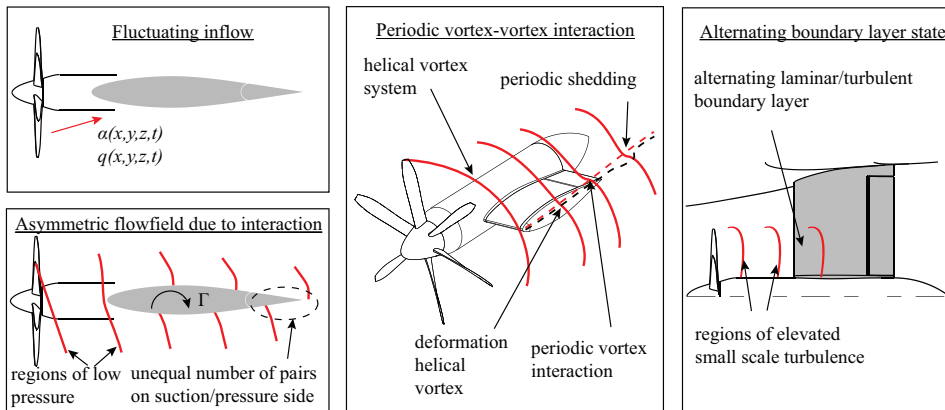
Figure 8.40: Different causes of propeller-induced unsteady loading on a lifting surface, based on Refs. [94, 110, 174, 248, 249].

Direct lifting-effects

- *Fluctuating inflow.* The fluctuations of local angle of attack and dynamic pressure ahead of the airfoil directly change the local lift and drag coefficient of the airfoil. The two regions that entail the largest fluctuations in terms of magnitude and gradient are the tip vortex and the viscous wakes that trail from the blades (see e.g. Fig. 2.19). This fluctuating inflow could therefore be seen as a two-dimensional effect, comparable to a two-dimensional airfoil experiencing a disturbance such as a gust [111]. Although the frequency of the disturbance is the same along the span, the time-scale of the perturbation highly depends on the radial coordinate and therefore spanwise location. This strongly varying flowfield is depicted in Fig. 8.38. In Ref. [112] it is highlighted that the reduced frequency $\sigma \frac{knc}{4\pi V}$ of the perturbation on a lifting surface has a profound effect on the magnitude and phase delay of the response, i.e. unsteady lift and drag. For a given magnitude of the perturbation, the response is larger if the reduced frequency of the perturbation is lower. In other words, not only the magnitude of the disturbance is important, also the advance ratio.

- *State of boundary layer.* The elevated turbulence level in the turbulent wakes that trail from the propeller blades affects the transition location on the lifting surface, for example shown in Ref. [110]. Between the passing blade wakes, the flow can be laminar. This alternating state of the boundary layer introduces periodic loading in drag and lift direction. This contribution can be expected to be small compared to the lift and drag due to a fluctuating inflow. Moreover, at typical flight Reynolds numbers, this contribution is even reduced, since it can be expected that a smaller chordwise fraction of the boundary layer is laminar. Therefore, this not further discussed in this dissertation.

LIFTING-EFFECTS DUE TO INTERACTION

Due to the three-dimensional character of the aerodynamic interaction, the unsteady response also depends on this interaction. Reference [243] presents a fundamental study on vortex–surface interactions, together with an extensive literature review on the vortex deformation, redistribution of vorticity, and interaction with a boundary layer. More specifically, the typical interaction of a helical vortex with a lifting surface is further discussed in Ref. [174]. That reference identifies the various phenomena that take place: the vortex bends around the leading edge, the helicity changes, the vortex interacts with the boundary layer, and there is periodic vortex shedding from the trailing edge. It is shown that the transport of the vorticity in downstream direction depends on the loading of the lifting surface as well as the viscous interaction with the boundary layer. The following distinction can be made in the effect of interaction on the unsteady loads:

- *Pressure effects.* A vortex that has a normal component to the chordline is split at the stagnation point. The low static pressure in the propeller tip vortex is therefore encountered by the lifting surface and the downstream convection of the vortex along the surface of the airfoil leads to local pressure fluctuations. If on each side of the lifting surface these are out-of-phase, the pressure difference leads to a net force [94, 253]. This is typically the case if there is circulation around the airfoil and in case of a shear of the slipstream in spanwise direction. An example of both is shown in Fig. 8.41, where there is a clear net pressure difference between suction and pressure side depending on the time instance. The magnitude of the pressure fluctuation is relatively small compared to the time-averaged pressure distribution. For higher thrust settings, the local fluctuating pressures may also lead to earlier (periodic) boundary layer separation, as the local adverse pressure gradient is increased, for example discussed in Ref. [243].

- *Vortex–surface interaction.* The spanwise displacement that is discussed in Section 8.3.1 induces a significantly different flowfield than an axisymmetric slipstream. The displacement of the split vortex at the trailing edge leads to vortex shedding. When the two displaced vortices on each side of the surface are shed, there is a downwash induced in between, which in turn affects the loading on the lifting surface periodically. Any response at spanwise location y due to a disturbance introduced by the propeller at the same spanwise location, is therefore spread in $\pm y$ directions. This is inherently a three-dimensional effect, as shown in Fig. 8.42.

- *Vortex–vortex interaction.* As discussed in Ref. [165], two vortices in proximity of each other interact. This means that the propeller helical tip vortex and the tip vortex of the lifting surface interact, especially when the two cores are sufficiently close to each other. This leads to a displacement and reorientation of the vorticity, which in its turn affects the induced angle of attack to the lifting surface in a time-dependent manner. The periodic shedding is clearly observable in Fig. 8.42.

  In Ref. [97] it is discussed that the helical vortex system can start to break down when it encounters a sufficiently large disturbance. Since the encounter with the lifting surface inherently leads to a deformed helical vortex system, this interaction can lead to a non-periodic flowfield, which in turn affects the loading on the lifting

8

surface. However, as demonstrated in Section 6.2, a displacement of the helical vortex far downstream has a negligible upstream effect.

(a) $2y/b_{ht} = -0.61$, $\alpha = 0$ deg and $\delta_e = +10$ deg

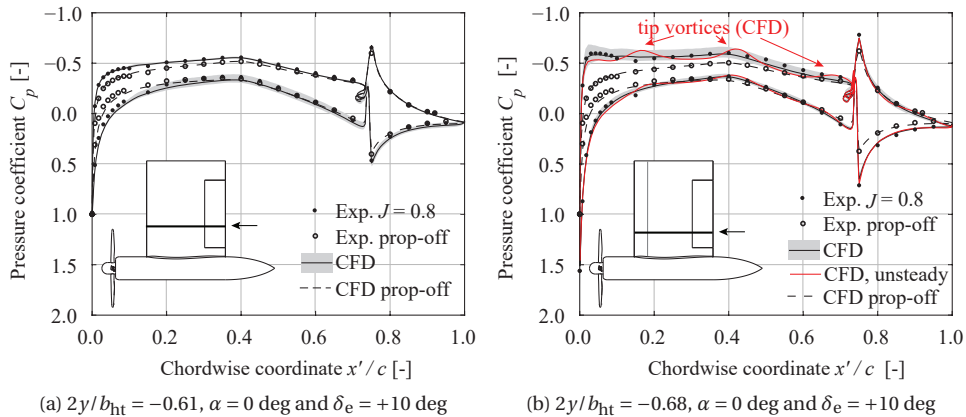(b) $2y/b_{ht} = -0.68$, $\alpha = 0$ deg and $\delta_e = +10$ deg

Figure 8.41: Time-averaged and time-dependent pressure distribution for the case *PROWIM-HTP* model $\alpha = 0$ deg and $\delta_e = +10$ deg. The shaded area indicates the spread of the pressure fluctuations over a full propeller rotation.
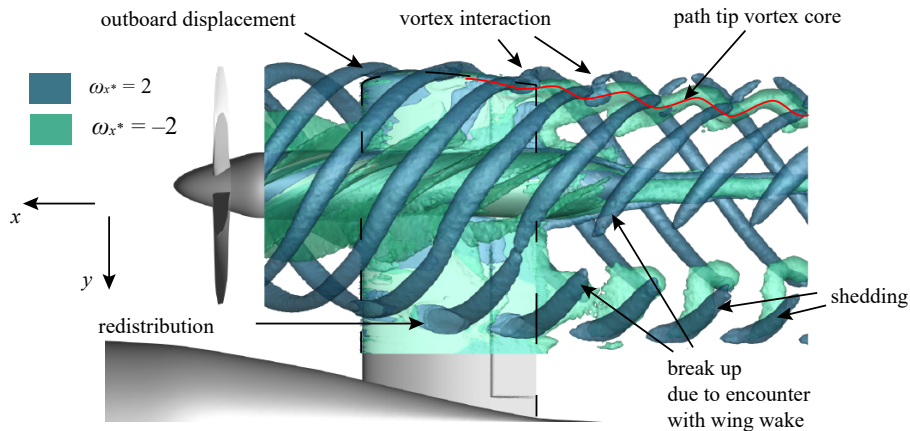

Figure 8.42: Instanteneous vortex field for inboard-up rotation on the *VGM-HTP* model in cruise conditions, $J = 1.8$, $\alpha = 0$ deg. Viewed from below, isosurface shown only part of the y-values.

8.5.2. QUANTIFICATION AND MITIGATION OF UNSTEADY LOADING

The magnitude, phase, and shape of the unsteady loads depend on various factors. Based on the slipstream shape (Chapter 2) and the knowledge of interaction between the helical vortex and lifting surface, it can be expected that the unsteady response depends at least on:

- Circulation around the lifting surface

- The chord length of the lifting surface relative to the pitch of the helical vortex system

- The gradients of the slipstream, which depend on the spacing between propeller and lifting surface, the drag coefficients of the propeller blade sections, and the strength of the tip vortices

- Aerodynamic characteristics of the lifting surface

- The relative position of the propeller vortex system to the vortex system of the lifting surface

A representative case ideally covers all these aspects to a certain extent. The relevance of propeller-induced vibrations is especially important for the configuration of a horizontal tail-mounted propeller configuration, since the main reason for the specific propeller location is improved passenger comfort. Since the design of the tailplane is less constrained than the wing design, the tailplane lends itself for more design freedom compared to a wing-mounted propeller installation. The selected configuration for the analyses is therefore the *VGM-HTP* model (see Section 3.3.5). This case allows for the distinction between the vortex system that impinges on an inboard part of the lifting surface, as well as the outboard part, which are two fundamentally different problems. It also illustrates the unsteady interaction between the tip vortex of the tailplane and the helical vortex system. Furthermore, the lift acting on the lifting tailplane greatly varies between flight conditions; from a downforce at low angle of attack, to a large lift at high angles of attack, which allows for the investigation of the effect that these parameters have on the unsteady loads. The combination of a relatively low aspect ratio of the tailplane (leading to strongly varying circulation along the span) and the mounting of the propeller at 70% of the span, allows for the assessment of spanwise location. More specifically, for a given design, the effect of lift coefficient, rotation direction, and layout of the tailplane on the unsteady loads are investigated.

First, to separate the propeller-induced loading in a mean and unsteady component, the normal-force distribution is depicted in Fig. 8.43. The spread indicates the minimum and maximum value at each spanwise location over a full propeller revolution. It is this force component that has the largest time-dependency; drag force fluctuations are a factor 10 to 30 smaller. Based on these distributions, several observations can be made:

- The spread is distributed relatively evenly within the slipstream and the force fluctuations are of the order of $\pm 10\%$ around mean value that is induced by the propeller, in line with Ref. [248]

- Outside of the slipstream, the unsteady effect is small, but still present. The varying circulation along the tailplane still influences the downwash behind the lifting surface, and therefore also the loading between the fuselage and slipstream edge.

251

- The unsteady loads on the outboard part of the tailplane are different in magnitude and the distribution does not resemble the distribution on the inboard part of the tailplane. The spanwise location of the slipstream impingement plays therefore an important role.

- On the outboard part of the tailplane, it appears that the amplitude of the time-dependent loads does not significantly depend the direction of the tailplane tip vortex relative to the direction of the helical vortex.
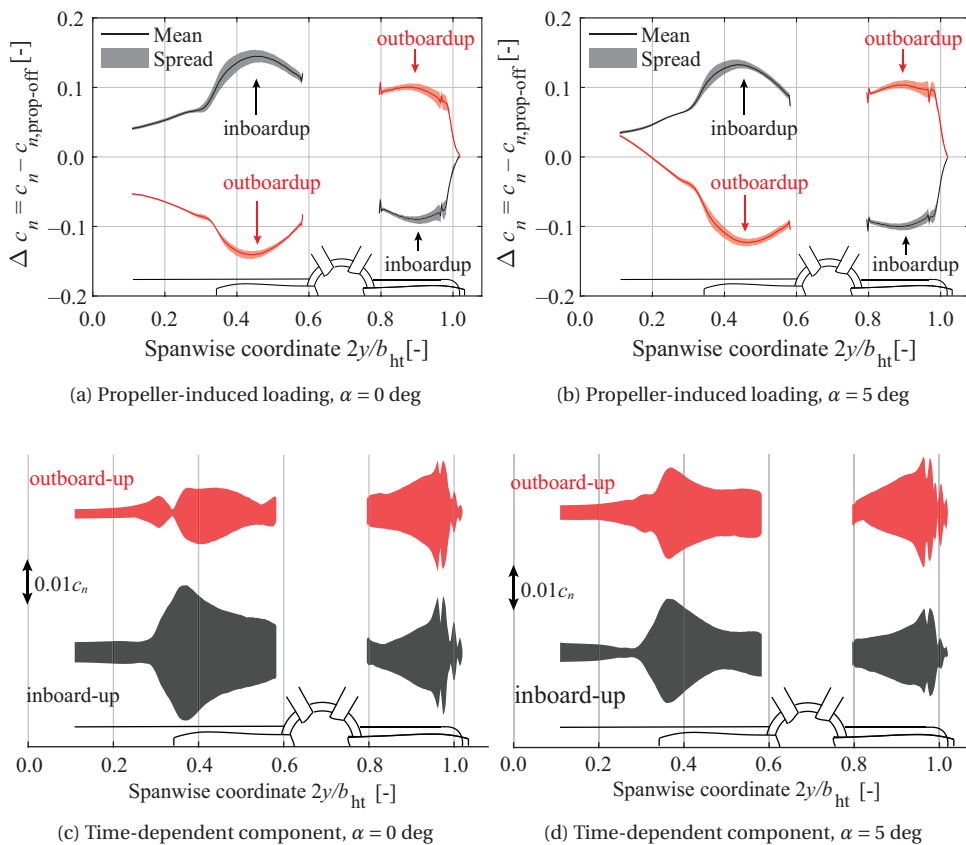

(a) Propeller-induced loading, $\alpha = 0$ deg

(b) Propeller-induced loading, $\alpha = 5$ deg

(c) Time-dependent component, $\alpha = 0$ deg

(d) Time-dependent component, $\alpha = 5$ deg

Figure 8.43: Time-averaged and spread of the propeller-induced normal-force distribution at $J = 1.8$, CFD results of the *VGM-HTP* model.

From Figs. 8.43a and 8.43b it appears that there is quite a difference in spread on the inboard loading between inboard-up and outboard-up rotation. Going from $\alpha = 0$ deg to $\alpha = 5$ deg, the spread is increasing for the outboard-up rotation, while it is reducing for the inboard-up rotation. Partially, this can directly be related to the strength of the propeller tip vortex (see Fig. 8.16b). Moreover, the spread appears to be more pronounced on the inboard part of the tailplane. On the outboard part of the tailplane the unsteady

loads are negligible. It is clear that the unsteady response of the lifting surface is not confined to the location where the tip vortices impinge, but instead is distributed over a large part of the tailplane. The different amplitudes of the fluctuations are summarized in Figs. 8.43c and 8.43d, indicating that especially for the inboard part of the tailplane, different patterns can be distinguished. The physical mechanism that underpins this behaviour is not clear.

More insight is gained by not only considering the variation, but also the power of the unsteady loads. The standard deviation is plotted along the tailplane span in Fig. 8.44a. A clear set of nearly self-similar distributions are shown with the largest amplitude slightly inboard of the impingement of the tip vortex core. This already suggests that not the low pressure in the vortex is the cause of unsteady loads, but it is the velocity field induced by the vortex that causes the strongest fluctuations. From the distributions in Fig. 8.44a it is clear that even though the distributions have similarities, there are clear differences in the shape. Especially the case of an outboard-up rotation at $\alpha = 0$ deg shows a very irregular unsteady loading and is an outlier.
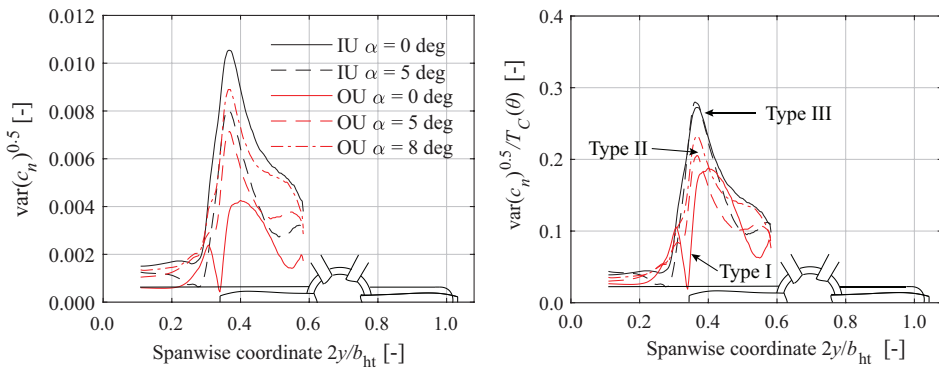
(a) Standard deviation of the normal-force coefficient. (b) Standard deviation of the normal-force coefficient normalized with average thrust over $\theta = [45, 135]$ deg.

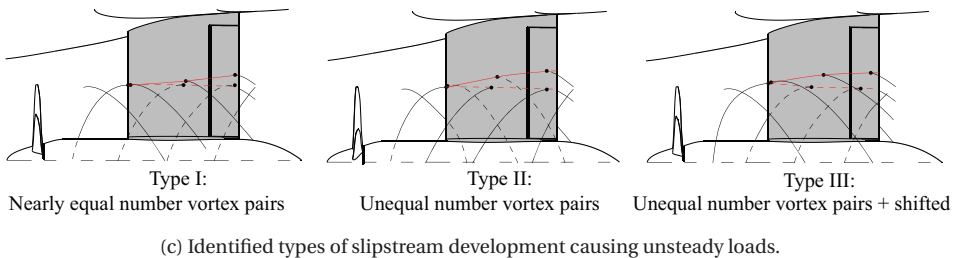(c) Identified types of slipstream development causing unsteady loads.

Figure 8.44: Computed unsteady loads induced by the propeller on the inboard part of the horizontal tailplane, CFD results of the *VGM-HTP* model.

The difference in amplitude of the unsteady loads between the different rotation directions and angles of attack is partially caused by the different blade loading for each of

these cases; the rotation direction and angle of attack lead to unequal strength of the tip vortices, and therefore in the unsteady response on the lifting surface. To demonstrate the importance of the different blade loading relative to the type of interaction, the distributions in Fig. 8.44a are normalized by the average thrust coefficient in the quadrant $\theta = [45, 135]$ deg. By applying this normalization, the effect of a varying vortex strength is removed, such that the type of interaction can be identified. In Fig. 8.44b, three different characteristic shapes (labelled I, II, III) are distinguished on the inboard part of the tailplane, based on the development of the propeller tip-vortex. The three patterns are reconstructed from the computed flowfields from the CFD simulations and are depicted in Fig. 8.44c. Types I and II have an equal number of vortex pairs that reside at the tailplane at each time-instance. For Type I, the helical vortex cut by the lifting surface reconnects at the trailing edge [174] nearly instantly without a chordwise displacement. For Types II and III, there is larger spanwise displacement of the helical tip vortices. Furthermore, Type I has a constant number of vortex pairs; at the time-instance a vortex impinges the leading edge, a vortex pair leaves the trailing edge. This is not the case for Type III, where there is an alternating number of vortex pairs residing on the tailplane. Table 8.1 summarizes the properties of these three types of tip-vortex interaction with the lifting surface.

Table 8.1: Qualitative rating of the factors of the helical vortex system that influences the unsteady loading on the lifting surface.

Type	Equal number of vortex pairs on each side	Number of vortex pairs	Spanwise displacement	Unsteady loads
I	✓	Constant	Small	Low
II	✓	Alternating	Large	Moderate
III	✗	Alternating	Large	High

For the outboard part of the tailplane, where the center core of the propeller tip vortex does not impinge on the tailplane (see Fig. 8.42), the spanwise distributions do not differ significantly between the rotation directions or different angles of attack. For this reason, only one distribution is shown in Fig. 8.45a. For $2y/b_{\text{ht}} = 0.8$ to 0.9, the fluctuations in the normal-force coefficient resemble the fluctuations between $2y/b_{\text{ht}} = 0.5$ to 0.6, although the magnitude is somewhat reduced, due to a weaker response to a disturbance if that disturbance is encountered near the tip of a lifting surface. Near the tip, two clear structures can be identified: initial impingement and vortex shedding. From the analyses of the flowfield from the CFD simulations it is clear that these are the consequence of the initial impingement of the helical vortex system and a periodic vortex shedding at the trailing edge. Due to the spanwise translation of the helical tip vortex as it is in the proximity of the tip of the tailplane, the vortex shedding occurs more inboard. A schematic of this vortex-vortex interaction is depicted in Fig. 8.45b. The results indicate that in case the unsteady loads are to be reduced, the span of the lifting surface should be selected such that its tip vortex is not in the vicinity of the helical vortex system. This means either a span extension of the tailplane or a reduction by at least 15-20% of the propeller radius. This is also a recommended value in aerodynamic and aeroacoustic

evaluations of the counter-rotating open-rotor system (CROR), see Ref. [260].

(a) Standard deviation of the normal-force coefficient normalized with average thrust in corresponding quadrants. Inboard-up, $\alpha = 0$ deg. (b) Schematic of tip-vortex interaction, extracted from Fig. 8.40
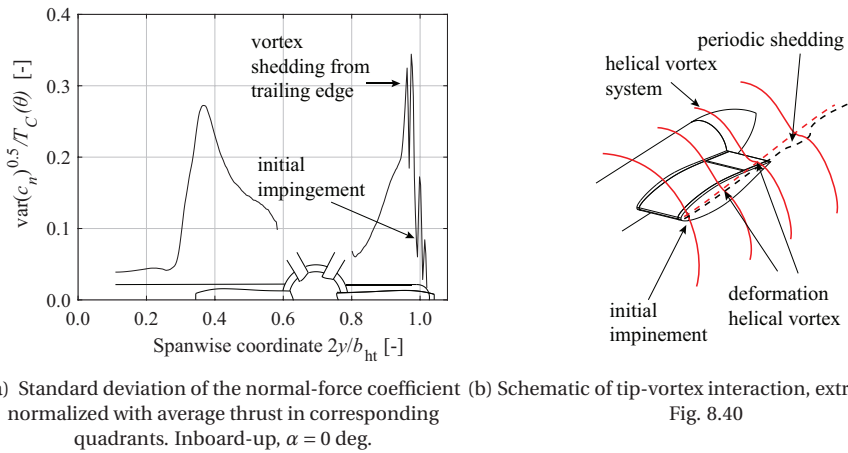
Figure 8.45: Computed unsteady loads on the horizontal tailplane induced by the propeller, CFD results of the *VGM-HTP* model.

To demonstrate that in many cases the most important part of the unsteady loads are introduced on the inboard part of the tailplane, the integral values of the normal-force coefficient over a $1/B$ propeller revolution for the inboard part of the tailplane are plotted in Figs. 8.46a and 8.46b. The loads on the outboard part are plotted in Figs. 8.46d and 8.46e. If there is no phase lag due to structural deformation and differences in stiffness along the tailplane, these values represent the forces at the root of the tailplane which are transferred to the fuselage. As can be seen from the figures, the phase shifts of the loads for $\alpha > 0$ relative to the case of $\alpha = 0$ are primarily caused by the apparent phase offset due to a deflected slipstream, as highlighted in Fig. 8.12. While for vortex Types II and III the response is nearly sinusoidal, for Type I the amplitude is greatly suppressed (Fig. 8.46a, $\alpha = 0$ deg). This is the result of the opposing rise in loading at the leading edge and a reduction in loading at the trailing edge. The figures also confirm the hypothesis of more pronounced unsteady loads on the inboard part of the tailplane by nearly a factor two.

The fact that the rise and reduction in load on each side of the propeller are not in-phase leads to a time-dependent shear force at the root of the fuselage. If they would be exactly $360/(2B)$ deg out of phase, the loads would partially cancel for this operating condition. Such a difference can be achieved by staggering the inboard and outboard part of the lifting surface, or by applying sweep. An even further reduction of unsteady loads can be achieved if the chord of the tailplane is chosen such that it is a multiple of the pitch of the helical vortex such that vortex Type I exists. It is noted that this only applies for a given advance ratio.

Another hypothetical way to reduce the unsteady loads that are transmitted to the fuselage, is to compare the phase angles of the propeller and tailplane loads. Provided that the propeller shaft load is also periodic, the spacing between propeller and
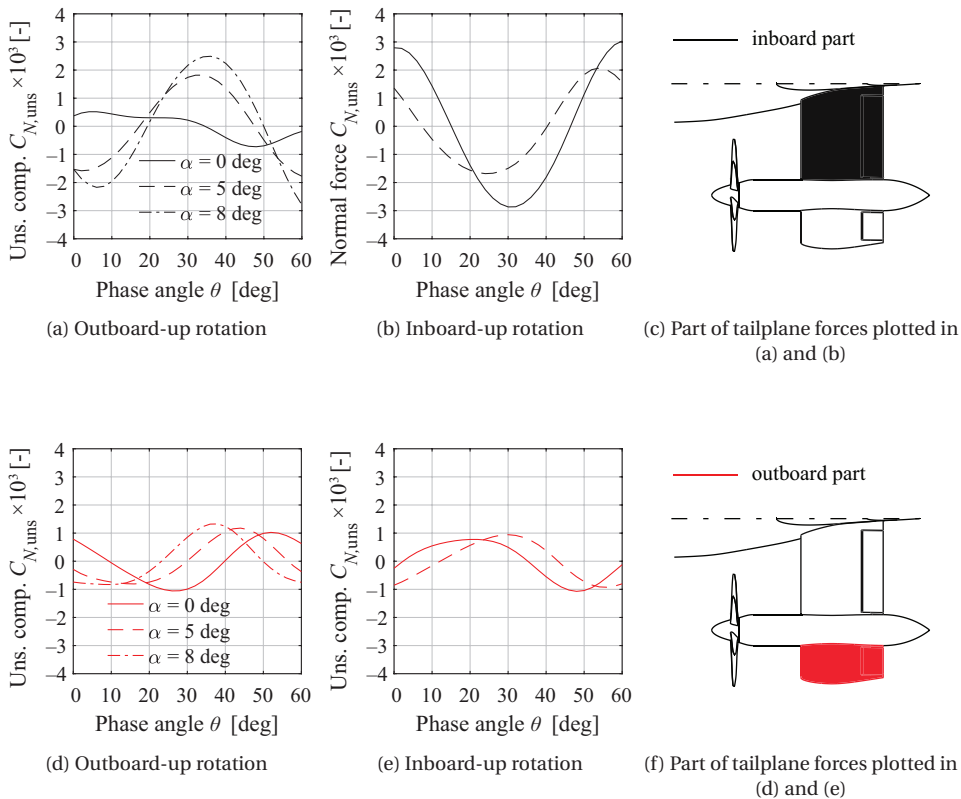
8

Figure 8.46: Time-dependent fluctuations of the normal-force coefficient on half of the tailplane, normalized with S_{ht}, CFD results of the *VGM-HTP* model.

8

tailplane can be selected such that the propeller shaft load is exactly out-of-phase with the tailplane loading. This would minimize the loads transmitted to the cabin. However, the unsteady load on the propeller shaft is an order of magnitude smaller than the loads acting on the tailplane. Therefore a selection of the spacing between the disk and tailplane should not be motivated to introduce a phase-offset between the propeller and tailplane loads. Instead, a larger spacing lowers the magnitude of the velocity perturbations in the slipstream and therefore the unsteady loads on the lifting surface.

8.6. CONCLUSIONS

This chapter has addressed the time-averaged and time-dependent loading on a lifting surface that is caused by installation of a tractor propeller ahead of it. It is a research topic that has been studied by a large number of authors, especially in the light of a wing-mounted propeller configuration. The previously identified trends of the response

of a lifting surface to a slipstream have also been confirmed in this chapter.

In the presented work, the complex interaction is further explored with the objective of providing handles that are useful for 1) developing an understanding what level of modelling is required to capture the relevant effects, 2) support design choices, and 3) further development of knowledge on the interaction between the vortex systems of the propeller and lifting surface. The test cases also provide insight in typical values and trends that can be expected, which may be useful for engineering problems. The main conclusions that have not been discussed in literature before are categorized as follows:

FUNDAMENTAL AND TIME-AVERAGED AERODYNAMIC INTERACTION
One of the effects of propeller installation is that the inflow to the lifting surface is no longer the inflow produced by an isolated propeller:

- The strongest changes of flowfield quantities with angle of attack occur at the edges of the slipstream. The smallest changes of flowfield quantities with angle of attack occur if the lifting surface is positioned at the propeller rotation axis.

- The gradient of the local angle of attack α' relative to the freestream value, $\frac{d\alpha'}{d\alpha_\infty}$, is reduced by the propeller due to the change loading on the disk.

- Outside the slipstream the change in the flowfield with respect to angle of attack is larger than inside the slipstream caused by both the deflected slipstream and the presence of the nacelle. The effect of the slipstream deflection is estimated to be three times more prominent than the presence of the nacelle.

- An angle of attack leads to a phase shift of the helical tip vortices on the advancing side and retreating side of the propeller. This directly affects the unsteady loads on the lifting surface.

- The installation effect of adjacent propellers is twofold. First, at the symmetry planes larger velocity and pressure gradients are introduced. Secondly, the slipstream is less contracted at the symmetry plane, while more contraction is observed on the upper/lower side of the array of slipstreams. The slipstream area is nearly constant, as the reduction in thrust is negligible. The larger contraction on the upper/lower side of the array of slipstreams leads to a smaller angle of attack in case the propellers are mounted below the wing chord line, compared to a case where there is no interaction between the adjacent propellers.

On the interaction of the slipstream with a lifting surface, the following can be concluded:

- The results show that the *change* in loading due to an angle of attack is more concentrated towards the leading edge. When the propeller is spinning and the angle of attack is raised from α_1 to α_2, the *change* in loading resembles the distribution of the propeller-off case if the two pressure distributions are normalized. Therefore, the propeller-tailplane combination behaves in the same way as the propeller-off case: the presence of the slipstream can be described as a change in local lift curve slope.

- If the change in loading is obtained through a change in advance ratio, i.e. going from $T_{C,1}$ to $T_{C,2}$, the pressure distribution is not the same as a change in angle of attack. This is caused by a finite height of the slipstream relative to the chord of the lifting surface. Therefore, for low D_p/c ratios, the design of the leading edge of the wing becomes relatively more important. This is, for example, the case for distributed propellers along the leading edge.

- The propeller increases the effectiveness of the flap/elevator and this increase is nearly inversely proportional with advance ratio. By the deflection of a control surface/high-lift device, there is *relatively* more loading toward the leading edge of the main element and the leading edge of the control surface.

- Slipstream deformation is, in addition to the variation of spanwise loading, caused by a change in helicity of the propeller tip vortex.

- The portion of the span that is washed by the propeller, the local downwash angle is reduced. Outside this region, the downwash angle increases.

- Independent of rotation direction, the largest reduction of in-plane kinetic energy is observed between the leading edge and quarter chord of the lifting surface due to the presence of a nonpermeable boundary. More downstream, the kinetic energy deposition is further reduced if the propeller is rotating against the tip vortex direction of the lifting surface.

- For a tip-mounted propeller configuration with the propeller rotating against the wing tip-vortex, the portion of the wing washed by the propeller has:

    - A higher lift coefficient at the same α
    - A higher lift curve slope
    - The angle of attack at which maximum lift coefficient is reached is approximately independent of the propeller installation
    - A higher lift-to-drag ratio at the same angle of attack
    - The maximum c_l/c_d is achieved at higher c_l
    - At low lift coefficients, the c_l/c_d is lower compared to the propeller-off condition

By varying the relative spanwise position of the vortex systems from the propeller and lifting surface, the following can be concluded:

- Compared to a tip-mounted propeller, if the propeller is mounted close to the fuselage, the jump in circulation at the propeller rotation axis is stronger than the propeller hub vorticity. This is the result of a higher gradient of the section lift coefficient with angle of attack if it is further away from the tip.

- Compared to a tip-mounted propeller, if the propeller is mounted close to the fuselage, the main installation effect on the gradient of the normal force is obtained on the inboard part of the tailplane. This is driven by the three vortices

shed from the lifting surface at three distinct locations: at the root, at the edge of the slipstream, and at the propeller rotation axis. For an inboard-up rotating propeller, these three lead to a larger downwash gradient compared to the outboard-up rotating propeller. An inboard-up rotating propeller in such installation therefore leads to a lower normal-force gradient of the lifting surface compared to an outboard-up rotation.

UNSTEADY AERODYNAMIC INTERACTION AND MITIGATION STRATEGIES

The analysis of the time-dependent load distributions on the lifting surface do not only gain insights for structural design perspective, also opportunities are revealed to reduce the unsteady loads produced by the propeller–lifting surface combination. The observations made from those analyses may drive design choices such as rotation direction, propeller position relative to the airframe, and the tail size. The following main conclusions are formulated that have not been identified in previous literature:

- Three types of slipstream deformation have been identified that lead to vastly different unsteady loads on a lifting surface. The local chord length relative to the pitch of the helical vortex is found to be the driving parameter to affect the unsteady loads.

- The largest unsteady loads can be expected on the inboard side of the lifting surface.

- The fact that the rise and reduction in load on each side of the propeller are not in-phase leads to a net shear force and bending moment at the root of the fuselage.

- Close proximity of the helical tip vortex to the tip vortex of the lifting surface is undesired because the associated periodic vortex interaction introduces unsteady loads on the lifting surface.

- The strongest unsteady loading increase even further with angle of attack in case the propeller rotates outboard-up since the strength of the tip vortices increases.

- At elevated angle of attack, a phase difference arises between the response of the normal force on the inboard and outboard part of the lifting surface.

- The unsteady loading is strongly dependent on angle of attack, rotation direction, and therefore is directly dependent on the propeller loading distribution.

8

9

ASPECTS OF AIRCRAFT STABILITY, CONTROL, AND PERFORMANCE FOR UNCONVENTIONAL PROPELLER INTEGRATIONS

9.1. INTRODUCTION

Previous chapters have investigated several propeller installation effects on component level for unconventional propeller configurations. More specifically, the installation effects on the aerodynamic characteristics of lifting surfaces (i.e. a wing or tailplane) and the effect of the presence of the airframe on the propeller forces and moments have been quantified. An advantage of the assessment of the aerodynamic interactions on component level is that the conclusions can be generalized, at least to a certain extent. However, the installation effect on aircraft level based on these studies is not evident, e.g. in case the aerodynamic interaction influences multiple surfaces, when the shift in the neutral point is to be determined, or when the trimmed lift-to-drag curve is to be quantified. Furthermore, the construction of aircraft moment curves with the purpose of designing a control system or flight dynamics model is challenging as the superposition of individual components is generally not possible because of the aerodynamic coupling between components.

The relative location of the propellers to the wing, fuselage, and stabilizing surfaces will determine the propeller contribution to static stability, trim drag, maximum lift coefficient, and ultimately, the fuel consumption for a given mission profile. Examples of 'direct contributions' are the changed aircraft lift-to-drag ratio, propeller efficiency, and available excess thrust. Examples of 'indirect contributions' are design adaptations such as the tail size (and weight), the control surface area, the wing area, and the effectiveness

---

Parts of this chapter have been published in Ref. [119].

of high-lift devices [39, 61, 63, 65–67]. Moreover, indirect performance benefits could also be achieved if weight reductions are realized while vibration and noise levels are maintained relative to a reference case.

In this chapter several 'direct contributions' of propeller installation on aircraft level are investigated in detail. The key quantities that are of interest for unconventional configurations include:

- **The product $\eta_p \frac{C_L}{C_D}$** is a measure for the fuel consumption [261].

- **Offsets in pitching and yawing moment curves** as these determine the required trim input to nullify the moment about a reference point.

- The change in the **slope of the moment curves** determine the changes in static stability. Practically, the shift in the neutral point, together with a static margin, determines whether the range of allowable center of gravity locations is compromised or extended. Furthermore, the dependency of the slope of the moment curves also affects the flight dynamic behaviour (which is out of the scope of this dissertation).

- **Control effectiveness**. The effect of propeller installation on the effectiveness of the control surfaces does not only determine their size for the sizing flight condition, also the change in drag due to deflection is relevant when deflected to trim the aircraft. The dependency of the moment due to a control deflection on thrust is also indicative of the initial dynamic response to a control surface deflection.

- **Airframe lift**. Changes in lift due to a change in thrust also affects the aircraft attitude during (optimal) cruise, as well as the flight dynamic behaviour. For example, a large drop in lift with higher thrust coefficient is undesired in case of a balked landing.

- **Airframe maximum lift**. The maximum lift coefficient determines the low-speed performance for transport aircraft, and thereby is a constraint on the sizing of the wing. As is presented in the following sections, propeller installation leads to changes in aircraft stability, and the maximum useable lift coefficient may be compromised when the true maximum lift coefficient is achieved in an unstable flight condition.

- **Aircraft axial force.** The airframe drag in cruise condition directly affects the fuel consumption, while climb and manoeuvring performance are also affected by the airframe drag [67]. Moreover, the propeller installation may reduce or increase the (specific) excess thrust in accelerating or climb conditions by changes in the installed airframe drag and propeller thrust.

- **Propeller efficiency in the direction of flight**. In Chapter 7 it is shown that the installation of propellers leads to a resultant force vector which generally is not in the direction of flight.

Conclusions on these indicators can also provide a direction on the installation impact on overall aircraft design and performance. It is noted that besides these quantities,

9

also required design changes impact aircraft performance. For example, an aft empty-aircraft center of gravity for tail-mounted propellers leads to a large excursion of the center of gravity and a fully loaded aircraft therefore has large trim drag [25, 29, 86, 132, 262–265], while structural design challenges arise for tip-mounted propellers [266]. Such aircraft design studies in terms of weight estimations and the sizing (procedure) of lifting surfaces are not discussed in this chapter. For comparisons of propeller installation effects on overall aircraft design to estimate e.g. fuel efficiency, the reader is referred e.g. Refs. [25, 265, 267].

The translation of the aerodynamic interaction on component level to aircraft level requires the definition of a certain configuration, together with an assumed range of center of gravity locations and operating conditions. To this end, two aircraft configurations (depicted in Fig. 9.1), which have been used throughout this dissertation act as test cases. These are selected since they differ substantially from each other in several ways:

- *VGM-HTP*. In this case the propeller is influenced by the airframe and is mounted behind the center of gravity. In turn, the slipstream directly influences the stabilizing surfaces at the back of the aircraft.

- *A320-DP*. In this case the wing is influenced by multiple propellers that are mounted to its leading edge. This means the propellers are positioned ahead of the center of gravity, and their slipstreams and the modified downwash field trailing from the wing both influence the stabilizing surfaces at the back of the aircraft. This aircraft has a moderately swept wing and resembles a short to medium range aircraft. Although the introduction of such (a high) sweep is not envisioned for (near) future propeller-driven aircraft, it introduces several unique interaction phenomena that are not displayed for wing with low or no sweep angle. Therefore, the presented findings are still useful for propeller-driven aircraft at high subsonic flight Mach numbers that could become reality.

(a) *VGM-HTP* model to investigate longitudinal & directional stability, control and performance aspects

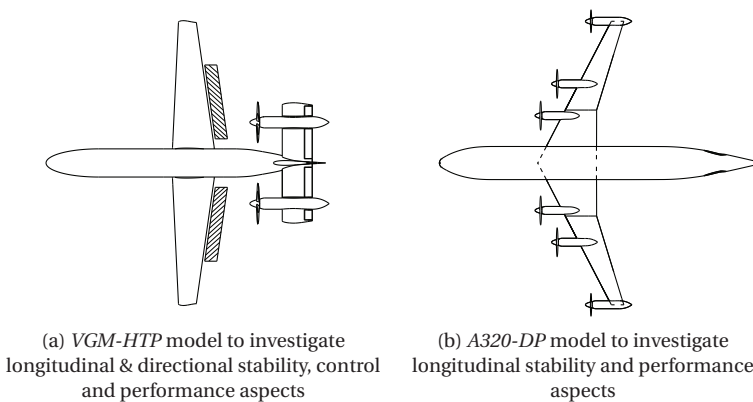(b) *A320-DP* model to investigate longitudinal stability and performance aspects

Figure 9.1: The two aircraft models selected to identify and quantify the propeller installation effects on aircraft level.

Several studies have already investigated aspects of stability, control, and performance for these configurations. Especially on the wing-mounted propeller configuration numerous publications appeared since the early days of aviation. Those findings also apply to a certain extent for distributed propulsion systems, where a larger part of the wing is affected by the propellers. For those configurations, typically more design freedom is available in the particular placement of the propellers. For wing-mounted propeller configurations, the following conclusions are found in open literature:

- The slope of the lift curve of the full aircraft (including propeller contribution) significantly increases with higher thrust coefficients [268].

- The wing aerodynamic characteristics, i.e. lift, drag, pitching moment, yawing moment, and rolling moment, are highly influenced by the spanwise location and rotation direction of the wing-mounted tractor propeller [36, 45, 242, 269].

- The high-lift capabilities in take-off condition and approach condition can significantly be enhanced [38–44].

- The downwash angle ϵ and the (average) downwash gradient $\frac{d\epsilon}{d\alpha}$ at the horizontal tailplane typically increases with thrust coefficient [160], even when the slipstream is not impinging on the horizontal tail. The complex flowfield at the tail surfaces leads to large variations of static longitudinal stability between various aircraft attitudes [39, 62–66].

- The wing-induced cross-flow to the vertical tailplane affects the directional stability and trim [39, 62, 173, 251, 270]. For a high-wing configuration with one engine inoperative, this interaction effect is of the same order as the propeller-only contribution to the yawing moment [271].

- In case of a co-rotating configuration, the drag difference between each side of the wing leads to a net yawing moment [37].

- While the installation effect of a nacelle on the propeller is small [272], the effect of the nacelle on the wing is significant, leading to lower maximum lift coefficients, a disturbed wing loading, and higher drag [273].

9

For configurations where the propellers are either mounted to a pylon behind the wing or to the horizontal tailplane, the following main conclusions are presented in open literature:

- In Refs. [25, 86, 131, 229, 268, 274] it is concluded that a rear-installation of two co-rotating propellers does not adversely affect the longitudinal and directional stability characteristics compared to the uninstalled configuration. The installation effect is typically described as 'small' while stronger effects had been hypothesized in most of these studies. An experimental campaign performed by Ref. [229] shows an appreciable effect of the propeller installation on the change in trim, static stability, and control authority.

- The vertical tailplane size can be reduced because of the smaller moment arm to the fuselage symmetry plane and the lower sidewash on the vertical tailplane in case of a one-engine-inoperative condition, leading to an estimated 4% reduction of total aircraft drag [268].

- The propeller also impacts the flow angle outside the slipstream since the contraction of the slipstream leads to curved streamlines outside the slipstream. This effectively increases the downwash angle in case of a T-tail configuration. At the same time, the propeller reduces the dynamic pressure at the T-tail by approximately 1% of the freestream dynamic pressure [268]. For a pylon-mounted contra-rotating open-rotor, the pressure drag on the fuselage could increase by 3% compared to the propeller-off case.

- Aerodynamic performance benefits that arise from a clean wing, such as an extended region of laminar flow [132] and the reduced adverse compressibility effects on the wing caused by the elevated Mach number inside the slipstream [175], are promising.

- In Ref. [86, 275] it is estimated that the fuel saving potential of using propellers instead of turbofans could reduce with 50% compared to the wing-mounted propeller configuration for missions of over 1,500 nautical miles due to increased trim drag.

The quantified or estimated impact of the installation effects for both wing- and aft-mounted configurations ranges between 'small' to 'significant'. Even for relatively similar layouts, quite a spread is found on the impact of propeller installation. There are several reasons for the discrepancy in the observations. First, a more detailed assessment of the aerodynamic interaction up to high angles of attack, especially for the aft-mounted propeller configurations, is missing in the majority of these studies, while in Chapters 6 and 8 it is shown that these conditions introduce the largest installation effects. Second, the available studies also acknowledge the limited detail of the complex propeller–airframe aerodynamic interaction that was included in the performance assessments, especially on aircraft design level. For example, to assess the impact on static stability, the aft-mounted propeller was treated as an isolated propeller at a distance from the aircraft center of gravity, neglecting the changes in the airframe and propeller forces due to the aerodynamic interaction. The propeller contribution to aircraft stability and trim are often estimated using linearized models [63] and typically, the propeller forces are determined without including the influence of the airframe [61]. Moreover, simplified models of the prediction of the slipstream on local flow angles at the horizontal tailplane omit slipstream deformation and the presence of swirl in the slipstream, which will be shown in this chapter to be an important factor. Finally, in the experimental and numerical studies, the propellers are often co-rotating, and the individual characteristics on each side of the aircraft therefore are being averaged and the installation effect appears as small. For a symmetric rotation direction however, the installation effect could be (unexpectedly) more pronounced.

A general observation from the existing literature is that the relative contributions of the propeller and airframe compared to the overall vehicle performance have not been

9

not assessed, while these are key in order to understand the relevant interaction phenomena. A more detailed breakdown of the propeller–airframe interaction in unconventional configurations is required, as this can lead to improved performance predictions and, ultimately, improved design choices. In this chapter part of this knowledge gap is filled with a systematic breakdown of the interaction problem on aircraft level in case the propellers are mounted to the wing leading edge or to the horizontal tailplane. More specifically, the following main research questions are addressed in this chapter:

- *RQ 9.1:* What are the key drivers for each propeller configuration to alter the aircraft static stability, control, and trim characteristics?

- *RQ 9.2:* What is the importance of the installation effect on the propeller relative to the airframe for the estimation of the directional and longitudinal stability characteristics?

- *RQ 9.2:* How does the installation effect on propellers compare to the installation effect on the airframe in terms of changes in directional and longitudinal stability characteristics?

- *RQ 9.3:* What is the relevance of the forces introduced by a slipstream on airframe components that are in the vicinity of a propeller slipstream but not submerged in it?

- *RQ 9.4:* What is the difference in aircraft performance when a certain rotation direction is selected for a tail-mounted propeller compared to a wing-mounted propeller?

- *RQ 9.5:* Can a co-rotating case be represented as the average of the two rotation directions?

- *RQ 9.6:* What is the implication of wing sweep on the longitudinal static stability characteristics of distributed leading-edge propeller installation?

- *RQ 9.7:* How does the interaction between the slipstreams of two adjacent propellers affect the flowfield at the horizontal tailplane?

- *RQ 9.8:* Is the propeller installation effect on longitudinal stability proportional with angle of attack?

This chapter is split into two parts, where in the first part the tail mounted propeller configuration is discussed (Section 9.2), followed by the assessment of a distributed propulsion configuration in Section 9.3.

9.2. Horizontal-Tailplane-Mounted Propeller Configuration

Based on the findings of Chapters 6 and 8, the expected trends of the installation effects of tail-mounted propellers on the integral moment curves, lift curves, propeller efficiency, and lift-to-drag ratio can already be formulated. Recalling the conclusions from those chapters, it can be expected that:

- The change in the aircraft pitching moment curve is not linear due to the varying inflowfield to the propeller and tailplane with angle of attack.

- The neutral point shifts aft as a function of thrust for the linear part of the lift curve from a more effective tailplane.

- Even at $T_C = 0$, the presence of the propeller still increases the pitch and yaw stability because of its nonzero normal-force gradient.

- The elevator effectiveness is increased as function of thrust coefficient.

- For co-rotating propellers, a net sidewash is introduced due to the interaction of the slipstream with the tailplane. This leads to a net yawing moment.

- The maximum lift-to-drag ratio is increased compared to the propeller-off configuration because of the higher lift and slightly reduced drag. At the same time, the maximum is reached at a higher lift coefficient.

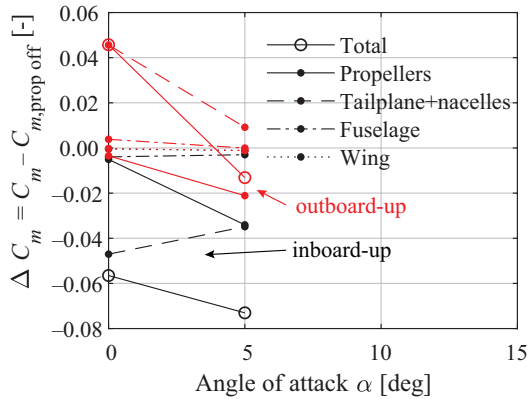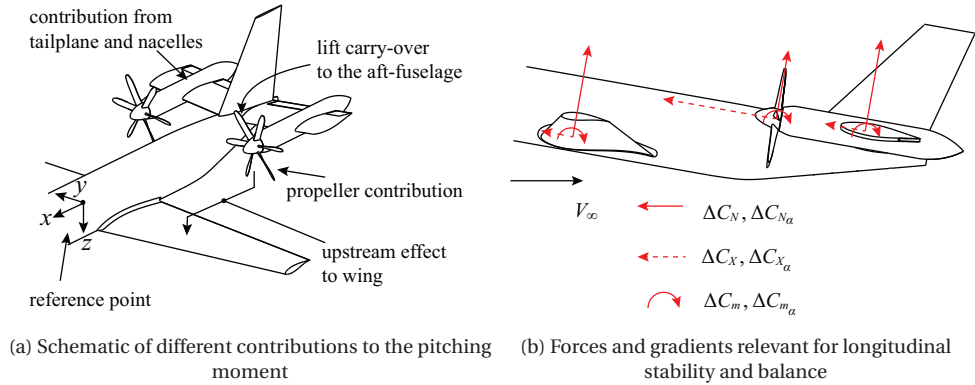- The maximum propeller efficiency is achieved at non-zero angle of attack.

These rather qualitative interpretations are put into perspective in the following sections by the evaluation of the integral force and moment curves. The forces acting on the propeller and airframe are evaluated separately, both using experimental and CFD data. More specific tracing of individual contributions is done using CFD data for a small range of conditions. In Ref. [268] it is shown that the propeller installation effect on the static stability characteristics is nearly independent of Mach number. This observation justifies the analysis at low-subsonic Mach number in this section. First, the installation effects on longitudinal static stability and trim are investigated, followed by the assessment on directional stability and one-engine-inoperative conditions. Finally, the effect of propeller installation on a few performance indicators is quantified, such as propeller efficiency, lift-to-drag ratio, and enhancement of lift.

9.2.1. Longitudinal Static Stability and Balance

The evaluations of the pitching moment coefficient in a reference point at $x/\bar{c} = 0.25$ as well as the location of the neutral point provide insight into the impact of propeller installation on the longitudinal stability characteristics. The largest changes in loading on the aircraft can be expected to occur far from this $x/\bar{c} = 0.25$ reference point, i.e. towards the aft of the aircraft. Therefore, the trends that are observed in this arbitrary reference point also apply to points that are close to this reference point. It is noted that often the center of gravity is close to this point [276] and tail arms are also defined with respect to $x/\bar{c} = 0.25$ [67], which further justifies this choice.

To confirm this hypothesis, the separate contributions of the airframe components on $C_m - \alpha$ are evaluated using Fig. 9.2, where Figs. 9.2a and 9.2b schematically show the different contributions of each airframe component to the pitching moment. Figure 9.2c shows that the upstream effects of the propeller, i.e. the induction of a higher dynamic pressure, an effective angle of attack, and a pressure gradient on the suction side of the wing, are negligible. The relative importance of the effect on the derivative of the wing pitching moment becomes larger if the propeller–wing spacing would be reduced,

as demonstrated in Ref. [277], leading to a more negative $C_{m,\alpha}$ [98, 267]. Figure 9.2c also shows that the carry-over of the loading acting on the horizontal tailplane to the fuselage leads to a change in $C_{m,\alpha}$ in the same direction as the one of the tailplane, but its contribution is negligible. This confirmation of the dominant contributions allows to use the findings on the horizontal tailplane and propeller to explain the trends on aircraft level. Figure 9.2c shows several important characteristics for the tailplane and propeller, which will be discussed later.

(a) Schematic of different contributions to the pitching moment

(b) Forces and gradients relevant for longitudinal stability and balance

(c) Contributions about $0.25\bar{c}$ for the clean configuration, $J = 1.8$ (cruise condition)

Figure 9.2: Different contributions of the airframe and propeller to the aircraft pitching moment for the *VGM-HTP* model.

The overall impact of propeller installation is shown in Fig. 9.3 as a $\Delta C_m = C_{m,\text{prop-on}} - C_{m,\text{prop-off}}$. The following is observed:

- The offset of the pitching moment curve increases with lower J. This is relevant for the trim condition, shown in Figs. 9.3a and 9.3b.

- At zero thrust, the co-rotating configuration has approximately no pitching mo-

ment at a low angle of attack and becomes negative for higher thrust settings; $\frac{dC_m}{dT_C} < 0$ for $\alpha > 0$. For a symmetric rotation direction, there is a finite change of the pitching moment.

- The slope of the pitching moment curve with angle-of-attack at constant advance ratio, as well as at constant T_C, becomes more negative with higher thrust settings over the majority of angles of attack, shown in Fig. 9.3c.

- The moment curve of the co-rotating configuration is the average between inboard-up and outboard-up rotation directions, until the onset of stall, as shown in Fig. 9.3d. This means that there is a negligible coupling between each side of the tailplane.
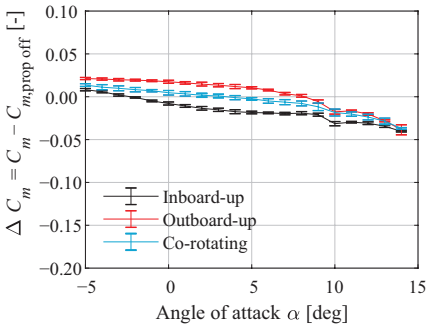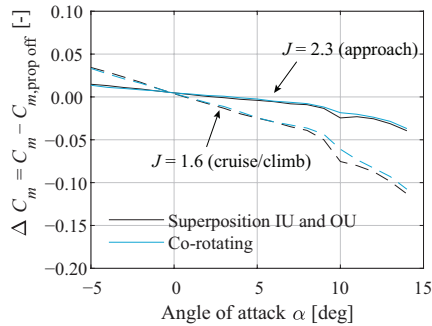

(a) $J = 2.3$ (approach)
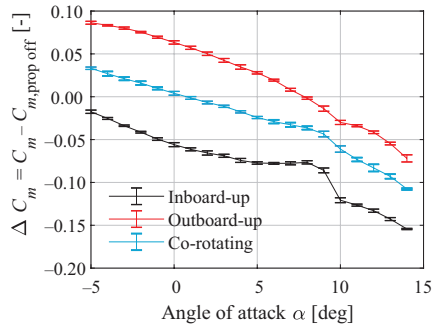
(b) $J = 1.6$ (cruise/climb). The offset from 0 impacts the trim condition.
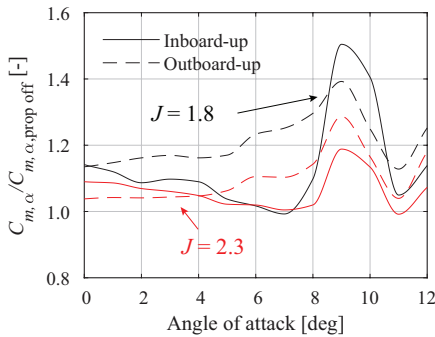
(c) Effect of propeller installation on aircraft C_{m_α}

(d) Demonstration of negligible aerodynamic coupling between starboard and port side

Figure 9.3: Effect of the propeller installation on the aircraft pitching moment about $0.25\bar{c}$. Experimental results, $\beta = 0$ deg for the clean configuration of the *VGM-HTP* model.

Figure 9.3a and especially Fig. 9.3b reveal several important characteristics for either symmetric rotation directions. For an outboard-up rotation, the propeller installation leads to a nose-up pitching moment, that needs to be compensated with an el-

evator deflection. This means that, despite the propellers that are mounted above the moment reference point in z-direction, the tailplane-induced pitching moment is dominant compared to the thrust-induced moment, in line with findings on an aft-mounted propeller configuration with a T-tail [268]. The figure also indicates a progressively more negative $C_m - \alpha$ curve at higher angles of attack for the outboard-up rotation, while between $\alpha = 5$ deg and $\alpha = 8$ deg, the inboard-up rotation leads to a *destabilizing* effect by the propellers. This is an observation that has not been made in previous studies which do not consider a symmetric rotation direction.

To investigate this trend of a destabilizing propeller effect for inboard-up rotating propellers, the relative contributions of the propeller and tailplane are analyzed. In Section 8.4.2 it is shown that the inboard-up and outboard-up rotation decrease and increase the normal-force gradient of the tailplane, respectively. This is confirmed in Fig. 9.4a, which shows the different contributions of the airframe and propeller, measured in the experiment. The inboard-up rotation leads to a destabilizing airframe contribution to the moment coefficient up to $\alpha = 8$ deg. The contrary is the case for the outboard-up rotating configuration. This is in line with the findings on the normal-force gradient of the tailplane in Chapter 8. The rapid change of the airframe contribution to C_{m_α} at $\alpha = 8$ deg, in particular with the inboard-up configuration, is a consequence of two aspects. Firstly, the rapid reduction in C_{m_p} for the inboard-up propeller indicates that the loading on the upgoing blade is increased. The consequence is locally a larger swirl on the inboard part of the tailplane, leading to a stabilizing normal force, and hence a more negative C_{m_α}. The second aspect is that the fuselage-induced vortex in streamwise direction (Γ_{II} in Fig. 6.35b), which initiates between $\alpha = 5$ deg and $\alpha = 8$ deg, is altered by the propeller installation. Around $\alpha = 8$ deg, these two vortices are situated slightly above the tailplane, near the junction with the fuselage. The inboard-up rotating propeller leads to an opposite vortex at the tailplane–fuselage junction, which is thereby reducing the influence of Γ_{II} on the tailplane.
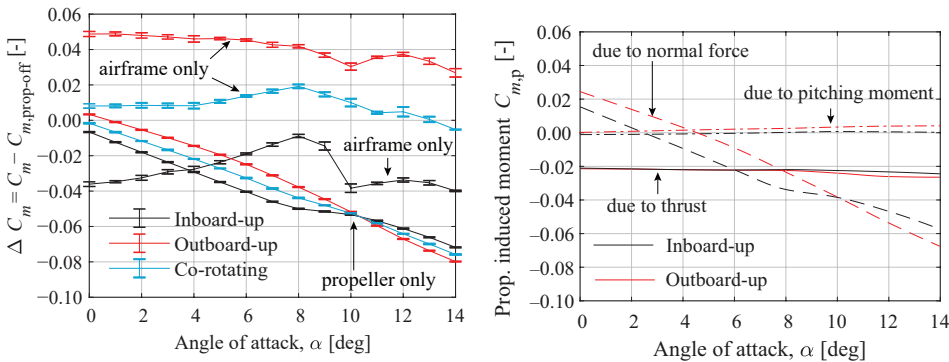
(a) Airframe and propeller contributions split-up, experimental results

(b) Separate contributions of each force component of each propeller, experimental results

Figure 9.4: Different contributions of the airframe and propeller to the aircraft pitching moment about $0.25\bar{c}$ for the clean configuration of the *VGM-HTP* model with $J = 1.8$.

Of the propeller contribution to the aircraft pitching moment, the individual propeller force and moment components are depicted in Fig. 9.4b. The normal-force contribution is dominant and enhances the aircraft longitudinal stability because the propellers are behind a hypothetical aircraft center of gravity location. Trends regarding this force component are therefore indicative of the direct propeller contribution on aircraft level. The moment about the propeller y_p axis is negligible, as is also concluded in Refs. [195, 196]. The thrust is primarily an offset of the C_m curve, and therefore affects the trim condition. Because the thrust contribution to longitudinal stability is small, the vertical location of the propeller relative to the airframe can be expected to have a small impact on longitudinal stability. In that case, the changing flowfield from the wing that affects C_{N_p} is likely to dominate.

A more complete overview of the installation effect on aircraft stability is provided in Fig. 9.5, which depicts the slope of the $C_m - \alpha$ curve compared to the propeller-off case, $C_{m_\alpha}/C_{m_\alpha,\text{prop-off}}$. For the inboard-up rotation, this ratio varies between 0.95 to 1.40; while smaller variations of 1.0 to 1.25 are induced by the outboard-up configuration. Three distinct regions can be recognized, denoted with letters A through C for the inboard-up rotation, and two regions are distinguishable for the other rotation direction. In both regions A, there is a progressively more negative pitching moment curve with angle-of-attack for the outboard-up rotation, while for the inboard-up rotation this is the opposite. The large variations of C_{m_α} starting from the onset of the nonlinearity of the lift curve, i.e. $\alpha > 7$ deg and are directly related to the changing normal-force curves of the propeller and tailplane. The contour plot in Fig. 9.5 shows that for a given α, increasing T_C only leads to a moderate change in pitch stability, contrary to a change in α, which has a significant impact on longitudinal stability. This rather unexpected result has an important implication: an assessment of the impact of the propeller installation on static stability does not require a large number of evaluations at different thrust settings. By evaluating only two cases, i.e. a propeller-off case and a propeller-on case (e.g. maximum thrust coefficient), will provide a rather conclusive result on the propeller installation effect on longitudinal static stability.
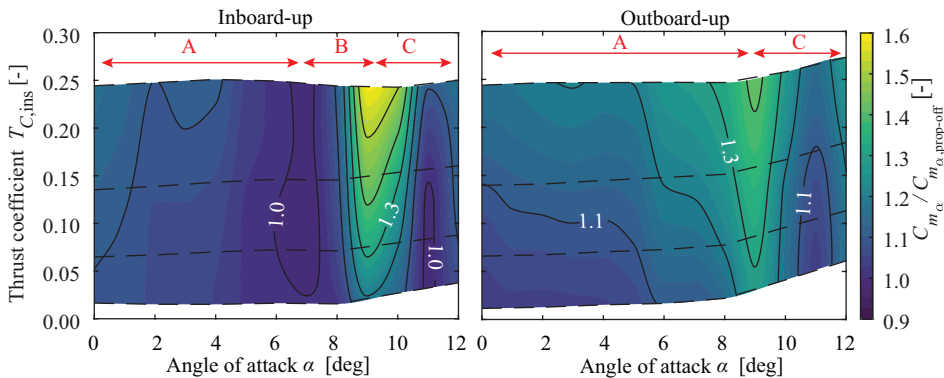

Figure 9.5: Effect of the propeller installation on the gradient of the aircraft pitching moment about $0.25\bar{c}$ of the *VGM-HTP* model. Dashed lines represent constant advance ratio. Experimental results, $\beta = 0$ deg. Contour map is computed using the interpolation in both directions, using multiple data sets with $\Delta\alpha = 1$ deg.

The gradient of the moment coefficient with angle of attack at a constant T_C and α is not necessarily a quantity of interest, since for most combinations of thrust and angle of attack the aircraft is either accelerating or decelerating. An indication of such an accelerating flight is depicted in Fig. 9.6 for both rotation directions. The curves represent a constant lift coefficient (and thereby varying angle of attack) as function of advance ratio. The red arrows indicate a sequence of J and C_L of an accelerating flight, from high J and high C_L to a low J and low C_L. This could be a balked landing. The schematic indicates that in no condition the C_{m_α} drops below the value of the propeller-off condition, but reaches a less negative value, followed by a more negative value. Combined with a varying elevator input required to nullify the pitching moment (next subsection), this varying stability characteristic impacts the handling qualities.
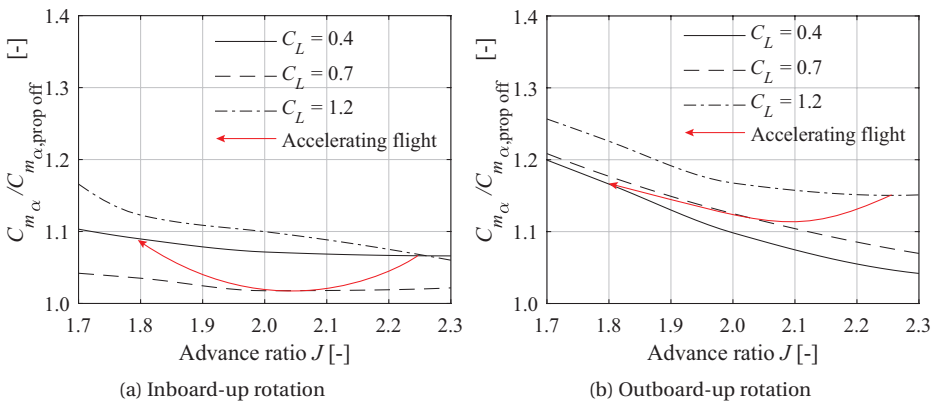

Figure 9.6: Indication of propeller installation effect when the aircraft is accelerating from low T_C and high C_L to a high T_C and low C_L. The arrow gives an *indication* of a possible thrust-lift coefficient scheduling. Clean configuration, experimental results of the *VGM-HTP* model.

As already shown in Fig. 9.3c, the co-rotating case resembles the average between the two symmetric rotation directions. For a co-rotating configuration no destabilizing contribution is found for any angle of attack and (positive) thrust values. This is evident in Fig. 9.7, which depicts the shift in the neutral point as a function of angle of attack at two different advance ratios. At the thrust setting that is representative for approach conditions ($J = 2.3$, $T_C \approx 0.03$), the neutral point shifts rearwards relative to the propeller-off condition from $\frac{\Delta x}{\bar{c}} = -0.05$ at low angles-of-attack, to $\frac{\Delta x}{\bar{c}} = 0.00$ at $\alpha = 7$ deg. At higher thrust settings, the rearward shift is larger. As the most forward location of the neutral point is at low angle of attack in the clean configuration, it is the most critical of all flight conditions in terms of stability. The overall stability is not adversely affected, which is in line with the findings of Ref. [194].

In addition to the characterization for the clean configuration, the propeller installation effect for the high-lift condition is of interest as well. As discussed in Section 6.6.2, a flap deflection results in a larger propeller normal force in Z-direction at the same lift coefficient. The significant nose-down pitching moment from the flaps (Fig. 9.8a) is only partially offset by the propeller installation. It follows that a slightly smaller eleva-
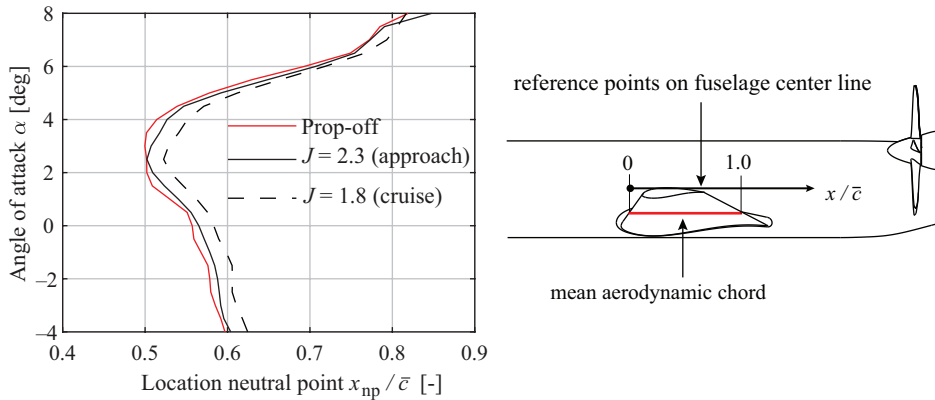
Figure 9.7: Effect of co-rotating propellers on the neutral point. Experimental results of the *VGM-HTP* model, $\beta = 0$ deg, $J = 1.8$.

tor deflection is required to trim the aircraft, but these shifts in C_m still indicate that a trim scheduling is required to maintain a constant lift coefficient. The figure also shows that the overall installation effect of two co-rotating propellers on the pitching moment is an offset and a nearly constant change in slope up to the non-linear region of the lift curve, where the slope changes rapidly and remains approximately constant again for the higher angles of attack. Compared to the clean configuration, there is no significant difference in $C_{m_\alpha}/C_{m_{\alpha,\text{prop-off}}}$ (see Fig. 9.8b): for the clean configuration on average it is increased by 13%, while for the high-lift configuration it increases by 14% over the interval $\alpha = [0,4]$ if the propellers are co-rotating at $J = 1.8$. This is primarily due to a lower variation of the wing-induced flowfield at the plane of the propeller.

(a) Change of pitching moment vs. lift coefficient

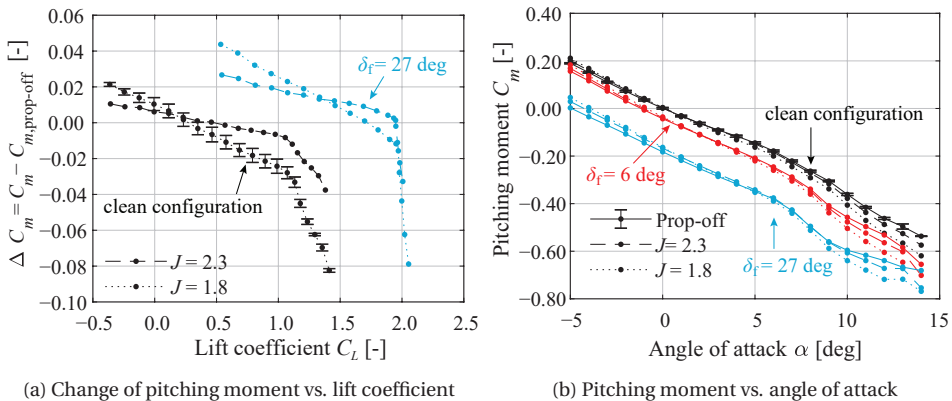(b) Pitching moment vs. angle of attack

Figure 9.8: Effect of the propeller installation on the aircraft pitching moment about $0.25\bar{c}$ for the clean and high-lift configurations of the *VGM-HTP* model. Experimental results, $\beta = 0$ deg. Errorbars representative for all curves.

9.2.2. Control Effectiveness and Trim

The effect of propeller installation on the elevator effectiveness, i.e. $C_{m_{\delta_e}}$, is a relevant parameter from a design perspective, as well as to design a thrust-dependent control law. In Section 8.4 it is shown that a trailing edge device becomes more effective if it is emerged in a slipstream. This effect is confirmed in Fig. 9.9a as a higher $C_{m_{\delta_e}}$ compared to the propeller-off condition. For a given angle of attack, the elevator effectiveness $C_{m_{\delta_e}}$ increases with T_C due to the rise of dynamic pressure in the slipstream. The maximum achievable normal-force coefficient is not compromised by the propeller installation, and therefore it is sufficient to investigate the control effectiveness at low angles of attack. It is clear that even at $T_C \approx 0$, $C_{m_{\delta_e}}$ is larger than $C_{m_{\delta_{e,\text{prop-off}}}}$. This is expected to be the result of the propeller normal force that is introduced by the upwash from the tailplane, schematically shown in Fig. 9.9b. In other words, the propeller could be considered an extension in upstream direction of the main element of the tailplane. A possible implication is that a smaller elevator is required if this interaction effect is included in the design process since independent of the thrust and elevator deflection, the combination of the propeller and tailplane can produce a larger downforce.

(a) Effect of propeller setting on elevator effectiveness, $\alpha = 0$ deg

(b) Illustration of the cause of higher elevator effectiveness at $T_C = 0$

(c) Increase of elevator effectiveness

(d) Change in net force in x-direction, $\alpha = 0$ deg

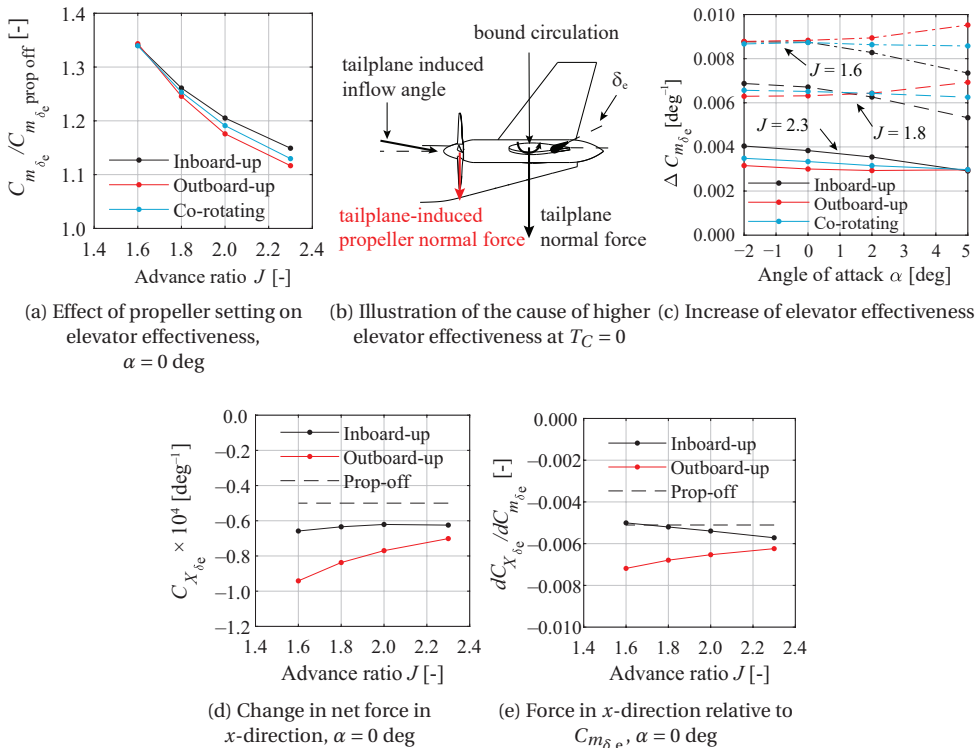(e) Force in x-direction relative to $C_{m_{\delta,e}}$, $\alpha = 0$ deg

Figure 9.9: Effect of propeller installation on elevator effectiveness. Gradients determined over $\delta_e = [0, 15]$ deg. Experimental results of the clean configuration, $\beta = 0$ deg.

The dependency of the elevator effectiveness on rotation direction is attributed to the vortex systems of the tailplane and propeller, similar to the explanation of the difference in normal-force gradient for the tailplane with no elevator deflection. An elevator deflection leads to an increase in C_{m_α} (for the propeller-off case by +30% for $\alpha = [0,5]$ deg), governed by on the one hand a rearward shift of the aerodynamic center and a higher section lift curve slope [67], and on the other hand more trailing vortices are shed for this specific elevator design, which effectively reduce the aspect ratio of the tailplane and therefore its lift-curve slope. Provided that, depending on the rotation direction of the propeller, there is either a favourable or unfavourable interaction between the propeller and tail plane vortices, the $C_{N_{ht,\alpha}}$ increase/reduces if the elevator is deflected. Following the principle of superposition for the co-rotating configuration, $C_{m_{\delta_e}}$ is nearly independent of angle of attack, shown in Fig. 9.9c.

In Fig. 8.25d it is shown that the *relatively* more effective elevator due to propeller installation also means that a higher pressure-drag is associated with it. This is clearly observable in Figs. 9.9d and 9.9e, where the relative increase in drag by an elevator deflection is larger than the propeller-off configuration. The more effective elevator for the outboard-up rotation also means that the drag increase is relatively high, around 25% higher for a typical cruise condition.

The required elevator deflection to compensate for the offset and change in slope of the aircraft C_m curve due to the propeller installation is partially offset by the higher elevator effectiveness. In Fig. 9.10 it is shown up to a thrust setting representative for cruise ($J = 1.8$), the required elevator deflection as a result of propeller installation remains within ± 4 deg compared to the propeller-off condition for a large range of moment reference points. A lower thrust setting leads to smaller required elevator deflection since the impact on the tailplane is smaller. Since the pitching moment coefficient that is introduced by the propeller is not linear with T_C and the elevator effectiveness is a function of the installed thrust coefficient, the required elevator deflection to maintain $C_m = 0$ for various moment reference points is nonlinear. Therefore, a thrust input at a constant C_L and V_∞ needs to be coupled with an elevator scheduling scheme to maintain a certain pitching moment coefficient.

Several previous studies [25, 86] have concluded that the trim drag associated with the large center of gravity excursion is a major drawback for aircraft with tailplane-mounted propellers. In addition to this, the propeller installation also alters the pitching moment curves. However, the consequence of the elevator deflections on the aircraft trim drag for a constant lift coefficient is shown to be minimal for the outboard-up rotating case, see Fig. 9.11. For an inboard-up rotation, the added trim drag is approximately 25% of the propeller-off condition for a typical cruise lift coefficient, and remains a finite offset for the full range of C_L. This property is useful, since the trim drag is therefore only a function of T_C, which simplifies a mission analysis of such aircraft configuration. It is noted that a in case the wing is shifted more rearwards to account for the aft center of gravity, the difference in trim between propeller-on and propeller-off is expected to increase.
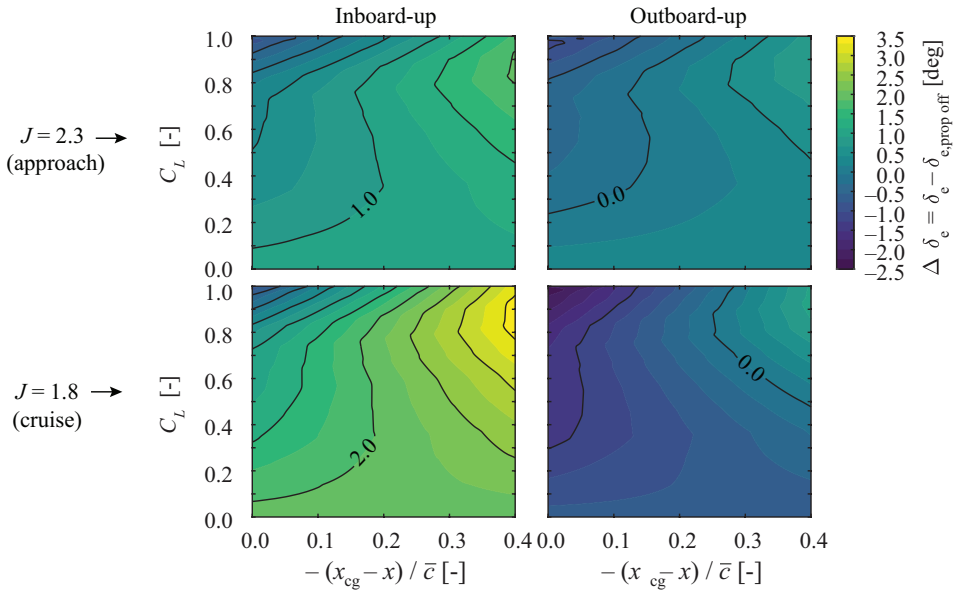
9

Figure 9.10: Difference in elevator deflection relative to the propeller-off condition of the *VGM-HTP* model to maintain $C_m = 0$ in the moment reference point, indicated on the horizontal axis.
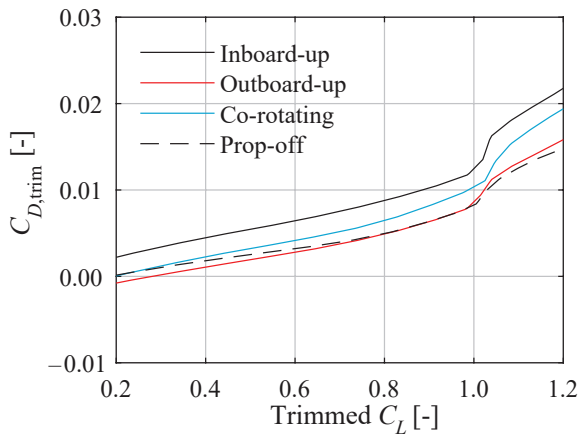

Figure 9.11: Trim drag for $C_m = 0$ at $(x, y, z) = (0, 0, 0)$, clean configuration at $J = 1.6$, $\beta = 0$ deg. Experimental results of the *VGM-HTP* model.

9.2.3. Directional Stability and Trim

The directional stability and trim are influenced by the propeller installation in three ways. First, the propellers introduce a yawing moment due to the thrust line having a distance from the moment reference point. Second, the airframe induces a nonuniform inflow to the propeller, that affects the propeller forces, and thus their contribution to the moments. Finally, the (sheared) propeller slipstream introduces sidewash on the aft-fuselage and vertical tailplane [62, 173, 174]. The separate contributions are indicated in Fig. 9.12.
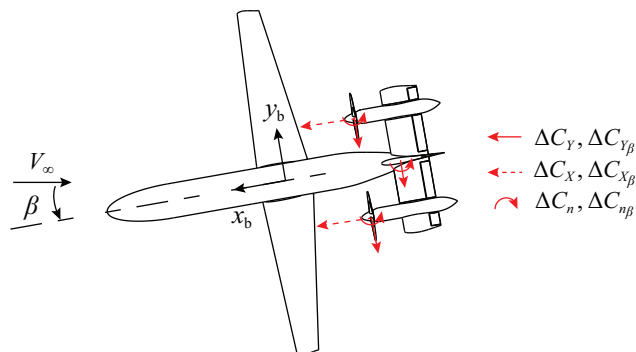

Figure 9.12: Forces and force gradients with sideslip angle relevant for directional stability and trim.

Figure 9.13 depicts the change in yawing moment coefficient for a range of angles of side slip for a cruise condition ($J = 1.8$). For the co-rotating configuration (Fig. 9.13a), the main effect is a larger yawing moment that is proportional to β, hence a higher C_{n_β}. At least for the measured range of $\beta = \pm 10$, the increment in C_n is almost a proportional to β, while at significantly higher angles of sideslip it is expected to become more nonlinear. The initial onset of nonlinearity is already starting at $\beta = -7$ deg and $\beta = +5$ deg, respectively. In Fig. 6.39a in Chapter 6 it is shown that the propeller side-force coefficient remains linear for $\beta \pm 10$ deg. Therefore, this nonlinearity is expected to originate from the slipstream that approaches the trailing edge of the vertical tail, and thereby affecting the pressure distribution on the vertical tail. This is not symmetric for $\pm \beta$ for the co-rotating case, since the slipstream deformation is not symmetric with respect to the aircraft center plane. For this particular case, in Fig. 9.13b it is shown that the installation effect on directional stability depends on rotation direction, with the outboard-up rotation providing the largest increment in directional stability. The same figure also shows that the co-rotating configuration is not the average between the two symmetric rotation directions, and there is an offset in the $C_n - \beta$ curve. These two observations will be addressed later in this section. From the figure is it clear that the main contribution to C_{n_β} comes from the yawing moment of two isolated propellers that are mounted at the respective (x, y, z) locations and the installation effect on the vertical tailplane is at least an order of magnitude smaller.

(a) Co-rotating configuration
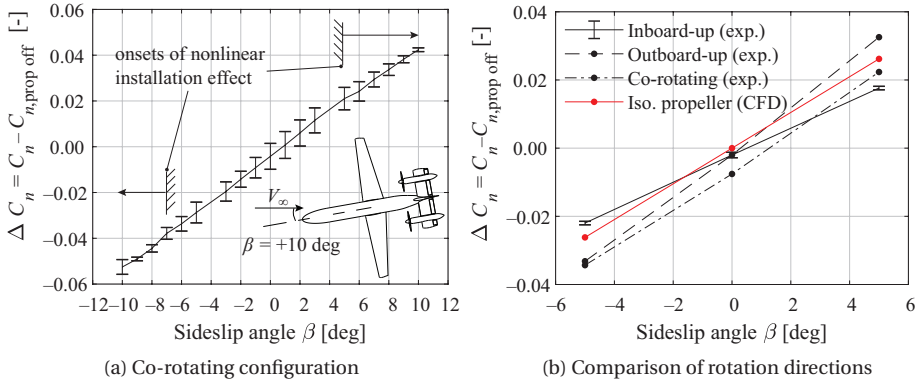
(b) Comparison of rotation directions

Figure 9.13: Effect of propeller installation on the aircraft yawing moment coefficient, $\alpha = 0$, clean configuration, $J = 1.8$. Experimental results of the *VGM-HTP* model.

To understand the role of the rotation direction on the directional stability, the C_{n_β} is evaluated for different thrust coefficients in Fig. 9.14a. The figure shows the gradient of the yawing moment with sideslip angle, relative to the propeller-off configuration. Figure 9.14a also depicts the yawing moment caused if a propeller in isolated conditions is positioned at the same (x, y, z)-location as the installed propellers. Nearly independent of thrust coefficient, the propeller installation enhances the directional stability by approximately 6% to 12%. The low dependency of the propeller side-force coefficient on T_C is also the case for an isolated propeller (indicated in the same figure). The difference between values of C_{n_β} is caused by the installation effect, partially coming from the changes in forces on the airframe, and partially due to the different forces acting on the propeller.
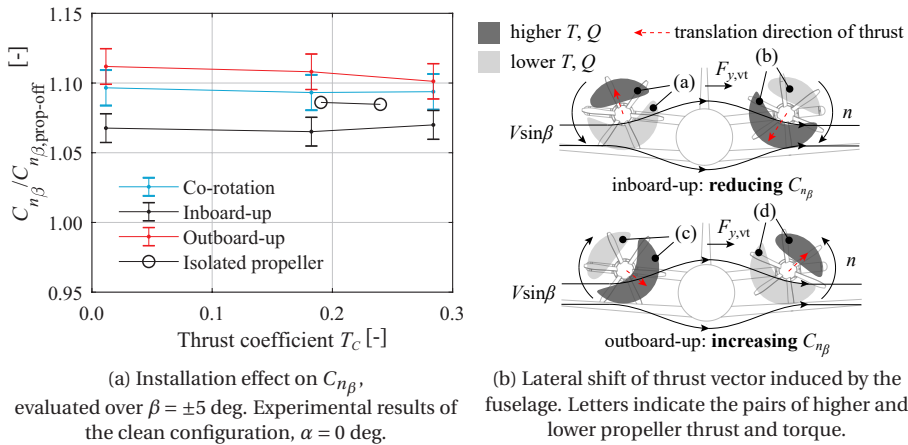
(a) Installation effect on C_{n_β}, evaluated over $\beta = \pm 5$ deg. Experimental results of the clean configuration, $\alpha = 0$ deg.

(b) Lateral shift of thrust vector induced by the fuselage. Letters indicate the pairs of higher and lower propeller thrust and torque.

Figure 9.14: Effect of propeller installation on directional stability for the *VGM-HTP* model.

The fuselage-induced non-uniform inflow to the propeller, schematically shown in Fig. 9.14b, can be observed in the propeller side-force coefficient in Fig. 6.39a in Chapter 6. The fuselage induces an in-plane flowfield such that the regions (a) and (b) translate in opposite direction to the side force on the vertical tail $\left(F_{y_{vt}}\right)$, while pair (c) and (d) translate in the same direction as $F_{y_{vt}}$. The consequence is an enhanced and reduced C_{n_β} for an outboard-up and inboard-up configuration, respectively.

Besides the forces on the propeller, the presence of a slipstream on each side of the vertical tail also influences the contribution of the vertical tail to the yawing moment by the introduction of a sidewash and gradient of the flowangle between these slipstreams [278]. This results in an offset and change in slope of the $C_n - \beta$ curve as a function of thrust. For a wing-mounted propeller configuration with corotating propellers, there is also a sidewash to the vertical tail, induced by the non-symmetric lift-distribution [278]. For a rear-mounted configuration, the slipstream deformation due to the horizontal tail occurs close to the leading edge of the vertical tail, thereby reducing its impact on the sidewash to the vertical tail. For the configuration studied herein, the sidewash is equivalent to a sideslip angle of approximately 2 deg for a typical cruise/climb thrust setting of $T_C = 0.28$, as shown in Fig. 9.15a, with the sidewash observable in the flowfield depicted in Fig. 9.15b.
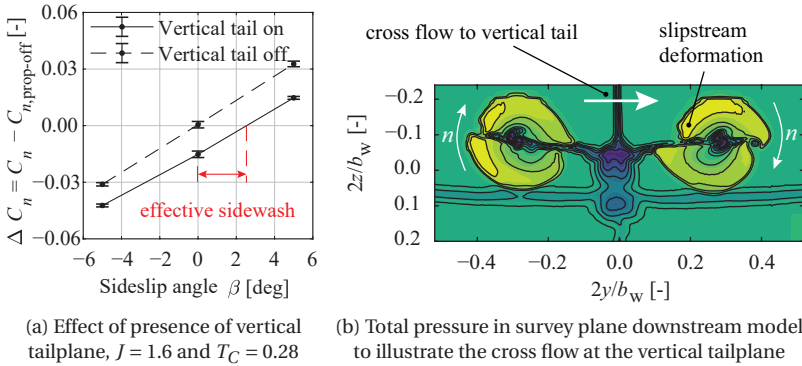

(a) Effect of presence of vertical tailplane, $J = 1.6$ and $T_C = 0.28$

(b) Total pressure in survey plane downstream model to illustrate the cross flow at the vertical tailplane

Figure 9.15: Effect of co-rotating propellers on the vertical tail, $\alpha = 0$ deg, $J = 1.8$. Experimental results of the *VGM-HTP* model.

Without the vertical tail, the yawing-moment coefficient is zero at $\beta = 0$ deg, indicating that the propeller-induced sidewash primarily affects the vertical tail and not the fuselage. Figure 9.15a also indicates that the installation of the vertical tail partially offsets the increased directional stability enhancement by the propellers. This reduction is attributed to the position of the vertical tail between two slipstreams. The dynamic pressure and the effective inflow at the vertical tail are both reduced with an increasing thrust setting, which leads to a reduction of $C_{n_{\beta_{vt}}}$ of 2.5% compared to zero thrust. This value is therefore representative of the reduction in effective sidewash to angle of sideslip for a vertical tailplane.

For the one-engine-inoperative condition, the yawing moment introduced by the operating propeller needs to be compensated by a rudder deflection if the flight path is to

be maintained. Figure 9.16 depicts the yawing moment as the result of the port propeller not operating, as well as the moment that is introduced as thrust multiplied with the moment-arm, $n = -Ty_p$. As expected, the sidewash on the vertical tail introduced by the outboard-up rotating propeller is opposing the thrust-induced yawing moment. If the outboard-up propeller is inoperative, the sidewash adds to the yawing moment and a larger rudder input is required to trim the aircraft at zero sideslip angle. Hence, the outboard-up propeller is the critical engine.
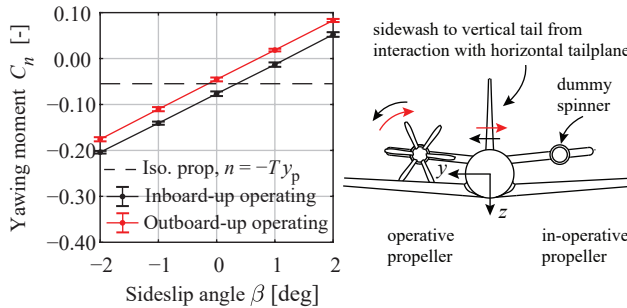

Figure 9.16: Effect of one-engine-inoperative condition on yawing moment, $J = 1.6$. Inoperative port propeller replaced by a dummy spinner. Experimental results of the *VGM-HTP* model.

9.2.4. Installation Effect on Lift, Drag, and Lift-to-Drag Ratio

The installation of the propellers also affects the integral airframe lift and drag, and propeller lift, leading to a net change in lift-to-drag ratio. While for a wing-mounted tractor configuration the propellers enhance L/D and maximum lift [37, 269, 279, 280], for the tail-mounted propeller configuration this is not evident. From the different contributions of the propeller, fuselage, and tailplane, it is not directly clear how the overall lift is affected by the propeller installation. In Refs. [194, 229] it is demonstrated that the effect on integral lift for a tail-mounted configuration is relatively small, with a ΔC_L introduced by the propeller of an order of magnitude smaller than for a wing-mounted configuration. This is attributed to the typically lower aspect ratio of the tailplane and the relatively small size compared to the propeller. A more elaborate analysis of the integral forces introduced by the propeller will allow for the interpretation of the relevance of the different contributions found in previous chapters.

Figure 9.17a depicts the change in lift coefficient for a typical cruise condition. As expected, the outboard-up rotation direction introduces a small reduction in $C_L = -0.020$ at $\alpha = 0$, while the inboard-up rotation increases the lift by $C_L = +0.015$. At higher angles of attack, especially the propeller force components lead to a higher lift, shown in Fig. 9.17b. Of the propeller forces, the normal force contributes most to added lift. If the propellers were to be mounted to the leading edge of a wing, a larger propeller lift component could be expected due to the wing upwash. The co-rotating configuration is again approximately the superposition of the two rotation directions, and the added lift by the propeller can be reasonably approximated using force data of an isolated propeller.

(a) Change in lift coefficient as a function of α, $J = 1.8$ (cruise condition)

(b) Approximate contribution of two isolated propellers with $\alpha = \alpha_\infty$, $J = 1.8$ (cruise condition)
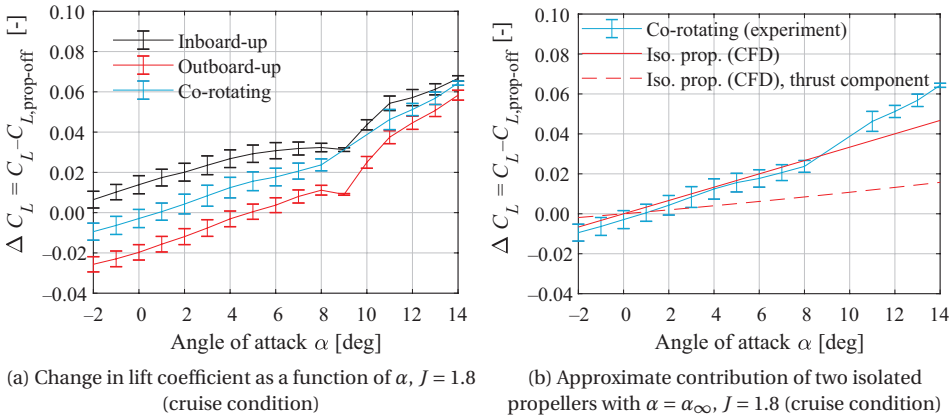
Figure 9.17: Change in aircraft lift due to propeller installation (contributions from both propeller and airframe). Experimental results of the *VGM-HTP* model, $\beta = 0$ deg.

At typical cruise angles of attack ($\alpha = 2$ deg to $\alpha = 4$ deg), the thrust induced lift for the co-rotating configuration is slightly positive, i.e. $\frac{dC_L}{dT_C} > 0$. This is particularly visible in Fig. 9.18, with a gradual larger effect for higher T_C values. For the outboard-up configuration at $\alpha = 5$ deg, the response $C_L - T_C$ is rather flat. In this case, the negative lift on the tailplane and the positive contribution of the propeller are compensating each other.
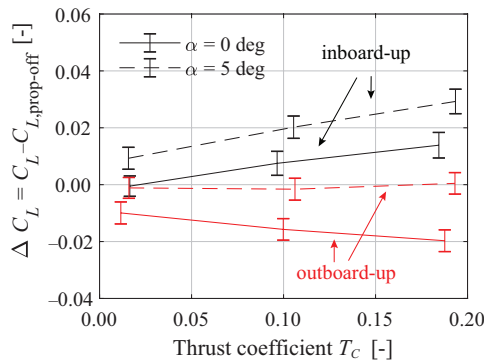
Figure 9.18: Change in lift as function of installed thrust. Experimental results of the *VGM-HTP* model, $\beta = 0$ deg.

Although the maximum lift coefficient for the clean configuration is at $\alpha > 14$ deg (out of the measured range), Fig. 9.19a depicts a small positive effect on maximum lift. Unlike a wing-mounted configuration, this is not the result of the higher dynamic pressure at the same angle of attack, but primarily coming from the forces acting on the propellers, as already shown in Fig. 9.17b. This observation is further supported by Fig. 9.2.

281

A flap deflection leads on the one hand to a reduced normal force on the propeller, but on the other hand to higher thrust values. The decomposition of the airframe and propeller contributions in the high-lift conditions, depicted in Fig. 9.19b, puts the relative propeller contribution in perspective. The propeller contribution to lift is approximately linear with α and is, similar to the clean configuration, again the dominating contribution to ΔC_L. The strong wing-induced downwash field causes C_{L_p} to be negative for low to moderate angles of attack. The nonlinear part in the airframe ΔC_L for $\alpha > 6$ deg is the consequence of the added lift on the tailplane on the inboard-up rotating side. The figure also shows that the *change* in airframe lift does not vary significantly with angle of attack. This is due to the compensating normal force on each side of the tailplane and nacelle (see Fig. 8.36c).

The difference in maximum lift coefficient between the clean and high-lift condition (simulated with a flap deflection) is minor. The propeller and airframe combined lead to only a moderate increase in C_{L_max} by up to 0.05, and this is nearly independent of propeller thrust (since the normal force is dominating), contrary to a wing-mounted propeller configuration, where the maximum lift enhancement is thrust dependent [42, 107, 116].
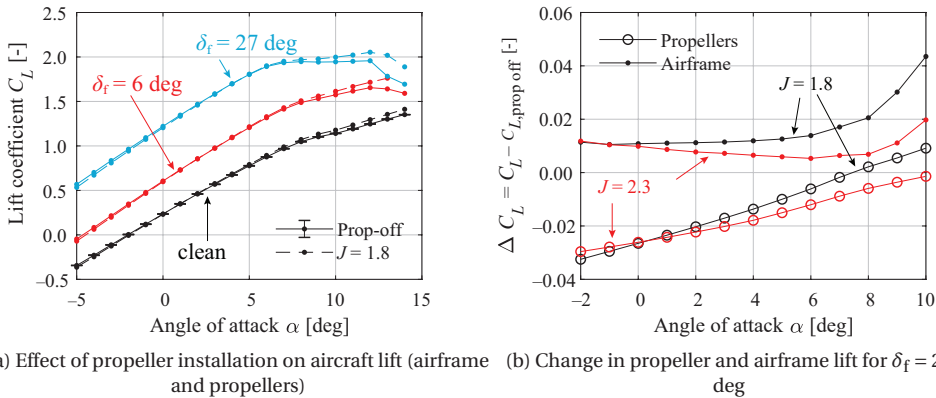

(a) Effect of propeller installation on aircraft lift (airframe and propellers) (b) Change in propeller and airframe lift for $\delta_\mathrm{f} = 27$ deg

Figure 9.19: Change in propeller and airframe lift in installed conditions for the co-rotating configuration with a flap deflection of $\delta_\mathrm{f} = 27$ deg. Experimental results of the *VGM-HTP* model, $\beta = 0$ deg.

In Section 8.4 it has been demonstrated that, depending on the rotation direction and angle of attack, the drag of the tailplane is either reduced or increased compared to the propeller-off condition. The implication of propeller installation the airframe drag for the co-rotating configuration is depicted in Fig. 9.20a. At the same lift-coefficient, the drag curve of the installed case falls nearly within the experimental uncertainty of the propeller-off case. Despite the small reduction in tailplane drag for the co-rotating case (Fig. 8.37), has nearly no effect on aircraft level. The airframe drag is slightly reduced for $\alpha \leq 2$ deg, due to the swirl recovery by the tailplane at $\alpha = 0$ and $J = 1.8$ and the drag is reduced by 20 drag counts.

Figure 9.20 depicts the product of the installed lift-to-drag ratio curves with the efficiency in flight direction. If the lift of the propeller is included in the aircraft lift-

coefficient, the *total* lift-to-drag ratio is slightly higher at higher angles-of-attack. At these conditions, both the thrust vector and normal force enhance lift. The lower propeller normal force at positive angles of attack leads to a higher propeller efficiency in freestream direction compared to an isolated propeller. This makes the propeller efficiency in flight direction multiplied with the lift-to-drag ratio up to 2% higher compared to the situation in which the interaction is not included.

It is noted that for this particular aircraft the maximum lift-to-drag ratio is at a high value ($C_L = 0.9$), and $(L/D)_{\text{max}}$ is relatively low because of the suboptimal design of the aircraft. As the benefit of a propeller normal force particular is present at higher angles of attack ($\alpha > 5$ deg), the benefit would be smaller if the maximum airframe efficiency would be at a lower C_L, for example by selecting a different wing incidence angle.

(a) Airframe drag

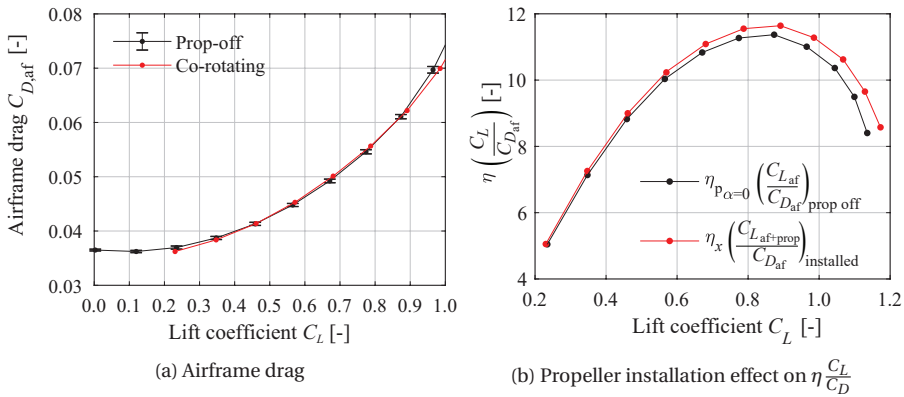(b) Propeller installation effect on $\eta \frac{C_L}{C_D}$

Figure 9.20: Installation effect on C_D and $\eta \frac{C_L}{C_D}$ untrimmed the clean configuration at $J = 1.8$. Experimental results of the *VGM-HTP* model, $\beta = 0$ deg.

An interesting quantity from a flight-mechanics perspective is the gradient of the axial force component with angle of attack. For a propeller-off configuration, this value is negative; a perturbation $\Delta\alpha > 0$ leads to higher drag force. In case the propellers are installed and operate at constant advance ratio, it is not directly clear whether the change in axial force is less/more negative compared to the propeller-off case. Figure 9.21a shows that the propeller installation leads to a slightly less negative value of C_{X_α}, while it becomes more negative at higher thrust settings. In a practical sense, this means that at low thrust setting, a perturbation in angle of attack (and therefore lift coefficient) is less critical for the axial force balance in case the airspeed is to be maintained, compared to a situation where the airframe and propellers are modelled individually. At higher thrust settings for an outboard-up rotation, C_{X_α} is more negative, attributed to the higher normal-force coefficient that points in the drag-direction. Finally, in Fig. 9.21c the gradient $\frac{dC_X}{dC_L}$ is plotted as a function of lift coefficient. These curves indicate the change in axial force for a change in lift coefficient. This figure shows that the installation effect is small: a first estimation of the dynamic behaviour along the x-direction can be obtained without taking the propeller-installation effects into account, especially for the co-rotating case.
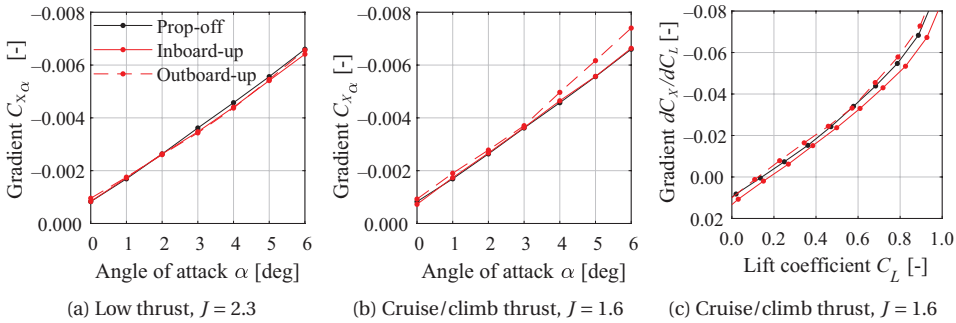
Figure 9.21: Installation effect the gradient of the axial force component. Experimental results of the clean configuration of the *VGM-HTP* model.

The current study displays that even for a suboptimal design, the beneficial propeller–airframe aerodynamic interaction could partially offset the drawbacks identified for the configuration [25, 86, 280]. These benefits are present despite the fact that an aerodynamic performance benefit historically has not been the objective to study the configuration.

9.2.5. Propeller Efficiency

In Chapter 6 it is shown that a propeller installation to the horizontal tailplane slightly increases the propeller efficiency due to the lower axial velocity at the aft of the aircraft. Since the propeller inflow varies between flight conditions, i.e. angle of attack, angle of sideslip, and the deployment of high-lift devices, the propeller efficiency is not constant. This section puts these variations of η_p into perspective.

The propeller efficiency map, i.e. $\eta_p - \alpha$, is depicted in Fig. 9.22a for the two rotation directions. As expected, the efficiency along the propeller rotation axis slightly increases with angle of attack, with a maximum for the inboard-up rotating case around $J = 1.9$. This is close to the advance ratio at which the isolated propeller has its maximal efficiency. Approximately the same trend is followed by the outboard-up rotating propeller. However, the reduction of η_p at $\alpha = 8$ deg is only present for the inboard-up rotating propeller. This corresponds to the condition with swirling inflow (see Section 6.6.3)and the inboard-up rotating propeller operates locally at a higher effective advance ratio. The efficiency of the outboard-up rotating propeller continues to increase up to values close to unity. These high efficiencies are possible because η_p is defined with V_∞ as reference velocity, while there is kinetic energy deposition induced by the airframe at the propeller plane. Figure 9.22b also shows that in case a fixed blade pitch is selected for operation, the advance ratio, i.e. rotational speed, should be adapted to operate at the maximum efficiency (further discussed in Chapter 7). However, in essence this is not different from wing-mounted propeller configurations.

A more interesting quantity from an aircraft performance perspective is the propeller efficiency in the direction of flight, η_x, as it directly affects the fuel consumption for a given flight condition. Typically, for an isolated propeller, η_x decreases with angle of
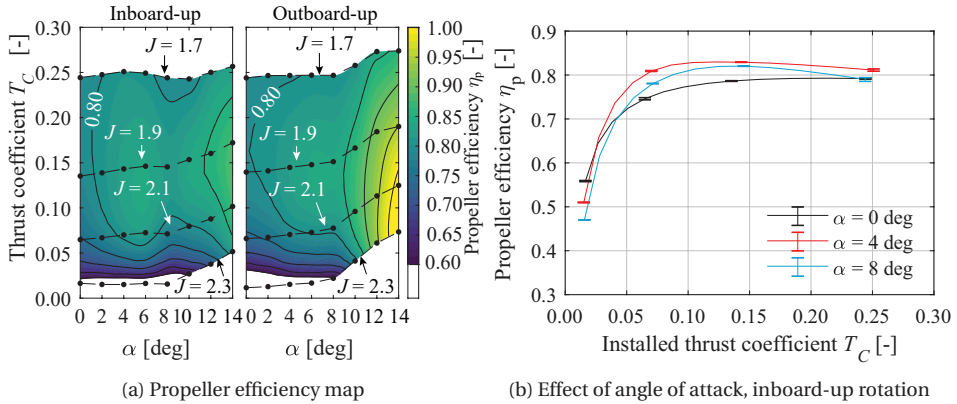
(a) Propeller efficiency map

(b) Effect of angle of attack, inboard-up rotation

Figure 9.22: Installation effect on propeller efficiency η_p. Experimental results of the *VGM-HTP* model. Clean configuration, $\beta = 0$ deg.

attack because the normal force has a negative contribution in flight direction which completely offsets the higher efficiency due to the reduced axial inflow. To the contrary, for the installed propeller, η_x can be expected to increase for the linear part of the lift-curve, as schematically shown in Fig. 9.23a. For the $VGM - HTP$ model, this is indeed the case from $\alpha = 0$ up to $\alpha = 5$ deg, as plotted in Fig. 9.23b. This increase is caused by the reduced propeller normal force that is minimal at a positive angle of attack due to the propeller operating in the wing-induced flowfield. The second peak around $\alpha = 14$ deg for the outboard-up rotating propeller is in line with the trend of η_p. This means that the outboard-up configuration has a larger range of angle of attack at which η_x is close to the maximum. Therefore, this rotation direction potentially has a better climb performance from a propulsive efficiency point of view than the inboard-up configuration.

(a) Effect of angle of attack, inboard-up rotation
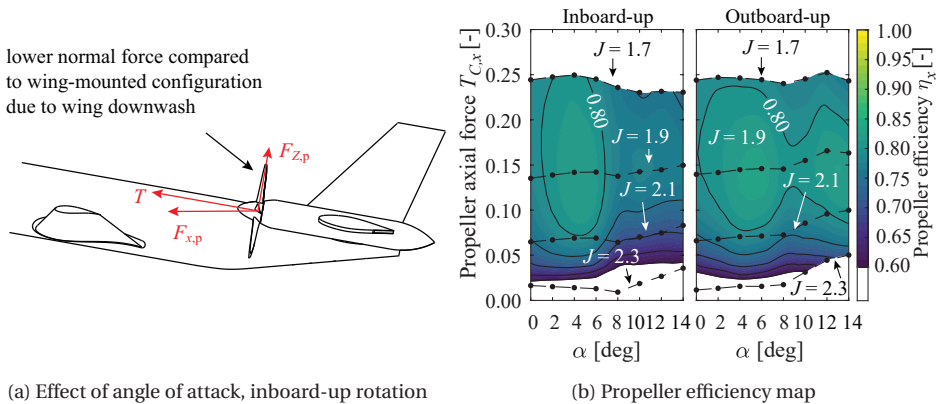
(b) Propeller efficiency map

Figure 9.23: Installation effect on propeller efficiency $\eta_x \left(= \frac{F_{x,\mathrm{p}} V_\infty}{P_\mathrm{s}} \right)$. Experimental results of the *VGM-HTP* model. Clean configuration, $\beta = 0$ deg.

The results in this section once again confirm that the propeller performance in the installed condition is affected by the installation. If the installed propeller is to be operated at the maximal efficiency (along the direction of flight) the advance ratio and blade pitch are to be adapted relative to an isolated propeller, which is in line with the conclusions in Chapter 7. If a co-rotating configuration is to be selected that operates at the same advance ratio (to avoid an annoying vibratory frequency [83, 281]), one propeller may not operate at its highest efficiency point. If it would, a thrust imbalance would arise that needs to be compensated by a rudder deflection.

9.3. Leading-Edge Distributed Propeller Configuration

In this section the propeller installation effect of an array of leading-edge-mounted propellers on various aircraft performance indicators is investigated. As mentioned before, the *A320-DP* model is used (Section 3.4.4). The propeller forces are computed using the method described in Chapter 5. The implementation in the CFD model is described in Section 3.4.3, while the design choices for this particular aircraft are explained in Section 3.4.4. The fact that the wing has a rather high sweep angle, which is not necessary for the envisioned flight Mach numbers, does limit the quantitative projection of the results to a more representative geometry that has no sweep. On the other hand, it allows to investigate particular features including the effect on flow separation and the shift in aerodynamic center that would also occur on moderately swept wings.

In this section, specifically several design considerations are addressed from a fundamental interaction perspective. These include the effect of rotation direction and the nacelle integration on:

- Longitudinal static stability

- Maximum lift coefficient

- Aircraft lift-to-drag ratio

Moreover, also the effect of tip-propeller radius is investigated on the propeller efficiency and wing drag.

Since there is a resemblance with the conventional wing-mounted configuration, the findings that pertain to either the wing sweep angle, the tip propeller, and the slipstream–slipstream interaction of the inboard propellers are of special interest. However, there is also still overlap with the conventional twin-prop configuration with propellers mounted to the inboard part of the wing. First, aspects of nacelle-integration are discussed in Section 9.3.1. The effect of rotation direction on airframe and propeller performance is discussed in Section 9.3.2, followed by a discussion on propeller installation effects on the pitching moment curve. Finally, a trade-off study is presented on the size of the tip-propeller relative to the airframe performance.

9.3.1. Aspects of Nacelle Integration

In Chapter 8 it has been shown that a nacelle introduces a significant velocity perturbation to the wing in case of a crossflow, i.e. an upwash from the wing or angle of at-

tack. The result is a higher angle of attack, especially near the leading-edge of the wing, causing a higher suction peak. At high-speed flight, the additional suction can cause compressibility losses [282, 283]. At low angle of attack, this suction increases the local lift coefficient, while at high angle of attack, the maximum lift coefficient of the wing is compromised [250, 273, 284] as flow separation is likely to initiate at that particular location. On the other hand, for the portion of the wing where the nacelle is mounted, typically the circulation is reduced compared to the clean wing.

At low thrust coefficients, the nacelle-induced flowfield dominates the installation effect by a propeller—nacelle combination to the wing. At higher thrust coefficients, this installation effect is further enhanced on the upgoing blade side. In case the wing is swept, it is known from literature [162, 282, 285–287] that the installation of the nacelle leads to a higher suction peak and a steeper adverse pressure gradient on the inboard portion of the wing. While the local flow separation on a swept wing will change the wing aerodynamic center, the effect of a nacelle mounted to the wing on the aircraft stability characteristics are not frequently quantified. This aspect of nacelle integration is discussed in Section 9.3.3. For the interpretation of some of the trends that are discussed in the following sections, it is required to investigate the installation effect of the propeller-off case first, which serves as the baseline.

The local perturbations to the spanwise lift distribution caused by the nacelle are visible in Figs. 9.24a and 9.24b. It is noted that since the nacelles are already tilted down by 3 deg, the upwash effect to the wing is relatively small at a cruise condition with $\alpha = 4$ deg. It is also noted that in this case the wing design is not adapted to account for these local increased in inflow. The rising lift coefficients are caused by the additional upwash from the nacelles, while the reductions are an indication of flow separation, especially observable for $\alpha > 4$ deg. The drag increases from both a higher pressure drag that arises from the flow separation, while also the induced drag increases, caused by the additional spanwise vortices that are shed. The locations that are most influenced by the nacelles are likely to achieve the local maximum lift coefficient of the section at a lower angle of attack than in case of no nacelles. This leads to premature flow separation and therefore a reduction of aircraft maximum lift coefficient. In Figs. 9.24c and 9.24d it is clear that the local pressure distribution on the inboard side of the nacelle is affected as the result of the adverse pressure gradient caused by the swept leading-edge. At $\alpha = 6$ deg, the inboard side already shows a leading-edge separation, where the region of reversed flow extends further in chordwise direction for higher angles of attack. The flow separation is absent on the outboard side of the nacelle.

To reduce the adverse installation effect of the nacelles, several studies have suggested local adaptations of the nacelle [250] or to the wing—nacelle junction to suppress the suction peak [282, 284, 288]. A rather complete overview of various techniques is presented in Ref. [283]. The adverse installation effect can be reduced by a translation of the nacelle in z-direction, with the purpose of reducing the w-velocity component. To demonstrate that this is an effective method, the inboard nacelle is translated downwards (positive z-direction) by a distance equal to 0.5 times the nacelle radius (Figs. 9.25a and 9.25b). This translation would have a relatively small effect on the propeller-installation as discussed in Section 8 (although not quantified herein).

By translating only the inboard nacelle for illustration purposes (while maintaining

(a) Lift distribution

(b) Drag distribution

(c) Pressure distribution, inboard side
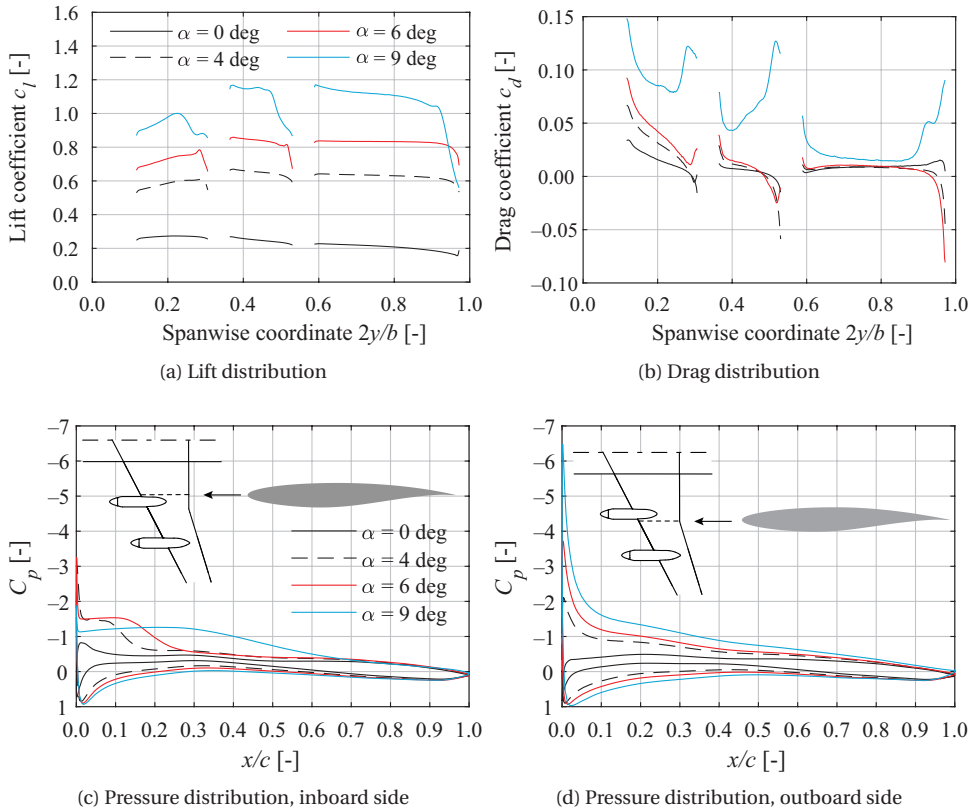
(d) Pressure distribution, outboard side

Figure 9.24: Effect of nacelle installation on the wing lift, drag, and pressure distributions (propeller-off)

the other nacelle locations), the lift increment on each side of this nacelle is reduced, as is evident in Fig. 9.25c. The drag is reduced on the inboard side and increased on the outboard side, which is as expected. The absence of the upwash on the outboard side leads to a resultant force vector that is tilted more backward. Even for $\alpha = 6$ deg and with one nacelle translated, the aircraft lift-to-drag ratio is increased by 2.5% (from 14.9 to 15.3), while the lift is reduced by $\Delta C_L = -0.01$.

Since the aim is not necessarily to improve the cruise performance but instead improve the high angle-of-attack condition, the suction peak followed by a flow separation is successfully suppressed for the translated nacelle for the case of $\alpha = 6$ deg, as is evident in Fig. 9.26a. On the outboard side of the nacelle (Fig. 9.26b) the influence is clearly visible in the front part of the airfoil, but does not impact the overall pressure distribution. The less severe flow separation from the nacelle–leading-edge junction is also shown in the flow structures, shown in Figs. 9.26c and 9.26d. The figure depicts discrete flow pathlines to visualize the corner-flow separation, as well as additional pathlines that remain close to the wing surface to distinguish between the attached and separated flow regions. Although not well visible, an isosurface is plotted with the axial velocity compo-
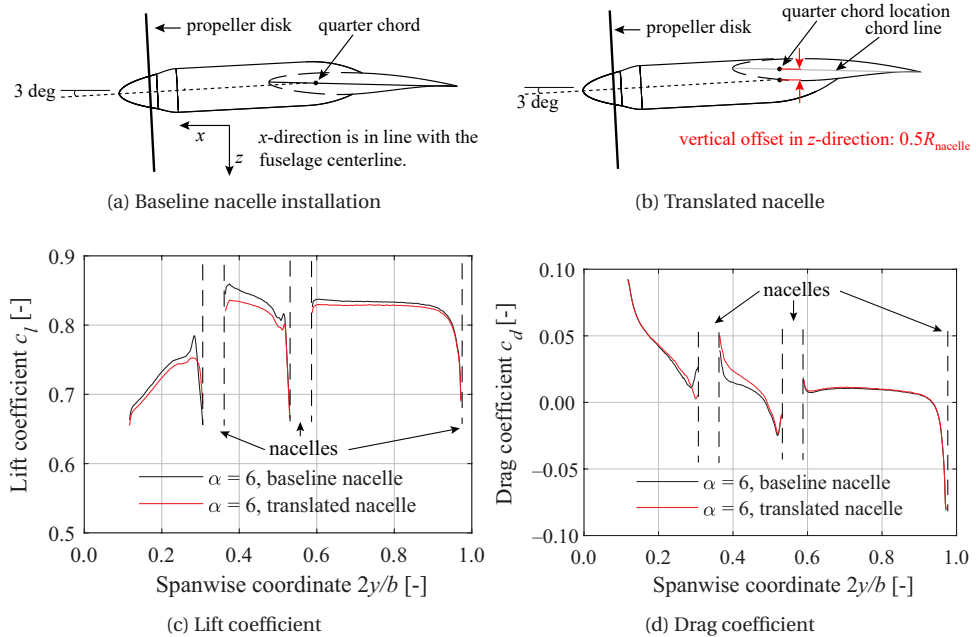
(a) Baseline nacelle installation

(b) Translated nacelle

(c) Lift coefficient

(d) Drag coefficient

Figure 9.25: Effect of a translated inboard nacelle on the wing lift and drag distributions, prop-off, $\alpha = 6$ deg.

nent equal to zero, to identify the region of flow reversal. Even at this low angle of attack, the corner-flow separation for the baseline case extents over nearly 25% of the chord and incudes a strong vortex (also observed in Refs. [273, 289]). For the translated nacelle, the corner-flow separation is still present, but its extent is limited. A small fillet to reduce the curvature in this junction even further is expected to nearly remove the local flow separation. Another advantage of a more downward mounted nacelle is the larger part of the wing that is undisturbed. The wake that leaves the baseline nacelle on the suction side greatly reduces the local effective curvature, and therefore the lift coefficient at the nacelle y-location. Furthermore, for this swept-wing design, the streamlines on the suction side are curved towards the fuselage. A nacelle that has no toe-out angle introduces an additional pressure gradient since it is experienced as a diverging channel. This is highlighted by the dashed lines in Fig. 9.26d.

The remaining results in the following sections are computed with the baseline nacelle, since the nacelle adaptation was only done at a later stage of the evaluation of the *A320-DP*. Because the phenomena of a corner-flow separation are still present with the translated nacelle (and could be even further suppressed), the presented results are considered a more extreme case. Therefore, the conclusions of the severity of this installation on the stability characteristics should be interpreted with care and should be considered as qualitative. Furthermore, by interpreting the benefits from the propellers on airframe lift-to-drag ratio, it should be remembered that the baseline values are rather low compared to a well-designed wing–nacelle combination.

(a) Pressure distribution on the inboard part of the nacelle

(b) Pressure distribution on the outboard part of the nacelle

(c) Isometric view

(d) Top view. Dashed black lines indicate the average flow direction above the wing surface.
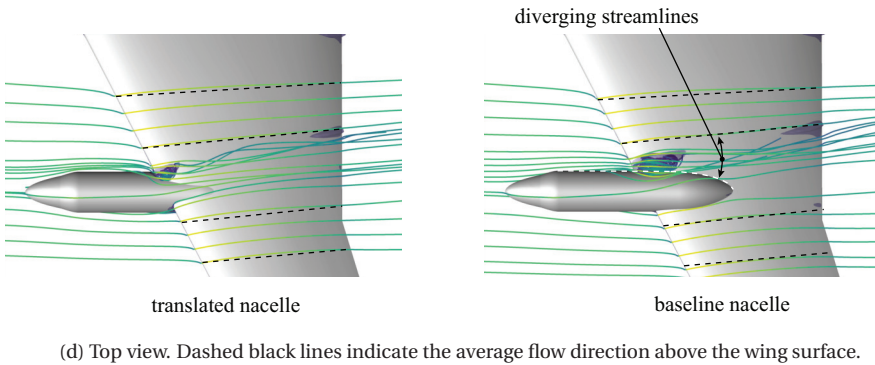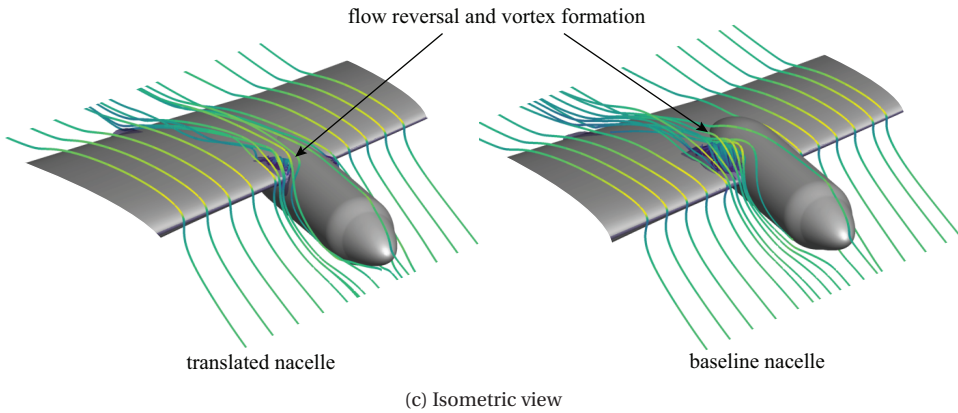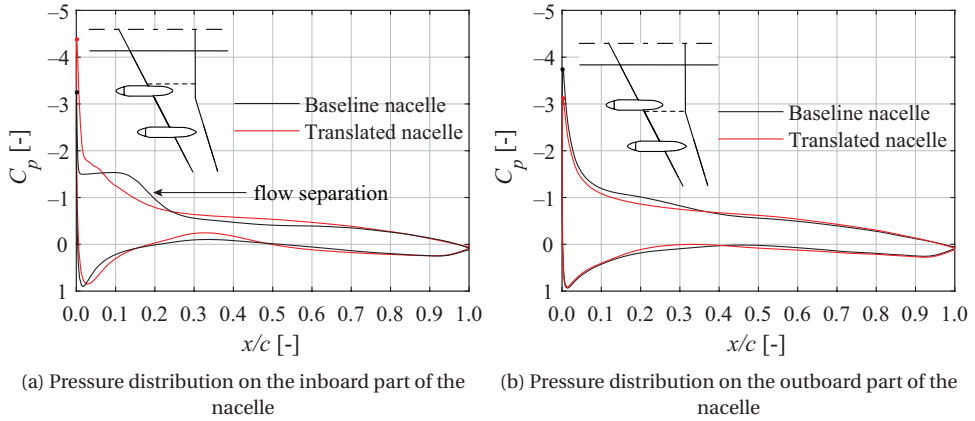
Figure 9.26: Flow separation on inboard side of inboard nacelles, prop-off. Colors of the pathlines in c and d indicate the axial flow velocity. The blue isosurface indicate the edge of flow reversal. Conditions: $\alpha = 6$ deg, $M = 0.14$, $Re_{\bar{c}} = 1.7 \cdot 10^6$.

9.3.2. Effect of Rotation Direction on Airframe and Propeller Performance

The rotation direction of propellers mounted to a swept wing can be expected to be a more important parameter for the airframe performance (i.e. change in lift at given angle of attack, the lift-to-drag ratio, trim drag), propeller performance (i.e. efficiency and unsteady loads), and static stability characteristics (i.e. slope of the moment curves), because the airframe-induced inflow is skewed with respect to the propeller, and additionally, the previous section has shown that the nacelle-installation can significantly impact the wing aerodynamic performance. This section discusses the installation effect on the wing, propeller, and full aircraft in the cruise condition (despite a low Mach number of $M = 0.14$ is used as inflow condition).

Prior to the analyses of any performance changes related to the airframe, the effect of the airframe on the propeller is estimated first. The varying load distribution, and therefore upwash, along the span leads to a larger installation effect in case the propellers are mounted more inboard. On top of this, the wing leading-edge is swept, while the y-axis of the propeller disks are perpendicular to the freestream flow. In Fig. 9.27a it is schematically shown that a larger upwash is experienced on the inboard side of the disk since it is closer to the wing leading-edge. The result is that at $\alpha = 3$ deg (propeller disks normal to direction of freestream) an outboard-up rotating propeller generally has a higher efficiency. The average efficiency in flight direction, η_x, is shown in 9.27b, and confirms this hypothesis. For the OU-OU-IU configuration, the difference is approximately $\Delta\eta_x = 0.01$ compared to IU-IU-IU. In other words, the installation coefficient κ, as introduced in Chapter 6, is higher for an outboard-up rotating propeller. At higher angles of attack, the normal-force coefficient of this rotation direction also increases. Since this is a force that has a component in drag direction, the benefit in η_x becomes smaller at higher angle of attack. The difference in loading on the propeller disk is also evident in Fig. 9.27c, which shows the thrust distribution for each propeller of the IU-OU-IU configuration. In this case, while the most inboard propeller experiences the largest disturbance in inflow, the largest changes in loading are present for the middle propeller. The corresponding flowfield, i.e. the varying swirl and increment of dynamic pressure, determines the interaction with the wing.

9

(a) Schematic of the distributed upwash along the leading-edge caused by the fuselage and swept wing

(b) Installation effect on the average efficiency η_x for each rotation-direction

(c) Propeller loading distribution at $\alpha = 4$ deg, $J = 1.9$ for the IU-OU-IU rotation direction.
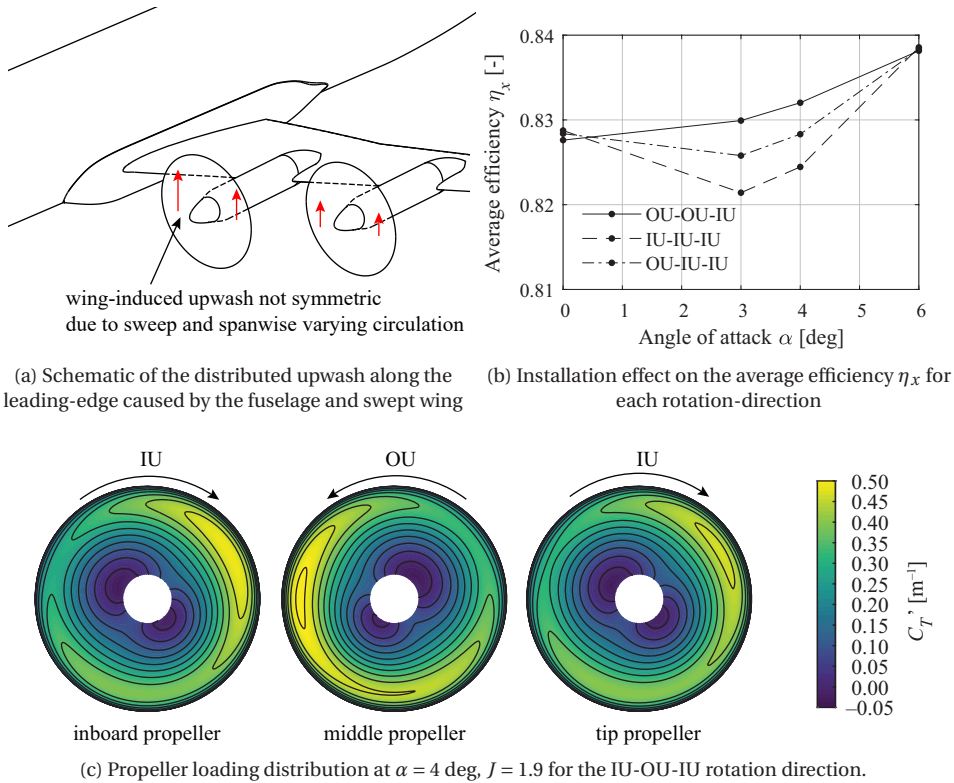
Figure 9.27: Installation effect of propellers mounted to the swept leading-edge.

The effect of the propeller on the wing lift distribution is depicted in Fig. 9.28. The lift coefficient is particularly enhanced in the tip region ($2y/b_\mathrm{w} > 0.8$), since the ratio D_p/c is higher in this region and the effect of induced drag reduction is largest in this region (see Section 8.4). This also means that the wing becomes prone to tip stall, especially in case of further enhancement of lift by means of an aileron deflection. The lift coefficient can be expected to increase even further for higher disk loadings since it comes with a higher swirl angle in the slipstream (Fig. 2.14c).

The rotation directions of the inboard propellers have a profound effect on the spanwise lift distributions. The following can be observed from the *relative* increase in lift in Figs. 9.28b and 9.28c:

1. For inboard-up rotating propellers: The more inboard the propeller is mounted, the larger the magnitude and the spanwise extent of that rise in lift is. The rise in lift is therefore more inboard.

2. For outboard-up rotating propellers: The more outboard the propeller is mounted, the larger the magnitude and the spanwise extent of that rise in lift is. The rise in lift is therefore more outboard.

3. Irrespective of the rotation direction, there is a net lift increase.

4. The part of the disk that is increasing the local angle of attack to the wing increases the lift and at the same time decreases drag. At these locations, the sectional lift-to-drag ratio increases significantly.

(a) Distribution of the lift coefficient

(b) Change in c_l distribution

(c) Normalized change in lift distribution
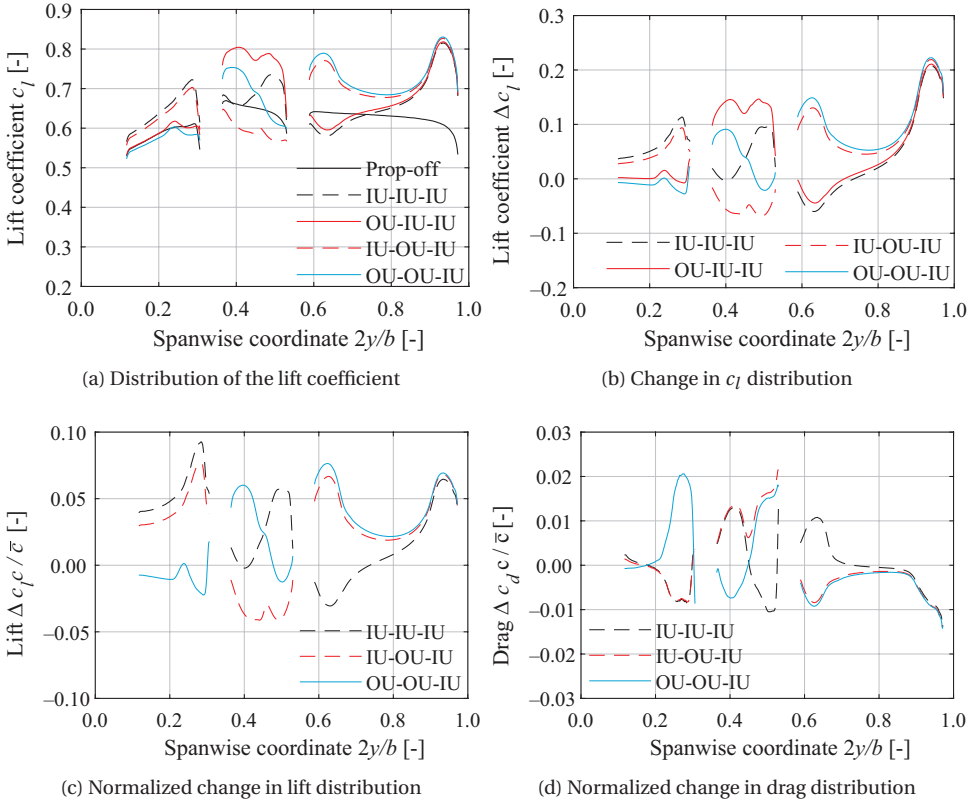
(d) Normalized change in drag distribution

Figure 9.28: Effect of propeller rotation on the lift and drag distributions for the cruise condition ($\alpha = 4$ deg, $J = 1.9$).

The rather large gradients of the lift and drag on the inboard parts of the nacelle is attributed to the local corner-flow separation, as discussed in the previous section. Since an inboard-up rotating propeller increases the suction peak further, the flow separation is more severe. This is clearly observable in the pressure distributions on each side of the nacelle, shown in Fig. 9.29. The flow separation that already is present for the propeller-off case due to the nacelle installation, is nearly completely suppressed by an outboard-up rotating propeller. This effect is clearly observable in the spanwise and chordwise extent of the stall cells that reside on the suction side of the wing in Figs. 9.29c and 9.29d. This strongly modified pressure distribution and flow structure at the nacelle–wing junction can be expected to result in more favourable high-lift characteristics in

case the propeller rotates outboard-up.

(a) Inboard side of nacelle

(b) Outboard side of nacelle

(c) Inboard propeller rotating inboard-up: more flow reversal

(d) Inboard propeller rotating outboard-up: less flow reversal
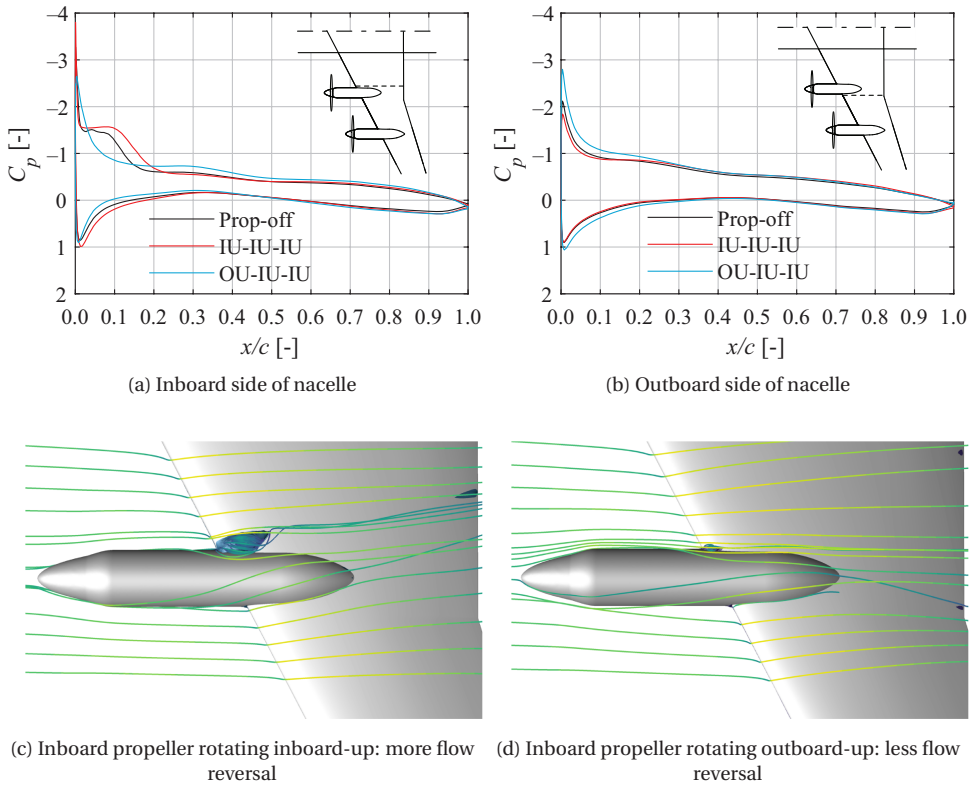
Figure 9.29: Effect of propeller rotation on the local pressure distribution on each side of the most inboard nacelle ($\alpha = 4$ deg, $J = 1.9$).

The net effect of propeller installation on the aircraft lift and drag is summarized in Fig. 9.30. In Fig. 9.30a it is shown that the lift curve is shifted ($\frac{dC_L}{dT_C} > 0$) up for the linear range of angles of attack. Furthermore, the slope of the lift curve is higher, as expected from the discussion in Chapter 8. The difference in ΔC_L is small, showing that the loss in lift from the corner-flow separation is not a dominant effect on the lift of the full airframe. In Fig. 9.30b it is clear that the *slope* of the OU-OU-IU configuration is higher compared to only inboard-up rotating propellers. This is the result of the reducing jump in circulation at the propeller y-locations when the angle of attack increases. For the IU-IU-IU case, it is the inverse [37]. The figure also shows that in case only the tip-propeller is operating, the lift increase accounts for approximately 1/3 of the lift increase of the all-propellers operating cases. This means that since the propeller is only increasing the angle of attack (there is no down-going blade to affect the wing), fact that the outboard wing is less sensitive to a local angle of attack is completely offset. The tip propeller is also responsible for a drag reduction, shown in Fig. 9.30c. Therefore, one can make a division of the 'functionality' for propellers that are mounted along the leading-edge

of a wing as sketched in 9.30d. All propellers cause a relevant lift enhancement, while especially the tip-propeller causes the (induced) drag of the wing to reduce.

(a) Airframe lift

(b) Change in aircraft lift coefficient

(c) Change in airframe drag coefficient
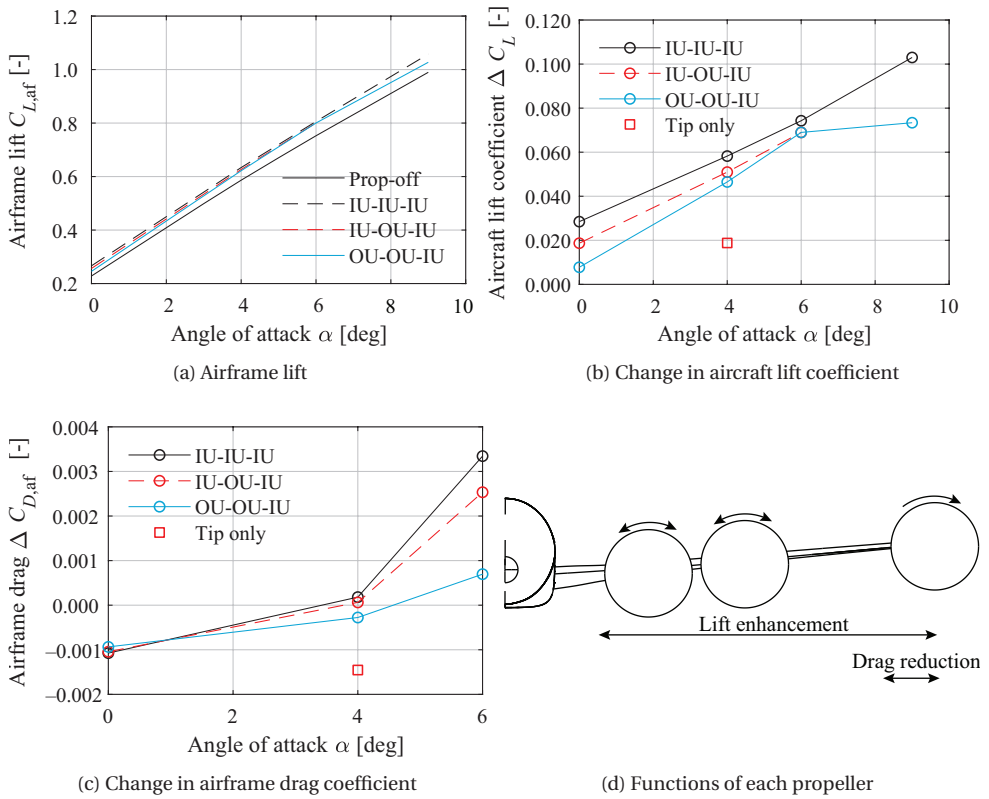
(d) Functions of each propeller

Figure 9.30: Lift-to-drag ratio compared to the propeller-off case.

The overall effect of the propeller installation is an enhancement of the airframe lift-to-drag ratio, at least for low angles of attack. The offset relative to the propeller-off curve is depicted in Fig. 9.31. At a constant angle of attack of $\alpha = 4$ deg, $\frac{L}{D}$ is increased by 6.5 % to 8.5%. The rotation direction has therefore a small effect on this increase. At higher lift coefficients, the nacelle-induced flow separation starts to dominate the aerodynamic efficiency of the wing: while the OU-OU-IU configuration shows still a high $\frac{L}{D}$ at $C_L = 0.9$, the IU-IU-IU case approaches the propeller-off condition. The reason is that the flow separation that is aggravated by inboard-up rotating propellers starts to dominate, and the added drag caused by this is not offset by the drag reduction from the tip propeller.
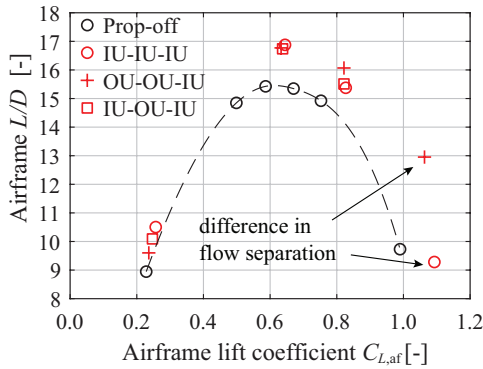
295

Figure 9.31: Lift-to-drag ratio compared to the propeller-off case, $J = 1.9$. Wing + nacelles + fuselage (tail surfaces and propeller contribution are not included). The IU-OU-IU case has not been evaluated at $\alpha = 9$ deg.

Finally, if the propeller efficiency along the x-direction (η_x), is taken into account, the overall beneficial installation effect is depicted in Fig. 9.32a. The same trend is observed as the L/D curve in Fig. 9.31, where there is a significant benefit in the cruise condition. The relative higher installation benefit at higher lift coefficients is the result of the nacelle installation, as addressed in the previous section. If the nacelles would have been translated down and a dedicated fairing would have been used, the drop-off of the $\eta_x \frac{L}{D}$ curve for the propeller-off case would already be less steep.

(a) $J = 1.9$

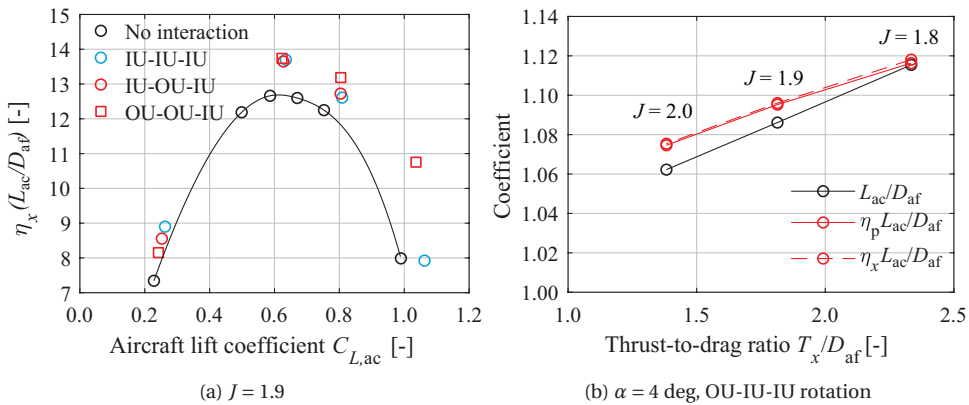(b) $\alpha = 4$ deg, OU-IU-IU rotation

Figure 9.32: Overall aerodynamic efficiency of the aircraft in (a). In (b) a sensitivity of performance indicators to the installed thrust to drag (which includes the interaction effects). The subscripts 'ac' and 'af' refer to aicraft and airframe, respectively. 'Aircraft' includes the propeller forces, while the 'airframe' excludes these.

Since in this particular thrust is not equal to drag (since the excrescences, tail surfaces, and gaps between lifting surfaces are not included in the simulations), the trend of the relevant aerodynamic and overall efficiency indicators are evaluated by running

the propellers at different advance ratios. In Fig. 9.32b these indicators are plotted relative to the uninstalled configuration, i.e. the propeller and airframe operate in isolation. Even at low thrust conditions, the efficiency of the propeller is increased due to the upstream effect of the airframe. Although the drag of the full aircraft is unknown, the linear trends indicate that the lift-to-drag can be expected to increase by 5% to 8%, and the product $\eta_x \frac{L}{D}$ even slightly more. The reader is reminded that this is compared to the wing+nacelle combination without propellers. Figure 9.32 also indicates that for accelerating flight or during a (climbing) manoeuvre, there is a consistent positive installation effect at this angle of attack in terms of $\frac{L}{D}$ and $\eta_x \frac{L}{D}$. This means that even for the present nacelle–wing combination and without adaptations to the propeller and wing to maximize the aeropropulsive $\eta_x \frac{L}{D}$, still a significant increase in $\eta_x \frac{L}{D}$ can be achieved for a wide range of lift coefficients and thrust settings.

9.3.3. Aspects of Propeller Installation on Pitching Moment and Pitching-Moment Derivative

The propeller installation changes the longitudinal static stability of the aircraft relative to the propeller-off case through three mechanisms: (1) the propeller normal force derivative, (2) the altered wing pitching moment curve , and (3) the flowfield at the horizontal tailplane. For the configuration evaluated herein, these three contributions are discussed separately.

The contribution of the propeller forces to stability is relatively independent on thrust setting, as the normal-force coefficient is quite insensitive to thrust, as can be observed in Fig. 9.14a. The main focus therefore is on the wing contribution to the pitching-moment derivative and the change in flowfield at the tailplane with angle-of-attack under power-on conditions. Since the wing is swept and the propeller–nacelle combinations are distributed along the span, the aerodynamic center shifts depending on where stall is initiated and what the rise is in local lift curve slope. The fact that there are distributed propellers makes the flowfield at the horizontal tailplane more complex compared to the conventional twin-propeller configuration, although the lessons learned on these configurations also supports the analyses presented herein. The relatively unconventional wing sweep compared to envisioned aircraft with leading-edge distribution propulsion has several unique characteristics:

- The axial positions of the propellers vary along the span. In case the reference point is at $0.25\bar{c}$, the normal force of the tip propeller is stabilizing, while the most inboard propeller has a destabilizing contribution.

- In case of flow separation introduced by the propeller, the effect on longitudinal stability is strongly dependent on the spanwise location of this flow separation

- Interference of the nacelle with the wing is known to cause premature stall at the inboard junction of the wing and nacelle for the geometry that is presently under consideration, as discussed in Section 9.3.1.

Based on these considerations, the trends and conclusions for the propeller-wing-body combination are specific for this particular aircraft geometry. The observations made for the (de)stabilizing flowfield at the tailplane are more general.

9

MOMENT CURVES OF PROPELLER-WING-BODY COMBINATION

Figure 9.33 depicts the definition of the reference point used for the computation of the pitching moment curves. The 35% location of the mean aerodynamic chord is a representative location of the center of gravity for the cruise condition of the Airbus A320 aircraft [276] on which the *A320-DP* aircraft is based. It is noted that the contribution of the horizontal tailplane is excluded.

(tailplane excluded)

mean aerodynamic chord $\bar{c}$
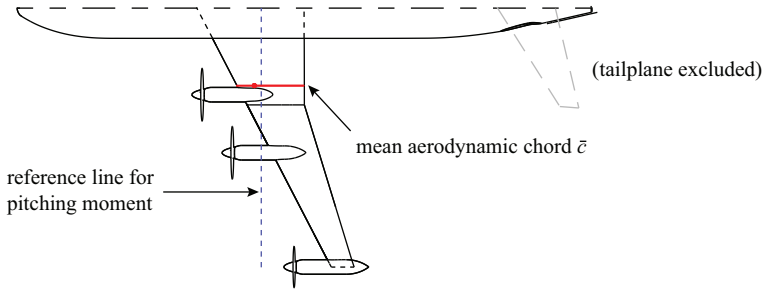
reference line for
pitching moment

Figure 9.33: Definition of the location of the reference point for the pitching moment at $\Delta x = 0.35\bar{c}$ from the leading-edge of the mean aerodynamic chord.

The forces acting on the propellers and their contribution to the pitching moment are summarized in Fig. 9.34. The variation of the propeller thrust with angle of attack is minimal, as shown in Fig. 9.34a. The difference between the three propellers is the upstream blockage and upwash, as well as the fuselage induced flowfield. The selected propeller incidence of −3 deg is such that at a cruise angles-of-attack up to $\alpha = 4$ the propeller normal force is slightly above zero, as shown in Fig. 9.34b. The effect of the upwash distribution is clearly observable in the same figure, as the most inboard propeller generates the largest normal force, while the tip propeller experiences only a low upwash angle and less blockage. The normal force acting on the tip propeller is further reduced as the wing is only situated on one side of the disk.

The *variation* of the thrust and normal force with angle of attack affects the slope of the pitching moment curve, where the normal-force component is dominant as the moment arm in vertical direction between the thrust force and the moment reference point is small. The contribution of each propeller to the aircraft pitching moment is shown in Fig. 9.34c. As expected, the inboard and center propeller have destabilizing contributions, while the tip propeller has a stabilizing contribution, which can already be observed by there respective locations. Provided that the normal-force coefficient is nearly independent of T_C (Fig. 9.14), even in wind-milling conditions, a one-engine inoperative situation will not significantly change the propeller contribution to longitudinal stability. If this wing were unswept, the destabilizing effect of the propellers would be larger [61].

Figure 9.35 depicts the effect of propeller installation on aircraft level. The relative contributions of the propeller compared to the wing-nacelle combination is small, as shown in Fig. 9.35a. The net effect on the fuselage is also negligible: any additional lift at the fuselage–wing junction is close to the moment reference point. In Fig. 9.35b the

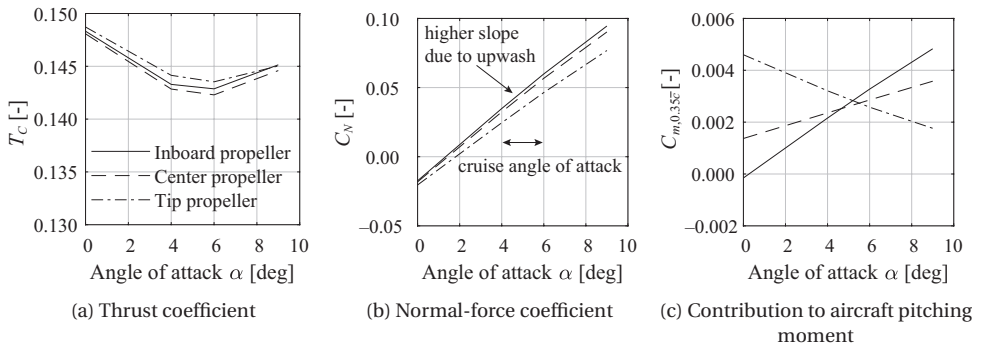(a) Thrust coefficient   (b) Normal-force coefficient   (c) Contribution to aircraft pitching moment

Figure 9.34: Difference in forces for the three propellers, cruise conditions. The rotation direction has negligible impact on the integral forces.

main effect of the installation is a shift in the $C_m - \alpha$ curve, primarily caused by the wing loading. The downward shift of the curve implies $C_{m_{T_C}} < 0$ up to an angle of attack of $\alpha = 6$ deg. Part of this more nose-down pitching moment is compensated by the larger down wash angle at the horizontal tailplane (shown in the next section). The slope of the moment curve becomes 5% more negative without significant difference between the rotation directions.
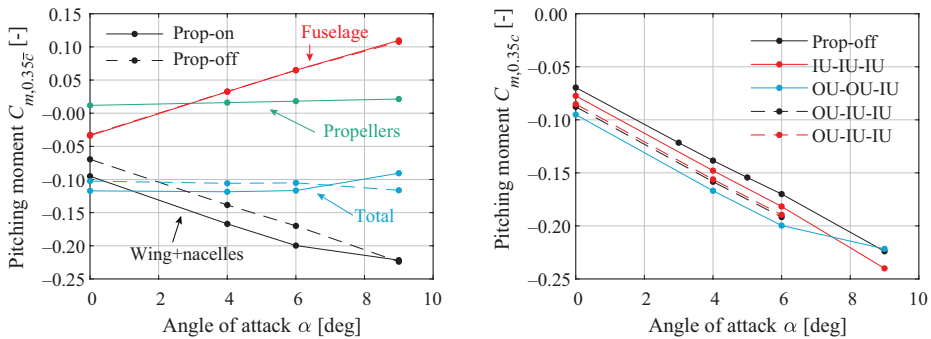
(a) Contributions of different components, OU-OU-IU configuration.   (b) Pitching moment of wing and nacelles (at $\alpha = 9$ not all conditions have been simulated)

Figure 9.35: Pitching moment about 35% of the mean aerodynamic chord for the clean configuration, $J = 1.9$ (cruise). Contribution of the horizontal tailplane is not included.

An interesting nonlinearity of the $C_m - \alpha$ curve arises for $\alpha > 6$ deg. The propeller-off case already shows a more negative C_{m_α}, even more negative for the IU-IU-IU case, and a less negative value in case the configuration is OU-OU-IU. It is found that this is due to the flow separation on the inboard part of the nacelles, as discussed in Section 9.3.1. Since the inboard part of the wing has a higher lift coefficient, flow separation initiates on the inboard and center nacelles. This shifts the neutral point aft, hence C_{m_α}

299

becomes more negative. In case the propellers rotate inboard up, the flow separation initiates at a net lower lift coefficient and angle of attack (see Section 9.3.2). In case the inboard propellers rotate outboard-up, the flow separation initiates at the tip, causing tip-stall. This is not only unwanted from a lateral control and stability perspective, it also means the neutral point shifts forward, leading to a less stable aircraft. Given the wing sweep angle, selecting the inboard propeller to rotate opposite to each other would be a compromise between maximum lift coefficient (see Section 9.3.2) and longitudinal stability characteristics of the wing–nacelle combination.

FLOWFIELD EXPERIENCED BY THE HORIZONTAL TAILPLANE

In the case of a wing-mounted propeller configuration, the interaction of the slipstream with the wing deforms the slipstream. The slipstream of the most inboard propeller is in the vicinity of the horizontal tailplane, while it also modifies the wing lift and down-wash distributions. In Section 8.2 it has been shown that a slipstream which approaches a lifting surface in vertical direction leads to a *destabilizing* effect as the gradient of the flowfield with angle of attack is lower than the change in flowfield without slipstream. In this section, the effect of rotation direction on the flowfield at the horizontal tailplane is investigated. Since the wing-mounted propeller configuration is relatively well known, the impact of the middle propeller on the flowfield near the tailplane is particularly of interest. Since the tailplane itself is not modelled in the current analyses, the evaluation of the flowfield characteristics at the tailplane is relatively straightforward as no correction is required to correct for the velocity induced by the tailplane.

To illustrate that indeed the rotation direction affects the location of the slipstreams to the horizontal tailplane, the edges of the slipstreams are visualized by a contour of axial vorticity, shown in Fig. 9.36. The figure shows that in case of an outboard-up rotation, the slipstream deforms such that on the suction side the slipstream is directed towards the fuselage. This is an expected result [37]. In case of an inboard-up rotation, the spanwise shear is significantly less, in line with the discussion in Section 8.3. The various cases show that especially the most inboard propeller rotation direction determines the amount of spanwise displacement. A slipstream from this inboard-up rotating propeller is less likely to impinge on the horizontal tail. Moreover, a slipstream from an adjacent propeller has negligible effect of the location of the first slipstream. This indicates that in a time-averaged sense the slipstreams do not interact such that the global flow structure is changed.

For a conventional layout with a fuselage-mounted horizontal tailplane, a slipstream that is approaching the horizontal tail leads to several unwanted effects. Firstly, the gradient of the local angle-of-attack $\frac{d\alpha'}{d\alpha_\infty} < 1$, leading to a destabilizing installation effect. Secondly, the flowfield is unsteady, and in case the edge of the slipstream impinges the horizontal tail, unsteady loads are generated. If these considerations drive the design choice for the inboard propeller (to rotate inboard-up), then the rotation direction of the center propeller can be selected to achieve highest $\frac{L}{D}$ or highest maximum lift, since its influence on the flowfield near the tailplane is relatively small.
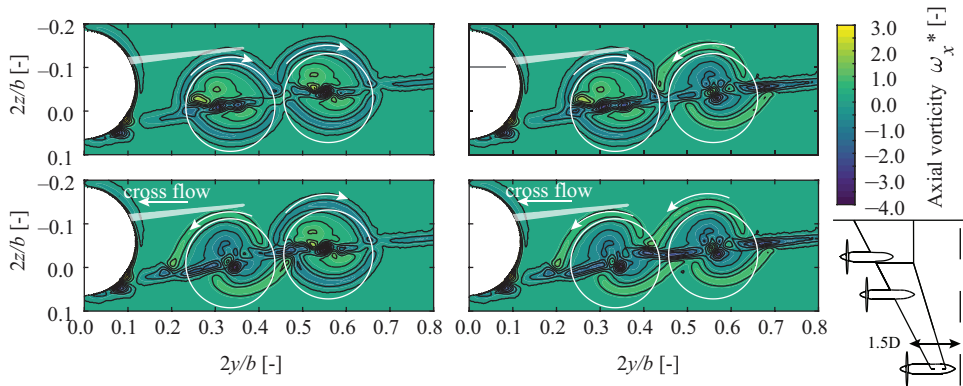
Figure 9.36: Axial vorticity (time-averaged) in a plane downstream of the wing in cruise condition to show that a crossflow due to slipstream deformation affects the flowfield near the stabilizing surfaces and is dependent on the rotation direction of the propellers. Cruise condition, $\alpha = 4$ deg, $J = 1.9$. The horizontal tailplane (excluded in simulation) is highlighted.

Figure 9.37 gives a more concrete picture of the distribution of the downwash angle in a plane just downstream of the wing. Since the wing lift distribution is not elliptical for the propeller-off condition, the downwash angle varies significantly along the span, typical for a more triangular or bell-shaped lift distribution [290]. From the contours, it becomes clear that the propeller installation especially modifies the downwash distribution locally, which is in line with the observations in Section 8.3.

On the inboard part of the wing, there is quite a variation of the local downwash, since the lift distribution is strongly affected by the propellers. The downwash distribution along vertical survey lines (indicated in the contours) show a typical distribution with a maximum downwash coinciding with the location of the wing wake. The direction of the downwash on the inboard part of the wing can be derived from the (change of the) lift distributions presented in Fig. 9.28a. When the propellers are operating, the downwash angle either increases (IU-IU-IU configuration) or decreases (OU-OU-IU configuration). This means that a high thrust condition requires a different trim setting compared to a low thrust setting. Figures 9.37b through 9.37d indicate that the rotation directions of the inboard and middle propeller do not influence the downwash angle in the tip region of the horizontal tailplane. On the surveyline at 15% of the wing semi-span, the downwash is changed by approximately 1 deg, depending on the rotation direction. Compared to the propeller-off condition, the downwash angle is reduced on the outboard part of the wing (even though the lift is higher compared to the propeller-off case), which is in line with the reduced drag caused by the tip propeller.

The propeller installation leads to a change in the lift distribution, and therefore in the *distribution* of the downwash angle along the tailplane. The change in the local angle of attack along the span of the horizontal tailplane is shown in Fig. 9.38a for the cruise condition with $\alpha = 4$ deg. The figure confirms that the inboard propeller is the cause of the flowfield along the majority of the span. The influence of the middle propeller is limited to outboard 40% of the tailplane. When the angle of attack is increased from $\alpha = 4$ deg to $\alpha = 6$ deg, the *change* in local flow angle is less severe in case the

9
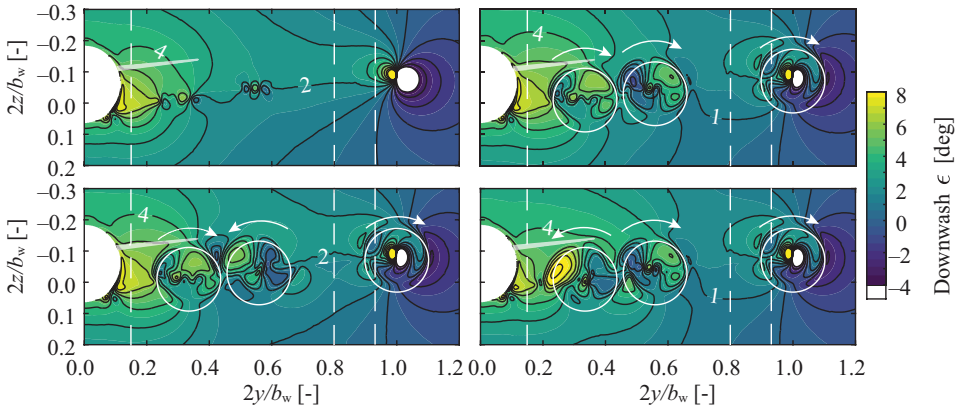
(a) Effect of rotation direction on the downwash distribution
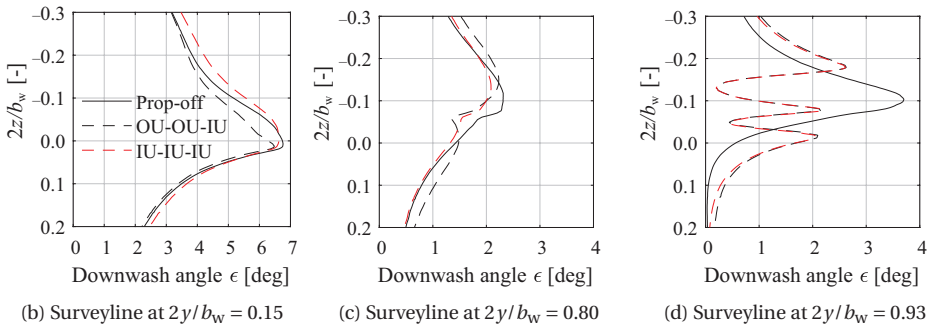
(b) Surveyline at $2y/b_\mathrm{w} = 0.15$

(c) Surveyline at $2y/b_\mathrm{w} = 0.80$

(d) Surveyline at $2y/b_\mathrm{w} = 0.93$

Figure 9.37: Downwash angle for a cruise condition ($\alpha = 4$ deg, propeller operate at at $J = 1.9$). The horizontal tailplane (excluded in simulation) is highlighted.

most inboard propeller rotates inboard-up, shown in Fig. 9.38b. In Fig. 9.38a it is clear that the edge of the slipstream is already impinging on the tip of the tailplane, and as expected, an outboard-up rotation leads to a larger portion of the tailplane submerged in the slipstream, as depicted in Fig 9.38c. Interestingly, the fuselage–tailplane junction also experiences a Δq. It is found that this is caused by the difference in loading the boundary layer development on the fuselage. On average, the IU-OU-IU rotation direction has the smallest impact, i.e. the smallest deviation of the downwash angle relative to the propeller-off case. This is the consequence of two phenomena. First, the rise in lift at the inboard part of the wing is smaller (Fig. 9.28c). Second, the slipstream deformation is smaller.

Like any lifting surface of finite span, the spanwise location where a perturbation of the flowfield occurs determines the net change in the force; a perturbation towards the tip has a smaller impact than the same perturbation that is experienced in the more inboard part. For this reason, often an average downwash angle is used along the tailplane [67]. The gradient of this average downwash value is depicted in Fig. 9.39. The relative downwash gradient $\frac{d\epsilon}{d\alpha}$ compared to the propeller-off value is shown to vary between
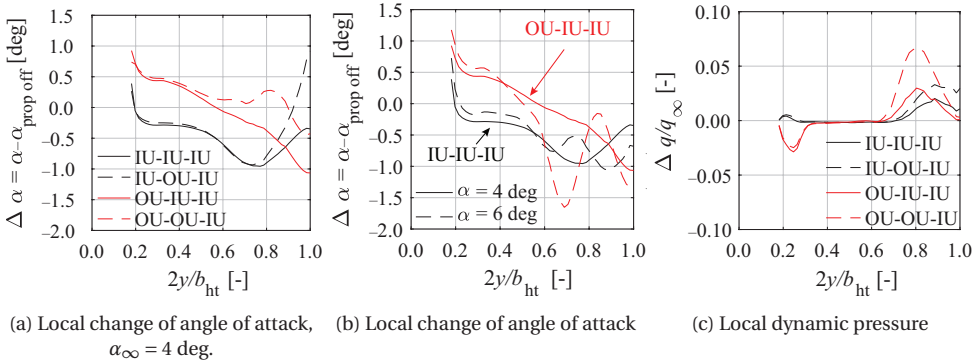
(a) Local change of angle of attack, $\alpha_\infty = 4$ deg.

(b) Local change of angle of attack

(c) Local dynamic pressure

Figure 9.38: Characteristics of local flowfield at the horizontal tailplane at low angle of attack.

+20% and −10%. This figure demonstrates that the propeller installation effect cannot be generalized as 'stabilizing' or 'destabilizing': depending on the angle of attack, the downwash gradient either decreases or increases.
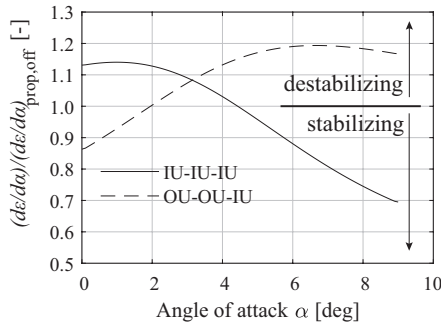

Figure 9.39: Average downwash gradient along the horizontal tailplane relative to the propeller-off case. Conditions: $J = 1.9$ (representative for cruise/climb), $Re_{\bar{c}} = 1.7 \cdot 10^6$

9

9.3.4. TRADE-OFF BETWEEN PROPELLER AND WING EFFICIENCY FOR THE TIP-MOUNTED PROPELLERS

In Chapter 8 it has been shown that the propeller can enhance the airframe lift-to-drag ratio, especially if it is mounted to the tip of the wing. Since the payload-range energy efficiency of an aircraft is proportional to the product of propeller efficiency and airframe L/D, a relevant question is how this product can be maximized for a tip-mounted propeller. This is addressed in Ref. [36]. However, often, the propeller operating condition is selected such that η_p is maximal as the motivation for such a choice seems reasonable; provided that the losses introduced by the propeller cannot be employed by the airframe to their fullest for drag reduction, the introduction of swirl loss should be minimum for the system to operate at its highest efficiency.

From an overall aircraft perspective, such an approach can be questioned for various reasons. Firstly, the weight of the propeller, motor, and nacelle components also determine the payload-range energy efficiency. Secondly, from an aerodynamic interaction perspective, the location of the introduced swirl by the propeller relative to the airframe is shown to be an important indicator for the change in airframe loading, i.e. a propeller designed for isolated conditions introduces a certain slipstream (see Chapter 2). For a given thrust requirement, the disk area can be selected to either operate at maximum efficiency, or at a lower efficiency to either maximize $\eta_x \frac{L}{D}$ or to reduce the weight of the propeller and other components related to the motor. Figure 9.40 depicts this design freedom. A higher (maximum) swirl can be achieved at the expense of propeller efficiency.
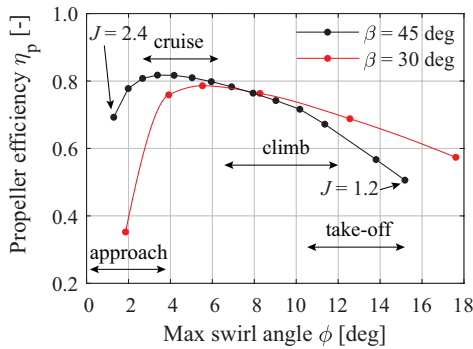

Figure 9.40: Relation between swirl angle and propeller efficiency for two blade pitches of the XPROP propeller. Typical operating conditions are indicated (for further reading, see Section 2.5).

In Section 2.3 it has been shown that the swirl distribution along the radius has a maximum value around $r/R_p = 0.5$, while the wing tip vortex has approximately a $1/r$ character. This suggests that, in case the propeller design is not adapted, the swirl imparted to the flow cancels a larger part of the wing tip vortex if the propeller is small. Therefore, there is a trade-off: for a smaller diameter, the propeller efficiency is compromised, while at the same time, the wing lift-to-drag ratio may be increased. In the end, the product of these two quantities is relevant. Besides $\eta_p \frac{L}{D}$, a smaller tip propeller can also be beneficial in terms of mass and clearance to the ground (to meet the maximum bank angle requirement).

To demonstrate that the optimal propeller performance is not necessarily the optimal solution on aircraft level, the propeller installation effect for the tip-mounted propeller of the *A320-DP* aircraft is evaluated for various propeller radii. The thrust is in these cases maintained to approximately 1/6 of the aircraft drag, which means T_C is not constant. It is noted that the nacelle geometry remains constant and therefore the hub radius as well. The loading on the inboard part of the disk is therefore not modelled, while the propeller loading distribution away from the hub remains consistent.

Figures 9.41a and 9.41b depict the effect of a constant thrust on the wing lift and drag coefficients. As expected, the lift increase and drag reduction are more concentrated towards the wing tip if the propeller is smaller, while their magnitude is increased. Figure

9.41a also indicates that the extent of the influence of the tip-propeller is limited to the outer 20% of the wing, which has also been found in Section 8.3. Provided that, relative to the propeller-off case, there is a lift increase, and at the same time a drag reduction, this leads to a net increase in wing $\frac{L}{D}$. This is clearly observed in Fig. 9.41c, with a 20% smaller propeller with the same thrust leading to a 0.5% increase in $\frac{L}{D}$. In case the thrust is not maintained but instead the propeller remains operating at its maximum efficiency point, the $\frac{L}{D}$ benefit reduces by 1.5%.

(a) Lift coefficient

(b) Drag coefficient

(c) Airframe L/D

(d) Total efficiency, $\eta_x L/D$
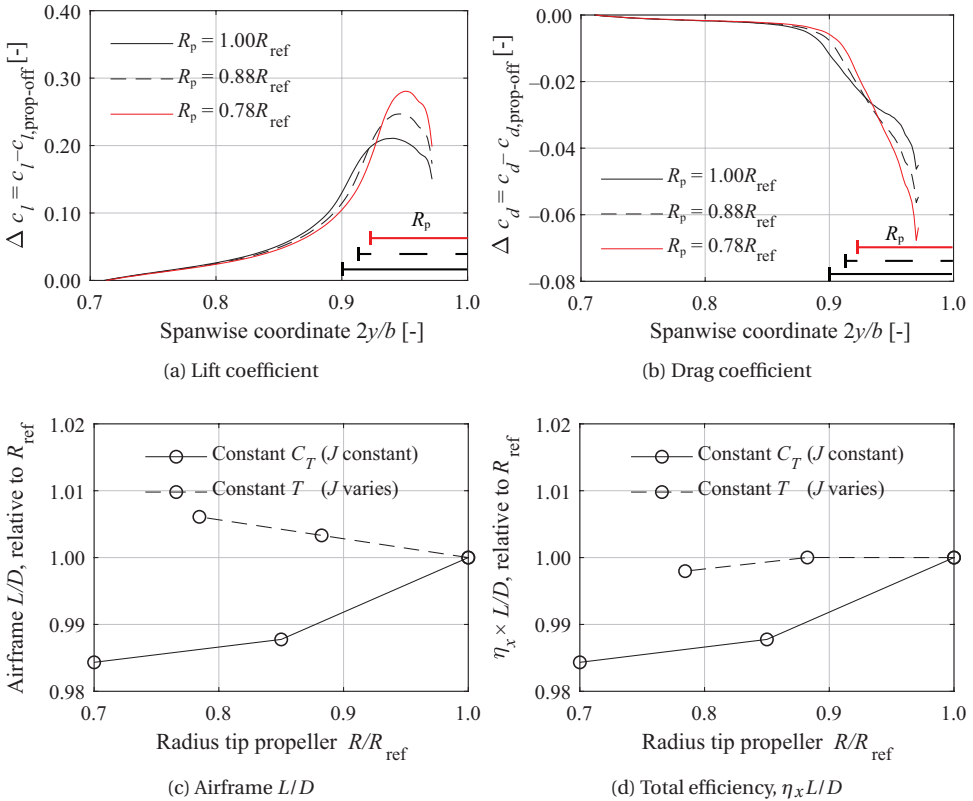
Figure 9.41: Impact of reduced diameter for the tip propeller on the airframe and system efficiencies of the A320-DP configuration, while maintaining the nacelle geometry. Condition: $\alpha = 4$ deg, $J = 1.9$. CFD results obtained using an actuator disk model with a nonuniform loading that is different for each radius.

To explain the observed trends, the in-plane velocity field behind the wing tip is investigated. The phase-averaged flowfield is presented in Fig. 9.42 and indeed reveals the more concentrated swirl that is added by the propeller. The figure shows that the swirl reduction is local. This is in line with the finding of Section 8.3, specifically Fig. 8.23. The downwash field introduced by the wing-tip vortex is therefore not reduced outside of the region of influence of the propeller, i.e. approximately the 1.2 times the propeller radius. In fact, for $r/R_{ref} > 1.2$, it may be observed that the tangential velocity

9

305

(and therefore downwash velocity) *decreases*: the result of a higher wing lift coefficient and a larger spanwise loading variation. The still existing tip vortex of the wing is evident near $r/R_{ref} = 0$. The propeller adds therefore axial vorticity in both hub and tip region, but is not compensating the tip vortex.
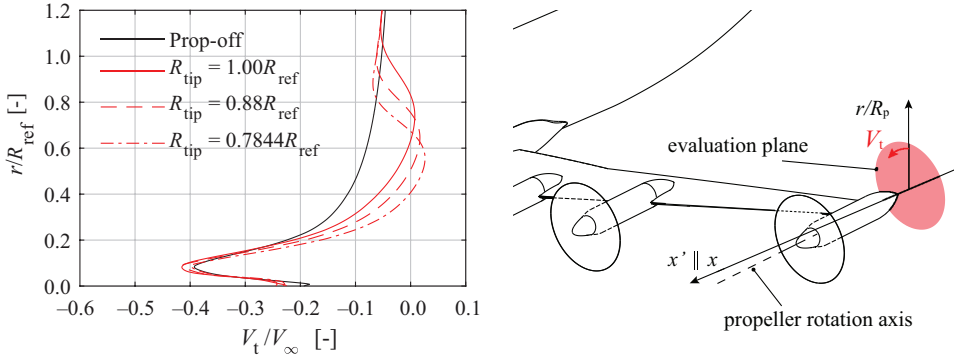

Figure 9.42: Phase-averaged tangential velocity just behind the nacelle at the tip of the wing to show the still finite swirl at the core of the wing-tip vortex, with $2R_{ref}/b_w = 0.2039$. Away from the propeller tip, there on average a higher tangential velocity (and therefore downwash). Conditions: $\alpha = 4$ deg, $J = 1.9$.

The relatively low dependency of the propeller diameter on the combined propeller–wing performance is an important result, as the weight of the propulsion system can be reduced without a large loss of the beneficial installation. Furthermore, in case the propeller is driven by an electric motor, a second advantage is employed: while maintaining the shaft power, the torque reduces nearly proportional to the propeller diameter, as shown in Fig. 9.43. This directly has advantages for either direct-drive and gearbox installations as in certain cases the torque requirement is the active sizing constraint for electric motors [291, 292].
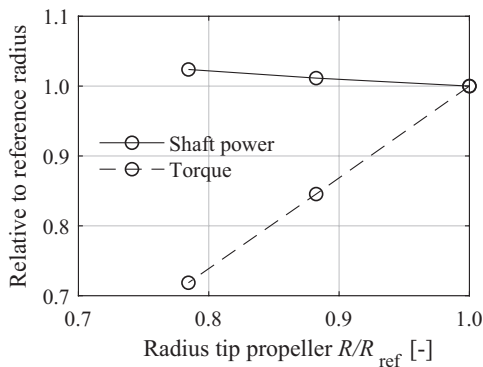

Figure 9.43: Effect of propeller tip radius on shaft power and torque, constant T_C. The significant reduction in torque at (nearly) constant power is indicative for lower electric motor mass.

9.4. CONCLUSIONS

This chapter has extended the knowledge of the installation effect of horizontal-tailmounted propellers on aircraft stability, control, and performance by employing more detailed and elaborate analyses compared to previous works. Furthermore, a better understanding has been developed on the effect of distributed propellers along the leading edge of a wing with specific characteristics on several aircraft performance indicators, as well as on the longitudinal stability characteristics. To limit the scope for both configurations, only a select number of operating conditions have been evaluated. Part of the conclusions of the analyses are common between these two configurations:

- The airframe-induced flowfield affects the direct propeller contribution to static stability. By simplifying the installation using an isolated propeller with a moment arm and in-plane force gradient, the static stability is either under- or overpredicted, depending on the propeller location and the gradient of the inflow field with angle-of-attack.

- The rotation direction that is most favourable from a performance and/or stability perspective depends on the configuration and the propeller size relative to the lifting surface downstream of it.

In addition to these common characteristics, the following more specific conclusions are formulated in the following.

HORIZONTAL-TAILPLANE-MOUNTED PROPELLER CONFIGURATION
The following is concluded regarding longitudinal static stability and trim:

- An aft-mounted propeller installation generally does not adversely affect the aircraft longitudinal static stability over a major part of the operating conditions, which confirms the findings in literature. The neutral point shifts aft with increasing thrust coefficient, up to 5% of the mean aerodynamic chord for a thrust coefficient typical for climb/cruise with co-rotating propellers. At higher thrust settings, the neutral point shifts more aft. Exceptions to this are observed at high angles of attack.

- The propeller normal force is the dominant component of the changes in aircraft pitching moment resulting from propeller installation. Its contribution is linear with angle of attack for the linear part of the lift-curve.

- On aircraft level, the propeller installation leads to a nonlinear contribution to the pitching moment due to angle of attack (C_{m_α}) which is dependent on rotation direction. The large variations of C_{m_α} start from the onset of the nonlinearity of the lift curve, because of the strong nonuniform inflow to the propeller. The slope of the pitching moment curve becomes up to 25% more negative for an outboard-up configuration, and up to 40% more negative for an inboard-up configuration. The dependency on thrust is low.

- The propeller slipstreams are not significantly displaced relative to the stabilizing surfaces for various flight conditions. For this reason, more predictable and more favourable static stability characteristics are achieved compared to the situation where propellers are mounted on the inboard part of the wing.

- The thrust-induced nose-down pitching moment is largely compensated by the propeller normal force induced by the wing downwash field. Therefore, only a small change in trim setting of ±2 deg in cruise conditions is required between propeller-off and propeller-on.

Regarding the directional static stability and trim:

- The propeller installation increases the C_{n_β} in a reference point at 25% of the mean aerodynamic chord by 6% for the inboard-up propeller configuration and up to 12% for the inboard-up propeller configuration. The difference between the two rotation directions is caused by the fuselage induced flowfield. The co-rotating configuration can be approximated by the sideforce of two isolated propellers multiplied with their moment arm. The rise is nearly independently of thrust coefficient.

- The presence of the slipstreams on each side of the vertical tail makes the vertical tailplane less effective. The C_{n_β} is reduced by 2.5% for a cruise thrust setting.

- The change in yawing moment coefficient remains approximately linear for $\beta = \pm 10$ deg.

- In the co-rotating configuration, a net yawing moment exists that is equivalent to a sideslip angle of two degrees. This is caused by the thrust-dependent sidewash of the slipstream due to interaction, in line with other research [62, 173, 174].

- The outboard-up rotating propeller is the critical engine. In case of an one-engine-inoperative situation, the yawing moment becomes zero at $\beta \approx 1$ deg in cruise conditions, if the thrust of the operating engine is not increased to arrive at an equilibrium condition of $T = D$.

Regarding the propeller efficiency and other performance indicators:

- The installation is beneficial for the propeller efficiency at a positive (aircraft) angle of attack as the normal force is suppressed. The maximum is found at approximately $\alpha = 5$ deg. For comparable configurations, it is hypothesized that the propeller installation angle should be chosen such that the net normal force is zero to achieve highest efficiency in the direction of flight.

- The propeller efficiency in flight direction multiplied with the lift-to-drag ratio is up to 2% higher for the co-rotating configuration compared to the situation in which the interaction is not included.

- The maximum lift coefficient is increased by up to $\Delta C_{L,\max} = +0.06$ for the co-rotating configuration. This increment is significantly smaller compared to wing-mounted propeller configurations. The propellers are the dominant contribution to lift.

As a final note, the current study displays that even for a suboptimal design, the beneficial propeller–airframe aerodynamic interaction could partially offset the drawbacks identified for the configuration [25, 86, 280]. These benefits are present despite the fact that an aerodynamic performance benefit historically has not been motivation for studying this configuration.

Leading-Edge Distributed Propeller Configuration

The geometry on which the analyses have been performed has a highly swept wing, comparable to an Airbus A320. Therefore, some of the conclusions only pertain to the swept wing geometry. However, by varying the rotation direction, thrust coefficient, and propeller diameter, design guidelines are formulated for comparable installations which do not necessarily have a swept wing.

The following is concluded on the nacelle installation on a swept wing:

- If the wing–nacelle junction is not adapted to lower the adverse pressure gradients, even at low angles of attack the flow is prone to separation on the inboard side of the nacelle, in line with other studies.

- Flow separation initiates at the inboard nacelles, which shifts the aerodynamic center rearwards. On the other hand, the tip becomes more prone to tip stall compared to the clean wing design due to the local higher angle of attack introduced by the propeller–nacelle combination

- A vertical translation by a distance equal to half the diameter of the nacelle already significantly postpones the onset of stall, in line with other studies. The lift-to-drag ratio in that case is raised by approximately 2.5% per nacelle for a cruise/climb angle of attack.

The following is concluded on the propeller installation on the aircraft performance:

- Due to wing sweep, an outboard-up rotating propeller has a higher efficiency (approximately 1%) than an inboard-up rotating propeller.

- The propeller installation leads to changes in lift, drag, and lift-to-drag ratio. The inboard propellers especially contribute to aircraft lift, while the tip propeller not only increases lift, but also reduces drag. The part of the disk that is increasing the local angle of attack to the wing increases the lift and at the same time decreases drag.

- Irrespective of the rotation direction, there is a net increase of the lift coefficient which is proportional to the thrust coefficient.

- For inboard-up rotating propellers: The more inboard the propeller is mounted, the larger the magnitude and the spanwise extent of that rise in lift is. The opposite is the case for the other rotation direction.

- The airframe lift-to-drag ratio increases between 5% to 8% depending on the reference drag and rotation direction. At high angles of attack, because of wing sweep, the airframe lift-to-drag ratio remains high in case of outboard-up rotating propellers, since the corner-flow separation at the nacelle junction is suppressed.

- A smaller tip propeller can be selected at the cost of propeller efficiency and to the benefit of airframe lift-to-drag ratio. The product of these two quantities remains approximately constant for the evaluated radii (up to 30% smaller diameter compared to a reference case). While the power increases by 2% to maintain the same thrust, the torque is reduced by more than 20%. A smaller tip propeller may therefore lead to a lighter nacelle, propeller, and (electric) motor.

The following is concluded regarding longitudinal static stability and pitching moment:

- The direct propeller contribution to longitudinal stability is small. The tip propeller is stabilizing, the inboard propellers are destabilizing for a moment reference location at 35% of the mean aerodynamic chord. The main effect of the propeller installation is a more negative tail-off pitching moment.

- The slope of the tail-off moment curve becomes 5% more negative without significant difference between the rotation directions.

- The propellers and horizontal tailplane should be positioned such that the slipstream does not impinge the horizontal tailplane. Among other considerations (such as unsteady loads), a slipstream impingement introduces rapid changes in the pitching moment curve with angle of attack.

- On average, the rotation direction "down between blades" has the smallest impact on the downwash angle at the horizontal tailplane relative to the propeller-off case.

9

10

CONCLUSIONS AND RECOMMENDATIONS

10.1. CONCLUSIONS

It is envisioned that the future generations of regional and short to medium-range aircraft employ a high level of propeller integration to achieve low-emission flight. The objectives of unconventional propeller installations include the enhancement of the airframe aerodynamic efficiency, increasing the propeller efficiency, improving cabin comfort, and improving the overall aircraft design. Furthermore, by introducing the aerodynamic interaction in specific phases of the flight, beneficial propulsion integration can also enable the use of alternative energy sources and increase the electrification level of the propulsion system.

The higher level of integration also means that typically a stronger aerodynamic coupling exists compared to the conventional configuration. The closer proximity of the propeller and airframe requires a more dedicated integral design (approach) of both the airframe and propulsion unit. This is partially driven by the impact of unconventional propeller installations on static stability, as various proposed unconventional configurations use propellers that are relatively far from the center of gravity. Therefore, new design guidelines need to be formulated.

In order to achieve significant efficiency gains on aircraft level, it is required that the aerodynamic interactions that lead to changes in aircraft performance, stability, and control are understood from a fundamental perspective, and from an application point of view. To contribute to the necessary knowledge required for further development of these aircraft, the objective of this dissertation is:

> "to characterize the role of the aerodynamic interaction between the propeller and the airframe on the performance and static stability characteristics for selected aircraft configurations which aim for a beneficial propeller–airframe interaction".

The associated main research question is:

> *What are the fundamental mechanisms that determine the airframe perfor-*
> *mance, static stability, and control characteristics when propellers are in close*
> *proximity to the airframe and how can these be predicted?*

To this end, a combination of experimental and numerical analyses on several configurations have been conducted. Three different types of analyses were performed. First, fundamental phenomena were investigated which provide insight for related configurations and derivatives thereof. Second, a configuration study indicated the expected trends on various performance indicators. Finally, two detailed studies on aircraft level demonstrate the relative importance and the coupling between aerodynamic interactions.

To limit the scope, the aerodynamic interactions are studied on a select number of configurations and conditions that would be representative for regional transport aircraft. For these types of aircraft, it is the airframe that typically produces the dominant flowfields and aerodynamic forces, while the propeller typically introduces a small change to these. Moreover, for these aircraft the wing has a low sweep angle and the operation is at subsonic Mach numbers. Conceptually, the following cases have been studied:

- Propellers that are mounted ahead of the wing
- Propellers that are mounted near the stabilizing surfaces
- Propellers that are mounted above or behind the wing

Two particular cases were investigated in detail. The first configuration had propellers that are mounted to the horizontal tailplane. This is an example where there is a strong interaction between the propeller and airframe that affects performance, stability, and control, and contains various interaction mechanisms that are of interest for other configurations as well. A second specific case is a distributed propulsion configuration with propellers mounted to the inboard part of the wing (in front of the high lift devices), together with a propeller mounted to the tip of the wing. In such configuration, the propellers are ahead of the center of gravity, and the dominant aerodynamic interaction is the effect of the propeller on the wing, which in turn influences the flowfield at the stabilizing surfaces.

Comprehensive wind-tunnel tests and numerical simulations have been performed on numerous specific propeller installations that are linked to these two configurations, including isolated propellers, various combinations of a propeller and a single lifting surface, and propeller–propeller interaction. The experimental results also provide a benchmark for both isolated propeller simulations and for propeller-installation studies on related configurations. This dissertation is therefore also useful as a reference to compare the installation effect of different configurations.

It is also noted that the focus in the dissertation is on the *aerodynamic phenomena*: the relative importance of certain observations (e.g. the impact of the nacelle or the (non)linearity of force curves) are dependent on specific geometries and not all findings can be generalized. For this reason, where possible, it is noted that a certain observation

10

is case-specific, or can be perceived as a (more) general conclusion. Along those lines, although the experiments and simulations were conducted at relatively low Reynolds and Mach number, several results indicate that the results can be properly scaled to determine installation effects at other Mach and Reynolds numbers as well.

In line with the objective of this dissertation, six research questions have been formulated and are answered in the following sections. First, the effect of nonuniform inflow on the propeller is discussed, followed by the conclusions on the impact of the propeller on lifting surfaces. Their combined interaction is then discussed on aircraft level, which provides an outlook of the installation effect on aircraft performance, stability, and control. Finally, conclusions are presented on the modelling of these aerodynamic interactions. Recommendations for further research are presented at the end of this chapter.

10.1.1. FUNDAMENTAL MECHANISMS OF NONUNIFORM INFLOW EFFECTS ON INSTALLED PROPELLERS

Nonuniform inflow generally leads to changes in the propeller efficiency curve, the gradient of in-plane and out-of-plane forces, maximum achievable thrust for a certain flight condition, and unsteady loads on the blades. Compared to the conventional configuration, for various unconventional propeller installations, the nonuniform inflow to the propeller differs both in type and magnitude. This is not only the case for a single flight condition. Since also the airframe-induced flowfield is not constant between flight conditions, there is a larger dependency of the inflow on the angle-of-attack, sideslip angle, and high-lift conditions. This directly affects the gradients and offsets of the propeller force curves and therefore the aircraft stability and trim, respectively. Moreover, the effect of nonuniform inflow to the propeller is not limited to the propeller forces only: the slipstream shape and consequently its interaction with lifting surfaces are affected as well. The understanding of nonuniform inflow effects on the propeller is therefore of importance for full aircraft studies, which has led to the following research question:

1. *What are the physical mechanisms that determine the propeller performance in installed conditions?*

To address this question, steady and unsteady RANS simulations have been performed of isolated and installed propellers. In Chapter 6 it was shown that airframe-induced flowfield, i.e. the axial and tangential momentum transport, at the propeller disk is the dominant factor that determines the propeller forces. Other effects that determine the local inflow condition are of secondary importance. For example, it is shown that the deflection of a slipstream as the result of an angle-of-attack, introduces only small velocity components at the propeller disk. Slipstream deformations that occur further downstream (for example due to the interaction with a wing) are not a relevant factor for the propeller loading.

A study has been performed on the *sensitivity* of the radial load distribution to a change in inflow condition that is expressed as a change in local advance ratio. The constructed distributions provide insight into what region of the disk is responsible for the largest changes of the propeller forces. This was demonstrated to be the region of highest loading. The analogy can be made to a three-dimensional wing, for which the local slope of the lift-curve along the span is proportional to its nominal lift distribution. This

10

particular distribution is a property of the propeller design. For propellers with a high number of blades and/or in case there is a duct around the propeller, the region most sensitive to inflow perturbations can be expected to be more outboard. Furthermore, it can be concluded that:

- A perturbation that is introduced at a certain radial location and phase angle leads to a change in load that is spread in radial direction, and has a phase delay that depends on the reduced frequency and Mach number.

- For a given blade design, it is shown that the normalized shape of the sensitivity distributions of the blade forces is virtually independent of propeller advance ratio.

- At constant rotational speed, the disk loading changes linearly with a velocity perturbation in in-plane direction, and quadratically with a velocity perturbation in tangential direction.

- Due to the nonlinear sensitivity distribution over the disk, a varying nonuniform inflow with angle-of-attack leads to a higher or lower gradient of the propeller integral forces compared to the same propeller experiencing a uniform angle-of-attack.

- The largest unsteady blade loads can be reduced if velocity perturbations at the annulus of highest loading are avoided.

Next to the understanding of the local changes in blade loading in a single condition, a prediction of the propeller efficiency curve in the installed case is of interest for an aircraft designer. It has been shown that for a given propeller design, nonuniform inflow can be represented by an 'installation coefficient' κ such that the efficiency curve of this uninstalled propeller is scaled along the J and η_p directions by κ to obtain the installed propeller efficiency. Using the data of the isolated propeller for an arbitrary blade angle, the advance ratio at which the installed case has highest efficiency, as well as the value of the maximum efficiency, can be quantified immediately. The computational intensive analyses to find the optimum blade angle for the installed cases are therefore redundant and the formulation of the installation coefficient is therefore highly valuable to the aircraft designer. The following can be observed from the definition of κ:

- For a given inflow disturbance, the largest installation effect occurs at high advance ratio, i.e. cruise and approach conditions.

- Any benefits/losses on the maximum efficiency will be more pronounced for large blade pitches, as these typically operate at high advance ratio.

- An axial disturbance results in an increase or decrease in efficiency as a fraction of η_iso. A tangential disturbance results in an increase or decrease in efficiency that is linearly varying with J.

To determine the installation coefficient, the propeller performance in a limited number of conditions should be quantified, preferably at low computational cost, since high fidelity time-dependent analyses and experiments are often out of the scope for

various stages in the aircraft design. Methods published in literature are either of high fidelity, or based on lower order methods that lack the required accuracy to even predict the propeller loads in uniform inflow conditions. The following question is therefore addressed:

2. *What aspects need to be captured by a low-order method in order to accurately esti-mate the propeller loading caused by nonuniform inflow?*

An engineering method has been developed to estimate the propeller load distribu-tion for propellers operating in arbitrary nonuniform flow. A quasi-steady approach is formulated by making use of the sensitivity distributions of the loading with advance ra-tio. This input can be obtained by e.g. high fidelity CFD simulations, lower-order meth-ods, or from experiments. Since the local torque and thrust are primarily dependent on the lift force on the blade sections, the quasi-steady approach is successfully extended by applying modified equations of unsteady aerodynamics for airfoils that predict the lift of two-dimensional airfoils.

In case the actual shape of the nonuniform inflow is not taken into account, but in-stead is averaged over the disk, the installation effect on the integral propeller forces is generally underestimated and in-plane force components are not representative. For ex-ample, by averaging the upwash introduced by a wing to a tractor propeller, the normal-force coefficient is overpredicted by 10%.

The method has been applied to four representative validation cases, each having a particular combination of nonuniform inflow. The integral forces on the individual blades over a full revolution as well as the integral propeller forces compared well with the validation data in terms of predicted trends and the magnitude. For the evaluated cases, it is shown that the change in the load due to the nonuniform inflow is predicted with errors ranging from 0.5% up to 12% compared to the validation data.

The proposed method provided a time-resolved solution within several CPU sec-onds, which was 7 orders of magnitude faster than with full-blade RANS CFD compu-tations. The unsteady analyses of the full annulus of the installed propeller are avoided, while still a time-resolved solution is obtained, with a temporal resolution depending on the spatial resolution of the inputs. The low computational cost makes the pro-posed method suitable for both design and analyses of propellers in arbitrary nonuni-form flows. Compared to relying on isolated performance data, this method allows for a better prediction of the performance of aircraft with tightly integrated propellers, as well as an estimation of the propeller contribution to the aircraft stability derivatives dur-ing the preliminary design phase. A prediction of the slipstream-effect on the airframe should be computed using a method in which this nonuniformity of the slipstream is described.

10.1.2. CONFIGURATION-SPECIFIC NONUNIFORM INFLOW EFFECTS ON INSTALLED PROPELLERS

In this dissertation, various propeller configurations have been evaluated. By making use of the definition of the installation coefficient and by employing the developed en-gineering method, the following questions are addressed:

10

3. *How do different propeller configurations compare in terms of cruise performance and what design guidelines can be formulated?*

4. *What approaches should be followed to reduce or avoid unsteady loads on the propeller when it is in close proximity to the airframe?*

A configuration study has been conducted where a large number of propeller locations relative to a representative aircraft in cruise conditions have been evaluated. Although the study focussed on the propeller only, the outcomes are useful for both propeller and aircraft design studies. For example, any loss in propeller efficiency is an indication of the minimum L/D benefit that needs to be achieved in order to still obtain a positive $\eta_p L/D$ gain. The study highlights the dependency of the installation coefficient, normal-force coefficient, and unsteady loads on propeller diameter and position. The study highlights that small adaptations (e.g. selecting a slightly different chordwise location or vertical position) can have a significant impact on the propeller performance in the order of 10% to 20% from the uninstalled condition. The study also shows that the propeller location that leads to the largest propeller normal-force coefficient and/or unsteady loads, does not necessarily coincide with the location that corresponds to the largest installation coefficient. It is found that the relative magnitude of the unsteady force compared to the thrust reduces when the propeller diameter increases.

Propeller ahead/behind a lifting surface

From all the evaluated configurations, a propeller ahead of a lifting surface experiences the smallest installation effect, in line with findings from other research. The installation coefficient was found to vary between $\kappa = 1.00$ and $\kappa = 1.02$. The blockage effect of the wing is the main cause of a higher installation coefficient. The upstream effect due to displacement of the streamlines is proportional to the airfoil thickness-to-chord ratio. The dependency of κ on propeller diameter, axial and vertical location is low, and the maximum value is reached when the propeller is slightly below the wing chord line. Provided that the installation coefficient is above unity, the blade pitch should be slightly increased (estimated to be up to 5 deg) to operate the desired thrust coefficient at maximum efficiency. The normal force and unsteady loads are largest if the propeller is mounted above the chordline.

Since the downwash and upwash gradient in the plane of the propeller (either upstream or downstream of the wing), depends on the wing aspect ratio, the (de)stabilizing contribution of the propeller depends on the wing aspect ratio as well. Compared to an isolated propeller, a wing with an aspect ratio lower than 10 reduces the normal-force gradient if the propeller is mounted ahead of the wing. A reduction of the normal-force gradient by 25% is found in case the propeller is mounted behind the wing with an aspect ratio of 10, irrespective of the distance behind the wing.

In case the propeller is mounted behind a wing, the dependency of the installation coefficient on diameter is significant, which ranges between $\kappa = 1.02$ and $\kappa = 1.10$ for $D_p = 1.0$ to $D_p = 0.1$, respectively, and is in line with other research. Besides being responsible for the higher installation coefficient, the encounter of a wake especially leads to unsteady loads, where the largest installation effects occur if the wake is encountered at $z/R_p = \pm 0.5$. The unsteady loads on the blades are either one-per-revolution or two-per-revolution, depending on the vertical location of the wake-encounter. Compared to

10

316

a propeller mounted ahead of a wing, the unsteady loads increase by a factor of four for this particular case.

In case a propeller operates in the flowfield induced by the wing-tip vortex, a moderate increase of the installation coefficient between $\kappa = 1.02$ and $\kappa = 1.06$ is primarily caused by the tangential velocity component. A smaller diameter leads to a larger installation coefficient. A small normal force is produced, depending on the vertical location of the propeller. The presence of the wake and downwash on the inboard side of the disk leads to unsteady blade loads of the order of 20% to 40% of the mean thrust, and are nearly independent of propeller diameter. If the propeller blade would have been designed to operate in the radially varying flowfield, the efficiency benefit could have been larger.

PROPELLER ABOVE/BELOW A WING

If a propeller is mounted above a lifting wing, the higher axial inflow leads to significant reduction in installation coefficient ($\kappa = 0.8$ to 1.0 have been found), which primarily depends on the chordwise location of the propeller for a given condition. Next to the chordwise location, the diameter is a key parameter that influences the propeller performance, while the tip-clearance is shown to have only a small impact. For the particular case investigated, the over-the-wing configuration can lead to significant downforce on the propeller (up to 40% of the thrust). The under-the-wing propeller leads to zero to moderate lift contribution (up to 20% of the thrust). Due to the strong varying velocity profile normal to the airfoil surface, these installations lead to the largest unsteady loads of all configurations.

ARRAY OF DISTRIBUTED PROPELLERS

In line with other research, installing propellers in a side-by-side arrangement reduces the propeller efficiency for any thrust coefficient. For this particular case with a tip spacing of 4% of the propeller radius, values ranging between $\Delta\eta_\mathrm{p} = -0.05$ at $T_C \approx 0.01$ to $\Delta\eta_\mathrm{p} = -0.005$ at $T_C = 1.0$ have been found. The main installation effect on the mean propeller efficiency and thrust is introduced by the nacelles, increasing the effective inflow velocity on adjacent propeller disks. The nacelle-effect becomes even more prominent at higher thrust coefficients.

The largest unsteady loads occur due to the boundary condition that limits the slipstream to contract. The corresponding in-plane velocities lead to periodic loading and these linearly increase with the thrust coefficient. The unsteady loads from the interaction between tip vortices only leads to very local changes in load. The magnitudes of the unsteady shaft loads are proportional to the installed thrust coefficient.

10

PROPELLERS MOUNTED TO THE HORIZONTAL TAILPLANE

When propellers are mounted to a horizontal tailplane, a distorted flowfield is experienced caused by the wing, by the fuselage (especially in case of a side-slip), and by the upstream effect from the tailplane. The dominant condition is when the separated flow from the wing–fuselage junction impinges on the propeller disk. The swirling character of this flowfield in particular leads to an increase in thrust and propeller normal force for the outboard-up rotating propeller.

The airframe-induced flowfield present at lower angles of attack leads to important implications for the forces acting on the propellers. The contribution of the propeller to longitudinal stability is reduced as the normal-force coefficient is lowered by up to 30% for the outboard-up rotating propeller for the cruise condition. The difference in rotation direction is caused by the fuselage-induced flowfield (especially a cross-flow component), that is not constant with angle-of-attack. In high angle-of-attack conditions, the normal-force gradient becomes even slightly negative for an inboard-up rotating propeller, while the magnitude increases by a factor of three times the value existing at $\alpha = 0$ deg for the outboard-up rotating propeller.

A propeller installation above the fuselage centerline leads to a rotation-dependent gradient of the side-force coefficient, estimated to be $\pm 10\%$ from the value of an isolated propeller. These changes in propeller loading are primarily caused by the fuselage-induced flowfield in case of a sideslip.

Due to the nonuniform inflow, the maximum propeller efficiency is achieved at a small positive angle-of-attack if the propellers are aligned with the fuselage centerline. The largest values are achieved at high angle-of-attack for an outboard-up rotation, while at angles of attack representative for cruise, the difference is small.

Finally, it has been shown that the consequence of nonuniform inflow significantly impacts the unsteady pressure fluctuations (and therefore noise) on the fuselage outer surface, the particular case showed that these doubled for angles of attack ranging from $\alpha = 0$ deg to $\alpha = 14$ deg. The rotation direction has a large impact on the magnitude of these, which is in line with other research.

10.1.3. Aerodynamic Response of Lifting Surfaces due to a Propeller Slipstream

The time-averaged effect of a propeller slipstream on the maximum lift coefficient, the change in lift at constant angle-of-attack, and the lift-to-drag ratio of a lifting surface that is submerged in this slipstream is in particular of interest from an aircraft performance point of view. From an aircraft stability and control point of view, the gradients of the forces with angle-of-attack and the change in control effectiveness are relevant. The time-dependent interaction is primarily of interest when it comes to the assessment of load-transfer to the cabin, structureborne noise, and the assessment of fatigue loads.

Fundamentally, these are research topics that have been studied by a large number of authors, especially in the light of a wing-mounted propeller configuration. While most of the previously identified trends have been confirmed in this dissertation, also opposite trends have been found for specific cases and several new findings have been presented on a fundamental interaction level, as well as from an application point of view. To arrive at those conclusions, the underlying research question was formulated:

5. *What are the physical mechanisms that determine aerodynamic forces on the airframe as the result of propeller installation?*

The various test cases that have been analyzed in Chapter 8 also provide insight in typical values and trends that can be expected for comparable geometries. These results may be useful for design (exploration) and other engineering/research problems.

DEVELOPMENT OF THE SLIPSTREAM THAT INTERACTS WITH A LIFTING SURFACE
In the installed condition, the inflow to the lifting surface is no longer the inflow produced by an isolated propeller. In open literature, such a distorted inflow has not extensively been addressed, while it is considered an important aspect. To further understand the trends of the forces and gradients of the forces with angle-of-attack, it was essential to evaluate the development of the propeller slipstream. From full-blade CFD simulations of a propeller–nacelle combination, the following key observations were made:

- The gradient of the local angle-of-attack α' relative to the freestream value, $\frac{d\alpha'}{d\alpha_\infty}$, is reduced by the propeller on each side of the disk due to the change in loading on the disk. The value varies along the radial direction and reductions have been found up to 10%. This reduction directly reduces the (local) slope of the lift curve of a surface that is submerged in the slipstream. It is expected that this reduction depends on the gradient of the propeller normal-force coefficient.

- Outside the slipstream the change in the flowfield with respect to angle-of-attack is larger than inside the slipstream and is opposite in sign, caused by both the deflected slipstream and the presence of the nacelle. The effect of the slipstream deflection on the local angle-of-attack is estimated to be two to three times larger than the presence of the nacelle.

- The strongest changes of flowfield quantities with angle-of-attack occur at the edges of the slipstream. The smallest changes of flowfield quantities with angle-of-attack occur if the lifting surface is positioned at the propeller rotation axis. Accounting for the varying slipstream with angle-of-attack is therefore even more important if the lifting surface has an offset from the rotation axis.

The installation effect of adjacent propellers (for leading-edge distributed propulsion) on the slipstream development is twofold. First, at the symmetry planes larger velocity and pressure gradients are introduced. Secondly, the slipstream is less contracted at the symmetry plane, while more contraction is observed on the upper/lower side of the array of slipstreams. The slipstream area is nearly constant, as the reduction in thrust is negligible. The larger contraction on the upper/lower side of the array of slipstreams leads to a smaller angle-of-attack in case the propellers are mounted below the wing chord line, compared to a case where there is no interaction between the adjacent propellers.

FUNDAMENTAL AERODYNAMIC INTERACTION
In Chapter 8 the aerodynamic interaction mechanisms that determine the changes in loading on the lifting surface have been discussed. New findings are presented on the pressure distributions that are affected by the propeller. Some of the findings from other authors have been confirmed, and at the same time, the link to aircraft performance, stability, and control has been made more apparent.

The interaction may be split up into a quasi-two-dimensional problem, where an airfoil section experiences a different dynamic pressure and angle-of-attack. On top of that, there is a three-dimensional interaction through the interaction of the vortex systems, which in turn affects the local induced angle-of-attack. These quantities were analyzed

10

using two test cases. The first case is a tip-mounted propeller which directly influences the flowfield by the tip-vortex of the lifting surface. The second test case was a more inboard mounted propeller, where the tip-vortex of the lifting surface resides between the propeller rotation axis and the edge of the propeller disk. From these comprehensive wind-tunnel tests and full-blade CFD simulations, the following is concluded:

- The results show that the *change* in loading due to an angle-of-attack is more concentrated towards the leading-edge. When the propeller is spinning and the angle-of-attack is raised from α_1 to α_2, the *change* in loading resembles the pressure distribution of the propeller-off case if the two distributions are normalized. Therefore, the propeller-tailplane combination behaves in the same way as the propeller-off case: the presence of the slipstream can be described as a change in lift curve slope.

- If the change in loading is obtained through a change in advance ratio, i.e. going from $T_{C,1}$ to $T_{C,2}$, the pressure distribution is not the same as a change in angle-of-attack. This is caused by a finite height of the slipstream relative to the chord of the lifting surface. Therefore, for low D_p/c ratios, the design of the leading-edge of the wing becomes relatively more important. This is, for example, the case for distributed propellers along the leading-edge.

- The propeller increases the effectiveness of the flap/elevator and this increase is nearly inversely proportional with advance ratio. By the deflection of a control surface/high-lift device, there is *relatively* more loading toward the leading-edge of the main element and the leading-edge of the control surface/high-lift device.

- Slipstream deformation is, in addition to the variation of spanwise loading, caused by a change in helicity of the propeller tip vortex near the surface.

- At constant angle-of-attack, for the portion of the span that is washed by the propeller, the local downwash angle is reduced. Outside this region, the downwash angle increases.

- Independent of rotation direction, the largest reduction of in-plane kinetic energy is observed between the leading-edge and quarter chord of the lifting surface due to the presence of a nonpermeable boundary. More downstream, the kinetic energy deposition is further reduced if the propeller is rotating against the tip vortex direction of the lifting surface.

- For a tip-mounted propeller configuration with the propeller rotating against the wing tip-vortex, the portion of the wing washed by the propeller has:
    - A higher lift coefficient at the same α
    - A higher lift curve slope
    - The maximum lift coefficient is achieved at the same angle-of-attack as the propeller-off case
    - A higher lift-to-drag ratio at the same angle-of-attack
    - The maximum c_l/c_d is achieved at higher c_l
    - At low lift coefficients, the c_l/c_d is lower compared to the propeller-off condition

10

Compared to a tip-mounted propeller, if the propeller is mounted close to the fuselage, the jump in circulation at the propeller rotation axis is stronger than the propeller hub vorticity. This is the result of a higher gradient of the section lift coefficient with angle-of-attack if it is further away from the tip. This is driven by the three vortices shed from the lifting surface at three distinct locations: at the root, at the edge of the slipstream, and at the propeller rotation axis. For an inboard-up rotating propeller, these three lead to a larger downwash gradient compared to the outboard-up rotating propeller, and therefore to a lower normal-force gradient of the lifting surface.

UNSTEADY AERODYNAMIC INTERACTION AND MITIGATION STRATEGIES

The vibration levels in the cabin for propeller driven aircraft are typically higher than for turbofan aircraft of the same class. Part of this is caused by the unsteady aerodynamic interaction between slipstream and airframe. From the analyses of the time-dependent load distributions on the lifting surface not only insight is gained from a structural design perspective, but also opportunities are revealed to reduce the unsteady loads produced by the propeller–lifting surface combination. The observations made from those analyses may drive design choices such as rotation direction, propeller position relative to the airframe, and the tail size. Therefore, the following research question has been posed:

6. *What approaches should be followed to reduce or avoid unsteady loads on the airframe it is in proximity to a propeller?*

Although a design study has not been conducted to fully address this question, the following conclusions have been formulated:

- Three types of slipstream deformation have been identified that lead to vastly different unsteady loads on a lifting surface. The case where there is an alternating number of vortex pairs residing on the surface and in case there is a strong shear of the slipstream, the unsteady loads at a spanwise station are maximum. The local chord length relative to the pitch of the helical vortex is found to be the driving parameter to affect the unsteady loads.

- The largest unsteady loads can be expected on the inboard side of the lifting surface due to the higher lift-curve slope in this region compared to the tip region.

- Generally, the tip vortex strength is not constant over a revolution. The interaction of a helical tip vortex with a lifting surface is therefore not symmetric on each side of the propeller axis. The unsteady loads therefore directly depend on the nonuniform inflow to the propeller, e.g. an angle-of-attack.

- An angle-of-attack leads to a phase shift of the helical tip vortices on the advancing side and retreating side of the propeller because the slipstream is deflected relative to the lifting surface. This directly affects the integral unsteady loads on the lifting surface, as the associated phase difference between the upgoing and downgoing blade sides partially cancel or enhance the integral time-dependent for the lifting surface.

10

- Close proximity of the helical tip vortex to the tip vortex of the lifting surface is undesired because the associated periodic vortex interaction introduces unsteady loads on the lifting surface.

10.1.4. ASPECTS OF AIRCRAFT STABILITY, CONTROL, AND PERFORMANCE FOR UNCONVENTIONAL PROPELLER INTEGRATION

The findings from the chapters on the fundamental aerodynamic interaction mechanisms have been put in perspective by addressing the following question:

8. *What are the key parameters that determine the airframe performance, static stability, and control characteristics when propellers are in close proximity to the airframe and what is their relation to aircraft design?*

The two configurations of interest serve as representative examples of unconventional propeller installation. The presented findings extend the knowledge of the installation effect of horizontal-tail-mounted propellers on aircraft stability, control, and performance by employing more detailed and elaborate analyses compared to previous works. Furthermore, a better understanding has been developed on the effect of distributed propellers along the leading-edge of a wing on several aircraft performance indicators, as well as on the longitudinal stability characteristics. Several more general conclusions have been formulated that apply to a wider range of configurations:

- A velocity field that reduces the effective advance ratio (i.e. lower axial inflow or a swirl that is against the propeller rotation direction) leads to a higher propeller efficiency and affects the optimal operating condition. In those cases, the optimal thrust coefficient is lower and the corresponding advance ratio is higher. For the same thrust coefficient, the blade pitch needs to be reduced to operate at maximum efficiency.

- The optimal propeller installation angle to achieve the maximum propeller efficiency and/or a favourable lift-contribution, is generally not parallel to the direction of flight.

- The airframe-induced flowfield affects the direct propeller contribution to static stability. By simplifying the installation using an isolated propeller with a moment arm and in-plane force gradient, the static stability is either under- or overpredicted.

- The rotation direction that is most favourable from a performance and/or stability perspective depends on the configuration and the propeller size relative to the lifting surface downstream of it. The rotation direction should therefore be a design variable already in the early stages of the aircraft design.

The following conclusions are more specific to the two propeller configurations:

10

Horizontal-Tailplane-Mounted Propeller Configuration

When the propellers are mounted to the horizontal tailplane, the following can be concluded regarding longitudinal static stability:

- An aft-mounted propeller installation generally does not adversely affect the aircraft longitudinal static stability over a major part of the operating conditions, which confirms the findings in Refs. [194, 229]. The neutral point shifts aft with increasing thrust coefficient, up to 5% of the mean aerodynamic chord for a thrust coefficient typical for climb/cruise with co-rotating propellers. At higher thrust settings, the neutral point shifts more aft. Exceptions to this are observed at high angles of attack.

- The propeller normal force is the dominant component of the changes in aircraft pitching moment resulting from propeller installation. Its contribution is linear with angle-of-attack for the linear part of the lift-curve.

- On aircraft level, the propeller installation leads to a nonlinear contribution to the pitching moment due to angle-of-attack (C_{m_α}) which depends rotation direction. The large variations of C_{m_α} start from the onset of the nonlinearity of the lift curve, because of the strong nonuniform inflow to the propeller. The slope of the pitching moment curve becomes up to 25% more negative for an outboard-up configuration, and up to 40% more negative for an inboard-up configuration. The dependency on thrust is low.

- The propeller slipstreams are not significantly displaced relative to the stabilizing surfaces for various flight conditions. For this reason, a more predictable and more favourable static stability characteristics are achieved compared to the situation where propellers are mounted on the inboard part of the wing.

Rear-mounting the propeller enhances the directional stability on aircraft level. The propeller installation increases the C_{n_β} with respect to a reference point at 25% of the mean aerodynamic chord by 6% for the inboard-up propeller configuration and up to 12% for the inboard-up propeller configuration. The difference between the two rotation directions is caused by the fuselage induced flowfield. The co-rotating configuration can be approximated by the sideforce of two isolated propellers multiplied with their moment arm. The rise is nearly independently of thrust coefficient. The change in yawing moment coefficient remains approximately linear for $\beta = \pm 10$ deg. On the other hand, tail-off measurements show that the presence of the slipstreams on each side of the vertical tail makes the vertical tailplane less effective. The effectiveness of the vertical tailplane reduces by 2.5% for a cruise thrust setting.

The propeller installation leads to a different trim setting compared to the propeller-off case. The thrust-induced nose-down pitching moment is largely compensated by the propeller normal force induced by the wing downwash field. Therefore, only a small change in trim setting of ± 2 deg in cruise conditions is required between propeller-on and propeller-off. The small elevator input required for the outboard-up rotating case leads to nearly no additional trim drag. For an inboard-up rotation, the added trim drag

10

is approximately 25% of the propeller-off condition for a typical cruise lift coefficient, and remains a finite offset over the full range of C_L.

In the co-rotating configuration, a net yawing moment exists that is equivalent to a sideslip angle of two degrees. This is caused by the thrust-dependent sidewash of the slipstream due to interaction, in line with other research. The outboard-up rotating propeller is the critical engine. In case of an one-engine-inoperative situation, the yawing moment becomes zero at $\beta \approx 1$ deg in cruise conditions, if the thrust of the operating engine is not increased to arrive at an equilibrium condition of $T = D$.

The propeller efficiency in flight direction multiplied with the lift-to-drag ratio is up to 2% higher for the co-rotating configuration compared to the situation in which the interaction is not included. Mounting the propeller to the tailplane does not significantly reduce the drag of the airframe. Moreover, the maximum lift coefficient is increased by up to $\Delta C_{L,\mathrm{max}} = +0.06$ for the co-rotating configuration, mainly caused by the propeller forces. This increment is significantly smaller compared to wing-mounted propeller configurations.

The current study displays that even for a suboptimal design, the beneficial propeller–airframe aerodynamic interaction could partially offset the drawbacks identified for the configuration. These benefits are present despite the fact that an aerodynamic performance benefit historically has not been the motivation for studying this configuration.

LEADING-EDGE DISTRIBUTED PROPELLER CONFIGURATION

The focus of the case with propellers mounted to the leading-edge of the wing is twofold. First, the performance benefit of the tip-mounted propeller is evaluated on aircraft level. Second, the effect of two propellers mounted close to each other on the downwash field at the tailplane is investigated. Although the geometry on which the analyses have been performed has a highly swept wing, by varying the rotation direction, thrust coefficient, and propeller diameter, design guidelines are formulated for the low angle-of-attack range of comparable installations which do not necessarily have a swept wing.

If the wing–nacelle junction is not adapted to lower the adverse pressure gradients, even at low angles of attack the flow is prone to separation on the inboard side of the nacelle, in line with other studies. Flow separation initiates at the inboard nacelles, which shifts the aerodynamic center rearwards. On the other hand, the tip becomes more prone to tip stall compared to the clean wing design due to the local higher angle-of-attack introduced by the propeller–nacelle combination. A vertical translation by a distance equal to half the diameter of the nacelle already significantly postpones the onset of stall, in line with other studies. The lift-to-drag ratio in that case is raised by approximately 2.5% per nacelle for a cruise/climb angle-of-attack. The following is concluded on the propeller installation on the aircraft performance:

- Irrespective of the rotation direction of the inboard propellers, there is a net increase of the lift coefficient which is proportional to the thrust coefficient. Especially the inboard propellers contribute to aircraft lift, while the tip propeller not only increases lift, but also reduces drag. The maximum airframe lift-to-drag ratio increases between 5% to 8% depending on the reference drag and rotation direction.

- A smaller tip propeller can be selected at the cost of propeller efficiency and to the benefit of airframe lift-to-drag ratio. The product $\eta_p \frac{L}{D}$ remains approximately constant for the evaluated radii (up to 30% smaller diameter compared to a reference case). While the power increases by 2% to maintain the same thrust, the torque is reduced by more than 20%. A smaller tip propeller may therefore lead to a lighter nacelle, propeller, and (electric) motor.

The direct propeller contribution to longitudinal stability is small. The tip propeller is stabilizing, the inboard propellers are destabilizing for a moment reference location at 35% of the mean aerodynamic chord. The main effect of the propeller installation is a more negative tail-off pitching moment and the slope of the tail-off moment curve becomes 5% more negative without significant difference between the rotation directions.

On average, the rotation direction "down-between-blades" has the smallest impact on the downwash angle at the horizontal tailplane relative to the propeller-off case. Among other considerations such as unsteady loads, a slipstream impingement introduces rapid changes in the pitching moment curve with angle-of-attack.

10.1.5. ANALYSIS METHODS AND APPROACHES FOR ESTIMATING PROPELLER-INSTALLATION EFFECTS

Provided that propeller–airframe aerodynamic interaction has a highly three-dimensional character, the interaction is time-dependent, and often involves rather complex geometries consisting of multiple lifting and non-lifting surfaces, it is important to determine the fidelity level that is required to achieve the objective of an analysis. In addition, the understanding of the effect of scale is relevant, especially when an experimental approach is selected using scaled-down models. In this section, the findings of employing a high-fidelity approach are presented.

There are several common flowfield characteristics between various propeller configurations. Through the assessment of a select number of cases, it has been concluded that the following flow phenomena play a relevant role in the changes in terms of *absolute* forces and moments, as well in terms of the changes in the *gradient* of the forces and moments with angle-of-attack, sideslip angle, deflection of high-lift devices, and thrust coefficient:

- The development of the slipstream in axial and radial direction
- The slipstream deformation as a consequence of interaction with the airframe
- The slipstream deflection/displacement as a consequence of the local flow field
- The effect of nonuniform inflow on the propeller forces and slipstream generation
- The effect of the nacelle through the potential-flow effects and the associated junction-flow
- The development and roll-up of the trailing vorticity from the lifting surface
- The fuselage-induced flowfield in case of propellers mounted close to the fuselage
- The relative size of the slipstream compared to the lifting surface that is submerged in it

10

- The time-dependency of the slipstream

An analysis method that can capture these phenomena is unsteady RANS using a full-blade approach, which was the selected method for the majority of the simulations. The advantage for the flowfield to be time-dependent becomes clear when considering the fact the propeller helical vortex system is generally nonsymmetric, especially when it encounters a lifting surface. This introduces a phase difference of the three dimensional flowfield that impacts the time-averaged forces acting on the lifting surface.

Moreover, a RANS approach was also chosen since the necessity of modelling the effect of viscosity is evident for high-lift conditions, for the slipstream development in downstream direction, and for vortex-vortex interactions. However, the effect of small-scale turbulent structures on the mean interaction have been discussed to be low, in case the (majority) of the boundary layer is turbulent. This hypothesis is strengthened by the fact that pressure distributions computed by unsteady RANS simulations correlate well with the experimental results. This demonstrates the ability of an unsteady RANS approach to capture the key factors of the aerodynamic interaction. Moreover, since in full-scale conditions the boundary layer is turbulent for the majority of the airframe components, enforcing the boundary layer to be turbulent is justified. The following is concluded about the unsteady RANS simulations:

- In line with other publications, the dependency of several force coefficients and the slipstream shape on the mesh size was low. No major differences were found in the flowfield using finer meshes, except in the shear layer of the slipstream.

- Numerical diffusion is responsible for the large difference in vortex core radius and the associated velocity gradients, while the circulation of the tip vortex is nearly independent of the grid choice. The fact that numerical diffusion plays such an important role in the vorticity transport was clearly observed in the roll-up process. In the experiment, the complete roll-up took place significantly further away from the propeller disk, while the velocity gradients are still large, even close to the disk.

- For installation studies where the unsteady component of lift is important, a combination of a higher-order (discretization) method and/or a fine grid is required.

The following was concluded about the differences between unsteady RANS simulations and experimental results:

- Already with a relatively coarse mesh, the propeller performance for a cruise setting compares well with the experimental results.

- The main deviation of CFD relative to experiment for the installed configurations was found at the slipstream edges. However, the results also show that excessive diffusion of the propeller tip vortices does not impact the integral forces on the lifting surfaces.

- The results on a full aircraft configuration demonstrate that the CFD simulations are well suitable to predict the aircraft performance. The estimated change in axial force component, i.e. the combined effect of propeller thrust variations and

10

airframe drag, is within 2% of the experimental result. The *change* in slope of the pitching moment curve is also predicted to differ up to 2% of the experimental result, which therefore falls nearly in the experimental uncertainty band.

- The largest differences between CFD and experiment for the propeller are found at low thrust settings. The slope of the $C_T − J$ curve is 20% higher in the experiment, which was found to be driven by the low Reynolds number. By reducing J, two phenomena occur simultaneously. First, the angle of attack to the blade sections increases, and second, the Reynolds number increases. Provided that the lift curve slope and α_0 increase with Re, an *effective lift curve* of each airfoil section can be constructed. This apparent curve has a relatively high slope. Therefore, the Reynolds number effect on a propeller is larger than for the rest of the airframe. The difference between CFD and experiment would be smaller if the airfoils were uncambered because there would be no shift of the lift curves.

- Given the differences in propeller loading, in case the thrust coefficient is matched at a different advance ratio, still good agreement is found in the shape of the slipstream.

A comparison between two well-established models (the one-equation Spalart-Allmaras model and the two-equation $\kappa − \omega$ shear stress transport model (SST) model) showed significant difference in the flow structures. While the pressure distribution from the simulation using the Spalart-Allmaras model coincides with experiment, the $\kappa − \omega$ SST model greatly overpredicts the flow separation. For the evaluated cases in this dissertation with a low Reynolds and Mach number, while strong pressure and velocity gradients are introduced, the Spalart-Allmaras turbulence models has proven to be most suitable. The fact that two well-known models display such a significant difference highlights the importance of validation data.

Despite the relatively large amount of computational resources required to obtain a single solution, the excellent agreement indicates that the main flow phenomena on each component can be studied in further detail. The power of a (well validated) CFD setup is therefore clearly displayed herein. On the other hand, if one is interested in trends (i.e. a large number of operating conditions), or in the time-accurate response of a lifting surface in an unsteady flowfield, experimental campaigns are in particular useful.

The wind-tunnel models employed in this research are scaled-down versions of the envisioned propeller installations. The maximal thrust coefficients of the scaled-down experimental setup are inherently lower because of the lower tip Mach number and lower Reynolds numbers of the blade sections. Due to compressibility, at a given advance ratio, the thrust and torque coefficients are increasing with freestream Mach number. Consequently, the total pressure and swirl angle in the slipstream are increasing accordingly. However, by normalizing the thrust distribution, it is shown that Mach number only has a minor effect on the *shape* of the radial distribution of propeller forces, in case there is no significant shock-induced separation on the outboard part of the blade. This leads to the conclusion that the same slipstream shape can be obtained if J and C_T are matched. This would be possible by slightly increasing the blade pitch for the scaled model that operates at a lower freestream Mach number.

10

10.2. Recommendations

Based on the expected trends of research topics that have not been covered in this dissertation, several recommendations for future research are made.

The aerodynamic interaction that determines the aircraft high-lift performance is especially complex for leading-edge mounted tractor propellers with multiple propellers that are in close proximity. Design guidelines in terms of propeller position, propeller design, nacelle integration, and high-lift design are required to quantify the benefit of such configuration that can be achieved in practice. For the leading-edge distributed propulsion configurations, there is a large number of nacelles and it is expected that the wing-nacelle interaction will be a prominent factor for the wing performance, both in cruise and high-lift conditions. The presence of the nacelle on the development of the flowfield and the interaction with the wing is probably the most underestimated factor in the available studies to date. Various studies even completely omit the nacelle, leading to very unrepresentative conclusions. Provided that the nacelle has a significant effect on the gradient of the flowfield, is apparent in the determination of maximum lift coefficient, locally reduces the lift-to-drag ratio along the span, and reduces the efficiency of adjacent propellers, it must be a key topic in any distributed propulsion study that attempts to predict performance of the system.

It has been shown that especially the leading-edge region of a lifting surface is affected by a slipstream. It is this region that should be designed such that the drag reduction is maximum, while maintaining (or improving) the maximum lift capabilities. For lower propeller-diameter-over-wing-chord ratios, the leading-edge region becomes even more important. For distributed propulsion concepts, resources should be spend on designing leading edge accordingly, where also the presence of the nacelle is included.

It has been shown that nonuniform inflow has a significant impact on the noise levels at the fuselage outer surface. At the same time, unsteady loads are transferred to the aircraft structure. Since these are periodic and well defined in terms of magnitude, selecting the frequency and phase, as well as adapting the structural design, are envisioned to greatly reduce these unwanted installation effects. In addition to these strategies, design adaptations regarding the propeller positioning may lead to partially cancelling/reducing of the vibrations. The current study has shown that even by changing the interaction with the airframe slightly, the propeller and airframe loads can be reduced. Concrete design rules have not been established yet, but are necessary for accurate weight estimations of the airframe, given a desired comfort level.

Although several conclusions have been formulated that relate to aircraft design, the implication of propeller installation on the sizing of the aircraft was out of the scope of this research. For example, the configuration study that has been presented only considered the effect of the airframe on the propeller performance. Much more interesting from an aircraft design perspective is the overall aircraft efficiency, i.e. the maximum $\eta_x \frac{L}{D}$ that is changed by the propeller installation, where the airframe $\frac{L}{D}$ is determined based on a converged aircraft design. By the knowledge of the author only a handful of such studies have been presented that capture sufficient detail. A broader design study covering multiple configurations would be beneficial to quantify the actual performance benefit/loss of a certain propeller configuration.

Regarding the configuration with propellers mounted to the horizontal tailplane, it is recommended to further investigate the noise benefits in the cruise condition in addition to the existing literature, especially for lower flight Mach numbers. Moreover, the noise penalty and mitigation strategies for the high angle-of-attack conditions should be investigated in detail. Minimizing the distortion at the propeller plane by redesign of the airframe could allow for larger propeller diameters with potentially higher overall system efficiency that otherwise would be constraint by, for example, the location of the wing wake.

The pylon-mounted configuration,as recently proposed by industry, is a configuration that is closely related to the tail-mounted configuration discussed herein. The demonstrated drawbacks of an aft location of a center of gravity in other studies indicate that this is a potential compromise between complexity of the mounting, the far aft center of gravity, the added weight, and the added wetted surface area. Such a mounting would allow more geometric and structural adaptations to further lower the impact of the propeller on cabin noise. Provided that the shifted mass to the back of the aircraft still would lead to large excursion of the center of gravity, it is recommended that also for this configuration, engineering solutions are investigated to limit this excursion (e.g. a trim tank that could be filled with water or fuel). Alternatively, a quantification of the effect of constraining the operational boundaries, e.g. by specifying a minimum payload, could be insightful for reshaping the regulations for future aircraft.

The substantial aerodynamic benefit in terms of lift-to-drag ratio of a tip-mounted propeller is in line with other research. Several research topics are to be addressed to support further development of this concept. An example is the understanding of the effect of an one-engine-inoperative condition on the aerodynamic interaction. This is especially relevant for the aircraft rolling and yawing moment in the high-lift and high-thrust conditions. Moreover, the 'best' location and orientation of the tip-mounted propeller relative to the wing tip has not been investigated sufficiently to quantify the maximum attainable aerodynamic benefit. The nacelle length, diameter, and aft-shape deserve a fundamental role in these studies.

In the experience of the author, changing the mesh setup has significantly more impact on the results than refining the same mesh. Most effort should therefore be spend on the mesh design instead of elaborate mesh refinement studies. A mesh refinement study is not a proof of the validity of the results, while it is often (indirectly) presented as such. Along the same line, a numerical study that is not validated against a comparable and well-characterized case, should be interpreted with great care. Therefore, it is recommended that various benchmark cases should be characterized prior to research these configurations using numerical tools. Resources have to be directed towards characterizing and publishing benchmark cases, rather than spending the resources on numerical studies that are comparable in type, for which the conclusions are already available in literature. Especially for studies that focus on high-lift conditions, benchmark data that includes the propeller installation effects are required.

As a final remark, it is the author's opinion that the quality, consistency, and clarity of reporting of an experimental and numerical study are significantly improved in case both simulations are conducted by the same researcher. The quality of the work is further improved if it is performed in collaboration with one or more colleagues.

10

A

DESCRIPTION OF THE DELFT UNIVERSITY 'DU 96-150' AIRFOIL

The airfoil coordinates listed in this appendix are used for the wing of the *VGM-HTP* airfraft. The DU 96-150 was originally designed by L. L. M. Veldhuis in 1996. Coordinates are digitized from these original drawings by N. van Arnhem. The final data points are obtained by fitting a smooth profile through these points. Figure A.1 depicts the airfoil contour and its first derivative with respect to the local *x*-direction. The data points are listed in Table A.1.

(a) Airfoil contour

(b) Gradient $\frac{dy}{dx}$
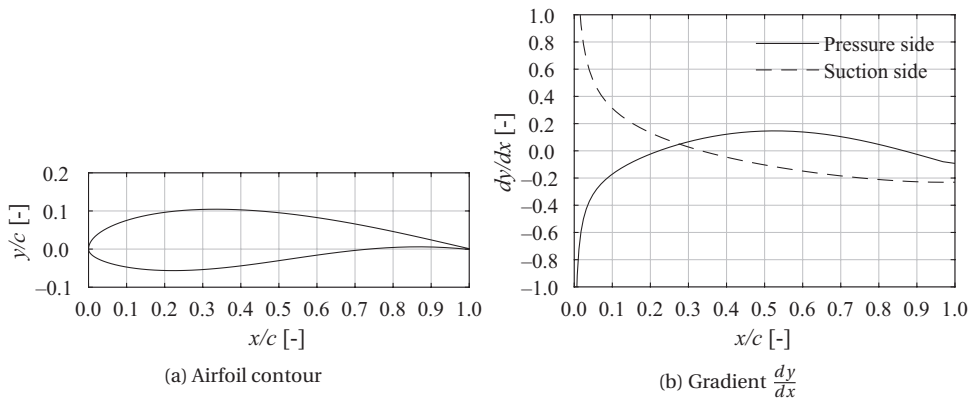
Figure A.1: Description of the 'DU 96-150' airfoil profile.

Table A.1: Description of the 'DU 96-150' airfoil profile.

x/c, pressure side	y/c, pressure side	x/c, suction side	y/c, suction side
1.0000000000000000	-0.0010000000000000	0.0000000000000000	0.0000000000000000
0.9685892409218720	0.0019043293718139	0.0004934396342684	0.0056532423052185
0.9372094804706870	0.0040215025431021	0.0019732715717284	0.0112971420613367
0.9058916866814860	0.0053536534757097	0.0044380353969200	0.0169211284138153
0.8746667664356960	0.0059174203115027	0.0078852986855221	0.0225141583362097
0.8435655349597690	0.0057427150920721	0.0123116594048622	0.0280645049368678
0.8126186854142750	0.0048713278894506	0.0177127492713113	0.0335595734581515
0.7818567586034570	0.0033554017798597	0.0240832380612526	0.0389857525824591
0.7513101128351450	0.0012558156236512	0.0314168388713689	0.0443283073517772
0.7210088939607710	-0.0013594886551398	0.0397063143230569	0.0495713184670513
0.6909830056250530	-0.0044171986191326	0.0489434837048465	0.0546976710180560
0.6612620797547090	-0.0078403097409807	0.0591192310457745	0.0596890938681777
0.6318754473153220	-0.0115497580723911	0.0702235141117487	0.0645262490506539
0.6028521093652200	-0.0154659783916419	0.0822453743160189	0.0691888686943582
0.5742207084349270	-0.0195103623610287	0.0951729475339805	0.0736559352586939
0.5460095002604530	-0.0236065948651789	0.1089934758116320	0.0779058992858903
0.5182463258982850	-0.0276818505819703	0.1236933199561360	0.0819169275367340
0.4909585842496290	-0.0316678368604546	0.1392579729960560	0.0856671733162751
0.4641732050210030	-0.0355016730479563	0.1556720744979850	0.0891350600631434
0.4379166221478690	-0.0391266004294150	0.1729194257254380	0.0922995689018148
0.4122147477075270	-0.0424925208308508	0.1909830056250530	0.0951405208604805
0.3870929463470230	-0.0455563656187176	0.2098449876243100	0.0976388448430794
0.3625760102513100	-0.0482823002307612	0.2294867572242110	0.0997768232031556
0.3386881346763480	-0.0506417724454073	0.2498889303695410	0.1015383078757610
0.3154528940713110	-0.0526134152906458	0.2710313725785880	0.1029089014441480
0.2928932188134520	-0.0541828177764844	0.2928932188134520	0.1038760992003360
0.2710313725785880	-0.0553421784856317	0.3154528940713110	0.1044293901414160
0.2498889303695410	-0.0560898584647901	0.3386881346763480	0.1045603168561890
0.2294867572242110	-0.0564298508241837	0.3625760102513100	0.1042624963219460
0.2098449876243100	-0.0563711849860255	0.3870929463470230	0.1035316056671110
0.1909830056250530	-0.0559272836427101	0.4122147477075270	0.1023653388788670
0.1729194257254380	-0.0551152902194486	0.4379166221478690	0.1007633421638290
0.1556720744979850	-0.0539553840170565	0.4641732050210030	0.0987271371269067
0.1392579729960560	-0.0524700992768831	0.4909585842496290	0.0962600420482383
0.1236933199561360	-0.0506836632032849	0.5182463258982850	0.0933671022501987
0.1089934758116320	-0.0486213665437221	0.5460095002604530	0.0900055040807833
0.0951729475339805	-0.0463089787076216	0.5742207084349270	0.0863322406329104
0.0822453743160189	-0.0437722176475571	0.6028521093652200	0.0822087682365492
0.0702235141117487	-0.0410362828737593	0.6318754473153220	0.0776964482476104
0.0591192310457745	-0.0381254580671169	0.6612620797547090	0.0728089960511306
0.0489434837048465	-0.0350627878354287	0.6909830056250530	0.0675622137484296
0.0397063143230569	-0.0318698312581365	0.7210088939607710	0.0619742520807612
0.0314168388713689	-0.0285664930177851	0.7513101128351450	0.0560659380705131
0.0240832380612526	-0.0251709311497565	0.7818567586034570	0.0498611650015347
0.0177127492713113	-0.0216995387792120	0.8126186854142750	0.0433873380791309
0.0123116594048622	-0.0181669956755810	0.8435655349597690	0.0366758657863011
0.0078852986855221	-0.0145863840566919	0.8746667664356960	0.0297626836982929
0.0044380353969200	-0.0109693618297603	0.9058916866814860	0.0226887944481901
0.0019732715717284	-0.0073263853750556	0.9372094804706870	0.0155008047675110
0.0004934396342684	-0.0036669730677752	0.9685892409218720	0.0082514381692086
0.0000000000000000	0.0000000000000000	1.0000000000000000	0.0010000000000000

B

# Role of Redistribution of Loading that is Caused by an Inflow Perturbation

The change in loading on a lifting surface as the result of a local inflow perturbation over a portion of the span is not limited to the spatial size of this inflow perturbation. The spanwise variation in circulation causes streamwise vorticity to be shed which induce a local downwash field. This downwash also changes the (induced) drag of the lifting surface. The quantification of these changes in loading for a wing is relatively straightforward, especially when the lifting surface is modelled as a lifting line.

The changes in the actual propeller vortex system that are caused by a local perturbation in the flowfield are not calculated directly in the engineering method presented in Chapter 5. Instead, these are approximated using the local 'sensitivity' of the loading to a perturbation. The spanwise redistribution is therefore treated as a second-order effect when computing the changes in propeller performance. This principle is demonstrated in this appendix for a wing to show that the impact of the redistribution is indeed relatively small. It is clear that the propeller vortex system consisting of the distribution of bound vorticity and the helical vortex system is more complex than this simple example and cannot directly be compared. Nevertheless, the results are indicative of the role of the redistribution on the integral loads.

For this example, the classical lifting line method is used to compute the lift and drag for a symmetric bell-shaped disturbance along the entire span of a straight and untwisted wing. The 'full solution' consists of the solution in which redistribution is taken into account. The 'approximated' solution is computed by evaluating the entire wing at each of the disturbed angles. This is equivalent to the main assumption and starting point of the engineering method.

Figure B.1a shows the example of a local perturbation with a peak at $2y/b = \pm 0.5$. From Figs. B.1b to B.1e it is clear that the shed vorticity reduces the peak load at the

location of the disturbance and redistributes part of the load towards adjacent wing sections. This example shows that the change in loading distribution can be approximated relatively well. It can be expected that the gradient of the disturbance in spanwise direction is a driving factor for the redistribution, since a perturbation with no gradient in spanwise direction would exactly resemble the 'full solution'. In Fig. B.2, it is shown that the error in neglecting the redistribution remains within a few percent for the integral lift. However, as the induced drag is driven by the spanwise variation of circulation, it is more dependent on the actual circulation distribution than the lift coefficient. The error in induced drag coefficient relative to the actual induced drag distribution becomes larger for disturbances with a higher spanwise gradient. Therefore the stated assumption in Chapter 5 has a larger impact on torque than on thrust. Nevertheless, even for a disturbance with a large gradient, the relative error is still acceptable for most applications, especially for thrust and torque as they are mostly dependent on the lift force acting on the blade sections (Chapter 2).
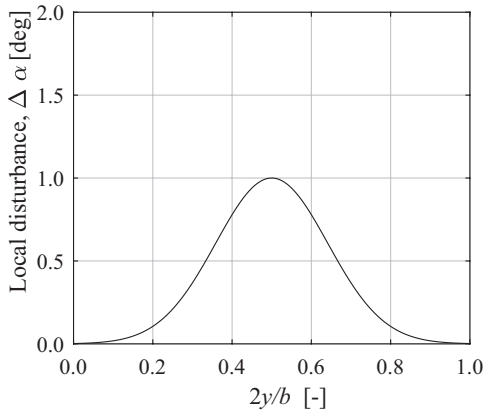
(a) Local disturbance along the semi-span
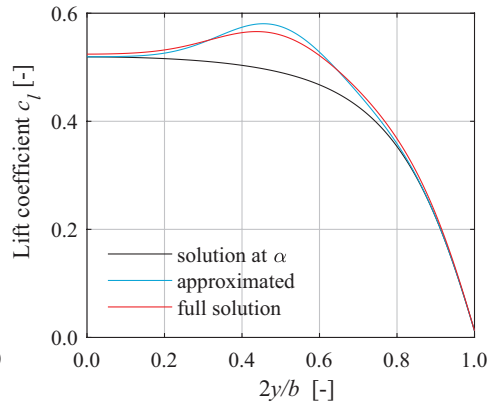
(b) Comparison of lift distributions
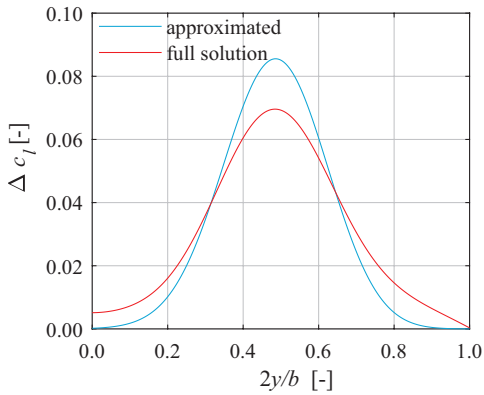
(c) Change in lift distribution
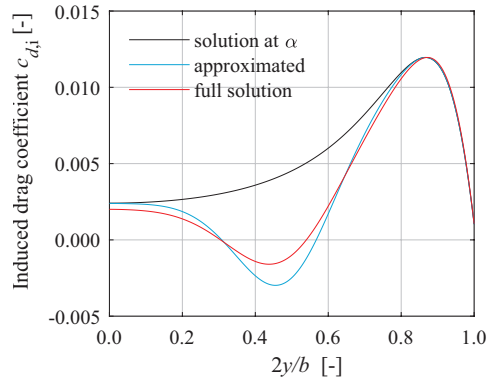
(d) Comparison of induced drag distributions
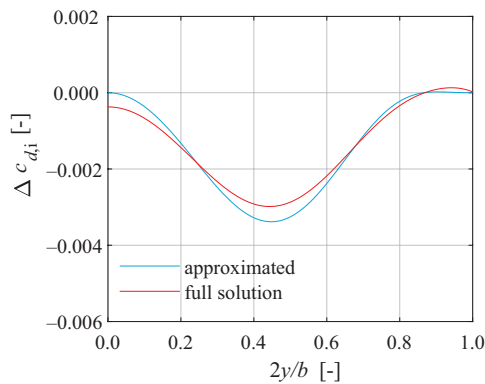
(e) Change in induced drag distribution

Figure B.1: Comparison of the computed and approximated loading distribution as the result of a bell-shaped disturbance along the semi-span. Straight and untwisted wing has an aspect ratio of 20 and a two-dimensional lift-curve slope of 2π.
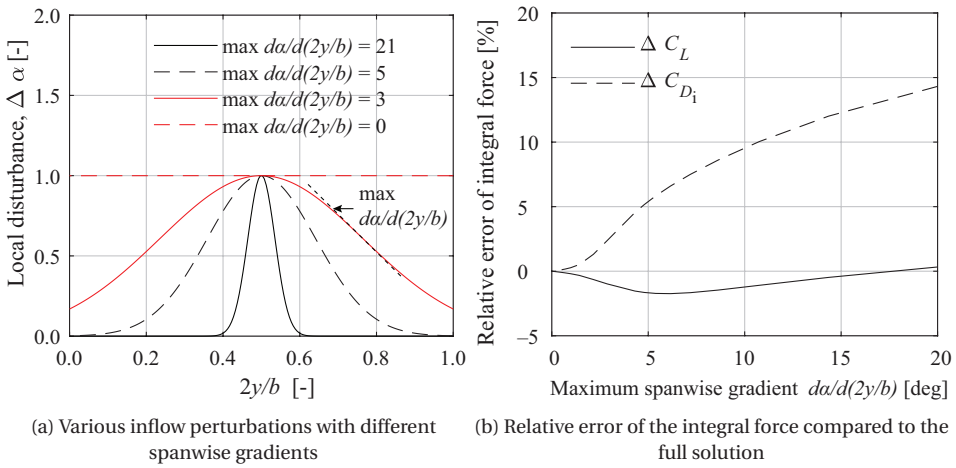
B

(a) Various inflow perturbations with different
spanwise gradients

(b) Relative error of the integral force compared to the
full solution

Figure B.2: Effect of spanwise gradient of the perturbation on the deviation between the approximated and
full solutions.

REFERENCES

[1] Edenhofer, O., Pichs-Madruga, R., Sokona, Y., Farahani, E., Kadner, S., Seyboth, K., Adler, A., Baum, I., Brunner, S., Eickemeier, P., Kriemann, B., Savolainen, J., Schlömer, S., von Stechow, C., Zwickel, T., and Minx, J.C., *Climate Change 2014 Mitigation of Climate Change Working Group III Contribution to the Fifth Assessment Report of the IPCC*, Cambridge University Press, Cambridge, 2014.

[2] Lee, D., Pitari, G., Grewe, V., Gierens, K., Penner, J., Petzold, A., Prather, M., Schumann, U., Bais, A., Berntsen, T., Iachetti, D., Lim, L., and Sausen, R., "Transport impacts on atmosphere and climate: Aviation," *Atmospheric Environment*, Vol. 44, No. 37, 2010, pp. 4678–4734. doi:10.1016/j.atmosenv.2009.06.005.

[3] "Air Passenger Market Analysis – September 2020," , International Air Transport Association, 2020.

[4] Airbus S.A.S., "Global Market Forecast - Cities, Airports and Aircraft 2019–2038," Airbus, 2019.

[5] Nygren, E., Aleklett, K., and Höö, M., "Aviation fuel and future oil production scenarios," *Energy Policy*, Vol. 37, No. 10, 2015, pp. 4003—4010. doi:10.1016/j.enpol.2009.04.048.

[6] "Air Transport and Energy Efficiency," Tech. Rep. TP-38, The World Bank, 2012.

[7] European Commission, "European Green Deal - Delivering on Our Targets," , 2021. NA-02-21-151-EN-N. doi:10.2775/595210.

[8] Singh, V., and Sharma, S. K., "Fuel consumption optimization in air transport: a review, classification, critique, simple meta-analysis, and future research implications," *European Transport Research Review*, Vol. 7, No. 12, 2015. doi:10.1007/s12544-015-0160-x.

[9] "Aircraft Technology Roadmap to 2050," , International Air Transport Association, 2020.

[10] Dahlmann, K., Koch, D., Linke, F., Lührs, B., Grewe, V., Otten, T., Seider, D., Gollnick, V., Schumann, U., "Climate-Compatible Air Transport System—Climate Impact Mitigation Potential for Actual and Future Aircraft," *Aerospace*, Vol. 3, No. 38, 2016. doi:10.3390/aerospace3040038.

[11] "Hydrogen-powered aviation. A fact-based study of hydrogen technology, economics, and climate impact by 2050," , 2020. Doi:10.2843/471510.

[12] Yaros, S. F., Sexstone, M. G., Huebner, L. D., Lamar, J. E., McKinley Jr., R. E., Torres, A. O., Burley, C. L., Scott, R. C., and Small, W. J., "Synergistic Airframe-Propulsion Interactions and Integrations," Tech. Rep. TM-1998-207644, NASA, 1998.

[13] Dugan, Jr., J. F., Gatzen, B. S., and, Adamson, W. M., "Prop-Fan Propulsion – Its Status and Potential," *SAE Paper*, 1979. doi:10.4271/780995.

[14] Durand, W. F., *Aerodynamic Theory Vol. IV.*, Julius Springer, 1935.

[15] Epstein, A. H., "Aeropropulsion for Commercial Aviation in the Twenty-First Century and Research Directions Needed," *AIAA Journal*, Vol. 52, No. 5, 2014, pp. 901–911. doi:10.2514/1.J052713.

[16] Küchemann, D., and Weber, J., *Aerodynamics of Propulsion*, McGraw-Hill Publishing Company, 1953.

[17] Rudnik, R., Rossow, C.-C., von Geyr, H. Frhr., "Numerical simulation of engine/airframe integration for high-bypass engines," *Aerospace Science and Technology*, Vol. 6, No. 1, 2002, pp. 31–42. doi:10.1016/S1270-9638(01)01139-7.

[18] Dron, S., "Toward ACARE 2020: Innovative Engine Architectures to Achieve the Environmental Goals?" *International Congress of the Aeronautical Sciences*, 2008.

[19] van Zante, D. E., "Progress in Open Rotor Research," *Encyclopedia of Aerospace Engineering*, 2015. doi:10.1002/9780470686652.eae1019.

[20] Schimming, P., "Counter Rotating Fans An Aircraft Propulsion for the Future?" *Journal of Thermal Science*, Vol. 12, No. 2, 2003, pp. 97—-103. doi:10.1007/s11630-003-0049-1.

[21] Whitlow, J. B., and Sievers, G. K., "Fuel Savings Potential of the NASA Advanced Turboprop Program," Tech. Rep. TM-83736, NASA, 1984.

[22] Jackson, Jr., A. H., and, Gatzen, B. S., "Multi-Mission Uses for Prop-Fan Propulsion," *AGARD Conference Proceedings*, 1976.

[23] Guynn, M. D., Berton, J., J., Haller, W. J., Hendricks, E. S., and Tong, M. T., "Performance and Environmental Assessment of an Advanced Aircraft with Open Rotor Propulsion," Tech. Rep. TM-2012-217772, NASA, 2012.

[24] Mikkelson, D. C., Mitchell, G. A., and, Bober, L. J., "Summary of Recent NASA Propeller Research," *AGARD Conference Proceedings*, Vol. AGARD-CP-366, 1984.

[25] Goldsmith, I. M., "A Study to Define the Research and Technology Requirements for Advanced Turbo/Propfan Transport Aircraft," Tech. Rep. CR-166138, NASA, 1981.

[26] Miley, S. J. and von Lavante, E., "Propeller Propulsion System Integration State of Technology Survey," Tech. Rep. CR-3882, NASA, 1985.

[27] Hager, R. D., and Vrabel, D., "Advanced Turboprop Project," Tech. Rep. SP-495, NASA, 1988.

[28] Dittmar, J. H., "An Experimental Investigation of Reducing Advanced Turboprop Cabin Noise by Wing Shielding," *AIAA Paper*, 1986. doi:10.2514/6.1986-1966.

[29] Revell, J. D., and, Tullis, R. H., "Fuel Conservation Merits of Advanced Turboprop Transport Aircraft," Tech. Rep. CR-152096, NASA, 1977.

[30] Khalid, S. A., Lurie, D., Breeze-Stringfellow, A., Wood, T., Ramakrishnan, K., Paliath, U., Wojno, J., Janardan, B., Goerig, T., and Opalski, A., "Open Rotor Engine Aeroacoustic Technology Final Report," Tech. Rep. DOT/FAA/AEE/2014-04, Federal Aviation Administration, 2012.

[31] Lange, R. H., "Review of Advanced Turboprop Transport," *Progress in Aerospace Sciences*, Vol. 23, No. 2, 1986, pp. 151–166. doi:10.1016/0376-0421(86)90003-5.

[32] Van Zante, D., Collier, F., Orton, A., Khalid, S., Wojno, J., and Wood, T., "Progress in open rotor propulsors: The FAA/GE/NASA open rotor test campaign," *The Aeronautical Journal*, Vol. 118, No. 1208, 2014, pp. 1181–1213. doi:10.1017/S0001924000009842.

[33] Fage, A., and Collins, H. E., "An Investigation of the Mutual Interference of Airscrews and Bodies of the Pusher Type," Tech. Rep. 1916-17, Advisory Committee for Aeronautics, 1920.

[34] Gohardani, A. S., Doulgeris, G., and Singh, R., "Challenges of future aircraft propulsion: A review of distributed propulsion technology and its potential application for the all electric commercial aircraft," *Progress in Aerospace Sciences*, Vol. 47, No. 5, 2011, pp. 369–391. doi:10.1016/j.paerosci.2010.09.001.

[35] Reckzeh, D., and Hansen, H., *High Reynolds-Number Windtunnel Testing for the Design of Airbus High-Lift Wings*, Springer, Berlin, Heidelberg, 2006. doi:10.1007/978-3-540-33287-9_1.

[36] Kroo, I., " Propeller/wing integration for minimum induced loss," *Journal of Aircraft*, Vol. 23, No. 7, 1986, pp. 561–565. doi:10.2514/3.45344.

[37] Veldhuis, L.L.M., "Propeller Wing Aerodynamic Interference," Ph.D. Thesis, Delft University of Technology, Delft, The Netherlands, 2005.

[38] Patterson, M. D., "Conceptual Design of High-Lift Propeller Systems for Small Electric Aircraft," Ph.D. Thesis, Georgia Institute of Technology, Atlanta, United States, 2016.

[39] Keller, D., and Rudnik, R., "Numerical Investigation of Engine Effects on a Transport Aircraft with Circulation Control," *Journal of Aircraft*, Vol. 52, No. 2, 2015, pp. 421–438. doi:10.2514/1.C032724.

[40] Borer, N. K., Patterson, M. D., Viken, J. K., Moore, M. D., Bevirt, J. , Stoll, A. M., and Gibson, A. R., "Design and Performance of the NASA SCEPTOR Distributed Electric Propulsion Flight Demonstrator," *AIAA Paper*, 2016. doi:10.2514/6.2016-3920.

[41] Takallu, M. A., and Gentry, Jr., G. L., "Aerodynamic Characteristics of a Propeller Powered High Lift Semi Span Wing," *AIAA Paper*, 1992. doi:10.2514/6.1992-388.

[42] Petrov, A., "Aerodynamics of STOL Airplanes with Powered High- Lift Systems," *International Council of the Aeronautical Sciences (ICAS) Paper*, 2012.

[43] Lange, R. H., "Review of Advanced Turboprop Transport Activities," *AGARD Conference Proceedings*, 1984.

[44] Guynn, M. D., Berton, J. J., Tong, M. J., and Haller, W. J., "Initial Assessment of Open Rotor Propulsion Applied to an Advanced Single-Aisle Aircraft," *AIAA Paper*, 2013. doi:10.2514/6.2011-7058.

[45] Snyder, Jr, M.H. and Zumwalt, G.W., "Effects of wingtip-mounted propellers on wing lift and induced drag," *Journal of Aircraft*, Vol. 6, No. 5, 1969, pp. 392–397. doi:10.2514/3.44076.

[46] Schaffer, A., "A Study of Vortex Cancellation," *Journal of the Aerospace Sciences*, Vol. 27, No. 3, 1960, pp. 193–233. doi:10.2514/8.8470.

[47] Miranda, L. R. and Brennan, J. E., "Aerodynamic effects of wingtip-mounted propellers and turbines," *AIAA Paper*, 1986. doi:10.2514/6.1986-1802.

[48] Patterson, Jr, J. C., and Bartlett, G.R., "Evaluation of Installed Performance of a Wing-Tip-Mounted Pusher Turboprop on a Semispan Wing," Tech. Rep. TP-2739, NASA, 1978.

[49] Sinnige, T., van Arnhem, N., Stokkermans, T. C. A., Eitelberg, G., and Veldhuis L. L. M., "Wingtip-Mounted Propellers: Aerodynamic Analysis of Interaction Effects and Comparison with Conventional Layout," *Journal of Aircraft*, Vol. 56, No. 1, 2019, pp. 295–312. doi:10.2514/1.C034978.

[50] de Vries, R., Hoogreef, M. F. M., and Vos, R., "Aeropropulsive Efficiency Requirements for Turboelectric Transport Aircraft," *AIAA Paper*, 2020. doi:10.2514/6.2020-0502.

[51] Johnson, J. L., and White, E. R., "Exploratory Low-Speed Wind-Tunnel Investigation of Advanced Commuter Configurations Including an Over-the-Wing Propeller Design," *AIAA Paper*, 1983. doi:10.2514/6.1983-2531.

[52] Müller, L., Heinze, W., Kožulović, D., Hepperle, M., and Radespiel, R., "Aerodynamic Installation Effects of an Over-the-Wing Propeller on a High-Lift Configuration," *Journal of Aircraft*, Vol. 51, No. 1, 2014, pp. 249–258. doi:10.2514/1.C032307.

[53] Veldhuis L. L. M., and Khajehzadeh, A., "Analysis and Design of a Wing Trailing Edge Mounted Over-The-Wing Distributed Propeller Propulsion System," *AIAA Paper*, 2019. doi:10.2514/6.2019-3692.

[54] de Vries, R., van Arnhem, N., Avallone, F., Ragni, D., Vos, R., Eitelberg, G., and Veldhuis, L. L. M., "Experimental Investigation of Over-the-Wing Propeller–Boundary-Layer Interaction," *AIAA Journal*, Vol. 59, No. 6, 2021, pp. 2169–2182. doi:10.2514/1.J059770.

[55] Mitchell, G. A., and, Mikkelson, D. C., "Induced Drag Elimination on Subsonic Aircraft," Tech. Rep. AFFDL-TR-66-115, U.S. Air Force, 1966.

[56] Stokkermans, T. C. A., van Arnhem, N., and Veldhuis, L. L. M., "Mitigation of propeller kinetic energy losses with boundary layer ingestion and swirl recovery vanes," *RAeS Applied Aerodynamics Conference*, 2016.

[57] Mark Janus, J., Chatterjee, A., and Cave, C., "Computational Analysis of a Wingtip-Mounted Pusher Turboprop," *Journal of Aircraft*, Vol. 33, No. 2, 2006, pp. 441–444. doi:10.2514/3.46959.

[58] Gearheart, W. S., and Henderson, R. E., "Selection of a Propulsor for a Submersible System," *Journal of Aircraft*, Vol. 3, No. 1, 1966, pp. 84–86. doi:10.2514/3.59270.

[59] Smith, L. H., "Wake Ingestion Propulsion Benefits," *Journal of Propulsion and Power*, Vol. 9, No. 1, 1993, pp. 74–82. doi:10.2514/3.11487.

[60] de Young, J., "Propellers at high incidence," *Journal of Aircraft*, Vol. 23, No. 3, 1965, pp. 241–250. doi:10.2514/3.43646.

[61] Phillips, W. F., Anderson, E. A., Kelly, Q. J., "Predicting the Contribution of Running Propellers to Aircraft Stability Derivatives," *Journal of Aircraft*, Vol. 40, No. 6, 2003, pp. 1107–1114. doi:10.2514/2.7221.

[62] Obert, E., *A Method for the Determination of the Effect of Propeller Slipstream on the Static Longitudinal Stability and Control of Multi-engined Aircraft*, Delft University Press, 1997.

[63] Perkins, C.D., and Hage, R.E., *Airplane Performance, Stability and Control*, John Wiley & Sons, New York, 1949, pp. 231–242, section 5.6.

[64] van der Vaart, J. C., and, Muhammad, H., "Static Longitudinal Stability and Control Characteristics of the Fokker F27 'Friendship' Calculated by Simple Handbook Methods," Tech. Rep. LR-394, Delft University of Technology, 1983.

[65] Eshelby, M. E., "On the Aerodynamics of Installed Propellers," *AGARD Conference Proceedings*, AGARD-CP-366, 1984.

[66] Qin, E., Yang, G., and Li, F., "Numerical Analysis of the Interference Effect of Propeller Slipstream on Aircraft Flowfield," *Journal of Aircraft*, Vol. 35, No. 1, 1998, pp. 84–90. doi:10.2514/2.2263.

[67] Torenbeek, E., *Synthesis of subsonic airplane design*, Delft University Press, 1982. ISBN 90-247-2724-3.

[68] Subramanian, S., and, Mueller, T. J., "An Experimental Study of Propeller Noise Due to Cyclic Flow Distortion," *Journal of Sound and Vibration*, Vol. 183, No. 5, 1995, pp. 907–923. doi:10.1006/jsvi.1995.0295.

[69] Magliozzi, B., "Advanced Turboprop Noise: A Historical Review," *AIAA Paper*, 1984. doi:10.2514/6.1984-2261.

[70] Schulten, J. B. H. M., "Effects of Asymmetric Inflow on Near-Field Propeller Noise," *AIAA Journal*, Vol. 34, No. 2, 1996, pp. 251–258. doi:10.2514/3.13058.

[71] Mitchell, G. A., and, Mikkelson, D. C., "Summary and Recent Results From the NASA Advanced High-Speed Propeller Research Program," Tech. Rep. TM-82891, NASA, 1982.

[72] Chirico, G., Barakos, G. N., and, Bown, N., "Propeller Installation Effects on Turboprop Aircraft Acoustics," *Journal of Sound and Vibration*, Vol. 424, 2018, pp. 238–262. doi:10.1016/j.jsv.2018.03.003.

[73] Brooks, B. M., and, Metzger, F. B., "Acoustic Test and Analysis of Three Advanced Turboprop Models," Tech. Rep. NASA-CR-159667, NASA, 1980.

[74] Unruh, J. F., "Installation effects on propeller wake/vortex-induced structure-borne noise transmissions," *Journal of Aircraft*, Vol. 27, No. 5, 1990, pp. 444–448. doi:10.2514/3.25296.

[75] Loeffler, I. J., "Structureborne Noise Control in Advanced Turboprop Aircraft," *AIAA Paper*, 1987. doi:10.2514/6.1987-530.

[76] Salikuddin, M., Tanna, H. K., Burrin, R. H., and, Carter, W. E., "Application of Active Noise Control to Model Propeller Noise," *AGARD Conference Proceedings*, AGARD-CP-366, 1984.

[77] Revell, J. D., Balena, F. J., and, Koval, L. R., "Analysis of Interior Noise-Control Treatments for High-speed Propeller-Driven Aircraft," *Journal of Aircraft*, Vol. 19, No. 1, 1982, pp. 31–38. doi:10.2514/3.57352.

[78] SenGupta, G., "Reduction of Cabin Noise During Cruise Conditions by Stringer and Frame Damping," *AIAA Journal*, Vol. 17, No. 3, 1979, pp. 229–236. doi:10.2514/3.61106.

[79] Metzger, F. B., "The State of the Art in Prop-Fan and Turboprop Noise," *AGARD Conference Proceedings*, AGARD-CP-366, 1984.

[80] Metzger, F. B., "Measurements and Predictions of Turboprop Noise at High Cruise Speed," *AIAA Paper*, 1983. doi:10.2514/6.1983-689.

[81] Succi, G. P., "Design of Quiet Efficient Propellers," *Society of Automobile Engineers Transactions*, Vol. 88, 1979, pp. 2039–2052.

[82] Jeracki, R., Mikkelson, D., and, Blaha, B., "Wind Tunnel Performance of Four Energy Efficient Propellers Designed for Mach 0.8 Cruise," *Society of Automobile Engineers*, Technical Paper 790573, 1979. doi:10.4271/790573.

[83] Blunt, D., M., "Optimisation and Adaptive Control of Aircraft Propeller Synchrophase Angles," Ph.D. Thesis, The University of Adelaide, Adelaide, Australia, 2012.

[84] Mixson, J. S., Farassat, F., Leatherwood, J. D., Prydz, R., and Revell, J. D., "Interior Noise Considerations for Advanced High-speed Turboprop Aircraft," *Journal of Aircraft*, 1983. doi:10.2514/3.44944.

[85] Renninson, D. C., Wilby, J. F., Marsh, A. H., and, Wilby, E. G., "Interior Noise Control Prediction Study for High-Speed Propeller-Driven Aircraft," Tech. Rep. CR-159200, NASA, 1979.

[86] Boeing Preliminary Design Department, "Energy Consumption Characteristics of Transports Using the Prop-Fan Concept," Tech. Rep. CR-137937, NASA, 1976.

[87] Sullivan, W. E., Turnberg, J. E., and Violette, J. A., "Large-Scale Advanced Prop-Fan Blade Design," Tech. Rep. CR-174790, NASA, 1984.

[88] Berton, J. J., "Empennage Noise Shielding Benefits for an Open Rotor Transport," *AIAA Paper*, 2011. doi:10.2514/6.2011-2764.

[89] Sinnige, T., Ragni, D., Malgoezar, A. M. N., Eitelberg, G., and Veldhuis, L. M. M., "APIAN-INF: an aerodynamic and aeroacoustic investigation of pylon-interaction effects for pusher propellers," *CEAS Aeronautical Journal*, 2017. doi:10.1007/s13272-017-0247-2.

[90] van Arnhem, N., de Vries, R., Sinnige, T., Vos, R., Eitelberg, G., and, Veldhuis, L. L. M., "Engineering Method to Estimate the Blade Loading of Propellers in Nonuniform Flow," *AIAA Journal*, Vol. 58, No. 12, 2020, pp. 5332–5346. doi:10.2514/1.J059485.

[91] Wald, Q. R., "The aerodynamics of propellers," *Progress in Aerospace Sciences*, Vol. 42, No. 2, 2006, pp. 85–128. doi:10.1016/j.paerosci.2006.04.001.

[92] Ortun, B., Boisard, R., and Gonzalez-Martino, I., "In-plane airloads of a propeller with inflow angle: prediction vs. experiment," *AIAA Paper*, 2012. doi:10.2514/6.2012-2778.

[93] Nallasamy, M., and Groeneweg, J. F, "Unsteady Euler Analysis of the Flow Field of a Propfan at an Angle of Attack," Tech. Rep. TM 102426, NASA, 1990.

[94] Sinnige, T., de Vries, R., Della Corte, B., Avallone, F., Ragni, D., Eitelberg, G., and Veldhuis, L. L. M., "Unsteady Pylon Loading Caused by Propeller-Slipstream Impingement for Tip-Mounted Propellers," *Journal of Aircraft*, Vol. 55, No. 4, 2018, pp. 1605–1618. doi:10.2514/1.C034696.

[95] Conway, J. T., "Analytical solutions for the actuator disk with variable radial distribution of load," *Journal of Fluid Mechanics*, Vol. 297, 1995, pp. 327–355. doi: 10.1017/S0022112095003120.

[96] Felli, M., Guj, G., and Camussi, R., "Effect of the number of blades on propeller wake evolution," *Experiments in Fluids*, Vol. 44, 2008, pp. 409–418. doi:10.1007/s00348-007-0385-0.

[97] Widnall, S. E., "The stability of a helical vortex filament," *Journal of Fluid Mechanics*, Vol. 54, No. 4, 1972, pp. 641–663. doi:10.1017/S0022112072000928.

[98] Catalano, F. M., and Stollery, J. L., "The Effect of a High Thrust Pusher Propeller on the Flow over a Straight Wing," *AIAA Paper*, 1993. doi:10.2514/6.1993-3436.

[99] Hapkins, J. P., and Wharton, H. E., "Study of the Cost/Benefit Tradeoffs for Reducing the Energy Consumption of the Commercial Air Transportation System," Tech. Rep. NASA CR-137926, NASA, 1976.

[100] Goldstein, S., "On the Vortex Theory of Screw Propellers," *Proceedings of the Royal Society of London Series A*, Vol. 123, No. 792, 1929, pp. 440—465. doi:10.1098/rspa.1929.0078.

[101] Prandtl, L., "Applications of Modern Hydrodynamics to Aeronautics," Tech. Rep. TR-116, NACA, 1921.

[102] Betz, A., " Schraubenpropeller mit geringstem Energieverlust–Mit einem Zusatz von L. Prandtl," *Nachrichten d. K. Gesellschaft d. Wissenschaften*, 1919, pp. 193–217.

[103] Drela, M., "Power Balance in Aerodynamic Flows," *AIAA Journal*, Vol. 47, No. 7, 2009, pp. 1761–1771. doi:10.2514/1.42409.

[104] Higgins, R. J., Barakos, G. N., Jinks, E., and Bown, N., "A Propeller Blade Design for Experimental Stall Flutter Investigations," *47rd European Rotorcraft Forum*, 2021.

[105] Traub, L. W., "Simplified propeller analysis and design including effects of stall," *The Aeronautical Journal*, Vol. 120, No. 1227, 2016, pp. 796–818. doi:10.1017/aer.2016.31.

[106] Snel, H., Houwink, R., and Piers, W.J., "Sectional Prediction of 3D Effects for Separated Flow on rotating blades," *18th European Rotorcraft Forum*, 1992.

[107] Page, V., Dickinson, S. O., and Deckert, W. H., "Large-Scale Wind-Tunnel Tests of a Deflected Slipstream STOL Model with Wings of Various Aspect Ratios," Tech. Rep. TN D–4448, NASA, 1968.

[108] Beck, N., "Experiments on Propeller Influence on a Wing with Active High Lift," Ph.D. Thesis, TU Braunschweig, Braunschweig, Germany, 2017.

[109] Stokkermans, T. C. A., "Aerodynamics of Propellers in Interaction Dominated Flowfields: An Application to Novel Aerospace Vehicles," Ph.D. Thesis, Delft University of Technology, Delft, The Netherlands, 2020. doi:10.4233/uuid: 46178824-bb80-4247-83f1-dc8a9ca7d8e3.

[110] Howard, R. M., Miley, S. J., and Holmes, B. J., "An Investigation of the Effects of the Propeller Slipstream on a Laminar Wing Boundary Layer," *SAE Transactions*, Vol. 94, No. 4, 1985, pp. 474–485.

[111] von Karman, T. and Sears, W. R., "Airfoil Theory for Non-Uniform Motion," *Journal of Aeronautical Sciences*, Vol. 5, No. 10, 1938, pp. 379–390. doi:10.2514/8.674.

[112] Sears, W. R., "Some Aspects of Non-Stationary Airfoil Theory and Its Practical Application," *Journal of the Aeronautical Sciences*, Vol. 8, No. 3, 1941, pp. 104–108. doi:10.2514/8.10655.

[113] Ruiz-Calavera, L. P., and Perdones-Diaz, D., "CFD computation of in-plane propeller shaft loads," *AIAA Paper*, 2013. doi:10.2514/6.2013-3798.

[114] Tenerowicz, T., "Flow Behind Single-and Dual-Rotation Propellers at Angle of Attack," *AIAA Paper*, 1987. doi:10.2514/6.1987-1750.

[115] Bass, R. M., "Small Scale Wind Tunnel Testing of Model Propellers," *AIAA Paper*, 1986. doi:10.2514/6.1986-392.

[116] Sinnige, T., "Aerodynamic and Aeroacoustic Interaction Effects for Tip-Mounted Propellers: An Experimental Study," Ph.D. Thesis, Delft University of Technology, Delft, The Netherlands, 2018.

[117] Stack, J., Draley, E. C., Delano, J. B., and Feldman, L., "Investigation of the NACA 4-(3)(08)-03 and NACA 4-(3)(08)-45 two-blade propellers at forward mach numbers of 0.725 to determine the effects of compressibility and solidity on performance," Tech. Rep. TR-999, NACA, 1950.

[118] van Arnhem, N., Vos, R., and Veldhuis, L. L. M., "Aerodynamic Loads on an Aft-Mounted Propeller Induced by the Wing," *AIAA Paper*, 2019. doi:10.2514/6. 2019-1093.

[119] van Arnhem, N., de Vries, R., Sinnige, T., Vos, R., and Veldhuis L. L. M., "Aerodynamic Performance and Static Stability Characteristics of Aircraft with Tail-Mounted Propellers," *Journal of Aircraft*, 2021. doi:10.2514/1.C036338.

[120] van Arnhem, N., Sinnige, T., Stokkermans, T. C. A., Eitelberg, G., and Veldhuis, L. L. M., "Aerodynamic Interaction Effects of Tip-Mounted Propellers Installed on the Horizontal Tailplane," *AIAA Paper*, 2018. doi:10.2514/6.2018-2052.

[121] Li, Q., "Towards Optimum Swirl Recovery Vanes for Propeller Propulsion Systems," Ph.D. Thesis, Delft University of Technology, Delft, The Netherlands, 2019.

[122] de Vries, R., "Hybrid-Electric Aircraft with Over-the-Wing Distributed Propulsion: Aerodynamic Performance and Conceptual Design," Ph.D. Thesis, Delft University of Technology, Delft, The Netherlands, 2021.

[123] Taverna, F., "Advanced airfoil design for general aviation propellers," *Journal of Aircraft*, Vol. 21, No. 9, 1984, pp. 649–657. doi:10.2514/3.45010.

[124] Ragni, D., "PIV-based load determination in aircraft propellers," Ph.D. Thesis, Delft University of Technology, Delft, The Netherlands, 2012.

[125] Chu, S., Linton, D., Verstraete, D., and Thornber, B., "Aerodynamic Analysis of Multi-Propeller/Wing Interaction using the Actuator Surface Model," *AIAA Paper*, 2021. doi:10.2514/6.2021-1661.

[126] Serpieri, J., "Cross-Flow Instability: Flow diagnostics and control of swept wing boundary layers," Ph.D. Thesis, Delft University of Technology, Delft, The Netherlands, 2018.

[127] Veldhuis, L. L. M., "Ijking weegsysteem," Tech. Rep. LSW 88-12, TUDelft, 1988.

[128] Molenwijk, L., and Bernardi, S., "Korte kalibratie van de balansen van de LTT windtunnel," Tech. rep., TUDelft, 2008.

[129] Gracey, W., Letko, W., and Russel, W. R., "Wind-Tunnel Investigation of a Number of Total-Pressure Tubes at High Angles of Attack," Tech. Rep. TN 2331, NACA, 1951.

[130] Ewald, B., "Wind Tunnel Wall Corrections," Tech. Rep. AGARD-AG-336, Advisory Group for Aerospace Research and Development, 1998.

[131] Coe, Jr., P., Applin, Z., and, Williams, L., "Stability and Control Results for Advanced Turboprop Aft-Mount Installations," *SAE Paper*, 1984. doi:10.4271/841479.

[132] Nicolosi, F., Corcione, S., Della Vecchia, P., Trifari, V., and, Ruocco, M., "Aerodynamic Design and Analysis of an Innovative Regional Turboprop Configuration," *31st Congress of the International Council of the Aeronautical Sciences*, 2018.

[133] Stokkermans, T. C. A., van Arnhem, N., Sinnige, T. and Veldhuis, L. L. M., "Validation and Comparison of RANS Propeller Modeling Methods for Tip-Mounted Applications," *AIAA Journal*, Vol. 57, No. 2, 2019, pp. 566–580. doi:10.2514/1.J057398.

[134] Hoerner, S.F., *Interference Drag*, Hoerner Fluid Dynamics, 1965.

[135] Tripp, J. S., and Tcheng, P., "First International Symposium on Strain Gauge Balances," Tech. Rep. CP-1999-209101/PT2, NASA, 1999.

[136] Hufnagel, K., and Quade, M., "The 2nd Generation Balance Calibration Machine of Darmstadt University of Technology," *AIAA Paper*, 2007. doi:10.2514/6.2007-148.

[137] Hanson, D. B., and, Magliozzi, B., "Propagation of Propeller Tone Noise Through a Fuselage Boundary Layer," *Journal of Aircraft*, Vol. 22, No. 1, 1985, pp. 63–70. doi:10.2514/3.45081.

[138] Catalano, F. M., "On the Effects of an Installed Propeller Slipstream on Wing Aerodynamic Characteristics," *Acta Polytechnica*, Vol. 44, No. 3, 2004, pp. 8–14. doi: 10.14311/562.

[139] ANSYS® Academic Research Release 18.1, "Help System, Fluent," ANSYS, Inc.

[140] Kundu, P. K., Cohen, I. M., and Dowling, D. R., *Fluid Mechanics*, 6th ed., Elsevier Academic Press, 1997.

[141] Wilcox, D. C., *Turbulence Modeling for CFD*, 3rd ed., DCW Industries, 2006.

[142] Bardina, J. E., Huang, P. G., and Coakley, T. J., "Turbulence Modeling Validation, Testing, and Development," Tech. Rep. TR-110446, NASA, 1997. doi:DOI:10.21236/adb072483.

[143] Meheut, M., "Thrust and Torque Far-Field Analysis of Propeller and Counter Rotating Open Rotor Configurations," *AIAA Paper*, 2013. doi:10.2514/6.2013-2803.

[144] Stürmer, A. W., "Unsteady CFD Simulations of Propeller Installation Effects," *AIAA Paper*, 2006. doi:10.2514/6.2006-4969.

[145] Falissard, F., Boisard, R., and Delattre, G., "Aeroacoustic Computation of a Contra Rotating Open Rotor Model with Test Rig Installation Effects," *AIAA Paper*, 2012. doi:10.2514/6.2013-2803.

[146] Stürmer, A., and Yin, J., "The Case for Counter-Rotation of Installed Contra-Rotating Open Rotor Propulsion Systems," *AIAA Paper*, 2012. doi:10.2514/6.2012-2785.

[147] Spalart, P. R., and Allmaras, S. R., "A one-equation turbulence model for aerodynamic flows," *AIAA Paper*, 1992. doi:10.2514/6.1992-439.

[148] Roosenboom, E. W. M., Stürmer, Schröder, "Advanced Experimental and Numerical Validation and Analysis of Propeller Slipstream Flows," *Journal of Aircraft*, Vol. 47, No. 1, 2010, pp. 284—291. doi:10.2514/1.45961.

[149] Yin, J., Stürmer, A., and, and Aversano, M. , "Aerodynamic and Aeroacoustic Analysis of Installed Pusher-Propeller Aircraft Configurations," *Journal of Aircraft*, Vol. 49, No. 5, 2012, pp. 1423—-1433. doi:10.2514/1.C031704.

[150] Béchet, S., Negulescu, C. A., Chapin, V., and Simon, F., "Integration of CFD Tools in Aerodynamic Design of Contra-Rotating Propeller Blades," *CEAS Air and Space Conference*, 2011.

[151] Márquez, C. O., Stürmer, A., Clemen, C., Grimminger, A., "Validation of Actuator Disk Simulations of CROR Propulsion Systems at Low-Speed Flight Conditions," *AIAA Paper*, 2012. doi:10.2514/6.2012-2787.

[152] Dacles-Mariani, J. Zilliac, G. G., Chow, J. S., and Bradshaw, P., "Numerical/Experimental Study of a Wingtip Vortex in the near Field," *AIAA Journal*, Vol. 33, No. 9, 1995, pp. 1561—-1568. doi:10.2514/3.12826.

[153] Spalart, P. R., and Rumsey, C. L., "Effective Inflow Conditions for Turbulence Models in Aerodynamic Calculations," *AIAA Journal*, Vol. 45, No. 10, 2007, pp. 2544–2553. doi:10.2514/1.29373.

[154] Morgado, J., Abdollahzadeh, M., Silvestre,M. A. R., and Páscoa, J. C., "High Altitude Propeller Design and Analysis," *Aerospace Science and Technology*, Vol. 45, 2015, pp. 398—-407. doi:10.1016/j.ast.2015.06.011.

[155] Francois, B., Costes, M., and Dufour, G., "Comparison of Chimera and Sliding Mesh Techniques for Unsteady Simulations of Counter Rotating Open-Rotors," *20th ISABE Conference*, 2011.

[156] Mark Janus, J., "General Aviation Propeller–Airframe Integration Simulations," *Journal of Aircraft*, Vol. 43, No. 2, 2006, pp. 390–394. doi:10.2514/1.15354.

[157] Baruzzi, G. S., Aliaga, C. N., Ozcer, I. A., Stokes, J., Svihla, K., and Saxena, S., "Numerical Simulation of an Integrated Propeller with Models of Progressively Increasing Fidelity," *AIAA Paper*, 2020. doi:10.2514/6.2020-2682.

[158] Aref, P., Ghoreyshi, M., Jirasek, A., Satchell, M. J., and Bergeron, K., "Computational Study of Propeller–Wing Aerodynamic Interaction," *Aerospace*, Vol. 5, No. 79, 2018. doi:10.3390/aerospace5030079.

[159] Steijl, R., and Barakos, G., "Sliding Mesh Algorithm for CFD Analysis of Helicopter Rotor–Fuselage Aerodynamics," *International Journal for Numerical Methods in Fluids*, Vol. 58, 2008, pp. 527–549. doi:abs/10.1002/fld.1757.

[160] Waller, G., "CFD Prediction of stability derivatives of a turboprop aircraft using a Cartesian grid based Euler code," *ICAS 2002*, 2002.

[161] de Vries, R., van Arnhem, N., Sinnige, T., Vos, R., and, Veldhuis, L. L. M., "Aerodynamic Interaction Between Propellers of a Distributed-Propulsion System in Forward Flight," *Aerospace Science and Technology*, Vol. 118, 2021. doi:10.1016/j.ast. 2021.107009.

[162] Little, B. H., Poland, D. T., Bartel, H. W., and Withers, C. C., "Propfan Test Assessment (PTA) Final Project Report," Tech. Rep. CR 185138, NASA, 1989.

[163] Roache, P. J., "Quantification of Uncertainty in Computational Fluid Dynamics," *Annual Review of Fluid Mechanics*, Vol. 29, No. 1, 1997, pp. 123–160. doi:10.1146/ annurev.fluid.29.1.123.

[164] Eça, L., and Hoekstra, M., "Discretization Uncertainty Estimation Based on a Least Squares Version of the Grid Convergence Index," *Proceedings of the Second Workshop on CFD Uncertainty Analysis*, 2006.

[165] Leweke, T., Le Dizés, S., and, Williamson, C.H.K., "Dynamics and Instabilities of Vortex Pairs," *Annual Review of Fluid Mechanics*, Vol. 48, 2016, pp. 507–541. doi: 10.1146/annurev-fluid-122414-034558.

[166] Ekaterinaris, J. A., "High-Order Accurate, Low Numerical Diffusion Methods for Aerodynamics," *Annual Review of Fluid Mechanics*, Vol. 41, No. 3–4, 2005, pp. 192–200. doi:10.1016/j.paerosci.2005.03.003.

[167] McCutchen, C. W., "A Theorem on Swirl Loss in Propeller Wakes," *Journal of Aircraft*, Vol. 22, No. 4, 1985, pp. 344—-346. doi:10.2514/3.45131.

[168] Drela, M., *XFOIL: An Analysis and Design System for Low Reynolds Number Airfoils*, Springer, Berlin, Heidelberg, 1989. doi:10.1007/978-3-642-84010-4_1, mueller T.J. (eds) Low Reynolds Number Aerodynamics. Lecture Notes in Engineering, Vol. 54.

[169] Winslow, J., Otsuka, H., Govindarajan, B., and Chopra, I., "Basic Understanding of Airfoil Characteristics at Low Reynolds Numbers (10^4–10^5)," *Journal of Aircraft*, Vol. 55, No. 3, 2018, pp. 1050–1061. doi:10.2514/1.C034415.

[170] Schlichting, H., *Boundary-Layer Theory*, McGraw-Hill, 1960.

[171] Schülein, E., Rosemann, H., and Schaber, S., "Transition Detection and Skin Friction Measurements on Rotating Propeller Blades," *AIAA Paper*, 2012. doi:10.2514/6.2012-3202.

[172] Jing, Z., and Ducoin, A., "Direct numerical simulation and stability analysis of the transitional boundary layer on a marine propeller blade," *Physics of Fluids*, Vol. 32, No. 12, 2020. doi:10.1063/5.0030070.

[173] van Rooyen, R. S., and Eshelby, M. E., "Assessment of propeller influence on lateral-directional stability of multiengine aircraft," *Journal of Aircraft*, Vol. 18, No. 5, 1981, pp. 364–371. doi:10.2514/3.44710.

[174] Felli, M., "Underlying mechanisms of propeller wake interaction with a wing," *Journal of Fluid Mechanics*, Vol. 908, No. A10, 2020. doi:10.1017/jfm.2020.792.

[175] Boctor, M.L., Clay, C.W. and Watson, C.F., "An Analysis of Prop-Fan Airframe Aerodynamic Integration," Tech. Rep. CR 152186, NASA, 1978.

[176] Ragni, D., van Oudheusden, B. W., and Scarano, F., "Stereoscopic Particle Image Velocimetry-Based Integral Load Determination on an Aircraft Propeller," *Journal of Aircraft*, Vol. 49, No. 5, 2012, pp. 1497–1506. doi:10.2514/1.C031853.

[177] Schetz, J. A., Mallory D. A., and Pelletier, D., "Numerical and Experimental Investigation of a Propeller Flowfield With a 3-D Non-Uniform Inflow," *AIAA Paper*, 1987. doi:10.2514/6.1987-607.

[178] Schulten, J. B. H. M., "Advanced Propeller Performance Calculation by a Lifting Surface Method," *Journal of Propulsion and Power*, Vol. 12, No. 3, 1996, pp. 477–485. doi:10.2514/3.24060.

[179] Hanson, D. B., "Compressible lifting surface theory for propeller performance calculation," *Journal of Aircraft*, Vol. 22, No. 1, 1985, pp. 19–27. doi:10.2514/3.45075.

[180] Gur, O. and Rosen, A., "Comparison between blade-element models of propellers," *The Aeronautical Journal*, Vol. 112, No. 1138, 2008, pp. 689–704. doi:10.1017/S0001924000002669.

[181] "Prediction of near-field and far-fieldharmonic noise from subsonic propellers with non-axial inflow," Tech. Rep. ESDU 11005, Engineering Sciences Data Unit, 2018.

[182] Finck, R., "USAF (United States Air Force) Stability and Control DATCOM (Data Compendium)," Tech. rep., McDonnell Aircraft, 1978. doi:doi:10.21236/adb072483.

[183] Whitfield, D. L., Swafford, T. W., Janus, J. M., Mulac, R.A., and Belk, D. M., "Three Dimensional Unsteady Euler Solutions for Propfans and Counter-Rotating Prop-fans," *AIAA Paper*, 1987. doi:10.2514/6.1987-1197.

[184] Allen, C. S., and Korkan, K. D., "Influence of a Non-Uniform Free Stream Velocity Distribution on Performance/Acoustics of Counterrotating Propeller Configurations," *AIAA Paper*, 1991. doi:10.2514/6.1991-195.

[185] Martinez, R., "Predictions of Wing and Pylon Forces Caused by Propeller Installation," Tech. Rep. CR-178298, NASA, 1987.

[186] Amiet, R. K., "Compressibility Effects in Unsteady Thin-Airfoil Theory," *AIAA Journal*, Vol. 12, No. 2, 1974, pp. 252–255. doi:10.2514/3.49212.

[187] Gérard, A., Berry, A., Masson, P., and Gervais, Y., "Evaluation of Tonal Aeroacoustic Sources in Subsonic Fans Using Inverse Models," *AIAA Journal*, Vol. 45, No. 1, 2007, pp. 98–109. doi:10.2514/1.21957.

[188] McCune, J. E., "Unsteady Wing Theory - The Kármán/Sears Legacy," *1st National Fluid Dynamics Conference*, 1988. doi:10.2514/6.1988-3539.

[189] Simpson, R. J. S., Palacios, R., and Murua, J., "Induced-Drag Calculations in the Unsteady Vortex Lattice Method," *AIAA Journal*, Vol. 51, No. 7, 2013, pp. 1775–1779. doi:10.2514/1.J052136.

[190] Stokkermans, T. C. A., Nootebos, S., and Veldhuis L. L. M., "Analysis and Design of a Small-Scale Wingtip-Mounted Pusher Propeller," *AIAA Paper*, 2019. doi:10.2514/6.2019-3693.

[191] Nallasamy, M., "Unsteady Blade Pressures on a Propfan: Predicted and Measured Compressibility Effects," *AIAA Paper*, 1992. doi:10.2514/6.1992-3774.

[192] Heidelberg, L. J., Nallasamy, M., "Unsteady Blade Pressure Measurements for the SR-7A Propeller at Cruise Conditions," *AIAA Paper*, 1990. doi:10.2514/6.1990-4022.

[193] Anand, N., "Progress in CFD-based Automated Design with Application to Unconventional Turbomachines," Ph.D. Thesis, Delft University of Technology, Delft, The Netherlands, 2021.

[194] Applin, Z. T., and Coe, P. L., Jr, "Low-Speed Stability and Control Characteristics of a Transport Model with Aft-Fuselage-Mounted Advanced Turboprops," Tech. Rep. NT-2535, NASA, 1986.

[195] Draper, J. W., and Kuhn, R. E., "Investigation of the aerodynamic characteristics of a model wing-propeller combination and of the wing and propeller separately at angles of attack up to 90 degrees," Tech. Rep. TN 3304, NACA, 1954.

[196] Bencze, D. P., Smith, R. C., Welge, H. R., and Crowder, J. P., "Predictions of Wing and Pylon Forces Caused by Propeller Installation," Tech. Rep. 780997, SAE, 1978. doi:10.4271/780997.

[197] Bousquet, J. -M., and Gardarein, P., "Improvements on computations of high speed propeller unsteady aerodynamics," *Aerospace Science and Technology*, Vol. 7, 2003, pp. 465–472. doi:10.1016/S1270-9638(03)00046-4.

[198] Yaggy, P. F., "A Method for Predicting the Upwash Angles Induced at the Propeller Plane of a Combination of Bodies with an Unswept Wing," Tech. Rep. TN 2528, NACA, 1951.

[199] "Airframe-induced upwash at subsonic speeds ," Tech. Rep. ESDU 90020, Engineering Sciences Data Unit, 2009.

[200] Custers, l. G. M., "Propeller-Wing Interference Effects at Low Speed Conditions," Tech. Rep. TP 96312, NLR, 1996.

[201] Lv, P., Rao, A. G, Ragni, D., and Veldhuis L. L. M., "Performance Analysis of Wake and Boundary-Layer Ingestion for Aircraft Design," *Journal of Aircraft*, Vol. 53, No. 5, 2016, pp. 1517–1526. doi:10.2514/1.C033395.

[202] Veldhuis, L. L. M., van Berkel, E., Kotsonis, M., and Eitelberg, G., "Non-Uniform Inflow Effects on Propeller Performance," *AIAA Paper*, 2013. doi:10.2514/6.2013-2801.

[203] Stokkermans, T. C. A., Voskuijl, M., Veldhuis, L. L. M., Soemarwoto, B., Fukari, R., and Eglin, P., "Aerodynamic Installation Effects of Lateral Rotors on a Novel Compound Helicopter Configuration," *AHS Forum*, 2018.

[204] Yang, Y., Zhou, T., Sciacchitano, A., Veldhuis, L., and Eitelberg, G., "Propeller and inflow vortex interaction: vortex response and impact on the propeller performance," *CEAS Aeronautical Journal*, Vol. 7, No. 3, 2016, pp. 419–428. doi:10.1007/s13272-016-0198-z.

[205] Sinnige, T., Ragni, D., Eitelberg, G., and Veldhuis, L. M. M., "Mitigation of Pusher-Propeller Installation Effects by Pylon Trailing-Edge Blowing," *Journal of Aircraft*, Vol. 54, No. 1, 2017, pp. 292–300. doi:10.2514/1.C034000.

[206] Block, P. J. W. and Gentry, Jr., G. L., "Directivity and Trends of Noise Generated by a Propeller in a Wake," Tech. Rep. TP 2609, NASA, 1986.

[207] Bushnell, P., Gruber, M., and Parzyck, D., "Measurement of Unsteady Blade Surface Pressures on a Single Rotation Large-Scale Advanced Propfan with Angular and Wake Inflow at Mach Numbers from 0.02 to 0.70," Tech. Rep. CR 182123, NASA, 1988.

[208] Neuwerth, G., Lölgen, T., and Staufenbiel, R., "Increased noise emission of propellers and propfans due to pusher installation," *17th ICAS Congress Proceedings*, Vol. 1, 1990, pp. 127–138.

[209] Geiselhart, K. A., Daggett, D. L., Kawai, R., and Friedman, D., "Blended Wing Body System Studies: Boundary Layer Ingestion Inlets with Active Flow Control," Tech. Rep. CR-2003-212670, NASA, 2003.

[210] Guo, Y., and Thomas, R. H., "System Noise Assessment of Hybrid Wing–Body Aircraft with Open-Rotor Propulsion," *Journal of Aircraft*, Vol. 52, No. 6, 2015, pp. 1767–1779. doi:10.2514/1.C033048.

[211] van Arnhem, N., "Design and Analysis of an Installed Pusher Propeller with Boundary Layer Inflow," MSc. Thesis 047-15-MT-FPP, Delft, The Netherlands, 2015.

[212] Caralano, F. M., and Maunsell, M. G., "Numerical and experimental analysis of the effect of a pusher propeller on a wing and body," *AIAA Paper 97-0038*, 1997. doi:10.2514/6.1997-38.

[213] Yoon, S. S., and Heister, S. D., "Analytical formulas for the velocity field induced by an infinitely thin vortex ring," *International Journal for Numerical Methods in Fluids*, Vol. 44, 2004.

[214] Rogallo, V. L., "Effects of Wing Sweep on the Upwash at the Propeller Planes of Multi Engine Airplanes," Tech. Rep. NACA TN 2795, NACA, 1952.

[215] Roberts, J. C., and Yaggy, P. F., "A Survey of the Flow at the Plane of the Propeller of a Twin-Engine Airplane," Tech. Rep. NACA TN 2192, NACA, 1950.

[216] Howe, D., and Rorie, G., *Aircraft conceptual design synthesis*, Professional Engineering Publishing London, UK, 2000.

[217] Kundu, A. K., *Aircraft design*, Vol. 27, Cambridge University Press, 2010.

[218] Raymer, D., *Aircraft design: a conceptual approach*, American Institute of Aeronautics and Astronautics, Inc., 2012.

[219] Roskam, J., *Airplane Design: Preliminary configuration design and integration of the propulsion system*, DARcorporation, 1985.

[220] Schaufele, R. D., *The elements of aircraft preliminary design*, Aries Publications Santa Anna, CA, 2000.

[221] Rogallo, V. L., Roberts, J. C., and Oldaker, M. R., "Vibratory Stresses in Propellers Operating in the Flow Field of a Wing-Nacelle-Fuselage Combination," Tech. Rep. NACA TN 1951, NACA, 1951.

[222] Wojno, J. P., Mueller, T. J., and, Blake, W. K., "Turbulence Ingestion Noise, Part 2: Rotor Aeroacoustic Response to Grid-Generated Turbulence," *AIAA Journal*, Vol. 40, No. 1, 2002, pp. 26–32. doi:10.2514/2.1637.

[223] Moore, K. R., and Ning, A., "Takeoff and Performance Trade-Offs of Retrofit Distributed Electric Propulsion for Urban Transport," *Journal of Aircraft*, Vol. 56, No. 5, 2019, pp. 1880–1892. doi:10.2514/1.C035321.

[224] Stokkermans, T. C. A., Usai, D., Sinnige, T., and Veldhuis, L. L. M., "Aerodynamic Interaction Effects Between Propellers in Typical eVTOL Vehicle Configurations," *Journal of Aircraft*, Vol. 58, No. 4, 2021, pp. 815–833. doi:10.2514/1.C035814.

[225] Harris, F. D., "Technical Note: Twin Rotor Hover Performance," *Journal of the American Helicopter Society*, Vol. 44, No. 1, 1999, pp. 34–37. doi:10.4050/JAHS. 44.34.

[226] Ramasamy, M., "Hover Performance Measurements Toward Understanding Aerodynamic Interference in Coaxial, Tandem, and Tilt Rotors," *Journal of the American Helicopter Society*, Vol. 60, No. 3, 2015, pp. 1–17. doi:10.4050/JAHS.60.032005.

[227] Alvarez, E. J., and Ning, A., "High-Fidelity Modeling of Multirotor Aerodynamic Interactions for Aircraft Design," *AIAA Journal*, Vol. 58, No. 10, 2020, pp. 4385–4400. doi:10.2514/1.J059178.

[228] Ffowcs Williams, J. E., and Hawkings, D. L., "Sound generation by turbulence and surfaces in arbitrary motion," *Philosophical Transactions of the Royal Society*, Vol. 264, No. 1151, 1969, p. 321–542. doi:10.1098/rsta.1969.0031.

[229] Ridder, S.-O., "Wind Tunnel of a Twin, Rear Propeller Transport Aircraft Configuration at Low Speeds," 14th *ICAS Congress*, Vol. 2, 1984, pp. 644–654.

[230] "Three-Dimensional Interactions and Vortical Flows with Emphasis on High Speeds," Tech. Rep. AGARD-AG-252, AGARD, 1980.

[231] Gand, F., Monnier, J.-C., Deluc, J.-M., and, Choffat, A., "Experimental Study of the Corner Flow Separationon a Simplified Junction," *AIAA Journal*, Vol. 53, No. 10, 2015, pp. 2869–2877. doi:10.2514/1.J053771.

[232] Surana, A., Grunberg, O., and Haller, G., "Exact theory of three-dimensional flow separation. Part 1. Steady separation," *Journal of Fluid Mechanics*, Vol. 564, 2006, pp. 57–103. doi:10.1017/S0022112006001200.

[233] Hubbard, H. H., "Aeroacoustics of Flight Vehicles: Theory and Practice. Volume 1: Noise Sources," Tech. Rep. NASA TR 90-3052, NASA, 1991.

[234] Willis, C. M., Mayes, W. H., and, Daniels, E. F., "Effects of Propeller Rotation Direction on Airplane Interior Noise Level," Tech. Rep. TP-2444, NASA, 1985.

[235] Smith, A. M. O., and Roberts, H. E., "The Jet Airplane Utilizing Boundary Layer Air for Propulsion," *Journal of the Aeronautical Sciences*, Vol. 14, No. 2, 1947, pp. 97—-109. doi:10.2514/8.1273.

[236] Kim, H. D., and Felder, J. L., "Control Volume Analysis of Boundary Layer Ingestion Propulsion Systems With or Without Shock Wave Ahead of the Inlet," *AIAA Paper*, 2011. doi:10.2514/6.2011-222.

[237] Atinault, O., Carrier, G., Grenon, R., Verbecke, C., and Viscat, P., "Numerical and Experimental Aerodynamic Investigations of Boundary Layer Ingestion for Improving Propulsion Efficiency of Future Air Transport," *AIAA Paper*, 2013. doi:10.2514/6.2013-2406.

[238] Stüper, J., "Effect of Propeller Slipstream on Wing and Tail," Tech. Rep. TM-874, NACA, 1938.

[239] Ting, L., Lui, C. H., and Kleinstein, G., "Interference of Wing and Multipropellers," *AIAA Journal*, Vol. 10, No. 7, 1972, pp. 906–914. doi:10.2514/3.50244.

[240] Keller, D., and Rudnik, R., "Investigation and Improvement of Directional Stability and Control of a Propeller-Driven STOL Aircraft," *CEAS Aeronautical Journal*, Vol. 10, 2019, pp. 909–924. doi:10.1007/s13272-019-00363-8.

[241] Rauleder, J., and Leishman, J. G., "Particle–fluid interactions in rotor-generated vortex flows," *Experiments in Fluids*, Vol. 55, No. 1689, 2014. doi:10.1007/s00348-014-1689-5.

[242] Cole, J. A. , Krebs, T., Barcelos, D., and Bramesfeld, G., "Influence of Propeller Location, Diameter, and Rotation Direction on Aerodynamic Efficiency," *Journal of Aircraft*, Vol. 58, No. 1, 2020, pp. 63–71. doi:10.2514/1.C035917.

[243] Colisk, A. T., "A Theory of Vortex-Surface Collisions," *AIAA Paper*, 1998. doi:10.2514/6.1998-2858.

[244] Obert, E., "The Effect of Propeller Slipstream on the Longitudinal Characteristics of a Model of the Saab 2000," Tech. rep., Fokker Report H-0-104, Appendix XXII, 2016.

[245] Sinnige, T., Stokkermans, T. C. A., Ragni, D., Eitelberg, G., and Veldhuis L. L. M., "Aerodynamic and Aeroacoustic Performance of a Propeller Propulsion System with Swirl-Recovery Vanes," *Journal of Propulsion and Power*, Vol. 34, No. 6, 2018, pp. 4719–4729. doi:10.2514/1.B36877.

[246] Li, Q., Öztürk, K., Sinnige, T., Ragni, D., Eitelberg, G., Veldhuis L. L. M., and Wang, Y., "Design and Experimental Validation of Swirl-Recovery Vanes for Propeller Propulsion Systems," *AIAA Journal*, Vol. 56, No. 12, 2018, pp. 4719–4729. doi:10.2514/1.J057113.

[247] Kleinstein, G., and Lui, C. H., "Application of Airfoil Theory for Nonuniform Slipstream Wing Propeller Interaction," *Journal of Aircraft*, Vol. 9, No. 2, 1972, pp. 137–142. doi:10.2514/3.44327.

[248] Thom, A., and Duraisamy, K., "Computational Investigation of Unsteadiness in Propeller Wake–Wing Interactions," *Journal of Aircraft*, Vol. 50, No. 13, 2013, pp. 985—988. doi:10.2514/1.C031866.

[249] Johnston, R. T. and Sullivan, J. P., "Unsteady wing surface pressures in the wake of a propeller," *Journal of Aircraft*, Vol. 30, No. 5, 1993, pp. 644–651. doi:10.2514/3.46393.

[250] Samuelsson, I., "Low speed wind tunnel investigation of propeller slipstream aerodynamic effects on different nacelle/wing combinations," Tech. Rep. FFA TN 1990-24, Flygtekniska Försöksanstalten, 1990.

[251] Schroijen, M. J. T., Veldhuis, L. L. M., Slingerland, R., "Propeller Empennage Interaction Effects on Vertical Tail Design of Multiengine Aircraft," *Journal of Aircraft*, Vol. 47, No. 4, 2010, pp. 1133–1140. doi:10.2514/1.46707.

[252] Ljunggren, S., Samuelsson, I. and Widig, K., "Slipstream-induced pressure fluctuations on a wing panel," *Journal of Aircraft*, Vol. 26, No. 10, 1989, pp. 914–919. doi:10.2514/3.45861.

[253] Chiaramonte, J. Y., Favier, D., Maresca, C., and Benneceur, S., "Aerodynamic Interaction Study of the Propeller/Wing Under Different Flow Configurations," *Journal of Aircraft*, Vol. 33, No. 1, 1996, pp. 46—53. doi:10.2514/3.46901.

[254] Icke, R. O., and Baysal, O., "Wing-Tip Mounted Propeller: Analysis and Adjoint Sensitivities of Noise Generation and Propagation," *AIAA Paper*, 2021. doi:10.2514/6.2021-2283.

[255] Zhou, B. Y., Morelli, M., Guardone, A., Dehpanah, P., and Gauger, N. R., "Aeroacoustic Analysis of a Wing-Tip Mounted Propeller Configuration," *AIAA Paper*, 2021. doi:10.2514/6.2021-2224.

[256] Sinnige, T., Della Corte, B., de Vries, R., Avallone, F., Merino-Martínez, Eitelberg, G., and Veldhuis L. L. M., "Alleviation of Propeller-Slipstream-Induced Unsteady Pylon Loading by a Flow-Permeable Leading Edge," *Journal of Aircraft*, Vol. 56, No. 3, 2019, pp. 1214–1230. doi:10.2514/1.C035250.

[257] Tinetti, A. F., Kelly, J. J., Bauer, S. X. S., and Thomas, R. H., "On the Use of Surface Porosity to Reduce Unsteady Lift," *AIAA Paper*, 2001. doi:10.2514/6.2001-2921.

[258] Lee, S., "Reduction of Blade-Vortex Interaction Noise Through Porous Leading Edge," *AIAA Journal*, Vol. 32, No. 3, 1994, pp. 480—488. doi:10.2514/3.12011.

[259] Favier, D., Ettaouil, A., and Maresca, C., "Numerical and Experimental Investigation of Isolated Propeller Wakes in Axial Flight," *Journal of Aircraft*, Vol. 26, No. 9, 1989, pp. 837–846. doi:10.2514/3.45849.

[260] Negulescu, C. A., "Airbus AI-PX7 CROR Design Features and Aerodynamics," *SAE International Journal of Aerospace*, Vol. 6, No. 2, 2013, pp. 626–642. doi:10.4271/2013-01-2245.

[261] Küchemann, D., and Weber, J., "5 - An Analysis of Some Performance Aspects of Various Types of Aircraft Designed to Fly Over Different Ranges at Different Speeds," *Progress in Aeronautical Sciences*, Vol. 9, 1968, pp. 329–456. doi:10.1016/B978-1-4831-9985-6.50008-4.

[262] Dorsey, A. M., and Uranga, A., "Design Space Exploration of Future Open Rotor Configurations," *AIAA Paper*, 2020. doi:10.2514/6.2020-3680.

[263] Nicolosi, F., Corcione, S., Trifari, V., Cusati, V., Ruocco, R., and Della Vecchia, P., "Performance evaluation and DOC Estimation of an Innovative Turboprop Configuration," *AIAA Paper*, 2018. doi:10.2514/6.2018-3662.

[264] Nicolosi, F., Corcione, S., Trifari, V., Della Vecchia, P., and, De Marco, A., "Design Guidelines for High Capacity Innovative Regional Turboprop Aircraft," *AIAA Paper*, 2019. doi:10.2514/6.2019-02561.

[265] Hoogreef, M. and Vos, R., "System-level assessment of tail-mounted propellers for regional aircraft," *31st ICAS Congress*, 2018.

[266] Hoover, C. B., Shen, J., Kreshock, A. R., "Propeller Whirl Flutter Stability and Its Influence on X-57 Aircraft Design," *Journal of Aircraft*, Vol. 55, No. 5, 2018, pp. 2168–2174. doi:10.2514/1.C034950.

[267] Johnson Jr., J. L., and White, E. R., "Exploratory Low -Speed Wind-Tunnel Investigation of Advanced Commuter Configurations Including an Over-the-Wing Propeller Design," *AIAA Paper*, 1983. doi:10.2514/6.1983-2531.

[268] Barth, M., Calmels, B., and Aupoix, B., "Aerodynamics of Counter-Rotating Open Rotors at High Speed," *AIAA Paper*, 2012. doi:10.2514/6.2012-2786.

[269] Sinnige, T., van Arnhem, N., Stokkermans, T. C. A., Eitelberg, G., and Veldhuis L. L. M., "Wingtip-Mounted Propellers: Aerodynamic Analysis of Interaction Effects and Comparison with Conventional Layout," *Journal of Aircraft*, Vol. 56, No. 1, 2018, pp. 295–312. doi:10.2514/1.C034978.

[270] Schroijen, M. J. T., Veldhuis, L. L. M., Slingerland, R., "Propeller Slipstream Investigation Using the Fokker F27 Wind Tunnel Model with Flaps Deflected," *31st ICAS Congress*, International Council of the Aeronautical Sciences (ICAS) Paper 2008-3.1.2, 2008.

[271] Schroijen, M. J. T., and Slingerland, R., "Propeller slipstream effects on directional aircraft control with one engine inoperative," *AIAA Paper*, 2007. doi:10.2514/6.2007-1046.

[272] Hurst D. W., and Owen, D. T., "Nacelle Installation Effects on Propeller Blade Surface Pressure Distributions," *SAE Transactions*, Vol. 96, No. 6, 1987, pp. 940–949.

[273] Wickens, R. H., "Viscous Three-Dimensional Flow Separations from High-Wing Propeller–Turbine Nacelle Models," Tech. Rep. ADP002255, National Research Council Canada, 1983.

[274] Dunham, D. M., Gentry, Jr., G. L., Manuel, G. S., Applin, Z. T., and, Quinto, P. F., "Low-Speed Aerodynamic Characteristics of a Twin-Engine General Aviation Configuration with Aft-Fuselage-Mounted Pusher Propellers," Tech. Rep. TP 2763, NASA, 1987.

[275] Schouten, T. J. E., Hoogreef, M., and Vos, R., "Effect of Propeller Installation on Performance Indicators of Regional Turboprop Aircraft," *AIAA Paper*, 2019. doi: 10.2514/6.2019-1306.

[276] Airbus S.A.S., "A320 Aircraft Characteristics - Airport and Maintenance Planning," , 2005.

[277] Traub, L. W., "Effect of a pusher propeller on a delta wing," *Aerospace Science and Technology*, Vol. 48, 2016, pp. 115–121. doi:10.1016/j.ast.2015.11.010.

[278] Wolowicz, C. H., and, Yancey, R. B., "Lateral-directional aerodynamic characteristics of light, twin-engine, propeller-driven airplanes," Tech. Rep. NASA TN-6946, NASA, 1972.

[279] Muehlbauer, J. C., Hewell, Jr., J.G., Lindenbaum, S. P, Randall, C. C., Searle, N., and Stone, Jr. F. R., "Turboprop Cargo Aircraft Systems Study Phase 1," Tech. Rep. NAS 1-15708, NASA, 1980.

[280] Mann, S. A. E., Stuart, C. A., "Advanced Propulsion Through the 1990s, An Airframers View," *AIAA Paper*, 1985. doi:10.2514/6.1985-1192.

[281] Sanderson, G. E., "The Influence of Propeller Synchrophasing on Aircraft Cabin Noise," *SAE Technical Paper*, Vol. 550177, 1955. doi:10.4271/550177.

[282] Welge, H. R., Neuhart, D. H., Dahlin, J. A., "Analysis of Mach Number 0.8 Turboprop Slipstream Wing/Nacelle Interactions," Tech. Rep. CR 166214, NASA, 1987.

[283] Smith, R. C., Levin, A. D., and Wood, R. D., "Summary of Studies To Reduce Wing-Mounted Propfan Installation Drag on an M = 0.8 Transport," Tech. Rep. TP 2678, NASA, 1987.

[284] Qui, Y., Bai, J., and Qiao, L., "Aerodynamic Effects of Wing-Mounted Engine Nacelle on High-Lift Configuration of Turboprop Airliner," *Journal of Aircraft*, Vol. 55, No. 3, 2018, pp. 1082–1089. doi:10.2514/1.C034529.

[285] Carlson, J. R., Pendergraft, Jr., O. C., "Comparison of Advanced Turboprop Installation on Swept and Unswept Supercriticail Wings at Transonic Speeds," *AIAA Paper*, 1985. doi:10.2514/6.1985-1264.

[286] Levin, A. D., Smith, R. C., and Wood, R. D., "Aerodynamic and Propeller Performance Characteristics of a Propfan-Powered, Semispan Model," Tech. Rep. TM 86705, NASA, 1985.

357

[287] Keller, D., Hasan, Y. J., and Rudnik, R., "Nacelle Strake Design for Short Takeoff and Landing Configuration with Turboprop Engines," *Journal of Aircraft*, Vol. 55, No. 6, 2018, pp. 2444–2453. doi:10.2514/1.C035065.

[288] Reckzeh, D., "Aerodynamic Design of the A400M High-Lift System," *ICAS Paper*, 2008.

[289] Scarano, F., Jux, C., and Sciacchitano, A., "Recent advancements towards large-scale flow diagnostics by robotic PIV," *Fluid Dynamics Research*, Vol. 53, No. 1, 2021, pp. 1–13. doi:10.1088/1873-7005/abe034.

[290] Prandtl, L., "Über Tragflügel kleinsten induzierten Widerstandes," *Zeitschrift für Flugtechnik und Motorluftschiffahrt*, Vol. 24, No. 11, 1933, pp. 305—-306.

[291] Fernando, W. U. N., Barnes, M., and Marjanovic, O., "Direct drive permanent magnet generator fed ac–dc active rectification and control for more-electric aircraft engines," *IET Electric Power Applications*, Vol. 5, No. 1, 2011, pp. 14–27. doi: 10.1049/iet-epa.2009.0280.

[292] Sarlioglu, B., "More Electric Aircraft: Review, Challenges, and Opportunities for Commercial Transport Aircraft," *IEEE Transactions on Transportation Electrification*, Vol. 1, No. 1, 2015, pp. 54–64. doi:10.1109/TTE.2015.2426499.

ACKNOWLEDGMENTS

for your flexibility, humour, and willingness to try out new designs and ideas. I also want to mention the help provided by the technicians at the Low Speed Laboratory: Leo, Stefan, and Emiel. Thanks for all the technical support, your efforts to make our experiments possible, and for your trust that we will manage.

Certainly the most important group of people that have made this dissertation possible are my friends from the faculty. Everyone has made me feel welcome every day of the duration of the PhD, in the office, in one of the bars in Delft, and into their homes. Not a single week has gone by absent of drinks, dinners, or sports, thanks to: Adam, Akshay, Alberto, Ale, André, Anne-Liza, Antonio, Biagio, Carmine, Elisa, Imco, Lucia, Malcom, Marco, Martijn Roelofs, Martijn van Sluis, Maurice, Max, Nitish, Pieter-Jan, Reynard, Sarah, Sebastian, Sonia, Sumit, Tom, and Tomas. The 'FPP trips' to Salzburg, Turin, Andalusia, and Tenerife were amazing. Thanks to all colleagues from the AWEP departments for the nice conversations: Dani, Fabrizio, Francesco, Gianfranco, Joris, Marios, Mark, Nando Timmer, Ruud, and many others.

Tom, thanks for convincing me to start a PhD and for the endless discussions that we had on technical topics; conversations that were not only held in the office or over dinner, but also during hiking in, for example, Alaska. Reynard, you supported me throughout the years on so many occasions. The long days (within official opening hours) in the wind tunnel are memorable. Thanks for always being there for me.

Special thanks to André for introducing me to this sport/activity called bouldering. In essence it is like doing PhD: before you could even finish the previous challenges, the climbing routes are replaced by new ones. Thanks to Reynard and Sumit for letting me join two times per week, and to all the others who joined regularly: Martijn, André, Ale, Sarah, Francesco, and the Wind Energy group.

Adam, Sumit, and Nitish: you've always been successful in bringing a group together in a matter of minutes to join for beers or dinner at Kloosters or at home. I very much enjoyed the diversity of all cuisines that were represented in FPP, from which I tried to inherit some skills. Important lessons include the formal definition of 'paella' (thanks to the Spanish), that a package of De Cecco pasta in a Dutch supermarket is different from the one in an Italian supermarket (thanks to the countless Italians), and that 'curry' is an ingredient and not a dish (thanks to Nitish, Akshay, Sumit).

I also want to acknowledge a number of key people in the Flying-V project that were responsible for our successful flight test campaigns in Faßberg. Roelof, Malcom, Alberto, Daniel, Dean Henri Werij, Femke, Ineke, and Gunnar Haasse (Airbus), those days were a great distraction from my office work in Delft. I'm glad I could be part of the team.

Finally, I want to thank my parents, Paul and Marijke, and my brother and sister, Silvan and Minka, for the support and patience throughout these long years, and for the years before that led to the start of my PhD adventure.

Nando van Arnhem
Delft, January 2022

CURRICULUM VITAE

Passionate about research and development of more sustainable aircraft technologies. I am particularly interested in wind-tunnel testing, aircraft design, and aerodynamic analyses of open-rotor installations. I developed a broad range of skills through wind-tunnel testing, by performing numerical simulations, and by working on scaled-flight demonstrators. I always enjoy to collaborate with my colleagues, to share ideas within the department, and to drink a beer with friends after a long day of work.

RESEARCH & WORK EXPERIENCES

2020-2021 **Postdoctoral Researcher**
Delft University of Technology, Delft, The Netherlands
- Performed aerodynamic analyses of a scaled flight demonstrator with distributed propulsion in the Clean Sky 2 framework for Large Passenger Aircraft.
- Pilot of the first scaled version of the Flying-V aircraft of 3 meter span. These flight test campaigns were conducted in collaboration with Airbus.

2016-2022 **PhD in Aerospace Engineering**
Delft University of Technology, Delft, The Netherlands
- Dissertation entitled: "*Unconventional Propeller–Airframe Integration for Transport Aircraft Configurations*". The dissertation entails the characterization and modelling of propeller–airframe aerodynamic interaction, quantified through comprehensive wind-tunnel tests, CFD simulations, and by the development of lower-order models.
- Designed an aircraft model to characterize different aircraft configurations in low-speed wind tunnels
- Provided supervision to MSc students and support for practicals
- Author and co-author of 16 scientific papers

2015-2016 **Researcher**
Delft University of Technology, Delft, The Netherlands
Designed, built, and piloted a scaled flight demonstrator for a novel aircraft with a propulsive empennage. Took the lead in the application of a patent (WO2017146579A1) for this concept.

2013-2014   **Internship**
NASA Ames Research Center, Mountain View, United States of America
Developed Simulink modules for a rotorcraft flight simulator for a real-time user interface to support assessment of handling qualities.

2013-2014   **Teaching Assistant**
Delft University of Technology, Delft, The Netherlands
Assistant for a 3rd year BSc course on Simulation, Verification, and Validation

EDUCATION

2016-2020   **Doctoral Education Program**
Delft University of Technology, Delft, The Netherlands
Courses on personal development and presentation techniques

2011-2015   **MSc in Aerospace Engineering**
Delft University of Technology, Delft, The Netherlands
- Thesis entitled: "*Design and Analysis of an Installed Pusher Propeller with Boundary Layer Inflow.* Developed and validated a propeller design tool for boundary layer ingestion configurations.
- Flight Performance & Propulsion track
- Participated in the Entrepreneurship Track and the Honours Track

2008-2011   **BSc in Aerospace Engineering**
Delft University of Technology, Delft, The Netherlands
Minor: Sustainable Energy Technology

LIST OF PUBLICATIONS

JOURNAL PAPERS

6. van Arnhem, N., de Vries, R., Sinnige, T., Vos, R., and Veldhuis, L.L.M., "Aerodynamic Performance and Static Stability Characteristics of Aircraft with Tail-Mounted Propellers," *Journal of Aircraft*, in press, 2021. doi:10.2514/1.C036338

5. van Arnhem, N., de Vries, R., Sinnige, T., Vos, R., Eitelberg, G., and Veldhuis, L.L.M., "Engineering Method to Estimate the Blade Loading of Propellers in Nonuniform Flow," *AIAA Journal*, Vol. 58, No. 12, 2020, pp. 5332–5346. doi:10.2514/1.J059485

4. de Vries, R., van Arnhem, N., Sinnige, T., Vos, R., and Veldhuis, L.L.M., "Aerodynamic Interaction Between Propellers of a Distributed-Propulsion System in Forward Flight," *Aerospace Science & Technology*, Vol. 118, 2021. doi:10.1016/j.ast.2021.107009

3. de Vries, R., van Arnhem, N., Avallone, F., Ragni, D., Vos, R., Eitelberg, G., and Veldhuis, L.L.M., "Experimental Investigation of Over-the-Wing Propeller–Boundary-Layer Interaction," *AIAA Journal*, Vol. 59, No. 6, 2021, pp. 2169–2182. doi:10.2514/1.J059770

2. Stokkermans, T.C.A., van Arnhem, N., Sinnige, T., and Veldhuis, L.L.M., "Validation and Comparison of RANS Propeller Modeling Methods for Tip-Mounted Applications," *AIAA Journal*, Vol. 57, No. 2, 2018, pp. 566–580. doi:10.2514/1.J057398

1. Sinnige, T., van Arnhem, N., Stokkermans, T.C.A., Eitelberg, G., and Veldhuis, L.L.M., "Wingtip-Mounted Propellers: Aerodynamic Analysis of Interaction Effects and Comparison with Conventional Layout," *Journal of Aircraft*, Vol. 56, No. 1, 2018, pp. 295–312. doi:10.2514/1.C034978

CONFERENCE PAPERS

10. van Arnhem, N., de Vries, R., Vos, R., and Veldhuis, L.L.M., "Aerodynamic Performance of an Aircraft Equipped with Horizontal Tail-Mounted Propellers," *AIAA Paper*, 2019. doi:10.2514/6.2019-3036

9. van Arnhem, N., Vos, R., and Veldhuis, L.L.M., "Aerodynamic Loads on an Aft-Mounted Propeller Induced by the Wing Wake," *AIAA Paper*, 2019. doi: 10.2514/6.2019-1093

8. van Arnhem, N., Sinnige, T., Stokkermans, T.C.A., Eitelberg, G., and Veldhuis, L.L.M., "Aerodynamic Interaction Effects of Tip-Mounted Propellers Installed on the Horizontal Tailplane," *AIAA Paper*, 2018. doi:10.2514/6.2018-2052

7. Ruiz Garcia, A., Brown, M., Atherstone, D., van Arnhem, N., and Vos, R., "Aerodynamic Model Identification of the Flying V from Sub-Scale Flight Test Data," *AIAA Paper*, 2022. doi:10.2514/6.2022-0713

6. Bölk, S., de Vries, R., van Arnhem, N., and Veldhuis, L.L.M., "Numerical Investigation of Propeller–Flap Interaction in Inclined Over-the-Wing Distributed-Propulsion Systems," *AIAA Paper*, 2021. doi:10.2514/6.2021-0603

5. Sinnige, T., Nederlof, R., and van Arnhem, N., "Aerodynamic Performance of Wingtip-Mounted Propellers in Tractor and Pusher Configuration," *AIAA Paper*, 2021. doi:10.2514/6.2021-2511

4. Sinnige, T., Stokkermans, T.C.A., van Arnhem, N., and Veldhuis, L.L.M., "Aerodynamic Performance of a Wingtip-Mounted Tractor Propeller Configuration in Windmilling and Energy-Harvesting Conditions," *AIAA Paper*, 2019. doi: 10.2514/6.2019-3033

3. de Vries, R., van Arnhem, N., Avallone, F., Ragni, D., Vos, R., Eitelberg, G., and Veldhuis, L.L.M., "Aerodynamic Interaction Between an Over-the-Wing Propeller and the Wing Boundary-Layer in Adverse Pressure Gradients," *AIAA Paper*, 2019. doi:10.2514/6.2019-3035

2. Stokkermans, T.C.A., van Arnhem, N., Sinnige, T., and Veldhuis, L.L.M., "Validation and Comparison of RANS Propeller Modeling for Tip-Mounted Applications," *AIAA Paper*, 2018. doi:10.2514/6.2018-0542

1. Stokkermans, T.C.A., van Arnhem, N., and Veldhuis, L.L.M., "Mitigation of propeller kinetic energy losses with boundary layer ingestion and swirl recovery vanes," *Proceedings of the 2016 Applied Aerodynamics Research Conference*, Royal Aeronautical Society, 2016, pp. 56--69

Always remember that you are absolutely unique. Just like everyone else.
Margaret Mead